INFORMATION TO USERS

This manuscript has been reproduced from the microfilm master. UMI films the text directly from the original or copy submitted. Thus, some thesis and dissertation copies are in typewriter face, while others may be from any type of computer printer.

The quality of this reproduction is dependent upon the quality of the copy submitted. Broken or indistinct print, colored or poor quality illustrations and photographs, print bleedthrough, substandard margins, and improper alignment can adversely affect reproduction.

In the unlikely event that the author did not send UMI a complete manuscript and there are missing pages, these will be noted. Also, if unauthorized copyright material had to be removed, a note will indicate the deletion.

Oversize materials (e.g., maps, drawings, charts) are reproduced by sectioning the original, beginning at the upper left-hand corner and continuing from left to right in equal sections with small overlaps.

Photographs included in the original manuscript have been reproduced xerographically in this copy. Higher quality 6" x 9" black and white photographic prints are available for any photographs or illustrations appearing in this copy for an additional charge. Contact UMI directly to order.

Bell & Howell Information and Learning
300 North Zeeb Road, Ann Arbor, MI 48106-1346 USA
800-521-0600

Cette thèse est incomplète.
This thesis is incomplete.

La page 84 manque.
Page 84 is missing.

Université d'Ottawa · University of Ottawa

Innovative Approaches to Column Confinement

by

Mongi Ben M. Grira

A thesis submitted to
the Faculty of Graduate Studies and Research
in partial fulfillment of
the requirement for the degree of

Doctor of Philosophy
in Civil Engineering*

Department of Civil Engineering
University of Ottawa
Ottawa, Ontario, Canada
September 1998

* The Doctor of Philosophy Program in Civil Engineering
is a joint program with the Carleton University,
administrated by the Ottawa-Carleton Institute for Civil Engineering

ABSTRACT

Reinforced concrete columns subjected to strong earthquakes may experience inelastic deformations. Inelastic deformability of these columns is of utmost importance for overall strength and stability of structures. Column deformability may be increased through confinement of core concrete.

Conventional confinement reinforcement for square and rectangular columns consist of closely spaced perimeter hoops, overlapping hoops, and crossties. The confinement steel requirements of current building codes often result in high volumetric ratios of transverse reinforcement which may lead to the congestion of column cages, which may result in concrete placement problems. Bends with 135-degree hooks and bend extensions may add to the problem of congestion, jeopardizing sound construction practice. Furthermore, the production and assembly of these individual ties within acceptable dimensional tolerances may be labor intensive and may require excessive time, resulting in significant increase in construction cost.

An alternative to conventional transverse reinforcement is to use welded reinforcement steel grids (WRG) prefabricated to the required size and amount of steel, double headed studs (DHS) made of high-strength steel with conventional perimeter hoops, or Fiber Reinforced Plastic (FRP) grids.

An experimental investigation was conducted to evaluate physical and mechanical properties of the new confinement reinforcement. Column tests were conducted to investigate structural performance of concrete columns reinforced with WRG, DHS, or FRP grids. Thirty-one large-scale columns with different volumetric ratios, spacings, and arrangements of confinement reinforcement were tested under simulated seismic loading. The columns were subjected to concentric compression of approximately 20% or 40% of their capacities while also subjected to incrementally increasing lateral deformation reversals.

Test results indicate that the welded reinforcement grids can be used effectively as confinement reinforcement provided that the steel used has sufficient ductility and the

welding process employed does not alter the strength and elongation characteristics of steel. The experimental program met these requirements and showed 7% to 10% strains prior to failure. The grids improved the structural performance of columns, producing lateral drift ratios in excess of 3% with volumetric ratios less than those required by the ACI 318-95 Building Code. The drift capacity further increased when grids with smaller cells (larger number of cross bars) were used. However, when the size of longitudinal reinforcement was reduced, the bars became more susceptible to buckling. High-strength concrete columns were less ductile compared to normal-strength concrete columns, but they resisted higher lateral forces.

Concrete columns confined with double head studs and conventional perimeter hoops also showed ductile behavior, developing lateral drifts of 4% to 6% prior to a significant loss in moment capacity, depending on the degree of confinement provided. The failure of these columns was characterized by the sudden opening of the 135-degree hooks of perimeter hoops followed by the crushing of core concrete and buckling of longitudinal bars. The double head studs performed satisfactorily when compared with welded reinforcement grids, and superior when compared with conventional reinforcement.

In addition, test results indicated also that concrete columns properly confined with fiber reinforced plastic grids showed ductile response and behaved as well as the companion columns confined with welded steel grids. The failure of these columns was caused by premature failure of FRP grids at the joints.

The research program also included analysis of columns tested in the experimental phase. A rational analytical model was developed for buckling of longitudinal reinforcement in columns. The model was incorporated in the analytical procedure to compute the ultimate deformation capacity of concrete columns, many of which failed due to bar buckling.

ACKNOWLEDGEMENTS

I would like to express my gratitude to Dr. M. Saatcioglu, thesis supervisor, for his guidance and encouragement throughout the course of this study. A sincere gratitude is expressed to my fellow graduate students who assisted me in the fabrication and testing of the column specimens, in particular Mr. Darek Mes, Mr. Haki Sherifi, and Dr. Cem Yalcin.

This undertaking could never been possible without the patience, continuous encouragement, relentless support, and sacrifices of my wife Ilhem. I am also very grateful to my son Louay for his patience and understanding even at his young age.

My sincere appreciation to my mother for her continuous prayers and my father for his moral support. Many special thanks are extended to my mother-in-law for her understanding and baby-sitting my son. The support, encouragement, and advice of my father-in-law are sincerely appreciated. The encouragement of my brother-in-law Samir is not forgotten. The understanding for my brothers-in-law Moez, Imed, and Youssef, and my sister-in-law Suzane is much appreciated.

To my wife Ilhem and my son Louay

TABLE OF CONTENTS

LIST OF TABLES

LIST OF FIGURES

Chapter 1

INTRODUCTION

1.1 General

Performance of reinforced concrete buildings during recent earthquakes has demonstrated that unconfined columns, especially at the first story level, suffer significant damage. Although current design practice calls for strong columns and weak beams to dissipate seismic induced energy by yielding in the beams, it is difficult to prevent inelasticity in lower story columns during a strong earthquake. Therefore, earthquake resistant columns are designed to develop a large number of inelastic deformation reversals without a significant loss of strength. This is referred to as inelastic deformability of columns and can be attained through confinement of the core concrete by closely spaced transverse and longitudinal reinforcement. Column confinement is a requirement of building codes for seismic regions. Parameters of confinement include the amount, spacing, grade, and arrangement of the transverse reinforcement. A proper combination of these parameters results in strength and ductility enhancements in core concrete, which in turn improves the behavior of the column. Conventional rectilinear confinement reinforcement used in square and rectangular columns consists of perimeter hoops, overlapping hoops and crossties. The hoops are usually provided with either 90 or 135-degrees bends, whereas the crossties come with either 90, 135 or 180-degree bends. These bends have enough development lengths to be properly anchored into the core concrete. The close spacing of lateral reinforcement as required by building codes and the use of overlapping hoops with bends and bend extensions often results in congestion of the reinforcement cage, occasionally creating construction problems. Therefore, practical and cost efficient solutions are needed, different from those conventionally used to confine concrete. It is further evident that more research is needed to develop an analytical approach to the behavior of compression reinforcement in concrete columns.

A first alternative to conventional transverse reinforcement is welded reinforcement steel

grids (WRG), prefabricated to the required size and amount of steel. These grids, when used as column transverse reinforcement can potentially lead to savings associated with easy and fast cage assembly, and reductions in steel consumption since the overlapping reinforcement, bends and bend extensions are eliminated. The joint welds prevent opening of the ties under lateral concrete pressure, improving column behavior in the inelastic range. Furthermore, the precision of welded grid corners, as compared to bent conventional hoop corners, provides better and consistent support to longitudinal reinforcement. The grid corners may also provide additional confinement pressure peaks, even without any longitudinal reinforcement in these corners, improving the uniformity of pressure.

The second alternative is to use double headed studs (DHS) with conventional perimeter hoops, replacing cross ties and overlapping hoops. The studs can be inserted easily across the reinforcement cage, and provide sufficiently good support to longitudinal bars. This also helps eliminate the congestion of steel in column cage. The construction process becomes faster, and the labor cost is reduced. The studs also provide improved precision in supporting longitudinal bars. The heads of the studs were designed such that any stress concentration and the resulting concrete crushing is prevented while the longitudinal bars are supported against buckling.

Another alternative to confine reinforced concrete columns is to use Fiber Reinforced Plastic (FRP) grids in place of conventional hoops and ties. The FRP grids have the same benefits as those mentioned earlier for steel welded grids. Furthermore, they are easier to handle and they have superior long-term performance. More specifically, they are extremely light and non-magnetic. They do not corrode, and they have excellent resistance to alkalis, acids, and chemicals. The FRP grids are made of continuous fibers that are oriented in one direction. Hence, they have high reinforcing characteristics, and fatigue strength equal to or more than that of reinforcing steel.

1.2 Research Needs

More research is needed to experimentally investigate alternative ways of confining concrete columns and provide necessary explanations for mechanism of confinement in these new and

innovative approaches. As it is discussed in Chapter 2, it is further evident that more research is needed to develop an analytical approach for the behavior of compression reinforcement in concrete columns. The following provides a summary of research needs in the area of column confinement:

- Development of new confinement techniques to mitigate seismic vulnerability of concrete columns.
- Experimental research to substantiate the new techniques developed.
- Assessment of the validity of current analytical approaches for concrete confinement.
- Development of an analytical model /procedure for reinforcement bar buckling.

1.3 Objective

The main objective of the research project presented in this thesis is to develop economically feasible and structurally superior new techniques for column confinement. The objective also includes generation of test data on new and innovative confinement methods and investigation of the behavior of compression reinforcement within the inelastic range.

1.4 Scope

The objective of the research program was realized within the following scope:

- Review of previous research on the behavior of concrete columns tested under different load conditions to determine relevant parameters for the present study.
- Review of proposed analytical models for concrete confinement.
- Review of proposed analytical models for bar buckling.
- Design, construction, instrumentation, and testing of 31 full-scale reinforced concrete columns under constant axial load and simulated earthquake loads. The specimens include 13 columns confined with welded steel grids, of which 3 are built of high-strength concrete, 4 columns confined with steel hoops and double head studs, and 14 columns confined with fiber reinforced plastic grids.
- Evaluation and interpretation of test data with respect to specific parameters.
- Theoretical analysis of columns and comparison with experimental results.

- Development of a rational and comprehensive model for buckling of longitudinal steel bars in concrete columns subjected to gravity and seismic loads.
- Preparation of thesis and presentation of results.

Chapter 2

PREVIOUS RESEARCH

2.1 General

Review of previous research on confinement of reinforced concrete columns was organized such that it was consistent with the scope of the current research project. Experimental works done on columns confined using conventional and non-conventional lateral reinforcement were reviewed first, followed by the review of proposed analytical models for concrete confinement. Finally, the previous research on stability of longitudinal bars was reviewed.

The column tests can be viewed in three groups. Columns tested under; i) monotonically increasing concentric compression, ii) monotonically increasing eccentric loading, and iii) constant axial load accompanied by simulated seismic loading.

2.2 Conventional Lateral Confinement

Behavior of confined concrete columns under axial compression was a topic for many researchers early this century. Most of the previous researchers before 1975 tested small-scale specimens with or without corner longitudinal bars and with conventional hoops and ties (Szulczynski and Sozen 1961, Bresler and Gilbert 1961, Bertero and Felippa 1964, Pfister 1964, Stokl 1964, Hudson 1966, Shah and Rangan 1970, Burdette and Hilsdorf 1971). Little work was done on columns under eccentric load or columns under axial load and lateral deformation reversals. Tests on large-scale columns were tested starting in early 1970's.

Review of previous work was reported by various researchers in the past (Sheikh 1978, Razvi 1988, Sakai 1989). Saatcioglu (1991) reviewed deformability of 91 square reinforced concrete columns tested under either constant axial load and lateral deformation reversal or monotonically increasing concentric compression. Razvi and Saatcioglu (1994) evaluated up

to 250 high-strength concrete columns in terms of load, ductility, and drift capacity. It was reported that the behavior of columns under axial load, with or without bending, was significantly affected by their size (Martinez et al. 1984, Razvi 1995). Therefore, the detailed review of column tests, conducted in this research program, is limited to large and full-scale columns. In addition, the emphasis is placed mainly on square or rectangular columns, as the scope of current research does not include circular columns.

2.2.1 Columns Tested Under Concentric Loading

Most of the columns in this category were tested using deformation-controlled universal testing machines. The first comprehensive investigation was reported by Richart et al. (1928). They tested a large number of concrete cylinders subjected to lateral hydrostatic fluid pressure and axial compression. An expression was proposed, relating the lateral pressure to axial strength. This provided the basic understanding of concrete confinement in circular columns. A year later, Richart et al. (1929) reported test results of cylinders confined by circular steel spirals without any longitudinal reinforcement. Although their research was limited to only small cylindrical concrete columns, their finding was of great importance to concrete researchers. It was reported that the passive pressure provided by lateral reinforcement was very similar to the active lateral hydrostatic pressure. Subsequently, many researchers conducted experiments on small size columns tested under concentric axial loading. Only conventional ties and hoops were used in these research programs. In the late 1970s advances in industrial and electronic technology led researchers to start testing large-scale columns.

Sheikh and Uzumeri (1980) reported results of twenty square columns tested under monotonic axial compression. Four different tie configurations of square and octagonal hoops were used. Among the parameters studied were the distribution and amount of longitudinal steel around the core perimeter, volumetric ratio, spacing, and characteristics of lateral steel. The effect of longitudinal bar size on stability of columns was not considered in the experimental study. The researchers concluded that in addition to improvements in ductility, the strength of concrete increased up to 70% when columns were confined with rectilinear ties and well distributed longitudinal reinforcement. Strength and ductility were

improved by reducing tie spacing or by increasing the amount of lateral steel. The amount of longitudinal steel, within the range of 1.7% to 3.7%, had small effect on concrete confinement.

Basset and Uzumeri (1986) conducted experimental investigation on fifteen reinforced and three unreinforced square columns loaded under monotonically increasing axial compression. The specimens had a cross-sectional core dimension of 267 *mm*, measured from center to center of perimeter ties. They were made of high-strength low-density concrete (37 – 40 *MPa*) and confined using conventional steel hoops and ties with 135-degree hooks. The test variables considered were the distribution of longitudinal steel, hoop and crosstie configuration, vertical tie spacing, amount of transverse reinforcement, and amount of longitudinal reinforcement. The test results indicated that large amounts of lateral steel with well-distributed longitudinal reinforcement could improve the brittle behavior of high-strength concrete significantly. The ductility of columns was also improved by increasing the amount of longitudinal reinforcement. The ratio of in-place strength to-cylinder strength of concrete was found to be 0.98, different from 0.85 commonly assumed. Razvi and Saatcioglu (1994) reported that this ratio varied between 0.85 and 1.0 for high-strength normal-density concrete, and the average value of this variation increased with concrete strength.

Sheikh et al. (1986) reported test results of fifteen and sixteen columns tested under concentric and eccentric compressive loads, respectively. Among the parameters investigated were the distribution of laterally supported and unsupported longitudinal steel bars, overlapping hoops and cross ties, amount of lateral steel, tie spacing, and level of axial load. The emphasis was mostly on the level of axial load. Their test results showed that ductility of reinforced concrete columns was highly affected by the amount of axial load and lateral reinforcement.

Mander et al. (1988) conducted tests on thirty-one nearly full-size reinforced concrete columns of circular, square, or rectangular cross-section. Various arrangements of lateral and longitudinal reinforcement were investigated. Spirals were used for circular sections. Square or octagonal hoops with 135-degree hooks at both ends were used for square sections. Rectangular hoops and cross ties, with 135-degree hooks at both ends, were used for

rectangular columns. The axial compression load was applied at various strain rates. Their test results confirmed the finding of the previous researchers that the shape of the stress-strain curve of confined concrete of all shapes was significantly affected by the quantity of confining reinforcement.

Yong et al. (1988) tested 24 square high-strength concrete columns under monotonic concentric load. The compressive strength of concrete ranged from 84 *MPa* to 94 *MPa*. The columns were confined using conventional square hoops with 135-degree hooks at both ends. The program was designed to study the effect of the volumetric ratio of lateral steel reinforcement, the longitudinal steel arrangement and the cover concrete on the stress-strain relationship of rectilinearly confined high-strength concrete columns. Test results indicated that proper confinement of high-strength concrete columns produced a significant ductility increase. The lateral steel did not yield at the peak stress, and the cover concrete spalled at low stain values. Reduction of the amount of longitudinal reinforcement resulted in lower ductility of columns. Columns did not develop any effect of confinement when the tie spacing was increased to cross-sectional dimension.

Polat (1992) tested twelve near full-scale square columns to investigate the behavior of normal and high-strength concrete columns. The columns were tested under monotonic concentric load. The parameters considered included concrete strength, yield strength and volumetric ratio of lateral reinforcement, and gauge length. It was reported that an increase in the volumetric ratio of lateral reinforcement resulted in a significant improvement of column strength and ductility. The improvement was proportional to the square root of the yield strength of lateral steel. However, it was observed that high-strength concrete columns failed in a brittle manner compared to normal-strength concrete. The researcher concluded that high-strength concrete columns could fail at loads significantly lower than those computed based on the *ACI-318-89* building code. Yielding of lateral reinforcement was observed at the peak load when high-strength steel was used. The gauge length significantly affected column ductility. The researcher used confinement models proposed earlier for normal-strength concrete (Sheikh and Uzumeri 1982, Kent and Park 1979, Muguruma et al. 1983, Bjerkeli et al. 1990) to reproduce the experimentally obtained stress-strain curves. It was found that none of the models considered predicted accurately the test results.

Al-Hussaini et al. (1993) tested square columns under monotonic concentric axial load as part of research program aimed at developing design guidelines for high-strength concrete columns. The columns had 250 *mm* x 250-*mm* square cross-section and 2000 *mm* height. Among the parameters investigated were amount of longitudinal reinforcement, vertical spacing and amount of lateral reinforcement. It was concluded that the minimum lateral steel specified in the British Standard code (BS 1985) was insufficient and inadequate to prevent buckling of longitudinal reinforcement.

Cusson and Paultre (1994) reported test results of twenty-seven high-strength concrete columns confined by conventional square, rectangular, or octagonal hoops with 135-degree hooks at the ends. The columns had a cross-sectional dimension of 235 *mm* and a height of 1400 *mm*. They were tested under compressive concentric loading. Test variables included compressive strength of concrete (53 to 100 *MPa*), tie configuration, tie yield strength (392 to 770 *MPa*), lateral reinforcement ratio (1.4% to 4.9%), vertical tie spacing (50 and 100 *mm*), longitudinal reinforcement ratio (2.2% and 3.6%), and cover concrete. It was reported that the amount of transverse reinforcement was the most important parameter that influenced the behavior and the ductility of high-strength concrete columns. Because high-strength concrete is very brittle compared to normal strength concrete, the authors observed that cover concrete in all columns spalled early during testing. Thus, they recommended that the axial capacity of high-strength concrete columns should be calculated based on core area rather than on the whole cross-section area. Razvi and Saatcioglu (1994) also endorsed this idea for columns with certain level of confinement.

Li (1994) conducted an experimental investigation on normal and high-strength reinforced concrete columns. Two series of columns were tested under concentric loading. The first series included twenty-seven square and circular columns having a 240-*mm* cross-sectional dimension and 720 *mm* height. The second series included eleven square and four circular columns with the same dimensions as the first series. While the first series of columns were tested under low strain rate, the second series were tested under high strain rate. The test parameters included concrete strength, vertical spacing, yield strength and volumetric ratio of lateral steel reinforcement, and the arrangement of longitudinal reinforcement. Test results indicated that strength and ductility of confined concrete was improved by increasing the

amount and/or the strength of lateral steel. It was observed during tests that transverse steel of grade 430 *MPa* yielded at/or shortly after the peak column load was reached, whereas, grade 1300 *MPa* steel did not yield at peak load. Columns confined with high-grade steel behaved better than those confined with normal-grade steel. The researcher reported that columns tested under high strain rates produced higher strength and higher modulus of elasticity, but steeper slope of the descending branch of the stress-strain curve compared to columns tested under low strain rates. However, concrete columns confined with high-strength steel did not show higher strengths when tested under high strain rates.

Razvi and Saatcioglu (1996) reported experimental results of twenty-six square and twenty circular high-strength concrete columns tested under monotonically increasing concentric compression. The parameters investigated were concrete strength, cross-sectional shape, vertical spacing and volumetric ratio of transverse reinforcement, longitudinal reinforcing bar arrangement, yield strength of transverse steel, type of circular reinforcement, and the presence of longitudinal reinforcement on circular columns. The columns had a 250-*mm* cross-sectional dimension and 1500 *mm* height. It was reported that higher confinement pressure was required for high-strength concrete columns to increase ductility to similar levels observed in normal-strength concrete columns. High-strength concrete columns could benefit from the use of high-grade lateral steel reinforcement if properly arranged. In addition, it was found that closely spaced longitudinal reinforcement in columns with small vertical spacing of lateral steel, provided improvement in confinement efficiency. During tests, it was observed that spalling of cover concrete occurred before reaching the unconfined column capacity in most columns. This depended on the concrete strength, cover thickness and the nature of the reinforcement grid that separated the cover from the core. The researchers proved that circular spirals and circular hoops were more effective in confining high-strength concrete than rectilinear ties. Longitudinal reinforcement in circular columns had an effect on concrete confinement unlike what was commonly believed in the past.

Hoshikuma et al. (1997) conducted experimental work to investigate the behavior of small and large-scale reinforced concrete bridge piers subjected to monotonically increasing axial compression. The columns were 600 *mm*, 1000 *mm*, or 1500 *mm* high. They were of circular, square or rectangular (wall-type) geometry. The columns were built without cover concrete.

Thirty-one columns were constructed and tested. The concrete strength was relatively low (18.5 *MPa* - 28.8 *MPa*) to simulate actual strength of concrete used in Japanese bridges. The effect of confinement was evaluated in terms of volumetric hoop ratio, hoop spacing, configuration of hooks at hoop ends, cross-sectional shape and crossties. The volumetric ratio of hoop reinforcement ranged from 0.19 to 4.66% representing typical bridge columns built in Japan. The vertical spacing of hoops varied between 12.5 ***mm*** and 300 ***mm***. Hoops having 90, 135, and 180-degree hooks were used in three columns to investigate the effects of hook configuration. All other columns were laterally reinforced with hoops anchored by filled welds. The axial load was applied at a rate of 1.0 ***mm***/min. and the strain was measured over the entire length of columns. It was observed that all specimens exhibited the same type of failure. Specimens with large vertical tie spacing failed just after the concrete reached peak stress. Vertical cracks were developed followed by buckling of longitudinal bars that led to the crushing of core concrete. However, when close hoop spacing was used, column failure was caused by hoop fracture followed by longitudinal bar buckling and sudden crushing of core concrete. It was also recorded that buckling of longitudinal bars and crushing of core concrete occurred when the compressive stress dropped below 50% of peak stress. It was observed that the rupture of hoop reinforcement did not occur near the hook or the weld. Thus, no conclusion was reached about the performance of welds compared to conventional hooks. The ductility of wall-type sections increased significantly when crossties were used. The researchers used some of the available models (Kent and Park 1971, Mander et al. 1988, Saatcioglu and Razvi 1992, and Muguruma et al. 1980) to predict the stress-strain relationship of tested specimens. It was claimed that none of the above models was able to predict accurately the test results. All of them predicted larger slope for the ascending branch than those observed experimentally. It was concluded that the available models could not predict accurately the stress-strain behavior of columns confined with low volumetric ratio of hoop reinforcement. Therefore, the researchers proposed a new model. This model is reviewed later in this chapter, along with other confinement models.

2.2.2 Columns Tested Under Eccentric Loading

Conflicting views were expressed about the effects of eccentricity on column confinement. Sturman et al. (1965) indicated that the peak concrete stress and the corresponding strain

could be enhanced by the strain gradient. Karsan and Jirsa (1970) later contradicted this view. They reported that only the ductility improved with presence of strain gradient.

Scott et al. (1982) reported the results of twenty-five large-scale square reinforced concrete columns tested under eccentric loading. The columns were reinforced with conventional overlapping square or octagonal hoops and cross ties. Twelve or eight longitudinal steel bar configurations were used. The tests were conducted under low and high strain rates. The test variables included the effect of distribution of longitudinal reinforcement, the vertical spacing and the amount of lateral reinforcement. The researchers concluded that the peak stress of core concrete increased by increasing the lateral steel and the slope of the descending branch of the stress-strain curve of core concrete decreased. It was also reported that the analysis based on stress-strain relationships obtained from concentric column tests underestimated the deformability of columns recorded during these tests. Hence, it was concluded that stress-strain relationship with a less steep falling branch would be more appropriate for members subjected to eccentric loading.

Ozden (1992) tested ten square columns under strain gradient. The columns had a square section (230-x 230 *mm*) and 1500-*mm* height. They were constructed using concrete with strengths ranging between 55 *MPa* and 65 *MPa*. The strain gradient was applied such that the strain on one side of the cross-section was maintained at zero level. Test variables included the concrete strength, the vertical spacing and volumetric ratio of lateral ties. The main observation was reported to be that when the vertical spacing of ties was greater than one half of the cross-sectional dimension (h/2) of a column, the confinement was not effective. Whereas, with closed vertical spacing of lateral reinforcement, column strength and ductility improved significantly.

Saatcioglu et al. (1995) reported test results of twelve square columns compressed under two levels of end eccentricity to examine the characteristics of confined concrete under strain gradient. They used #10 (11.3 *mm* diameter) longitudinal reinforcement and 6.6-*mm* diameter plain hoops with 135-degree hooks. The variables studied were the arrangement, spacing, and volumetric ratio of transverse reinforcement. It has been shown that columns with large vertical spacing of transverse steel lost strength immediately after the peak load. The loss of

strength was caused mainly by buckling of longitudinal bars. Well-confined columns showed extremely ductile behavior with inelastic deformations exceeding a drift ratio of 4% without developing strength decay.

Lloyd and Rangan (1995) conducted an experimental study to investigate the behavior of high-strength concrete columns tested under eccentric compression. Thirty-six average-size columns were tested. The columns had either rectangular (100 x 300 *mm*) or square (175 x 175 *mm*) cross-section. They were laterally confined with 4-*mm* diameter high-strength ties at 60-*mm* vertical spacing. The control variables considered were concrete compressive strength, eccentricity of applied compressive load, and the longitudinal reinforcement ratio. The compressive strength of concrete was 58, 92, or 97 *MPa*. Eccentricity of applied load ranged from 0.1 to 0.4 times the column depth, and the longitudinal reinforcement ratio was 1.5 % or 2%. It was reported that even though the lateral confinement steel was more than the requirements of the Australian code (AS 3600 1994), it was not sufficient to produce ductile behavior for columns with low eccentricity. However, columns tested under an eccentricity of higher than 0.3 times the column depth behaved in a more ductile manner.

Setty and Rangan (1995) tested twelve high-strength concrete columns under eccentric compression. The columns were either 1386 *mm* or 936 *mm* high, and had 100 *mm* x 300-*mm* rectangular cross-section. They were built using 79 *MPa* concrete and were laterally reinforced with conventional ties made of 6-*mm* wire. The ties were provided with 135-degree hooks and were spaced at 50 *mm* at the middle of the column section. Four or six 12-*mm* longitudinal bar arrangement was provided. The eccentricity of the applied axial load was 10, 30, or 40 *mm*. Test results indicated that all columns failed in flexural mode without buckling of longitudinal bars. The increase in the longitudinal reinforcement resulted in an increase in failure load. However, failure load decreased with an increase in eccentricity.

2.2.3 Columns Tested Under Axial and Lateral Reversal Loads

Tests of concrete columns under reversed cyclic loading are scarce in the literature, especially prior to 1990s. The severe damage in concrete structures observed during earthquakes of the last two decades and the resulting high repair costs urged researchers to examine the performance of plastic hinges of concrete columns under reversed cyclic loads.

Furthermore, because of the increased emphasis placed on high-strength concrete and the availability of suitable testing machines in recent years, numerous tests of high-strength concrete columns were also conducted under simulated earthquake loading.

Ozcebe and Saatcioglu (1987) conducted an experimental investigation on columns confined with conventional crossties and hoops. They tested fourteen full-size columns under constant axial load and lateral load reversals. Both unilateral and bilateral displacement histories were included in the test program. The test variables studied were the effect of axial compression or tension load level, configuration and spacing of lateral reinforcement, and deformation path. The test results showed that the hysteretic responses of columns were affected significantly with the level of axial load. Columns under high axial load exhibited less ductility and accelerated strength and stiffness degradation. The ductility of columns was improved significantly with the use of proper confinement configuration. The use of cross ties with 90-degree hook at one end, and 135-degree at the other end was found satisfactory and resulted in a similar behavior as that of ties with 135-degree hooks at both ends. The stability of longitudinal bars was not of concern since the lateral reinforcement ratio was high (1.95%) and the axial load level was low (10.6% of the section capacity). Also, the #25 bars used as longitudinal reinforcement were less susceptible to bar buckling than smaller size bars used in most previous column tests. The authors also concluded that bi-directional lateral cyclic loads could produce severe stiffness and strength degradations.

Muguruma et al. (1990) conducted tests on eight high-strength concrete columns subjected to constant axial compression and reversed cyclic lateral loads. The specimens had 200-*mm* square cross sections and 1500-*mm* height, and made of concrete having a compressive strength of 86 *MPa* or 116 *MPa*. Each specimen consisted of heavily reinforced stub of 200 x 300 *mm* in cross section and 500 *mm* in length, placed in the middle of two half span columns. The lateral load was applied at the stub whereas both ends of the columns were hinged at the top and bottom of the loading setup. The lateral reinforcement consisted of welded square and rectangular ties, and it was made out of grade 320 *MPa* or 792 *MPa*. The applied axial load corresponded to 25.4%, 40%, 42.3%, and 62.3% of column section capacity. The experimental program was conducted to investigate the effects of concrete compressive strength, lateral steel yield strength, and axial load level. It was reported that

ductility of high-strength concrete columns could be achieved by using high-strength lateral steel with properly designed vertical spacing. Tests showed that the effect of lateral confinement on ductility was reduced with increasing concrete strength. Nothing was reported on the effect of welded stirrups compared to ordinary hoops.

Sakai et al. (1990) tested eight high-strength (100 *MPa*) square concrete columns under compression and lateral load reversals. The parameters investigated were the stability of longitudinal reinforcement, the yield strength of transverse reinforcement and the axial load level. The arrangements of longitudinal reinforcement used were either 4-bars, or 12-bars with four crossties or no crossties. Tests showed that columns confined with crossties were more stable and ductile because longitudinal bars were well supported against buckling. Smaller longitudinal spacing and higher yield strength of transverse steel improved the ductility of high-strength concrete columns especially under high axial load level.

Sugano et al. (1990) tested eight square reinforced concrete columns under earthquake type loading. The columns had 250 *mm* cross sectional dimension and 2000 *mm* height. The compressive strength of concrete varied between 39 *MPa* and 78 *MPa*. The yield strengths of lateral reinforcing steel considered were 315 *MPa*, 833 *MPa*, and 1362 *MPa*. Lateral reinforcement with 1362 *MPa* steel was used in the form of square spirals and inner hoops with 135-degree bends, in two columns. All other columns were confined with butt-welded square and rectangular hoops. The vertical spacing was chosen to be 35 *mm* and 55 *mm*. Two levels of axial load were used; 30% and 55% of concentric section capacity. The test variables included concrete strength, axial stress level, and capacity of lateral reinforcing steel $\left(\rho_s f_{yt}\right)$; where ρ_s and f_{yt} are the area ratio, and yield strength of lateral reinforcement, respectively. It was reported that the use of high-strength lateral steel could improve the ductility of high-strength concrete columns significantly. The columns confined with high-strength concretes of 59 *MPa* and 78 *MPa* exhibited lateral drifts larger than 5%, under axial compression of 30% of the concentric capacity. However, when the axial load level in companion columns was increased to 55% of the column concentric capacity, the ductility was reduced significantly. Furthermore, it was observed that the displacement ductility increased proportionately with yield strength of lateral reinforcement. The researchers recommended that the ductility of high-strength concrete columns should be evaluated as a

function of the ratio ($\rho_s f_{yt} / f_c'$) where f_c' is the concrete compressive strength. They suggested that the above ratio must be greater than 0.10 in order to achieve 2% lateral drift in a column subjected to axial compression of $0.60 f_c'$.

Sheikh and Khoury (1993) tested large-scale columns under high axial load and lateral load reversals. The columns were made of normal-strength concrete. The variables considered were the level of axial load, the amount and configuration of lateral reinforcement, and the stub effect. It was reported that the energy absorption capacity of columns and the effectiveness of confinement on concrete decreased with the increase of axial load. Then, Sheikh et al. (1994) tested, under the same conditions as above, four more large-size columns made of high-strength concrete (55 *MPa*). It was observed that ductility and energy-absorption of high-strength concrete columns are highly dependent on the amount of lateral steel as in normal-strength concrete columns.

Azizinamini et al. (1994) reported test results of near full-scale square reinforced concrete columns. The columns were designed according to the seismic provisions of the ACI 318-89 code. The columns were tested under a simulated earthquake load and constant axial load. Only eight longitudinal bar arrangement and conventional hoops and ties were used. The parameters investigated included concrete strength, axial compression load, spacing, and the yield strength of lateral reinforcement. The concrete strength ranged between 27 *MPa* and 104 *MPa*, whereas the yield strength of transverse reinforcement consisted of either 414 *MPa* or 828 *MPa*. The spacing of ties in the critical region was 41 *mm* in some specimens and 67 *mm* in others. The maximum axial compression applied was 40% of the section axial capacity. Test results showed that all specimens exhibited good energy-dissipation characteristics and possessed adequate curvature and displacement ductilities when subjected to axial load levels less than 20% of column axial capacity. Ductility improved with the increase of transverse reinforcement, and decreased with high axial compression. It was reported that confined high-strength concrete could have the same ductility as normal-strength concrete, and high-strength lateral reinforcement was inactive at low axial load levels. Thus, the use of high-strength transverse reinforcement to confine high-strength concrete column can result in larger spacing than what is recommended by the ACI 318-89

code. This can lead to premature failure of column due to buckling of longitudinal bars.

Li (1994) tested five large size square high-strength concrete columns with 350 *mm* cross-sectional dimension and 3900 *mm* height. The concrete strength was either 93 *MPa* or 98 *MPa*. The columns were tested under constant compression and lateral deformation reversals, simulating seismic action. Test parameters included the spacing and yield strength of lateral steel, as well as the level of axial load. It was reported that columns designed based on the New Zealand code (NZS 3101: 1982) behaved in a brittle manner, and that the envelopes of the hysteretic stress-strain curves agreed well with stress-strain curves of similar columns tested under monotonic compression.

Lipien (1995) investigated strength and deformation characteristics of confined high-strength concrete columns. Ten square columns were tested under constant axial compression of up to 28% of section capacity, and incrementally increasing lateral deformation reversals. The columns had 250-*mm* square section and were 1640 *mm* high. Two columns were made of 64 *MPa* concrete and eight were built of 104 *MPa* concrete. Eight or twelve longitudinal bars were used. Standard hoops and ties with 135-degree hooks at both ends were used as lateral reinforcement. The yield strength of lateral steel ranged between 400 *MPa* and 1000 *MPa*. The volumetric ratio of transverse reinforcement varied between 1.9% and 5.58% of the core concrete section. The vertical spacing of hoops and ties was investigated and varied between 45 *mm* and 62.5 *mm*. The test results showed that high-strength concrete columns behaved in a brittle manner. They required more lateral confinement to increase their ductility to approximately that of normal-strength concrete columns. The volumetric ratio of transverse steel was an important parameter to prevent buckling of longitudinal bars and properly confine core concrete. In addition, beneficial effects of high-grade transverse steel were reported. Columns confined with higher-grade steel and increased tie spacing behaved similarly to those with lower grade steel and decreased tie spacing. However, the use of high-strength steel as lateral reinforcement did not have significant effect on ductility when the axial load level was low. Lipien (1995) used the confinement concrete model proposed by Saatcioglu and Razvi (1992) to predict the experimental results. A good agreement between the analytical predictions and the experimental results was reported.

An experimental research program was carried out by Bayrak and Sheikh (1995) to test seven full-scale columns. The specimens had 305-*mm* square cross-section and 1473 *mm* height. They were confined with conventional hoops and ties. The compressive strength of concrete varied between 30 *MPa* and 102 *MPa*. The columns were tested under reversal cyclic loads simulating earthquake forces, and constant axial compression between 36% and 63% of column axial capacity. Also, among the variables considered were steel configuration and amount of lateral reinforcement. The main observations reported were: high-strength concrete columns were less ductile than those with normal-strength concrete, and increase in axial load reduced columns ductility and accelerated stiffness degradation. Also proper lateral steel arrangement provided lateral support to longitudinal bars and improved deformability and energy dissipation of both normal and high-strength concrete columns significantly.

Legeron and Paultre (1995) reported results of six large-scale high-strength concrete columns. The specimens had 305-*mm* square cross-section and 2150 *mm* height. They were fabricated using concrete with compressive strength of 100 *MPa*, and confined with conventional hoops and ties. The columns were tested under cyclic lateral deformations and a constant axial load ranging from 15% to 40% of concentric column capacity. The vertical spacing of ties used was either 60 *mm* or 130 *mm*. The first spacing was selected to be used in three columns to obtain a ductile behavior, whereas the second one was chosen for the rest of the columns based on minimum spacing for shear design. The main conclusion was that the ductility of the columns was highly affected by the level of axial load and the ACI and CSA codes were too conservative for high-strength concrete columns under high axial load.

Kuramoto et al. (1995) conducted an experimental investigation to study the effect of axial deformation on ductility of high-strength reinforced concrete columns under varying tri-axial forces. Four *1/3* scale-model columns were tested. The columns had a 250-*mm* square cross-section and 1000 *mm* height. All specimens were reinforced with 12 13-*mm* diameter longitudinal bars and square hoops with crossties having 135-degree hooks at the ends. The compressive strength of concrete was 64 *MPa*. The yield strength of longitudinal bars was 700 *MPa*, whereas the lateral reinforcement has a yield stress of 1350 *MPa*. An initial axial compressive load of 500 *kN* was applied for two columns, whereas the third and forth

columns were subjected to 1000 and 1500 *kN* initial compression, respectively. During testing, the axial load ranged between a tension of -400 *kN* and a compression of +2500 *kN*. It was reported that the ductility of columns under varying biaxial or triaxial forces decreased with the increase of axial force, similar to columns subjected to constant axial load and bending. In addition, the loading histories of concrete and longitudinal steel affected the axial deformability of columns under varying triaxial forces. It was observed that axial deformations of columns were controlled by the stability of longitudinal bars.

2.3 Non-Conventional Confinement Techniques

The non-conventional confinement techniques for reinforced concrete columns considered here include welded reinforcement steel grids, double headed studs, and fiber reinforced plastic grids. The applications of these techniques in construction industry have been recent, and research on their characteristics is scarce in the literature.

2.3.1 Welded Reinforcement Steel Grids (WRSG)

There has been no attempt in the past to investigate the effect of welded reinforcement steel grids on concrete confinement. However, few researchers tried to use welded wire fabric (WWF) as an alternative for conventional steel hoops and ties. The first study in recent years on the use of WWF as lateral reinforcement for concrete columns was conducted by Razvi and Saatcioglu (1988). They tested thirty-four small-scale square columns under concentric loading. The research program involved the use of conventional WWF, and hence was limited to low volumetric ratios of transverse reinforcement. In addition, the researchers investigated the use of WWF in combination with conventional hoops and the performance of 90 and 135-degree hooks of ties. The test program indicated potential benefits of confining column concrete with transverse reinforcement that consisted of conventional ties used in combination with WWF. Columns confined with hoops having 135-degree hooks showed superior performance compared to those with 90-degree hooks. With sufficient anchorage length into core concrete and closer vertical spacing of ties, the effect of hooks became more pronounced with WWF.

Furlong et al. (1991) studied strength, stiffness, and ductility behavior of columns reinforced with WWF and compared them with conventionally reinforced columns. A total of eight near full size columns were designed, fabricated, and tested under eccentric loading. Two square columns were built with conventional hoops and longitudinal reinforcement, where the longitudinal bars consisted of either four #5 (16 *mm*) bars or four #7 (22 *mm*) bars. Two similar columns were fabricated using WWF designed such that the vertical bars of the wire mesh would have the same area as the four corner bars used in companion conventionally reinforced columns. The other four columns had a rectangular cross-section: Two were reinforced with hoops and ties, and the other two with WWF. The columns had either 280 x 280 *mm*, or 200 x 380-*mm* cross-section, and 1530-*mm* height. It was reported that although the yield strength of WWF was higher than that of conventional reinforcement, the columns reinforced with WWF resisted less axial load than companion specimens. This phenomenon was explained by the fact that the absence of longitudinal corner bars and the large spacing of the transverse ties (mesh) could not confine the concrete properly. It was recommended that crossties were needed. It was also recommended that further studies be conducted to investigate the presence of corner longitudinal bars along with WWF and its effect on the ductility of columns.

More recently, however, grids with larger diameter reinforcement have become available in the United States of America. The material was tested in boundary elements of concrete shear walls at the University of California at Berkeley (Miranda et al., 1990). A total of six of specimens were tested under cyclic axial load to study their mechanical behavior and ascertain the practical implications of the test results. The test results indicated that the deformability of the specimens confined with welded grids was highly dependent upon the strength of the resistance welds, which join the wires of the grids. The failure of the steel grids occurred at the resistance weld or in the heat-affected zones near the resistance welds. Hence, it was highly recommended that proper quality control of the manufacturing process should be maintained, so that the strength of the resistance of the weld is guaranteed to be greater than the tensile strength of the wire.

Welded reinforcement grids were also used as transverse reinforcement in beams and columns of specimens used for beam-column connection tests at the National Institute of

Standards and Technology (Cheok and Stone 1994). The steel grids were custom made out of smooth wires to fit necessary requirements for the specimens. They were mainly used to avoid the congestion caused by the hooks in the stirrups and crossties. The performance of the grids was not reported, because it was not the main objective of the tests.

2.3.2 Double Headed Studs (DHS)

Shear studs have been originally developed in Europe and used as shear reinforcement in heavily reinforced sections in some offshore oil drilling platforms. Then, they were introduced to the North American market by the University of Calgary (Dilger and Ghali 1997) as punching shear reinforcement in flat slabs. They were proven to be effective in increasing the punching shear strength of slabs (Lim and Rangan 1995). A so-called "Stud Rails" is presently manufactured by Decon® in a form of vertical studs with circular anchor heads, welded to a steel strip at the bottom. Shear stud reinforcement for slabs, rafts, and footing has been used also in many buildings worldwide. A similar concept was used to develop studs by welding anchor plates at the ends. They have been used recently in walls of several major offshore structures in Europe, North America, Asia, and Australia

Bjerkeli et al. (1990) tested 10 large-scale rectangular columns with shear-studs under monotonic axial compression. The columns were made of high-strength concrete, with concrete strength varying between 80 *MPa* and 108 *MPa*. They had a 300 ***mm*** x 500 ***mm*** cross section and 2000 ***mm*** height. Eighteen-bar and twelve-bar arrangements were used as longitudinal reinforcement. The columns were laterally confined by conventional rectangular hoops with 135-degree hooks at both ends. In addition to the hoop ties, each longitudinal bar was supported by shear-studs. The shear studs were made of 12, 16, and 20 ***mm*** round bars anchored by friction welded plates. The aim of the investigation was to study the effect of longitudinal bar distribution on the stress-strain behavior of confined cover concrete. Not many details were reported on the performance of the shear studs, except that the axial load capacity of columns with 18-bar arrangement did not drop as fast as that of columns with 12-bar arrangement after the spalling of the cover concrete.

Dilger and Ghali (1997) conducted an experimental investigation on five short columns using

studs with anchor heads at both ends, to replace conventional crossties. These Double-Head Studs (DHS) were produced by Decon® Corp., Brampton, Ontario. They were designed such that the anchor heads were sufficiently large enough to prevent crushing of concrete rather than to support longitudinal reinforcing bars. The columns had 150 x 500-*mm* cross-section with and a height of 800 *mm*. The main objective of the test was to study the effect of the DHS on the strength and ductility of columns under axial compression, compared to conventional lateral reinforcement. Although their tests were limited to five rectangular specimens, the authors proved that the 180-degree and the 90-degree hooks did not provide sufficient anchorage for the hoops to develop their yield strengths prior to the failure of columns. Whereas the DHS exhibited large strains beyond yielding, when they were used as cross ties. In addition, columns reinforced with DHS showed more ductility and exhibited higher strength than columns reinforced with conventional crossties. Hence, it was recommended that design codes should allow reduced cross sectional area and/or larger spacing when the studs are used as cross ties.

2.3.3 Fiber Reinforced Plastic (FRP) Grids

Composite Fiber Plastic materials were introduced to the concrete industry in early fifties. Rubinsky and Rubinsky (1954) were the first researchers to use fiberglass on prestressed concrete structural elements. Recently, advances in manufacturing technologies made composite materials competitive to conventional structural materials such as steel. Numerous composite materials such as Fiber Reinforced Plastic (FRP) products have become commercially available in the market, worldwide. The FRP reinforcement has good durability characteristics, high strength to weight ratio, good fatigue strength, and low relaxation losses compared to steel. These properties motivated structural engineers to use FRP as prestress tendons. Recently, FRP got the attention of bridge engineers, especially in North America, where extensive deterioration of bridge structures have been occurring in regions of cold climate due to the use of salt and associated corrosion of steel reinforcement. Hence, many bridges have been constructed throughout the world using composite reinforcement to take advantage of the unique characteristics of FRP.

FRP products have also shown significant promises in recent structural rehabilitation

projects. They present several advantages and have been recently investigated all over the world. Numerous demonstration projects are under way in the United States, Canada, and Europe mainly for retrofitting bridge piers and repairing damaged bridge columns. Recently in California, retrofitting of bridge columns with carbon-fiber wraps has been demonstrated to be more cost-effective than steel jacketing. In addition, significant enhancement of deformation capacities of structural elements was reported by Seible and Karbhari (1996) in members with FRP jackets.

Japan is more advanced in the composite material technology than any other country in the world. Japanese scientists are the pioneers on introducing FRP material to civil engineering applications. In addition, Japan is the only country in the world to have a draft code for use of composite materials in construction. Much research work has been reported and a large number of field applications have been claimed. More than four millions of square feet of FRP have been used in the past 15 years in Japan to reinforce concrete structures built in corrosive environment (Charles 1993). FRP products was widely used in different type of structures in Japan such as tunnel supports, roads, railways, water-conveyances and underground rock caverns for petroleum storage, airport runways, road pavement, bridge slabs and handrails, offshore and inshore structures, water inlet and out channels, general architectural structures such exterior walls, verandahs and handrails (Sekijima et al. 1988).

FRP products take the form of cables, bars, planar (2-D) grids and three-dimensional (3-D) cages, sheet materials, plates, etc. The 2-D grids and 3-D cages constitute a significant innovation with respect to conventional steel reinforcement. Grid shaped FRP reinforcement has been developed to prevent the deterioration of concrete structures caused by corrosion of steel reinforcement. The 2-D grids were designed to control surface cracks in concrete structural element such slabs and pavements. The 3-D cages are useful to reinforce concrete beams for shear and flexure.

Much research work was devoted to study and improve the material properties of FRP. Because of low modulus of elasticity, sudden rupture mode of failure and inability to resist compression, the FRP products could not replace the serviceability of steel entirely. The use of FRP for shear and confinement reinforcement has not been fully recognized due to the

unidirectional characteristics of the material and presence of shear cracks at an angle with the fibers. Very few studies have been reported on shear strength or confinement behavior of concrete elements reinforced with FRP products. Although many publications were written in recent years about FRP, only the studies related to the current research project are reviewed here.

Recently a new fiber material was introduced to the market, in the form of grids, for reinforcing concrete (NEFMAC™). NEFMAC™ is a 2-D grid type reinforcement, consisting of glass and carbon fibers impregnated with resin. It was developed by Shimizu Corporation, one of the largest Japanese general contractors. NEFMAC™ is formed into a flat or curved grid shape by a pin-winding process similar to filament winding. Its cross sectional area can vary between 5 to 400 mm^2. It is also available in Canada through Autocon Composites Inc. of Weston, Ontario that produces it under a license from Japan.

Many reinforced concrete slabs were built using NEFMAC™ reinforcement grids. Rahman and Taylor (1992) used Finite Element method to estimate the service load deflections of a slab reinforced with FRP and compared the results with similar slabs reinforced with steel bars. The program was first validated using the data available from experiments carried out by Schmeckpeper (1992) on one-way strips of slabs reinforced with FRP or steel rebars. It was reported that FRP reinforced slabs would suffer large deflections because of the low modulus of elasticity of FRP grids. Then, Rahman et al. (1993) conducted a research program to investigate the suitability of NEFMAC™ grids to reinforce concrete elements such as flat slabs. Short-term tension, creep, fatigue, and durability tests were carried out. Tests indicated that small change might occur in strength and stiffness of NEFMAC™ grids with changes in temperature. Creep deformation was very small. It was also reported that satisfactory fatigue behavior was obtained under tensile load cycles between 10% and 30% of tensile strength.

NEFMAC™ grids were also used by Banthia et al. (1995) to test three small-size concrete slabs and compare them to a control slab reinforced with steel rebars. It was reported that FRP reinforced concrete slabs absorbed less energy than slabs reinforced with steel, and various code equations did not require significant changes when extended to slabs with FRP

reinforcement.

The FRP products were also used as shear reinforcement in beams. Nagasaka et al. (1993) tested thirty-five half-scale concrete beams under anti-symmetric loading. The beams had 250 x 300-*mm* cross section and were reinforced with two steel and four FRP bars at both top and bottom sides. The beams were also reinforced for shear with FRP in the form of rectangular spiral stirrups or rectangular closed hoops. The experimental results showed that the ultimate shear capacity of the beams was determined by tensile breaking of stirrups or crushing of diagonal compression struts. In addition, shear capacity of the beams depended on the amount and type of FRP used, as well as on the axial rigidity of stirrups.

Ozawa et al. (1987) tested ten concrete beams to study the effect of FRP reinforcement on their flexural fatigue behavior. The beams made with 3-D FRP grids were tested under monotonic and cyclic loadings. The modulus of elasticity of the FRP grids was 27.1 GPa. Test results indicated that the bond strength of longitudinal bars was provided by shear stirrups (vertical grids) and the fatigue performance of beams was satisfactory. It was reported that at beam failure, the FRP grids ruptured under tension at the joint connections.

NEFMEC™ grids were also used in shear walls by Fujisaki and Kobayashi (1988). Three concrete shear walls were built and tested under constant axial load and laterals deformation reversals. It was reported that the walls had the same strength as those reinforced with steel bars until a curvature of 0.01.

The aging infrastructure and the need for improved structural performance are among reasons for the desire to use FRP for repair and strengthening. Nanni et al. (1993) used aramid FRP tape or filament winding with glass fiber to confine reinforced concrete columns by means of spiral wrapping. The modulus of elasticity of the FRP was 60,000 *MPa* and the compressive strength of concrete was 35.6 *MPa*. Concrete cylinders (300 x 600 *mm*) and 1/4 scale circular columns were tested under cyclic flexure with and without axial compression. The limited experimental results indicated that lateral confinement significantly increased the compressive strength and ductility of compressed concrete.

2.4 Analytical Models for Stress-Strain Relationship of Confined Concrete

With the limited data available in the past, researchers had difficulties to properly model concrete behavior under different types of loading. Chan (1955) was the first to propose an analytical model using the principle of active hydrostatic pressure suggested early by Richart et al. (1927, 1928). A tri-linear curve was proposed for the stress strain relationship of confined concrete, depending on the volumetric ratio of lateral reinforcement. Although his model was based on small size specimens, the attempt was the first to evaluate the effect of passive confinement of ties on behavior of concrete under eccentric compression. Almost a decade later, Roy and Sozen (1964) suggested a bilinear model for confined concrete based on test data of small size specimens. The model considered only the effect of passive confinement on the descending branch of stress-strain curve. The model was very simple to use, and considered a constant strain value of 0.002 at peak stress. This simplification was refined by other researchers afterwards.

Soliman and Yu (1967) proposed a more comprehensive model. The stress-strain curve was composed of a parabola for the ascending branch, a horizontal plateau, and a linear descending branch. The model considered dependence of confinement on the spacing and amount of transverse reinforcement. Then, Sargin (1971) suggested a continuous curve to better represent the whole stress-strain curve of confined concrete under axial compression. The proposed equation was empirical in nature and its parameters were calibrated for small-size square cross-sections. The ultimate strength was predicted by three equations.

In the same year, Kent and Park (1971) developed a model based on test results reported by Chan (1955), Roy and Sozen (1964), as well as those reported by Bertero et al. (1964). The stress-strain curve was composed of a parabolic ascending branch similar to that proposed by Soliman and Yu (1967), and then a linear descending branch with a slope depending on the amount of confinement. The descending branch joined a constant stress linear segment at 20% of peak stress. The model did not take into account the increase in concrete strength but considered the increase in ductility due to lateral confinement. A 0.002 level of strain was assumed at peak stress. The model was later modified by Park et al. (1982) to include the

effect of lateral confinement on concrete strength. The later model was examined for its application to high-strength concrete columns by Muguruma and Watanabe (1990). It was reported that the model overestimated the curvature ductility of high-strength concrete columns. Hence, the model was modified again, by latter researchers, by increasing the slope of descending part of stress-strain curve. The slope depended on concrete strength and the yield strength of lateral reinforcement.

Leslie and Park (1974) developed a new confinement model for circular columns. The stress-strain relationship was modeled with a curve having an ascending branch composed of two parabolas, and a linear descending branch, then a sustained stress equal to 20% of peak stress. Vallenas et al. (1977) suggested a confinement model similar to that proposed by Kent and Park (1971). The peak stress was a function of both the volumetric ratio of lateral and longitudinal reinforcement. Two empirical equations were developed to determine peak confined concrete stress and the corresponding strain.

Sheikh and Uzumeri (1982) presented a rational model for square sections to determine the stress-strain curve of confined concrete. The enhanced strength of confined concrete was calculated using the concept of effectively confined core area. The model incorporates the effect of tie spacing, and distribution of longitudinal steel around the core perimeter. An empirical equation was developed to compute the peak stress of confined concrete. The confinement coefficients were calibrated only for square columns confined with ordinary hoops and ties and loaded under concentric compression. A critical review of the above analytical models was compiled by Sheikh (1982). It was concluded that, in addition to the amount of lateral reinforcement, strength and spacing of reinforcement played important roles. Furthermore, the distribution of longitudinal steel around the core perimeter and the resulting tie configuration were found to be important in determining the behavior of confined concrete. It was shown that the models that did not consider reinforcement arrangement as a parameter were not able to predict differences in behavior resulting from the tie arrangement. Subsequently, Sheikh and Yeh (1986) modified the Sheikh and Uzumeri model for the effects of eccentricity of loading. The modification was done based on the test data reported by Sargin (1971). They extended the flat portion of the stress-strain curve to reflect the ductility enhancement associated with strain gradient. Hence, an additional

ductility was introduced for eccentrically loaded columns. The model is similar to that proposed early by Soliman and Yu (1967) except that the strength enhancement was considered in the new model. Then Sheikh and Yeh (1992) modified the Sheikh and Uzumeri (1982) stress-strain model for confined concrete again, because the previously proposed model overestimated the flexural column behavior under high levels of compression. The researchers incorporated the strength reduction in concrete associated with increased axial compression. The descending branch of the original model was also modified based on the same data.

Martinez et al. (1982) proposed a stress-strain relationship for circular concrete columns. The stress-strain curve consisted of a parabolic ascending branch and a linear falling branch. The strength enhancement was expressed as a function of lateral stress and spacing of hoops, whereas the ductility improvement of a column was determined as a function of concrete strength, lateral pressure, and spacing of hoops. The model is limited to reinforcement with a grade not exceeding 414 *MPa*. The expressions were empirically derived and their coefficients were calibrated using test data obtained form small concrete cylinders confined with circular spiral, without any longitudinal reinforcement.

Scott et al. (1982) used the modified Kent and Park model to predict their test results. They proposed an empirical equation to compute the maximum longitudinal strain in core concrete. The equation was determined based on their test results and the assumption that the compression concrete is limited by the first hoop fracture. Although the equation is more accurate than those previously proposed by Baker and Amarakone (1965) and Corly (1966), it is still very conservative for columns under combined axial compression and lateral load reversals.

Ahmed and Shah (1982) developed a model for circular reinforced concrete columns confined by spirals. They used the same equation proposed by Sargin (1971) to determine the stress-strain curve. The confining lateral pressure was expressed as a function of the pitch of the spiral, the concrete core dimension, as well as the volumetric ratio and yield strength of confining steel. The parameters defining confined concrete stress and the corresponding strain were determined by fitting experimental data. The effect of the distribution of

longitudinal reinforcement was not considered.

Muguruma et al. (1983) modified the Watanabe et al. (1980) model, originally proposed for normal strength concrete, to increase the applicable range of concrete strength. The modification was incorporated based on test data obtained from testing small square columns confined with high-strength steel. The curve of the stress-strain relationship consisted of discontinuous functions with three different curves. The ascending branch consisted of two second-degree parabolas. The first parabola started from the origin and ended at the peak stress of the unconfined concrete. The curve was followed by the second parabola that ended at the confined strength of concrete. The third curve was a linear segment, describing the descending branch of the relationship and terminated at a point referred to as available limit strain of confined concrete. The model does not consider the effect of longitudinal reinforcement. The proposed expressions were empirically derived and calibrated. The same model was modified once again by Muguruma and Watanabe (1990) to reflect more recent results obtained from their experimental investigation on large scale high-strength concrete columns under constant axial load and simulated earthquake deformations. The modification involved an increase in the limiting compressive strain. The model, however, failed to accurately predict the behavior of another set of columns. The new set consisted of four large-scale high-strength concrete columns, tested by Mugumura et al. (1991), under constant axial load and lateral deformation reversals. Therefore, the model was re-modified again to reflect the latest test data, by introducing an assumption that the concrete strength should not fall below 50 % of peak stress. The non-rationality of the model presented many problems in predicting reliable results. This obliged Muguruma et al. (1993) to modify the model for the fourth time. Consequently, a new set of equations was suggested.

Fafitis and Shah (1985) derived simple equations to predict stress-strain relationship of confined concrete. The model was developed for circular columns and its application was extended into square sections. Distribution of longitudinal steel and tie configuration was not included in the approach. An analytical investigation was also carried out to modify the proposed model to incorporate high-strength concrete. The test results reported by Martinez et al. (1983) and Muguruma et al. (1983) was used to calibrate the confinement parameters.

Mander et al. (1988) proposed a new rational stress-strain model for circular, rectangular and square reinforced concrete columns confined with conventional hoops and subjected to concentric compression. The model was developed on the concept of effectively confined core concrete previously proposed by Sheikh and Uzumeri (1982). The confined compressive strength of concrete was determined as a function of lateral pressure defined by the yield stress of lateral reinforcement. The equation developed by Popovics (1973) was used to predict the stress-strain curve of confined concrete. The model included the effect of strain rate and allowed for cyclic loading. An energy balance approach was used to determine the ultimate compression strain of concrete corresponding to the first fracture of transverse steel. The strain energy stored in the confined core concrete was equated to that of the transverse reinforcement.

Yong et al. (1988) used early confinement models (Sargin 1971, Vallenas et al. 1977, Park et al. 1982, Sheikh and Uzumeri 1982, and Fafitis and Shah 1985) to predict the stress-strain curve of their small-size high-strength concrete columns tested under concentric compression load. All the above models failed to predict their experimental results. Thus, the researchers suggested an empirical stress-strain relationship for high-strength concrete columns confined with rectilinear ties. The stress-strain curve was represented by a discontinuous function, consisting of two polynomial; one for the ascending branch and a second one for the descending branch. The strength enhancement due to confinement was assumed as a function of diameter and number of longitudinal reinforcement, concrete strength, vertical tie spacing, as well as the diameter and yield strength of lateral steel. This model was later modified by Azizinamini et al. (1994) by incorporating their test results. The stress-stain curve was simplified as a linear ascending branch, and a linear descending branch, followed by a sustained constant stress level at 30% of the confined strength.

Bjerkeli et al. (1990) suggested an analytical model to describe the stress-strain behavior of confined normal-density concrete and lightweight aggregate concrete. The stress-strain curve was determined based on expressions originally proposed by Martinez et al. (1982). It consisted of three parts: An ascending branch represented by a polynomial curve; a descending branch represented by a linear line segment followed by a horizontal line. The expressions for the peak concrete stress and the stress-strain curve were empirically derived

and calibrated separately for normal and high-strength concrete. Conflicting expressions were presented to account for the effect of longitudinal reinforcement on peak confined stress, as discussed by Razvi and Saatcioglu (1991).

Saatcioglu and Razvi (1992) developed a rational model for confined concrete. It was based on the concept of equivalent lateral pressure. The model is general enough to treat different concrete sections with rectangular or square hoops with or without cross ties, circulars ties or spirals, welded wire fabric or combination of the above mentioned lateral reinforcement. It was used to predict the behavior of confined concrete columns under strain gradient and compare them with experimental results. The comparison indicated that the behavior of columns under combined axial and flexural load can be predicted accurately using the same model developed for concentric loading, provided that the strain hardening of the longitudinal bars is considered and all the relevant confinement parameters are incorporated in the model. The proposed model was later extended by Razvi (1995) to analyze behavior of high-strength concrete columns.

Madas and Elnashai (1992) presented a model to determine the stress-strain relationship for confined concrete columns. The same equation proposed by Ahmed and Shah (1982) was used to calculate the lateral confining pressure. The increase in transverse steel stress due to the variation of Poisson's ratio of core concrete was considered in the model. Knowing the inelastic behavior of concrete, the Poisson's ratio was empirically related to the axial strain, and an iteration process was used to determine the confining pressure.

Nagashima et al. (1992) suggested new expressions to determine the stress-strain curve of confined high-strength concrete. The peak confined concrete stress was calculated based on the concept of effectively confined core concrete area suggested by Sheikh and Uzumeri (1992). The strain corresponding to the peak stress was expressed empirically as a function of concrete strength, area of lateral reinforcement, yield stress of lateral reinforcement and arrangement of longitudinal reinforcement. The stress-strain curve was composed of a parabola for the ascending branch as proposed by Popovics (1973) and a linear descending branch followed by a horizontal line representing a sustained pressure at 30% of the peak stress.

Cusson and Paultre (1993) developed an analytical model to predict the stress-strain curve of high-strength concrete columns confined with ordinary hoops and ties. They used the principle of effectively confined concrete area proposed earlier by Sheikh and Uzumeri (1982) and modified by Mander et al. (1988). The proposed stress-strain curve consisted of a discontinuous function of two polynomials. The ascending branch was represented by Popovics' (1973) equation, whereas the descending branch was a modification of the relationship proposed by Fafitis and Shah (1985). The coefficients used to express certain parameters were determined empirically, and calibrated using the researchers test data. The model is valid only for high-strength concrete columns confined with conventional ties and hoops, subjected to concentric compression.

The model was later modified by Cusson and Paultre (1995) based on data of columns tested by Nagashima et al. (1992). Some empirical coefficients were changed and an iteration process was proposed to calculate the stress in lateral reinforcement. Beside the complication of the iteration process, a very small variation in material properties can lead to the divergence of analytical predictions and completely different shape of stress-strain curve. The researchers compared the prediction of their model and reported only a 1 % improvement over Nagashima et al.'s model.

Li (1994) proposed a general model to predict the stress-strain curve of confined and unconfined concrete. The model is applicable to circular and square columns made of normal or high-strength concrete and confined with normal or high-strength lateral steel. A large number of columns with a wide range of concrete strength, tested under different conditions, were evaluated. The stress-strain curve of unconfined concrete was represented by a modified version of Popovics' (1973) expression, whereas the confined concrete curve was defined by a discontinuous function represented by a modified version of equations originally proposed by Muguruma et al. (1993). Different empirical expressions were proposed, similar to those suggested by Mander et al. (1988), to calculate the peak stress of confined concrete for different column cross-sections and steel yield strengths.

Hoshikuma et al. (1997) studied some of the previously proposed models (Kent and Park 1971, Mander et al. 1988, Saatcioglu and Razvi 1992, and Muguruma et 1980) and found

that they could not predict accurately the behavior of their columns confined with low volumetric ratios of lateral reinforcement. Hence, the researchers proposed a new model for such columns. The proposed stress-strain curve was represented by a discontinuous function consisting of a parabolic ascending branch followed by a descending straight line. The ultimate strain was considered as a strain corresponding to 50% of peak stress on the descending branch. No effort was made to formulate the sustaining branch of the stress-strain curve. Different empirical equations were suggested to calculate the confined peak stress and the corresponding strain for different cross-sectional shapes. All the empirical coefficients were calibrated using their test results.

Diniz and Frangopol (1997) claimed that some selected models failed to predict accurately the stress-strain relationship of confined high-strength concrete columns. They modified the model proposed by Fafitis and Shah (1985) by changing slightly the confinement index and introducing a correction factor to the descending branch of the stress-strain curve. The correction factor was originally proposed by Martinez et al. (1984) and Bjerkeli et al. (1990). The curve of stress-strain was represented by a discontinuous function at the peak stress, unlike Fafitis and Shah model. The ascending part was a parabola whereas the descending branch was represented by inverse of an exponential function. The empirical coefficients of functions were calibrated using test data under concentric compression. The peak concrete stress and corresponding strain were empirically determined. The confining pressure was calculated based on an arbitrary selected limit stress value of lateral reinforcement. The maximum usable stress in lateral steel was limited to 482.7 *MPa* for concretes of up to 89.6 *MPa* and 413.7 *MPa* for higher strength concretes. This is a contradiction to what had been observed during experimental tests. High-Strength steel of up to 1000 *MPa* is effective in confining high-strength concrete columns (Razvi and Saatcioglu 1994). During his experimental investigation, Razvi (1995) reported that lateral steel of grade 1000 *MPa* yielded at, or shortly after, reaching the peak resistance. Baingo (1995) investigated this phenomenon by testing high-strength concrete (90 *MPa*) under a high level of axial compression accompanied by lateral load reversals. The columns were confined with high-strength steel (1000 *MPa*). It was reported that lateral expansion of high-strength concrete was able to fully utilize the full capacity of lateral reinforcement. In addition, columns confined with high strength lateral steel developed higher deformability compared to

companion columns confined with lower grade steel (425 *MPa*). In addition, when the model was incorporated for sectional analysis, the stress-strain relationship of longitudinal steel in compression was assumed to be the same as that established through tension coupon tests. The expression proposed by Park and Pauley (1975) was adopted in their model. The validity of the model was only checked with data on a few selected test results.

2.5 Longitudinal Bar Stability

Little research was conducted on buckling of column reinforcement due to the complexity of the phenomenon. The majority of previous research was conducted analytically, with practically no experimental research undertaken on the topic. Scribner (1986) tested six cantilever reinforced concrete beams to investigate the effect of tie size and spacing on stability of longitudinal bars. Specimens were tested under repeated load reversal. Tests showed that longitudinal bars could buckle over a length greater than two-stirrup interval. The researcher discussed the relationship of the flexural stiffness of confining ties with inelastic buckling of longitudinal reinforcement. He developed an analytical model to determine the spacing of stirrups required for a given diameter of longitudinal bars and a diameter of ties. The energy method was used to determine the buckling load over a length equal to three stirrup-intervals (3S). A relationship between the ratio of tie spacing and the unsupported length of stirrup-tie leg was determined by considering the flexural stiffness of ties, and neglecting their axial stiffness.

Papia et al. (1988) developed an analytical model to predict the maximum compressive load that a longitudinal steel bar can resist before buckling. The authors modeled the reinforcing bar as a built end column, supported by intermediate elastic supports at intervals equal to the spacing of ties. The stiffness of the elastic supports was considered as a contribution of the axial rigidities of crossties. The flexural rigidity was neglected. In addition, neither the variation of transverse strains in concrete with axial strains, nor the effect of lateral pressure of core concrete on the longitudinal bar was considered. However, the effect of strain hardening on axial stiffness of ties was taken into account by replacing the value of the Young's modulus of elasticity by the tangent modulus of elasticity. The tangent modulus of elasticity was defined as the tangent slope of stress-strain curve within the strain-hardening

region. The criterion of the proposed model was given by determining first the unknown length of the region of the longitudinal reinforcement involved in relation to the geometrical and mechanical characteristics of column, then determining the buckling load. The researchers used the reduced modulus of elasticity theory to express the buckling load. The model is difficult for practical application and may be limited to square columns under concentric compression. The analytical predictions obtained for the critical buckling load were higher than those recorded experimentally. Consequently, a reduction factor of 1.20 was introduced to the buckling load expression.

Papia and Russo (1989) suggested a procedure to calculate the ultimate strain of concrete columns based on the limit stability condition of longitudinal reinforcement proposed earlier by Papia et al. (1988). The ultimate compressive concrete strain was assumed to coincide with the critical strain producing the buckling of longitudinal reinforcement. An empirical equation was proposed to relate the so-called reduced modulus of elasticity to Young's modulus of elasticity and the tangent modulus in strain hardening. In addition, an empirical equation relating the critical stress of longitudinal bars to the stiffness of the elastic system was presented. The authors acknowledged that the proposed equation could lead to about 10% error compared to that proposed earlier by Papia et al. (1988). The proposed expression for the stiffness of the spring system did not take the effect of flexure rigidity and it is valid only for square columns. A wide scatter between experimental and theoretical values was shown, although the new proposed procedure had a fair degree of accuracy compared to the previous one.

Mau and El-Mabsout (1989) developed a beam-column element to investigate bar buckling, and implemented it in a Finite Element program. The program was used to analyze the stability of longitudinal reinforcement between two consecutive transverse reinforcement layers in columns. It was assumed that ties are stiff enough to force the longitudinal bar to buckle in first mode, i.e., between the ties. Using the principle of virtual work and tangent modulus theory, the analysis showed that the critical aspect ratio was in the range of 5 to 7. When the aspect ratio was higher, the critical buckling load was lower than or equal to the yield load. However, the buckling load could be higher than the yield load even when the aspect ratio was smaller than the critical value and the stress-strain relationship in

compression was the same as that in tension. Conversely, the stress in compression bar drops rapidly prior to or at yield, as the strains continue increasing. The model could be suitable for computer use for a single element, but it can not be employed in models of real reinforced concrete structure. The complexity results from extensive numerical integration over the cross-sectional area and over the length of the element.

Mau (1990) used finite element method to study inelastic buckling of longitudinal reinforcement in concrete columns. In his study, he considered only the buckling between two consecutive transverse reinforcement layers. He applied the tangent modulus theory to predict the buckling load when the stress in compression steel passes the yield plateau region and goes into strain hardening. It was found that the critical aspect ratio of compression bar varied according to the hardening behavior of steel, but it was in the range of 5 to 7 for grade 400 *MPa* steel. When the aspect ratio was below the critical value, and transverse reinforcement were sufficiently stiff, the axial load deflection history of compression bar followed closely that of the material stress-strain relationship. However when the aspect ratio was larger than the critical ratio, the actual load-deflection path could be unstable beyond yielding. In this case, the tangent modulus theory could not be used to predict accurately the critical buckling load.

Monti and Camillo (1992) performed a series of monotonic and cyclic tests on FeB44 steel rebars of the Italian production. The objective of the research program was to study the effect of monotonic and cyclic behavior on inelastic buckling of reinforcing steel bars. The bars had 12, 16, or 24-*mm* diameter and a nominal strength of 440 *MPa*. Three different aspect ratios were considered: 5.0, 8.0, and 11.0. The test results showed that for an aspect ratio of 5.0, the compressive monotonic stress-strain curve was the same as that in tension. When the aspect ratio was 8.0, the difference between the two curves became obvious, and the slope of the stain-hardening region of the compression curve became lower. However, samples with an aspect ratio of 11 showed that as soon as the yield point was reached, the compression curve deviated from that in tension and developed a negative slope. Samples tested under symmetric cyclic loads showed that the envelope of cycles in tension was not affected by buckling. However, the envelope of cycles in compression depended on bar aspect ratio, and coincided with monotonic stress-strain curve in compression.

Ooya and Kato (1994) studied the inelastic buckling of intermediate and corner longitudinal bars in square concrete columns. Based on their experimental results, the researchers proposed an empirical equation to determine the buckling strain of longitudinal reinforcement. The buckling strain is the smallest calculated strain for different modes of buckling. There was a wide scatter between the predicted values and the test results, because the proposed equations were purely empirical.

Suda et al. (1996) carried out an experimental investigation of four columns to investigate the buckling behavior of reinforcing bars in concrete. The columns had a rectangular cross section (200 x 300 *mm*) and were reinforced with 22 10-*mm* longitudinal bars, confined with 3 or 5-*mm* hoops. The steel had yield strength of 366 *MPa* and an ultimate tensile strength of 544 *MPa*. The compressive strength of concrete was 46 *MPa*. The columns were tested under constant axial load and lateral deformation reversals. A new method was used to measure the stress in longitudinal bar beyond the yield point. A very small area around the measuring position of the reinforcing bar was heated using a special heating coil to raise the yield point to more than 1.4 times the initial value. A strain gauge was mounted at the center of the hardened portion that served as a loading cell. The experimental results indicated that the buckling behavior of reinforcing bars was affected by the splitting strength of cover concrete, the flexural stiffness of transverse reinforcement, and the flexural stiffness of the longitudinal bars. The researchers proposed an analytical model to determine the stress at which longitudinal bars buckled. The cover concrete was assumed to be the only dominant factor. The total splitting force of cover concrete was equated to the horizontal force caused by the curvature of longitudinal bar. The proposed model can not predict accurately the buckling load of steel bars in concrete columns, because it is difficult to predict the splitting strength of concrete accurately. Further, there is a wide scatter between the proposed equations in codes and disagreement among concrete researchers on how to determine tensile strength of concrete.

2.6 Conclusions from Previous Work

The following conclusions may be drawn from the review of previous research presented in the preceding sections:

- Most researchers agree that deformability of reinforced concrete columns is a function of concrete strength, amount and distribution of laterally supported longitudinal bars, tie arrangement, volumetric ratio, spacing and yield strength of lateral steel, level and eccentricity of axial load, direction and rate of lateral load, and loading history.
- Conflicting views were reported about the effectiveness of high-strength steel as confinement reinforcement. Some researchers believe that high-strength steel is necessary to confine high-strength concrete while others stated that its effectiveness is limited by a stress lower than the yield strength. However, there appears to be consensus among researchers that high-strength steel is effective under high axial compression.
- The brittle behavior of high-strength concrete, relative to normal-strength concrete has been established. Furthermore, it has been recognized that the confinement requirements for high-strength should be more stringent than those for normal-strength concrete. However, there is lack of test data to quantify the confinement requirements for high-strength concrete. Tests of large-size columns are needed to establish inelastic deformation characteristics of high-strength concrete columns.
- Reduction in spacing of lateral reinforcement improves strength and deformability of reinforced concrete columns. Well-distributed longitudinal bars may increase the confinement of concrete, but small-size bars are more susceptible to buckling if they are not properly supported.
- The 90-degree hooks tend to open during inelastic response of concrete columns and hence are not effective. Hooks with 135, and 180-degree bends, well anchored into confined core, perform well during inelastic response of concrete columns
- Welded hoops and square spirals used to confine concrete columns were reported only by Japanese researchers. However, the performance of welds was not properly investigated since it is believed that the weld must be stronger than the welded material.
- Researchers reported that performance of concrete columns confined with conventional welded wire fabric (WWF) was not satisfactory. Specially designed welded grids were recently tested in concrete shear walls and beams, but not in columns.
- Fiber reinforced plastic (FRP) products were widely used in different types of structural applications in Japan, and recently gained more attention from structural engineers in

North America to retrofit bridge columns and other infrastructures. No literature was found on the use of FRP grids as column transverse reinforcement.

- Shear studs were used world wide to reinforce concrete slabs for punching shear. Double headed studs were recently used in offshore structures mainly in Europe. No literature was found about the performance of the double head studs when used in columns subjected to constant axial load and simulated earthquake deformations.
- Most of the existing analytical models used to predict stress-strain relationships of confined concrete continue to have limitations. Many of them were developed for normal-strength concrete and they are not applicable to high-strength concrete and vice-versa. Most analytical models are empirical in nature. The reliable and rational models for rectilinear reinforcement are based on the "effectively confined core area" concept, with the exception of Saatcioglu and Razvi model, which was developed based on the concept of equivalent lateral pressure.
- The stress-strain curves predicted by confinement models were defined by discontinuous functions consisted of at least two expressions defining two distinctly different segments. All models were calibrated for a maximum concrete strength of 130 *MPa*.
- All confinement models, except those developed by Cusson and Paultre (1995), and Madas and Elnashai (1992), considered lateral confining pressure as a function of yield stress of transverse reinforcement and did not account for strain hardening in transverse steel. The iterative procedure proposed by Cusson and Paultre (1995) for high-strength square concrete columns has a convergence problem, whereas Madas and Elnashai's (1992) method is complicated and was never accepted by other researchers.
- The ultimate lateral deformation-capacity of reinforced concrete columns was determined by most researchers in terms of ultimate compressive strain of concrete, without considering the stability of compression reinforcement.
- The analytical models reviewed in the previous section for bar buckling were developed to determine the limiting compressive strength of concrete under concentric compression only. In addition, the behavior of bars was simulated under monotonic loading.
- All the previously proposed buckling models, with the exception of the model used by Mau, are complicated for an average structural engineer to use. The simplicity of Mau's

model was introduced by the assumption that longitudinal bars buckle only in the first mode, i.e., between two steel ties with an unsupported length equal to tie spacing.

- When sectional analysis of concrete was performed, all concrete researchers assumed that the stress-strain relationship of reinforcement in compression was the same as that in tension.
- Relatively few experimental studies were conducted on cyclic behavior of reinforcing bars, including inelastic buckling.

Chapter 3

EXPERIMENTAL INVESTIGATION

PART1- MATERIAL PROPERTIES

3.1 General

Three new types of transverse reinforcement were considered in the experimental program as potential alternatives to conventional confinement reinforcement. These included; i) welded reinforcement grids (WRG), ii) fiber reinforced plastic grids (FRPG), and iii) double headed studs (DHS) used in combination with perimeter hoops. Since they are not standard reinforcement elements, they were custom made for the current research project. Therefore, it became especially important to undertake a comprehensive study on their material properties prior to investigating their performance in columns. This chapter presents a detailed description of physical and mechanical characteristics of these elements, with relevant discussion on their potential benefits. Furthermore, because there are no standard tests developed for these materials, quality control testing procedures are proposed. The results of standard concrete cylinder tests, as well as longitudinal reinforcement coupon tests are also presented.

3.2 Need for New Confinement Reinforcement

Transverse reinforcement in reinforced concrete members serves three main functions. These include; i) stability of longitudinal reinforcement, ii) enhancement of shear (diagonal tension) and torsion capacities, and iii) confinement of core concrete. The conventional transverse reinforcement used in practice consists of spirals, circular hoops, perimeter and overlapping hoops of rectilinear geometry, perimeter ties, and crossties.

An important feature of transverse reinforcement is its detailing, without which it can not serve the function that it is designed for. For example, the stability of longitudinal reinforcement is maintained only if a bar is laterally braced by hooks or bends of transverse

reinforcement. Longitudinal reinforcement between the bends receives negligible support since the lateral restraint in this case would depend on flexural resistance of perimeter ties, which is often very small. Circular hoops and spirals develop sufficient rigidity as they experience hoop tension and provide lateral support along the perimeter. It is important to have the longitudinal bars fully engage in the hooks and bends, as well as the perimeter of circular hoops and spirals for proper lateral support. This requires a certain level of precision and workmanship which may complicate the construction process, sometimes leading to scarifies from optimal performance. Similarly, shear and torsion reinforcement used in the form of ties and closed hoops must conform to specific detailing requirements pertaining to bends and bend extensions. The same is also true for confinement reinforcement. Confinement reinforcement often results in high volumetric ratios of steel, producing congestion of reinforcement in steel cages. The detailing requirements for confinement reinforcement are more stringent than those specified for others. This type of reinforcement is produced with specific bend angles and extensions as well as crossties details to ensure satisfactory performance in the inelastic range of deformations. These details often increase the complexity of construction process, sometimes leading to concrete placement problems and compromises in quality and performance. It is clear that the assembly of reinforcement cage does require precision, skilled labor and diligence to achieve the functions for which they are designed.

Even with currently available modern equipment, the cross dimension tolerances of hoops and crossties can easily vary within ± 12 *mm*. The fabrication process usually involves bending of five rebars simultaneously, resulting in wide gaps between longitudinal bars and hoops at 135-degree bends. The ends of the hoops are often out of plane as shown in Fig 3.1, and the gap between the ends can be as much as 75 *mm* wide in the case of #15 reinforcement. This gap tends to be larger as the bar diameter increases and tie dimensions decrease. Figure 3.2 depicts the problems associated with delivery, handling, and storage of rebars. The problems associated with cage fabrication and steel congestion are shown in Fig. 3.3 and Fig. 3.4.

The lack of precision and related performance problems, as well as high installation cost associated with conventional ties necessitated a search for new types of transverse

reinforcement. Three potential alternatives to conventional ties were considered, in the form of welded reinforcement grids, fiber reinforced plastic grids, and a combination of double headed studs and perimeter hoops. These new forms of confinement reinforcement were developed to perform as good, or better than conventional reinforcement. The dimensional accuracy, structural performance, and installation time were the main considerations. The characteristics and advantages of these new elements are described in detail in the following sections.

3.3 Description of New Confinement Reinforcement

3.3.1 Welded Reinforcement Grids (WRG)

3.3.1.1 Description of WRG

WRG is made out of cold drawn wires, welded to form grids. Cold-drawn wires are often used in the form of welded wire fabric (WWF) or wire mesh. Hence, WRG may be confused with WWF. However, there are significant differences in terms of size and structural performance. WWF consists of smooth or deformed wires welded to form square or rectangular grids. They are often used in walls and floors where small size reinforcement is placed with uniform spacing in two orthogonal directions. The wire mesh is fabricated from small diameter wires. Although the wire diameter ranges between 3.429 *mm* (0.135 *in.*) and 15.951 *mm* (5/8 *in.*); and the grid dimension ranges between 51 *mm* (2 in) to 305 *mm* (12 in) squares, common stocks of WWF include wires of 1.47 *mm* (0.058 in) to 4.19 *mm* (0.165 in) in diameter. Usually, large size wires are used to produce large size grids. Hence, the steel area ratio produced by WWF becomes small. While this area ratio may be sufficient for walls and floors, it is not sufficient for beams and columns. The yield strength of standard WWF varies between 480 *MPa* (70 *ksi*) and 550 *MPa* (80 *ksi*). A major drawback of conventional WWF is the relatively brittle behavior of material as compared to re-bars. Smaller size wires tend to be less ductile than larger wires. Furthermore, the welding process may reduce material ductility. Therefore, the conventional WWF, with small size wires were not widely accepted by the construction industry, and often used cautionary in special structural applications.

Welded reinforcement grids (WRG) resemble WWF in terms of geometry and manufacturing process. Primary differences between the two come from the sizes of wires and grids, as well as the stress-strain relationship. WRG is designed to be used as transverse reinforcement in beams, columns, beam-column joints, and shear wall boundary elements. They are made from cold-drawn smooth wires, fuse welded in jigs to obtain desired grid size and configuration. WRG shows similar ductility as hot-rolled rebars, developing 7% to 10% strain at rupture, as illustrated later in this chapter, although they do not exhibit a clear yield plateau and any appreciable strain hardening.

The welded reinforcement grids were used as transverse confinement reinforcement in this experimental program to construct thirteen full-size concrete columns, three of which were built using high-strength concrete. They were manufactured and supplied by BauMesh Company, Newport Beach, California, U.S.A. They had a square configuration with a 292-*mm* (11 ½ in) out-to-out dimension. Three different types of grids were employed consisting of; i) 9.53 *mm* (3/8 in) diameter steel reinforcement welded to form 4 equal-size square grids, ii) 9.53 *mm* (3/8 in) diameter steel reinforcement welded to form 9 equal size square grids, and iii) 6.60 *mm* (1/4 in) diameter steel reinforcement welded to form 9 equal-size square grids. Figure 3.5 shows the geometric details of welded reinforcement grids used. Because of the welding process used, the reinforcement in each direction protrudes by 6.35 *mm* (1/4 in) beyond the perimeter welds.

3.3.1.2 Advantages of WRG

The main advantages in using WRG can be summarized as follows:

- WRG insures fast installation, reducing construction time and bringing related economic benefits.
- WRG costs less to install, as compared to convential transverse reinforcement, reducing labour cost. They require less manpower to place and inspect.
- Steel consumption is reduced as hooks, bends and their extensions are eliminated. Also, WRG is made out of a higher grade steel. Higher tensile strength allows reduction in steel areas resulting in savings in tonnage of steel.

- Accuracy in placement and longitudinal bar support can be achieved due to small dimensional tolerances and high quality control associated with the prefabrication process, resulting in improved structural performance.

3.3.2 Double Headed Studs (DHS)

3.3.2.1 Description of DHS

Double-headed studs were originally developed as shear reinforcement. They were used in the past to improve shear capacity of heavily reinforced concrete sections and flat slabs. Careful examination of the test results reported by Dilger and Ghali (1997) on shear walls indicated that this type of stud could also be used as crossties in combination of conventional perimeter hoops in columns. A typical DHS consist of a steel rod with plate welded at each end as anchor head.

In this experimental program, double headed studs were used with conventional square hoops to build four full size concrete columns for testing under simulated seismic loading. Two different types of studs were used in columns. The first type consisted of 9.53-*mm* (3/8 in) diameter steel rod with square plates welded at the ends as anchor heads. The second type had a 6.35-*mm* (1/4 in) diameter steel rod and circular end plates. The anchor heads were designed by the manufacturer to have sufficiently large bearing area to prevent crushing of concrete. The square plates had 28-*mm* sectional dimension and 4 *mm* thickness, whereas the circular plates had 25-*mm* diameter and 3 *mm* thickness. The double-headed studs were manufactured and supplied by Decon® Corp., Brampton, Ontario. Figures 3.6 and 3.7 illustrate typical double-headed studs used in test columns.

The steel rods of DHS were made of C1018 type steel (0.18% Carbon, 0.23% Silicon, 0.72 Manganese, 0.009% Phosphorus, 0.009% Sulfur, 0.09 Copper). The material properties of the anchor head plates were not available. However, hardness tests indicated that the circular head plates were made of cold rolled steel with approximately 675 *MPa* tensile strength and the rectangular head plates were cut from hot rolled plate having approximately 520 *MPa* tensile strength. It should be noted that the mechanical properties of the plates may have been changed as a result of heating during the welding process. The conventional type square

hoops used with the DHS to confine the columns were made of the same material as the studs.

3.3.2.2 Advantages of DHS

The benefits of using DHS as transverse reinforcement in concrete columns can be summarized as follows:

- The anchor heads eliminate the need for hooks and bends to be anchored in concrete core.
- Distribution of DHS across the column section as crossties increase the uniformity of lateral confinement, thus increasing the strength and ductility of concrete in columns.
- DHS are easy to install and hence less labor intensive. This results in savings associated with installation and inspection.
- Congestion in reinforcement cage is avoided. Bends and hooks that are used in conventional crossties are eliminated, resulting in improved concrete placement.
- The studs are often produced from high strength steel, enabling increased tensile strength and associated reduction in the amount of steel needed.

3.3.3 Fiber Reinforced Plastic Grids (FRPG)

3.3.3.1 Description of FRPG

Long term durability problems observed in many civil engineering structures and constant deterioration of steel and even wooden structures provided the impetus for growth of corrosion and degradation resistant materials such as fiber reinforced plastic (FRP). In addition, the need for lighter construction materials and more seismic resistant structures has placed high emphasis on the use of new and advanced materials.

Recently, a "New Fiber Composite Material for Advanced Concrete" (NEFMAC™) grid was introduced to the market by Shimizu Corporation, one of the largest Japanese general contractors. It has also become available in Canada through Autocon Composites Inc. of Weston, Ontario, that produces them under a license form Japan. NEFMAC™ is a 2-D grid type of reinforcement, consisting of glass and carbon fibers impregnated with resin.

NEFMAC™ is formed into a flat or curved grid shape by a pin-winding process similar to filament winding. A representative NEFMAC™ grid structure is shown in Fig 3.8.

The fiber reinforced plastic grids (FRPG) used in this project as transverse column reinforcement is of 2D-NEFMAC™ type. The size of a typical 2D-NEFMAC™ grid is specified by the area of the crossbars and the interval spacing. The cross-sectional area varies between 32 mm^2 and 3806 mm^2. Typical interval spaces are 25, 50, 75, 100, 150 *mm* (1, 2, 3, 4, 6 *in.*). The fiber reinforced plastic grids used in fourteen full size columns, tested in this investigation were manufactured and supplied by Autocon Composites Inc. of Weston, Ontario. The FRPG were made by impregnating continuous carbon fibers only with Vinyl ester resin. The carbon has a specific gravity of 1.4 and a modulus of elasticity of 100,000 *MPa* as reported by the manufacturer. They had a square configuration with about 300-*mm* out-to-out dimension. Five types of grids were employed consisting of; i) 6x10-*mm* rectangular bars forming four equal-size square grids; ii) 6x10-*mm* rectangular bars forming nine equal-size square grids; iii) 6x8-*mm* rectangular bars forming nine equal-size square grids; iv) 8x10-*mm* rectangular bars forming four equal-size square grids; v) 8x10-*mm* rectangular bars forming nine equal-size square grids. Figure 3.9 illustrates the geometric details of FRP grids used. The cross bars in each direction protruded by about 6 *mm* (1/4 *in.*) beyond the perimeter of joints to ensure proper strength of exterior joints.

3.3.3.2 Advantages of FRPG

The main advantages of using fiber plastic reinforced grids are:

- Non-corrosive material, reducing the need for concrete cover.
- Excellent resistance to alkalis, acids, and chemicals, improving durability of concrete members. FRPG can be used in conditions where damage/deterioration by salt and other chemicals are expected.
- Precision and easy assembly when used in concrete columns as transverse reinforcement, resulting in improved performance and reduced labor cost.
- FRP is non-magnetic. Electromagnetic transparency results in a suitable structure for hospital and rooms where electromagnetic transparency is required for medical equipment.

- Specific gravity of less than 2.0 results in ease of transportation and placement, and overall lighter structures.

3.3.4 Material Tests Proposed for New Reinforcement

Material properties of lateral reinforcement play an important role in performance of concrete columns under axial and seismic loads. The welded reinforcement grids, double headed studs, and the fiber reinforced plastic grids have not been adopted by the building industry as standard forms of transverse reinforcement for structural use. Therefore, no standard test procedure and guideline have been developed for these new products. However, it is essential that material test procedures be developed to verify and control material properties, before any one of these new materials can be adopted as standard reinforcement for use in structural concrete. A set of test methods and procedures are proposed in this section.

3.3.4.1 Coupon Tests

Strength and ductility (elongation) of lateral reinforcement play important roles on structural performance of reinforced concrete elements. Both of these two qualities can be established by a standard coupon test (ASTM E8). For reinforcing bars forming grids, coupons have to be cut from the grids such that a grid joint with a cross-reinforcement is located in the test region. This should be done for the case of welded steel grids to ensure that potentially adverse effects of joint weld and/or any imperfection that may be present in the joint are recorded during testing. The above consideration also applies to FRP grids where the bonding quality and continuity of fibers in two orthogonal directions are verified. A mechanical extensometer or an electronic displacement transducer can be placed over the joint to measure the elongation of material in direct tension. The coupon is gripped by the heads of the testing machine at the ends, and is subjected to uni-axial tension until failure.

Using tension coupon test results, a stress-strain relationship can easily be established. Among the parameters that can be determined from stress-strain curves are the yield strain ε_y, strain hardening ε_{sh}, ultimate strain ε_u, rupture strain ε_{up} and their corresponding stress at yield f_y, strain-hardening f_{sh}, ultimate f_u, and rupture f_{rup}, respectively. An additional

parameter useful for modeling the complete stress-strain curve of steel reinforcement is the initial slope E_h of the hardening curve. This easily determined graphically as shown in Fig. 3.10. It should be noted that the stress values are computed on the basis of original cross-section, and the strains are based on the original gauge length. This is referred to as engineering-type stress-strain curves and will be used throughout this thesis. The "true-stress-true-strain curves" based on instantaneous values of area and gauge length are often thought to be of more fundamental significance.

The yield strength is perhaps the most important quantity for application to columns. In conventional reinforcing bars the yield strength is easy to determine since their stress-strain curves show a well-defined yield point followed by a straight yield plateau. However, in the case of cold-drawn steel bars, such as the one used to make the welded reinforcement grids and the double-headed studs, a well-defined yield point does not exist. In this research program, the yield stress f_y is defined as the stress corresponding to the first deviation from perfectly elastic behavior. The corresponding yield strain is denoted as ε_y.

According to the ASTM standards, the yield strength is usually specified in either one of two ways. For steels with a specific value not exceeding 550 *MPa* (80 *ksi*), yield strength $f_{y0.5}$ is considered as the stress at which the test specimen reaches a 0.5% extension under tension load. For higher strength steels, the yield strength, $f_{y0.2}$ is the stress at which the specimen reaches a strain 0.2% greater than that for perfectly elastic behavior. However, the ACI code defines the yield strength $f_{y0.35}$ of reinforcing steel (rebars) as the stress at a strain of 0.0035, a value at which normal strength concrete roughly crushes.

3.3.4.2 Bursting Test for Grids

The stress condition that exists in column transverse reinforcement is more complex than that can be established by a direct tension coupon test. Hoops and ties are subjected to combined bending and axial tension as they stabilize compression reinforcement and confine laterally expanding concrete. Furthermore, they control diagonal tensile stresses that result in inclined cracks. The stress condition is further complicated in reinforcement grids due to the rigidity

of welded or bonded joints, increasing flexural rigidity of reinforcement. This raises a concern with regard to the ability of the grid joints to maintain their integrity until desired levels of strength and inelastic deformability are attained. While a standard coupon test may provide insight into the grid joint strength, this may not be sufficient, as this type of direct tension test may not simulate the stress condition imposed on the grid joints during response of an actual structural member to combined stresses. Therefore, the grids must be tested under a loading condition which is representative of the forces exerted by longitudinal compression reinforcement and laterally expanding concrete. A test procedure was developed to simulate stresses induced by a longitudinal bar on corner joints, as it tends to bust out laterally. This condition can be created approximately by a diagonal tension test as illustrated in Fig 3.11. The test is called " Bursting Test," and can be used to verify the strength of a grid joint while also establishing elongation characteristics of the grid as a whole.

The bursting test consists of a reinforcement grid subjected to diagonal tension along one of the diagonals while it is restrained against contraction in the orthogonal diagonal direction. A pair of hinges and a restraining rod assembly is used to apply the load as illustrated in Figs. 3.12, 3.13, and 3.14. The diagonal restraining piece is manufactured from two steel rods of sufficient rigidity and strength, bolted together, one on each side of the grid so that they do not yield or buckle prior to the failure of the grid. It can be manufactured to be adjustable for use with different size grids, and must contain sufficient number of bolts at an appropriate spacing to prevent buckling. The ends must be equipped with machined cylindrical pins of the same diameter as the longitudinal bar being simulated, engaging in joint corners just like a longitudinal column bar engages in the corner of a grid. A hinge assembly that contains a similar cylindrical steel piece forming the pin of the hinge, to apply diagonal tension, fits the loading end. The hinge assembly is attached to a steel bar, which is gripped by the head of the test machine.

The hinge must allow torsional twist so that the grid is free to rotate while pulled in the diagonal direction. This reduces the application of a twisting moment that results from the eccentricity of force components illustrated in Fig. 3.15. The twisting action does not develop in FRP grids because of the manufacturing process used, that puts the cross-bars at joints in the same plane, in contrast to WRG grids that are welded by pressing steel reinforcement

together. The WRG reinforcement in two orthogonal directions do not lie in the same plane, but in two parallel planes separated from each other by a distance equal to approximately the diameter of the reinforcement. This creates an eccentricity between the points of contact of the cylindrical pin and the grid, as illustrated in Fig. 3.15, and produces a twisting action until the lines of action of the two force components coincide, eliminating further twist during loading. Elimination of the twisting moment during a bursting test creates an idealized loading condition. In an actual concrete column, the longitudinal bar in the corner tend to bend and rotate as it applies lateral forces, minimizing the eccentricity between the points of application of lateral forces and associated twisting moment.

The grids should be instrumented for elongation measurements in the direction of loading. The instrumentation consists of either a mechanical dial gauge or an electronic displacement transducer placed between the diagonally opposite corners, or the loading pins. If the gauge is placed on the loading pins, it is important to eliminate any slack in the system so that the movement of the pins is equal to the elongation of the grid corners. This can be verified by examining the force-deformation relationship. If the relationship is linear within the initial loading stage, starting immediately with the initial application of load, this is an indication of proper measurement with zero slack in the system. The applied load is plotted against measured deflections to establish the force-deformation relationship of grid along its diagonal. The test is continued under a monotonically increasing tensile force until failure. The failure occurs either due to rupture of the material or due to joint failure. The force and corresponding deformation at failure give the strength and elongation capacity of grid.

A typical force-deformation relationship of WRG reinforcement is illustrated in Fig.3.16, and consists of an elastically linear segment, followed by an inelastic region. The elastic segment occurs during initial loading when the steel remains elastic. As the applied tension increases, one of the legs starts yielding. This causes a marked reduction in the slope of the force-deformation relationship. Subsequently, redistribution of stresses within the grid spreads yielding into the other legs. The yielding occurs near the welds, as in the case of coupon tests. The post-yield region becomes approximately linear, with a reduced slope. Hence, the force-deformation relationship can be idealized as a bilinear relationship. If the failure occurs in the weld, before significant yielding of steel, the grid may be disqualified as

reinforcement. The failure may be either due to steel rupture, or due to a weld failure. However, it must occur after a significant inelasticity, allowing the grid to develop the required inelastic deformability. Inelastic deformability may be expressed in terms of diagonal elongation of a grid.

The force deformation relationship of fiber reinforced plastic grids is different than that of welded reinforcement grids, because the stress strain relation of FRP bars is linear up to failure (Fig.3.16). The failure of FRPG reinforcement is associated either with the rupture of the crossbars or by failure of joints due to delaminating of fiber sheets.

3.3.4.3 Pullout Test of DHS

The main purpose of using double-headed studs is to increase the uniformity of lateral resistance to expansion of concrete under axial compression and maintain the stability of longitudinal bars in compression. This can not be achieved unless the steel head plates are properly connected to the studs. This is done through welding. The adequacy of weld can be verified by the proposed pullout test. The pullout test involves application of direct tension to a DHS specimen through the head plates. A pair of hinges, equipped with collars at the ends, is used to apply the load as shown in Fig. 3.17. Each collar is made out of two pieces placed under a plate around the stud and assembled with two bolts. The hinge assembly is attached to a steel bar, which is gripped by the head of the testing machine. The stud is instrumented by either a mechanical dial gauge or an electronic displacement transducer to measure axial elongations. Testing should continue under monotonically increasing tension force until failure. The failure occurs either due to the rupturing of stud, failure of weld, or yielding of head plates.

3.4 Material Properties of Lateral Reinforcement

3.4.1 Coupon Tests of WRG

Tests of WRG coupons were conducted as described above to establish stress-strain characteristics of steel. The coupons were taken from two different batches of grids with two

different wire and grid sizes such that a cross reinforcement with a welded joint was included in the test region. The coupons were randomly selected from two different batches with two different wire and grid sizes. The tests were performed using a 1500 kN (300 kip) Tinius Olsen universal testing machine. Two strain gauges were placed on each coupon; one at the back of welded joint, and the other between the joints. An Alsmer Extensometer with a 51 *mm* (2 in) gauge length was used, spanning the cross bar location, to record strains at large extensions where strain gauges usually cease to function. Figure 3.18 illustrates the instrumentation of a typical coupon. The data, consisting of elongations, strains, and forces, was recorded continuously until failure. It was found that the extensometer readings agreed closely with strain gauge readings at the joint.

The first yielding was recorded by the strain gauge behind the weld and the Extensometer over the joint. The weld survived the tests without any failure, and none of the coupons tested failed at the welds. The necking of steel started at the joint, behind the weld after a significant elongation was recorded. The necking led to the fracture of steel on one side of the welded joint, while the weld itself remained intact. Figures 3.18b and 3.18c show views of "necking" and rupturing of steel observed during coupon tests.

The WRG coupons were also tested under repeated cyclic loading. Figures 3.19 and 3.20 illustrate the stress-strain relationships for (1/4-*in.*) 6.60-*mm* and 9.53-*mm* (3/8 *in.*) steel grid reinforcements, respectively, obtained through coupon tests under monotonic and cyclic loading. The ultimate strength was attained at about 7% and 6.5% strains for 9.53 *mm* (3/8 *in.*) and 6.60-*mm* (1/4 *in.*) diameter grid reinforcement, respectively. The 9.53 *mm* (3/8 *in.*) coupons ruptured at approximately 10% strain while the 6.60 *mm* (1/4 *in.*) coupons ruptured at a strain slightly higher than 7.5%. The coupons showed yield strengths of approximately 580 *MPa* and 570 *MPa* for 6.60 *mm* and 9.53-*mm* reinforcement, respectively. These material characteristics of the welded reinforcement grids are illustrated in Table 3.1.

3.4.2 Bursting Tests of WRG

A total of 7 bursting tests were conducted according to the procedure described above, to illustrate the behavior of grids in diagonal tension. These are labeled as grids 1 through 7.

Table 3.2 provides geometric and material properties of the grids. The first three grids were instrumented by electric-resistance strain gauges and linear voltage displacement transducers (LVDT) to measure steel strains. An LVDT was also placed between the top and bottom hinges to measure the overall grid displacement along the diagonal, except the first sample. Fig. 3.21 shows steel strains at selected locations under increasing diagonal force, F. The LVDT readings give strain measurements over designated joints with a gauge length varying between 62 *mm* and 146 *mm*. The strain gauges, on the other hand, reflect localized behavior of steel over a 5-*mm* gauge length. The strain data shown in Fig. 3.21 indicate significant yielding of steel near the joints, developing strains as high as approximately 10% at two locations. This is consistent with observed failure of grids. All the grids showed signs of significant yielding and necking of steel near the grid joints prior to failure. Of the 7 grids tested, 4 failed by rupturing of steel near a welded joint, in exactly the same manner as observed in coupon tests. The remaining three exhibited weld failure after significant yielding of steel, at approximately the same elongation level. The failure patters are illustrated in Figs. 3.22 through 3.25. The deformed shape observed is consistent with that observed in actual column tests. Figure 3.26 shows the behavior of reinforcement grids in actual column tests. The comparison of grids subjected to bursting tests with those used in concrete columns as transverse reinforcement, indicates that the bursting test provides a close representation of actual grid behavior in columns as described in Chapter 5. However, 3 of the 7 bursting test grids failed due to the weld failure. One may conclude from this observation that, while the bursting test is representative of grid behavior in columns, it may be more critical on the weld. Therefore, it may be viewed as a conservative approach to verifying weld strength.

The diagonal force-diagonal elongation relationships recorded by bursting tests are shown in Fig. 3.27. The relationships show an initial elastic segment, followed by gradual yielding and redistribution of stresses among the grid legs as indicated by curving of the relationship with gradually decreasing slope. The sample tests included two different sizes of reinforcing steel, either 9.53 *mm* (3/8 *in.*) or 6.60 *mm* (1/4 *in.*) diameter, and two different grid patterns, either 4-cell or 9-cell. Although the load capacity was affected by these properties, they all exhibited similar elongation capacities. The measured elongation at failure ranged between

6.8% and 8.3% of the initial diagonal dimension. The failure pattern did not appear to affect the elongation capacity significantly. All the grids exhibited excessive yielding prior to failure as indicated by significant necking of steel near the weld, irrespective of whether the failure was caused by steel rupturing or weld failure.

The diagonal force applied by test machine results in longitudinal forces in reinforcement that make up the grid. Simple force equilibrium can be used to derive the force components as depicted in Fig. 3.15. Stress in steel can than be calculated from the axial force component in reinforcement, and can be compared with those recorded during a standard coupon test. It is important, however, to recognize the change in geometry during testing. The following equations can be used for this purpose (Refer to Fig. 3.15):

$$F = 2\left[T\cos\left(\frac{\theta}{2}\right) - V\sin\left(\frac{\theta}{2}\right)\right] \tag{3.1}$$

$$T = \frac{F + 2V\sin\left(\frac{\theta}{2}\right)}{2\cos\left(\frac{\theta}{2}\right)} \tag{3.2}$$

$$f_1 = \frac{T}{A_1} \tag{3.3}$$

where, F is the total applied load by the machine, V is the shear imposed on each leg of reinforcement. In 4-cell grids, the shear force V may be taken equal to ½ of the compressive force C in the perpendicular leg. The same force may be taken equal to C in 9-cell grids. Angle θ is the angle between the grid reinforcement in two orthogonal directions. This angle is 90° prior to testing, and reduces to approximately 80° at the end of the test, because of the extension of grid in the direction of loading. The actual angles recorded at the end of tests are listed in Table 3.2.

3.4.3 Coupon Tests of DHS

Double-headed stud coupons were tested under tension according to the ASTM E8 standard to establish sample stress-strain relationships. The coupons were randomly selected from two different batches with two different wire sizes. It should be noted that the conventional square hoops used in SD columns were made of the same material as that used to manufacture DHS. The tests were performed using a 1500 kN (300 kip) Tinius Olsen universal testing machine. The loading speed was maintained constant throughout the test. A linear voltage displacement transducer (LVDT) or an Alsmer mechanical extensometer was used to measure strain over a 51 *mm* (2 *in.*) gauge length in addition to a strain gauge placed at mid-length of bar. In addition, three other coupons were tested under repeated cyclic tension loading. Close examination of coupons after testing indicated that the DHS bars fractured in partial cup-cone manner indicating that coupons behaved in ductile behavior (see Fig. 3.28). Figures 3.29 and 3.30 illustrate the average stress-strain relationships for monotonic and cyclic tension loads for 6.35 *mm* (1/4 *in*) and 9.53-*mm* (3/8 *in*) DHS bars, respectively. The ultimate strength was attained at about 8% and 7% strains in 9.53-*mm* (3/8 *in*) and 6.35-*mm* (1/4 *in*) reinforcement, respectively. The coupons showed yield strengths of approximately 570 *MPa* and 630 *MPa* in 9.53 *mm* (3/8 *in*) and 6.35 *mm* (1/4 *in*) DHS, respectively. The material characteristics of the double-headed studs are illustrated in Table 3.1.

3.4.4 Pullout Tests of DHS

Pulling tests were performed on double-headed studs to check the adequacy of the welds between the studs and the head plates. The tests were done following the procedure described earlier in this Chapter. Three samples of 6.35-mm (1/4-in.) studs and three samples of 9.53-mm (3/8-in.) studs were tested under monotonic tension load. The samples were selected randomly from two different stud-size batches. The tests were performed using a 1500 kN (300 kip) Tinius Olsen universal testing machine. A strain gauge was placed at mid-length of each stud to monitor its deformation and record the ultimate strain corresponding to potential weld failure. The pullout tests proved that the end plates were properly welded to the studs. The failure was characterized by the rupture of the studs either at mid-point or about 50-mm

from the head plates. Some of the strain gauges ceased working after yielding of steel studs, while others recorded high values, close to the ultimate strain of studs.

3.4.5 Coupon Tests of FRPG

The fiber reinforced plastic products are known to have high tensile strength under short-term loading. Therefore, tension coupon tests are needed to determine the usable limit of the material. Special grips were designed for testing a single-bar specimen of NEFMAC® grid in tension. These grips were manufactured, consisting of internally threaded pipes having a 20-*mm* inside diameter, similar to that employed by Rahman et al (1993). The coupons were cast in the pipes with a special epoxy at both ends. The epoxy resin adhesive used was of Sikador 31, Hi-Mod Gel, consisting of two component pastes. The coupons were cut from the grids so that a cross bar extended 3-*mm* on either side of the bar, at each end. These cross bars at the ends were necessary to attain sufficient anchorage to the steel pipes. Figure 3.31 shows FRPG coupons prior to testing.

The tests were performed using a 1500 kN (300 kip) capacity Tinius Olsen universal testing machine. Two strain gauges were placed on each coupon; one at the joint, and the other between the joints. A linear voltage displacement transducer (LVDT) was also placed over the test region, spanning over a cross bar, to record strains at large extensions where the strain gauges usually cease to function. Elongation, strain, and force data were recorded continuously until failure, using a "Vishey" data acquisition system.

The stress-strain relationships for fiber reinforced plastics, obtained through coupon tests, are illustrated in Fig. 3.32. Figure 3.33 illustrates typical FRP coupons failures. Examination of the test results indicates that the elongation of FRP in the middle portion between the joints is slightly higher than that at the joint. The average recorded strain at ultimate was 1.78%, corresponding to an average ultimate strength of 1483.0 *MPa*. The modulus of elasticity was measured to be about 83,000 *MPa*, although it was specified by the manufacturer to be 100,000 *MPa*. The tensile properties of FRP coupons are presented in Tables 3.1 through 3.3.

3.4.6 Bursting Tests of FRPG

Bursting tests were conducted on five different types of NEFMAC® grids. The tests were performed using 1500 kN (300 kip) capacity Tinius Olsen universal testing machine. The grids were instrumented by electric resistance strain gauges and a linear voltage displacement transducer (LVDT). The strain gauges were placed at grid joints, as well as between the joints, as indicated in Fig 3.34. The LVDT was placed between the top and bottom hinges to measure the overall diagonal grid displacement.

The experimentally obtained diagonal displacements at peak load varied from one type of a grid to another. It was governed by delamination of corner joints. The grids failed at the joints before the crossbars reached 10% of their ultimate tension capacity. Figure 3.34 shows recorded strains at selected locations under increasing diagonal force F. Figure 3.35 depicts experimentally obtained diagonal force–diagonal deflection relationships. Although the FRP material has a low modulus of elasticity, the recorded deflection at peak load was very low compared to ultimate deflection of welded reinforcement grids. A maximum deflection reading of 22 *mm* was recorded in Type 1 grid and a minimum reading of 13 *mm* was recorded in Type 3. It appeared that the peak load varied with FRP cross sectional dimensions and grid configuration. The failure of the joints was mainly due to the low strength of epoxy resin compared to the carbon fibers. This is a setback for the superior performance of FRP material in tension. The bursting test of FRP grids provided a close representation of the actual grid behavior in column tests, as described in Chapter 5. The failure patterns of the joints are shown in Fig. 3.36.

3.5 Longitudinal Reinforcement Properties

3.5.1 Tension Test

Performance of longitudinal reinforcement under plastic load cycles plays an important role on overall ductility of reinforced concrete columns. Hence, the ductility of rebars has to be established by performing standard coupon tension tests in accordance with ASTM procedures. Ductility is measured by percent elongation over a given gauge length. Also, other tensile properties of reinforcing steel are of interest to structural engineers and are

generally determined from coupons tension tests. The behavior of coupons in these tests is closely related to the behavior of rebars in concrete structural members under static loads.

Three different sizes of grade 400 *MPa* bars were used as longitudinal steel reinforcement in concrete columns tested in this research program. These were #15 (16 *mm* diameter), #20 (19.5 *mm* diameter) and # 30 (29.9 *mm* diameter) bars, manufactured to conform CSA Standard G30.12 (ASTM A616). The steel reinforcement was supplied by a local company in two different batches. The first batch was used to build cages of the BG columns, whereas the second batch was used for the rest of the columns. Sample coupons of different size rebars from each batch were tested using a 1500 kN-Tenius Olsen universal testing machine. The tests were performed in accordance with ASTM A370-72 standard procedures. The strain was measured within a gauge length of 100-*mm* using an LVDT. The load and the deformation were recorded using a "Vishey" data acquisition system.

Coupon tests were also conducted under repeated tension load. The stress-strain curves of coupons are shown in Figs. 3.37, 3.38, and 3.39. Examination of the test results indicates that the stress-strain curves under monotonic tensile loading coincide with envelopes of stress strain relationships under cyclic loading. The relationship under monotonic loading exhibits an initial linear elastic portion and an inelastic portion. The inelastic range consists of two parts; a post-yield range in which strains increase with no appreciable increase in stress, followed by a strain-hardening range, in which strains increase with a gradual and significant increase in stress. Table 3.1 illustrates steel properties obtained from tension coupon tests.

3.6 Concrete Properties

Three different batches of ready mix concrete were used to cast the columns. Two of the batches had normal–strength concrete with a specified minimum 28-day strength of 30 *MPa*. The third batch had high-strength concrete with a specified strength of 80 *MPa*. Mix designs and fresh concrete properties are shown in Tables 3.4 and 3.5, respectively. Precautionary measures were taken in specifying the mix design for high-strength concrete. Since the workability and mix proportions of concrete are significantly affected by the gradation of aggregates, it was decided to perform grading of aggregates according to CSA Test Method

A23.2-2A (ASTM C125). The coarse aggregates used were either 10-*mm* or 20-*mm* crushed limestone. The fine aggregates consisted of sand having a fineness modulus of 2.75. The results of sieve analysis, shown in Fig. 3.40, satisfied the CSA requirements. The material proportions for high-strength concrete were specified to the ready-mix plant prior to delivery of concrete. Aggregates, cement and *retarder* were mixed at the ready-mix plant. The moisture content of the aggregates was measured and reported by the ready-mix company. Water and *Superplasticizer* were added at the Structures Laboratory of the University of Ottawa. The concrete was then mixed in the read-mix truck while the truck was in the laboratory, prior to taking samples for slump tests and casting columns.

While casting columns, a large number of control cylinders were prepared using 152 *mm* by 305 *mm* (6 in x 12 in) single-use plastic molds. The concrete was poured into the molds and compacted according to CSA Test Method A23.2-3C (ASTM C192-20a). For normal-strength concrete, the cylinder molds were filled in three layers of equal volume. Each layer was consolidated through rodding 25 strokes by a 16-*mm* diameter-tamping rod. An internal vibrator was used to consolidate high-strength concrete. The vibrator had 20 *mm* outside diameter and a frequency of 120Hz. The concrete cylinders were kept in the plastic molds for two days. The top surfaces were kept under wet burlap and covered by 4-mil-thick white opaque polyethylene film to prevent drying. After demolding, the concrete cylinders were placed with column specimens to continue curing under identical conditions.

A 2200 kN-capacity Fourney hydraulic testing machine was used to perform standard cylinder compression tests in accordance with CSA Test Method A23.2-9C (ASTM C39). The testing machine, shown in Fig. 3.41, had a bottom fixed platen and an upper loading platen equipped with a swivel. The compressive strength of concrete was monitored by testing cylinders at 7, 14, 21, 28 days as well as on the day of column test. The normal-strength concrete cylinders were capped according to CSA Test Methods A23.1 and A23.2-9 (ASTM C617) with high strength Sulfur compound, two hours prior to testing. The Sulfur compound had a compressive strength (70 *MPa*) less than that of high-strength concrete. An alternative to capping high-strength concrete cylinders was to grind the bearing surface using silicon carbide abrasion. The grinding was done using a "HI-KENMA Deluxe Specimen End Grinder" machine shown in Fig. 3.42, until the bearing surfaces were plane and square to

satisfy the CSA A23.1 requirements. The average 28-day concrete strength for each batch was found to be 33.7 *MPa*, 81.6 *MPa*, and 37.2 *MPa* for the first, second and third batches, respectively. The variation of concrete compressive strength with age is presented in Table 3.6 for each batch.

High-strength concrete cylinders failed in an explosive manner, compared to normal-strength concrete cylinders. Figure 3.43 shows normal and high-strength concrete cylinders at the end of testing. Close examination of cylinder failure surfaces indicated that the cement-paste and aggregates debonded in normal-strength concrete, whereas the shear plane passed through the cement paste and aggregates in the case of high-strength concrete.

A 1500 kN-Tenius Olsen universal testing machine was used to establish the stress-strain relationship of concrete cylinders under uniaxial compression. A spherical bearing block, shown in Fig. 3.44, was placed at the bed-plate of testing machine to eliminate accidental eccentricities. A compressometer was used to record deformation and strain characteristics of concrete (ASTM C 469). The compressometer with three-point contacts was placed around a concrete cylinder. The axial deformations were measured within 200-*mm* (8-*in.*) gauge length using two Linear Voltage Displacement Transducers (LVDT's) mounted on the compressometer on two opposite sides of a cylinder. The load and the deformation readings were recorded using a high speed "Vishey" data acquisition system. The tests were performed during the same time period of column tests. The complete compressive stress-strain curve could easily be established for normal-strength concrete. However, the data for high-strength concrete was limited to the ascending branch of the curve up to the peak stress. This was because of the brittleness of high-strength concrete and the steep falling branch of the stress-strain curve. Recording points within the descending branch requires a very high-speed data acquisition system and a close loop servo controlled machine, which were not available. An alternative testing procedure was adopted to obtain the full compressive stress-strain curve of concrete, consisting of repeated compressive load cycles. This procedure produces a pronounced hysteresis effect in the stress-strain curve. Under the effect of cycling, the concrete stiffness decreases as the compressive strain increases. Hence the concrete material becomes softer and a full stress-strain curve can be generated. It is widely accepted by concrete researchers that the envelope of cyclic curve would be identical to the

stress-strain curve under monotonic loading. The average monotonic compressive stress-strain curves and the cyclic loading curves for the three concrete batches are shown in Figs. 3.45, 3.46, and 3.47. The engineering parameters of the concrete curves are presented in Table 3.7.

Although concrete is not usually designed to resist direct tension, a knowledge of tensile strength is important to estimate cracking load of a structural member or to perform a detailed analysis. Hence, splitting tension tests of concrete cylinders were performed to evaluate the tensile strength of concrete, according to CSA Test Method A23.2-13C (ASTM C 496-90). A concrete cylinder, of the same type used for compression tests, was placed horizontally between the two platens of a 1500 kN capacity Tinius Olsen testing machine and loaded in compression (See Fig. 3.48). Two plywood strips, 3 *mm* (1/8 *in.*) thick and 25 *mm* (1*in.*) wide were placed between the bottom and top concrete cylinder surfaces and the platens as bearing strips. The load was increased until failure took by indirect tension, in the form of splitting along its longitudinal axis. Figure 3.49 illustrates the fracture planes of normal and high-strength concrete cylinders after testing. High-strength concrete is distinguished by its dark color fracture plane. Test observations indicate that fracture planes of normal strength concrete cylinders passed through the cement paste only, whereas there was no evidence of aggregates debonding from cement paste, in the case of high-strength concrete cylinders. Test results indicated that the tensile strength of concrete varied between 6% and 10% of compressive strength. The ratio of tensile strength to compressive strength decreased as the compressive strength of concrete increased. The tensile test results of concrete cylinders are summarized in Table 3.6.

Table 3-1: Reinforcement Properties

Bars Size	ε_y	ε_{sh}	ε_u	ε_{rup}	f_y (*MPa*)	$f_{y0.5\%}$ (*MPa*)	f_{sh} (*MPa*)	f_u (*MPa*)	f_{rup}	E_h (*MPa*)
BG-1 – BG-13										
# 15	0.002135	0.0092	0.106	0.106	427.0	427.0	427.0	672.0	672.0	3846.0
# 20	0.002275	0.012	0.104	0.104	455.0	455.0	455.0	660.0	660.0	6839.6
# 30	0.002350	0.010	0.097	0.097	470.0	470.0	470.0	703.0	703.0	6976.7
¼" Grids	0.002900	-	0.065	0.076	580.0	610.0	-	735.0	530.0	7666.0
3/8" Grids	0.002850	-	0.075	0.098	570.0	580.0	-	680.0	650.0	
SD-1 – SD-4										
# 20	0.00204	0.010	0.110	0.134	408.0	408.0	408.0	639.0	628.0	7826.0
¼" Studs	0.00285	-	0.070	0.087	570.0	625.0	-	700.0	480.0	6400.0
3/8" Studs	0.00270	-	0.065	0.080	540.0	580.0	-	655.0	570.0	8772.0
FRP-1 – FRP-2										
# 20	0.00204	0.010	0.110	0.134	408.0	408.0	408.0	639.0	628.0	7826.0
# 30	0.00230	0.012	0.128	0.176	460.0	460.0	460.0	698.5	674.0	5333.4
FRP Grids	-	-	0.018	0.018	-	-	-	1480.0	1480.0	-

Note: ε_y is based on rounded off experimental average value of 200,000 Mpa.

Table 3-2: Properties of WGR samples tested

Grid Samples	Steel Diameter (*mm*)	No. of Cells	Yield Strength (*MPa*)	Failure Mode	Elongation Capacity (%)	θ at end of test (Degrees)
Grid – 1	9.53	4	570	Weld Failure	--	79.5
Grid – 2	9.53	4	570	Steel Rupture	8.2	80.5
Grid – 3	9.53	9	570	Steel Rupture	8.3	79.0
Grid – 4	9.53	9	570	Weld Failure	6.8	77.0
Grid – 5	9.53	9	570	Weld Failure	7.0	73.0
Grid – 6	6.60	9	580	Steel Rupture	7.6	79.0
Grid – 7	6.60	9	580	Steel Rupture	7.3	81.0

Table 3-3: Properties of FRP Tension Coupons

	Ultimate Strain ε_u (%)	Ultimate Stress σ_u (*MPa*)	Modulus of Elasticity E_{FRP} (*MPa*)
Coupon 1	1.72	1455.0	84100.0
Coupon 2	1.73	1447.0	83600.0
Coupon 3	1.90	1547.0	81400.0
Average Value	1.78	1483.0	83033.0
Standard Deviation	0.08	45.4	1173.0

Table3-4: Mix proportion of $1m^3$ of concrete

	Batch #1	Batch # 2	Batch # 3
Specified Concrete Strength	30 *MPa*	80 *MPa*	30 *MPa*
Cement	204.0 Kg	342.5 Kg	246.5 Kg
Slag	83.0 Kg	141.3 Kg	64.5 Kg
Aggregate	1130.0 Kg	1100.6 Kg	1070.3 Kg
Sand	873.0 Kg	798.1Kg	853.5 Kg
Water	132.0 Kg	75.6 Kg	142.0 Kg
Superplasticizer	N/A	2.1 litters	N/A
Retarder	N/A	1.5 litters	2.2 litters

Note: Water included relative humidity of aggregates

Table 3-5: Properties of Concrete Mixes

	Batch #1	Batch # 2	Batch # 3
Specified concrete strength	30 *MPa*	80 *MPa*	30 *MPa*
Measured slump	80 *mm*	100 *mm*	75 *mm*
Type of cement	Type 10 Lafarge	Type 10 Lafarge	Type 10 Lafarge
Type of slag	St. Mary's	St. Mary's	St. Mary's
Type of Celica fume	N/A	Force 10000-D	N/A
Type of aggregate	Crushed lime stone	Crushed lime stone	Crushed lime stone
Type of Sand	Gatineau Sand	Gatineau Sand	Gatineau Sand
Type of Superplasticizer	N/A	Conchem S.P.N.	N/A
Type of Retarder	Conchem Protard	Conchem Protard	Conchem Protard
Maximum aggregate size	20 *mm*	10 *mm*	20 *mm*

Table 3-6: Variation of concrete compressive strength with age

	Compressive Strength of Concrete in *MPa*				Splitting Tensile Strength (*MPa*)
Age:	7 days	14 days	21 days	28 days	
			First Batch		
Cylinder 1	21.0	27.2	31.8	34.5	2.92
Cylinder 2	21.5	27.6	31.2	33.3	2.88
Cylinder 3	19.3	25.1	29.2	33.3	2.73
Average	20.6	26.6	30.7	33.7	2.84
Standard Dev.	0.94	1.09	1.13	0.57	0.08
			Second Batch		
Cylinder 1	63.9	71.9	78.1	82.2	5.06
Cylinder 2	64.7	73.0	78.5	81.3	4.82
Cylinder 3	66.4	70.2	80.1	81.4	4.94
Average	65.0	71.7	78.9	81.6	4.94
Standard Dev.	1.04	1.15	0.86	0.40	0.10
			Third Batch		
Cylinder 1	27.3	33.5	35.9	36.4	3.94
Cylinder 2	26.2	34.9	35.8	38.2	3.86
Cylinder 3	26.9	33.6	34.4	37.0	3.54
Average	26.8	34.0	35.4	37.2	3.78
Standard Dev.	0.45	0.64	0.68	0.75	0.17

Table 3-7: Properties of concrete

Columns	$f_{co}^{'}$ (*MPa*)	ε_{01} (%)	ε_{cu} (%)
BG-1 – BG-10	33.7	0.206	1.8
BG-11 – BG-13	81.6	0.262	0.5
SD-1	36.8	0.221	1.4
SD-2	35.4	0.213	1.4
SD-3	36.0	0.214	1.4
SD-4	35.8	0.213	1.4
FRP-1 – FRP-14	37.2	0.221	1.4

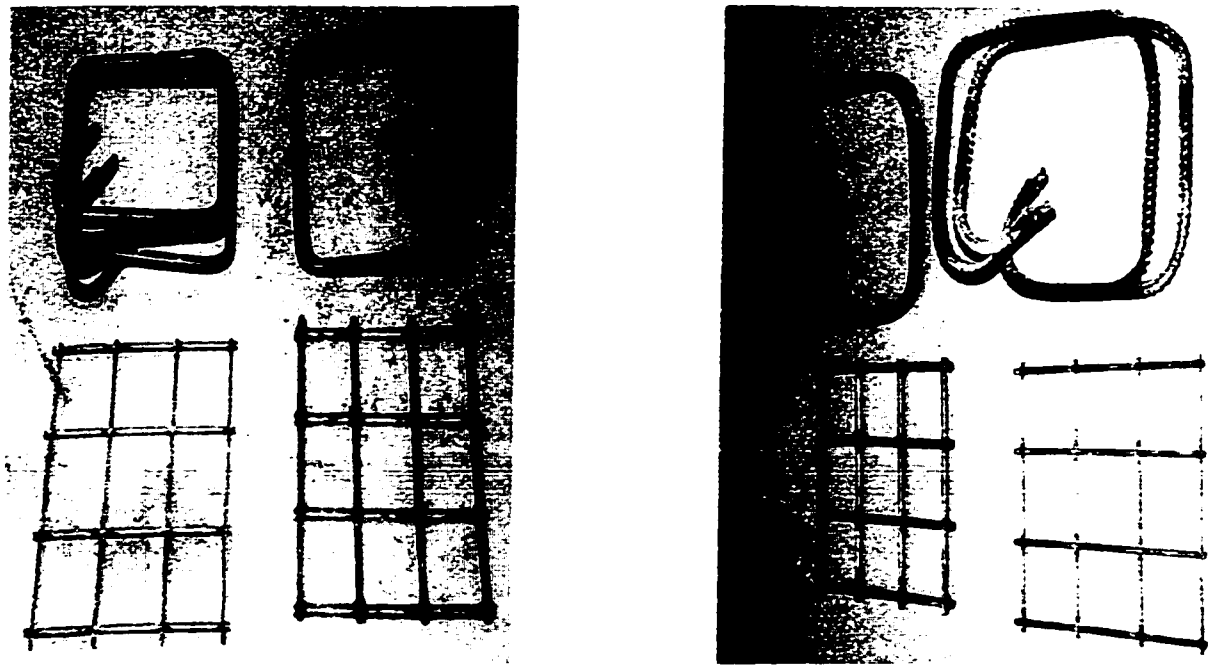

Figure 3-1: Problems associated with hoop fabrication (#15 and #20 hoops versus WRG)

Figure 3-2: Problems associated with handling of rebars

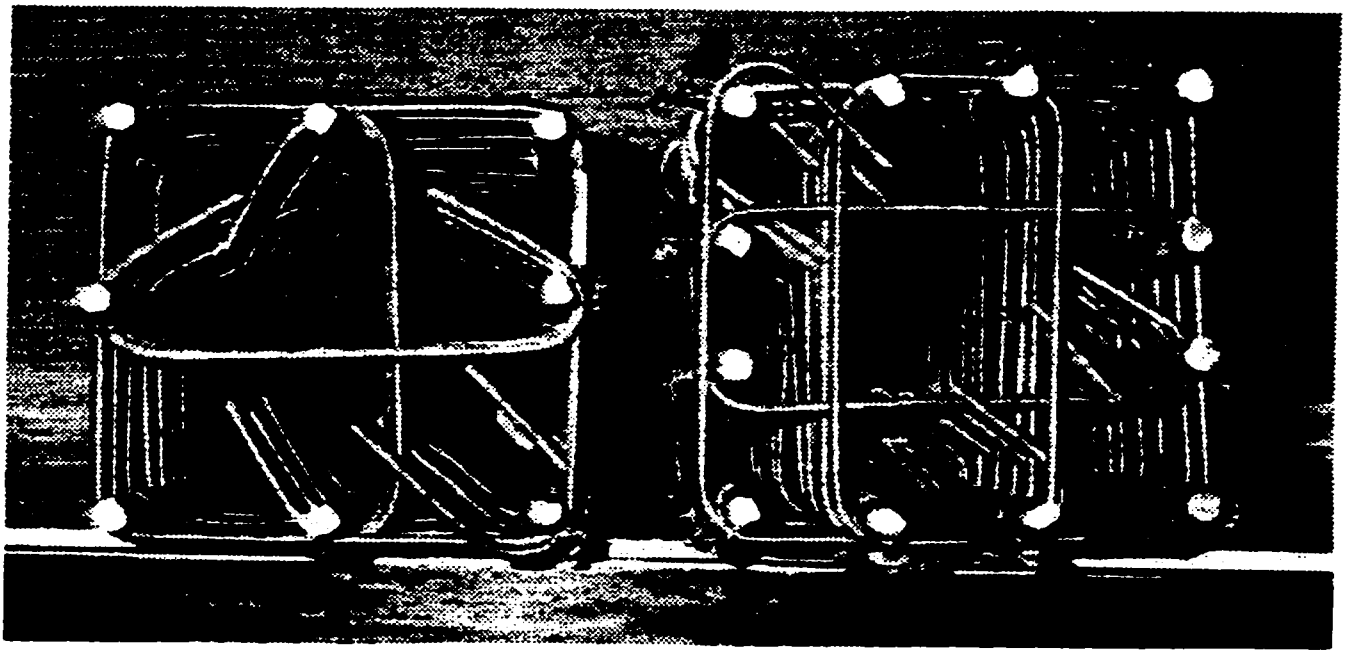

a) Razvi (1995)

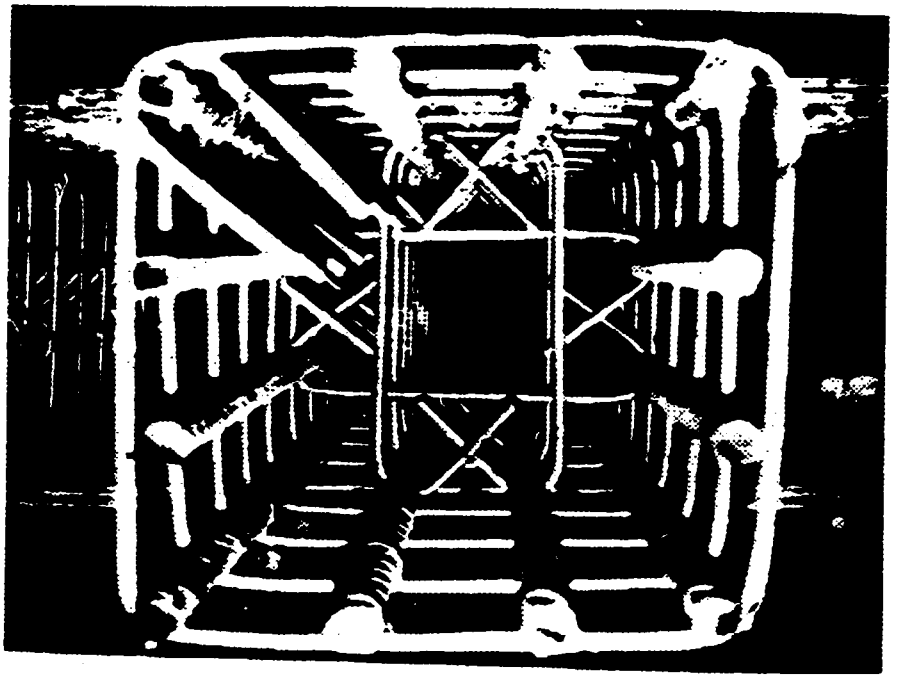

b) Lipien (1995)

Figure 3-3: Congestion of reinforcement

Figure 3-4: Precision of placing hoops and ties in concrete columns (Baumann, 1993)

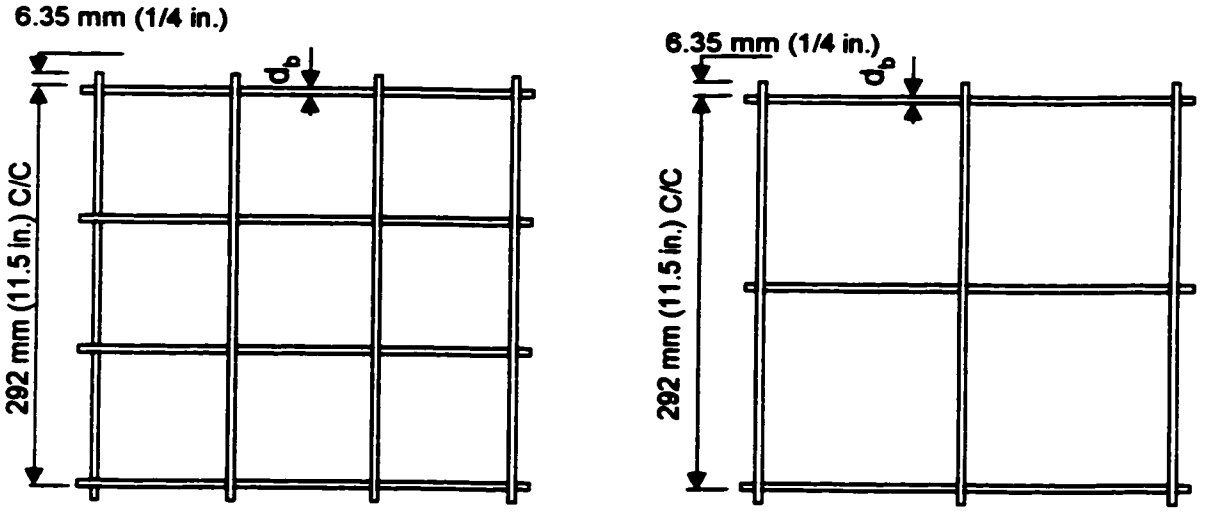

Figure 3-5: Geometric details of Welded Reinforcement Grids

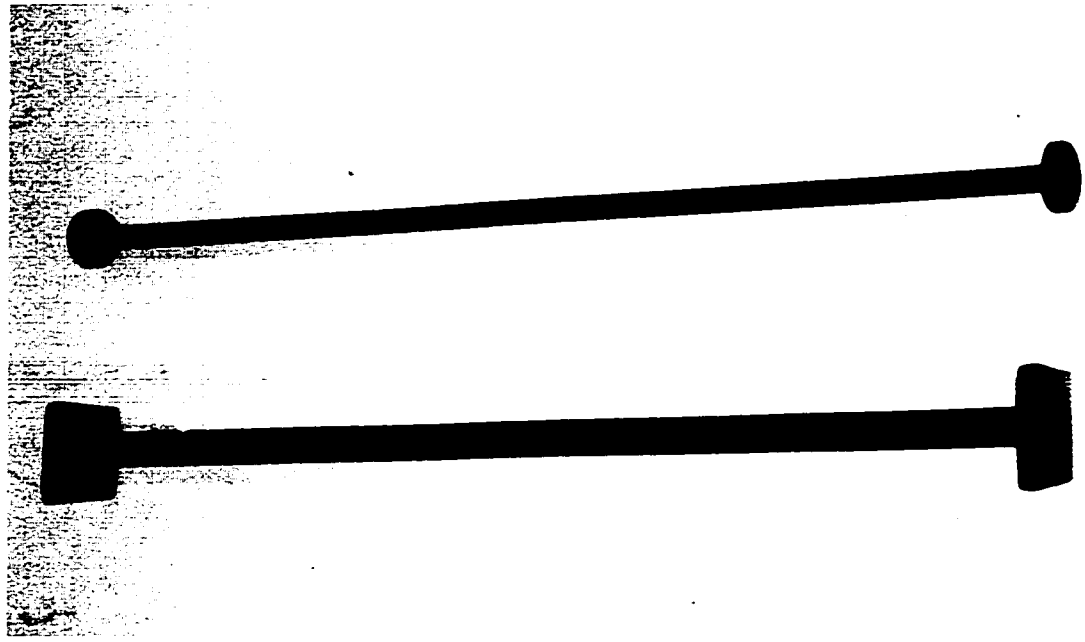

Figure 3-6: Photo of Double Headed Studs

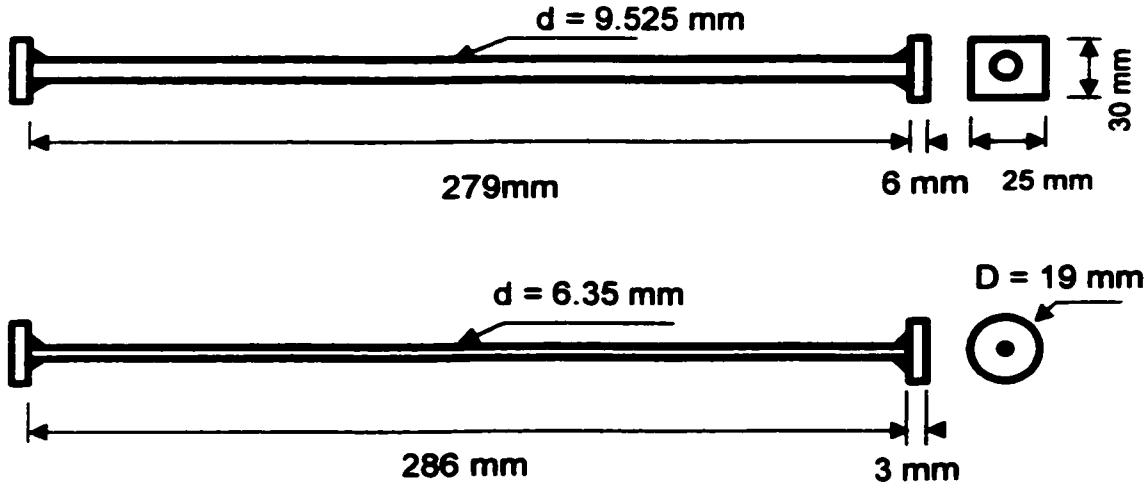

Figure 3-7: Geometric details of Double Headed Studs

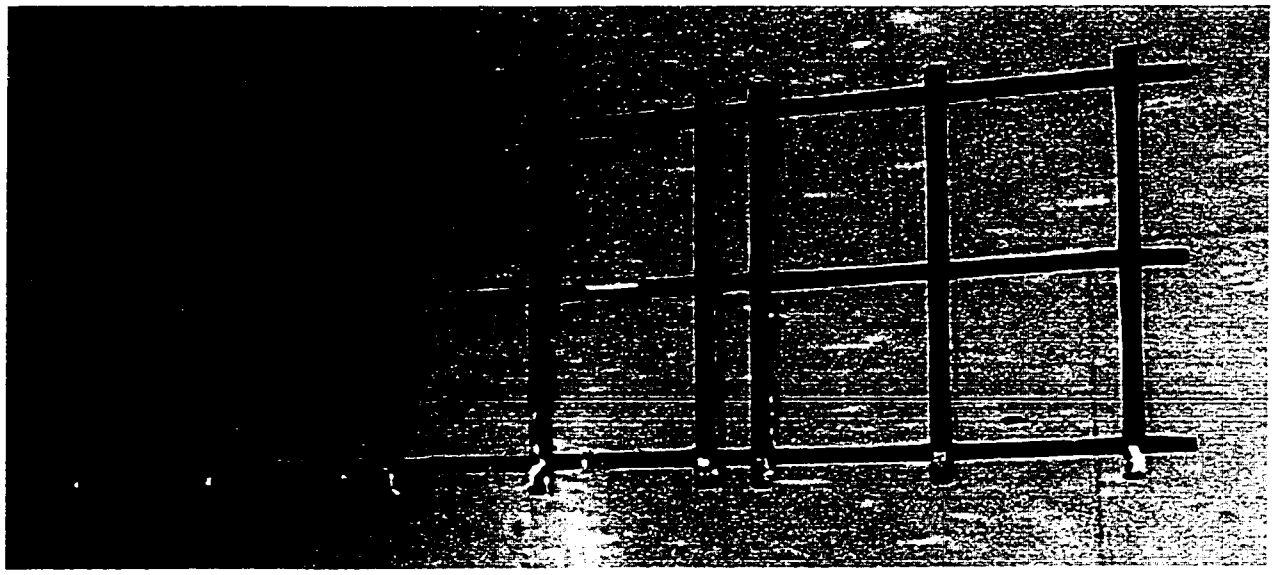

a) 2D-grid

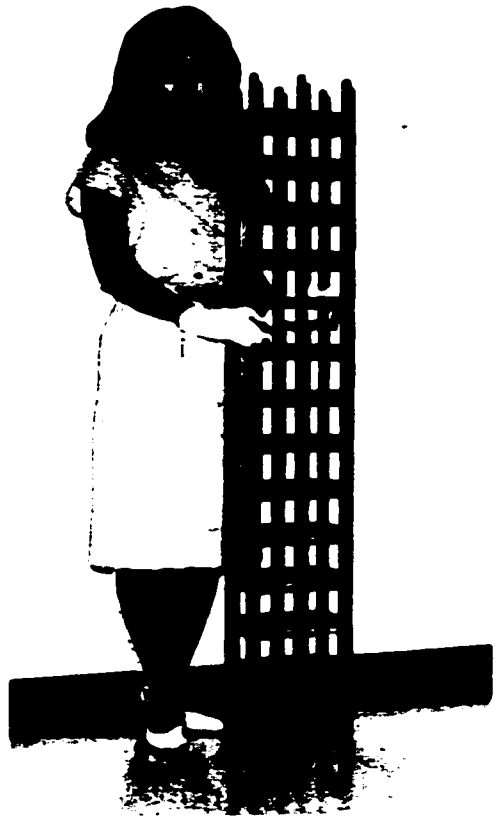

b) 3D-Grid

Figure 3-8: NEFMAC Grids

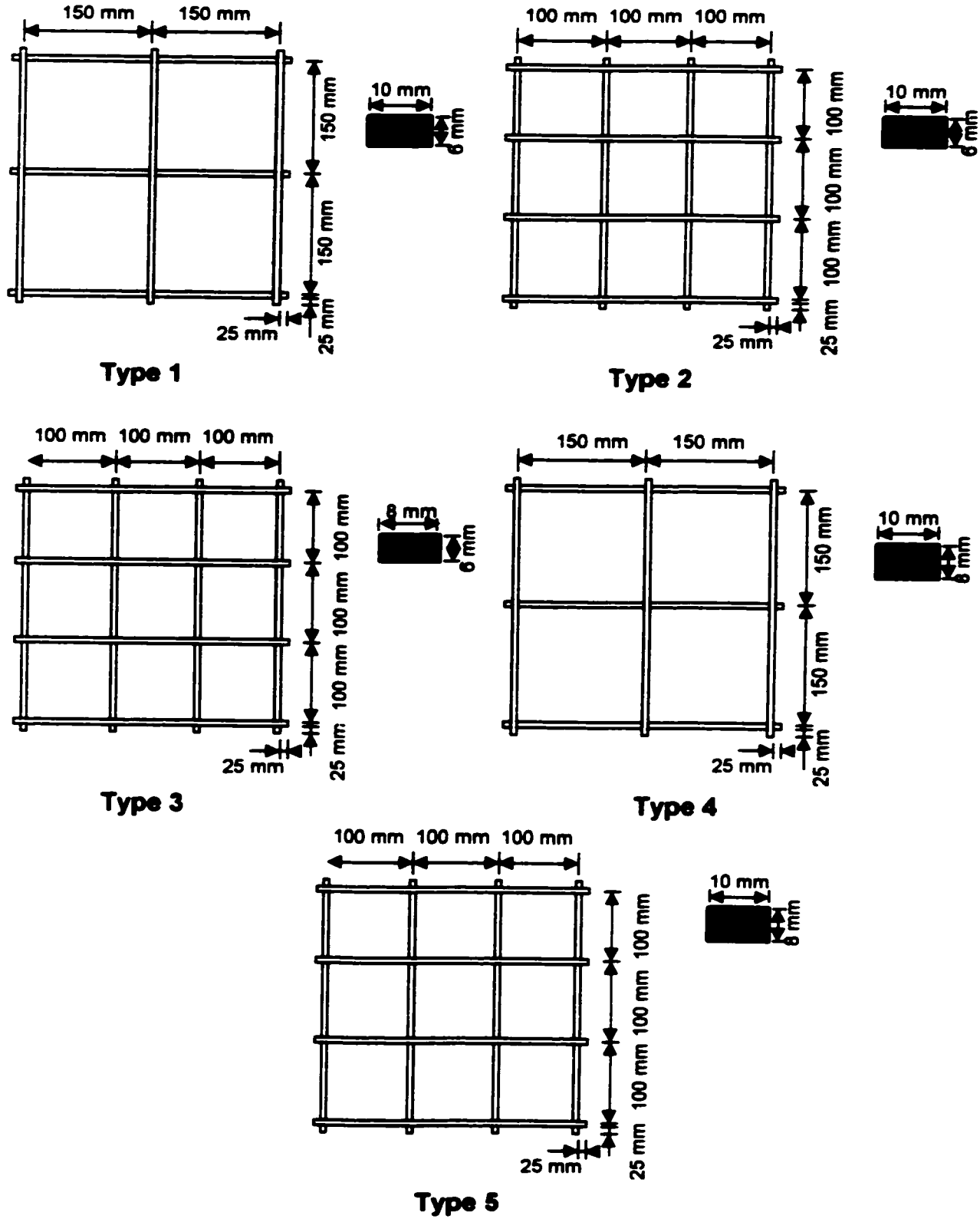

Figure 3-9: Geometric details of FRP grids used in the experimental investigation

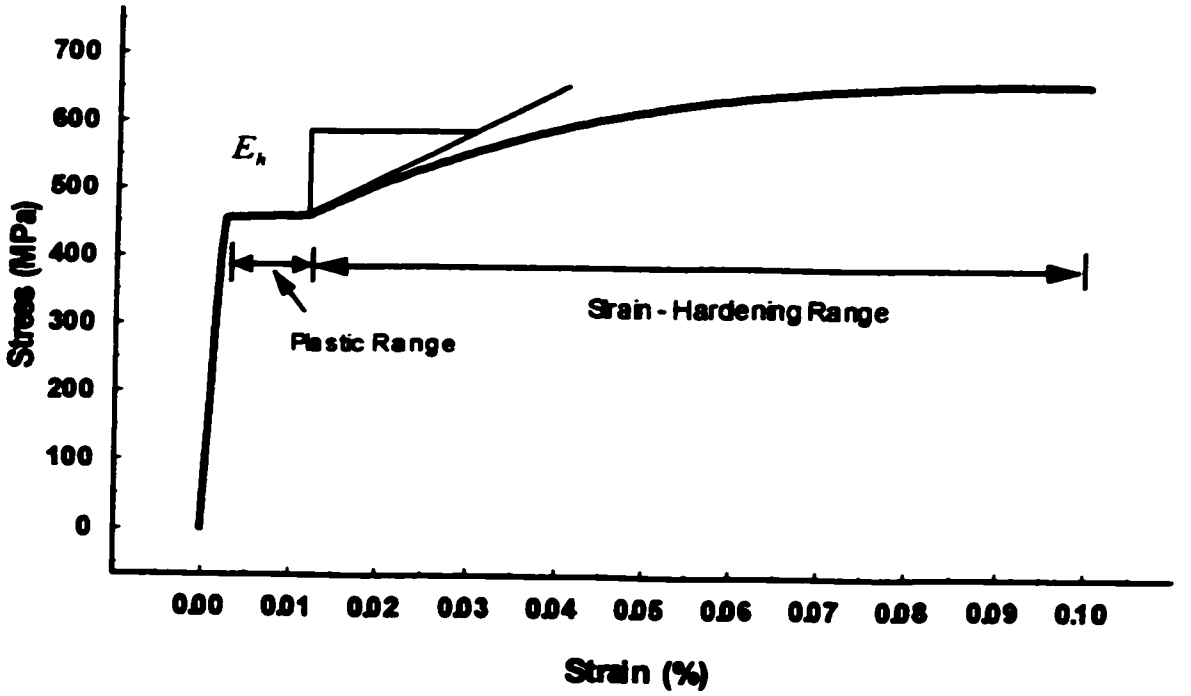

Figure 3-10: Typical stress-strain relationship of steel

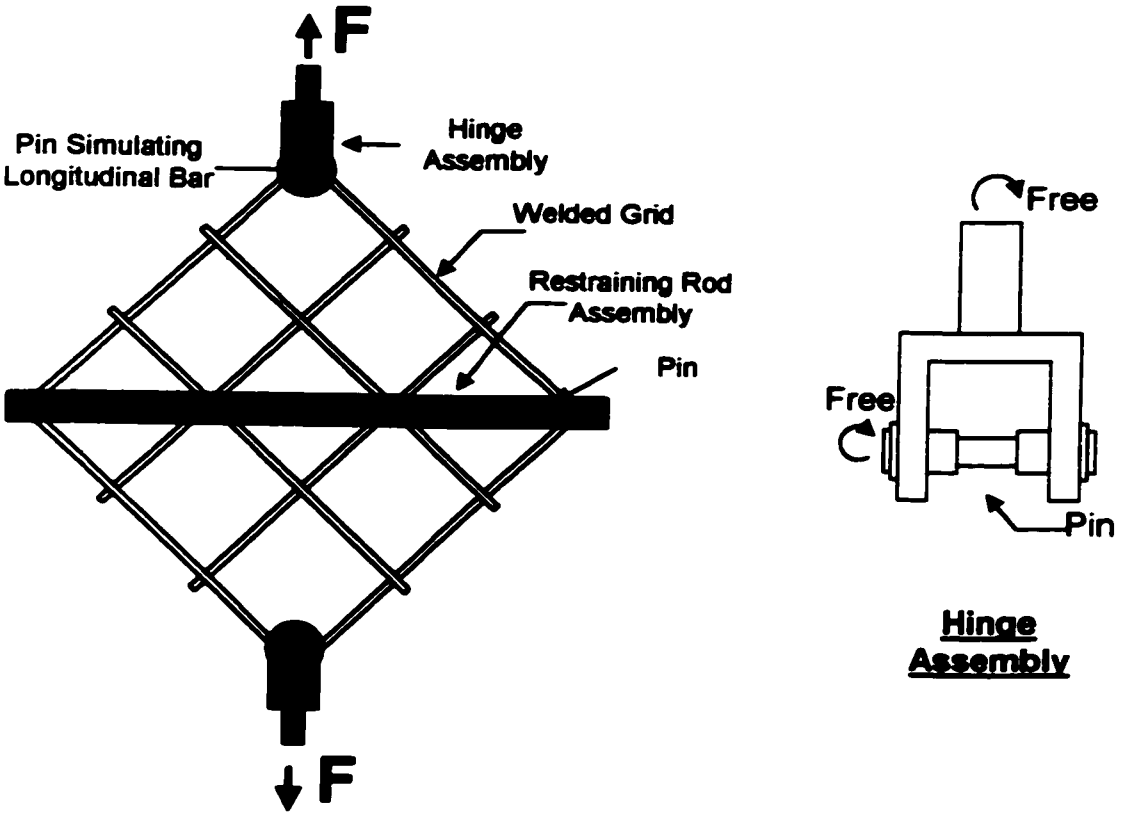

Figure 3-11: Bursting test setup

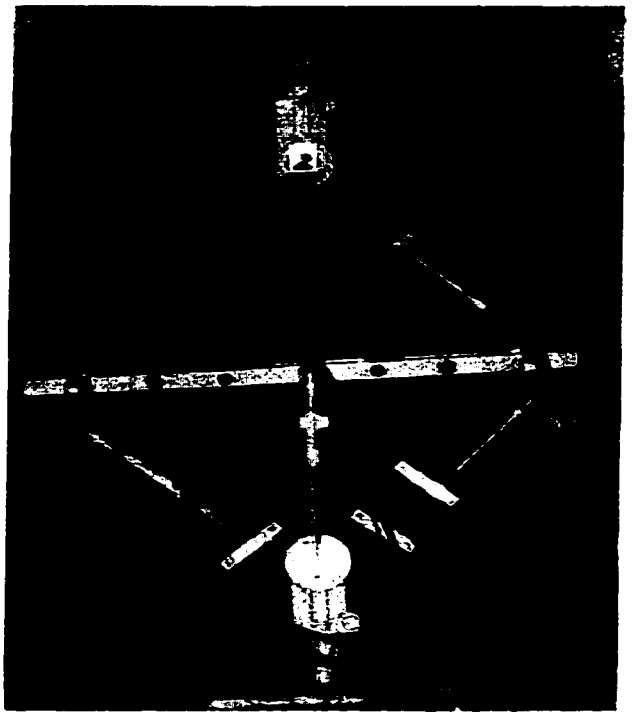

Figure 3-12: Bursting test setup with non-adjustable restraining rod assembly

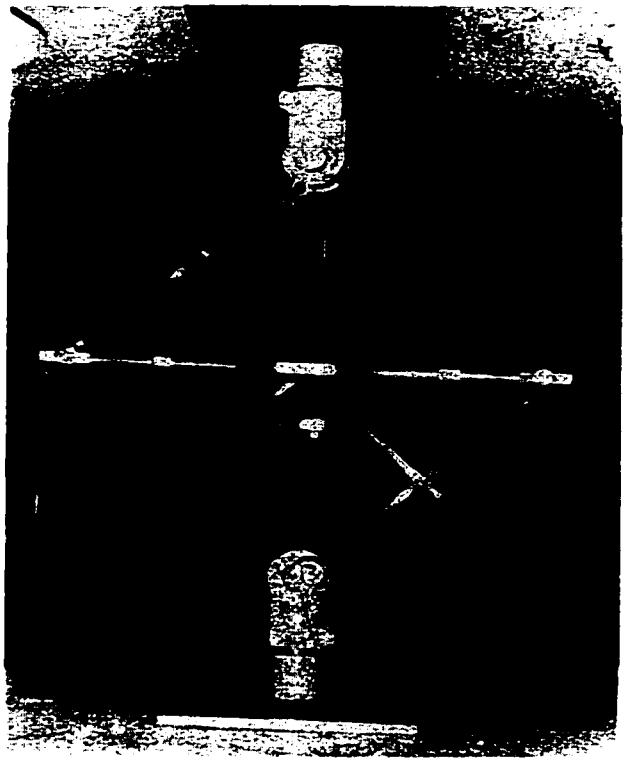

Figure 3-13: Bursting test setup with adjustable restraining rod assembly

Figure 3-14: View of testing machine and equipment for grid bursting test

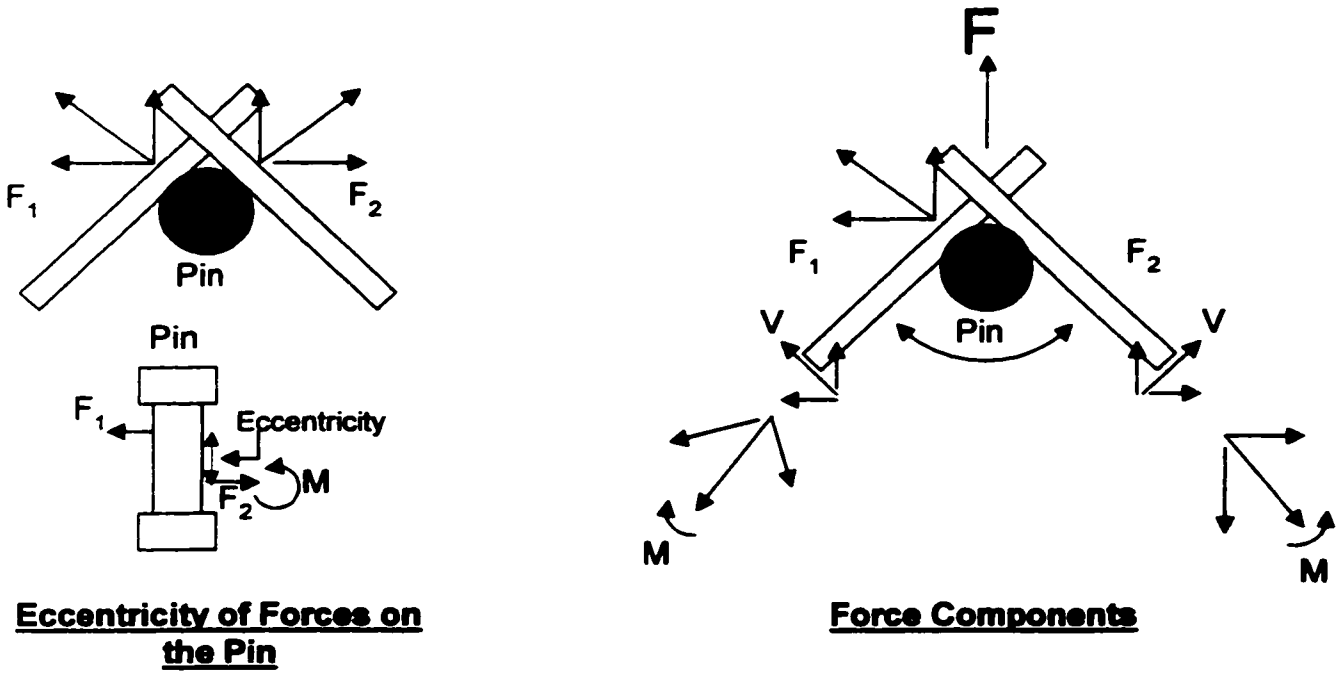

Figure 3-15: Eccentricity of forces and force components

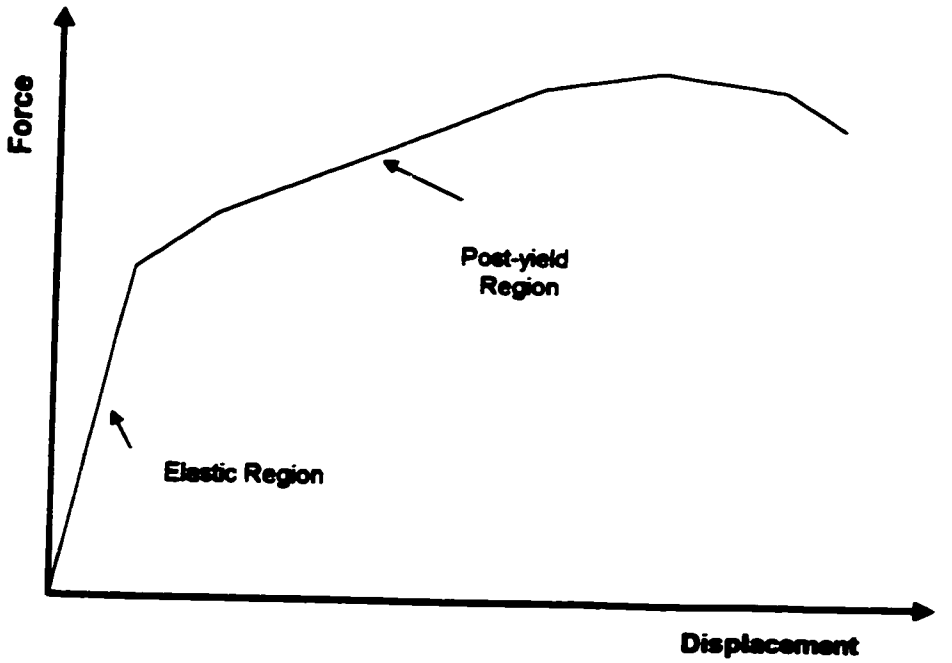

Figure 3-16: Typical diagonal force-diagonal displacement relationship obtained from a bursting test

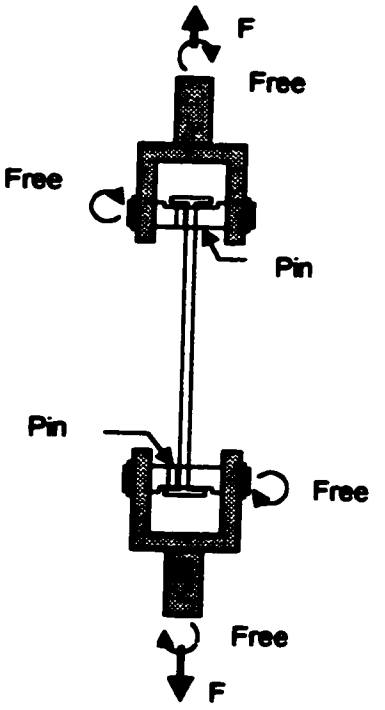

Figure 3-17: Pull-Out test setup

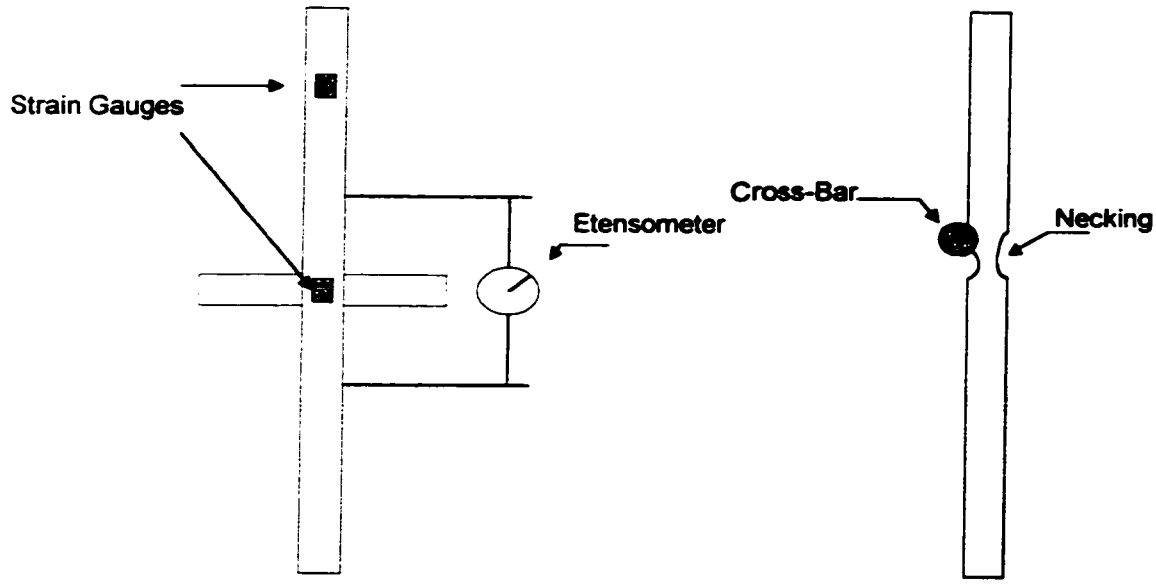

a) Instrumentation of a typical WRG coupon

b) location of "Necking"

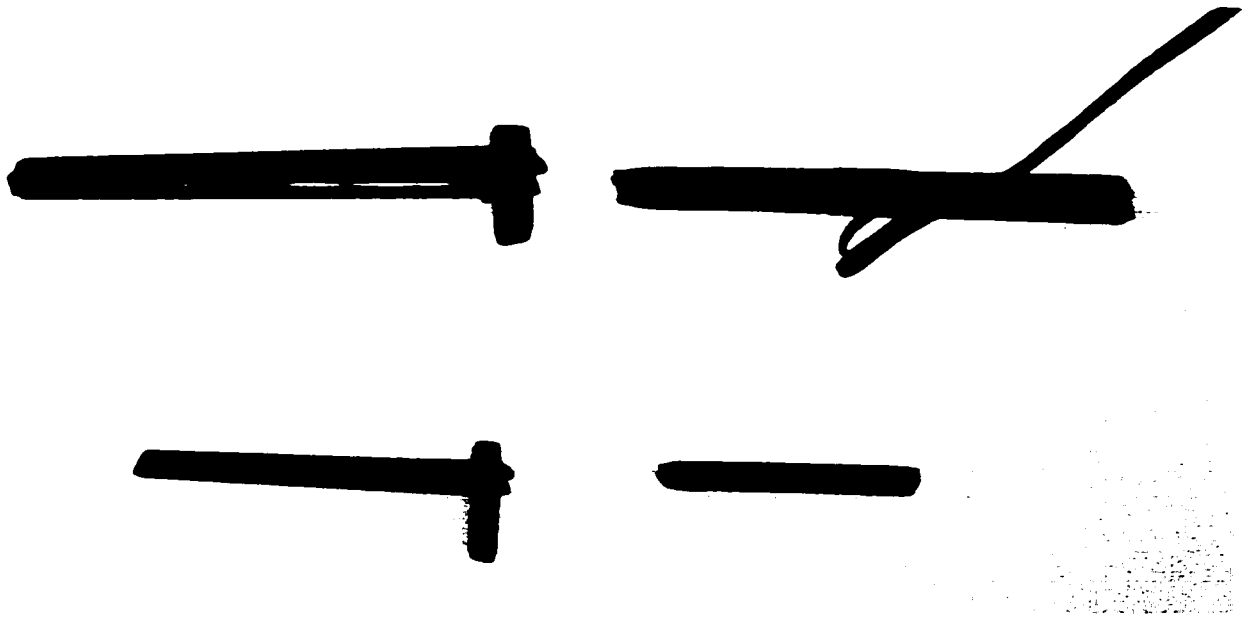

c) Typical coupon failures

Figure 3-18: Instrumentation of a typical WRG coupon and location of "Necking"

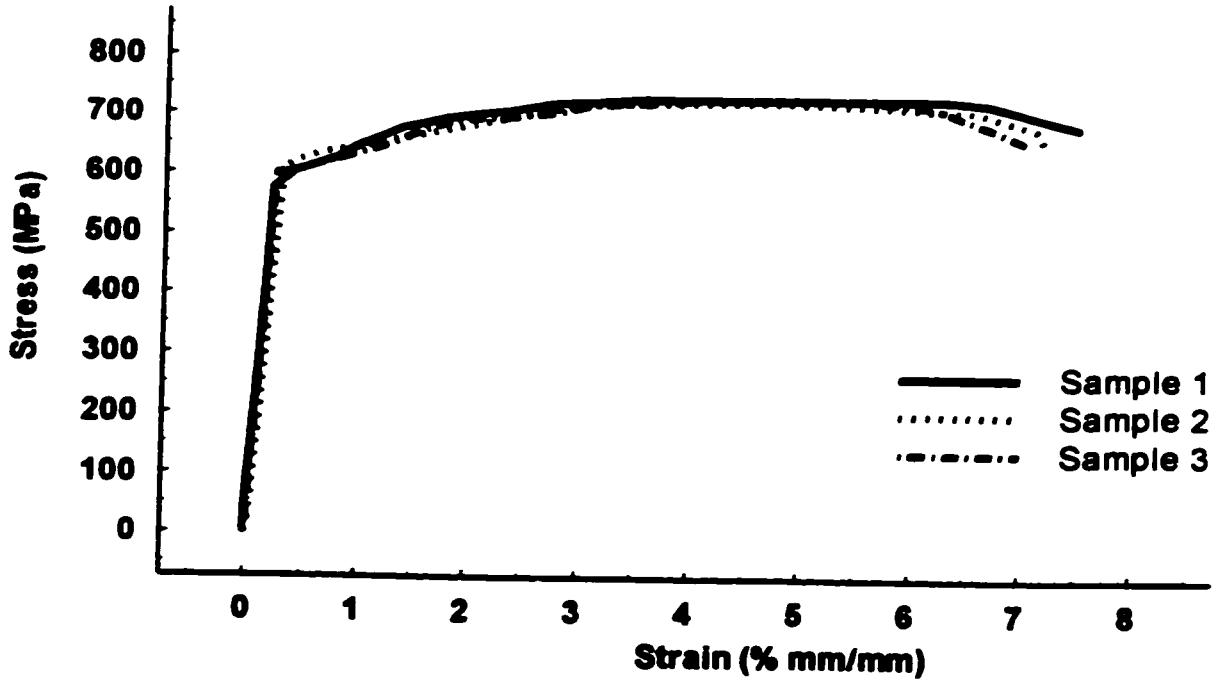

a) Monotonic load

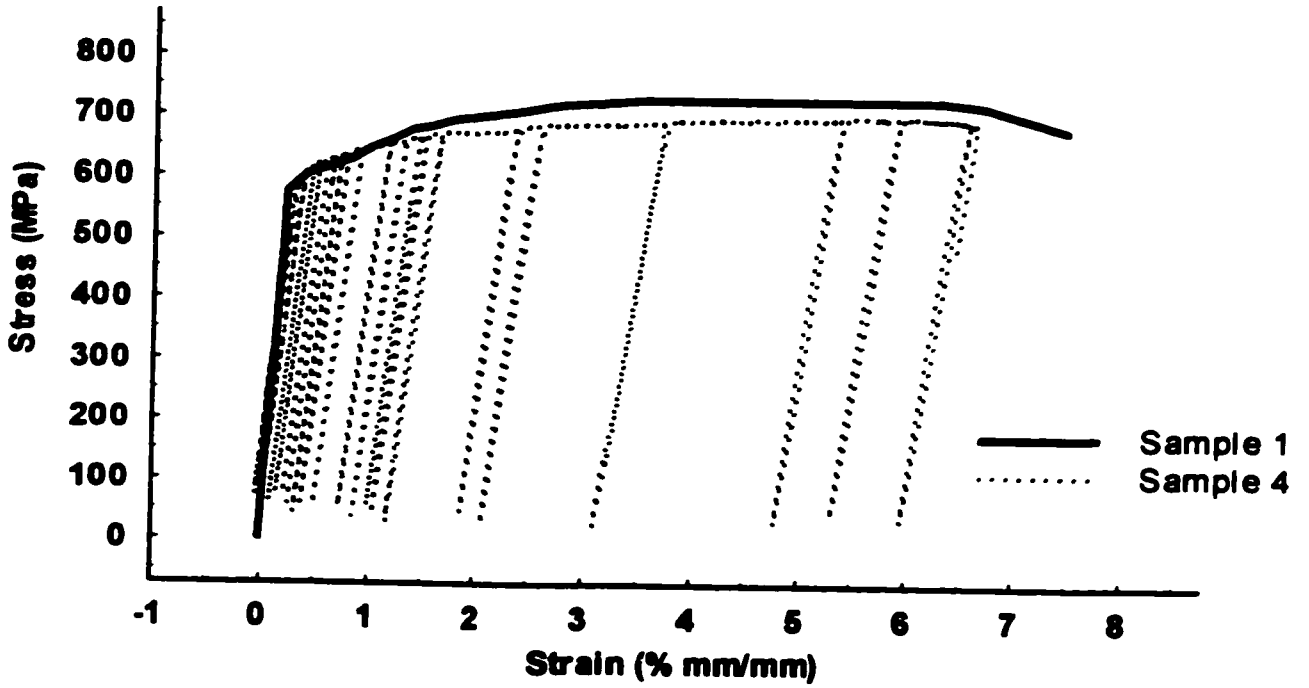

a) Cyclic load

Figure 3-19: Stress-strain relationship of 6.6 mm (1/4 in.) WRG steel coupon

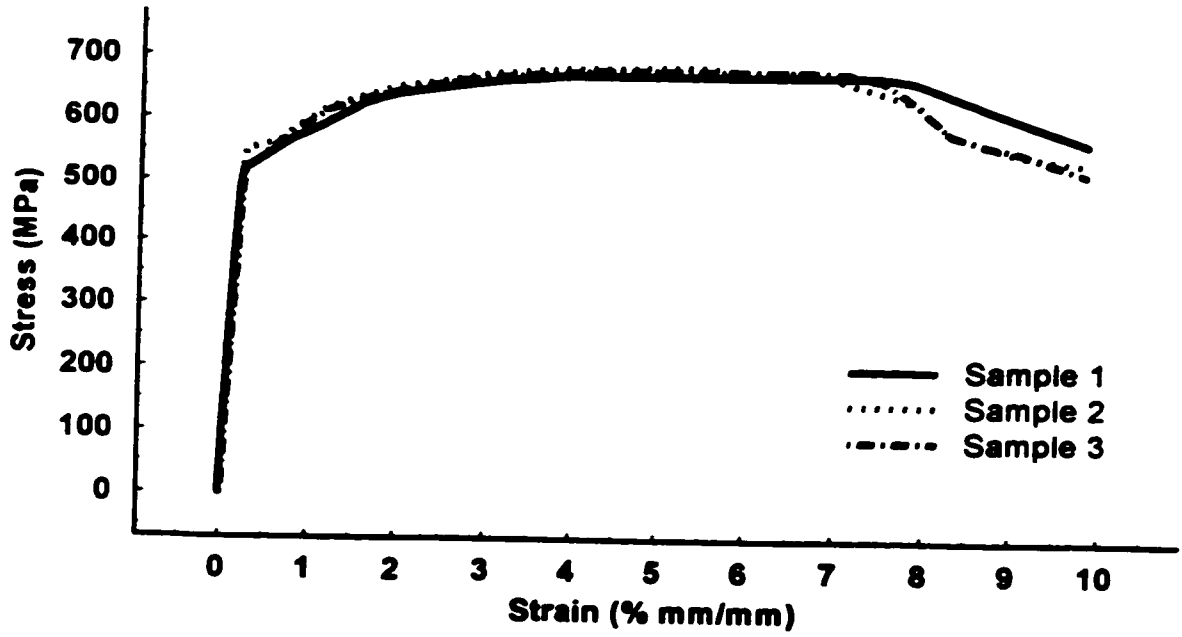

a) Monotonic Load

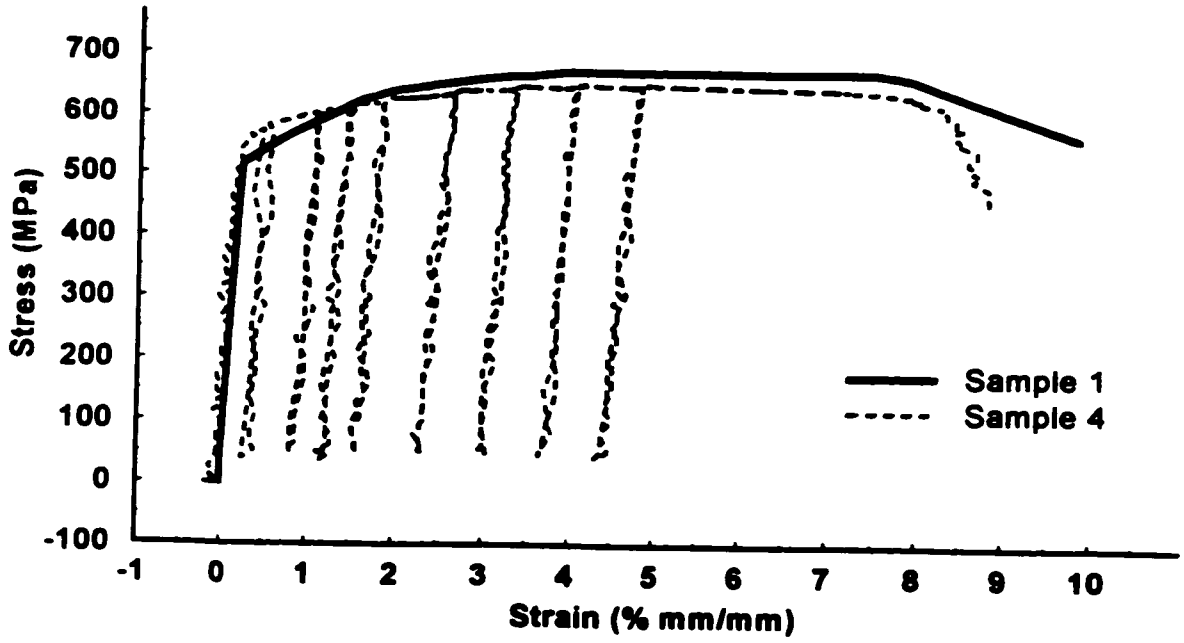

b) Cyclic load

Figure 3-20: Stress-strain relationship of 9.5 mm (3/8 in.) WRG steel coupon

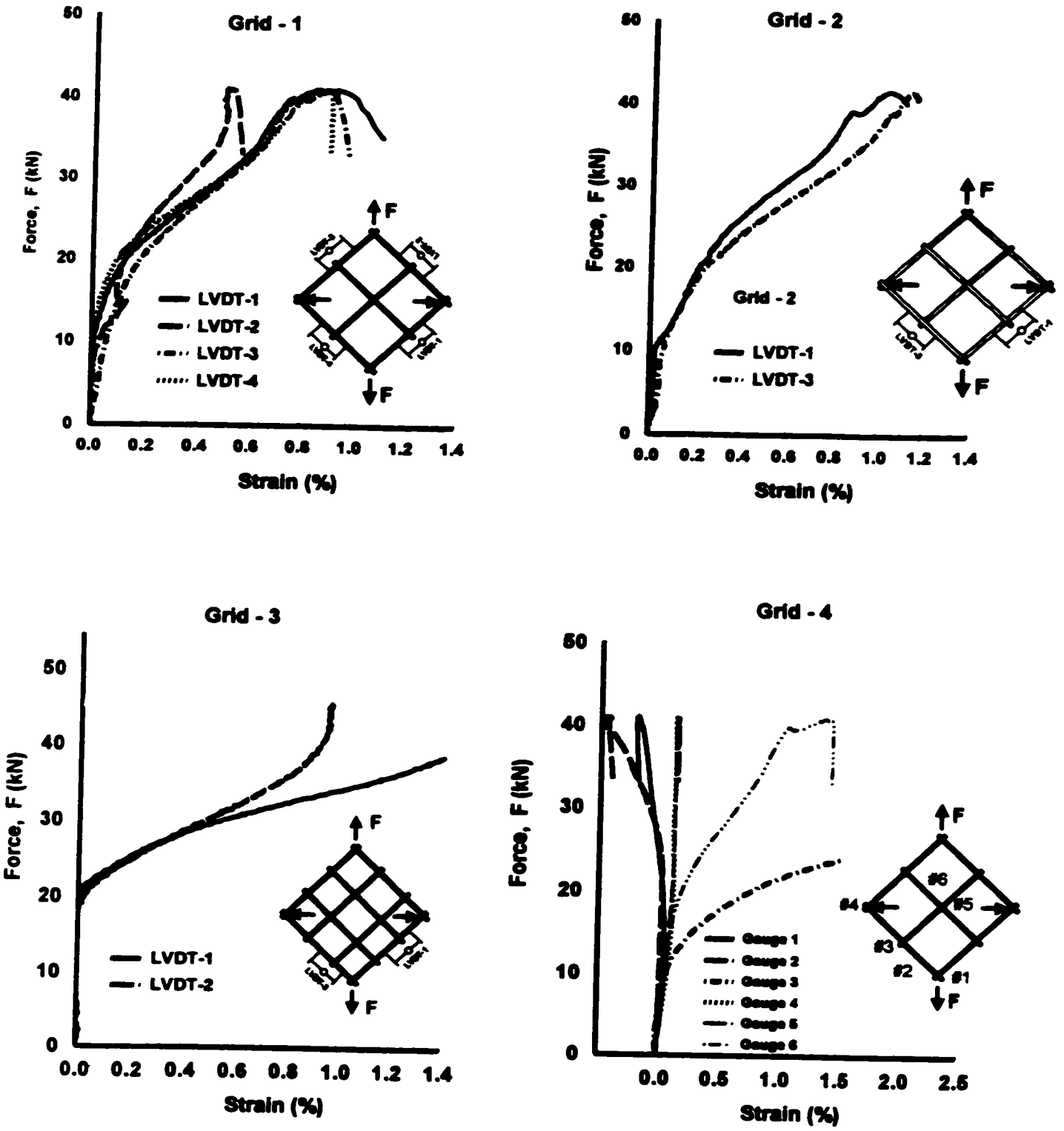

Figure 3-21: Steel strain recorded on WRG during bursting test

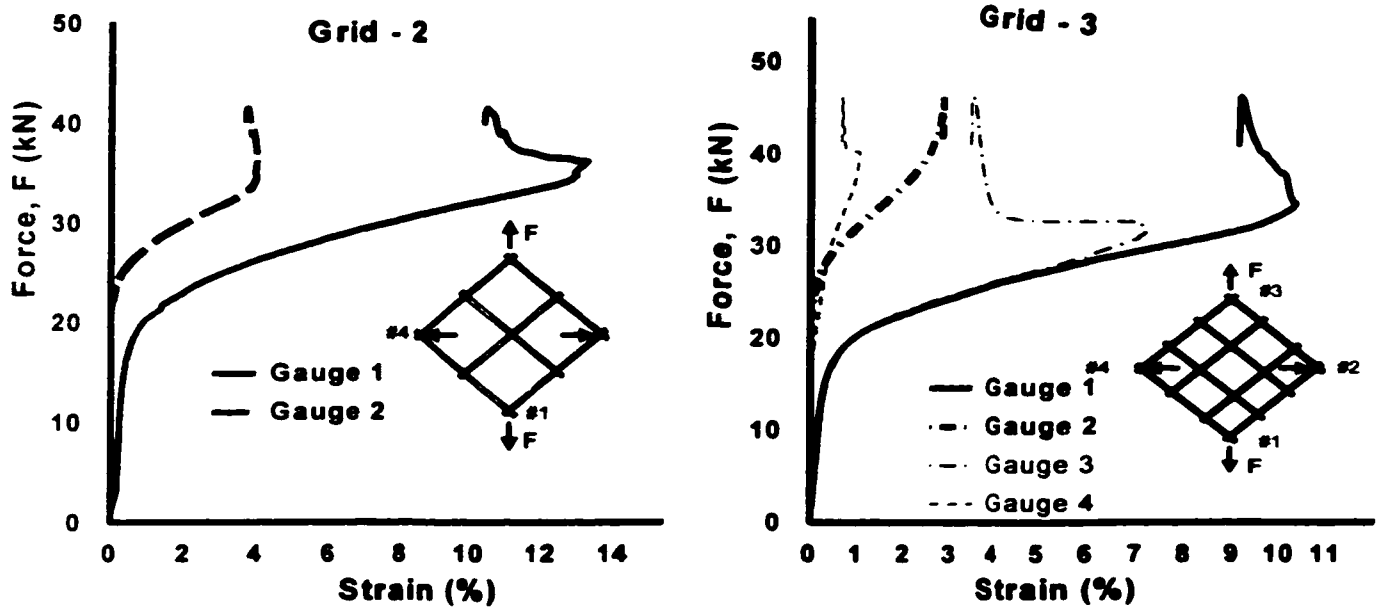

Figure 3-21: Cont.

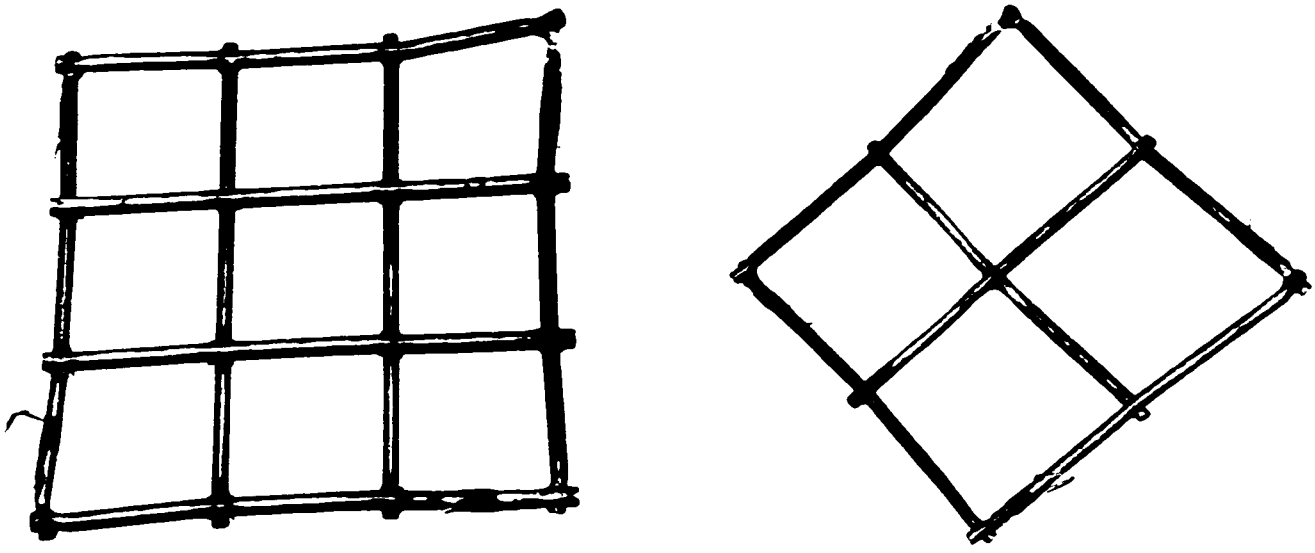

A 9-Cell Grid

A 4-Cell Grid

Figure 3-22: Fracturing of 9.53 mm (3/8in.) diameter steel WRG during bursting tests

A 9-cell grid

A 4-cell grid

Figure 3-23: Close-up of 9.53 mm (3/8in.) diameter steel rupture during bursting tests

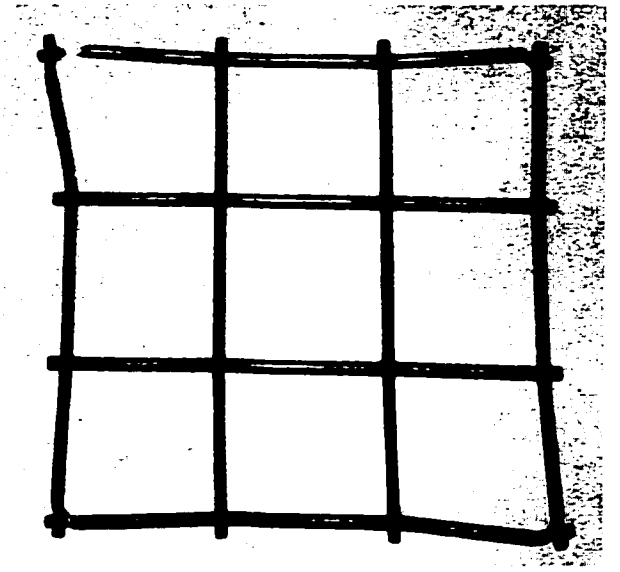

Overall view

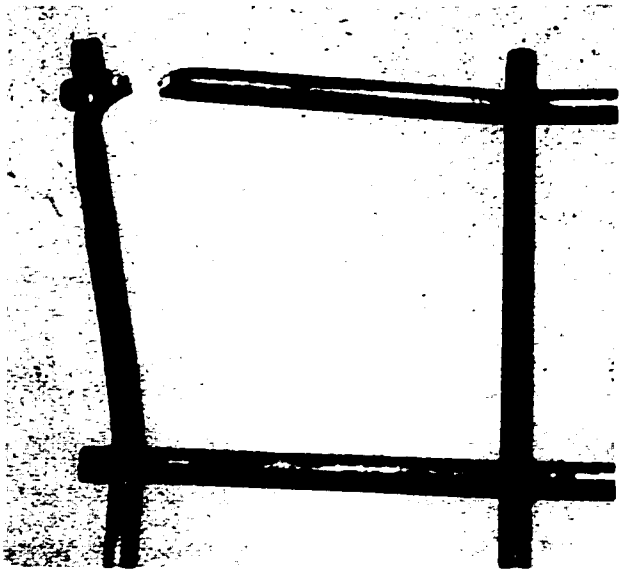

Close-up view

Figure 3-24: Close-up of 9.53 mm (3/8in.) diameter steel rupture during bursting tests

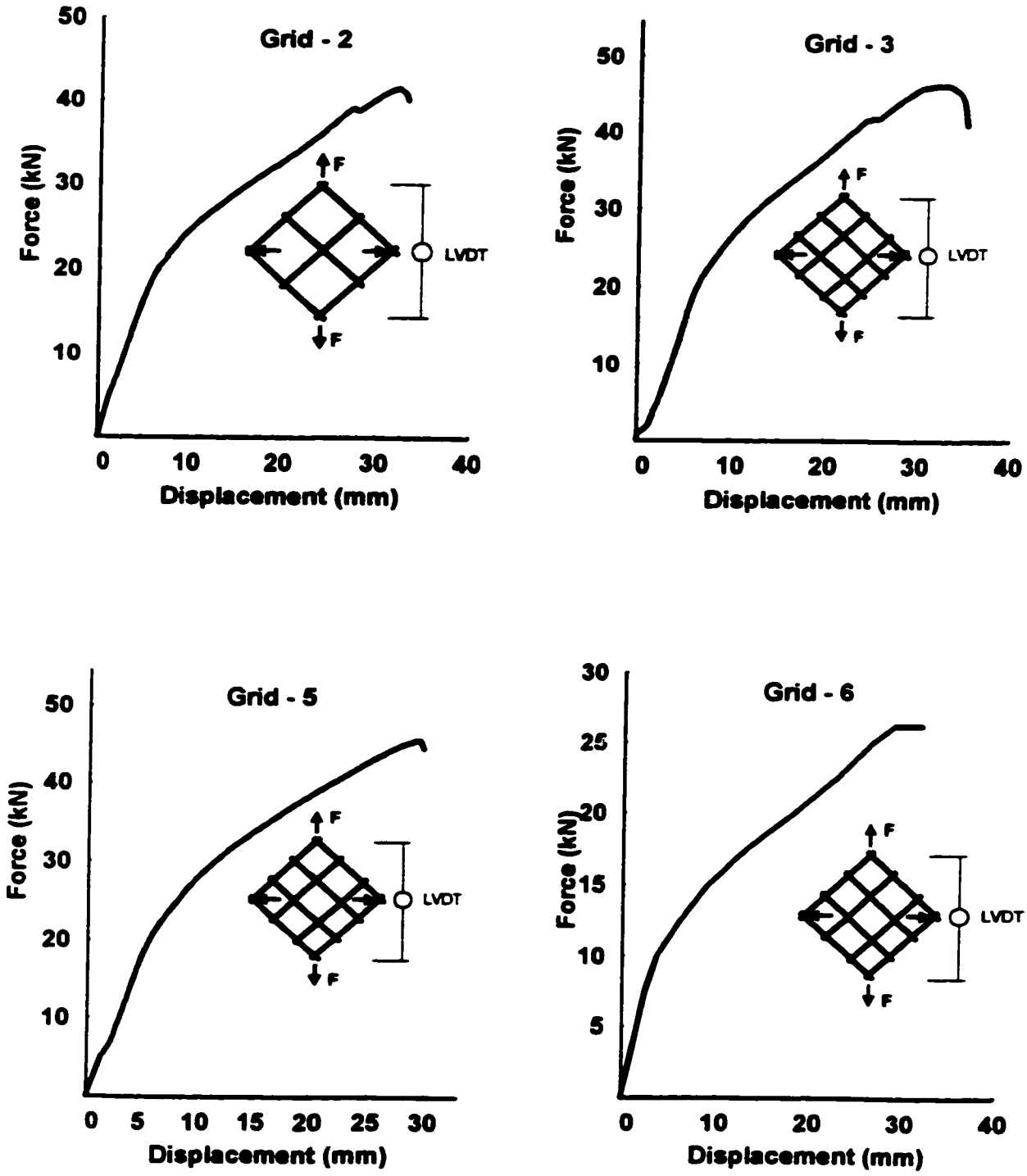

Figure 3-27: Diagonal force displacement relationships of WRG during bursting tests

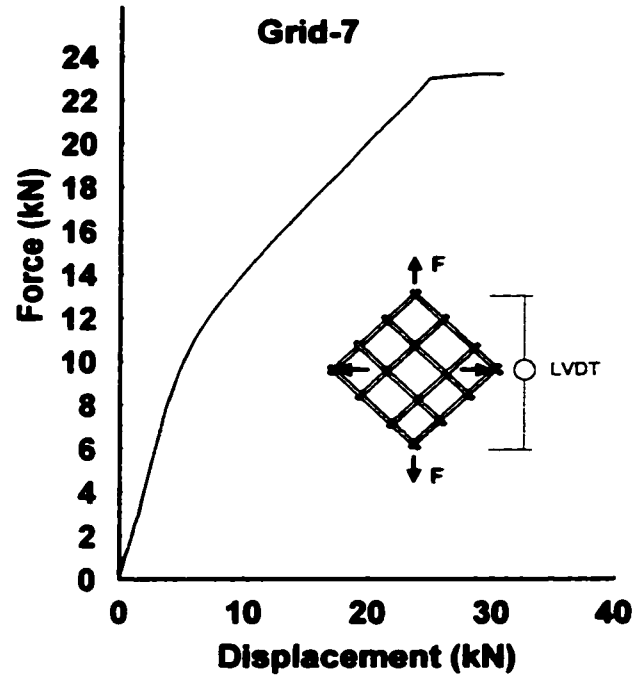

Figure 3-27: Cont.

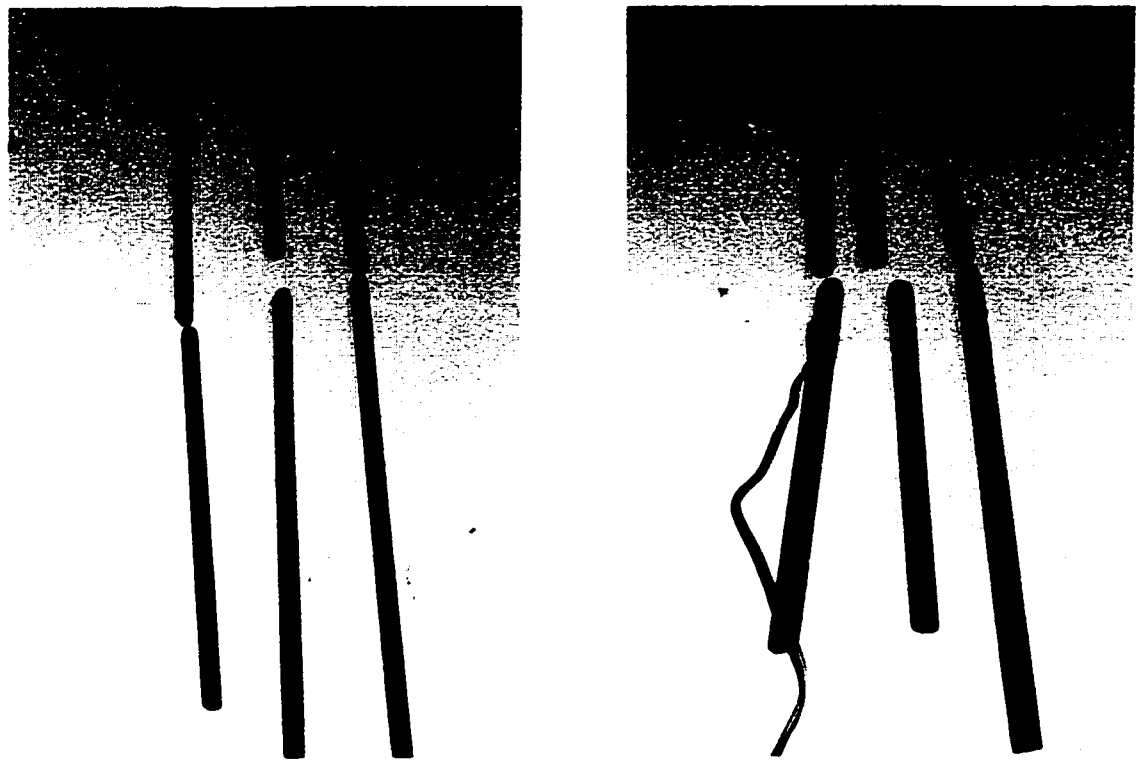

Figure 3-28: Test coupons of Double Headed Studs

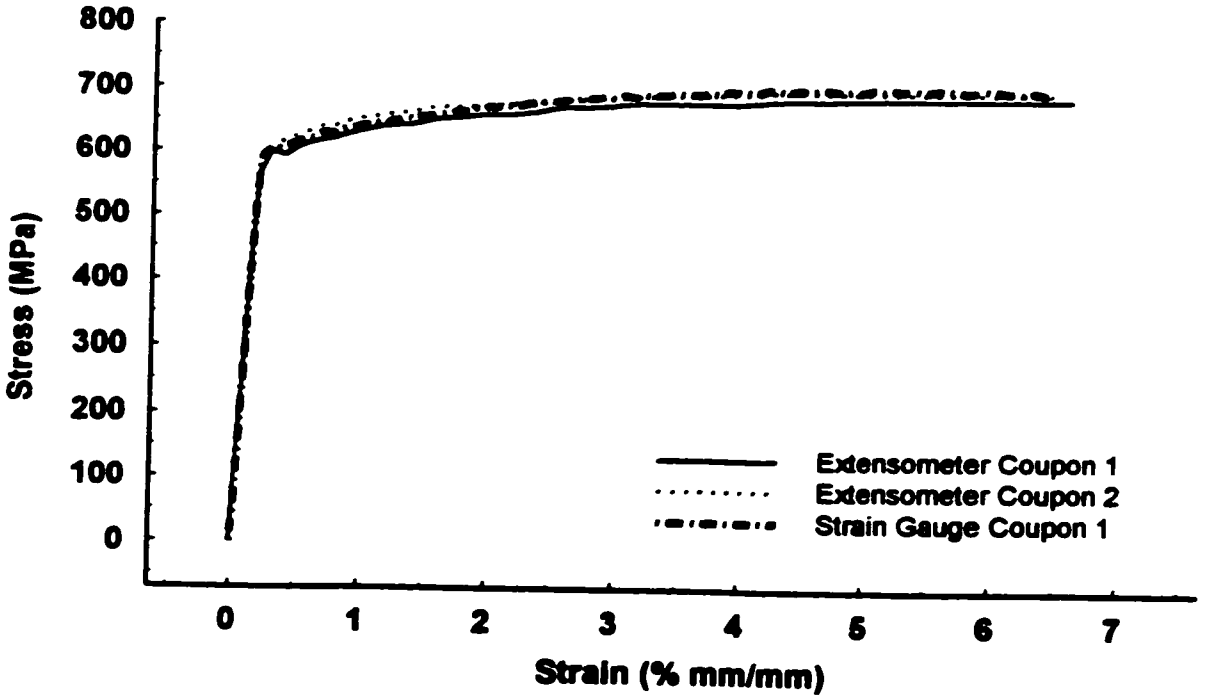

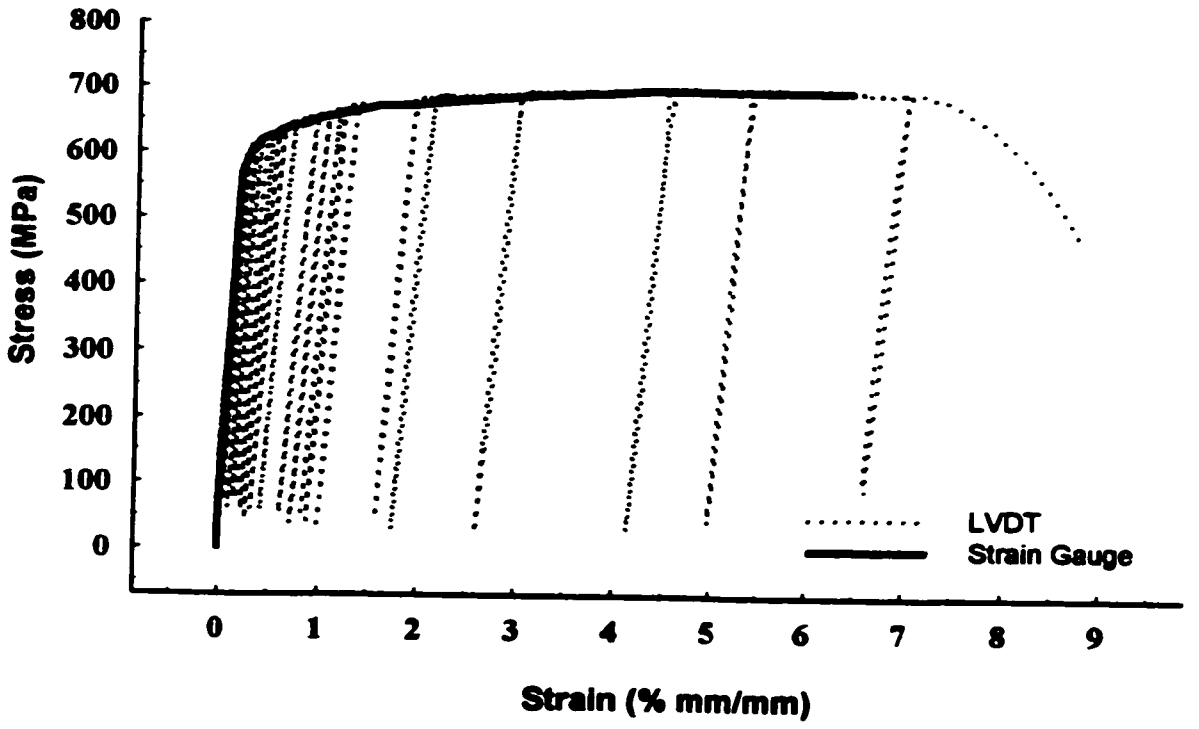

Figure 3-29: Stress-strain relationship of 6.6 mm (1/4 in) double-headed stud

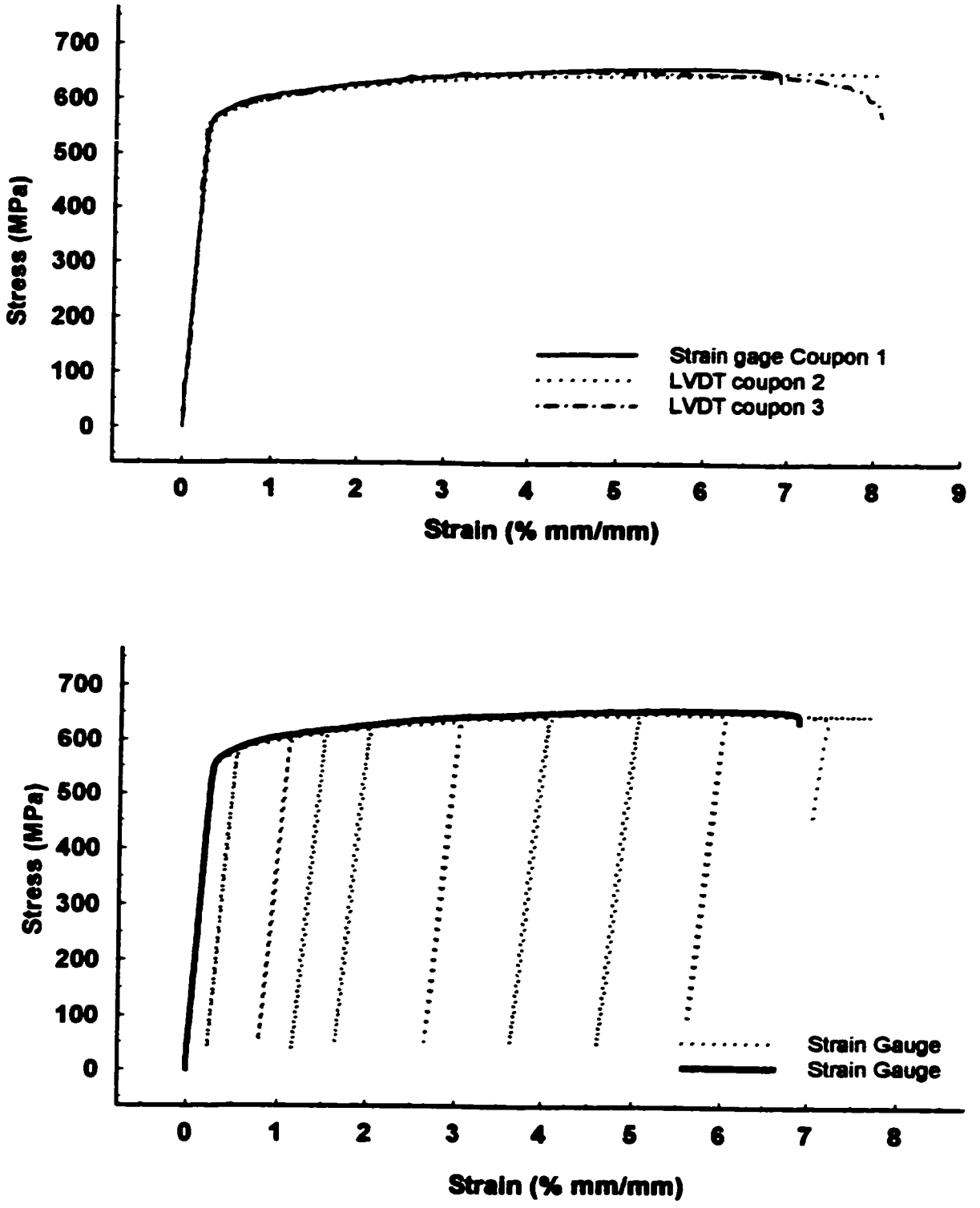

Figure 3-30: Stress-strain relationship of 9.5 mm (3/8in.) Double Headed Stud

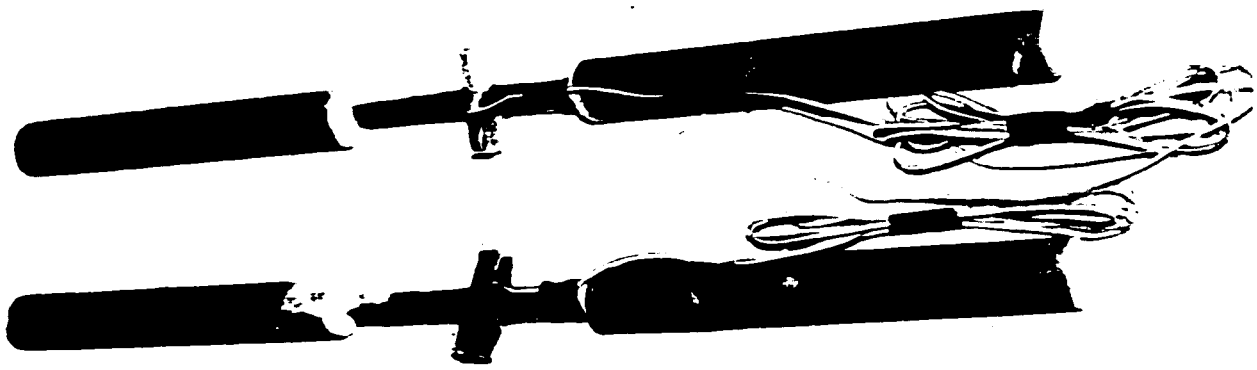

Figure 3-31: FRP coupons with ends cast in steel pipes

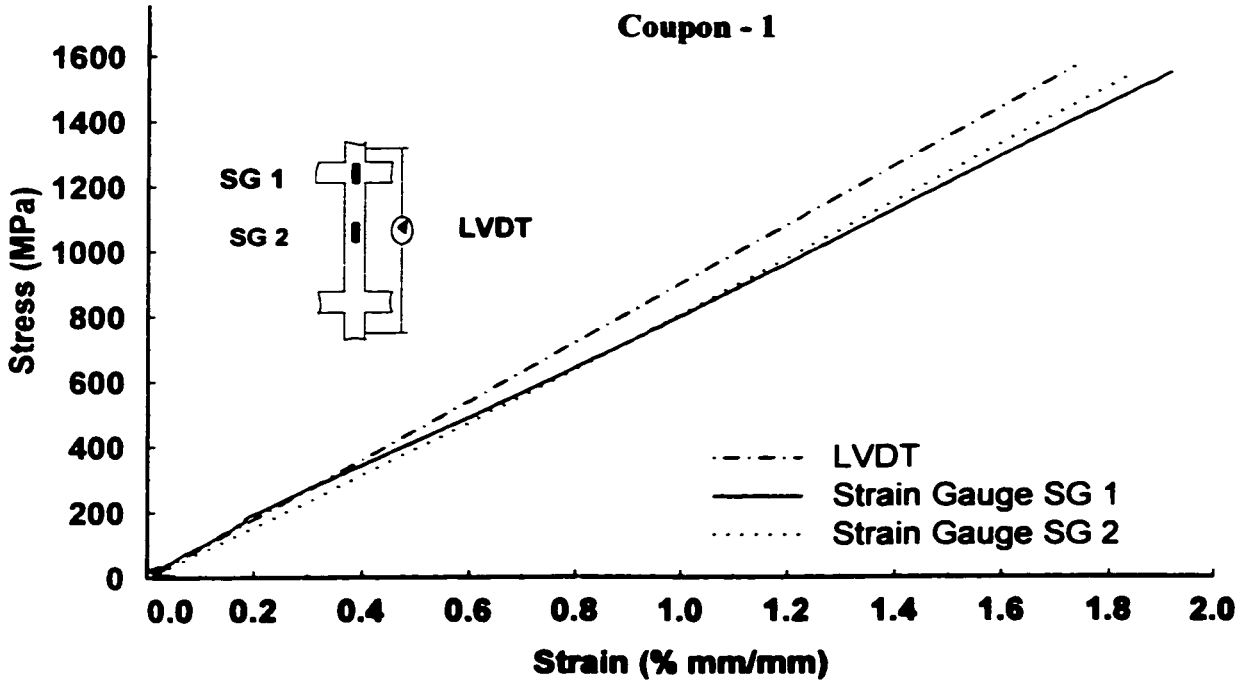

Figure 3-32: Stress-strain relationship of FRP coupons

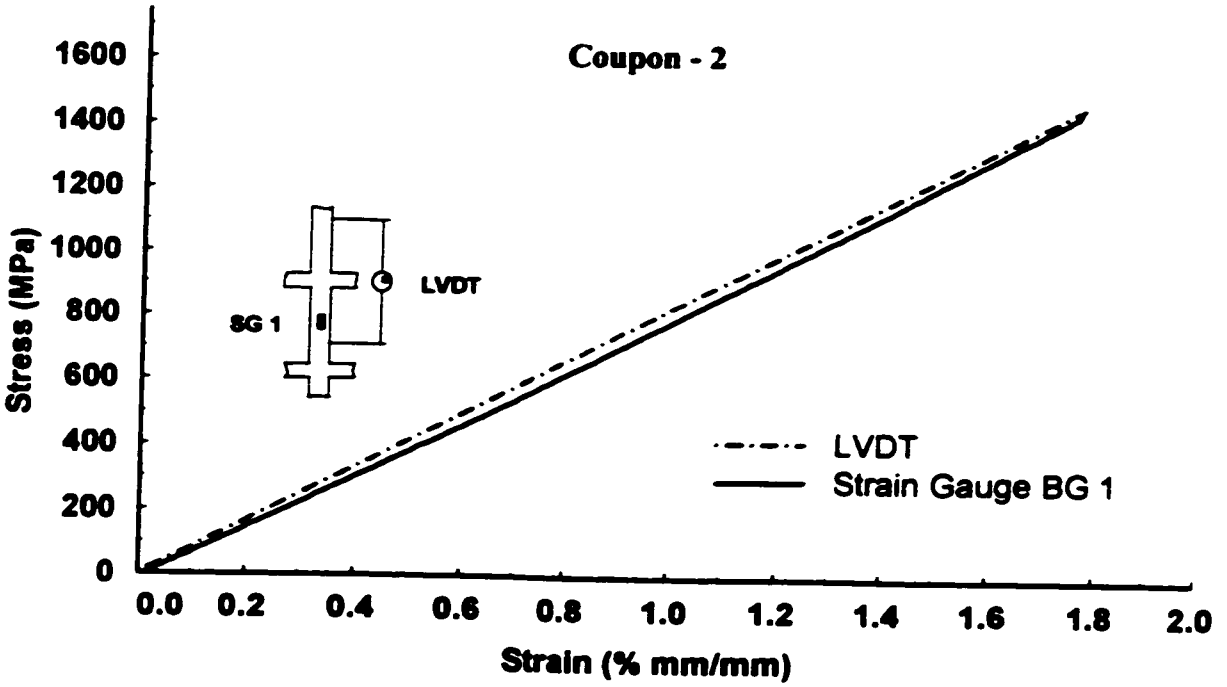

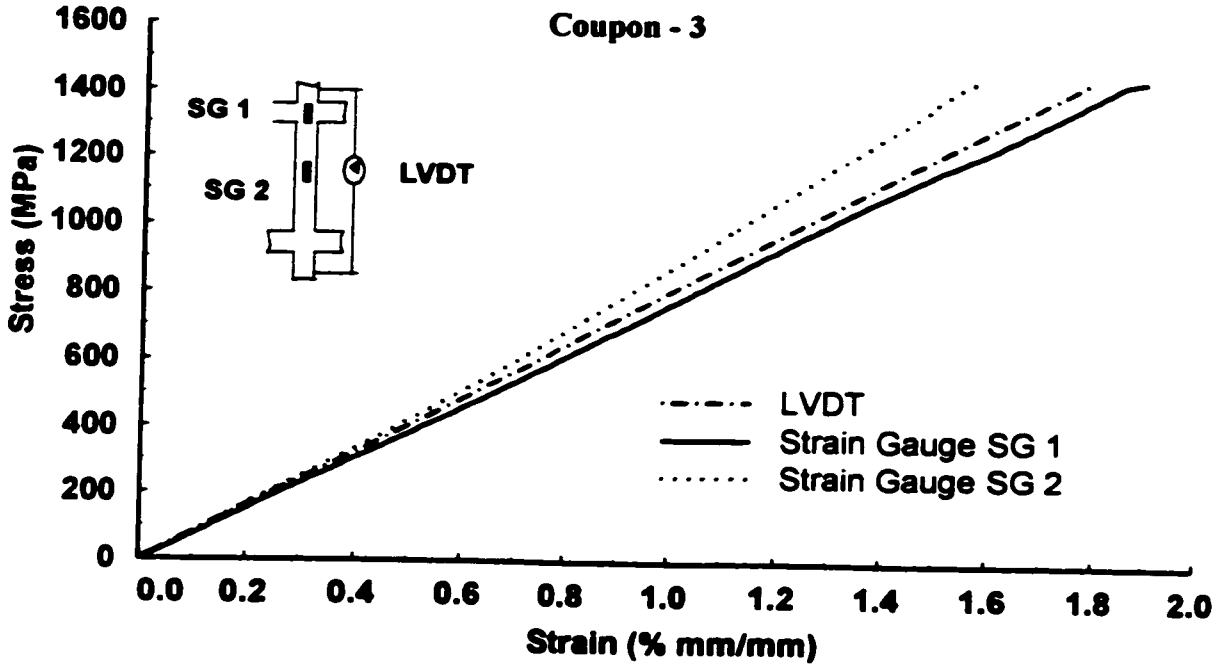

Figure 3-32: Cont.

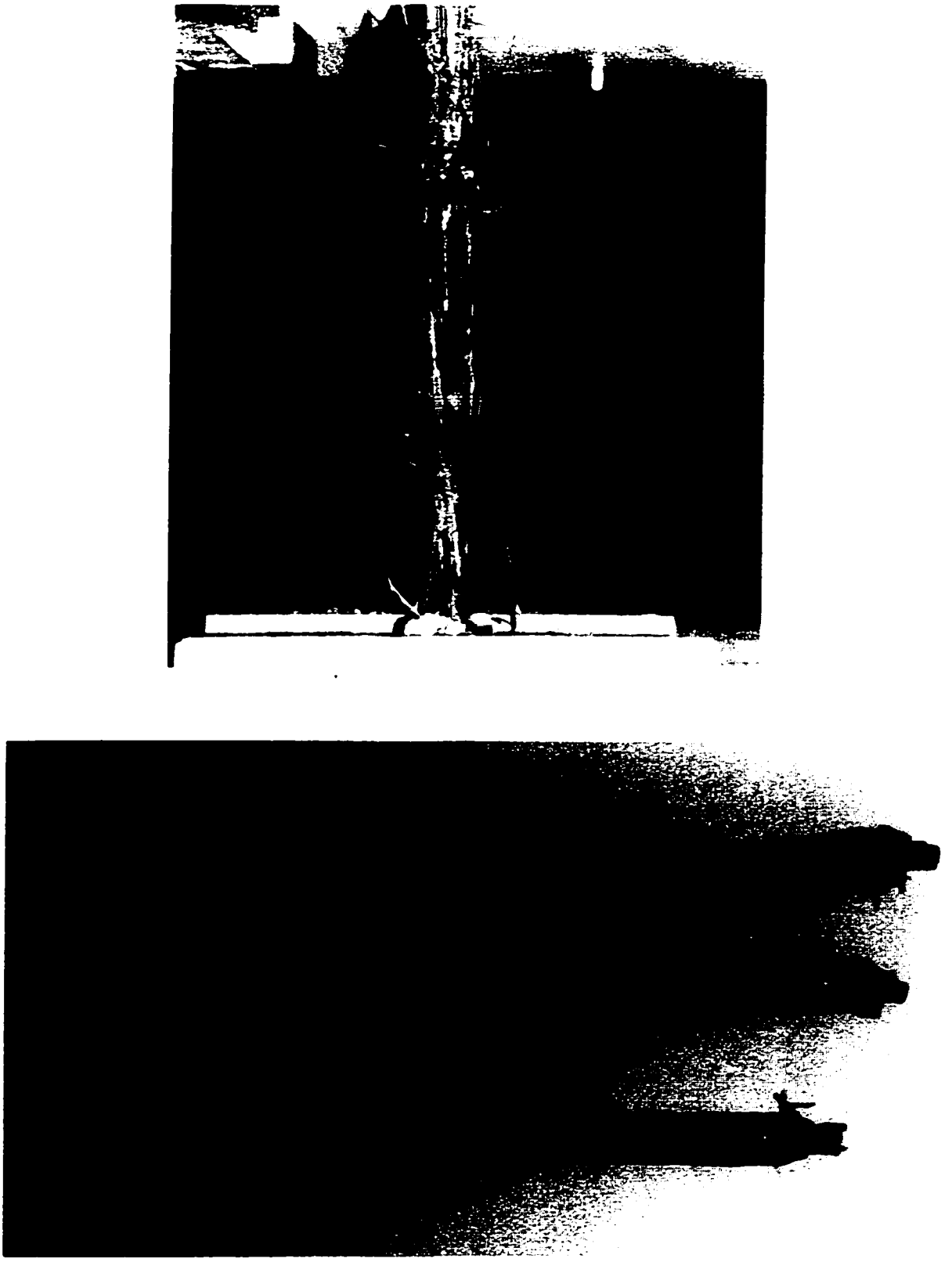

Figure 3-33: Typical FRP Coupon failures

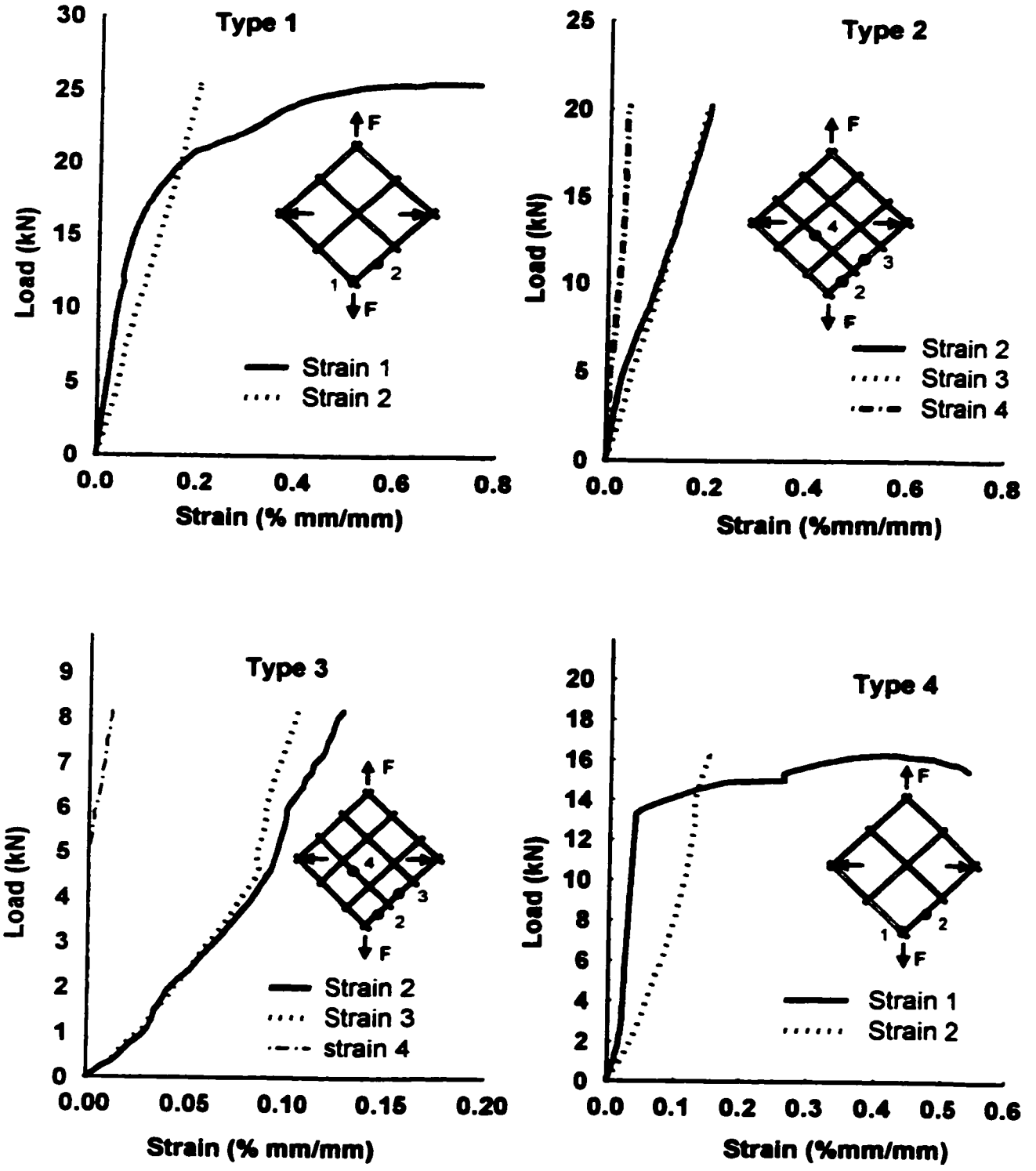

Figure 3-34: Strains recorded by strain gauges during bursting tests of FRP grids

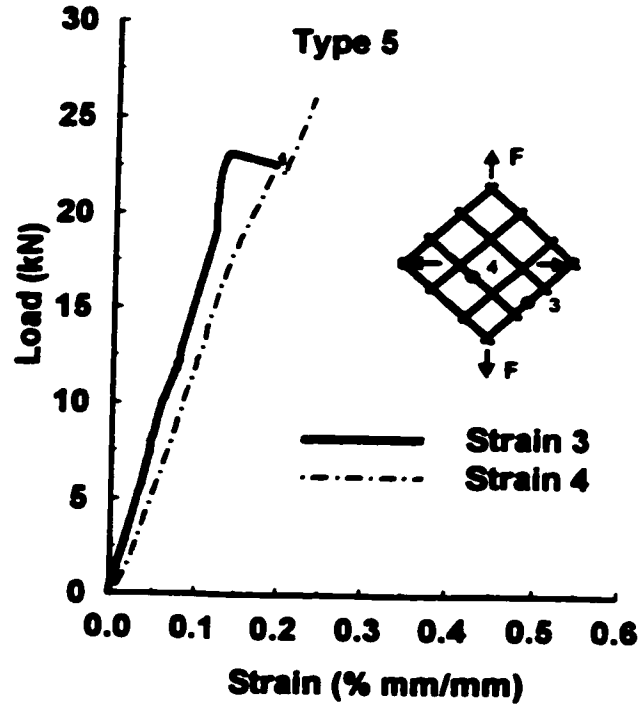

Figure 3-34: Cont.

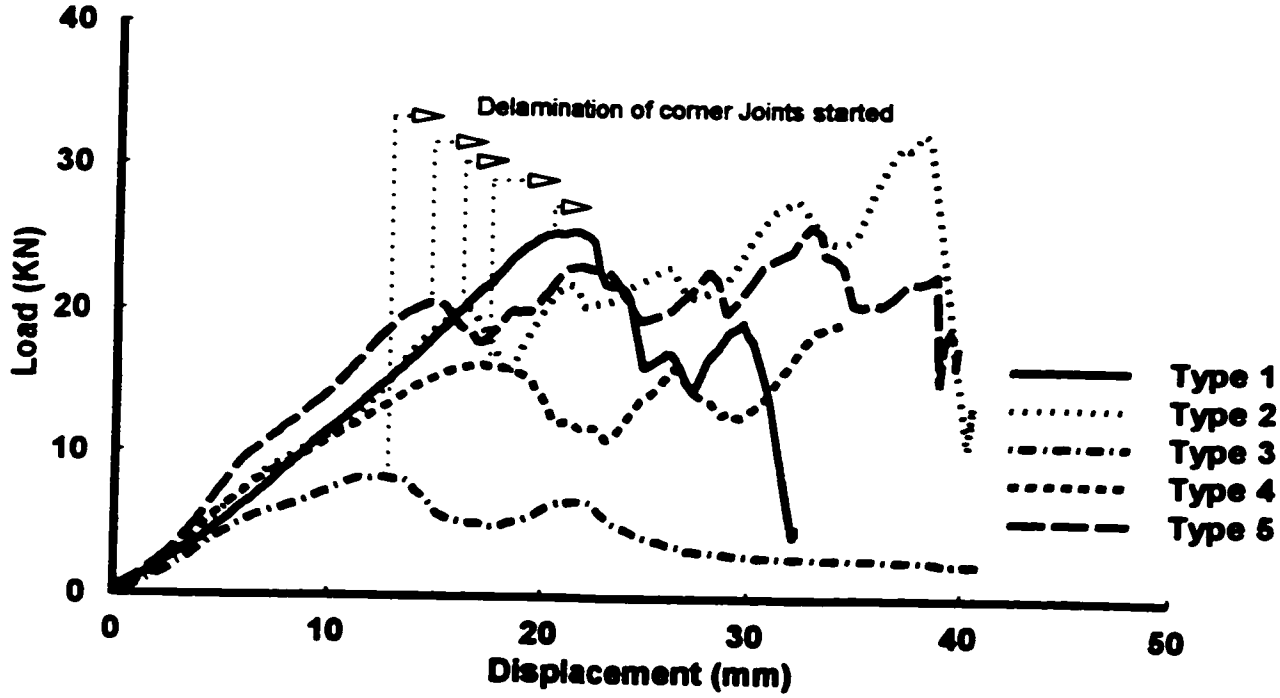

Figure 3-35: Diagonal force – diagonal displacement relationships of FRP grids

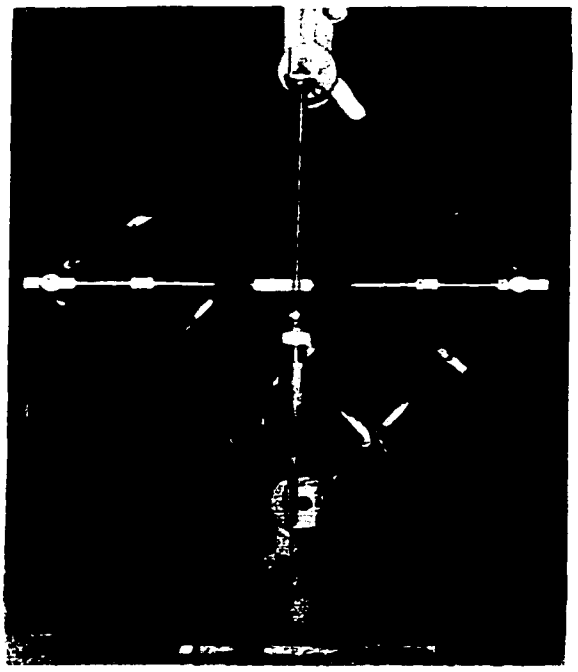

a) Deflected shape of the grid

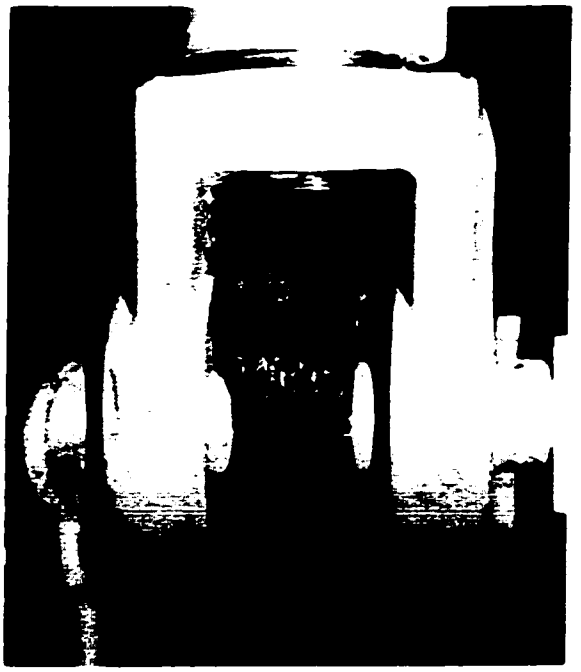

b) Close-up view of top grid corner

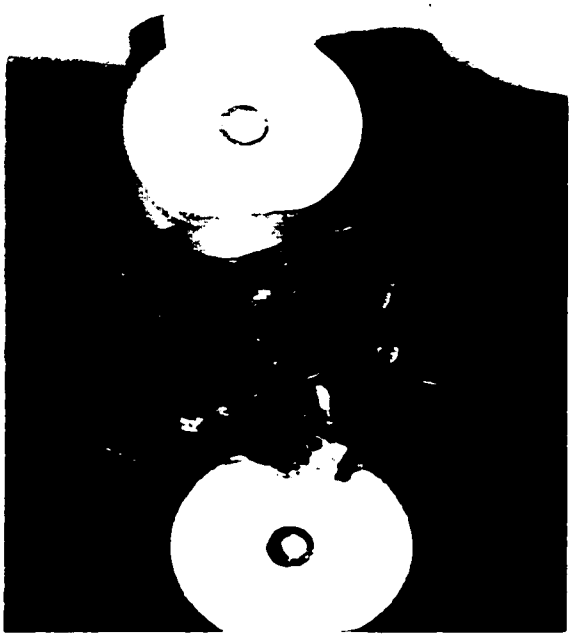

c) Close-up view of left grid corner

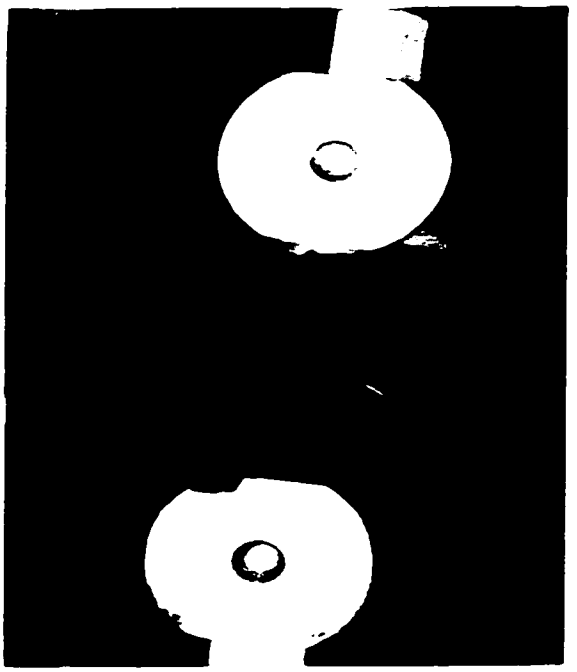

d) Close-up view of right grid corner

Figure 3-36: a) Fracturing of FRP grids during bursting tests

Figure 3-36: b) Behavior of FRP grids during columns tests

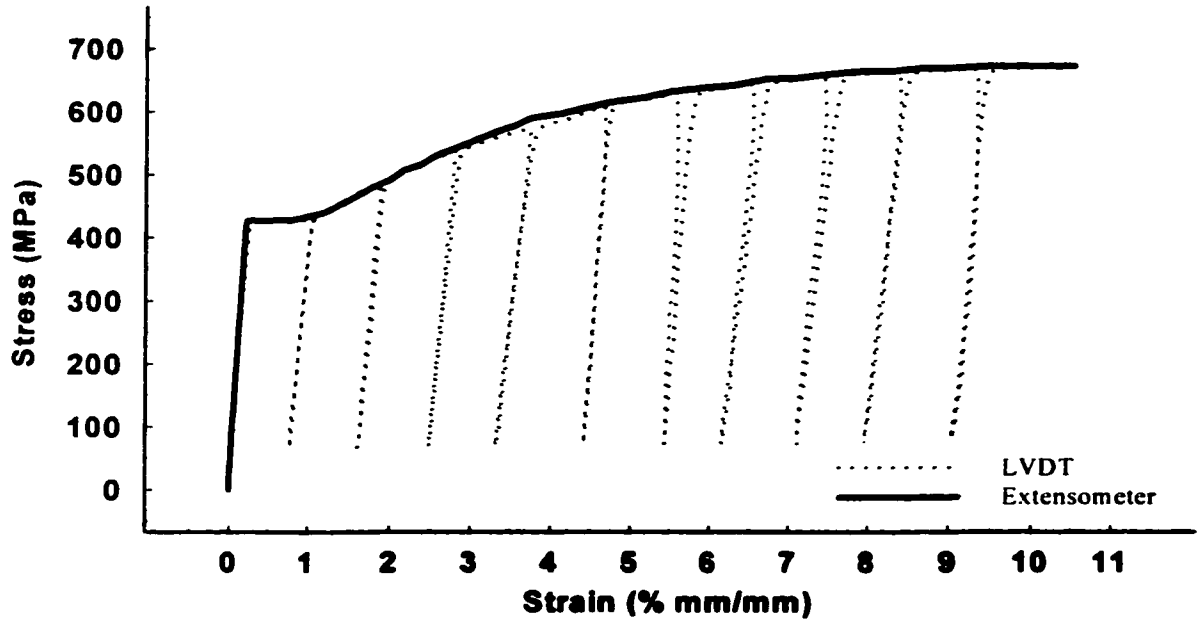

Figure 3-37: Stress – strain relationship of # 15 rebar

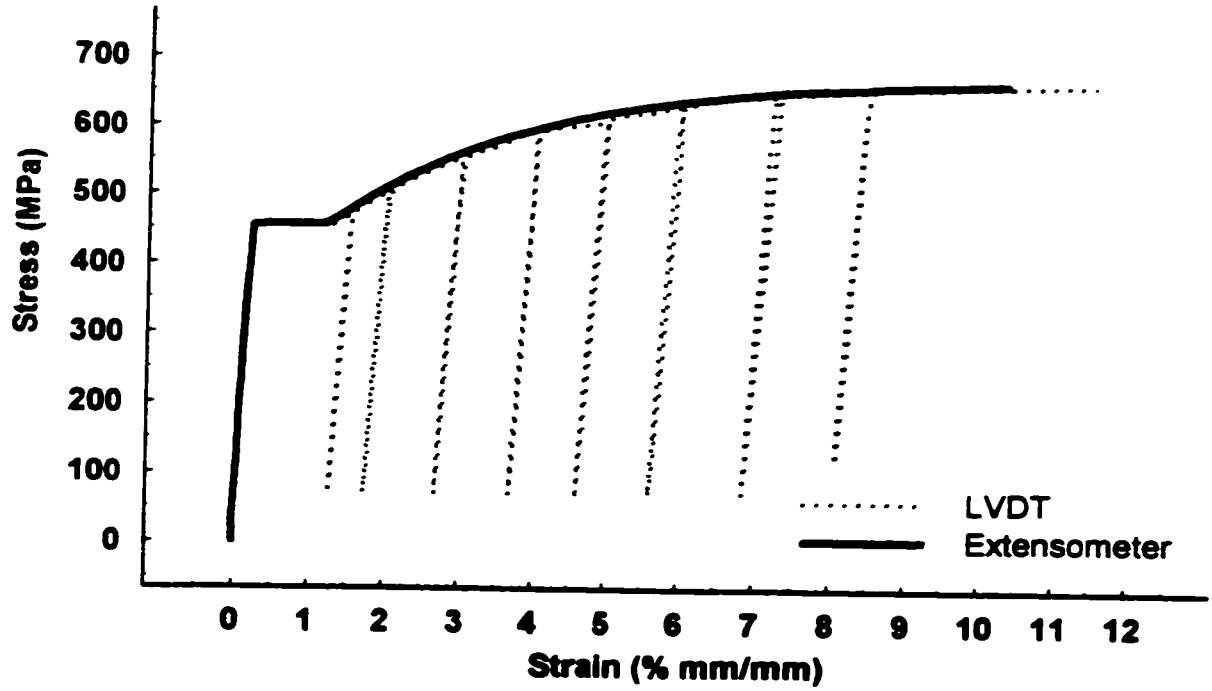

a) # 20 re-bars used in BG columns

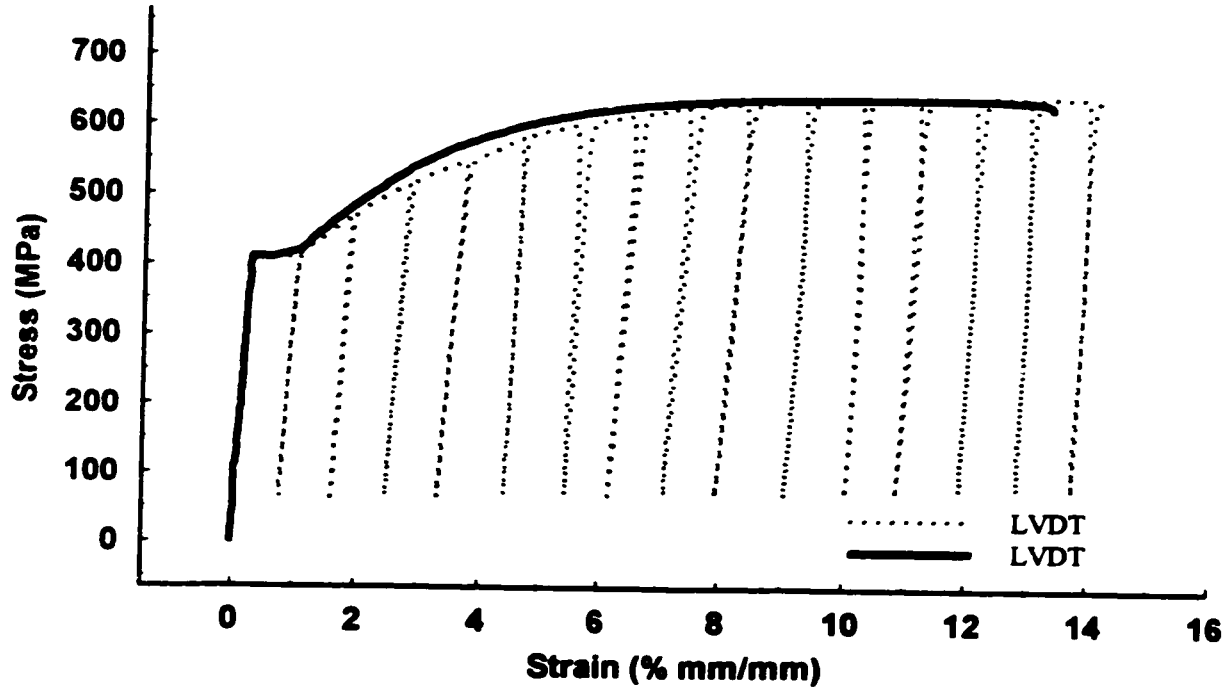

b) # 20 re-bars used in SD and FRP columns

Figure 3-38: Stress – strain relationships of #20 rebars

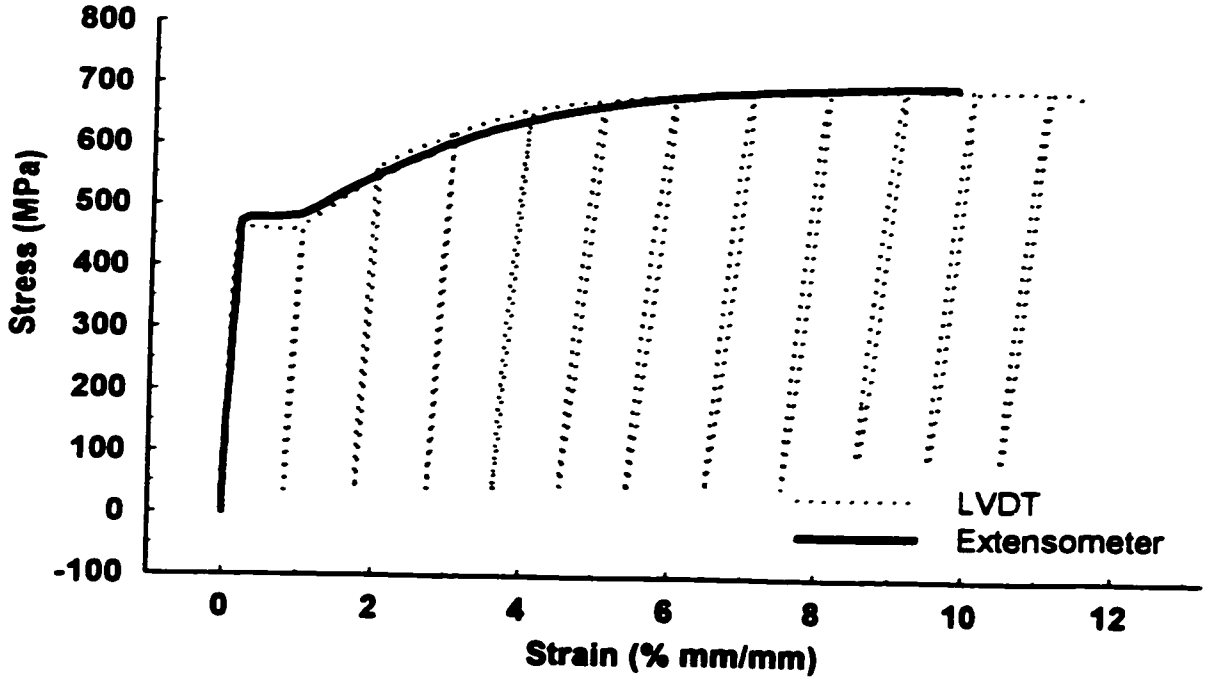

a) # 30 re-bars used in BG columns

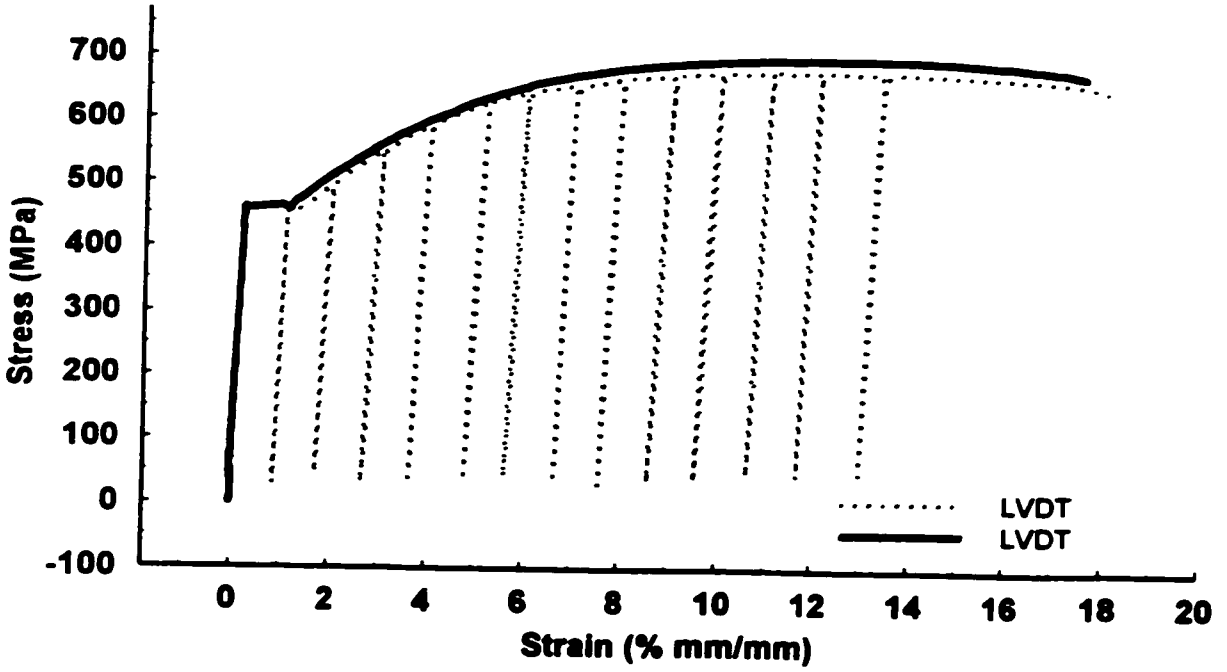

b) # 30 re-bars used in SD and FRP columns

Figure 3-39: Stress – strain relationships of #30 rebars

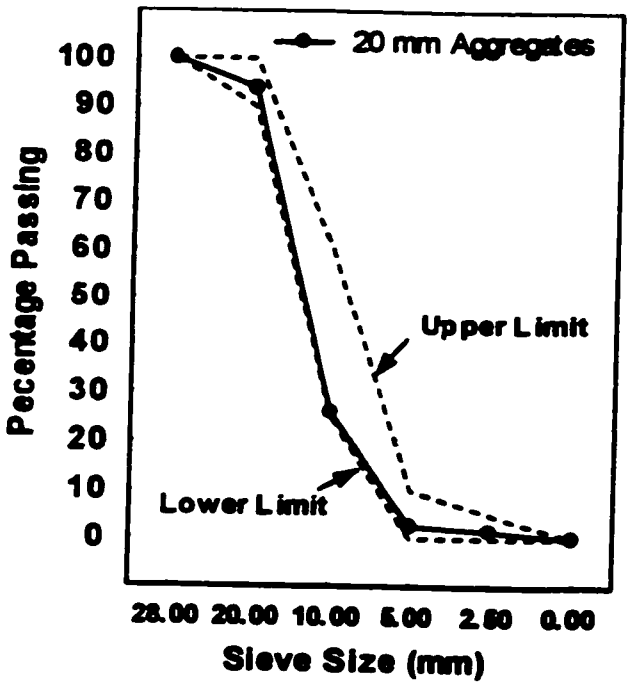

a) 20 mm Aggregates

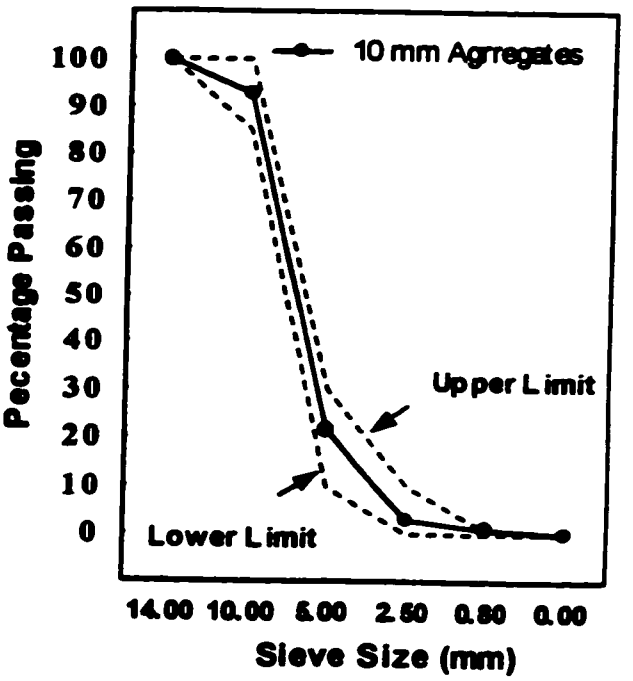

b) 10 mm Aggregates

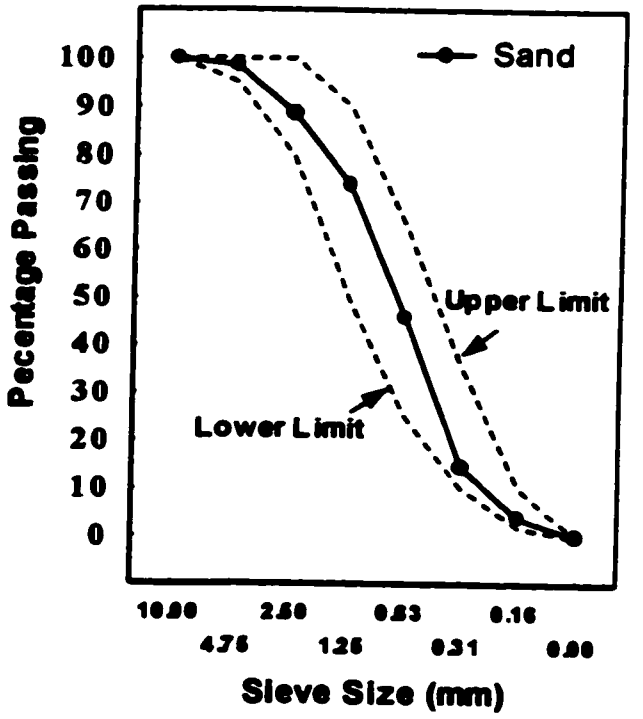

d) Sand

Figure 3-40: Grading of aggregates

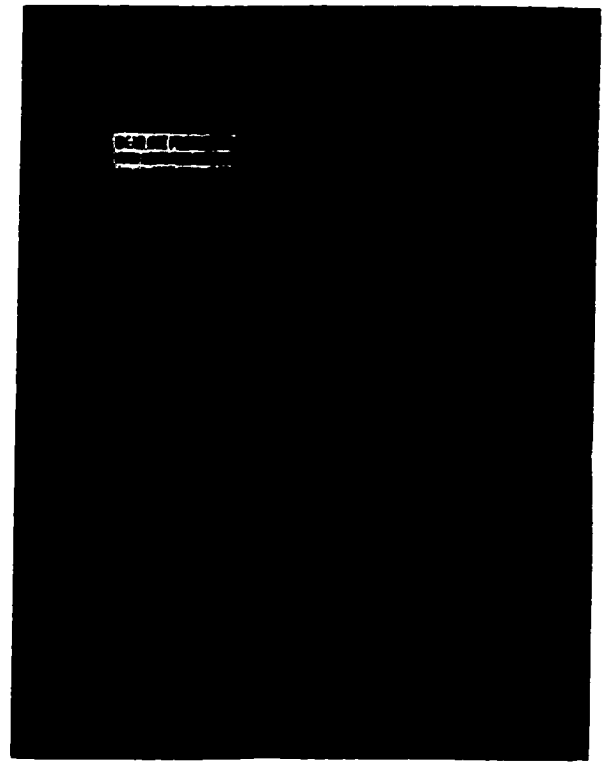

Figure 3-41: Concrete testing machine

Figure 3-42: Surface grinding machine

a) Normal - strength concrete

a) High - strength concrete

Figure 3.43: Failure pattern of concrete cylinders

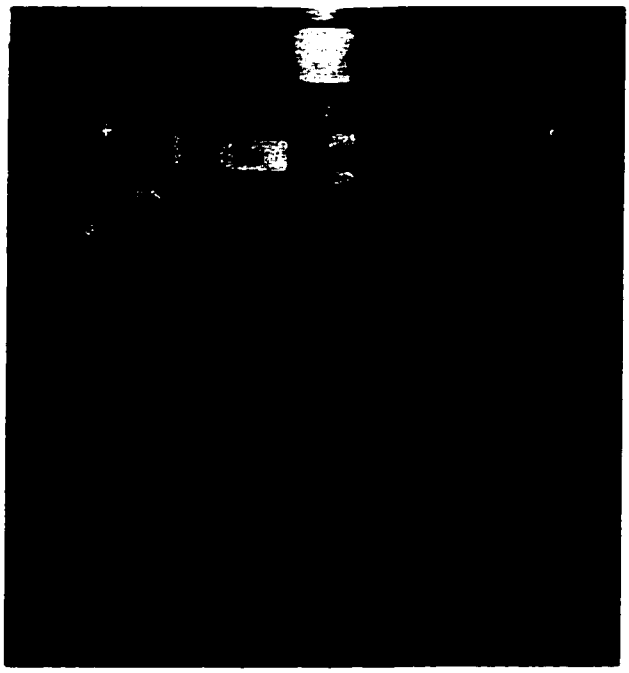

Figure 3.44: Test setup to generate stress-strain relationship of concrete

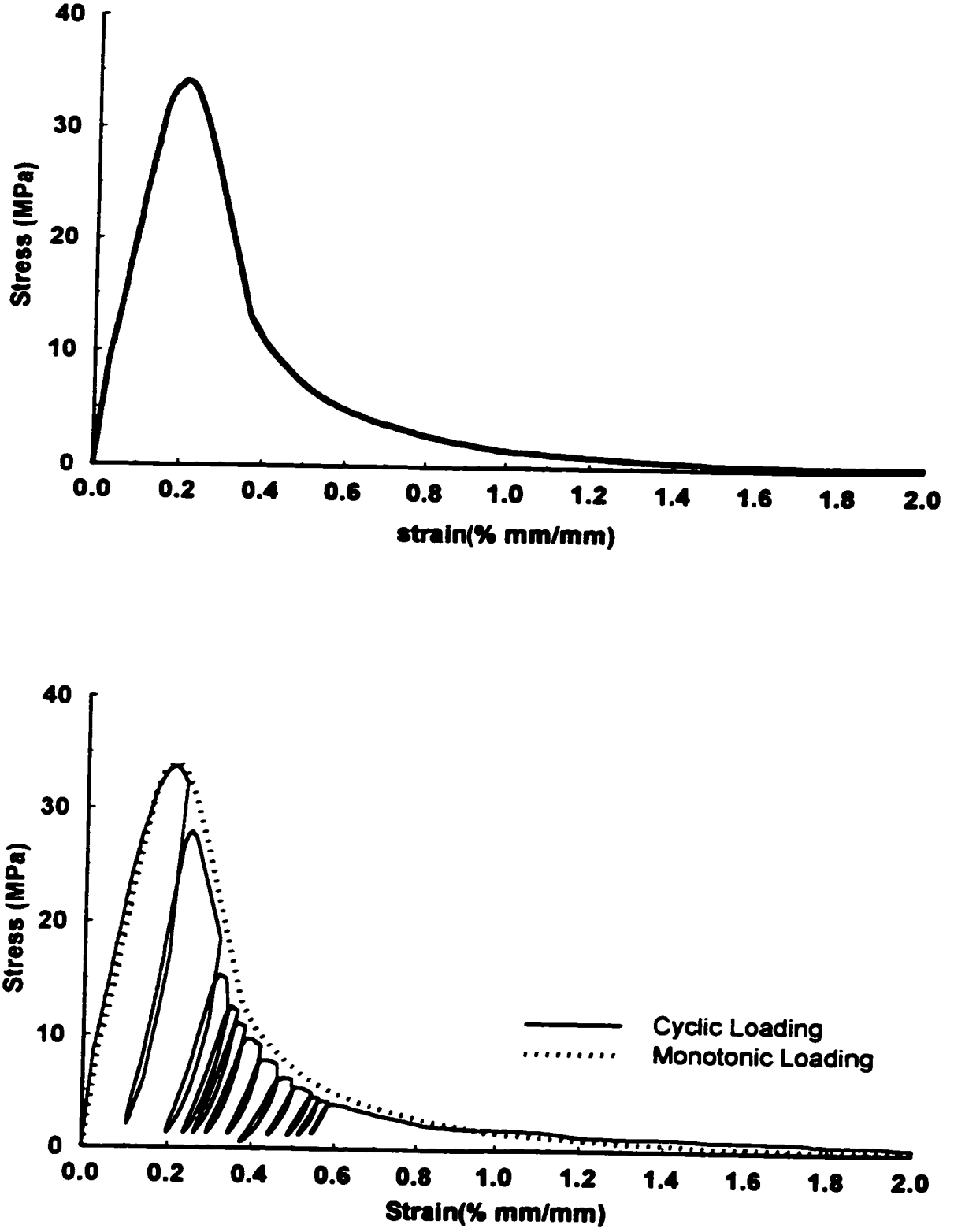

Figure 3-45: Stress-strain relationships of normal-strength concrete (Batch # 1)

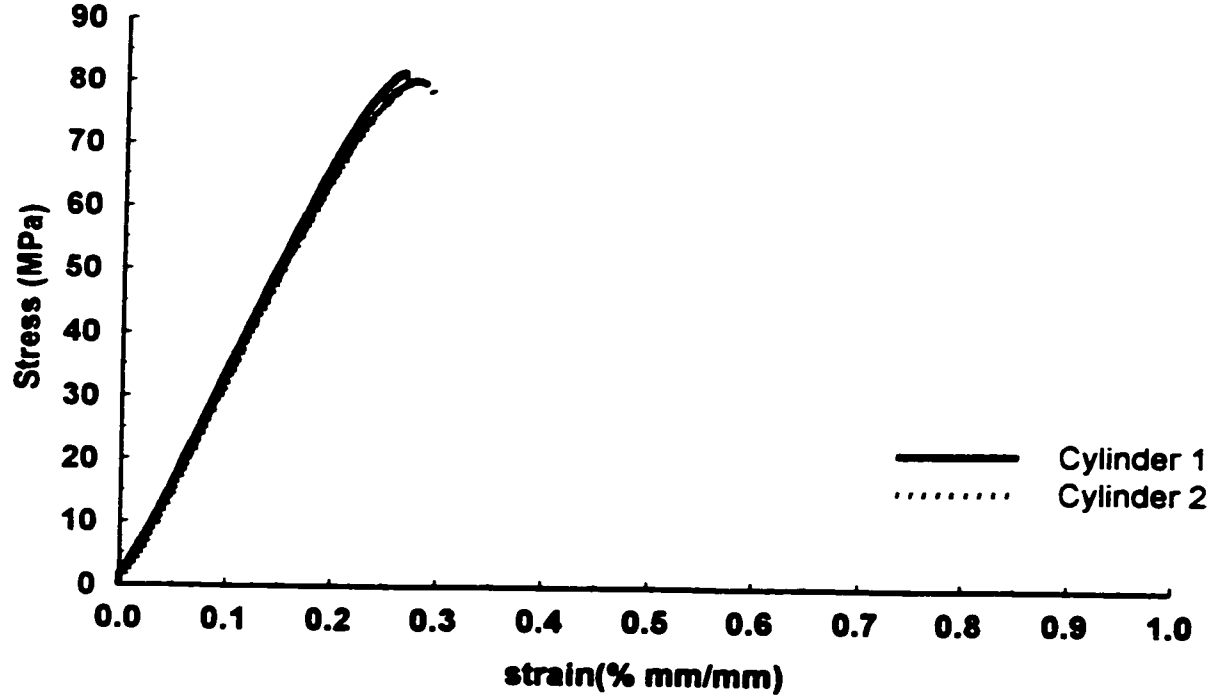

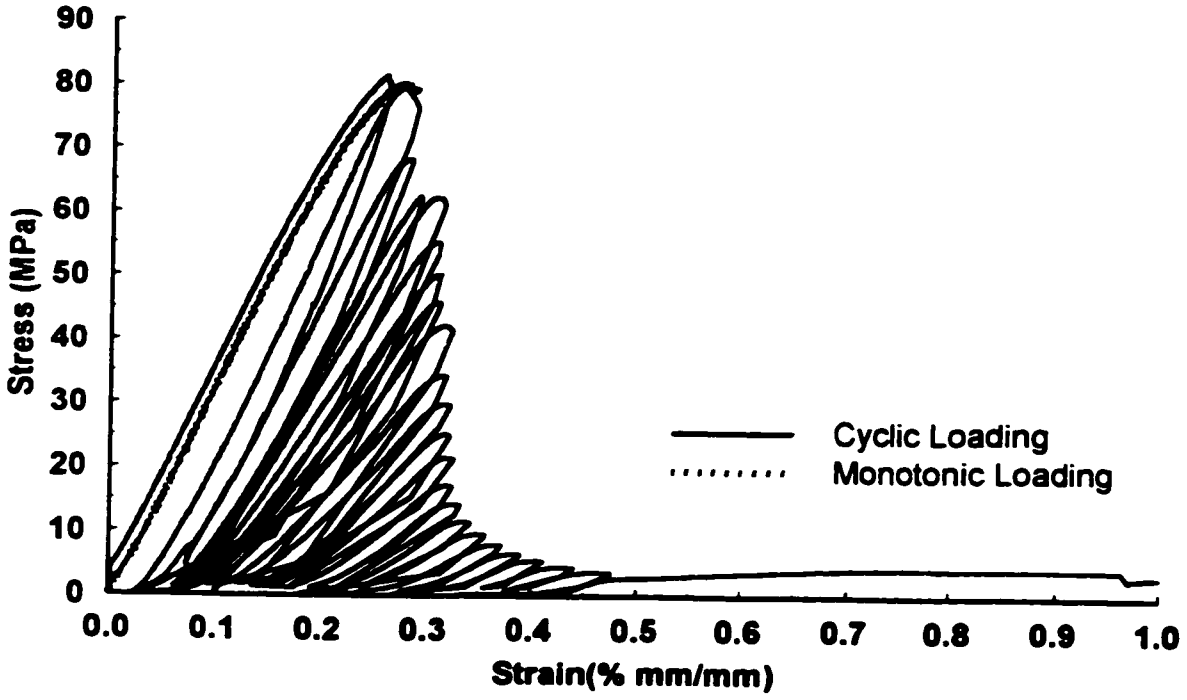

Figure 3-46: Stress-strain relationship of high-strength concrete (Batch #2)

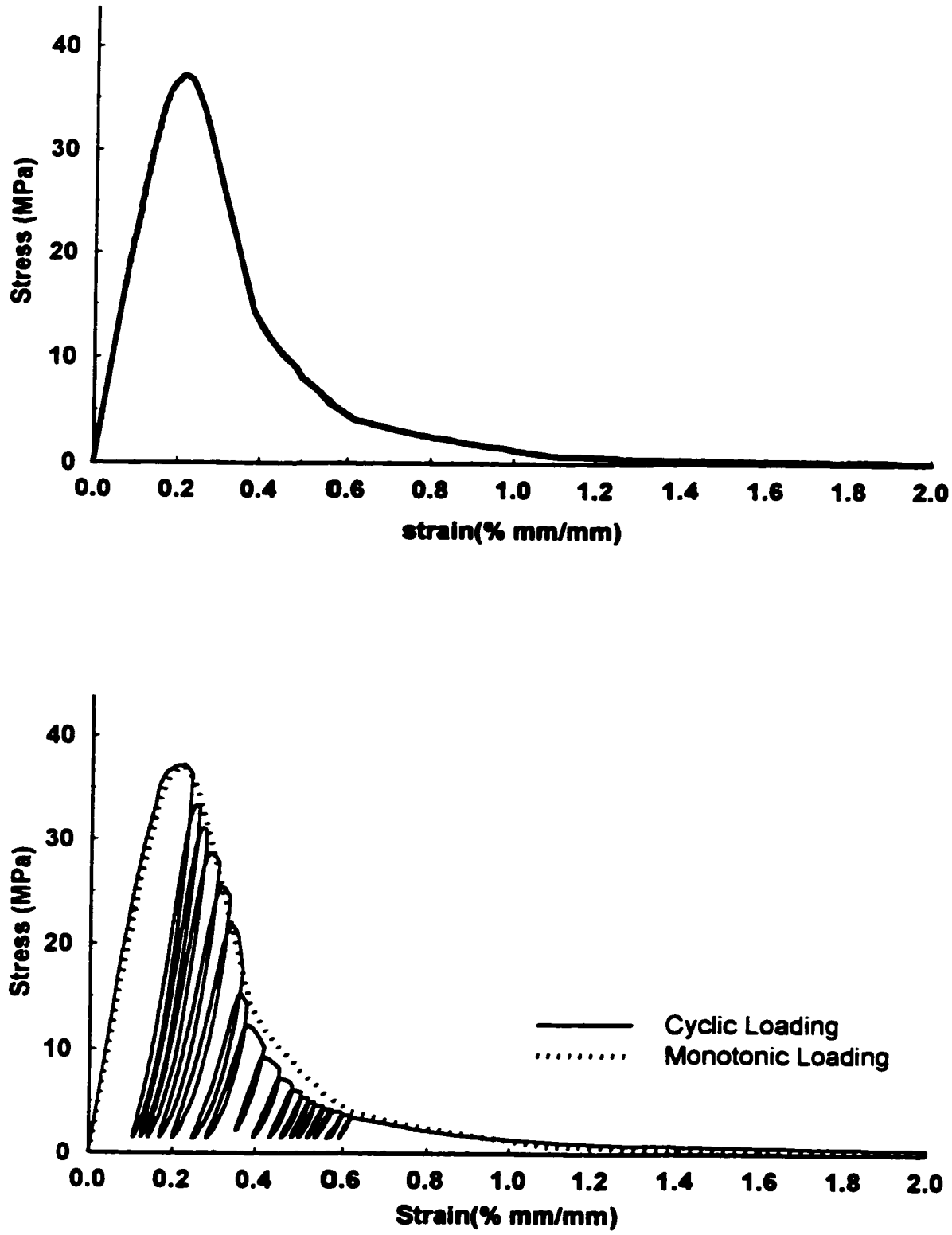

Figure 3-47: Stress-strain relationship of normal-strength concrete (Batch # 3)

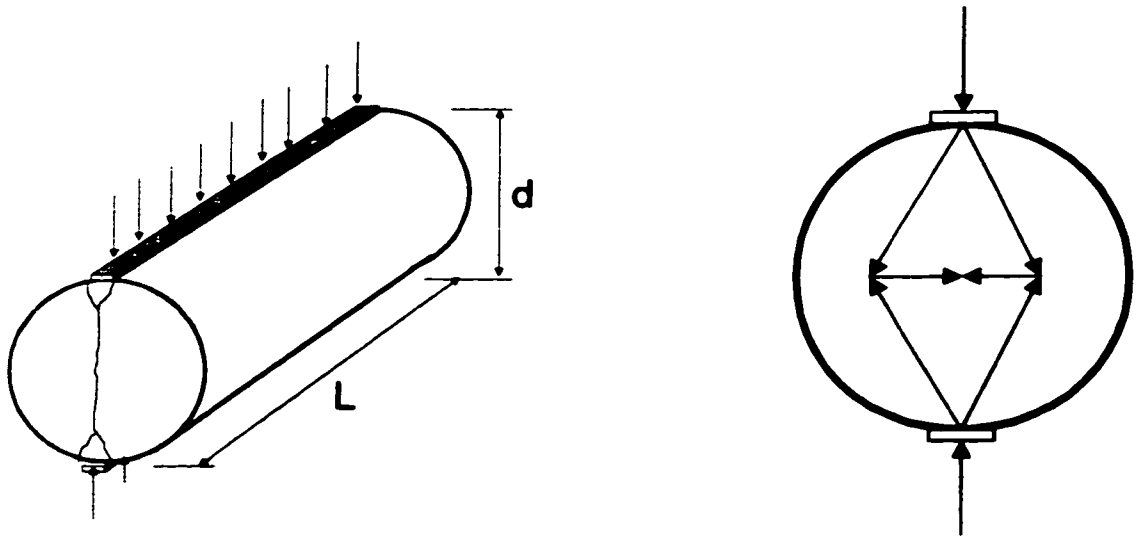

Figure 3-48: Split test of concrete cylinder

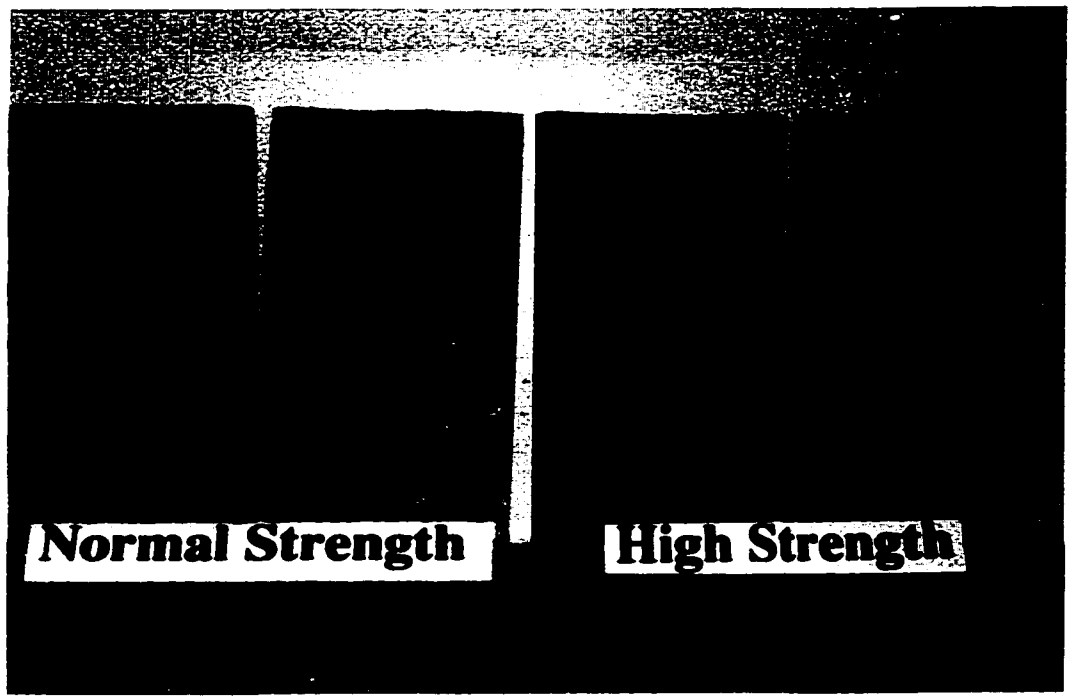

Figure 3-49: Splitting fracture planes of concrete cylinders

Chapter 4

EXPERIMENTAL INVESTIGATION

PART2- COLUMN SPECIMENS

4.1 Introduction

Large-scale reinforced concrete column specimens were designed, built and tested in the experimental phase of current research program. The material properties and relevant material tests are discussed in Chapter 3. This chapter contains the description of column specimens, their preparation, test setup, and test procedure. The results of column test are presented in Chapter 5.

4.2 Design of Column Specimens

The column specimens were chosen to be representatives of a lower portion of a first story column between the footing and point of inflection (Fig. 4-1), with a *1645 mm* shear span. The columns were designed to investigate confinement parameters based on specified material strengths and reinforcement arrangements. The choice of column height was dictated by the required mode of behavior, as well as dimensions of the already built load setup that had been used in previous column tests. The cross-sectional dimension was selected to be *350 mm* x *350 mm* to accommodate the prefabricated grid dimensions. Prefabricated grids were available in multiples of *100-mm (4 in.)* or *150 mm (6-in.)* square cells. The resulting shear span-to-depth ratio of *4.7* is typical for most columns used in building structures. Figure 4-2 illustrates the geometric properties of column specimens. The columns were designed to behave in flexure mode and show ductile response. The design was based on *ACI 318-95* building code. The design variables included compressive strength of concrete, arrangement of longitudinal bars, volumetric ratio of transverse reinforcement, vertical spacing of grids, and level axial load. The columns were designed such that the effects of design variables could be assessed by comparing companion columns.

reinforcement, vertical spacing of grids, and level axial load. The columns were designed such that the effects of design variables could be assessed by comparing companion columns. This is indicated in Table 4-1. The column specimens were labeled as BG, SD, or FRP based on the type of transverse reinforcement used, in the form of welded reinforcement grids (Bau-grids), conventional hoops and double head studs, and fiber reinforcement plastic grids, respectively.

4.2.1 Building Code Requirements

The seismic design provisions of *ACI 318-95* code require transverse confinement reinforcement. Accordingly, the total cross-sectional area of square hoop reinforcement is not to be less than;

$$A_{sh} = 0.3\left(\frac{Sh_c f'_{co}}{f_{yh}}\right)\left(\frac{A_g}{A_{ch}} - 1\right) \tag{4.1}$$

or;

$$A_{sh} = 0.09\left(\frac{Sh_c f'_{co}}{f_{yh}}\right) \tag{4.2}$$

where;

S = Spacing of transverse reinforcement measured along the longitudinal axis of column, *mm*.

h_c = Cross sectional dimension of column core, measured center-to-center of perimeter hoop, *mm*.

A_{ch} = Cross sectional area of the core concrete, mm^2.

A_g = Gross area of column section, mm^2

A_{sh} = Total cross sectional area of transverse reinforcement, (including cross ties) within spacing, s, and perpendicular to dimension, h_c, mm^2

f'_{co} = Specified compressive strength of concrete, *MPa*

f_{yh} = Specified yield strength of transverse reinforcement, *MPa*

The *CSA* standard *CAN3-A23.3-M84* uses a factor *0.12* instead of *0.09* in the second equation. The *ACI* and *CSA* codes also specify that transverse reinforcement shall be spaced at distances not exceeding one-quarter of the minimum member dimension *(h/4)*, *100 mm*, or 6 times the diameter of the smallest longitudinal bar. Hence, the columns were designed accordingly with a vertical spacing of *76 mm (3 in.)* which is equal approximately to *h/4*. A spacing of *152-mm (6-in.)* was used when the spacing was a parameter to study

4.2.2 Description of Column Specimens

Thirty-one full-size column specimens were designed and constructed for testing. The specimens represented part of a first-story column between the footing and the point of inflection, with a *1645-mm* shear span. This implies that each specimen was a representative of a prototype column with inter-story height of *3290 mm*. The shear span consisted of 1365 *mm* concrete column and *280 mm* steel loading plate up to the point of application of lateral force. The top steel portion of the column is subjected to little bending moment, remaining well below the elastic limit of concrete column. Hence, its deformation can be neglected in analysis. A *350-mm* square cross-section was used with different configurations of longitudinal reinforcement. The longitudinal bars had *90-degree* hooks, with *200-mm* extensions into the footing. This was done to avoid anchorage failure.

The columns had footings that were *405-mm* wide, *405-mm* high, and *1100 mm* long. They were heavily reinforced with #25 rebars as main reinforcement and conventional square hoops made of #15 rebars. Each footing contained four holes to fix the column to the foundation of the loading setup by means of high strength threaded rods. Figure 4-2 illustrates the geometric details of a typical specimen.

The columns were subjected to approximately *40%* of their concentric capacities, computed based on Eq. 4.3, except when the effect of axial compression was investigated as a parameter, in which case approximately *20%* of concentric capacity was also applied.

$$P_0 = 0.85 f_c' \left(A_g - A_s \right) + A_s f_y \qquad (4.3)$$

Table 4.1 provides a summary of material and geometric properties of all columns. The following sections explain in detail the reinforcement arrangements used in columns.

4.3 Reinforcement Arrangements

4.3.1 BG Columns

Ten columns were fabricated using normal-strength concrete, confined with welded reinforcement grids (*WRD*). Three of the columns were built with 8 #20 (*19.5 mm* diameter) bars as longitudinal reinforcement, confined with 4-cell grids having *9.53 mm* (*3/8 in.*) diameter reinforcement. Four columns were built with 12 #20(*19.5 mm* diameter) longitudinal bars, confined with 9-cell grids having either *9.53 mm (3/8 in.*) diameter or *6.6 mm (1/4 in.*) diameter reinforcement. One column was reinforced with 4 #30 (*29.9 mm* diameter) longitudinal bars and 9-cell grids having *9.53 mm* diameter transverse reinforcement. This column had four corner bars only, without any longitudinal reinforcement in the remaining perimeter corners of grids. Two additional columns were prepared with 20-#15 (*16.0 mm* diameter) bars as longitudinal reinforcement, one at each of the perimeter corner of 9-cell grids, having either *9.53 mm (3/8 in.)* or *6.60 mm (1/4 in.*) diameter transverse reinforcement. Different spacings of grids were used resulting in different volumetric ratios of transverse reinforcement. The volumetric ratio varied between *65%* and *172%* of that required by *ACI318-95*.

Three more columns were fabricated using high-strength concrete, confined with the same type of welded reinforcement grids. One column was built with 8 #20 bars used as longitudinal reinforcement and confined with 4-cell grids having *9.53-mm (3/8-in.*) diameter reinforcement. The other two columns were built with 12 #20 longitudinal bars, confined with 9-cell grids having either *9.53-mm (3/8-in.*) diameter or *6.6 mm (1/4-in.*) diameter reinforcement. Figures 4-3 and 4-4 depict details of cross-sectional configurations used for these columns.

4.3.2 SD Columns

Four column specimens were built using normal-strength concrete confined with ordinary steel hoops (having 135-degree bends) and double headed studs. Two of the specimens were fabricated using 8 #20 bars as longitudinal reinforcement, confined with *9.53-mm (3/8-in.)* diameter steel hoops and *9.53 mm (3/8 in.)* double headed studs. The other two specimens had 12 longitudinal bar arrangement, confined with either *9.53 mm (3/8 in.)* or *6.35 mm (1/4 in.)* diameter steel hoops, and *9.53 mm (3/8 in.)* or *6.35 mm (1/4 in.)* double headed studs. The studs were inserted across the column section as cross ties to laterally support longitudinal bars. The insertion of double-headed studs formed 4-cell grids for 8-bar arrangement and 9-cell grids for 12-bar arrangement. This is shown in Fig. 4-5. A *76-mm* vertical spacing was used in all columns. This resulted in volumetric ratio of transverse reinforcement varying between *57%* and 120% of that required by *ACI 318-95*.

4.3.3 FRP Columns

A total of 14 columns were built using FRP grids as lateral reinforcement. The columns were made of normal strength concrete. Four specimens were built using 4 #30 bars as longitudinal reinforcement, confined with either 4-cell or 9-cell grids having either *6x10-mm* or *8x10-mm* cross-section. Four columns were built with 8 #20 longitudinal bars, confined with 4-cell grids having either *6x10-mm* or *8x10-mm* cross-section. The other six columns were reinforced with 12 #20 longitudinal steel bars and 9-cell grids having *6x8-mm*, *6x10-mm*, or *8x10-mm* cross-sections. Two vertical spacings of grids were used resulting in different volumetric ratios varying between *0.79%* to *2.81%*. Figures 4-6 and 4-7 depict details of the reinforcement arrangement used for the FRP columns.

4.4 Preparation of Column Specimens

Each specimen consisted of a heavily reinforced footing and a cantilever column, reinforced with non-conventional transverse reinforcement. The preparation of each column involved i) installation of strain gauges on longitudinal and transverse reinforcement, ii) assembling reinforcement cages, iii) building formwork, and iv) casting and curing concrete. These preparation stages will be discussed in detail in the following subsections.

4.4.1 Strain Gauge Installation

Strain in reinforcement is an important part of test data that provides valuable information pertinent to the effectiveness of reinforcement. Therefore, strain gauges were placed on longitudinal and transverse reinforcement. The procedure used was the same as most universal methods of measuring strain indirectly, involving use of metallic foil-grid-resistance strain gauges, bonded to desired locations. The strain is obtained by measuring the variation in electrical output of gauge, multiplied by a calibration factor.

General-purpose strain gauges, model *CEA-06-250UN-120*, with integral solder dots were used in this project. They were supplied by Measurement Group Inc. The gauges were self-temperature-compensated and had a gauge factor of 2.085 at 24 °C. The strain limit was approximately 5%. Ribs of deformed bars were first filed off at gauge locations. The gauging area of the reinforcement was dry-abraded with 220 and 320-grit silicon-carbide paper. Then, it was cleaned with M-Prep Conditioner A and a liberal amount of M-Prep Neutralizer 5 was applied. The strain gauge was then picked up with a cellophane tape, type PCT-2A supplied by Measurement Group Inc., and properly centered on the bar. A little catalyst was applied to the bond surface of the stain gauge to enable the M-Bond 200 adhesive to be hardened quickly and reliably. Immediately upon completion of wipeout of the adhesive, firm pressure was applied to the gauge. The pressure was held for at least one minute. Once the gauge was solidly bonded in place, the cellophane tape was removed. Figure 4.8 shows a typical FRP grid being instrumented with strain gauges.

The strain gauges were connected to a data acquisition system through lead wires (type *DVF 326*) supplied by Measurements Group Inc. Since the gauge circuits were quarter bridges, a three-wire connection was preferred in order to minimize temperature effects and lead wire desensitization. The lead wires were selected of sufficient length to reach the data acquisition system and maintain their resistance at a level below 1% of strain gauge resistance. The lead wires were soldered to strain gauges using a temperature regulated soldering station.

The presence of moisture in fresh concrete can affect the performance of strain gauges. It usually results in low electrical resistance to ground, causing circulating currents, electrical noise, and desensitization of measurements. In addition, water can cause corrosion of strain

gauge grids and results in negative or positive drift in outputs. Therefore, a protective coating, *(M-coat)* was applied on each strain gauge immediately after the installation to prevent moisture from being collected in the gauging area. Then, the *M-coat* was covered by a portion of window seal, and wrapped with an electrical tape to protect the gauges from being damaged by vibrators during concrete casting.

Two of the longitudinal reinforcements in each column were instrumented with strain gauges. These gauges were placed on bars near the extreme compression and tension fibers at 50 *mm* below the footing surface. The first two grids, immediately above the footing of normal-strength concrete BG specimens, were also instrumented. These grids were labeled as the first and second, the first grid being the closest to the footing. All other columns had only the second grid (or level of transverse reinforcement) instrumented.

4.4.2 Fabrication of Reinforcement Cages

The reinforcement cages were assembled at the Structure Laboratory of the University of Ottawa. The longitudinal column bars and the reinforcement for foundations were cut and bent by a local supplier according to design specifications. The *WRG* grids were supplied by BauMesh Company, Newport Beach, California, U.S.A. The double-headed studs were manufactured to given specifications by Decon® Corp., Brampton, Ontario. The stirrups of the SD columns were manufactured at the structure laboratory using the same steel as that used to manufacture the double-headed studs. The FRP grids were ordered form Autocon Composites Inc. of Weston, Ontario, Canada.

The column cages were first assembled, prior to the footing cages. BG and FRP column cages were assembled by first aligning the longitudinal bars horizontally on supports and then inserting and positioning the grids. The use of grids as transverse reinforcement enabled easy assembly and perfect support for the longitudinal reinforcement. The SD columns were first assembled using only steel hoops, and then the studs were inserted, with cages standing in vertical position.

The fabrication of a typical reinforcement cage involved positioning first the longitudinal steel bars at the corners of grids or stirrups using wooden jigs. The grids and stirrups were then inserted and tied to the longitudinal bars by gauge 16 steel wires, ensuring proper and uniform spacing (Fig. 4.9). The column cage was then suspended above the floor, and the footing cage was built around and through the column cage (Fig. 4-10). The footing cages were made of #25 reinforcing steel bars, bent as illustrated in Fig 4-2, and closely spaced stirrups, made out of #15 bars.

4.4.3 Preparation of Formwork and Casting of Specimens

The formwork was made of 19-*mm* (3/4-*in.*) plywood sheet. A coat of white paint was applied on the interior surface to avoid water absorption, and also to act as a bond breaker. The formwork for footing was stiffened by wooden and steel brackets. Threaded rods with a diameter of 10-*mm* (3/8-*in.*) were used to tie the opposite faces of the footing formwork to prevent bulging during casting. The formwork for columns was also laterally reinforced with 30 *mm* x 30 *mm* x 3 *mm* (1¼ *in* x 1¼ *in* x 1/8 *in*) steel angles to prevent warping and bulging of the plywood due to lateral concrete pressure.

The reinforcement cages were placed in formwork by means of an overhead crane and properly checked for alignment. Four steel chairs, 38 *mm* (1.5 *in.*) high, were placed on the bottom of each footing cage, and four others were attached to the sides to hold the reinforcement in position. Small circular steel pieces, each measuring approximately 50-*mm* in length, were attached to the sides of column reinforcement at approximately 150-*mm* from the foundation, to allow for concrete cover of 29 *mm*. Braced wooden frames were constructed to stabilize column reinforcement and maintain its position during casting. Two 6 *mm*, (1/4 in) diameter threaded rods were placed in column cages, at approximately 20 *mm* and 350 *mm* from footing, to allow for rotation measurements. Four 38-*mm* (1.5-*in.*) diameter ABS pipes were placed in designated locations in footing to allow for attachment to laboratory strong floor. Figure 4-11 shows prepartion of column cages and positioning them in the formwork. Installation of column formwork and curing of concrete foundation are illustrated in Fig. 4-12.

The columns were cast vertically to simulate the actual construction practice. All specimens were cast in two stages, except high-strength concrete specimens. The footings were cast first, then the columns. The columns were cast two days after casting the footings. The ready mix concrete was ordered from a local supplier. Prior to casting, the ready-mix concrete was checked for workability by performing slump tests. The concrete was poured directly into the footing formwork from truck chute. However, the columns were cast with the aid of a concrete bucket, carried by the overhead crane. Concrete was consolidated using an internal electric vibrator, having a diameter of 40 *mm* and a frequency of 160 Hz confirming to *CSA standard A23.1 (ACI 309R)* requirements. Vibration of concrete was carefully done to prevent damage to strain gauges mounted on reinforcement. The top footing surface was floated with a metal hand float, then trawled by a steel toweling. The proper roughness of the footing-column joint was achieved by leaving the area without trawling. Four 19-*mm* (34-*in*) high-strength bolts, with 300-*mm* (12-*in.*), were inserted at the top of each column while the concrete was fresh. These bolts were placed in either 100 *mm* or 175-*mm* square configuration. They were designed to attach specimens to the steel loading beam. Large number of control cylinders were also cast along with column specimens using 152 *mm* by 305 *mm* (6 *in.* x 12*in.*) single use plastic molds.

The formwork was removed after two days from casting. The specimens were wrapped with burlap clothes and sprayed daily with water. The moisture was maintained by covering the wet burlap with 6-mil. thick white opaque polyethylene film. The strength of concrete was monitored by testing cylinders periodically. A thin layer of white latex paint was applied to concrete surface prior to testing, for better visibility of cracks during testing. The location of longitudinal and lateral reinforcement was also marked on each column using a black marker.

4.5 Test Setup

An overall view of the setup used for column tests is shown in Fig. 4.13. It consists of four major components, and includes a loading frame, a hydraulic system, a load control system, and a data acquisition system. Each of these components is described in detail in the following sections.

4.5.1 Loading Frame

The columns were tested under constant axial compression and variable lateral displacement reversals. This necessitated the fabrication of a special loading frame that allowed the application of axial load using two vertical actuators, and lateral load using a horizontally mounted actuator. One end of the horizontal actuator was attached to a *51-mm (2-in)* thick steel plate by means of four *38 mm* (*1.5 in*) high strength bolts. The other end of the horizontal actuator was bolted to the loading "T" beam. The bolts were torqued to *678 N.m* (*500 ft-lb.*) each, to assure a total fixity. The plate was attached to a lateral frame that consisted of a pair of *1200 mm* high "A" frames, mounted on a pair of three sets of *460 mm (18 in)* C-channels that were placed back to back. The C-channels were connected to each other using *25-mm (1-in)* grade 6 bolts. The lateral frame was secured to the laboratory strong floor by means of six *1400-mm* long bolts. These bolts had 70-*mm* (2.75-*in*) diameter and were made of AISI C 12L14 cold finished steel round bars (Yield strength = *480 MPa*). The horizontal loading frame was designed to resist a maximum load of *1000 KN*.

A special foundation was designed, built, and connected to the laboratory strong floor to secure the specimens and vertical actuators. The foundation consisted of a steel-concrete composite structure that included two C-channels welded to a *75-mm (3-in.)* thick steel plate and heavily reinforced high strength concrete *(90 MPa)* beams. The steel plate was *1.0 m* x *1.2 m*, manufactured from grade *300* steel. The C-channels were used to reinforce the sides of the foundation and increase the stiffness of the bottom plate. Eight countersink holes were made on the steel plate to connect the vertical actuators. Four *70-mm (2.75-in)* diameter bolts were used to fix the foundation to the strong floor of the structures laboratory. These bolts were *1800 mm* long and made also of AISI C 12L14 cold finished steel round bars. The middle reinforced concrete "H shaped" beam of the strong foundation had four *38-mm (1.5-in*) diameter holes forming *850-mm* by *400-mm* rectangular configuration in the middle. These holes were used to attach the footing of a column specimen by means of four *32 mm (1.25 in*) diameter high strength (Grade *7*) threaded rods. The threaded rods were approximately *900 mm* long, and were very well tied to prevent movement of specimens with respect to the foundation. The vertical actuators were placed on either side of the middle

reinforced concrete "*H*" beam and mounted on the thick plate of the foundation by means of *38-mm (1.5-in)* diameter and *400-mm* long high strength bolts.

The axial load was applied to columns by through a "*T shaped*" loading beam. It was constructed using weldable grade *44W (300 MPa)* steel plates. It consisted of an upper part, which was a built up box section, and a bottom part, which was a built up I-section. The I-section was stiffened in the direction of horizontal load by welding steel plates as stiffeners. It also served as a spacer to accommodate the vertical actuator length. The bottom and top pieces of the loading beam were connected together by eight *25-mm (1-in)* diameter, *100-mm* long high strength (Grade 8) bolts. The beam was secured to the top of each column by four *19-mm (3/4 in)* diameter, high strength (Grade 8) bolts that had been cast in concrete. Figures 4-14 through 4-16 illustrate the details of the loading setup.

Two steel frames were used to brace columns for possible out-of-plane instability during testing. The frames, shown in Figs. 4-13, were fixed to the laboratory strong floor, one on each side of specimen. The frames were also tied together at the top by means of *150* x *150* x *6-mm* (*6* x *6* x *3/16 in*) hollow steel box section.

4.5.2 Hydraulic System

The hydraulic system consisted of a hydraulic power supply unit and a single channel hydraulic service manifold (Fig. 4-17). The hydraulic power supply unit was equipped with two *380-liter (100 Gallons)* capacity tanks, connected together, and two piston pumps. The pumps were mounted in parallel and were set to operate at *20.7 MPa (3000 psi)* maximum pressure. They were capable of delivering *125 liters per minute (33 GPM)* of hydraulic oil, each. However, only one pump was needed for the static-loading test conducted in the current investigation.

A single channel hydraulic service manifold (model *MTS 290.22*) was installed between the hydraulic power supply and the servo-valves of actuators. The manifold was connected electrically to a digital controller. It was operated by a Load Control Unit. Hence, the control pressure was independent of the main hydraulic power supply. The manifold was set to operate at two pressure levels; a low pressure of *3.45 MPa (500 psi)* and a high pressure of

20.7 MPa (3000 psi). The low pressure is used during the placement of test column. Two piston-type accumulators (model *MTS-111.12C*) were installed in the manifold, one on the pressure line and the other on the return line. This was done to reduce the inertia and line restriction considerations. When the servo-valve opened and the line pressure began to drop, the accumulator supplied part of the fluid and maintained line pressure. Also at low frequencies, in which the horizontal actuator operated, fluid flow in the lines could stop completely and fluid inertia could become an operational factor. The accumulator in the return line reduced pulsing caused by varying amounts of fluid being discharged into the lines as the actuator moved. Movement of hoses and/or "*Hammering*" of hard lines were then reduced. Since the two vertical actuators were operating at full capacity at all times, the movement of the horizontal actuator could affect their operating pressure if the accumulators were not properly charged with Nitrogen gas. Thus, the pressure and return accumulators were checked and charged to their typical pressures *7 MPa (1000 psi)* and *0.35 MPa (50psi)*, respectively, before each test.

The hydraulic actuators (Model *MTS 243.70*) used in the loading system were heavy duty, single-ended and double acting units. They were *2655 mm* long when they were completely contracted, with a total stroke of 500-*mm* (20-*in*). Each actuator weighed about *900 kg* and had a force capacity of *1460 kN (328 kips)* in compression and *960 kN (216.0 kips)* in tension. The compression capacity of each actuator was limited by the capacity of the self-contained force transducer. A relief valve was installed on each actuator to limit the compression force to *960 kN (216 Kips)* less the capacity of the force transducer (*1000 kN (220 Kips)*). Actuators were also equipped with swivels and displacement transducers

Swivels (Model *MTS 249.51*) were mounted on actuator base from one end and the piston rod from the other end. They were rated for *1000 kN* force. They were designed to tilt from *-8* to *+8 degrees*. The swivel angle ranged from *-90* to *+30 degrees*. The swivels were primarily used to align the actuators with tensile or compression forces. Their backlashes were properly adjusted by loosening the swivels' bearings. Proper adjustment of backlash enabled the swivels to tilt and rotate without any damage to bearings.

The hydraulic manifold supplied oil pressure to the actuators through "*Moog*" hydraulic servo-valves (Model *MTS 252-55B*), which were also mounted directly to the actuators. The servo-valves regulated the rate and direction of hydraulic fluid flow to and from the actuators. Their flow was rated at *56 liters per minute (15 GPM)*. The polarity of the servo-valves could be inverted depending on the control mode wanted and the signal's feedback from the load and displacement transducers.

The actuators were equipped with internal Linear Variable Differential Transformers (*LVDT*). The *LVDTs* provided piston displacement feedback signals to the electronic control system. They were properly calibrated with a margin of error of 0.005 *mm*. Before each test, all the *LVDTs* were shunt calibrated using software "Test Star." The *LVDT* of horizontal actuator was used as control command, but not to measure the lateral displacement of columns, because the lateral frame was not stiff enough to resist lateral deformations.

Force transducers (Model *MTS 661.31E*) were also mounted directly on actuators between the pistons and the swivel heads. They were used to measure the magnitude and sense of applied load. Each load cell had a force capacity ranging between *-1000 kN* (tension) and *+1000 kN* (compression), and was calibrated with a margin of error of *0.010 kN*. The load cells of the vertical actuators were used to provide feedback to the control unit in order to maintain constant axial compression applied on each column.

4.5.3 Control System

The control system consisted of a workstation and a digital controller (Fig. 4-18). The workstation consisted of a personnel computer (Model *Dell 486/MXV*) with *16 Meg* RAM, and a Load Unit Control Panel. The "*OS/2*" operating system was used because of its multitasking functions. The Load Unit Control Panel was attached to a freestanding pedestal. It was mainly used to control the pressure out of the manifold, and command the movement of actuators manually.

A software package, consisting of a number of computer programs was used for testing columns. An application called "*TestStar*" was the main program that set up a test and communicate with the digital controller. A Function Generator program used created and ran

test commands. It could produce simple monotonic or cyclic test commands, using triangle, sine, and square wave shapes. It was used mainly to tune the system before testing. An application program called "*TestWare-SX*" was used to generate the loading sequence. *TestWare-SX* was a flexible, general-purpose program that combined processes, which produced a test command, acquired data, and could interface with external devices. *TestStar* had many other features and applications which were not needed for the tests conducted in the current project.

The digital controller consisted of a data acquisition system, A/D converter, AC conditioners, DC conditioners, drive valves, I/O analog bus, and connections for external equipment. The interface between the computer and the rest of the system was provided through a digital controller, which updated the servo loop at a speed of *5000 Hz*. All actuator's sensors were connected to the back of the controller that in turn was connected to the computer and the Load Unit Control Panel. The system was configured for three channels representing one horizontal actuator and two vertical actuators. The horizontal actuator was operated on displacement control mode, while the vertical actuators were operated on force mode.

4.5.4 Data Acquisition Systems

The data were collected using either a "*Sciemetric 200*" or "*Vishay*" data acquisition systems. The network diagram of the data acquisition system is described schematically in Fig. 4-19. The digital controller of the *MTS* system had a built-in data acquisition system as well. The "*TestWare-SX*" process acquired data from *MTS* "*Temposonic*" Linear Variable Differential Transformers (referred hereafter as *Temposonic LVDTs*), actuators inside *LVDT*, and load cells. The data was stored as ASCII files. Data acquisition was sequenced in parallel with command process and data was recorded using a level crossing mode. This implies that data from connected sensors were recorded when the point of inflection of test column deflected by a specified amount (*0.5 mm* in this case). The *MTS* Data Acquisition System was used as a backup to record feedback from the *MTS* sensors only.

The strain gauge and "*APEK*" Linear Voltage Displacement Transducer *(LVDT)* data were collected using either a *"Sciemetric 200"* or *"Vishay"* data acquisition system. The

Temposonic LVDT and actuator sensor data were collected by connecting these two data acquisition systems to the *MTS* digital controller. A "*Sciemetric 200*" data acquisition system was used to collect data for the BG normal strength-concrete columns. It had 64 channels, 12 of which configured to be used for full electric circuit bridge and 52 for 1/4 bridge. The full bridge circuits were exited internally with 10 DC *Volts*, whereas the 1/4 bridges used 2.5 DC Volts. Computer software *"COPILOT"* was used to process the data. *COPILOT* is a high-level *DOS* based program that takes care of the operation of individual sensors and data acquisition equipment. All data reduction operations were done automatically based on built in functions. The data were scanned, processed and displayed on the monitor every second, and saved on the hard disk every 5 seconds.

The "*Vishay*" data acquisition system was used to collect data for the rest of the columns. It consisted of two scanners (Model *5520*) each providing static acquisition and digitization of 20 channels of various analog inputs. The scanners were configured with 7 (5 channel) strain gauge cards and one (5channel) high-level input cards. The latter was used to collect data from *Temposonic LVDTs* and horizontal force through the *MTS* digital controller. Computer software, called *WIN5000*, was used to configure the data acquisition system. A Pentium computer *(166 MHz)* with "*Windows 95*" operating system was used to interface with "*Vishay*" data acquisition system. Sensors were shunt calibrated and zeroed before each test. Data were scanned and saved every 2 seconds.

4.6 Installation and Instrumentation of specimens

Each column specimen was positioned inside the loading system and securely fixed to the foundation by means of four-*32mm (1¼-in)* high-strength threaded rods. The specimen was leveled and checked for vertical and horizontal alignment. A thin layer of mortar was placed at the top of column, under the loading plate, for leveling purpose. The loading plate was securely connected to the top of the column by means of four *20-mm (3/4-in)* high-strength bolts that had been cast in the column. Then, the actuators were connected to the loading plate using *38-mm (1½-in)* diameter high-strength bolts. Figure 4-20 shows the column installation sequence.

Once a column was securely positioned inside the loading setup, it was instrumented to measure applied forces, lateral displacements, rotations of the hinging region, and strains in longitudinal and lateral reinforcement. Two *Temposonic LVDTs* were placed to measure horizontal displacements, one at the point of application of horizontal load (1645-*mm* from the footing), and the other immediately below the loading beam (1365 *mm* from the footing). Each *Temposonic LVDT* had a stroke of *±250 mm* with a *0.001 mm* reading precision. Fishing wires were fixed to the middle of the loading beam and the tip of column, and were ran through a pulley system to be fixed to the movable magnetic rings of *Temposonic LVDTs*. (Fig. 4-21) A light frame was constructed around the specimen using 50 *mm* slotted steel angles. The frame was then fixed to column footing. It was used to support the pulleys and electronic bases of *Temposonic LVDTs*. Thus, all displacements were measured with respect to column footing.

Four additional strain gauge-based Linear Voltage Displacement Transducers *(LVDTs)* were placed vertically near the critical section to measure rotations of hinging region and rotations caused by anchorage slip (extension of longitudinal reinforcement within the footing). These *LVDTs* were of spring type (*"APEK"* model), with *51-mm (2-in)* stroke. Hangers were made of slotted steel angles and mounted on the threaded rods, which had been cast in columns so that the reading could be taken beyond the spalling of concrete cover. Figure 4-22 illustrates the locations of displacement transducers.

The positions of *LVDTs* with respect to columns were very important for calculating rotations and curvatures. These positions varied from one specimen to another. Therefore they were measured each time before testing. One pair of vertical *LVDTs* was placed on faces perpendicular to the direction of loading to measure vertical displacements of the hinging region relative to the footing, with a gauge length of *350 mm*. The other pair was set to measure the displacement of bottom column section relative to footing with a gauge length of approximately *25-mm*. The difference between the readings of opposite *LVDTs* divided by the horizontal distance between the two would give rotation. The difference between total hinge rotation and anchorage slip rotation gives the rotation of the hinging region due to flexure alone.

4.7 Calibration of Instruments

The results and the performance of a test depend mainly on the precision of measuring instruments. Therefore a calibration of each transducer is essential before testing. Generally, the sensitivity of an electrical instrument depends on its capacity and on the range of measurement needed for a test. For small load or amplitude tests, higher sensitivity is recommended, while for large load or amplitude tests, lower sensitivity may be sufficient. Transducers can have numerous sensitivity ranges.

The *Temposonic LVDTs*, the load cells, and the self-contained actuator LVDTs were factory pre-calibrated. All of these sensors had two ranges of sensitivity, except the *Temposonic LVDTs*, which had only one sensitivity range with dual polarities. The *TestStar* program loads the database calibration prior to each test. The four *51-mm (2-in.) LVDTs* were calibrated in the laboratory, using a specially designed calibrator, which utilized a precise mechanical micrometer caliper with divisions of *0.001 mm*. These *LVDT's* have a sensitivity of *3.7 mV/V* and a non-linearity of *±0.1%* of full-scale range, and they were set to operate with an input voltage of *10 VDC*.

4.8 Test Procedure and Loading Program

A standard procedure was used to test the columns. The *TestWare-SX* software, in conjunction with *TestStar* software, was used to design the loading program. The axial load was applied first, and was maintained at a constant level through the test. The horizontal load was applied in the deformation control mode. Lateral deformation reversals were applied, starting with three elastic cycles at *0.5%* lateral drift, followed by three cycles at 1% drift, which approximately corresponded to the yield displacement. The subsequent stages of loading included three cycles at each of incrementally increasing drift level. The loading history shown in Fig. 4-23 was used to test each column.

Table 4-1: Properties of Test Specimens

Col. Label	$f_{cc}^{'}$ *MPa*	Reinf. Arrng.	ρ (%)	d_b (*mm*)	s (*mm*)	f_{yt} (*MPa*)	ρ_s (%)	$(\rho_s)_{ACI}$ (%)	$\frac{\rho_s}{(\rho_s)_{ACI}}$	P (kN)	P/P_0
BG-1	33.7	8-#20	1.96	9.53	152	570	1.00	1.55	0.65	1782	0.39
BG-2	33.7	8-#20	1.96	9.53	76	570	2.00	1.55	1.29	1782	0.39
BG-3	33.7	8-#20	1.96	9.53	76	570	2.00	1.55	1.29	831	0.18
BG-4	33.7	12-#20	2.94	9.53	152	570	1.33	1.55	0.86	1923	0.38
BG-5	33.7	12-#20	2.94	9.53	76	570	2.66	1.55	1.72	1923	0.38
BG-6	33.7	4-#30	2.29	9.53	76	570	2.66	1.55	1.72	1900	0.40
BG-7	33.7	12-#20	2.94	6.60	76	580	1.26	1.52	0.83	1923	0.38
BG-8	33.7	12-#20	2.94	6.60	76	580	1.26	1.52	0.83	961	0.19
BG-9	33.7	20-#15	3.26	6.60	76	580	1.26	1.52	0.83	1923	0.38
BG-10	33.7	20-#15	3.26	9.53	76	570	2.66	1.55	1.72	1923	0.38
BG-11	81.6	12-#20	2.94	9.53	76	570	2.66	3.75	0.71	1920	0.20
BG-12	81.6	12-#20	2.94	6.60	76	580	1.26	3.69	0.34	1920	0.20
BG-13	81.6	8-#20	1.96	9.53	76	570	2.00	3.75	0.53	1920	0.20
SD-1	36.8	8-#20	1.96	9.53	76	540	2.00	1.79	1.12	1920	0.40
SD-2	35.4	8-#20	1.96	9.53	76	540	2.00	1.70	1.17	912	0.20
SD-3	36.0	12-#20	2.94	9.53	76	540	2.66	1.75	1.52	1920	0.37
SD-4	35.8	12-#20	2.94	6.35	76	570	1.26	1.65	0.76	1920	0.37

$$(\rho_s)_{ACI} = 0.6\left(\frac{A_g}{A_{ch}} - 1\right) * \frac{f_c^{'}}{f_{yt}}$$

Table 4-1: Cont.

Col. Label	f'_{cc} *MPa*	Reinf. Arrng.	ρ (%)	d_b (*mm*)	s (*mm*)	ρ_s (%)	P (kN)	P/P_0
FRP-1	37.2	8-#20	1.96	6x10	152	0.79	1920	0.39
FRP-2	37.2	8-#20	1.96	6x10	76	1.59	1920	0.39
FRP-3	37.2	8-#20	1.96	6x10	76	1.59	978	0.20
FRP-4	37.2	12-#20	2.94	6x10	152	1.05	1920	0.36
FRP-5	37.2	12-#20	2.94	6x10	76	2.10	1920	0.38
FRP-6	37.2	12-#20	2.94	6x10	76	2.10	1080	0.20
FRP-7	37.2	4-#30	2.29	6x10	76	2.10	1920	0.38
FRP-8	37.2	4-#30	2.29	6x10	76	1.59	1920	0.36
FRP-9	37.2	12-#20	2.94	6x8	76	1.69	1920	0.39
FRP-10	37.2	12-#20	2.94	6x8	76	1.69	1080	0.20
FRP-11	37.2	8-#20	1.96	8x10	76	2.10	1920	0.36
FRP-12	37.2	12-#20	2.94	8x10	76	2.81	1920	0.38
FRP-13	37.2	4-#30	2.29	8x10	76	2.10	1920	0.38
FRP-14	37.2	4-#30	2.29	8x10	76	2.81	1920	0.38

Table 4-2: Research Parameters and Comparison

Specimens Parameter Studied	Comparison Specimens
Concrete Compressive Strength f_c'	BG-3 and BG-13/ BG-7 and BG-12
Spacing of Transverse Reinforcement S	BG-1 and BG-2/ BG-4 and BG-5/ FRP-1 and FRP-2/ FRP-4 and FRP-5
Axial Load Level P/P_o	BG-2 and BG-3/ BG-7 and BG-8/ SD-1 and SD-2/ FRP-2 and FRP-3/ FRP-5 and FRP-6/ FRP-9 and FRP-10
Volumetric Ratio of Transverse Reinforcement	BG-5 and BG-7/ BG-11 and BG-12/ SD-3 and SD-4/ FRP-5, FRP-9, and FRP-12/ FRP-6 and FRP-10/ FRP-2 and FRP-11/ FRP-7 and FRP-14/ FRP-8 and FRP-13
Number of cells of Transverse Reinforcement Grids	FRP-7 and FRP-13
Arrangement of Longitudinal Reinforcement	BG-5, BG-6, and BG-10/ BG-7 and BG-9/ FRP-2 and FRP-8/ FRP-5 and FRP-7/ FRP-12 and FRP-14/ FRP-11 and FRP-13
Type of Lateral Reinforcement	BG-1 and FRP-1/ BG-2, SD-1, FRP-2, and FRP-11/ BG-3, SD-2, and FRP-3/ BG-4 and FRP-4/ BG-5, SD-3, FRP-5, FRP-9, and FRP-12/ BG-6, FRP-7, and FRP-14/ BG-7, SD-4, FRP-5, FRP-9, and FRP-12/ BG-8, FRP-6, and FRP-10

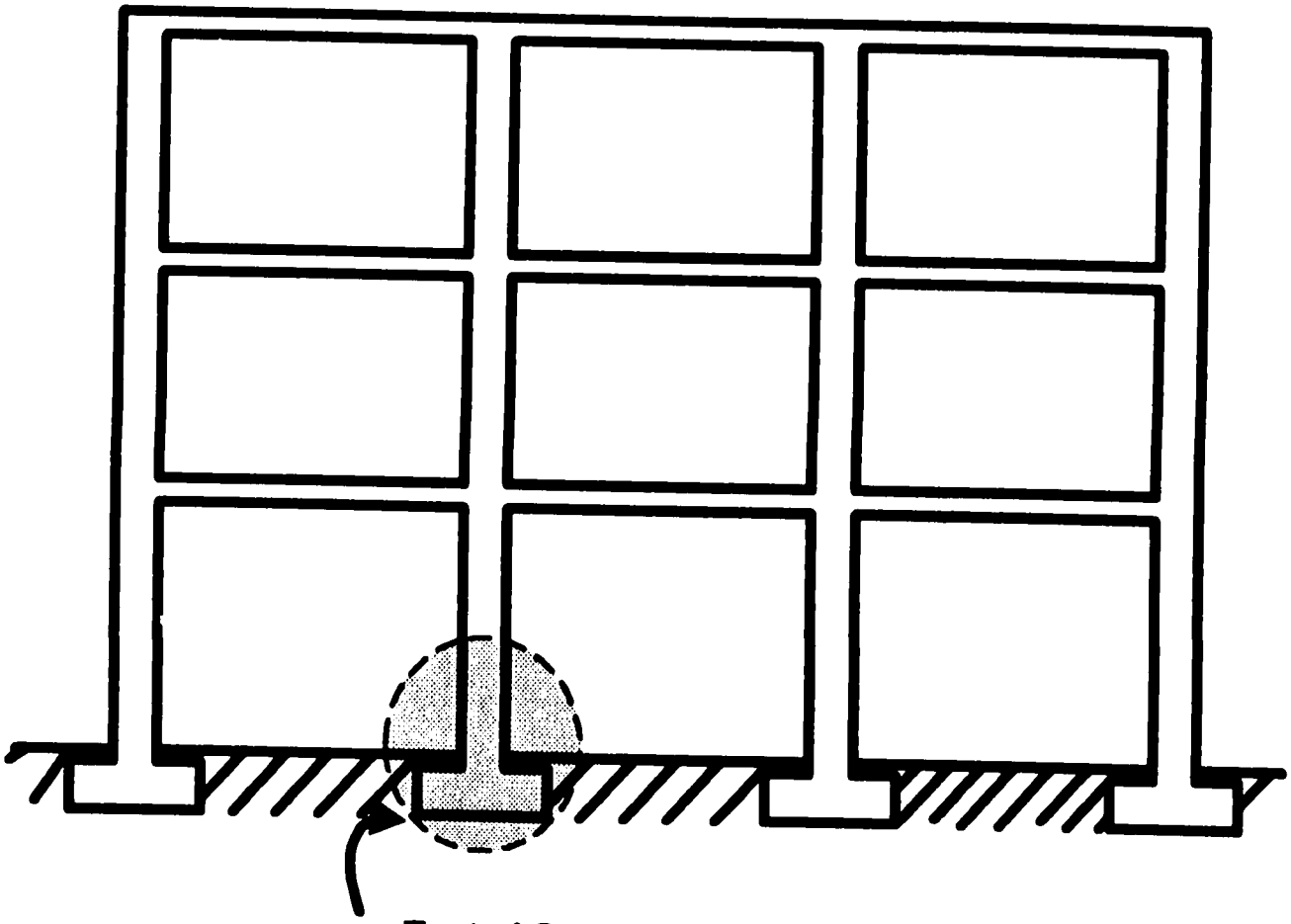

Figure 4-1: Tested column specimen in structure

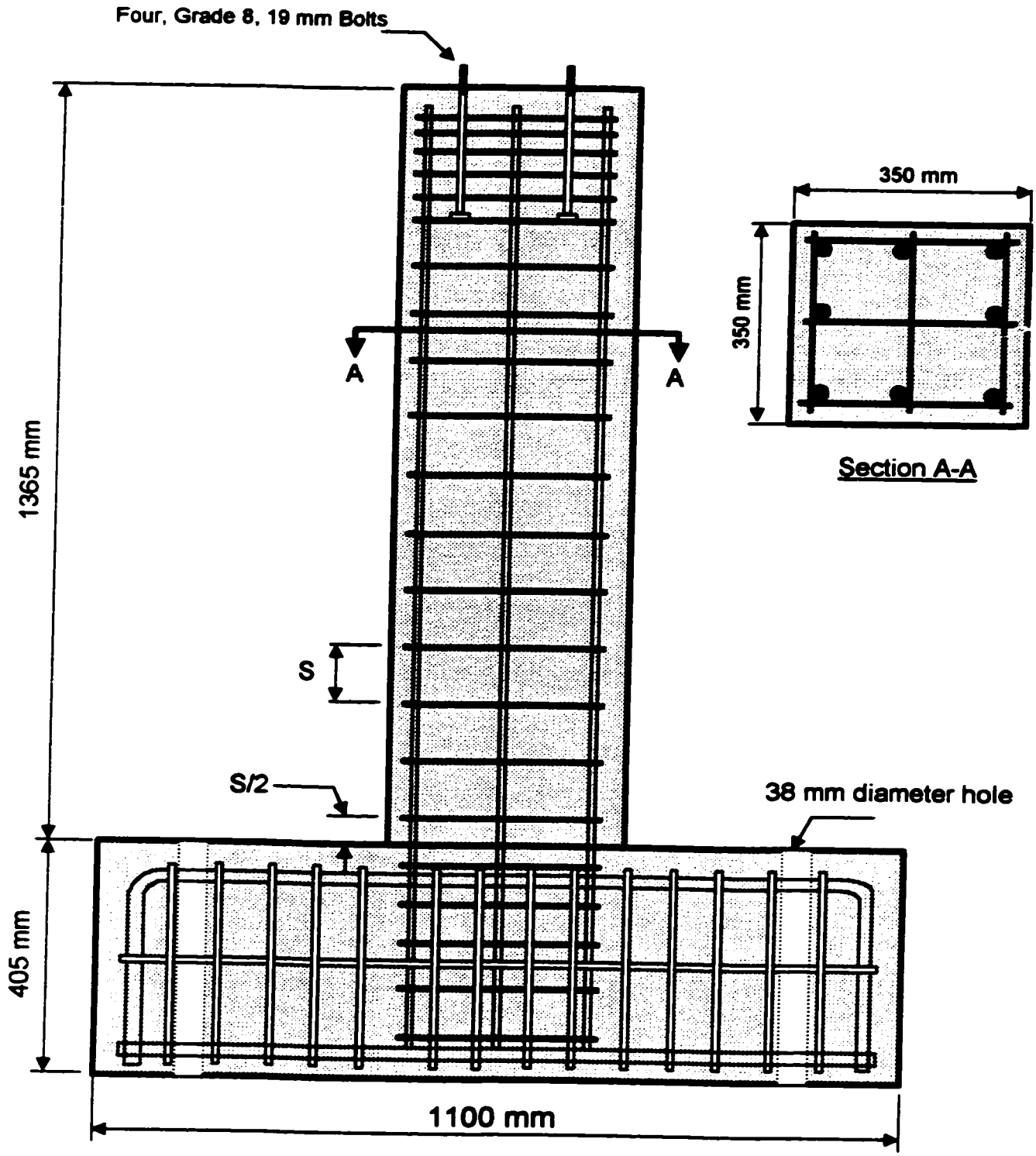

Figure 4-2: Geometry and reinforcement arrangement of column specimens

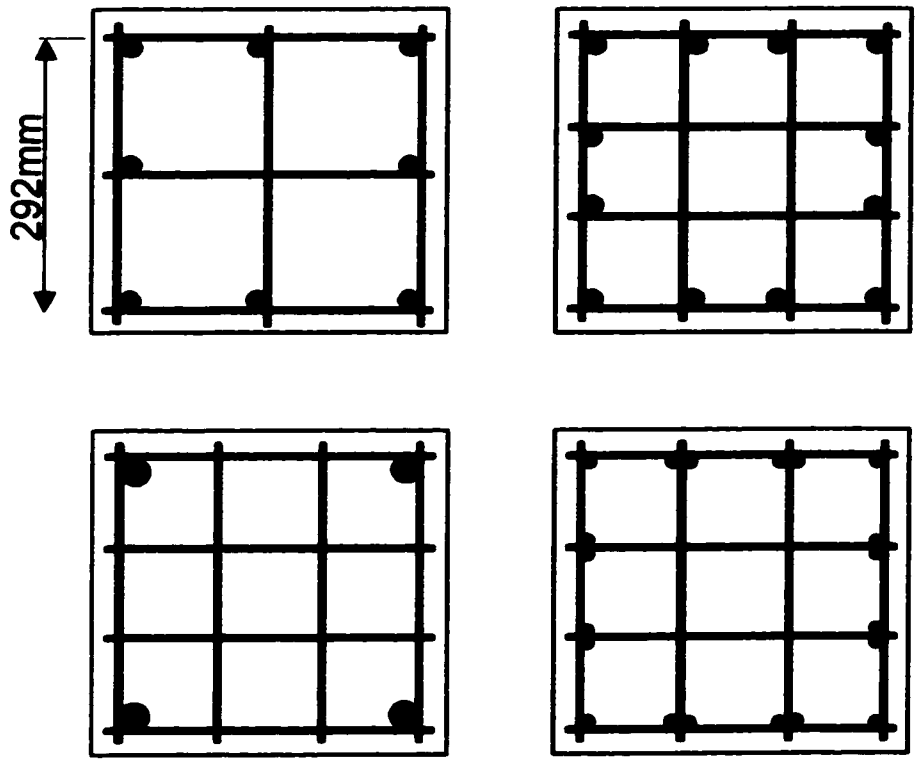

Figure 4-3: Cross-sectional arrangements used in BG columns

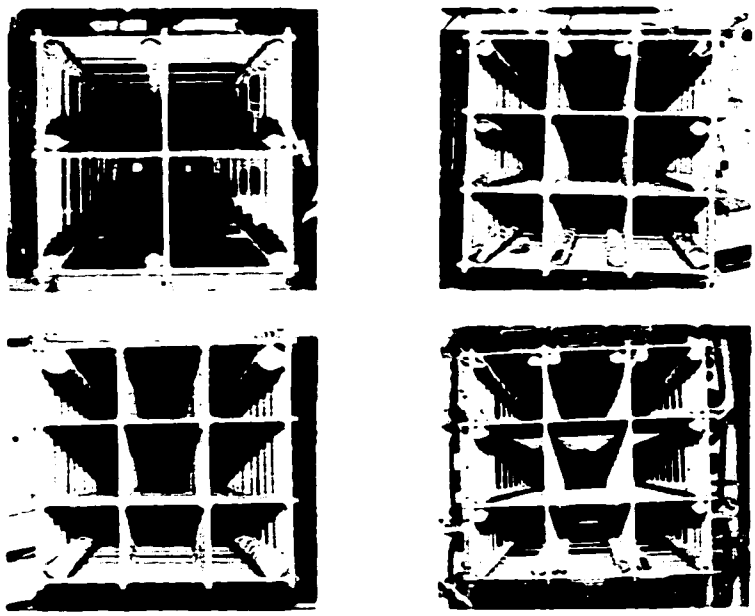

Figure 4-4: Top view of welded reinforcement grid cages

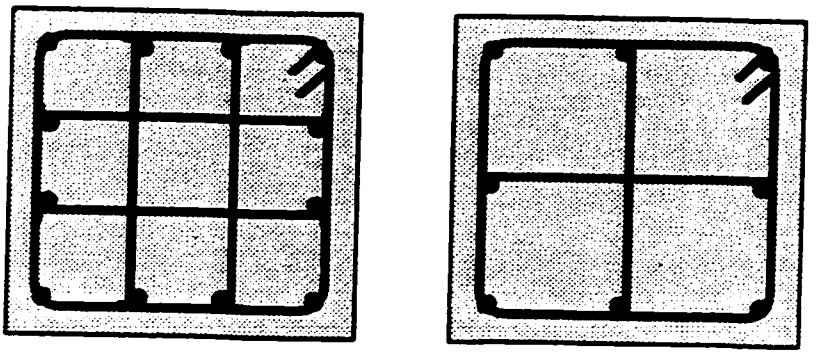

Figure 4-5: Cross-sectional arrangements used in SD columns

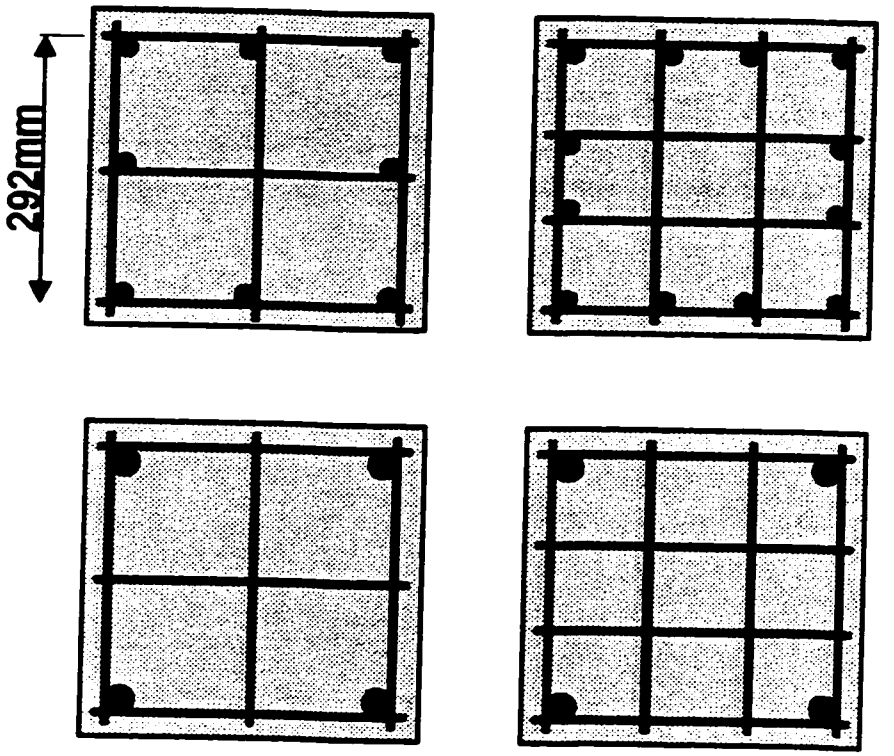

Figure 4-6: Cross-sectional arrangements used in FRP columns

Figure 4-7: Top view of FRP cages

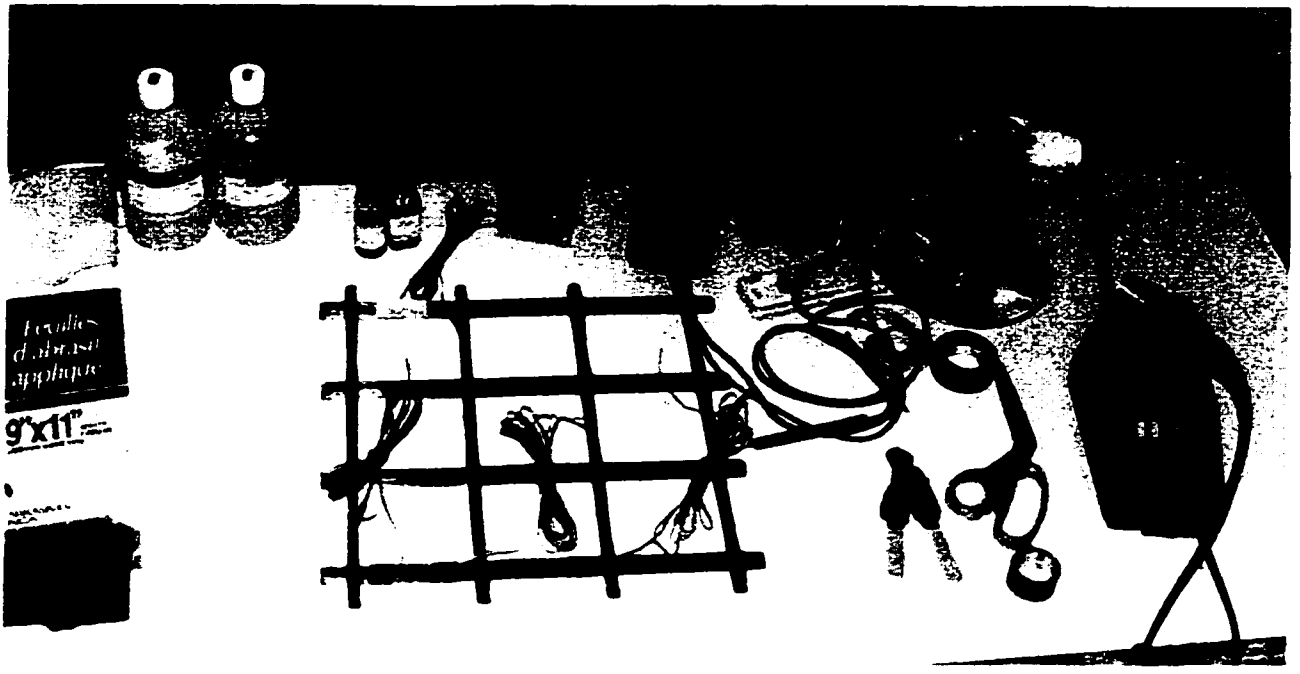

Figure 4-8: Strain gauge installation on typical grid reinforcement

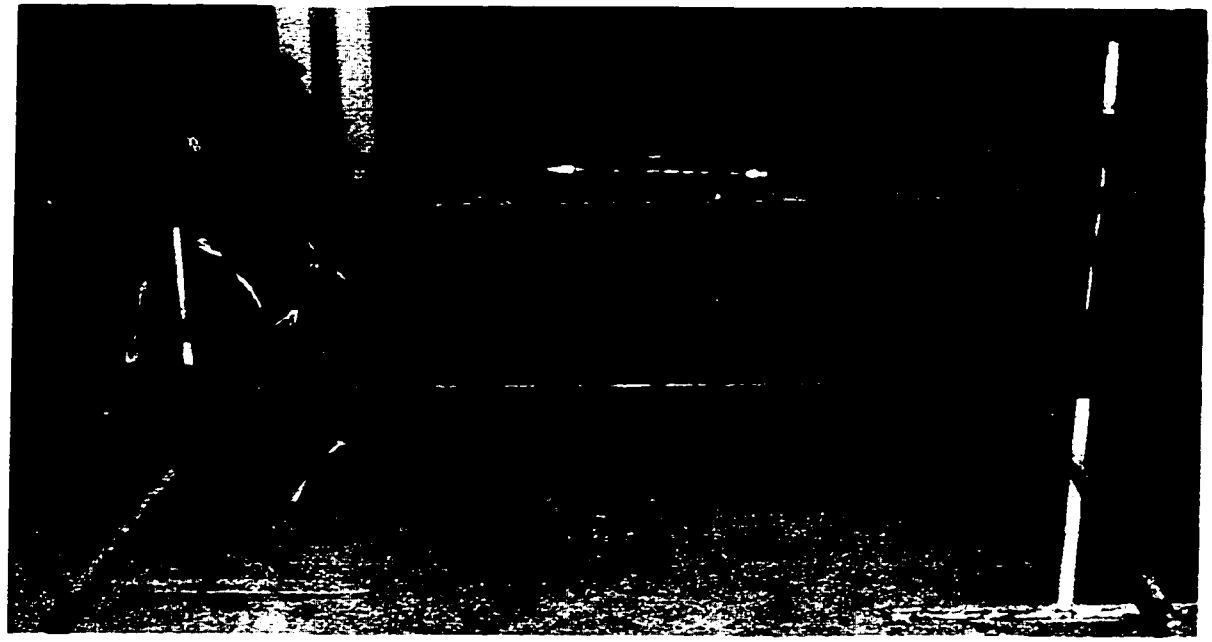

Figure 4-9: Preparation of a column cage

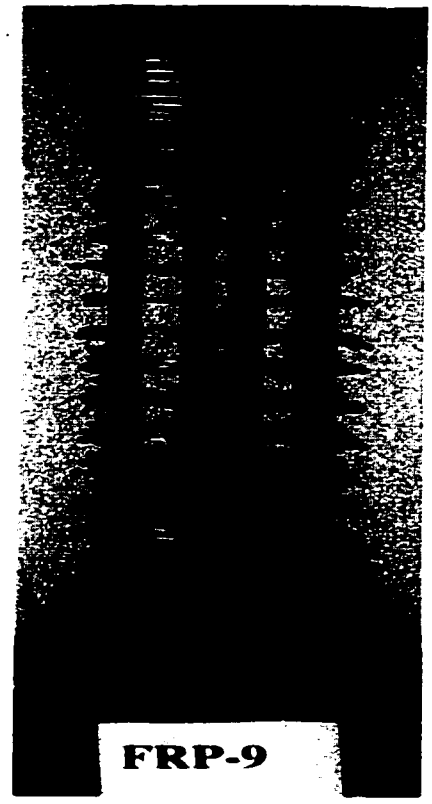

Figure 4-10: Preparation of a footing cage

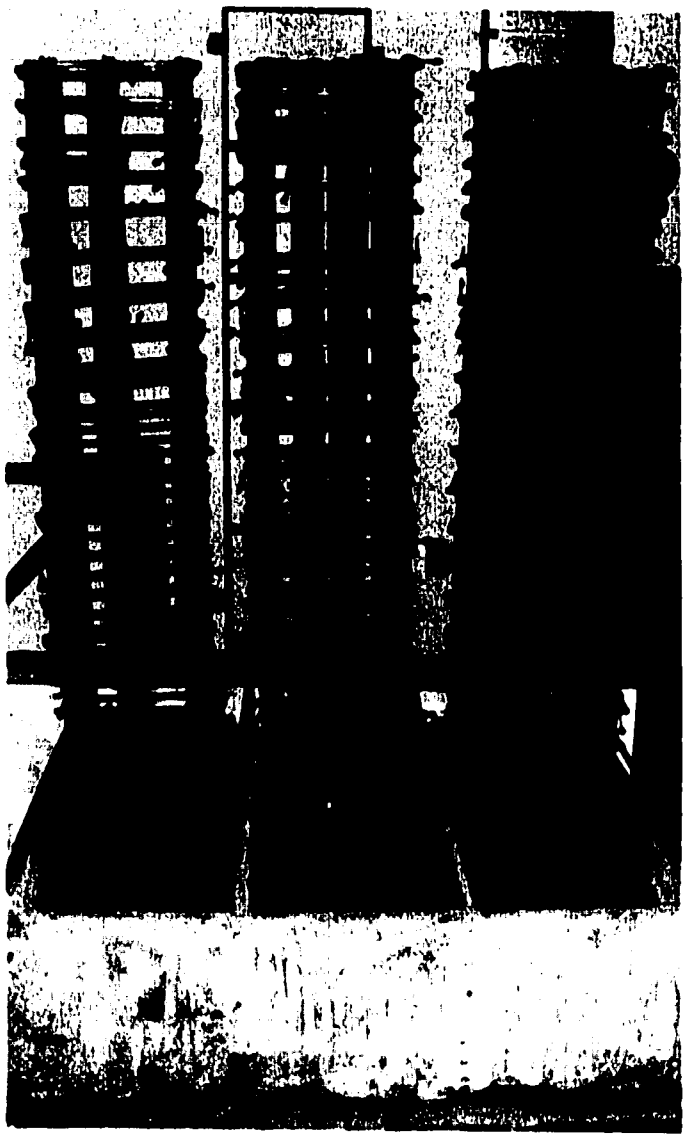

a) BG columns

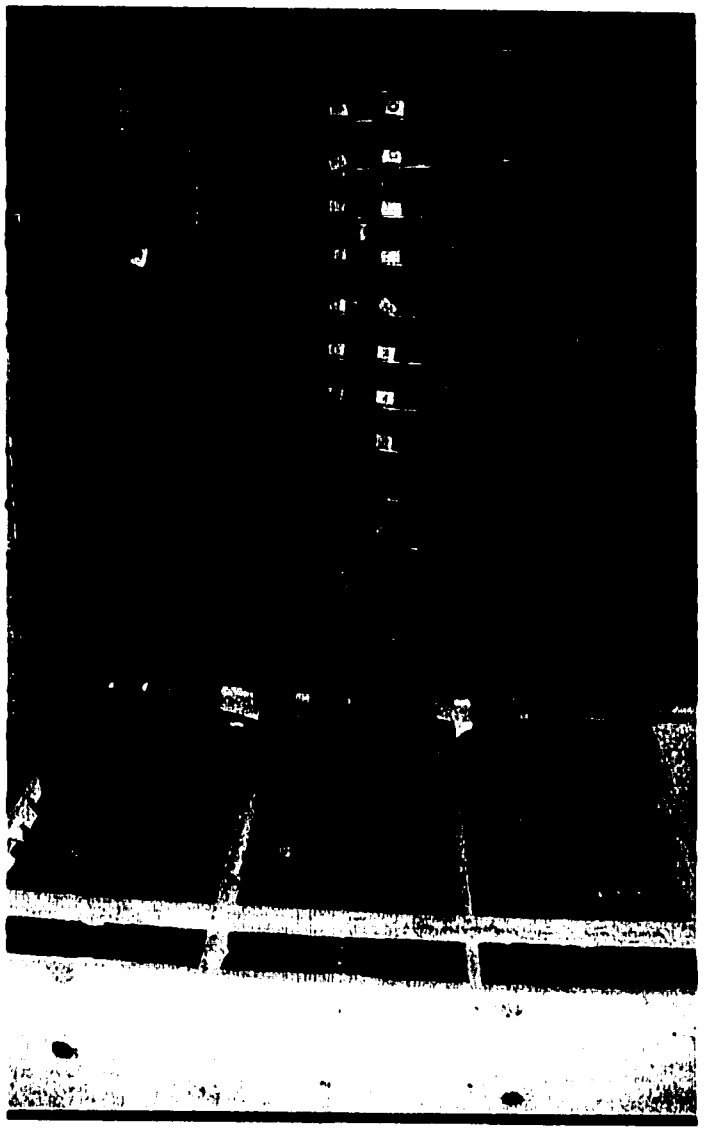

b) SD columns

Figure 4-11: Column cages placed in formwork

c) FRP columns

Figure 4-11: Cont.

Figure 4-12: Curing of concrete foundation and preparation for columns casting

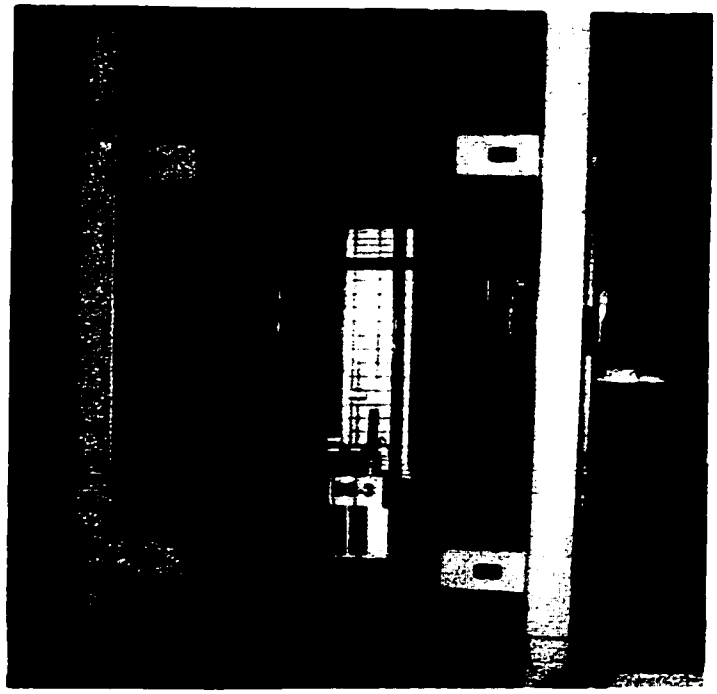

a) Front view

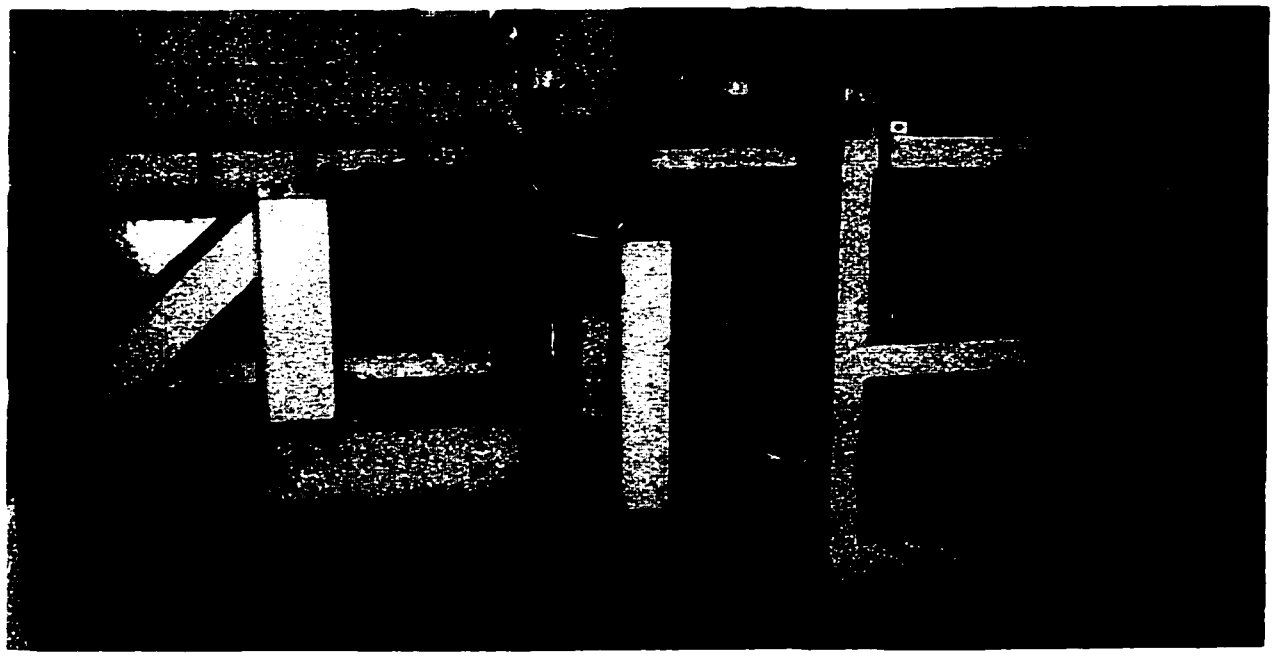

b) Side view

Figure 4-13: General view of test setup

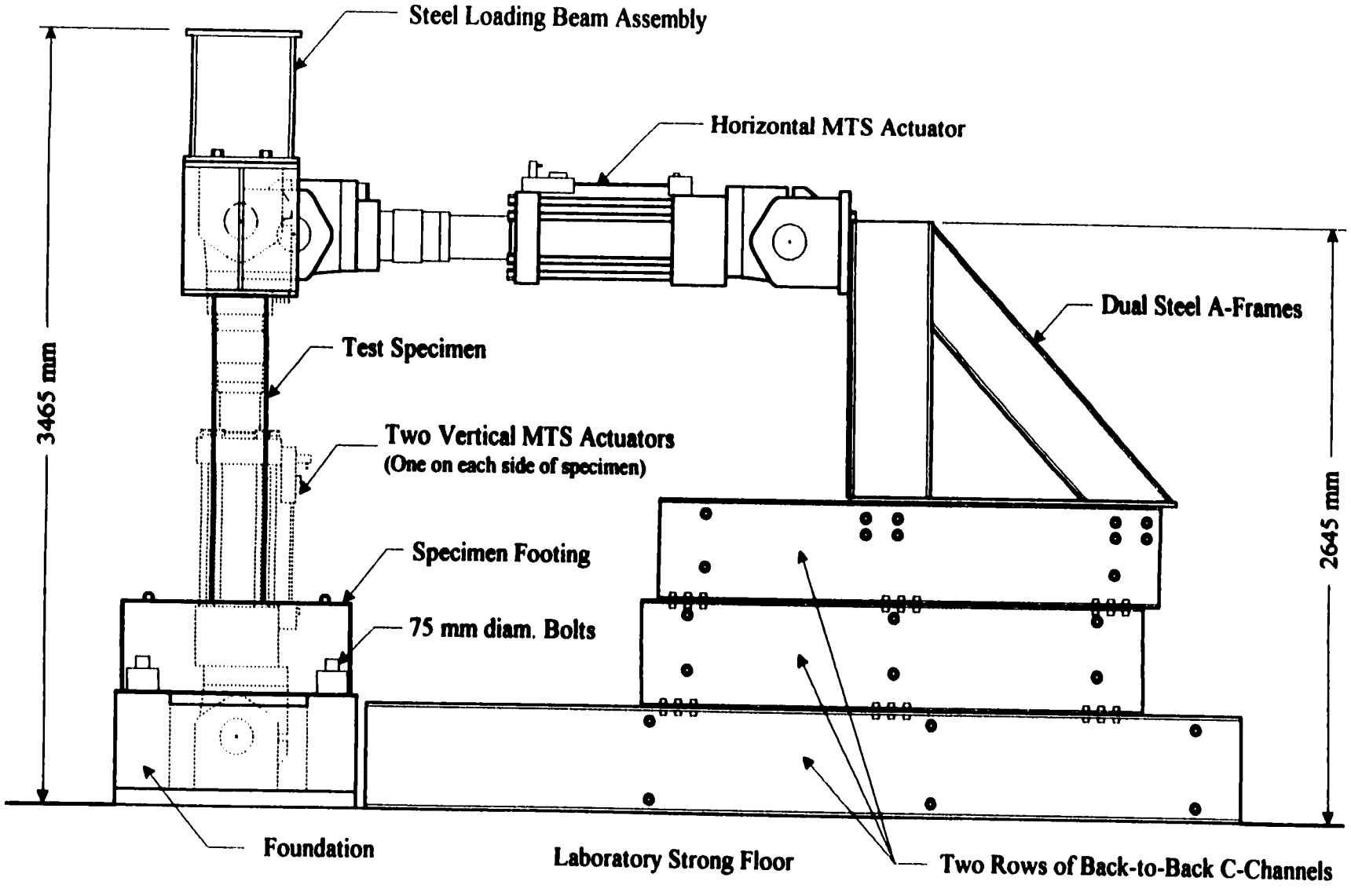

Figure 4-14: Side elevation of the test setup

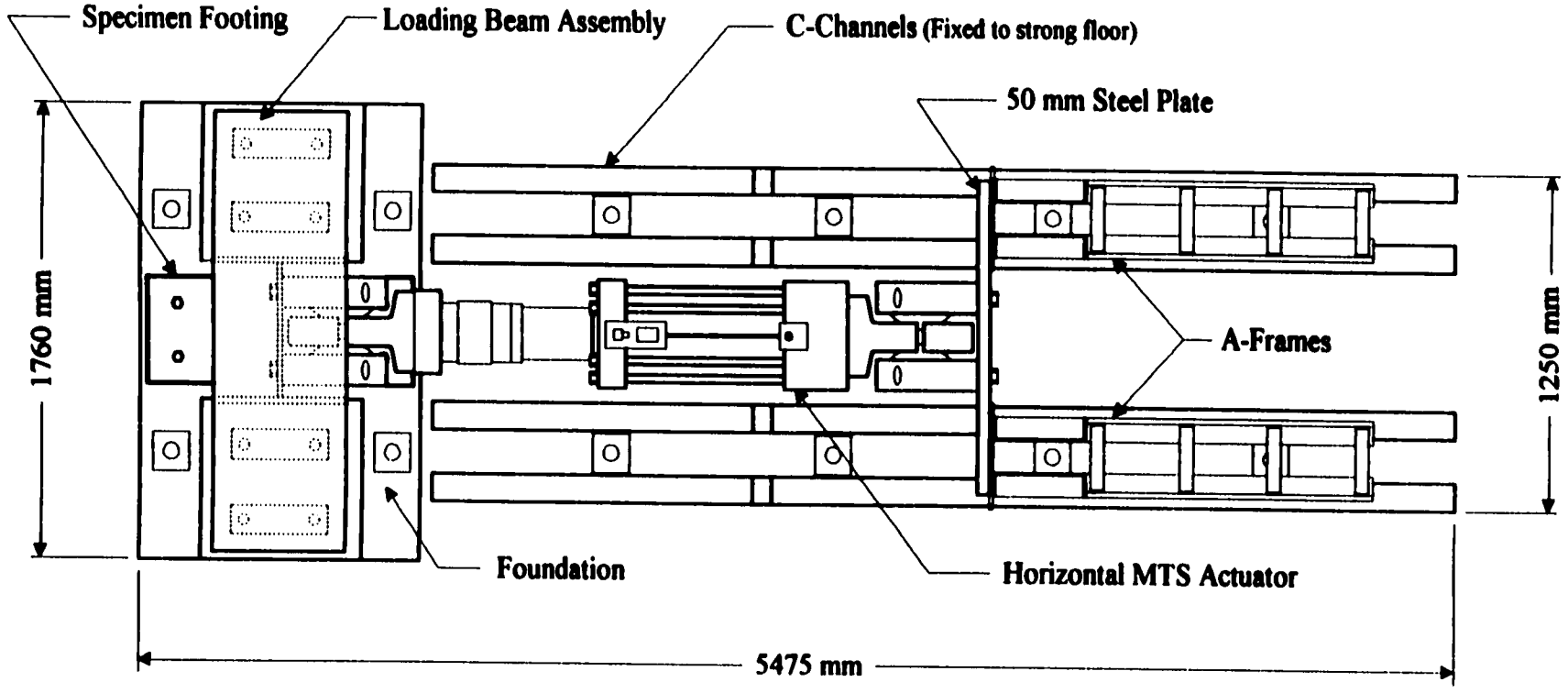

Figure 4-15: Plan view of test setup

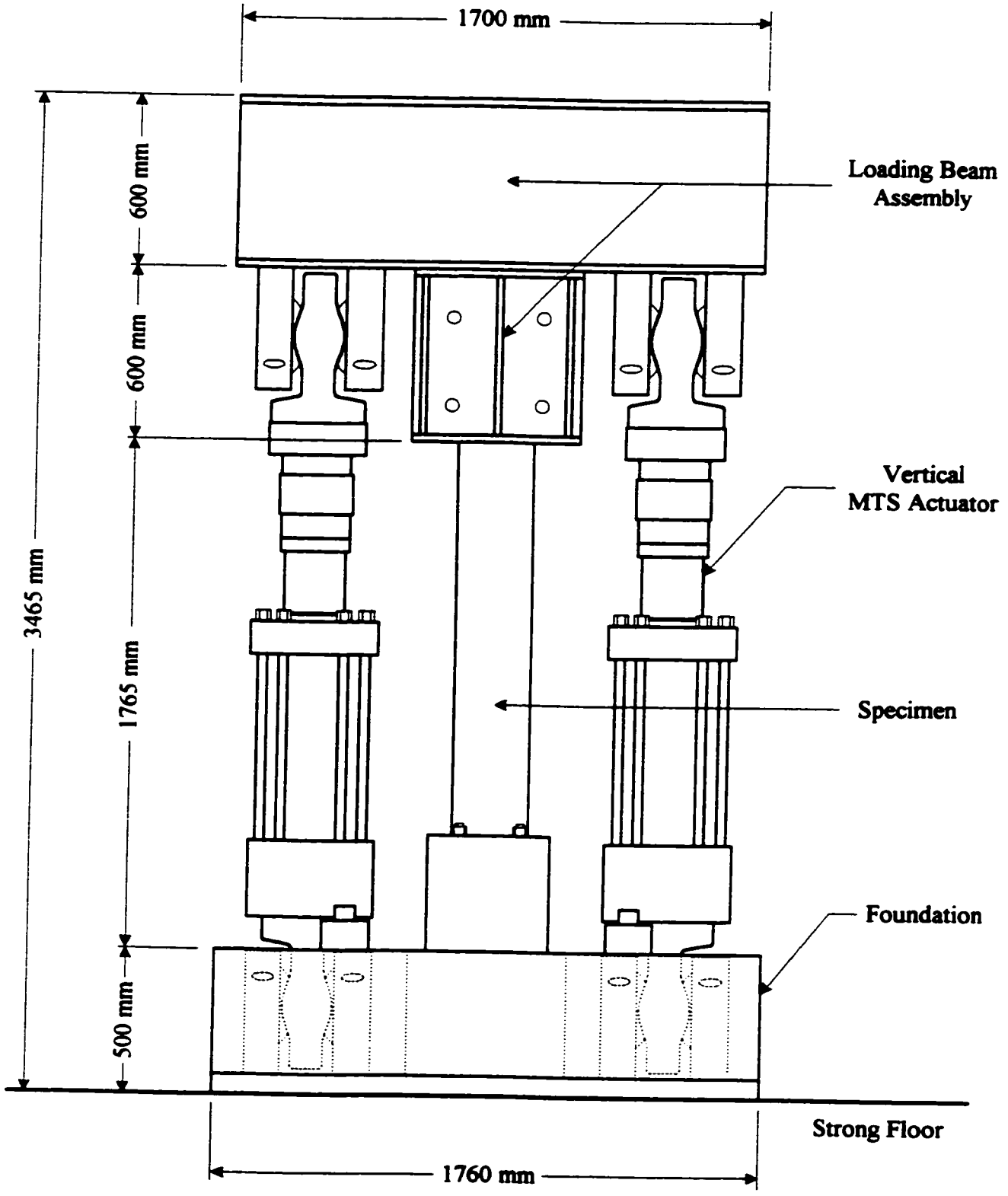

Figure 4-16: Front elevation of the test setup

a) Hydraulic Pump

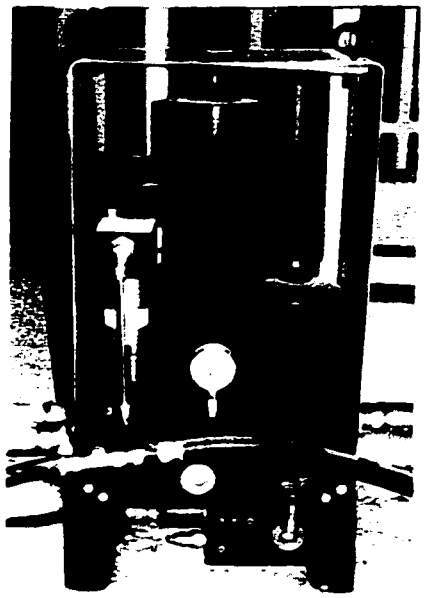

b) Hydraulic Manifold

Figure 4-17: Hydraulic power System

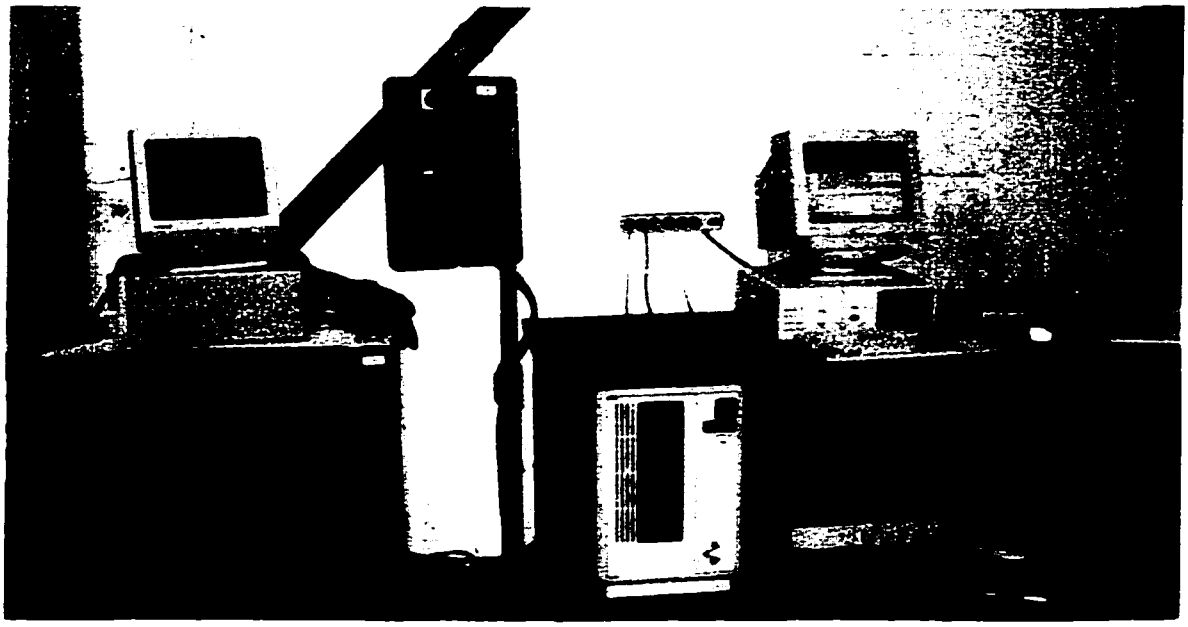

Figure 4-18: Loading control system

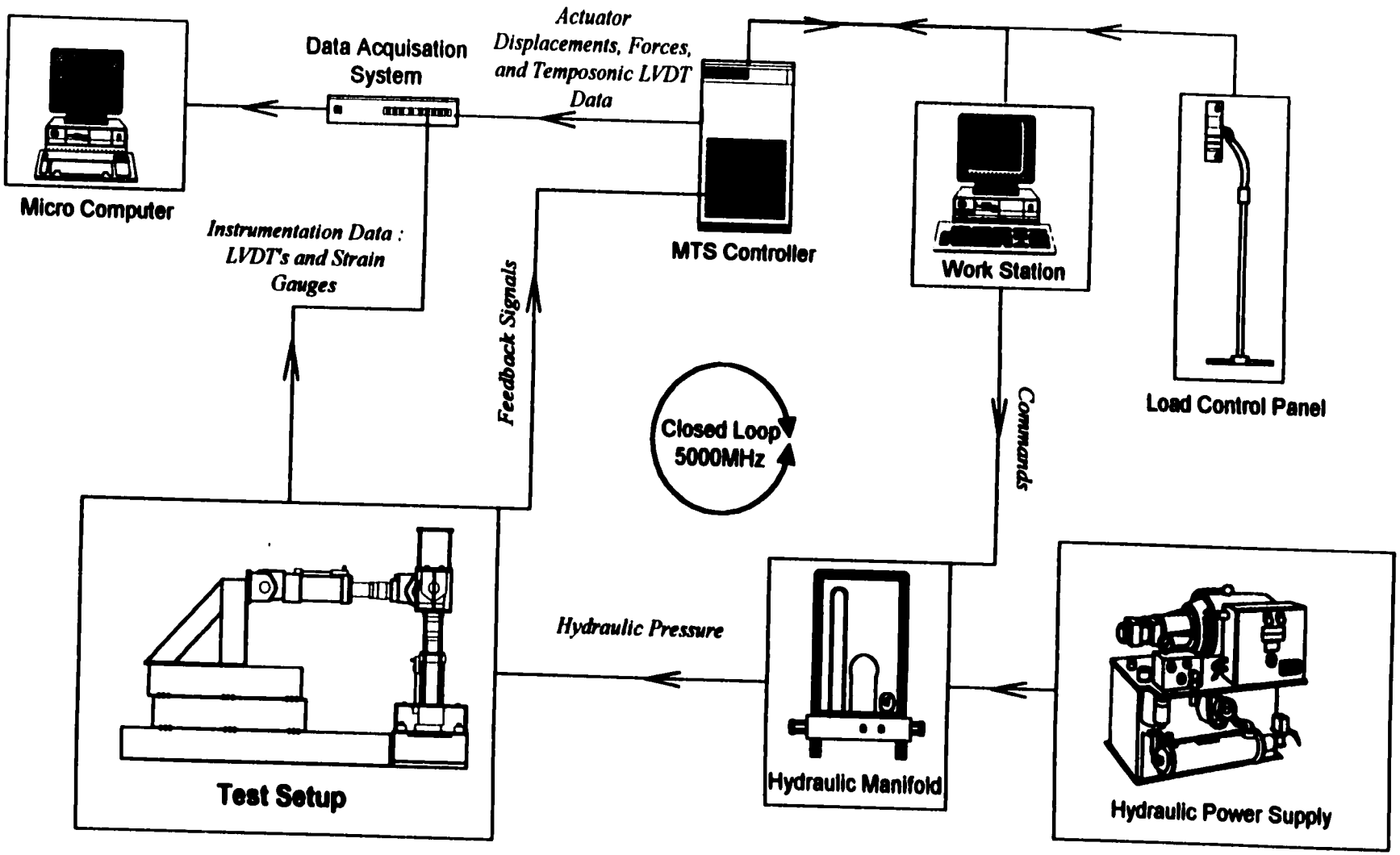

Figure 4-19: Schematic Network Diagram

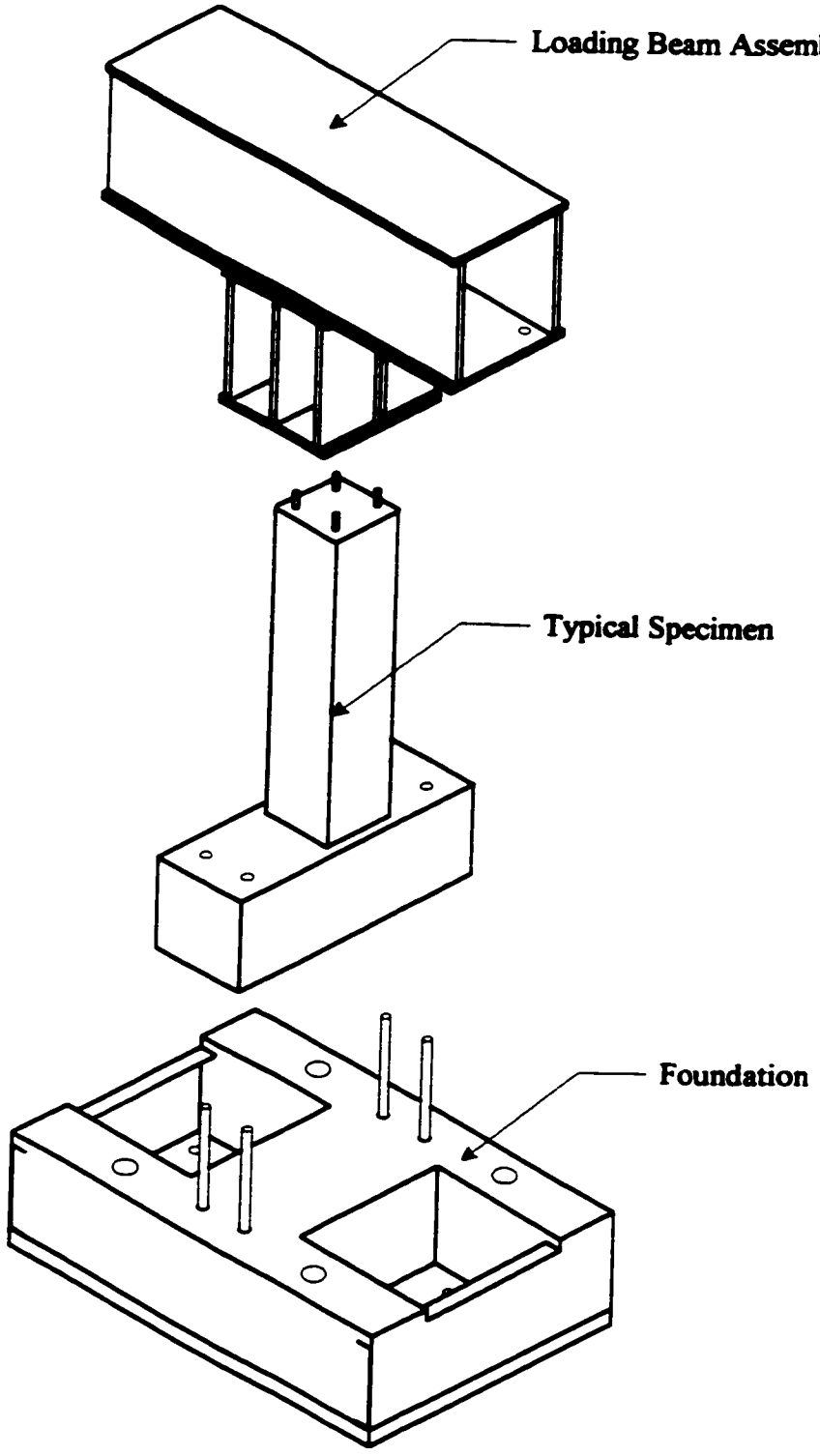

Figure 4-20: Sequence of column installation

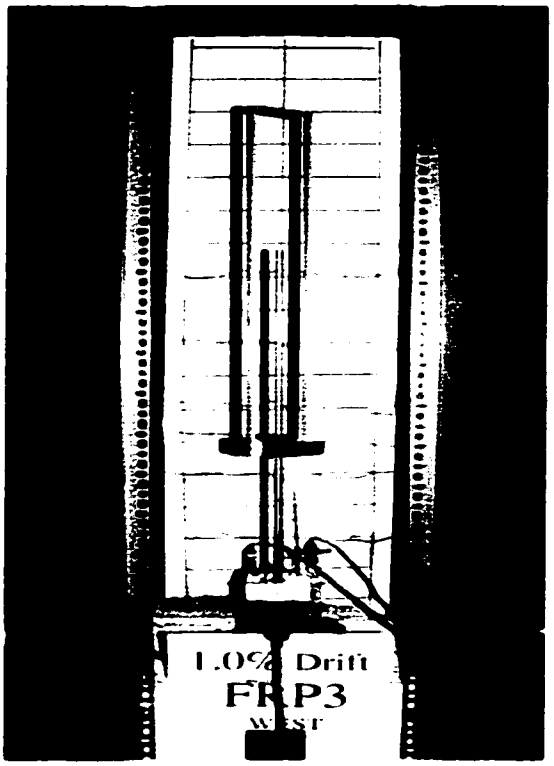

a) Front side

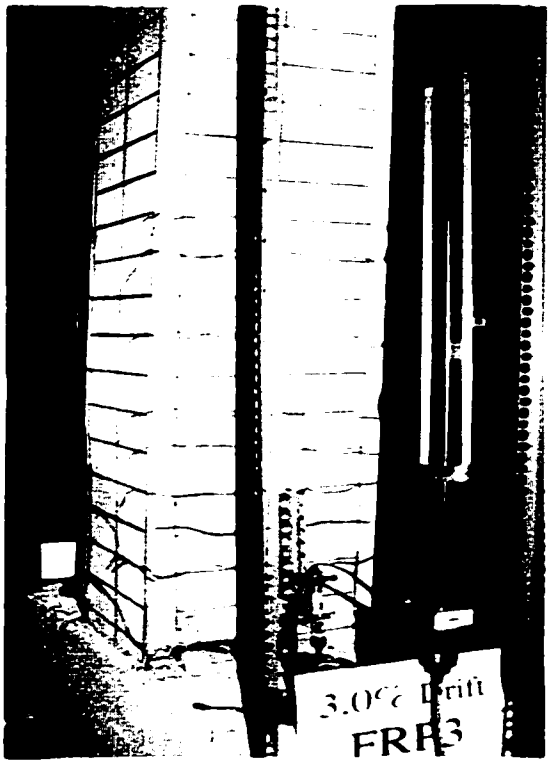

b) East Side

Figure 4-21: Instrumentation of a typical specimen during testing

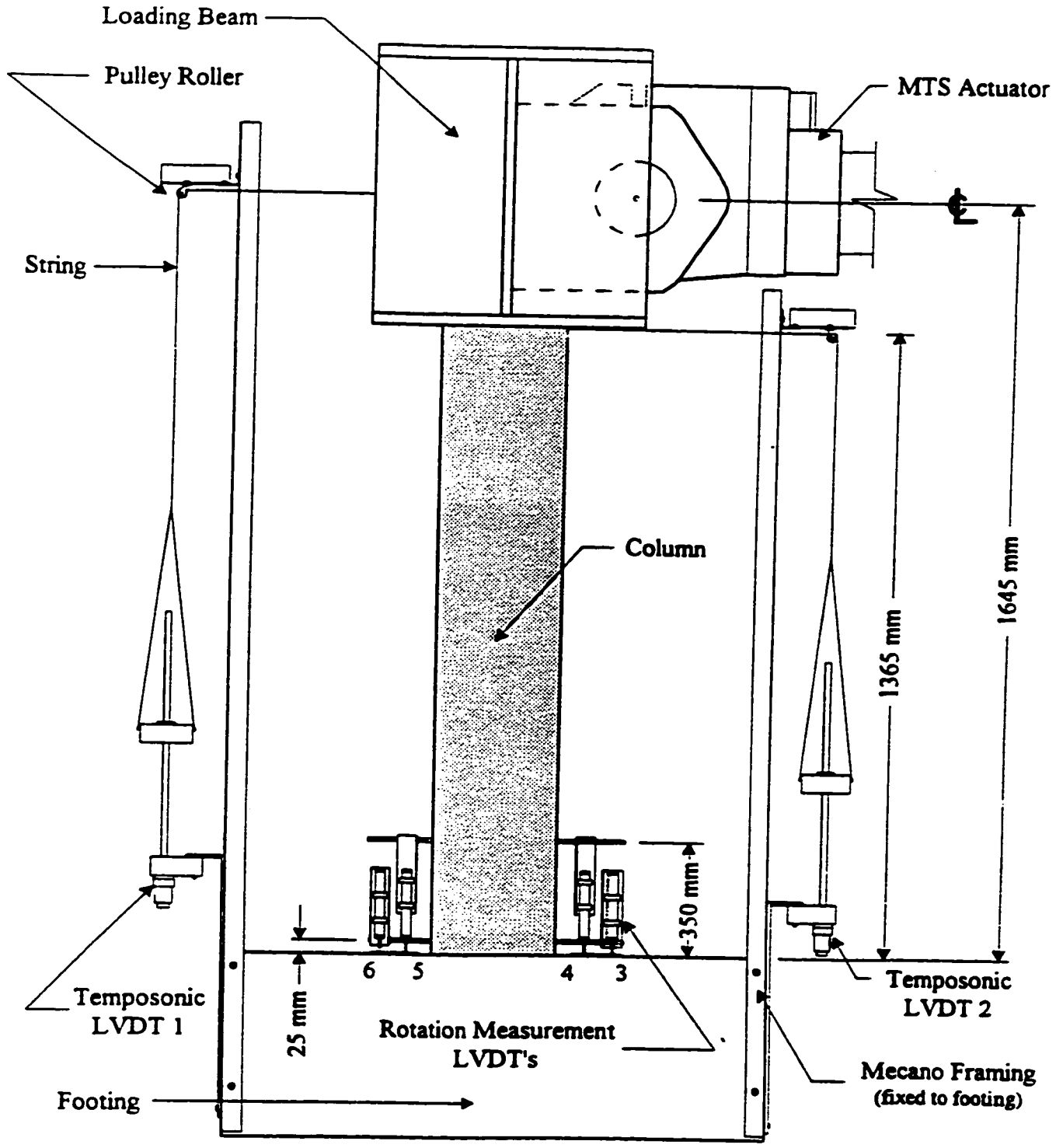

Figure 4-22: Instrumentation of a column specimen

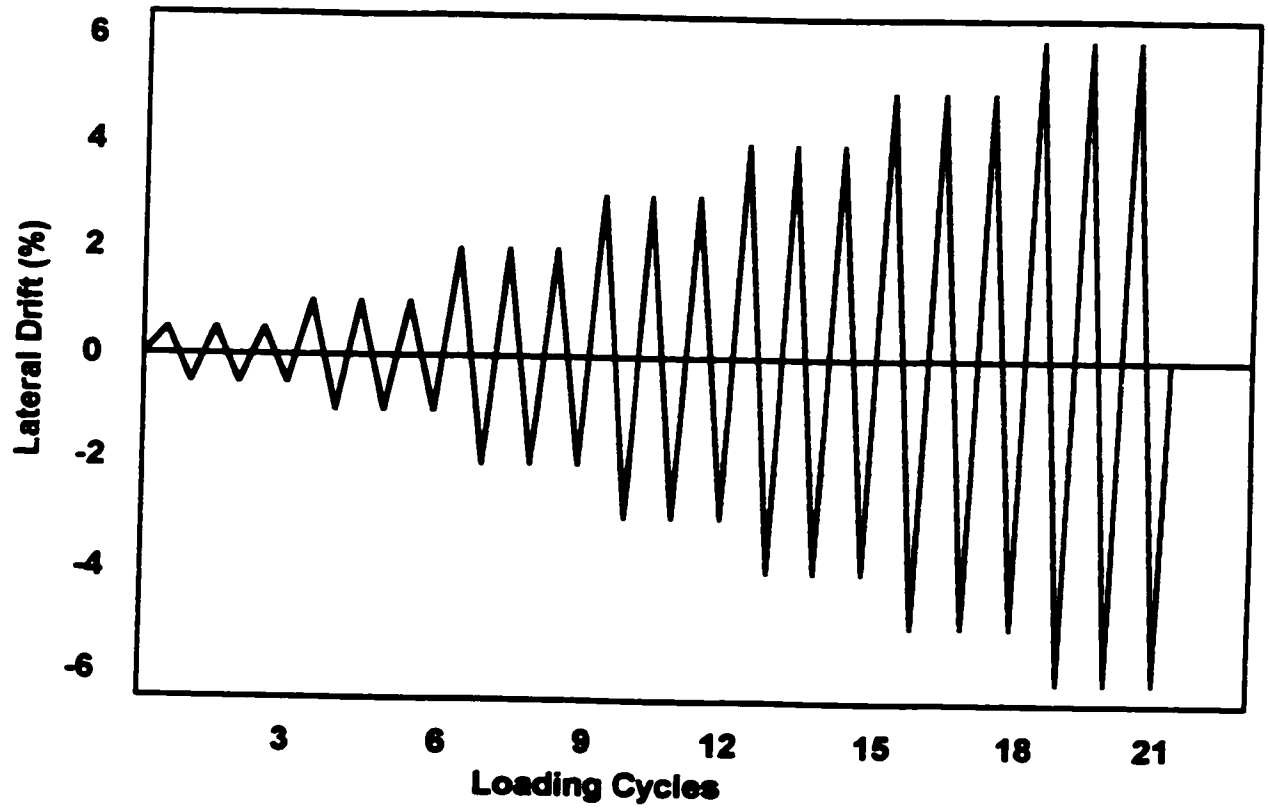

Figure 4-23: Loading History

Chapter 5

OBSERVED BEHAVIOR AND TEST RESULTS

5.1 Introduction

Thirty-one near-full-scale reinforced concrete columns were tested under heavy axial load and accompanying simulated lateral seismic loading as described in the preceding Chapter. A review of observed behavior for each column is presented and discussed in this Chapter. The performance of each column specimen is illustrated by photographs taken at selected load stages. The hysteretic behavior is presented both in terms of moment-displacement and force-displacement relationships. The moments plotted in these relationships are computed from recorded test data as the net lateral-force times the shear span plus the vertical axial force times the horizontal displacement (*P-Delta* moment). These moment-displacement relationships correspond to lateral force-lateral displacement relationships when the axial load passes through the critical column section at the base. Hence, these relationships do not show the degradation of lateral load resistance caused by *P-Delta* effect. Lateral force-lateral displacement hysteretic relationships, on the other hand, are plotted using the net horizontal resistance of columns as recorded during test, and the corresponding horizontal displacements while the vertical axial load component is acting on the column. Therefore, these relationships reflect the decay in lateral load resistance caused by *P-Delta* effect.

Hysteretic moment-total rotation, moment-anchorage slip rotation, and moment-flexural rotation relationships are presented and discussed also in this Chapter. Columns were instrumented to measure two sets of rotation readings within the potential hinge region. The hinging region was defined as the column segment between the column-footing interface and the section 350-*mm* above footing (equal to the cross-sectional dimension). The first set of readings gave total rotation of the assumed hinging region relative to footing. This set of readings consisted of rotations mostly due to flexure and also due to anchorage slip. The latter resulted from slippage and/or extension of reinforcement within footing, caused by the

penetration of yielding into the footing. Rotations due to anchorage slip were measured and formed the second set of readings. These readings were taken as the rotation of a column section near the column-footing interface relative to the footing. Ideally, these readings should have reflected the rotation of the critical column section at the interface. However, the *LVDT*'s used required some gauge length to be positioned on the column. Hence, they were mounted on a section approximately 25 ***mm*** above the interface. Therefore, these readings also include flexural rotations of the lowest 25-***mm*** segment of the column and hence are not accurate representation of anchorage slip. Furthermore, these readings were taken within the most disturbed region of columns because of concrete crushing. Hence, additional errors may have occurred especially near the end of testing when significant damage was observed in column hinging regions. The relatively small magnitude of anchorage slip readings provides a good indication of the significance of this deformation component in columns. The difference between total and anchorage slip rotations give rotations due to flexure.

Hysteretic relationships, depicting the variation of strains in both longitudinal and transverse reinforcement, are also presented. Each column specimen had two longitudinal bars instrumented with strain gauges placed at 50 ***mm*** below the column-footing interface. Normal-strength concrete BG columns had strain gauges placed on the first two grids above the footing. The closest to the footing was labeled as the first grid and the other as the second. All other columns had only the second transverse reinforcement instrumented. The strain gauges ceased to function at different stages of inelastic loading, either due to excessive damage or exceeding the gauge limit. Hence, the data presented may not represent the behavior of reinforcement until the end of testing.

5.2 General Observations

All columns showed similar behavior during the initial elastic cycles of deformation. Some flexural cracking was observed on the tension side near the critical column section. No sign of concrete damage was detected at this stage of loading. Deformation reversals at 1% drift resulted in additional flexural cracking. It was noticed that all the flexural cracks occurred near lateral reinforcement locations. Slight crushing of concrete cover was observed at the corners of the column-footing interface. Diagonal tension cracks were also observed on side

faces. Very little additional flexural cracks formed during subsequent levels of inelastic deformation. Instead, the existing cracks opened wider. Unlike the flexural cracks, new X-shaped diagonal tension cracks appeared on side faces every time an increased level of inelastic deformation was imposed. Spalling of concrete cover usually took place beyond 2% drift. Subsequent inelastic reversals of deformations resulted in further cover spalling and concrete crushing, followed by failure of transverse reinforcement or longitudinal bar buckling at large deformations. The amount of damage on each column varied depending on the level of axial compression, reinforcement arrangement, spacing, type, and volumetric ratio of transverse reinforcement. A summary of observed strength and drift capacities for all columns are tabulated in Table 5-1 along with nominal moment capacities computed following the *ACI 318-95* building code.

5.3 BG Columns

BG columns, confined with welded steel reinforcement grids and built from either normal or high-strength concrete, showed ductile response. With the exception of column BG-1, which had a grid spacing equal to approximately one half the cross-sectional dimension, and a volumetric ratio equal to 65% of that required by *ACI 318-95*, and developed 1% lateral drift, all other columns showed drift capacities of 2% and higher, even when *P-Delta* effects were considered. Columns conforming to the spacing requirements of *ACI 318-95*, with volumetric ratios ranging between 83% and 129% of that required by the code, showed ductile response even under high axial compression of approximately 40% of nominal concentric capacity. These columns developed lateral drifts of 3% to 6% prior to 20% degradation in moment resistance. Companion columns, tested under 20% of nominal concentric capacity, showed significantly higher deformabilities, developing 6% to 7% drift prior 20% degradation in moment resistance, and 4% drift at 20% decay in lateral force resistance. Columns confined with 9-cell grids showed higher deformability than those confined with 4-cell grids with the same volumetric ratio and spacing. Column BG-6, with only 4-corner longitudinal reinforcement and 9-cell grids showed ductile response similar to columns with 12-bar arrangement. Columns BG-9 and BG-10, with longitudinal bars placed on both sides of a perimeter grid joint, performed as good as those with single longitudinal bars placed on only one side of a grid joint. However, when the size of the longitudinal bars

was reduced, the bars became more susceptible to buckling. High-strength concrete columns were less ductile compared to normal-strength concrete columns. However, they resisted higher lateral forces. These columns developed 4% to 6% drift prior to 20% degradation in moment resistance and 2% to 4% drift at 20% decay in lateral force resistance. Column BG-11, confined with 9-cell grids, showed higher lateral force resistance and higher deformability than column BG-13, confined with 4-cell grids using the same size and spacing of reinforcement. Reduction in the amount of transverse reinforcement ratio in column BG-12 by about 50% resulted in a decrease of deformability by about 30%. A detailed description of the response of each of the BG columns is presented in the following sub-sections.

The welded reinforcement grids were instrumented to have strain gauges mostly placed at perimeter weld locations, on steel immediately behind the welds. Figure 5-1 illustrates the gauge location. During response, however, the protruding parts of reinforcement beyond the perimeter welds curved towards the welds, generating compression in the gauges. This is shown in Figs. 5-1(b) and 5-1(c). Consequently, these readings did not provide any information regarding the amount of tension in grid reinforcement. The compression strain is indicated by a negative reading, while the tension strain is indicated by a positive value.

5.3.1 Column BG-1

Column BG-1 was reinforced with 8#20 (19.5 *mm* diameter) longitudinal bars resulting in 1.96% reinforcement ratio. It was confined with 4-cell grids. The volumetric ratio of transverse reinforcement was 1.0%, which formed 65% of the amount required by *ACI 318-95*. The spacing of grids was 152 *mm* (6 *in*), which was approximately twice the maximum spacing required by *ACI 318-95*. The column was tested under a constant compressive force of 39% of its concentric capacity. The hysteretic relationships shown in Fig. 5-2 indicate that the column showed stable hysteresis loops up to 1% lateral drift but developed a significant strength decay during the second cycle at 2% drift. This was expected because of the low volumetric ratio of transverse reinforcement provided for the high level of axial compression imposed. The column failed due to the buckling of longitudinal reinforcement during the second cycle of 3% drift

Observations during testing indicated that the column experienced initial flexural cracks at 0.5% and 1% drift levels. The flexural cracks became visible within the lower 625-*mm* portion of the column. The cover concrete started crushing when the column was loaded to 2% lateral drift. The crushing of concrete became severe especially on the East Side of the column. At the end of 2% drift cycles the cover concrete below the second layer of grids near the base spalled off completely, exposing the reinforcement cage. The plastic hinging of the column near the base was visibly noticeable during the first cycle at 3% drift. During the second cycle at 3% drift level, the longitudinal reinforcement in the northwest corner buckled between the first and second grids from the base. Subsequently, the middle bars of the north side buckled between the second and the third layers of grids. The second grid from the base deformed excessively and bulged out under lateral expansion, while maintaining its integrity. There was no sign of weld failure or fracture of transverse steel even after the buckling of longitudinal reinforcement. The drop in load resistance was excessive during the second cycle at 3% drift, and the test was discontinued. Figure 5-3 illustrates the performance of column BG-1 at selected stages of loading.

Hysteretic moment-rotation relationships recorded during the test are shown in Fig. 5-4. The anchorage slip rotation includes flexural deformations within the bottom 25-*mm* segment because it was measured within a gauge length of 25 *mm*. Figure 5-4 indicates that at the end of the test, approximately 1/8th of total rotation was caused by anchorage slip, leaving the remaining 7/8th to flexure.

Strain gauge readings are presented in Fig. 5-5. Test results indicate that longitudinal reinforcement yielded during the first cycle of 3% drift. The second grid, located 125 *mm* (4.5 *in*) from the bottom of the column, was strained more than the first one. It yielded immediately after the yielding of longitudinal reinforcement.

5.3.2 Column BG-2

Column BG-2 was companion to BG-1, reinforced with 8#20 longitudinal bars. It was confined with 9-cell grids. Although the same size grids were also used in this column, the grid spacing was reduced by a factor of 2 resulting in doubling the volumetric ratio of transverse reinforcement. The grid spacing was 76 *mm* (3 *in*) and the volumetric ratio was

2.00%, exceeding the confinement steel requirement of *ACI 318-95* by 29%. The column was subjected to 39% of its concentric capacity. It behaved better than the companion column BG-1. The reduction in tie spacing increased the effectiveness of confinement and stability of longitudinal reinforcement. The moment-displacement hysteretic relationship shown in Fig. 5-6(a) indicates that the column showed stable hysteresis loops up to 3% drift with little strength decay, and failed at 5% drift due to bar buckling and concrete crushing. The force-displacement hysteretic relationship of Fig. 5-6 (b) shows reduced deformability due to *P-Delta* effect, and indicates about 2% column drift capacity at 20% loss in lateral load resistance.

Observations during the test indicated that the first flexural crack occurred when the column was subjected to the first cycle at 0.5% drift, near the second grid location from the base. Additional flexural cracks occurred at other grid levels during the subsequent cycles of 0.5% drift. Diagonal tension cracks started forming on side faces at 1% drift. Additional flexural cracks were also observed at this deformation level, although no cover crushing was evident. The cover concrete started to crush near the base at 2% drift level. Widening of diagonal cracks was also observed at this deformation level. Gradual spalling of cover concrete occurred during 3% drift cycles, which eventually led to the complete spalling of the hinging region at 4% drift. Cover spalling extended up to the fourth grid level, exposing reinforcement. Additional damage to concrete was noticed during the cycles at 5% drift. The hinging region became clearly visible and measured to be 350 *mm* from the base. The longitudinal reinforcement buckled during the second cycle at 5% drift and the column resistance dropped suddenly. When the column was pushed further to complete the second cycle at 5% drift, the rupturing of grid reinforcement was observed. Figure 5-7 illustrates the performance of column BG-2 at selected stages of loading.

Hysteretic moment-rotation relationships, recorded during the test, are shown in Fig. 5-8. The yield penetration into the footing was not observed until after 3% drift. Figure 5-8 indicates that at the end of the test, approximately 1/6th of total rotation was caused by anchorage slip, and 5/6th by flexure.

Figure 5-9 depicts the results obtained by strain gauges. The longitudinal reinforcement developed high tensile strains, showing 1.1% at 3% drift, 1.34% at 4% drift, and 1.7% at 5% drift, entering into the strain hardening region and implying significant yield penetration into the footing.

5.3.3 Column BG-3

Column BG-3 was identical to column BG-2 in every respect, with 129% of the confinement steel required by *ACI 318-95*. However, this column was tested under a lower level of axial compression, corresponding to 18% of its concentric capacity. The hysteretic relationships illustrated in Fig. 5-10 indicate that the column behaved in an extremely ductile manner, showing virtually no decay in moment resistance up to 7% drift, and 20% decay in lateral force resistance at 4% drift due to *P-Delta* effect. This confirms the expected trend of improvement in column deformability with reduced axial compression.

Observations during testing indicated that only hairline cracks formed at 0.5% drift cycles. These cracks became wider at 1% drift. No shear cracks were observed at this load stage. Slight crushing of cover concrete on the compression side was observed during the cycles at 2% drift. A wide flexural crack appeared at the column-footing interface, signifying yield penetration into the footing. Cover spalling started at 3% drift and continued during 4% and 5% drift cycles. The cover concrete completely spalled off within the hinging region, which was measured to be approximately equal to the cross-sectional dimension of the column. The column continued resisting loads during cycles at 6% drift, and was able to sustain the first cycles at 7% drift, during which the longitudinal bars started to buckle. When the column was pushed to the second cycle at 7% drift, the longitudinal and transverse reinforcement fractured in tension, marking the end of the test. Figure 5-11 illustrates the performance of column BG-3 at selected stages of loading.

Hysteretic moment-rotation relationships for column BG-3 are shown in Fig. 5-12. The yield penetration into the footing became significant near the end of the test, resulting in considerable slip rotations. The anchorage slip rotation was recorded to be approximately 1/7th of total rotation, while the flexural rotation constituted the remaining 6/7th.

It was observed that the longitudinal reinforcement yielded during at 1% drift. The recorded strains were 0.78% at 2% drift and 1.26% at 3% drift. The strain gauges ceased to function beyond 3% drift. The first grid above the footing gave low strain readings and remained elastic. However, the second grid yielded during the first cycle at 3% drift. Figure 5-13 illustrates the variation of strain in grid reinforcement with imposed lateral loading.

5.3.4 Column BG-4

Column BG-4 was reinforced with 12#20 longitudinal bars which resulted in 2.94% reinforcement. It was confined with 9-cell grids. The volumetric ratio of transverse reinforcement was 1.33%, which formed 86% of the amount required by *ACI 318-95*. The spacing of grids was 152 *mm* (6 *in.*), which was approximately twice the maximum spacing required by *ACI 318-95*. The column was subjected to 38% of its concentric capacity. The hysteretic relationships shown in Fig. 5-14 indicate that the column showed stable hysteresis loops up to 2% drift and failed during the second cycle of 4% drift when the longitudinal bars buckled and the core concrete crushed. The column behaved much better than column BG-1 which had slightly lower volumetric ratio but was otherwise similar to BG-4, mainly because of the difference in the number of grid cells. BG-4 was reinforced with 9-cell grids, producing closer spacing of transverse reinforcement in the cross-sectional plane, resulting in a more uniform distribution of lateral confinement pressure.

Observation during testing indicated that initial flexural cracking started at 0.5% and 1% drift cycles. Some shear cracking and cover crushing occurred during the cycles at 2% drift. The cover concrete started to spall off during the cycles at 3% drift. Severe damage to the hinging region concrete was also observed. The column failed due to the buckling of longitudinal reinforcement and crushing of core concrete during the cycles at 4% drift. No failure was observed in the grids. Figure 5-15 illustrates the performance of column BG-4 at selected stages of loading.

Hysteretic moment-rotation relationships for column BG-4 are shown in Fig. 5-16. Increased rotations due to anchorage slip were measured near the end of the test, indicating significant yield penetration into the footing. Figure 5-16 indicates that at least 1/5th of total rotation could be attributed to anchorage slippage, leaving the remaining 4/5th to flexure.

The variation of strains in reinforcement during testing is shown in Fig. 5-17. It was observed that the longitudinal reinforcement yielded during the last cycle of 1% drift, and developed tensile strains showing 0.9% at 2% drift, 1.0% at 3% drift, and 1.1% at 4% drift. This indicated that the longitudinal reinforcement was stressed into the strain-hardening region, implying significant yield penetration into the footing. The vertical spacing of transverse reinforcement was 150 *mm* (6 *in*). Hence, the first reinforcement grid was located at 75 *mm* (3 *in*) from the column-footing interface. The transverse reinforcement yielded at the same time as the longitudinal reinforcement. The first grid recorded strains of 0.35% at 2% drift and 0.6% at 3% drift, while the second grid showed strains of 0.45% at 2% drift and 0.72% at 3% drift.

5.3.5 Column BG-5

Column BG-5 was companion to BG-4 and was reinforced with 12#20 longitudinal bars confined with 9-cell grids. Although the grid size was kept constant, the spacing of grids was reduced in BG-5 by a factor of 2, resulting in an increase in the volumetric ratio. The grid spacing was 76 *mm* (3 *in*) and the volumetric ratio of transverse reinforcement was 2.66%, which was 72% higher than that required by *ACI 318-95*. The column was subjected to 38% of its concentric capacity. The hysteretic relationships shown in Fig. 5-18 indicate that the column showed no loss of moment resistance up to 5% drift, while the lateral load resistance dropped to approximately 80% of its peak at 3% drift, because of *P-Delta* effect. The failure was initiated by buckling of longitudinal reinforcement at 7% drift. The improved behavior relative to column BG-4 was attributed to reduced grid spacing, and the improvement relative to column BG-2 was attributed to the increased number of grid cells, providing better distribution of transverse reinforcement within the cross-sectional plane, improving the uniformity of confinement pressure.

Observations during testing revealed that the column developed initial flexural cracking during cycles at 0.5% and 1% drift. Some diagonal tension cracks also formed on the side faces during these cycles. No visible damage was observed until the column was subjected to 2% drift. Spalling of cover concrete started at 2% drift and continued during 3% drift cycles. Deformations at 4% and 5% drift resulted in the complete spalling of cover concrete within

the hinging region, which was measured to be approximately 350 *mm* from the footing. The longitudinal bars showed signs of buckling at 6% drift when the strain recorded was 1.4%. One longitudinal bar fractured in tension during the first cycle at 7% drift, resulting in a sudden drop of loading. Figure 5-19 illustrates the performance of column BG-5 at selected stages of loading.

Hysteretic moment-rotation relationships of the hinging region are shown in Fig. 5-20. It was concluded that approximately 1/5th of total rotation was caused by anchorage slip, leaving 4/5th to flexure.

The strain readings for reinforcement are plotted in Fig. 5-21. The longitudinal reinforcement yielded at 2% drift, and developed strains of 0.82% at 4% drift, 1.03% at 5% drift, and 1.38% at 6% drift. Strain gauge #3 showed compression and tension since it was placed at a weld location immediately behind a welded grid-joint. The protruding part of the transverse bar beyond the perimeter welds was curving up and down during cyclic loading. This caused the gauge being strained under cyclic compression and tension.

5.3.6 Column BG-6

Column BG-6 was reinforced with 4#30 (29.9-*mm* diameter) corner bars. The reinforcement grids had 9 cells, without any longitudinal reinforcement in the remaining perimeter grid corners. The volumetric ratio and spacing of transverse reinforcement were identical to those for column BG-5. It was loaded to 40% of its concentric capacity as constant axial compression. The hysteretic relationships shown in Fig. 5-22 indicate that the column behaved as good as the companion column BG-5, developing 5% drift without any sign of strength decay in moment resistance, and 3% drift in lateral force resistance at approximately 20% strength decay. This result has a significant practical implication, indicating that the grids are able to provide the required lateral restraint at grid joints without any longitudinal reinforcement. The close spacing of transverse reinforcement within the cross-sectional plane improved the distribution of lateral confinement pressure without the presence of longitudinal reinforcement. However, additional tests may be necessary to further confirm this point, as this specimen was the only column confined with this type of arrangement. Column BG-6 was one of the first columns tested and the test was discontinued prematurely

due to a safety concern at a high drift level of 5%, before developing a significant loss in strength.

Observations during testing indicated that only one flexural crack was observed during cycles at 0.5% drift. Additional four cracks were noticed at the bottom four-grid locations during cycles at 1% drift, in addition to a crack that formed at the column-footing interface. The concrete cover near the base started crushing at 2% lateral drift, while shear cracks were observed on the side faces. Some crushing of cover concrete was observed near the base at 3% lateral drift. No new flexural cracks were observed at this drift level although additional shear cracks became noticeable. Increased spalling of cover concrete was observed at 4% drift. The test was stopped at 5% drift due to a safety concern related to the lateral bracing system. Figure 5-23 shows the performance of column BG-6 during selected stages of testing.

Hysteretic moment-rotation relationships for column BG-6 are showed in Fig. 5-24. It can be concluded from this figure that approximately 1/5th of total rotation was caused by anchorage slip and the remaining 4/5th by flexure.

Column BG-6 was longitudinally reinforced with #30 rebars, which are less susceptible to buckling compared to smaller size bars. The longitudinal reinforcement yielded at 2% drift and showed a strain of 1.05% just before buckling. The transverse reinforcement yielded at 3% drift. This deformation level was higher than those that caused yielding in previously tested columns. This may be attributed to the stability of #30 bars as compared to #20 bars used in the previous columns, and the resulting delay in tendency of buckling and the development of restraining stresses in transverse reinforcement. Figure 5-25 shows hysteretic behavior of selected strain gauges placed on both longitudinal and transverse reinforcement.

5.3.7 Column BG-7

Column BG-7 was companion to BG-5 with 12#20 (19.5-*mm* diameter) longitudinal reinforcement and 9-cell grids spaced at 76 *mm* (3 *in.*). However, the diameter of grid reinforcement was reduced to 6.60 *mm* (1/4 *in.*), to reduce the volumetric ratio to 1.26%. This amount of transverse steel corresponded to 83% of that required by *ACI 318-95*. The axial

load level was kept constant at 38% of the concentric capacity. The hysteretic relationships shown in Fig. 5-26 indicate that the column showed ductile response even with a lower volumetric ratio than that required by *ACI 318-95*, because of the improved distribution of confinement pressure associated with 9-cell grids. The moment resistance was maintained until 4% lateral drift without any strength decay while the lateral force resistance showed 3% drift at 20% strength loss.

The observed behavior of column during testing indicated that some flexural cracks occurred during cycles at 1% drift, including a crack at the column-footing interface. No shear crack was observed at this load stage. More flexure and shear cracks were observed during the cycles at 2% drift level. The deformation cycles at 3% drift resulted in spalling of the cover concrete. Additional shear cracks were observed on side faces. The cycles at 4% drift resulted in the spalling of cover, exposing reinforcement. The plastic hinge length was measured to be approximately equal to the cross-sectional dimension. The column failed during the first cycle at 5% drift due to the buckling of longitudinal reinforcement and subsequent crushing of the core concrete. Figure 5-27 illustrates the performance of column BG-7 at selected stages of loading.

Column BG-7 showed increased yield penetration into the footing near the end of the test, causing significant rotations due to anchorage slip, especially on the West Side of column. Figure 5-28 indicates that approximately 1/5th of total rotation could be attributed to anchorage slip and about 4/5th to flexure.

Figure 5-29 shows plots of recorded strains in reinforcement. The longitudinal reinforcement yielded during the first cycle of 2% drift and showed almost symmetric hysteresis loops. In addition, the longitudinal bars were stressed into the strain-hardening region and developed 0.71% at 3% drift and 1.24% at 4% drift.

5.3.8 Column BG-8

Column BG-8 was companion to BG-7 with identical properties except the axial compression. The level of constant axial compression was reduced to 19% of the concentric capacity to investigate the effect of axial load. The hysteretic relationships shown in Fig. 5-

30 indicate that the column showed ductile response with no strength decay in moment resistance up to 6% drift, although the lateral load resistance dropped to 80% of its peak resistance at 4% drift, due to *P-Delta* effect.

Observations during testing indicated little flexural cracking at 0.5% drift. Additional cracks were observed at 1% drift, including a continuous crack at the column-footing interface. Shear cracks were observed to form at 2% drift, while additional flexural cracks were also observed to take place at this deformation level. Crushing of cover concrete started at 3% drift and continued during the cycles of subsequent deformation levels at 4% and 5% drift, exposing reinforcement within the hinging region. The longitudinal reinforcement showed signs of buckling during the cycles at 6% drift. One of the longitudinal bars buckled at 7% drift, which led to a sudden strength drop. Figure 5-31 illustrates the observed behavior at selected stages of loading.

Hysteretic base moment-rotation relationships for column BG-5 are shown in Fig. 5-32. It was observed that the longitudinal reinforcement was stressed into the strain-hardening region at high inelastic deformation levels, implying significant yield penetration into the footing. This resulted in increased rotations due to anchorage slip. Figure 5-32 indicates that at least 2/7th of the total rotation was attributed to anchorage slippage and the remaining 5/7th to flexure. The contribution of anchorage slip to total rotation was a factor of 2.0 higher than those in columns tested under twice the imposed axial compression.

The variation of strain in reinforcement is shown in Fig. 5-33. It was observed that the longitudinal reinforcement yielded during the last cycle of 1% drift, and developed compressive strains showing 0.61% at 2% drift, 0.81% at 3% drift. The lateral reinforcement recorded low strains compared to other columns. The first stirrup showed a strain of 0.16% at 5% drift, 0.17% at 6% drift, and 0.32% at 7% drift. The second grid above the footing recorded strains of 0.21% at 5% drift, 0.98% at 6% drift, and 1.10% at 7% drift.

5.3.9 Column BG-9

Column BG-9 was reinforced with 20#15 (16 *mm* diameter) longitudinal reinforcement, which resulted in 3.26% reinforcement ratio. The column was confined with 9-cell 6.6-*mm*

diameter (1/4 *in*) grids. There was one longitudinal bar in each of the perimeter grid corner, including one on each side of the interior perimeter joints. This resulted in 20 longitudinal reinforcement. The grid spacing was 76 *mm* (3 *in*) and the volumetric ratio of transverse reinforcement was 1.26% (83% of that required by *ACI 318-95*). The hysteretic relationships shown in Fig. 5-34 indicate that the column was able to develop 3% drift without a significant loss in strength. However, it was not able to sustain the deformation cycles at 4% drift. This column was companion to column BG-7, and although showed ductile response, was not able to develop the high ductility level exhibited by BG-7. This may be explained by the smaller size of longitudinal bars used in BG-9, which were more susceptible to buckling. The failure was observed to occur due to the buckling of one of the corner bars. Hence, the use of double longitudinal bars in perimeter grid corners was not likely to be the cause of the slight reduction in deformability.

Observations during testing indicated initiation of flexural cracks at 0.5% drift cycles. Additional flexural cracks formed at 1% drift, one at each grid location within the lower 600-*mm* segment. Shear cracks were observed during the cycles at 2% drift. Some crushing of cover concrete was evident near the base. Spalling of the cover concrete was observed at 3% drift. The column failed by buckling of one of the corner bars during the third cycle of deformation reversals at 4% drift. Figure 5-35 illustrates the performance of column at selected stages of loading.

Hysteretic base moment-rotation relationships are shown in Fig. 5-36. It was concluded that approximately 1/4th of total rotation was attributed to anchorage slippage and 3/4th to flexure.

The variation of strain in reinforcement is shown in Fig. 5-37. It was observed that the longitudinal reinforcement yielded during the last cycle of 1% drift and developed high compressive strains showing 0.74% at 2% drift, and 1.3% at 3% drift. The first grid above the footing recorded strains of 0.12% at 3% drift and 0.30% at 4% drift, while the second grid showed strains of 0.19% at 3% drift and 0.45% at 4% drift.

5.3.10 Column BG-10

Column BG-10 was companion to BG-9 with the same reinforcement arrangement, consisting of 20#15 (16 *mm* diameter) longitudinal bars and 9 cell grids. This time, however, the grid bar size was larger, increasing the volumetric ratio of transverse reinforcement to 2.66%. This amount of confinement steel represented 172% of that required by *ACI 318-95*. The grid spacing was maintained at 76 *mm* (3 *in*). The hysteretic relationships shown in Fig. 5-38 indicate superior performance than that for column BG-9, developing 5% drift without a significant loss in moment capacity. The lateral load capacity was reduced due to *P-Delta* effect, reaching approximately 80% of peak resistance at approximately 3% drift. The superior performance of this column can be explained by the increased volumetric ratio of transverse reinforcement.

Observations during testing indicated little flexural cracking at 0.5% and 1% drift. Additional flexural cracks, as well as shear cracks occurred at 2% drift. Some crushing of cover concrete was evident at this displacement level, near the base. Cycles at 3% drift and 4% drift resulted in gradual spalling of cover concrete, exposing reinforcement. Failure was initiated by buckling of a longitudinal reinforcement during the second cycle at 6% drift. Figure 5-39 illustrates the observed performance of column BG-10 at selected stages of loading.

Hysteretic moment-rotations relationships for column BG-10 are shown in Fig. 5-40. As in the case of previous columns, the yield penetration into the footing became significant near the end of the test, resulting in considerable amount of slip rotation. The anchorage slip rotation was recorded to be approximately 1/4th of total rotation while the flexure rotation constituted the remaining 3/4th.

It was observed during the test that the longitudinal reinforcement yielded during the first cycle at 2% drift. The recorded strains reached to 1.18% at 3% drift. The gauges ceased working after this deformation level. The maximum strain recorded on the first grid above the footing was 0.11% at 6% drift. The second grid that yielded during the first cycle of the 4% drift showed strains of 0.38% at 5% drift and 0.50% at 6% drift. Figure 5-41 illustrates the variation of strain in with imposed lateral force.

5.3.11 Column BG-11

Column BG-11 was built identical to column BG-5, except it was cast from high-strength concrete (81.6 MPa). It was reinforced with 12 longitudinal bars, which resulted in 2.94% reinforcement ratio, and confined with 9-cell grids. The volumetric ratio of transverse reinforcement was 2.66%, which formed 172% of the amount required by *ACI 318-95*. The spacing of grids was 76 ***mm*** (3 *in.*), corresponding approximately to the maximum spacing required by *ACI 318-95*. The column was tested under constant compressive force corresponding to 20% of its concentric capacity. The hysteretic relationships shown in Fig. 5-42 indicate that the column behaved in very ductile manner, showing almost no loss of moment resistance up to 6% drift. The lateral force resistance showed 20% strength drop at 4% lateral drift because of *P-Delta* effect.

Observations during testing indicated that hairline flexural cracks formed during the third cycle at 0.5% drift, at every grid level within the lower 350-***mm*** segment. These cracks extended diagonally on the sides during the first cycle at 1% drift. A flexural crack at the seventh grid level, and another one at column-footing interface formed during the subsequent cycles at the same deformation level. Additional flexural cracks were observed at 2% drift, especially within the lower 750-***mm*** portion of the column. The cover concrete started to crush in a brittle manner near the base, during the first cycle at 2% drift. The cover spalled off at the bottom corners, during the third cycle. The spalling continued during 3% drift cycles, exposing reinforcement within the bottom 300-***mm*** portion. Additional damage to concrete, widening of flexural cracks and extension of shear cracks were noticed during the cycles at 4% drift. Deformation cycles at 5% drift produced additional spalling of the cover, exposing the grids within the hinging region, up to about 340-***mm*** from the footing. A close observation during 6% drift cycles revealed that longitudinal bars under compression started bending, exerting high pressure on the grid joints. When the column was pushed further to complete the third cycle of 7% drift, the lateral load resistance dropped very fast. It was observed that 4 longitudinal bars failed in tension and the second grid from the footing ruptured, causing longitudinal bars to buckle under compression. Figure 5-43 illustrates the observed performance of column BG-10 at selected stages of loading.

Hysteretic base moment-rotation relationships are showed in Fig. 5-44. The anchorage slip rotation was measured to be small even at the end of the test. The rotation caused by anchorage slip was limited to about 1/6 of the total rotation.

Strain gauge readings are presented in Fig. 5-45. Test results indicated that longitudinal reinforcement yielded during the first cycle at 3% drift. The second grid from the footing yielded at 2% drift. It showed strains of 0.02%, 0.3%, 0.7%, and 1.0% at the third cycle of 1%, 2%, 3%, and 4% drift, respectively.

5.3.12 Column BG-12

Column BG-12 was built similar to BG-8, except it was cast from high-strength concrete (81.6 MPa). The column was reinforced with 12 longitudinal bars, which produced 2.94% reinforcement ratio, and confined with 9-cell welded reinforcement grids. The grids were made of 6.6-*mm* diameter wires. They were placed at a vertical spacing of 76 *mm* (3 *in.*), corresponding approximately to the maximum spacing required by the *ACI 318-95*. This resulted in a volumetric ratio of transverse reinforcement equal to 1.26%, forming 83% of the amount required by *ACI 318-95*. The column was tested under constant compressive force, corresponding to 20% of its concentric capacity. The hysteretic relationships shown in Fig. 5-46 indicate that the column showed about 20% loss of moment resistance at 4% drift, whereas the lateral force resistance dropped to approximately 80% of its peak at 3% drift because of *P-Delta* effect. The failure was characterized by rupturing of grids at joints, followed by the crushing of core concrete and buckling of longitudinal bars.

Observations during testing indicated that the column experienced initial flexural cracking at 0.5% and 1% drift levels. The flexural cracks became visible within the lower 500-*mm* portion of the column. Additional flexure cracks appeared up to the 10th grid level when the column was loaded to 2% lateral drift. The cover also started crushing at this deformation level. In addition, the previous flexural cracks extended diagonally to form shear cracks on the side faces. These shear cracks appeared all over the lower half of the column. At 3% drift, the cover concrete below the third layer of grids spalled off completely, exposing the reinforcement cage. The plastic hinging of the column near the base was visibly noticeable during the first cycle at 4% drift. The spalling of cover concrete extended up to the 4th grid

level, and wide shear crack occurred on the south side, as the cycles at 4% drift were completed. The third grid from the base ruptured at a joint on the south side, followed by the rupturing of the second grid at the same location when the column was deformed to 5% drift the first time. The lateral force resistance dropped significantly at this deformation level, and the bending of longitudinal bars became visibly noticeable. When the lateral load was reversed, the longitudinal bars on the East Side showed signs of buckling, and the load resistance dropped sharply. The grids within the hinging region deformed excessively on the East side, while bulging out under lateral expansion and maintaining their integrity. The drop in load resistance was excessive at the beginning of the second cycle of 5% drift and the test was discontinued when the core concrete crushed. Figure 5-47 illustrates the performance of column BG-12 at selected load stages.

Hysteretic base moment-rotation relationships are showed in Fig. 5-48. The anchorage slip rotation was measured to be very small even at the end of the test. It was concluded that the rotation caused by anchorage slip was limited to 1/10 of the total rotation.

Strain gauge readings are presented in Fig. 5-49. Test results indicated that longitudinal reinforcement yielded during the first cycle at 2% drift. The second grid from the footing yielded immediately after the yielding of the longitudinal bars. It showed strains of 0.6% and 0.98% at the third cycle of 2% and 3% drift, respectively.

5.3.13 Column BG-13

Column BG-13 was cast from high-strength concrete (81.6 MPa) and was reinforced with a cage similar to the ones used in Columns BG-2 and BG-3. The reinforcement cage consisted of 8#20 (19.5 *mm*) longitudinal bars, which produce 1.96% reinforcement ratio and 4-cell welded reinforcement grids made out of 9.53-*mm* (3/8 *in.*) diameter steel wires. The volumetric ratio of transverse reinforcement was 2.00%, which formed 129% of the amount required by *ACI 318-95*. The spacing of grids was 76 *mm* (3 *in.*) corresponding approximately to the maximum spacing required by *ACI 318-95*. The column was tested under a constant compressive force, corresponding to 20% of its concentric capacity. The hysteretic relationships shown in Fig. 5.50 indicate that the column experienced a 20% drop

in its moment resistance at 4% drift. The lateral force resistance showed a drop of 20% at 3% drift, essentially due to *P-Delta* effect.

Observations during testing indicated that the first flexural crack occurred during the first cycle at 0.5% drift, at the second grid level from the footing. Additional flexural cracks occurred at the third and fifth grid levels during the subsequent cycles at 0.5% drift. Flexural cracking extended to lower 600 *mm* of column during cycles at 1% drift, although no cover crushing was evident. However, diagonal tension cracks started forming on the side faces. The cover concrete started crushing near the base at 2% drift. Widening of diagonal cracks was also observed. The spalling continued during 3% drift cycles, and eventually lead to the complete spalling of the hinging region at 4% drift. Cover spalling extended up to the fifth grid level, exposing reinforcement, during the first cycle of this deformation level. Additional damage to concrete was noticed up to the 12^{th} grid level during the subsequent cycles at 4% drift. The hinging region became clearly visible and measured to be 450 *mm* from the base. The column did not survive the first cycle at 5% drift, due to stability problems. It leaned towards south, causing a significant drop in lateral load resistance. Figure 5-51 illustrates the progression of damage in Column BG-13, observed during testing.

Hysteretic base moment-rotation relationships are shown in Fig. 5-52. The yield penetration into the footing was not observed until after the 3% drift cycles. Figure 5-52 indicates that, at the end of the test, approximately 1/8 of total rotation was caused by anchorage slip and 7/8 by flexure.

Figure 5-53 depicts test results obtained from strain gauges. Strain gauge #1, placed 150 *mm* into the footing on the southeast corner bar, recorded a maximum of 0.18% strain at the end of the test. However, strain gauge #2 place on the same bar at the column-footing interface indicated that the longitudinal bar yielded in tension during the first cycle at 3% drift. Strain gauge #3, placed at 150 *mm* above the footing, showed that the bars were strained up to 1.15% under compression at 1% drift. Gauge #2 and #3 are presented here because the others ceased to work at early stages of testing when the connecting wires were cut by the sharp edges of falling concrete pieces. Strain gauges #4 and #5, placed on the outer perimeter of the second grid, indicated that the grid yielded in both directions at the first excursion of load to

1% drift. Average strain readings of 0.2%, 0.3%, and 0.4% was recorded at 0.5% drift, 1% drift, and 2% drift respectively. Strain gauge # 5 placed on a grid in the north-side direction, about 140 *mm* form perimeter bars, recorded a low reading of about 0.085% at 3% drift.

5.4 SD Columns

SD Columns were companions to four identical BG columns that were tested under similar loading conditions. They generally showed ductile behavior, developing lateral drifts of 4% to 6% prior to a significant loss in moment capacity, depending on the degree of confinement provided. They developed approximately the same drift capacities as those developed by companion BG columns. However, the SD columns showed instability of longitudinal bars at later stages of loading. The longitudinal bars in these columns suffered from instability near the end of testing, beyond approximately 4% drift due to the opening of 135-degree hooks of perimeter hoops. Furthermore, the middle longitudinal bars became free from the stud anchor heads. The lateral restraining action provided by the stud heads were no longer effective. Hence, they became more susceptible to buckling. The anchor heads of the studs were originally designed to prevent crushing of concrete, and not to restrain longitudinal bars against buckling. However, the tests conducted in the current investigation showed that the double-head studs performed satisfactorily when compared with welded reinforcement grids, and superior when compared with conventional reinforcement. The details of test data and observed behavior of columns are discussed in the following sections.

All SD-columns showed drift capacities in excess of 4% prior to 20% degradation in moment resistance. Column SD-1, with an 8-bar arrangement (one stud in each direction connecting the middle bars) and approximately the amount of confinement reinforcement required by *ACI 318-95* developed 4% lateral drift. The companion column SD-2, tested under a reduced axial compressive force equal to 20% of its nominal concentric capacity, showed significantly higher deformability, developing 6% drift. When two studs were used as cross ties in each direction with 12 longitudinal bars, the drift capacity increased to 6% even under an increased axial force of 37% of the column concentric capacity. Column SD-4, with a 12-bar arrangement, was able to sustain 4% drift even with a reduced volumetric ratio of 76% of that required by *ACI 318-95*.

Test results also showed that the double-head studs placed parallel to the direction of lateral loading experienced large strains, well exceeding the yield strain. The maximum strain recorded in columns with 8-bar and 12-bar arrangements were 1% and 1.4%, respectively. However, the strains recorded in transverse studs were limited to 0.27% and 0.7% for 8-bar and 12-bar columns, respectively.

5.4.1 Column SD-1

Column SD-1 was reinforced with 8 #20 (19.5 *mm* diameter) longitudinal bars, which resulted in 1.96% reinforcement ratio. The column was confined with square perimeter hoops and double-head-studs, manufactured from 9.53-*mm* (3-*in.*) diameter smooth steel bars. The double-head studs were placed on top of the hoops such that the middle longitudinal bars were engaged in the stud heads, and were supported by the heads against buckling. The resulting 8-bar arrangement can be compared with 4-cell grids used earlier in BG columns. In fact, Column SD-1 was companion to Column BG-2. The volumetric ratio of transverse reinforcement was 2.00%, which was equal to 179% of the amount required by *ACI 318-95*. The vertical spacing of transverse reinforcement was 76 *mm* (3*in.*), which was approximately equal to the maximum spacing required by *ACI 318-95*. The column was tested under a constant compressive force of 40% of its concentric capacity. The hysteretic relationships shown in Fig. 5-54 indicate that the column showed stable hysteresis loops up to 4% drift with little strength decay and failed during the initial loading towards 5% drift due to the buckling of longitudinal bars, followed by crushing of core concrete.

Observations during testing indicated that initially three hairline cracks formed at the 2nd, 4th, and 7th transverse steel levels from the footing, during 0.5% drift cycles. These cracks became wider at 1% drift. At 2% drift, additional flexural cracks were also observed and diagonal tension cracks started forming on the side faces. Widening of diagonal cracks was observed at this level, accompanied by cover crushing near the base. The spalling of cover concrete continued during 3% drift cycles, reaching complete spalling of the hinging region at 4% drift. The column failed due to bar buckling when it was pushed to 5% drift. It was observed that the column leaned towards the north side and the corner bars buckled between two transverse ties. Double-head studs prevented the buckling of middle longitudinal bars by

providing lateral restraints. Figure 5-55 illustrates the progression of damage in Column SD-1.

Base moment-rotation hysteretic relationships recorded during testing are shown in Fig. 5-56. The results indicate that 1/10th of total rotation was caused by anchorage slip and the remaining 9/10th by flexure. This observation is consistent with tensile strains recorded on longitudinal reinforcement. The longitudinal reinforcement developed low tensile strains showing 0.21% at 1% drift, 0.52%at 2% drift, and 0.59% at 3% drift. The readings in compression were very high, showing 0.80% at 1% drift, 1.10% at 2% drift, and 1.43 % at 3% drift. It was clear that the longitudinal steel was strained to its strain hardening long before it was buckled. The double-head studs developed tensile strains of were 0.21% at 2% drift, 0.41% at 3% drift and 0.95% at 4% drift in the loading direction. Studs in transverse direction gave lower strain readings, with a maximum value of 0.27% at 4% drift. Figure 5-57 illustrates the recorded strain readings for both longitudinal and transverse reinforcement.

5.4.2 Column SD-2

Column SD-2 was identical to SD-1 in every respect. However, this column was tested under a lower level of axial compression, corresponding to 20% of its concentric capacity. The column was also companion to BG-3, which was reinforced with welded grids. The hysteretic relationships illustrated in Fig. 5-58 indicate that the column behaved in a very ductile manner showing almost no decay in moment resistance up to 6% drift, and 20% decay in lateral force resistance at 3% drift due to *P-Delta* effect. The increase in ductility, compared to column SD-1, is attributed to reduced axial compression. The failure of the column was initiated by buckling of a middle longitudinal bar when it slipped off the head plate of the stud.

Observations during testing revealed that the column developed initial flexural cracking during cycles of 0.5% drift and 1% drift, at every other level of lateral reinforcement within the lower 700-*mm* portion. Diagonal shear cracks started forming at 2% drift on the side faces. The cover concrete started crushing at the same level of deformation, in the corners near the base. Widening of flexural cracks (4 *mm* at the second tie level) and additional concrete crushing were observed during the first cycle at 3% drift. Cover spalling continued

during the second and third cycles of this deformation level, which eventually lead to the complete spalling of hinging region at 4% drift. During 5% drift, cover spalling extended up to the fourth hoop level, exposing reinforcement. Additional damage to concrete was noticed in the hinging region, which became clearly visible during the cycles at 6% drift. The hinging region was measured to extend 350 *mm*. The column failed at the second cycle of 7% drift due to bar buckling. The perimeter hoops showed signs of opening at the hooks and gradual crushing of core concrete began. The head of the stud at the second hoop level slipped off and ceased holding the middle longitudinal bar against buckling. This lead to complete loss of lateral load resistance and the collapse of column under compression. Figure 5-59 illustrates observed performance of column SD-2 at selected stages of loading.

Base moment-rotation relationships are shown in Fig. 5-60. The results indicate that the column exhibited unsymmetrical anchorage slip rotations. Large anchorage slip rotations were recorded on the East Side, compared to the West. Approximately 1/4th of total rotation recorded was caused by anchorage slip, while the remaining 3/4 was caused mainly by flexure. Anchorage-slip rotations of SD-2 were almost twice the values recorded for SD-1. This was due to the difference in the level of axial load, and was consistent with the tensile strain readings recorded in longitudinal reinforcement, indicating a significant yield penetration into the footing.

Tensile strains recorded in longitudinal reinforcement ranged between 0.88% at 1% drift and 1.8% at 2%-drift, indicating significant yield penetration into the footing, giving rise to anchorage slip. The compression bars yielded during the second cycle at 1% drift, and developed a strain of 0.9% during the first cycle at 2% drift. Strains in the second hoop from the footing were monitored. The maximum tensile strain recorded in the hoop was 0.3% at 5% drift. Double head studs showed high-tensile strains as compared to hoops. The recorded strains in double-head studs in the direction of loading were 0.13%, 0.21%, 0.30%, 0.5%, and 0.96% at 2%, 3%, 4%, 5%, 6% drift levels, respectively. The double head studs in transverse direction developed a maximum strain of 0.08%. Figure 5-61 shows hysteric plots of strain readings.

5.4.3 Column SD-3

Column SD-3 was reinforced with 12 #20 (19.5 *mm* diameter) longitudinal bars, which result in 2.94% reinforcement ratio. It was confined with square perimeter hoops and double-head studs, both made out of 9.53-*mm* (3-*in.*) diameter smooth-steel reinforcement. The double-head studs were placed on top of the hoops to form two layers of cross ties, forming a geometry analogous to 9-cell grids. The column was companion to BG-5. The volumetric ratio of transverse reinforcement was 2.66%, which was 52 % higher than that required by *ACI 318-95*. The column was subjected to 37% of its concentric capacity during lateral deformation reversals. The hysteretic relationships shown in Fig. 5-62 indicate that the column showed no loss of moment resistance up to 6% drift, while developing 3% drift at 29% strength decay in lateral force resistance due to *P-Delta* effect. The failure of the column was initiated by buckling of longitudinal reinforcement and crushing of concrete. The improved behavior obtained in this column relative to column SD-1 was attributed to the confinement efficiency of the 12-bar arrangement.

Initially, only two hairline flexural cracks were observed at 0.5% drift cycles near the 3rd and 5th tie locations. Two more flexure cracks also developed during cycles at 1% drift at the 8th and 9th tie locations. A flexural crack was also visible at this load stage, at the column-footing interface. The cover concrete started crushing during the first cycle of 2% lateral drift. The crushing of concrete became severe especially at the corners. More flexural cracks and some diagonal tension cracks were also observed within the lower 700-*mm* portion of the column. The cover concrete started spalling gradually at 3% drift. The flexural cracks became wider and the shear-cracks extended to the middle of the column. Crushing and spalling of cover concrete continued during the cycles at 4% drift. The damage to cover concrete extended up to a height of 350 *mm* from the footing, exposing reinforcement. Additional damage to concrete was observed during the cycles at 5% drift. The longitudinal bars started bending during the second cycle at 6% drift. At the end of the second cycle of 6% drift, the head plate of the stud on the north side, located at 110 *mm* from the footing, slipped off the longitudinal bar. This caused that particular middle longitudinal bar to buckle. As a result, the horizontal load dropped faster and the North-East corner bar also buckled. This caused the column to lean towards north. The test was stopped prematurely because of

safety concerns. Figure 5-63 illustrates the observed behavior of column SD-3 at selected stages of loading.

Base moment-rotation hysteretic relationships recorded during testing are shown in Fig. 5-64. The results indicate that only about 1/6th of total rotation was caused by anchorage slip. The high level of axial load applied reduced anchorage slip in the footing. This observation is consistent with tensile strain readings recorded in longitudinal reinforcement, which indicate no significant extension of reinforcement at the column-footing interface.

The longitudinal reinforcement strain gauges recorded tensile strains of 0.12%, 0.32%, 0.47%, 0.88% and 1.00% at 1%, 2%, 3%, 4%, and 5% drifts, respectively. In addition, the longitudinal reinforcement was subjected to high levels of compression strains, entering the strain-hardening region. The recorded compressive strains were; 0.91%, 1.30%, 1.85%, 2.26%, 2.95% and 3.77% at 1%, 2%, 3%, 4%, 5%, and 6% drift levels, respectively. The hoops developed a maximum tensile strain of 0.25%. The double-head studs in the direction of loading strained excessively, reaching a maximum tensile strain of 2.60%, compared to a maximum tensile strain of 0.5% in the orthogonal direction. The strain gauge readings are presented in Fig. 5-65.

5.4.4 Column SD-4

Column SD-4 was companion to SD-3 with 12#20 (19.5 *mm* diameter) longitudinal reinforcement. The perimeter hoops and ties were arranged the same way to form 9-cell grids. The vertical spacing of transverse reinforcement was 76 *mm* (3 in). The diameter of hoops and double-head studs was reduced to 6.3 *mm* (1/4 *in.*), resulting in a reduced volumetric ratio of 1.26 %. This amount of transverse steel corresponded to 76% of that required by *ACI 318-95*. The column was tested under a constant axial compressive load of 37% of its concentric capacity, and was companion to Column BG-7. The hysteretic relationships shown in Fig. 5-66 indicate that column showed ductile behavior even with a volumetric ratio lower than that required by *ACI 318-96*. The ductile behavior observed was attributed to the superiority of the 12-bar arrangement used, which permitted a reduction in the volumetric ratio of transverse steel without adversely affecting column deformability. The moment resistance was maintained up to 4% lateral drift with almost no decay, while the

lateral load resistance showed 3% drift at 20% strength loss. The failure of the column was also initiated by buckling of longitudinal bars. The circular heads of the studs were not big enough to stabilize the longitudinal bars, and slipped off after the spalling of cover concrete.

The observed behavior of column during testing indicated that some flexural cracks occurred up to the 3rd tie level during the cycles at 1% drift. No shear cracks were observed at this defamation level, but a horizontal crack at the column-footing interface was also observed. The cover concrete started crushing while new flexure cracks developed at tie levels within the lower 650-*mm* portion of the column during cycles at 2% drift. Widening of flexural cracks, and formation of diagonal shear cracks were observed at 3% drift, while the cover started crushing near the base. Gradual crushing of cover concrete lead to complete spalling of the hinging region at 4% drift. The column started leaning towards south during the first cycle of 5% drift as the lateral load resistance dropped sharply. The test was then stopped for safety reasons. The longitudinal bars on the south side were bent and showed signs of buckling between the 3rd and 4th hoops. Figure 5-67 illustrates the performance of column SD-4 at selected load stages.

Moment-rotation hysteretic relationships, recorded during testing, are shown in Fig. 5-68. Although the SD-4 column was subjected to high axial compression, the results indicated that about ¼th of total rotation was caused by anchorage slip, leaving the remaining ¾th to flexure.

Figure 5-69 depicts the strain gauge reading taken on reinforcement during testing. The longitudinal reinforcement gauges recorded a maximum tensile strain of 0.7% and a maximum compressive strain of 3.0%. The perimeter hoops recorded a maximum tensile strain of 0.7%, whereas the double-head studs recorded maximum tensile strains of 1.2% and 0.6% in directions parallel and perpendicular to loading, respectively.

5.5 FRP Columns

FRP columns were reinforced with deformed steel bars as longitudinal steel, and FRP grids as transverse reinforcement. The majority of columns were designed to be companions to the BG columns tested earlier, for comparison. The results indicated that properly confined FRP

columns showed ductile response and behaved as well as companion BG-columns. The failure of FRP columns was characterized by premature failure of FRP grids at the joints. With the exception of columns FRP-1 and FRP-2, which had a grid spacing equal to approximately one half the cross-sectional dimension and a volumetric ratio equal to 39% and 52% of that required by *ACI 318-95*, respectively and hence developed 1% lateral drift, all other columns showed drift capacities of 2% and higher, even when *P-Delta* effect was considered. Columns conforming the spacing requirements of *ACI 318-95*, with volumetric ratios ranging between 79% and 140% of that required by the code showed ductile response even under high axial compression of approximately 40% of nominal concentric capacity, developing drifts of 2% to 6% prior to 20% degradation in moment resistance. Companion columns tested under 20% of nominal concentric capacity showed significantly higher deformabilities, developing 5% to 7% drift prior to 20% degradation in moment resistance and 4% to 5% drift at 20% decay in lateral force resistance. Columns confined with 9-cell grids showed higher deformability than those confined with 4-cell grids having the same volumetric ratio and spacing. Columns with only 4-corner longitudinal reinforcement and either 4 or 9-cell FRP grids showed ductile response similar to that of 8 or 12-bar arrangements. A detailed description of the response of each FRP column is presented in the following sub-sections.

5.5.1 Column FRP-1

Column FRP-1 was reinforced with 8#20 longitudinal bars which resulted in 1.96% reinforcement ratio, and was confined with 4-cell FRP grids. The volumetric ratio of transverse reinforcement was 0.79%, which formed 39% of the amount required by *ACI 318-95* when the FRP strength was assumed to be limited to 400 MPa, as required by the code. The spacing of grids was 152 *mm* (6 *in.*), which was approximately twice the maximum spacing required by *ACI 318-95*. The column was tested under constant compressive force of 39% of its concentric capacity. The hysteretic relationships shown in Fig. 5-70 indicate that the column showed stable hysteresis loops up to 1% drift, but developed a significant strength decay during the second cycle at 2% drift. This was expected because of the higher vertical spacing of the grids that resulted in a low volumetric ratio of transverse reinforcement and insufficient restraint to bar buckling. The column failed during the first

cycle at 3% drift due to the failure of FRP grids at corner joints and subsequent buckling of longitudinal reinforcement.

Observations during testing indicated that initial flexural cracking started at 0.5% and 1% drift cycles within the lower 450 *mm* portion of the column. During 2% drift cycles, a crack formed at the column-foundation interface and concrete started to crush at the lower corners. No shear cracks were observed, but the cover concrete started spalling off during the third cycle of this deformation level. When the column was deformed to 3% drift, a big shear crack was noticed. The FRP grids failed at the joints, causing the longitudinal bars to buckle under compression, which led to failure. Figure 5-71 illustrates the performance of column SD-4 at selected stages of loading.

Moment-rotation hysteretic relationships, recorded during testing, are shown in Fig. 5-72. The results indicate that about 3/7th of total rotation was caused by anchorage slip, and the remaining $4/7^{th}$ by flexure.

Strain gauge readings indicated that the FRP grids experienced a maximum of 0.5% tensile strain, whereas the longitudinal bars experienced high compression strains, reaching to 3.2% before buckling, and a moderate tensile strain of 1.2%. Figure 5-73 shows the hysteretic behavior of recorded strains.

5.5.2 Column FRP-2

Column FRP-2 was companion to FRP-1, reinforced with 8#20 longitudinal bars and confined with 4-cell grids. Although the same size grids were used in this column, the grid spacing was reduced by a factor of 2, resulting in an increase in the volumetric ratio of transverse reinforcement. The grid spacing was 76 *mm* (3 *in.*) and the volumetric ratio was 1.59%, which was 21% less than that required by *ACI 318-95* based on 400 *MPa* maximum strength of reinforcement. The column was subjected to 39% of its concentric capacity as constant axial compression. It showed better behavior than the companion column FRP-1. The reduction in tie spacing increased the effectiveness of confinement and stability of longitudinal reinforcement. The moment-displacement hysteretic relationship shown in Fig. 5-74 indicates that the column showed stable hysteresis loops up to 3% drift with little

strength decay and failed at the end of the second cycle of 4% drift due to FRP grid joint failure, followed by bar buckling and concrete crushing. The force-displacement hysteretic relationship of Fig. 5-74 shows reduced deformability due to *P-Delta* effect, and indicates 2% drift at approximately 20% strength decay.

Observations during 0.5% drift indicated that only four flexural cracks were noticed up to the fourth grid level. Additional flexural crack formed when the column was deformed to 1% drift. The cover concrete started crushing within the hinging region during the third cycles of this deformation level. Increased crushing of cover concrete and formation of diagonal tension cracks were noticed during the first cycle at 3% drift. The shear cracks widened during subsequent cycles. The cover concrete spalled off completely, exposing reinforcement within the lower 270-*mm* segment of column. The damage to cover concrete continued, and the hinging region became clearly visible during the first and second cycles of 4% drift. The height of the hinging region was measured to be 300 *mm* on the West Side and 400 *mm* on the East Side. The column failed during the third cycle of this deformation level as the corner longitudinal bars buckled in compression. Figure 5-75 illustrates the performance of column FRP-2 at selected load stages.

Moment-rotation hysteretic relationships recorded during testing are shown in Fig. 5-76. The results indicate that approximately $1/10^{th}$ of total rotation recorded was caused by anchorage slip, while the remaining 9/10th was caused by flexure.

Close examination of strain readings recorded during testing indicates that the FRP grids developed a maximum tensile strain of 0.22 percent during the last cycle of 2% lateral drift. The longitudinal bars developed high compressive strains, experiencing strain hardening. The strains recorded were 1.1% at 1% drift, 1.5% at 2% drift, 2.3% at 3% drift, and 3.2% at 4% drift. However, in tension the longitudinal bars strained to 0.22% at 1% drift, 0.61% at 2% drift, 0.75% at 3% drift, and 1.25% at 4% drift. These strain readings are also presented graphically in Fig. 5-77.

5.5.3 Column FRP-3

Column FRP-3 was identical to FRP-2 in every respect, with 129% of the confinement steel required by *ACI 318-95*. However, this column was tested under a lower level of axial compression, corresponding to 20% of its concentric capacity. This improved the deformability of column, as expected. The hysteretic relationships illustrated in Fig. 5-78 indicate that the column behaved in an extremely ductile manner, showing virtually no decay in moment resistance up to 6% drift, and 20% decay in lateral force resistance at 4% drift, due to *P-Delta* effect.

Observation during testing indicated that flexural cracks became visible during the third cycle of 0.5% drift, as well as during the cycles at 1% drift. A flexural crack formed at every grid location with the lower 750-*mm* portion of the column. These cracks extended diagonally to the sides, forming diagonal tension cracks. During the cycles at 2% drift, the flexural cracks became wider, shear cracks on the sides became longer, and cover concrete started crushing within the hinging region. In addition, a crack at the column-footing interface was formed. The shear cracks extended further and cover concrete spalled off completely below the second grid level at 4% drift. More damage to the cover concrete was observed during the cycles of 5% drift, exposing the reinforcement cage up to 350-*mm* from the footing. Close examination of column revealed bending of east-side longitudinal bars during the second cycle of 6% drift. The column failed due to bar buckling during the first cycle of 7% drift. Figure 5-79 illustrates the performance of Column FRP-3 at selected stages of loading.

Moment-rotation hysteretic relationships recorded during testing are shown in Fig. 5-80. The results indicate that approximately 1/3rd of total rotation was caused by anchorage slip. The high percentage of contribution of anchorage slip, compared to FRP-2, was attributed mainly to the low level of applied axial compression applied to Column FRP-3.

Figure 5-81 shows the hysteretic behavior of steel strains in longitudinal and transverse reinforcement. The examination of strain readings indicates that the second FRP grid from the footing, within the hinging region, strained to 0.03% at 1% drift, 0.08% at 2% drift, 0.19% at 3% drift, and 0.27% at 4% drift. After this deformation level, all strain gages placed

on FRP grids ceased to function. The strain gauges on longitudinal bars recorded lower strains in compression and higher strains in tension compared to those placed in Column FRP-2, due to the lower level of axial compression imposed. The compressive strains were 0.66%, 0.76%, 0.87% and the tensile strains were 0.9%, 1.3% and 1.9% at 2%, 3%, and 4% drifts, respectively.

5.5.4 Column FRP-4

Column FRP-4 was reinforced with 12#20 longitudinal bars, which resulted in 2.94% reinforcement ratio, and was confined with 9-cell grids. The volumetric ratio of transverse reinforcement was 1.05%, which formed 25% of the amount required by *ACI 318-95* when the maximum limit of 400 MPa is used on transverse reinforcement strength. The spacing of grids was 152 ***mm*** (6 ***in.***), which was approximately twice the maximum spacing required by *ACI 318-95*. The column was subjected to 38% of its concentric capacity during lateral deformation reversals. This column had some concrete placement problems, and hence was repaired within the hinging region. The hysteretic relationships shown in Fig. 5-82 indicate that the column showed stable hysteresis loops up to 1% drift and failed during the third cycle of 2% drift due to concrete crushing. This was not a surprise since the hinging region was not properly cast and vibrated. Close examination of the column after failure indicated that the column did contain many voids in the hinging region.

Observations during testing indicated that flexural cracks occurred within the lower portion of column during the cycles at 0.5% drift. These flexural cracks extended diagonally to the sides forming wide and long shear cracks at the first cycle of 1% drift. The cover concrete deteriorated under cyclic deformations at the same drift level. The column failed under compression at the end of the third cycle at 2% drift. A close examination of the hinging region indicated that the concrete at the bottom of the column on the south side was not well compacted. The concrete in this region crushed and failed prematurely, and a large portion of the compression force was transferred to the longitudinal bars. The column leaned towards the South and failed due to bar buckling. Although this column could not be used to study the effect of the test parameter for which it was designed, it confirmed that good workmanship

and concrete placement are paramount for desired performance. Figure 5-83 illustrates performance of column FRP-2 at selected stages of loading.

Moment-rotation hysteretic relationships recorded during testing are shown in Fig. 5-84. Although column FRP-4 was tested under high axial load, test results revealed that approximately 1/3rd of total rotation recorded was caused by anchorage slip, while the remaining 2/3rd was caused by flexure. The high contribution of anchorage slip to total rotation could be explained by the poor quality of core concrete.

The longitudinal reinforcement developed 0.75% compressive strain at peak lateral load corresponding to 1% drift. The FRP grids showed tensile strains ranging between 0.2% and 0.35% prior to column failure. Figure 5-85 shows the variation of strains in longitudinal and grids reinforcement.

5.5.5 Column FRP-5

Column FRP-5 was companion to FRP-4, and was reinforced with 12#20 longitudinal bars and 9-cell grids. Although the grid size was kept constant, the spacing of grids was reduced by a factor of 2, resulting in an increase in the volumetric ratio. The grid spacing was 76 *mm* (3 *in.*) and the volumetric ratio of transverse reinforcement was 2.10%, which was almost equal to that required by *ACI 318-95* based on the maximum strength of 400 MPa required in lateral reinforcement. The column was subjected to 38% of its concentric capacity. This column also experienced concrete placement problem, and was also repaired after casting. Therefore, the results were not as expected. The hysteretic relationships shown in Fig. 5-86 indicate that the column showed no loss of moment and lateral load resistance up to 1% drift. However, the peak lateral force resistance was smaller than the previous columns. The failure was initiated prematurely by crushing of the weak core concrete.

Observations during testing indicated that the column experienced same damage near the base under concentric compression. When lateral cycles were imposed at 0.5% drift, some flexural cracks, as well as diagonal tension cracks appeared, some wider than expected. At 1% drift cycles, the cracks became wider and the cover concrete started to crush. During the first cycle at 2% drift, the concrete cover spalled off completely within the lower 200-*mm*

segment. At the beginning of the second cycle, the column leaned towards its side and the longitudinal bars started bending. The column failed at the end of the second cycle due to the crushing of core concrete and buckling of longitudinal bars. Figure 5-87 illustrates the performance of column FRP-2 at selected stages of loading.

Column FRP-5 exhibited unsymmetrical moment-rotation hysteretic relationships, as shown in Fig. 5-88. The test results revealed that approximately 1/3rd of total rotations recorded were caused by anchorage slip, resulting in 2/3rd being attributed to flexure.

The variation of strains in reinforcement is shown in Fig. 5-89. The figure indicates that the longitudinal bars recorded a maximum compressive strain of 3.3% just before buckling. Strain gauges placed on FRP cross-bars (close to the perimeter bars) recorded maximum readings of 0.4% and 0.19% in directions parallel and perpendicular to lateral load, respectively. A gauge place at mid-cross-section location of column showed only a strain of 0.14% in the direction parallel to the lateral load. The FRP grids showed considerably high lateral strains ranging between 0.2% and 0.35% prior to column failure.

5.5.6 Column FRP-6

Column FRP-6 was identical to FRP-2 in every respect, with the amount of confinement reinforcement corresponding to 104% of that required by *ACI 318-95*. However, this column was tested under a lower level of axial compression, corresponding to 20% of its concentric capacity. The hysteretic relationships illustrated in Fig. 5-90 indicate that the column behaved in an extremely ductile manner showing virtually no decay in moment resistance up to 7% drift, and 20% decay in lateral force resistance due to *P-Delta* effect at 5% drift.

Observations during testing indicated that the column experienced initial flexural cracking during the cycles of 0.5% and 1% lateral drifts. The cracks were visible at every grid location within the lower 800-*mm* portion of column. They became wider while extending diagonally on side faces of column during 2% drift. A crack also formed at the column-footing interface, which was wide enough to suggest yielding of longitudinal reinforcement in tension. Further widening of cracks and crushing of cover concrete were observed at 3% lateral drift. Cracking extended up to 800 *mm* from the footing at the end of 3% drift cycles. The spalling

extended up to 110 *mm* above the footing during 4% drift cycles. More damage to cover concrete was observed when the column was deformed to 5% drift. The plastic hinging formed completely at 6% drift, exposing the reinforcement cage. The column continued resisting deformation cycles at 7% drift, during which the longitudinal bars started to buckle. The failure occurred at this deformation level and was initiated by the failure of FRP grids at joints, followed by the buckling of longitudinal bars. Fig. 5-91 illustrates the performance of column FRP-6 at selected stages of loading.

Moment-rotation hysteretic relationships recorded during testing are shown in Fig. 5-92. Although column FRP-6 was tested under a relatively high axial compression, the results revealed that only about 1/6th of total rotation was caused by anchorage slip, while the remaining 5/6 was caused by flexure. The contribution of anchorage slip was less than half the anchorage slip rotation recorded in column FRP-3 with the same level of axial compression. This could be attributed to the superior confinement characteristics of 9-cell grids used in Column FRP-6, as opposed to 4-cell grids used in FRP-3.

Close examination of strain gauge readings indicated that the longitudinal bars recorded maximum of 1.6% tensile and 2% compressive strains at 5% drift. Maximum tensile strains recorded on FRP grids were measured to be about 0.5% in the direction of loading and 0.5% in the perpendicular direction, at 6% drift. The strain readings of longitudinal and lateral reinforcement are presented graphically in Figure 5-93.

5.5.7 Column FRP-7

Column FRP-7 was reinforced with 4-#30 (29.9-*mm* diameter) corner bars. The reinforcement grids had 9 cells, without any longitudinal bars placed in the remaining perimeter grid corners. The volumetric ratio and spacing of transverse reinforcement were identical to those for column FRP-5 and FRP-6. It was loaded to 38% of its concentric capacity as constant axial compression. The hysteretic relationships shown in Fig. 5-94 indicate that the column behaved as good as expected, developing 4% drift without any sign of strength decay in moment resistance. The drift capacity was also 4% when a 20% strength decay was recorded in lateral load resistance. Close examination of the hysteretic relationships reveals that there is a slight pinching in the curves indicating that the column

might have experienced sizeable shear distortions. Despite that, the FRP grids were able to provide lateral restraint at perimeter grid joints without any longitudinal reinforcement. The close spacing of transverse reinforcement within the cross-sectional plane improved the distribution of lateral confinement pressure without the presence of longitudinal reinforcement.

Observations during testing revealed that the column experienced only one flexural crack at 0.5% drift and five more flexural cracks at 1% drift. During the cycles at 2% drift, more flexural cracks appeared and the previous cracks became wider, extending diagonally to the side faces, forming shear cracks. In addition, cover concrete started crushing during this deformation level. More shear cracks appeared and cover concrete started spalling when the column was pushed to 3% lateral drift. The cover concrete spalled off completely on the East and West sides of the column, exposing reinforcement during 4% drift cycles. The column started leaning towards north when 5% lateral drift was reached, while the lateral load resistance dropped rapidly. It was noticed that during the first cycle of this deformation level, the corner joint of the second FRP grid from the base, on the northeast side was subjected to high lateral pressure as the longitudinal bar was bent under compression. The column failed when an FRP joint grid opened causing the longitudinal bar to buckle between the first grid and the third grid. Figure 5-95 illustrates the performance of column FRP-7 at selected load stages.

Moment-rotation relationships, recorded during testing, are shown in Fig. 5-96. Test results indicate that Column FRP-7 showed high percentage of anchorage slip, forming approximately 50% of total hinging region rotation.

Strain gauge readings shown in Fig. 5-97 indicate that the longitudinal bars were subjected to cyclic strains, ranging from a compression of about 1.5% to a tension of about 0.9% at 3% lateral drift. The FRP grids were strained up to 0.31% in the loading direction at 4% drift, and 0.22% in the perpendicular direction at 3% drift.

5.5.8 Column FRP-8

Column FRP-8 was also reinforced with 4#30 corner bars. Unlike FRP-7, the reinforcement grids had 4-cells. The volumetric ratio of transverse reinforcement was 1.59%, which formed 79% of the amount required by *ACI 318-95*, based on the maximum reinforcement strength limit of 400 MPa specified in the code. The spacing of grids was 76 *mm* (3 *in.*), which was approximately equal to the maximum spacing required by *ACI 318-95*. The column was subjected to 36% of its concentric capacity as constant compression. It behaved in a less ductile manner than FRP-7. The reduction in number of grid cells decreased the effectiveness of confinement and stability of longitudinal reinforcement. The moment-displacement hysteretic relationship shown in Fig. 5-98 (a) indicates that the column showed stable hysteresis loops up to 2% drift with little strength decay and failed at the end of the third cycle of 3% drift due to rupturing of FRP grids and the joints, followed by bar buckling and concrete crushing. The force-displacement hysteretic relationship of Fig. 5-98(b) shows reduced deformability due to *P-Delta* effect, and indicates approximately 2% column drift capacity at 20% strength decay.

Observations during testing indicated that Column FRP8 experienced two flexural cracks at the second and forth grid levels during the cycles of 0.5% drift, though more flexural cracks appeared at 1% drift. The cover concrete started to spall off at 2% drift. Severe damage to the hinging region was observed during this deformation level. The damage continued to extend during the first cycle of 3% drift. In addition, wide and long shear cracks appeared on the sides faces of column. At the end of the second cycle, the cover concrete spalled off completely within the hinging region, which was measured to be approximately 300 *mm* from the footing. During the third cycle of 3% drift, the column started leaning towards south and the test was stopped prematurely for safety reasons. Figure 5-99 illustrates the performance of column FRP-8 at selected stages of loading.

Figure 5-100 shows the hysteretic moment-rotation relationships recorded during testing. The relationships indicate that approximately 1/5th of total hinging region rotation recorded was caused by anchorage slip, while the remaining 4/5th was attributed to flexure.

The maximum compressive strain in longitudinal reinforcement was recorded on the southwest corner bar to be 3.3% at 3% drift. The FRP grids recorded maximum tensile strains of 0.5% in the direction of loading and 0.3% in the perpendicular direction, at 2% drift. Figure 5-101 shows the hysteretic behavior of strains recorded on longitudinal and the FRP reinforcement.

5.5.9 Column FRP-9

Column FRP-9 was reinforced with 12#20 longitudinal bars, which resulted in 2.94% steel, confined with 9-cell FRP grids. The volumetric ratio of transverse reinforcement was 1.69%, which formed 84% of the amount required by *ACI 318-95*, based on the maximum reinforcement strength limit of 400 MPa. The grid spacing was 76 *mm* (3 *in.*), which was approximately equal to the maximum spacing required by *ACI 318-95*. The column was subjected to 38% of its concentric capacity as axial compression. The hysteretic relationships shown in Fig. 5-102 indicate that the column showed no loss of moment resistance until 4% drift. The lateral load resistance dropped to approximately 80% of its peak value at about 3% drift, because of *P-Delta* effect. The failure was initiated by the rupture of the FRP grids at the joints, followed by buckling of longitudinal bars at the beginning of the third cycle of 4% drift.

Non visible cracks were observed during the cycles at 0.5% drift. Two flexural and diagonal shear cracks were observed during the cycles at 1% drift. A flexural crack at the column-footing interface was observed. Additional flexural and shear cracks were observed at 2% lateral drift, within the lower 700-*mm* segment of the column. These cracks became wider and longer during the subsequent deformation reversals. The cover concrete started crushing during the first two cycles of 3% drift level within the plastic hinge region. The cover concrete crushed completely below the 4th grid level during the third cycle of 3% drift. The column started leaning toward north during the first cycle of 4% drift. The northeast corner joint of an FRP grid within the hinging region failed and opened up during the second cycle, resulting in bending of the longitudinal bar. The damage to the plastic hinging region became severe when the column was forced into the third cycle. Consequently, the second and third FRP grids from column base failed at the northwest corner, causing the longitudinal bars to

buckle in the second mode. The southwest corner bar buckled in the third mode, while the middle bar showed second mode failure on the West Side. The second FRP grid failed on the East side, leading to the buckling of northeast corner bar in second mode. Figure 5-103 illustrates the performance of column FRP-28 at selected load stages.

The hysteretic moment-rotation relationships are shown in Fig. 5-104. The test results indicate that approximately 1/3rd of total rotation recorded was caused by anchorage slip, while the remaining 2/3rd was attributed to flexure.

The hysteretic behavior of reinforcement strain readings recorded on longitudinal bars and FRP grids during testing is shown in Fig. 5-105. It is observed that the longitudinal bars recorded very high compressive strains, reaching 4.5% at 4% drift, while developing relatively moderate tensile strains of up to 1.2% at the same drift level. The maximum tensile strain recorded on FRP grids was limited to 0.35%.

5.5.10 Column FRP-10

Column FRP-10 was identical to FRP-2 in every respect, containing FRP lateral confinement equal to 84% of the steel required by *ACI 318-95*. However, this column was tested under a lower level of axial compression, corresponding to 20% of its concentric capacity. The hysteretic relationships illustrated in Fig. 5-106 indicate that the column behaved in an extremely ductile manner, showing virtually no decay in moment resistance up to 5% drift, while experiencing a 20% decay in lateral force resistance at 5% drift due to *P-Delta* effect. This conforms to the expected trend of improvement in column deformability with reduction in axial compression.

Observation during testing indicated that the column experienced initial flexural cracking at 0.5% and 1% lateral drift levels. The flexural cracks became visible within the lower 900-*mm* portion of the column. The cover concrete started crushing and diagonal tension cracks starting forming on side faces when the column was loaded to 2% lateral drift. The cover concrete below the third layer of grids near the base spalled off completely at 3% drift, exposing reinforcement cage. More damage to cover concrete was observed during the cycles at 4% drift, making the plastic hinge visibly noticeable. The column continued resisting

lateral forces when it was deformed to 5% drift. It was observed that during the first cycle of 6% drift level, the longitudinal reinforcement in the southwest corner bent between the second and third FRP grids from the base. The resistance to lateral force dropped during the second cycle of 6% drift because the second FRP grid from the base failed at the west corner. The drop in load resistance was excessive during the third cycle, because the longitudinal bars buckled on both east and west sides. Figure 5-107 illustrates the performance of the column at selected stages of loading.

The hysteretic moment-rotation relationships recorded during testing are shown in Fig. 5-108. Although the column was tested under low axial load, test results revealed that only 1/6th of total rotation recorded was caused by anchorage slip, while the remaining 5/6th was caused by flexure.

The strain gauge data indicates that longitudinal bars were subjected to maximum of 1.5% tensile and 2% compressive strains at 4% drift. The FRP grids developed 0.3% tensile strain in the direction of loading and 0.17% strain in the perpendicular direction. The hysteretic behavior of strains recorded on longitudinal and FRP reinforcement is shown in Fig. 5-109.

5.5.11 Column FRP-11

Column FRP-11 was companion to FRP-2, and was reinforced with 8 longitudinal bars. The grids used had 8-cells, with a larger FRP cross-section (8 *mm* x 10 *mm*). The spacing and volumetric ratio of grid reinforcement was 76 *mm* (3 *in*) and 2.01%, respectively. This represented 104% of the *ACI 318-95* requirement based on a maximum grid strength of 400 MPa. The column was subjected to 39% of its concentric capacity as constant axial compression. During casting this column experienced placement problems. Hence, it was repaired prior to testing. The failure of the column was characterized by crushing of core concrete, rupturing of grids at joint corners and subsequent buckling of compression reinforcement. The moment-displacement hysteretic relationship shown in Fig. 5-110 indicates that the column developed stable hysteresis loops up to 2% drift with little strength decay, and failed at the end of the first cycle at 3% drift. The force-displacement hysteretic relationship of Fig 5-110 shows reduced deformability due to *P-Delta* effect, indicating approximately 20% strength loss at 2% drift.

Initial flexural cracking occurred within the lower 150-*mm* segment of column, at 0.5% drift. These flexural cracks became wider and propagated diagonally on to the side faces during 1% drift cycles. The cover concrete started crushing at the southwest corner, when the column was deformed to 2% drift for the first time. More damage to cover concrete was observed during the subsequent cycles. The cover spalled off completely up to the fifth grid level, when the three cycles at 2% drift were completed. The grids ruptured at joints when the columns was deformed to 3% drift. This resulted in the instability of longitudinal bars. Closer examination of the grid behavior indicated that the grid joint failure initiated at the second and third grid levels from the base, at northwest and northeast corners. This resulted in the buckling of northwest corner bar in second mode, bending in double curvature, and northeast corner bar in third mode, deforming in triple curvature. Figure 5-111 illustrates the performance of column FRP-11 at selected stages of loading.

Hysteretic moment-rotations relationships recorded during testing are shown in Fig. 5-112. The results reveal that approximately 1/7th of total rotation recorded was caused by anchorage slip, while the remaining 6/7th was caused by flexure.

The variation of reinforcement strains during testing is shown in Fig. 5-113. The maximum tensile strain recorded on longitudinal reinforcement was 0.4%, while the reinforcement lost its stability and buckled at a compressive strain of about 3.5%.

5.5.12 Column FRP-12

Column FRP-12 was built similar to FRP-5, except the cross sectional size of the FRP grids used in Column FRP-12 was larger. The column was reinforced with 12#20 (19.5 *mm* diameter) longitudinal bars, resulting in 1.96% reinforcement ratio. It was confined by 9-cell grids. The volumetric ratio of transverse reinforcement was 2.81%, which formed 140% of the amount required by *ACI 318-95* based on maximum reinforcement strength of 400 MPa. The spacing of grids was 76 *mm* (3 *in.*), which was approximately equal to the maximum spacing required by the same code. The column was tested under constant compressive force of 38% of its concentric capacity. The hysteretic relationships shown in Fig. 5-114 indicate that the column showed stable hysteresis loops up to 4% drift but developed a significant strength decay during the first cycle at 5% drift. The column failed due to the instability of

longitudinal reinforcement, caused by the premature failure of FRP reinforcement at the perimeter joints.

Observations during testing indicated that the column experienced initial flexural cracking at 0.5% and 1% lateral drift levels, within the lower 450 *mm* portion. More flexural cracks was observed when the column was loaded to 2% lateral drift. The cover concrete started crushing and diagonal tension cracks began to appear on side faces at the same deformation level. More damage to concrete cover was observed during 3% drift cycles. The cover concrete spalled off completely below the fourth grid layer on the west and below the third grid layer on the east, during the first cycle at 4% drift. The reinforcement cage became clearly visible within the plastic hinge region. During the second cycle, the corner bars started bending and exerting pressure on FRP grids. The lateral force resistance started to drop when the column leaned toward north during the third cycle. The decay in strength became excessive during the subsequent level of deformation at 5% drift. At this stage, the second and third grids from the base ruptured and the longitudinal bars buckled. Figure 5-115 illustrates the performance of column FRP-10 at selected stages of loading.

Figure 5-116 shows the hysteretic moment-rotation relationships recorded during testing. The results indicate that approximately 1/7th of total rotation was caused by anchorage slip, while the remaining 6/7th was caused by flexure.

Strain gauge readings plotted in Fig. 5-117 show that the longitudinal bars were subjected to maximum tensile and compressive strains of 1.7% and 2.1%, respectively, during the cycles at 4% drift. The FRP grids recorded maximum tensile strains of about 0.3% and 0.16% in the direction and perpendicular to loading, respectively, at 2% drift.

5.5.13 Column FRP-13

Column FRP-13 was identical to column FRP-7, except for the grid size. Column FRP-13 was confined by grids, consisting of large size FRP (8 *mm* x 10 *mm*). It was reinforced with 4#30 (29.9-*mm* diameter) longitudinal corner bars. The reinforcement grids had four cells, without any longitudinal reinforcement in the remaining perimeter grid corners. The volumetric ratio and spacing of transverse reinforcement were identical to that of column

FRP-11. It was loaded to 38% of its concentric capacity as constant axial compression. The hysteretic relationships shown in Fig 5-118 indicate that the column behaved as good as expected, developing 4% drift without a significant strength decay in moment resistance. The drift capacity at 20% decay in lateral force resistance caused by *P-Delta* effect was about 3%. The column failure was characterized by rupturing of FRP grids at joint corners, followed by the buckling of longitudinal bars. The increase in FRP cross sectional area did not translate into improved behavior since the grids failed prematurely at the joints prior to developing their full direct tension capacity.

Observations during testing indicated that initial flexural cracks occurred during the first cycle at 0.5% drift, at the second, fourth, and sixth grid levels from the base. Diagonal tension cracks started forming on side faces during 1% drift cycles. Additional flexural cracks were also observed to form at this deformation level, up to the eighth grid level, although no cover crushing was evident. The cover concrete started crushing near the base during 2% drift cycles. Widening and extension of diagonal cracks were also observed. Gradual spalling of the cover occurred during 3% drift cycles, which eventually led to the complete spalling of hinging region at 4% drift. Cover spalling extended up to the fourth grid level, exposing reinforcement on the east and west sides. The hinging region became clearly visible and measured to be about 300 *mm* from the base. The column started leaning towards south as FRP grids experienced joint failure at the southeast corner, and the longitudinal bars started to bend and buckle. Figure 5-119 illustrates the performance of column FRP-13 at selected load stages.

Hysteretic moment-rotation relationships recorded during testing are shown in Fig. 5-120. The results indicate that approximately 1/5th of total rotation was caused by anchorage slip, while the remaining 4/5th was caused by flexure.

The longitudinal reinforcement developed a maximum tensile strain of 0.25% and a maximum compressive strain of about 2.7% just before the end of the test. However, the FRP grids recorded a maximum strain of 0.25% in the direction of loading and 0.40% in the perpendicular direction. The variation of reinforcement at selected locations during the test is illustrated in Fig. 5-121.

5.5.14 Column FRP-14

Column FRP-14 was reinforced with only 4-#30 corner bars as in the case of Column FRP-13. Unlike FRP-13, the reinforcement grids had 9-cells. The volumetric ratio of transverse reinforcement was 2.81%, which formed 140% of the amount required by *ACI 318-95* based on 400 MPa reinforcement strength. The grid spacing was 76 *mm* (3 *in.*), which was approximately equal to the maximum spacing required by *ACI 318-95*. The column was subjected to 38% of its concentric capacity prior to the application of lateral deformation reversals. The increase in the number of grid cells, relative to Column FRP-13, increased the uniformity of lateral confinement pressure and resulted in improved behavior. The moment-displacement hysteretic relationship shown in Fig. 5-122 indicates that the column showed stable hysteresis loops up to 5% drift with little strength decay. It failed at the end of the second cycle at 6% drift, due to the failure of FRP grid joints and associated buckling of longitudinal bars. The force-displacement hysteretic relationship of Fig. 5-123 shows reduced deformability due to *P-Delta* effect, showing 3% drift capacity at approximately 20% loss in lateral load resistance.

Observations during testing revealed that the column developed initial flexural cracking during cycles of 0.5% and 1% drift, at almost every level of FRP grid within the lower 680-*mm* segment. More flexural cracks and crushing of corner cover concrete were observed during the cycles at 2% drift. In addition, diagonal shear cracks started forming on side faces up to 750 *mm* from the base. Widening of flexural cracks and increased crushing of cover concrete on the compression side were observed during the initial cycle at 3% drift. A 240-*mm* vertical crack appeared on the East Side, about 120-*mm* from the north face. Cover spalling continued during the second and third cycles at 3% drift, as well as the cycles at 4% drift. During the cycles at 5% drift, spalling extended up to the fourth grid level on the West Side, and the fifth level on the East Side, exposing reinforcement. Additional damage to concrete was noticed and hinging region became clearly visible during the cycles of 6% drift. The height of the hinging region was measured to be 350 *mm*. The column failed at the second cycle of 6% drift deformation due to the instability of longitudinal reinforcement. The longitudinal bars buckled in the second mode, developing double curvature, when the FPR

grid failed at joints. Figure 5-123 illustrates the performance of column FRP-13 at selected stages of loading.

Hysteretic moment-rotation relationships are shown in Fig. 5-124. The results reveal that approximately 1/10th of total rotation recorded was caused by anchorage slip, while the remaining 9/10th was caused by flexure.

A maximum tensile strain of 0.9% was recorded on longitudinal reinforcement at the column-footing interface, indicating yield penetration into the footing. In addition, the longitudinal reinforcement developed a maximum compressive strain of about 3% just before the end of the test. Unlike the columns with 12-longitudinal bars, the 9-cell grids used in Column FRP-14 exhibited larger strains in the grids, in the direction perpendicular to loading. The maximum tensile strains recorded were 0.09% and 0.27% in the direction of loading and perpendicular to loading, respectively, at 3% drift. Figure 5-125 shows the hysteretic behavior of strains with lateral loading.

Table 5-1: Summary of strength and drift capacities

Column	Column Moment Resistance $(M_{test})_{Max}$ (kN.m)	Min.Drift@ $80\%(M_{test})_{Max}$	Column Force Resistance $(F_{test})_{Max}$ (kN)	Min. Drift @ $80\%(F_{test})_{Max}$	*ACI* 318-95 M_n (kN.m)
BG-1	320	1%	169	1%	242
BG-2	311	3%	164	2%	242
BG-3	260	7%	143	4%	242
BG-4	338	2%	177	2%	277
BG-5	363	5%	190	3%	277
BG-6	351	5%	180	3%	284
BG-7	348	4%	184	3%	290
BG-8	326	6%	179	4%	290
BG-9	359	3%	189	3%	286
BG-10	366	5%	192	3%	284
BG-11	437	6%	231	4%	453
BG-12	415	4%	214	3%	462
BG-13	379	4%	203	2%	428
SD-1	309	3%	160	2%	251
SD-2	271	6%	150	3%	245
SD-3	328	6%	173	3%	281
SD-4	335	4%	176	3%	285
FRP-1	282	1%	153	1%	261
FRP-2	317	3%	166	2%	261
FRP-3	266	6%	143	4%	261
FRP-4	204	1%	107	1%	296
FRP-5	209	2%	100	2%	296
FRP-6	339	7%	182	5%	296
FRP-7	372	4%	189	4%	320
FRP-8	330	2%	171	2%	320
FRP-9	318	3%	150	3%	297
FRP-10	341	5%	187	4%	297
FRP-11	248	2%	122	2%	261
FRP-12	337	4%	172	3%	296
FRP-13	356	4%	180	3%	320
FRP-14	372	6%	190	3%	320

Notes:

1. $(M_{test})_{Max}$ and $(F_{test})_{Max}$ quantities represent the average of maximum moments and lateral forces recorded in each direction of loading.

Minimum drift capacity is obtained from respective hysteretic relationship as lateral drift at which the column has completed a minimum of three deformation cycles with no more than 20% drop in strength. The readings are rounded off to the smaller whole number.

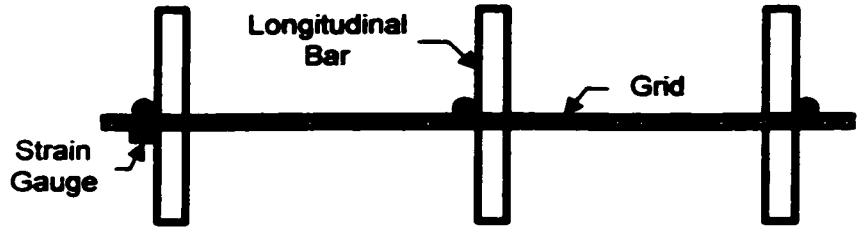

a) Strain gauge location (Side View)

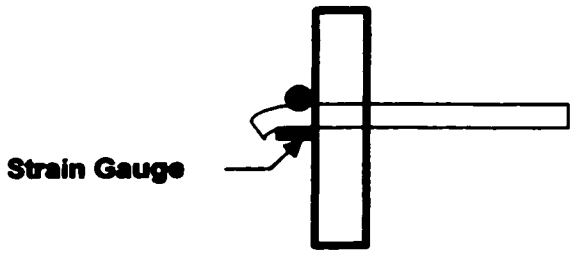

b) Bending of grid reinforcement

c) Observed behavior during column tests

Figure 5-1: Behavior of grids at perimeter joints

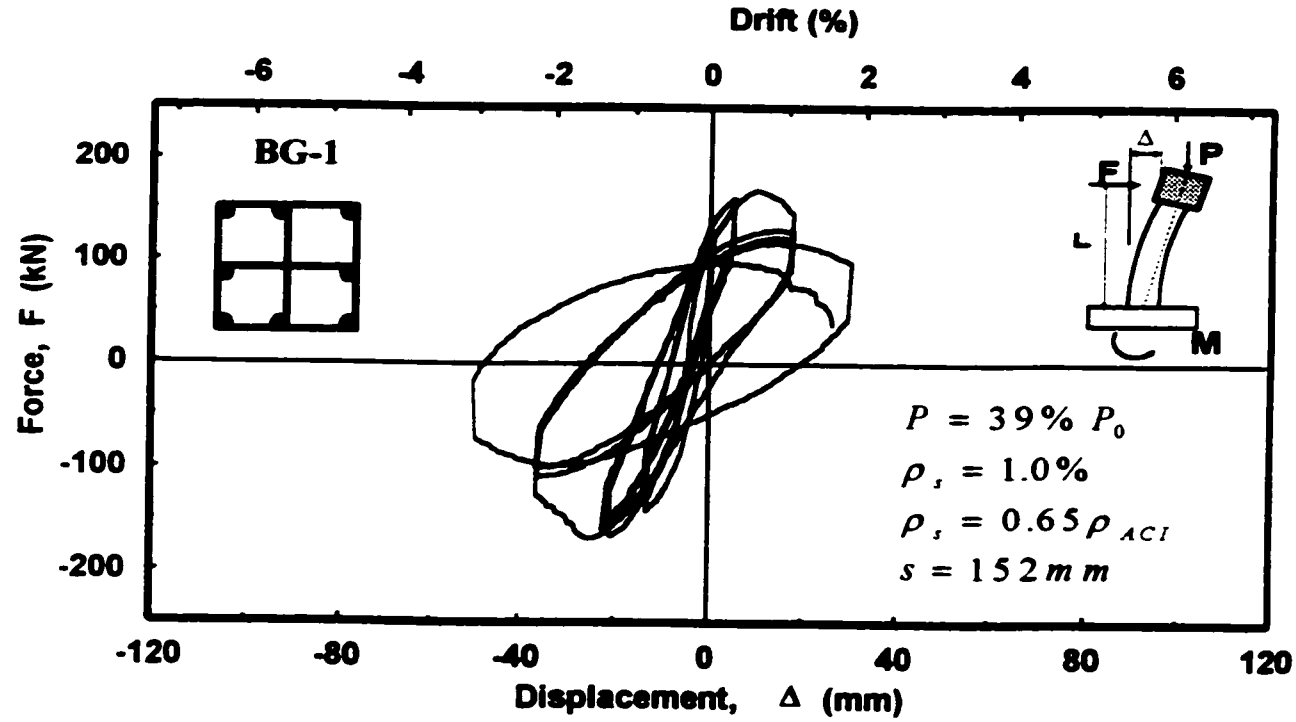

a) Hysteretic force-displacement relationship

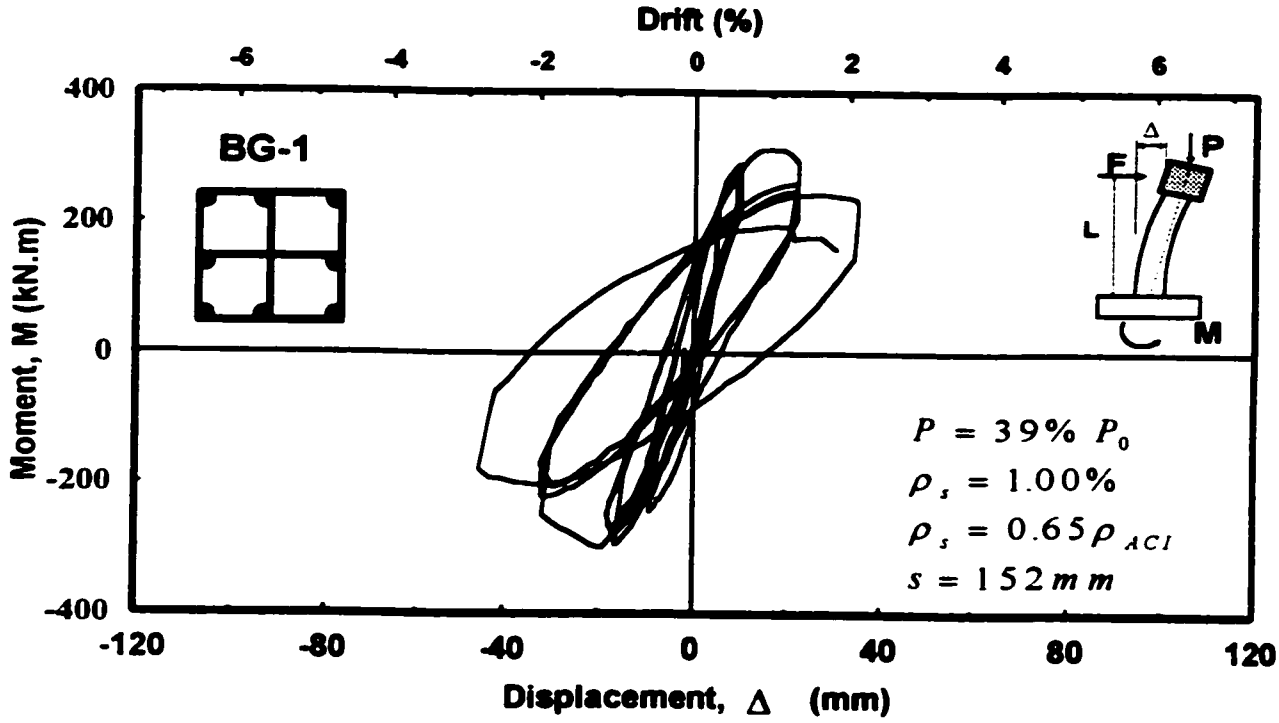

b) Hysteretic moment-displacement relationship

Figure 5-2: Hysteretic behavior of column BG-1

a) At 1% Drift

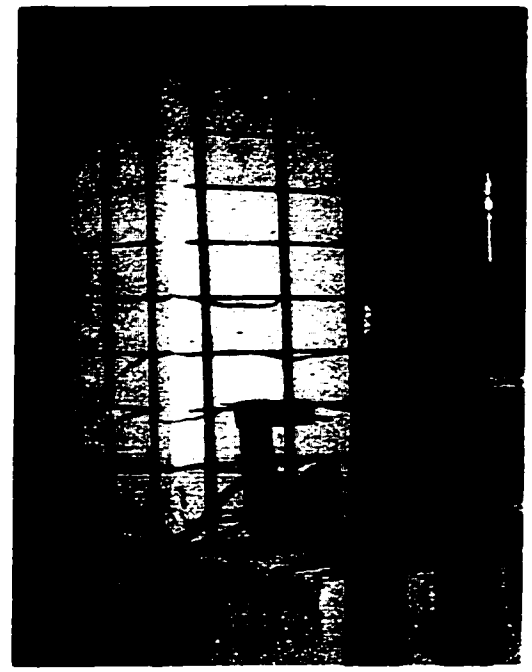

b) At 2% Drift

c) At 3% Drift

d) At Failure Zone

Figure 5-3: Observed damage in column BG-1 at selected stages of loading

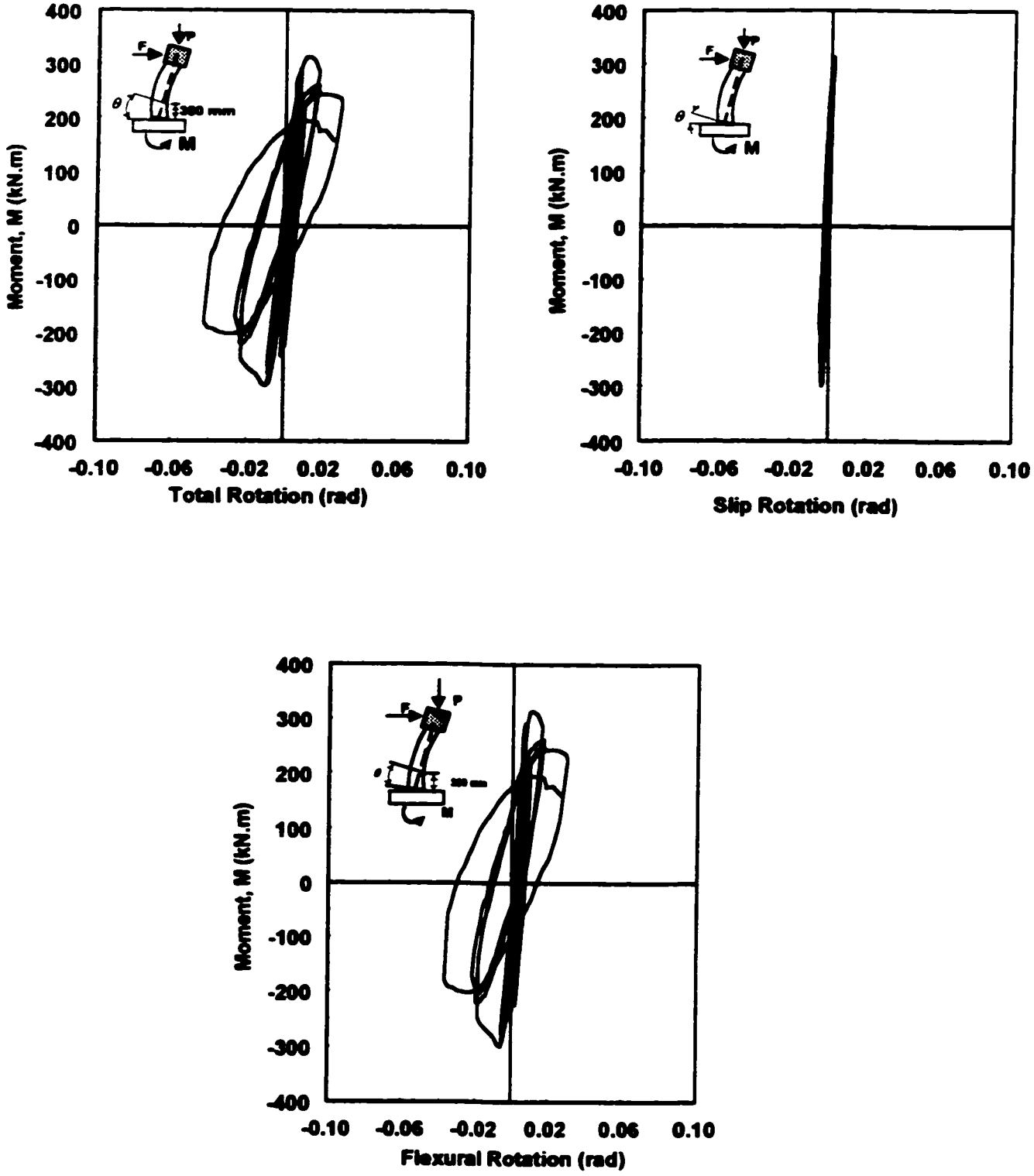

Figure 5-4: Moment-rotations relationships for column BG-1

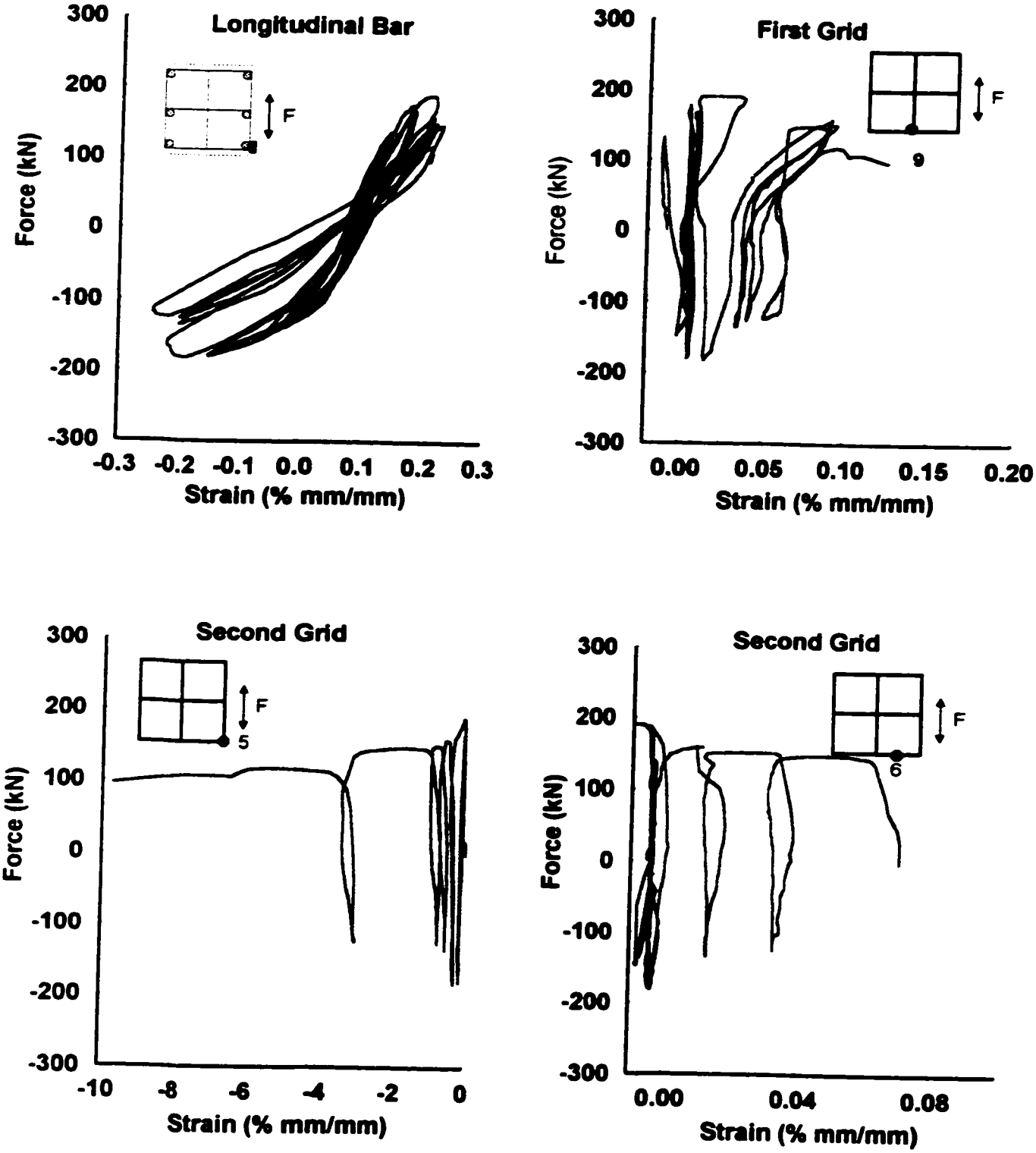

Figure 5-5: Reinforcement strain readings in Column BG-1

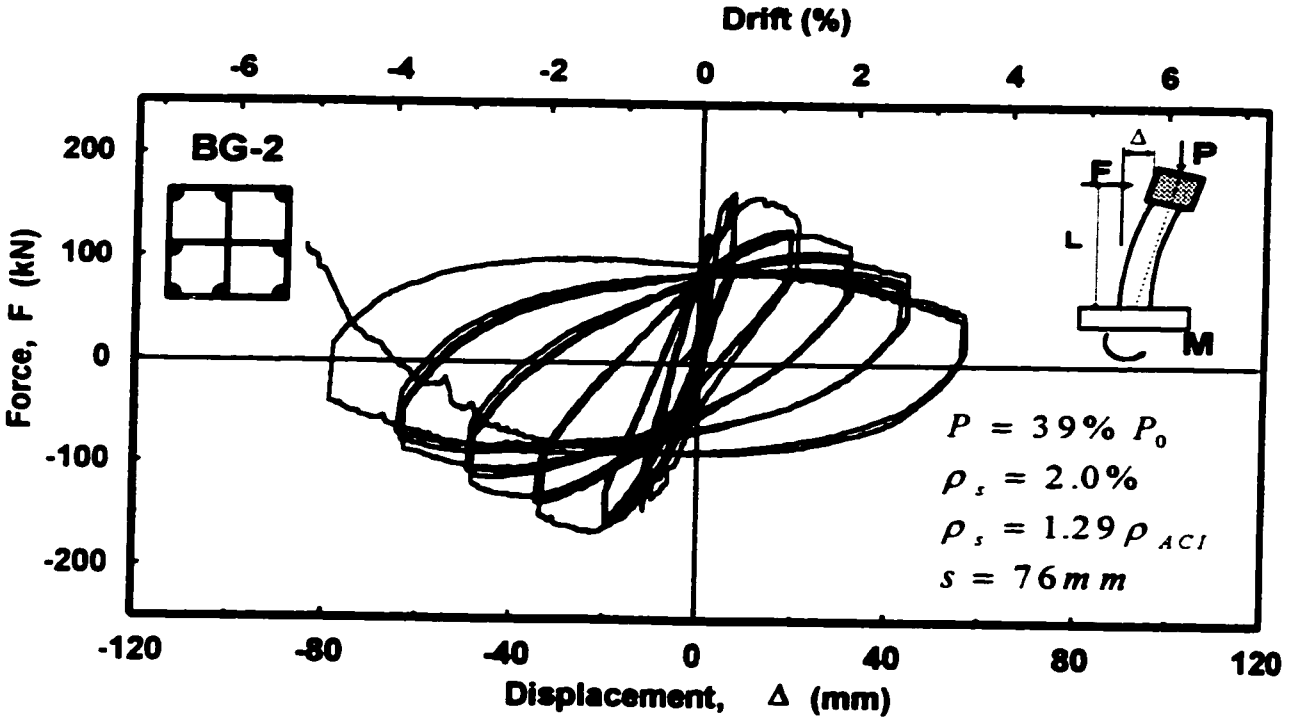

a) Hysteretic force-displacement relationship

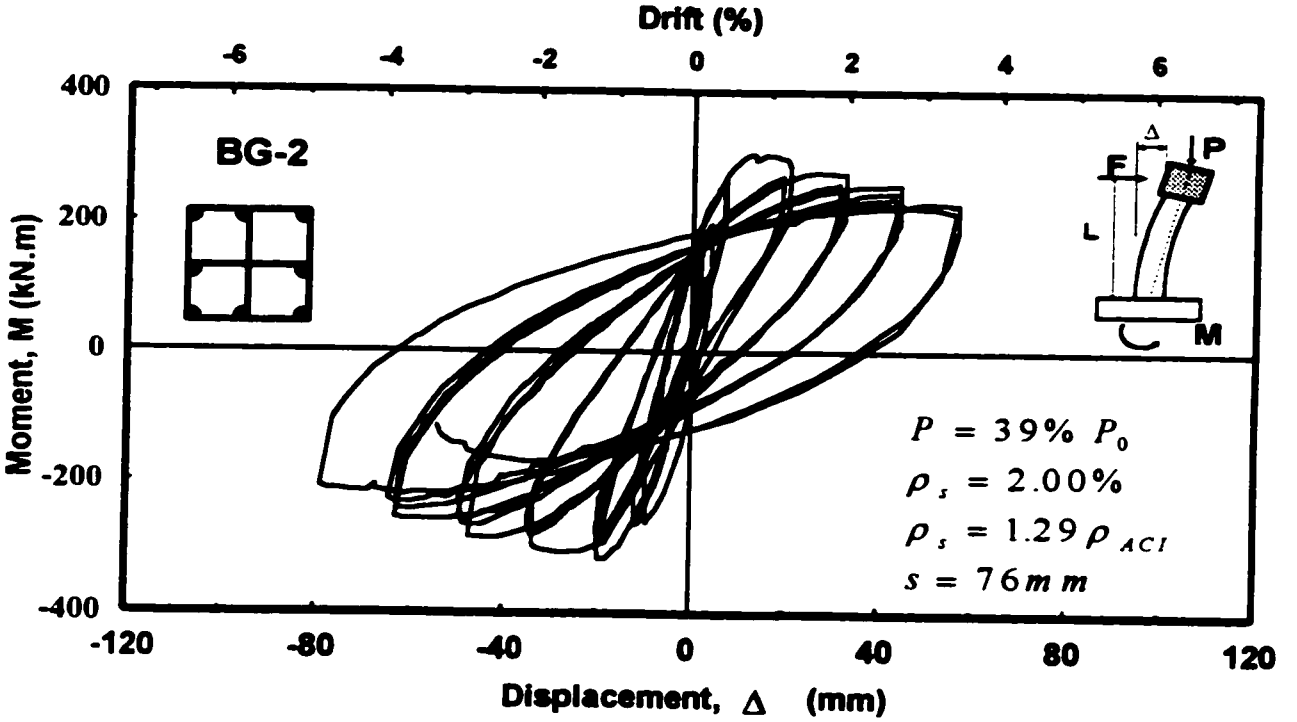

b) Hysteretic moment-displacement relationship

Figure 5-6: Hysteretic behavior of column BG-2

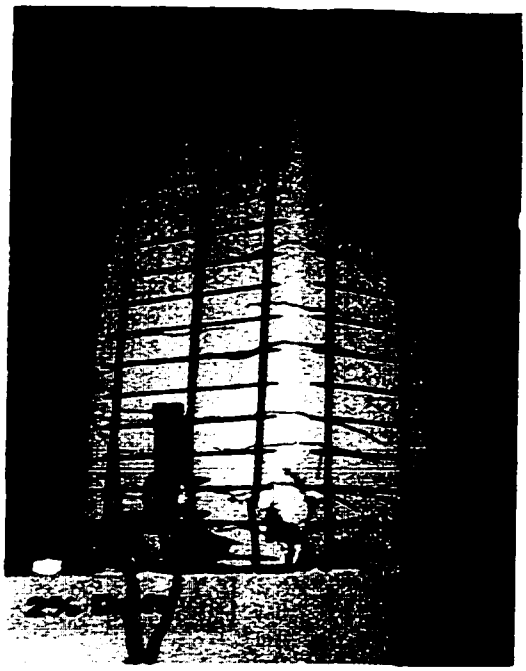

a) At 2% Drift

b) At 4% Drift

c) At 5% Drift (East View)

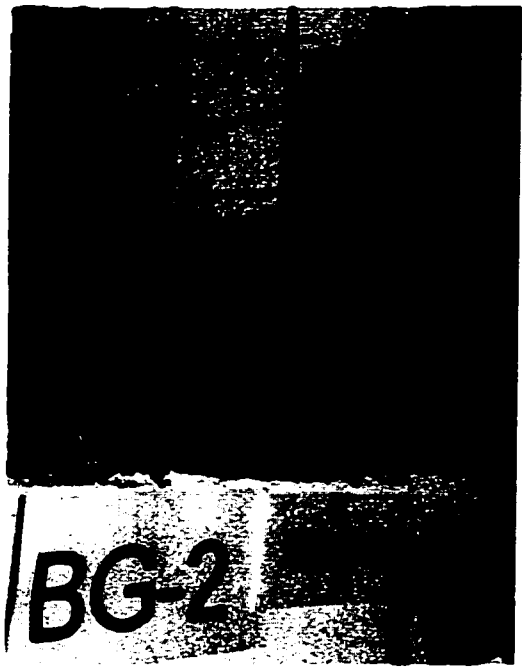

d) At 5% Drift, Close-up (West View)

Figure 5-7: Observed damage in column BG-2 at selected stages of loading

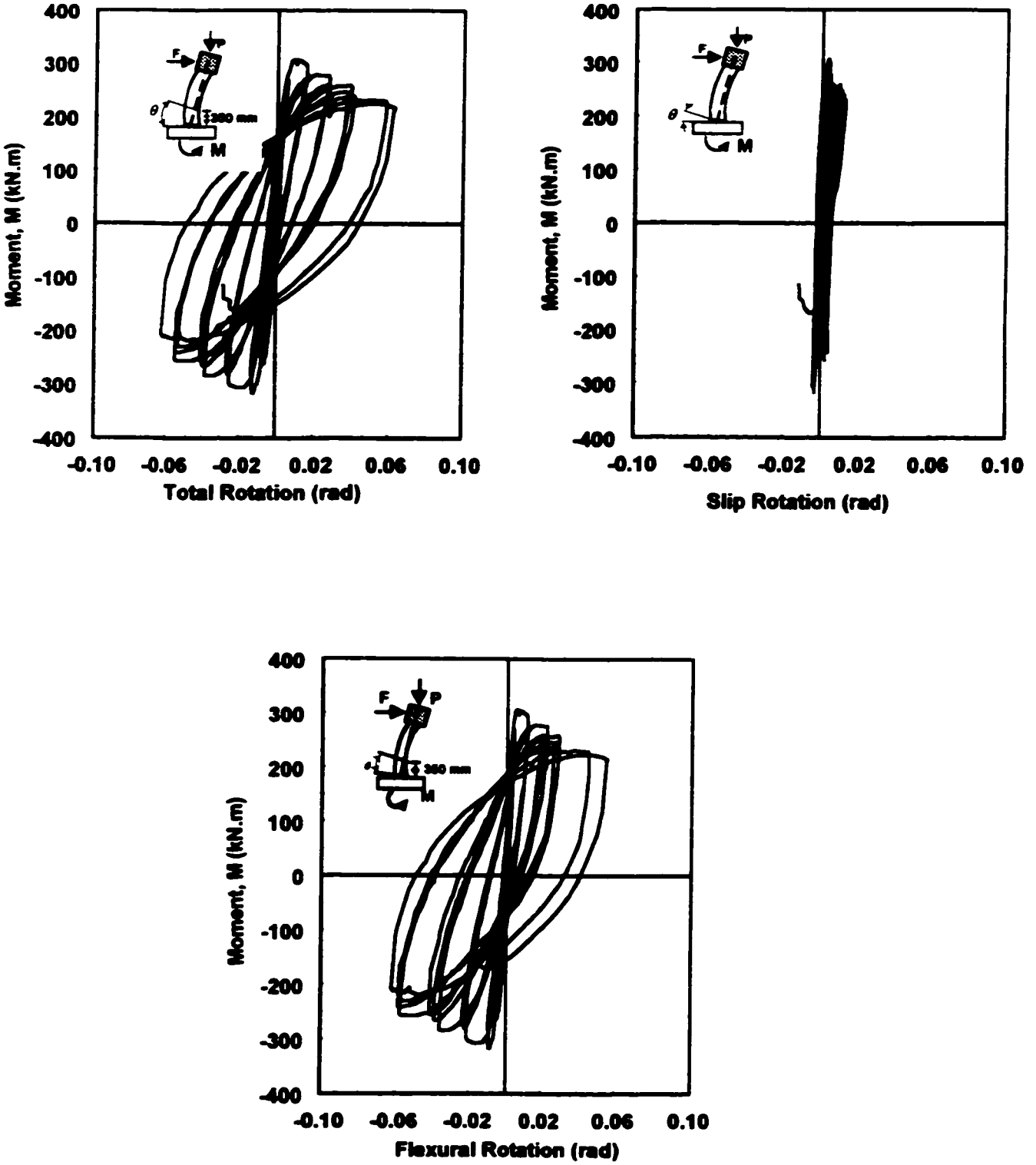

Figure 5-8: Moment-rotations relationships for column BG-2

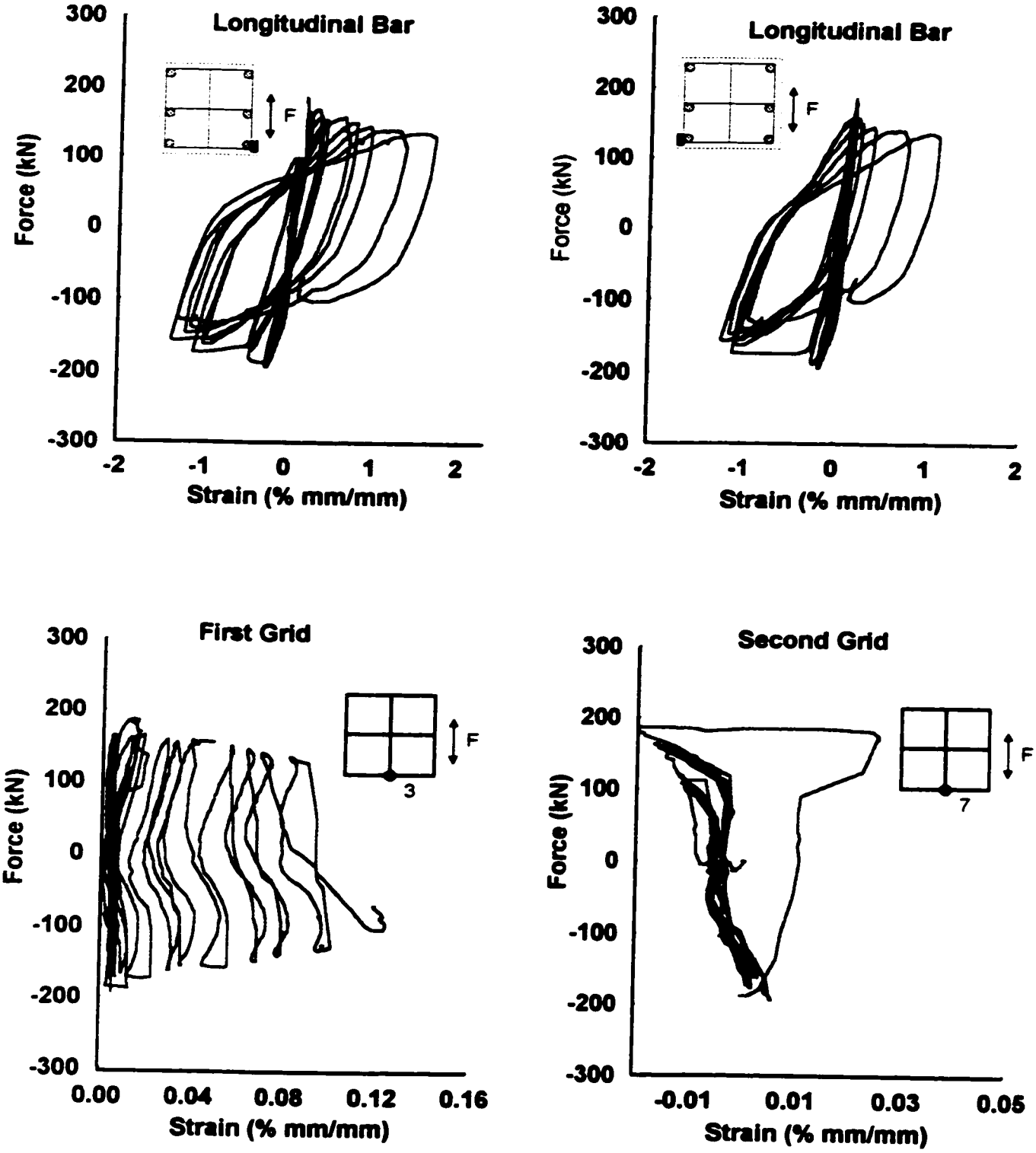

Figure 5-9: Reinforcement strain readings in Column BG-2

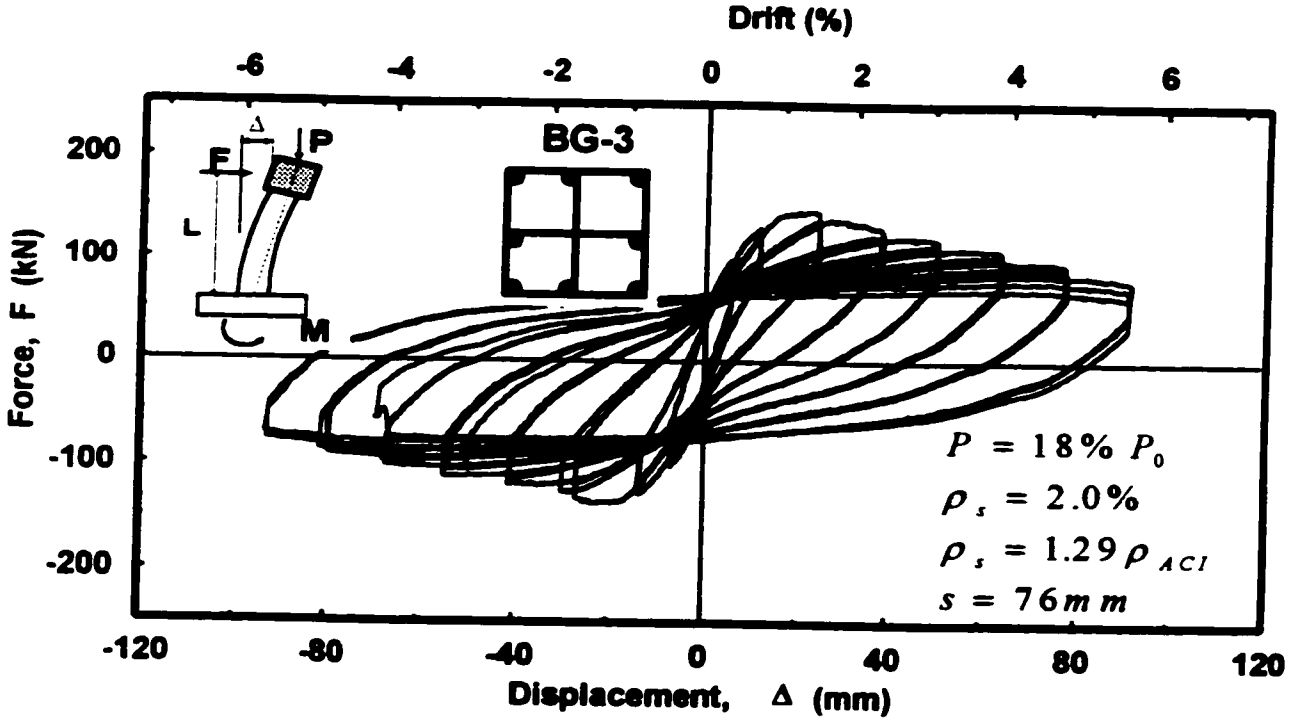

a) Hysteretic force-displacement relationship

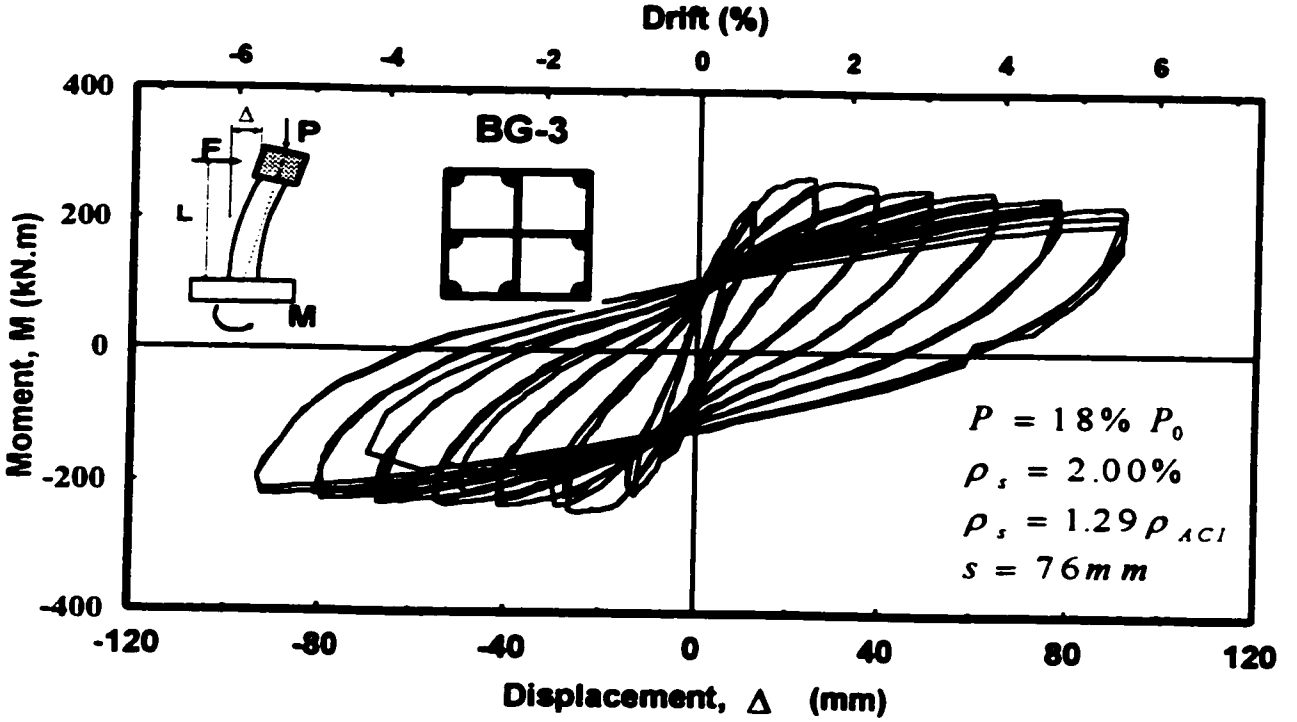

b) Hysteretic moment-displacement relationship

Figure 5-10: Hysteretic behavior of column BG-3

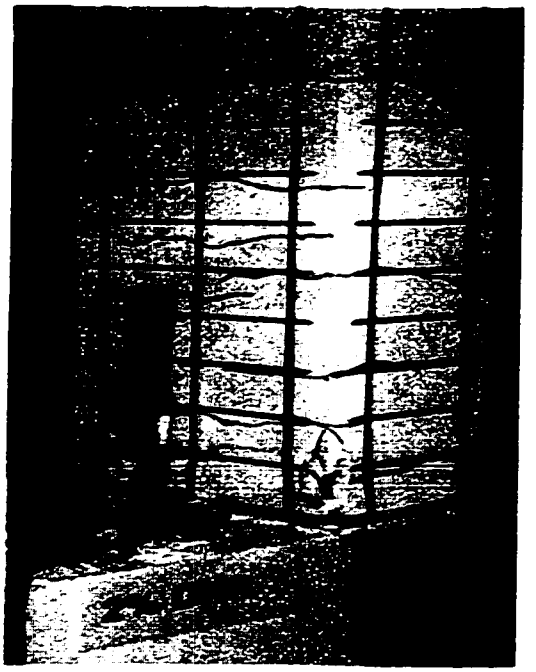

a) At 2% Drift

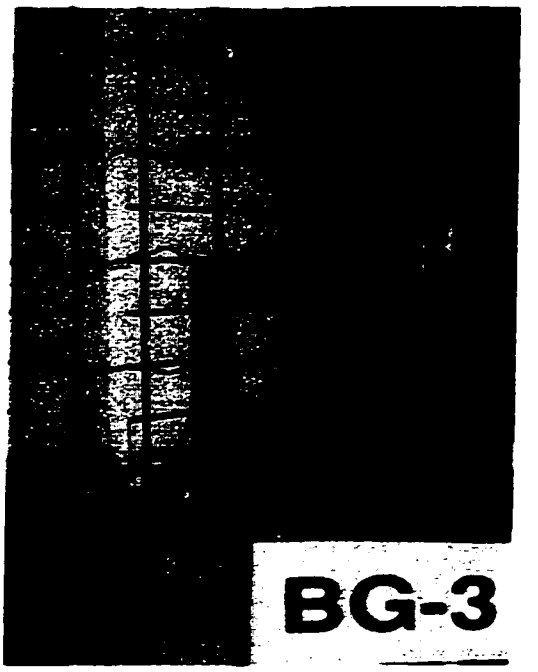

b) At 3% Drift

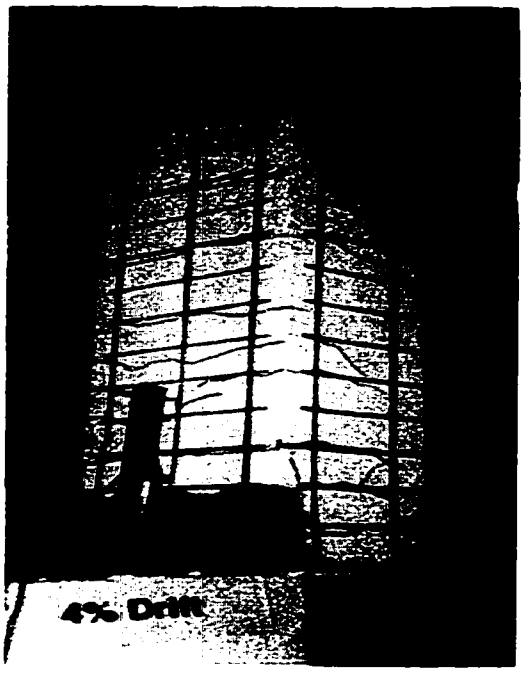

c) At 4% Drift

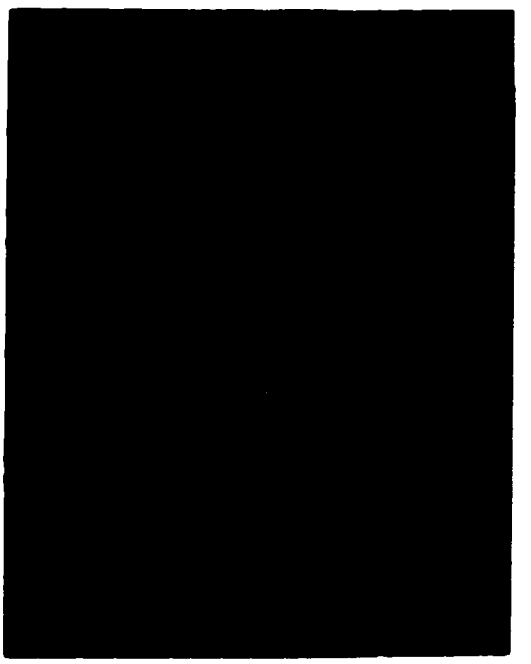

d) At 6% Drift

Figure 5-11: Observed Damage in Column BG-3 at Selected Stages of Loading

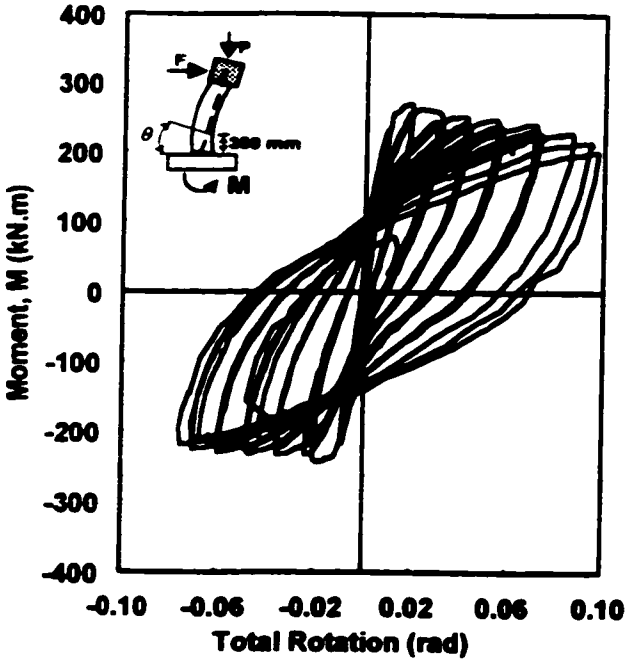

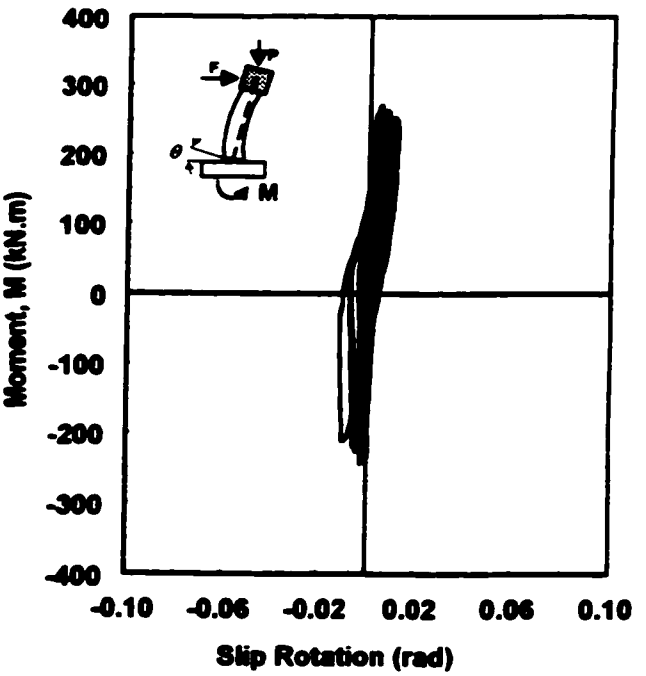

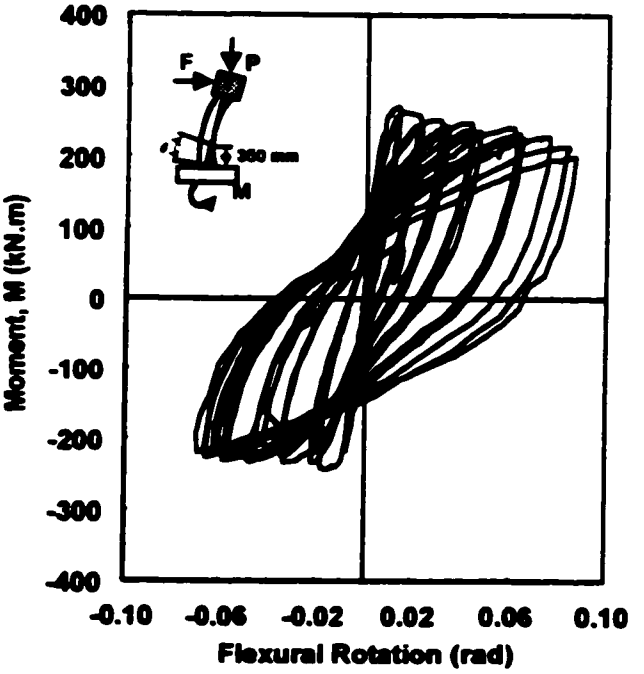

Figure 5-12: Moment-rotations relationships for column BG-3

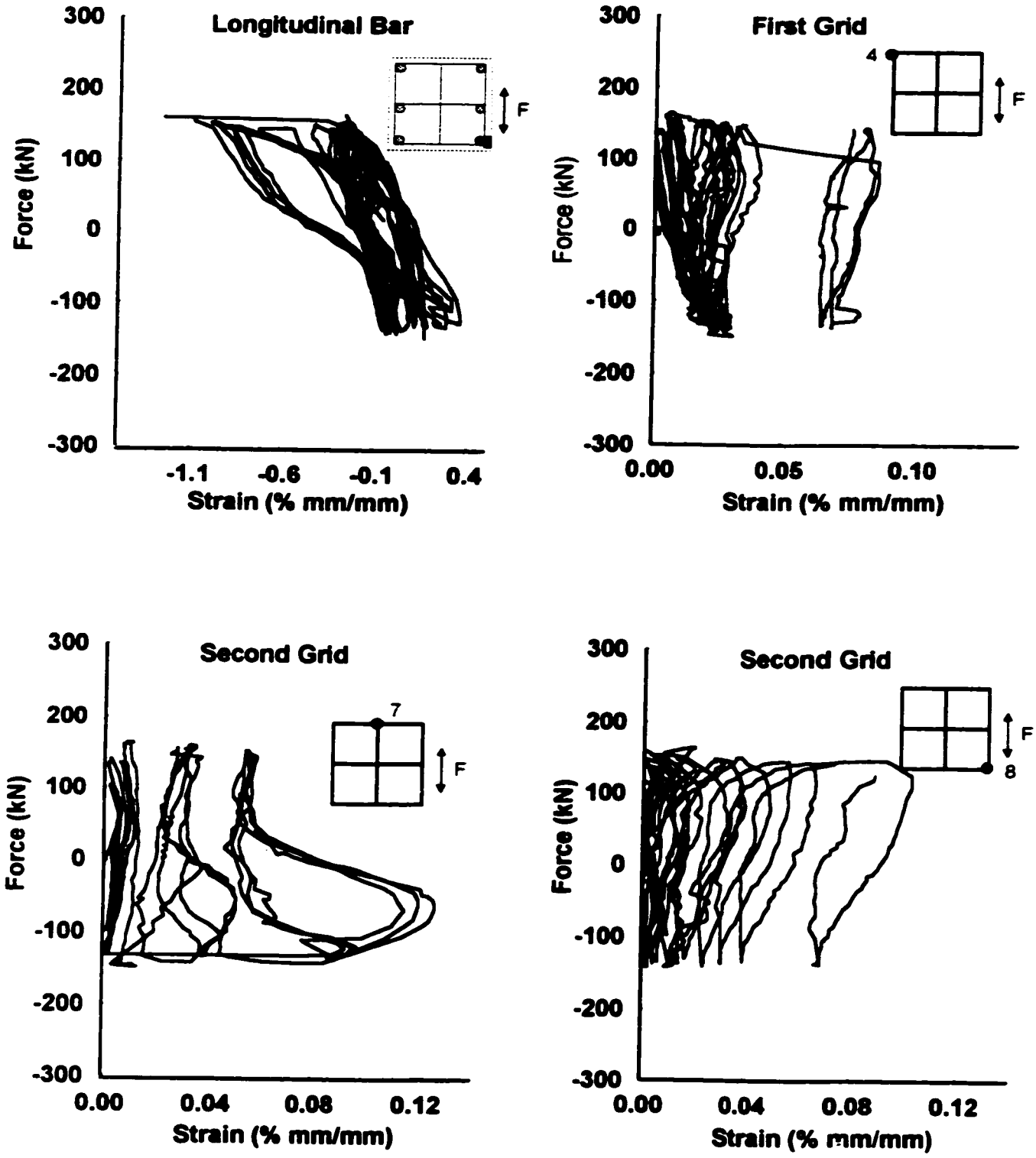

Figure 5-13: Reinforcement strain readings in Column BG-3

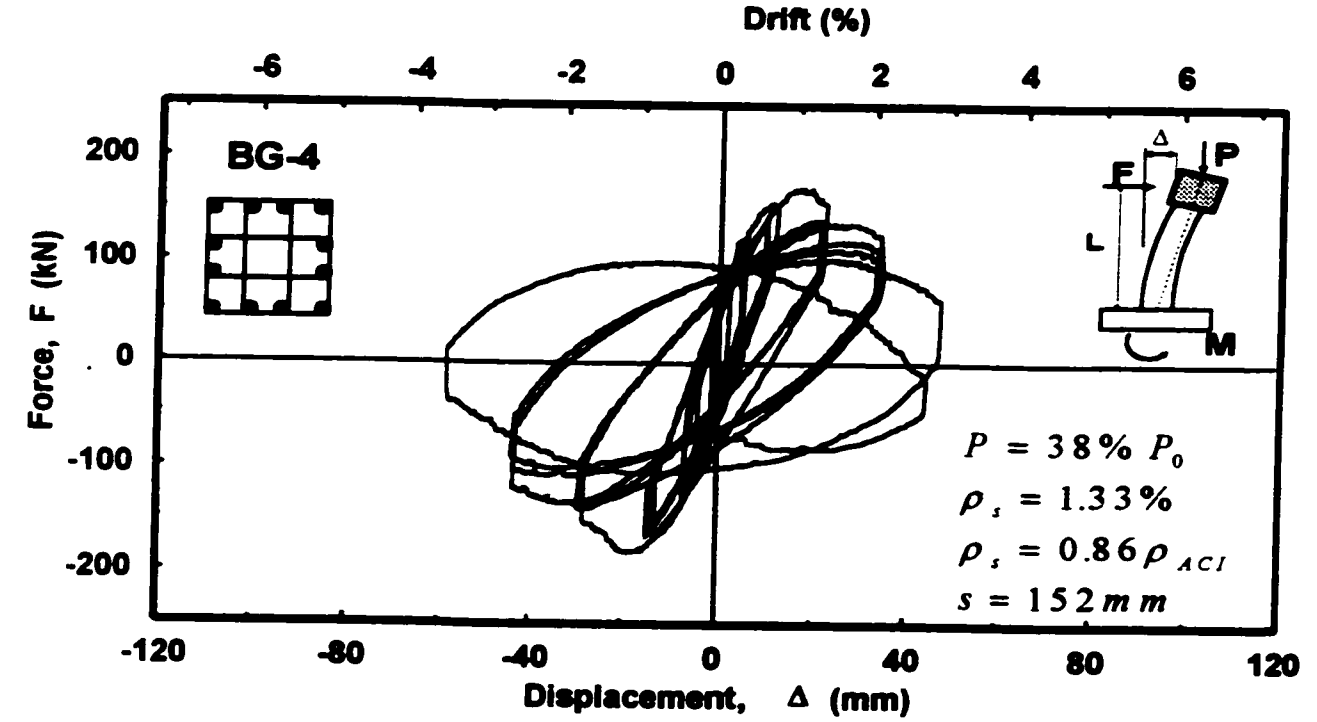

a) Hysteretic force-displacement relationship

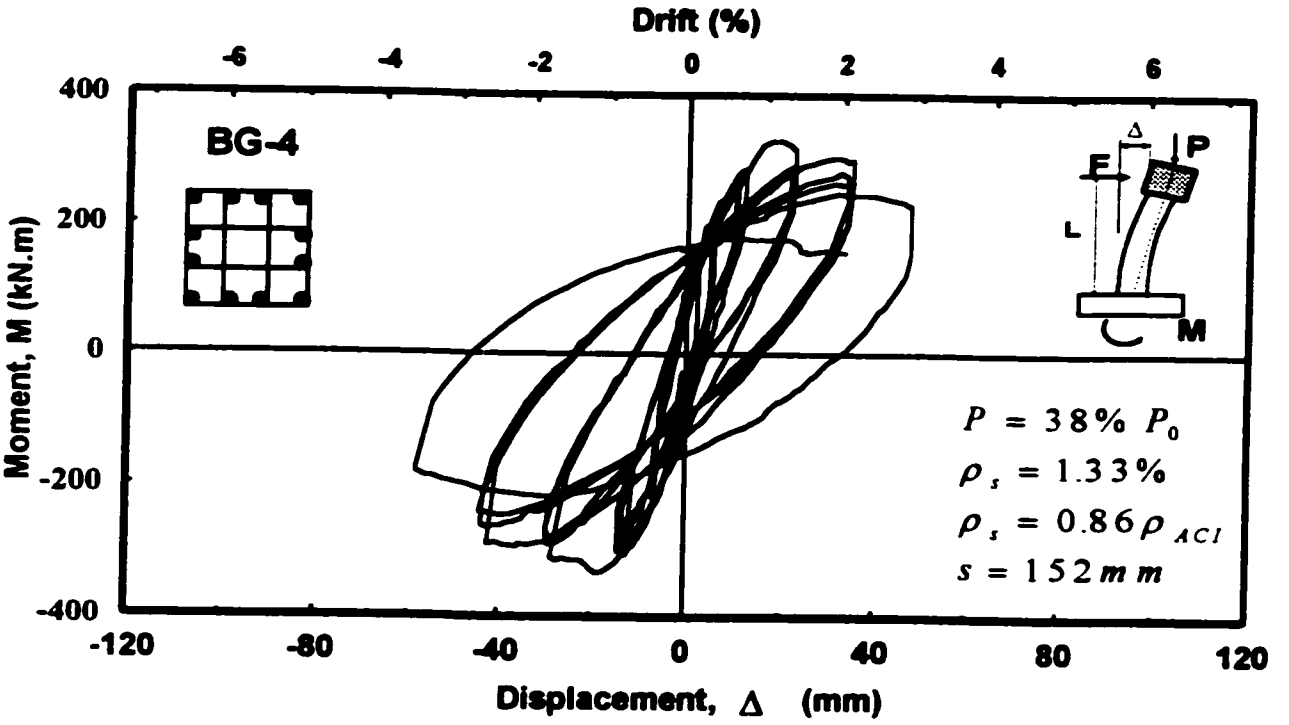

b) Hysteretic moment-displacement relationship

Figure 5-14: Hysteretic behavior of column BG-4

a) At 1% Drift

b) At 2% Drift

c) At 3% Drift

d) At 4% Drift

Figure 5-15: Observed damage in column BG-4 at selected stages of loading

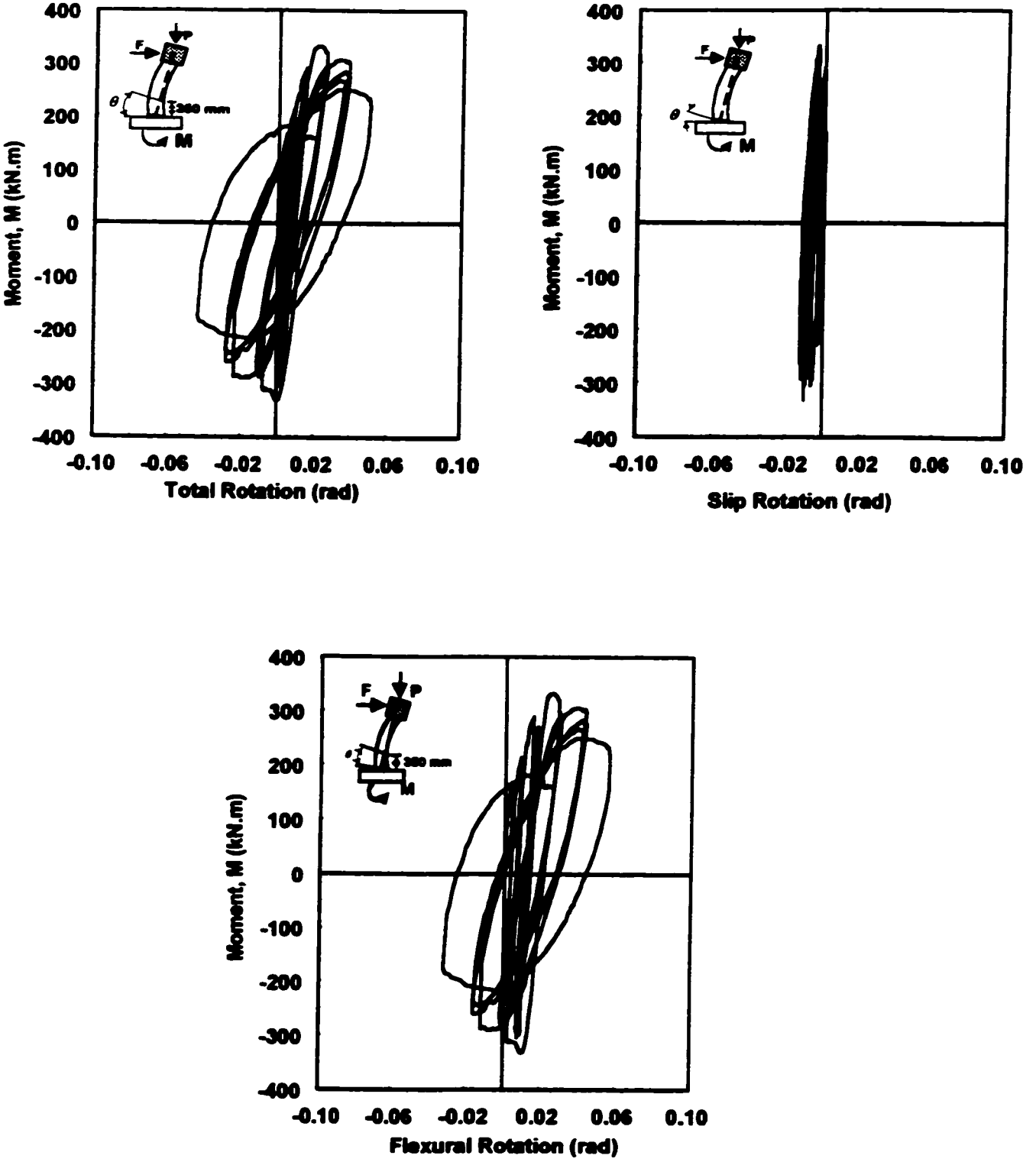

Figure 5-16: Moment-rotations relationships for column BG-4

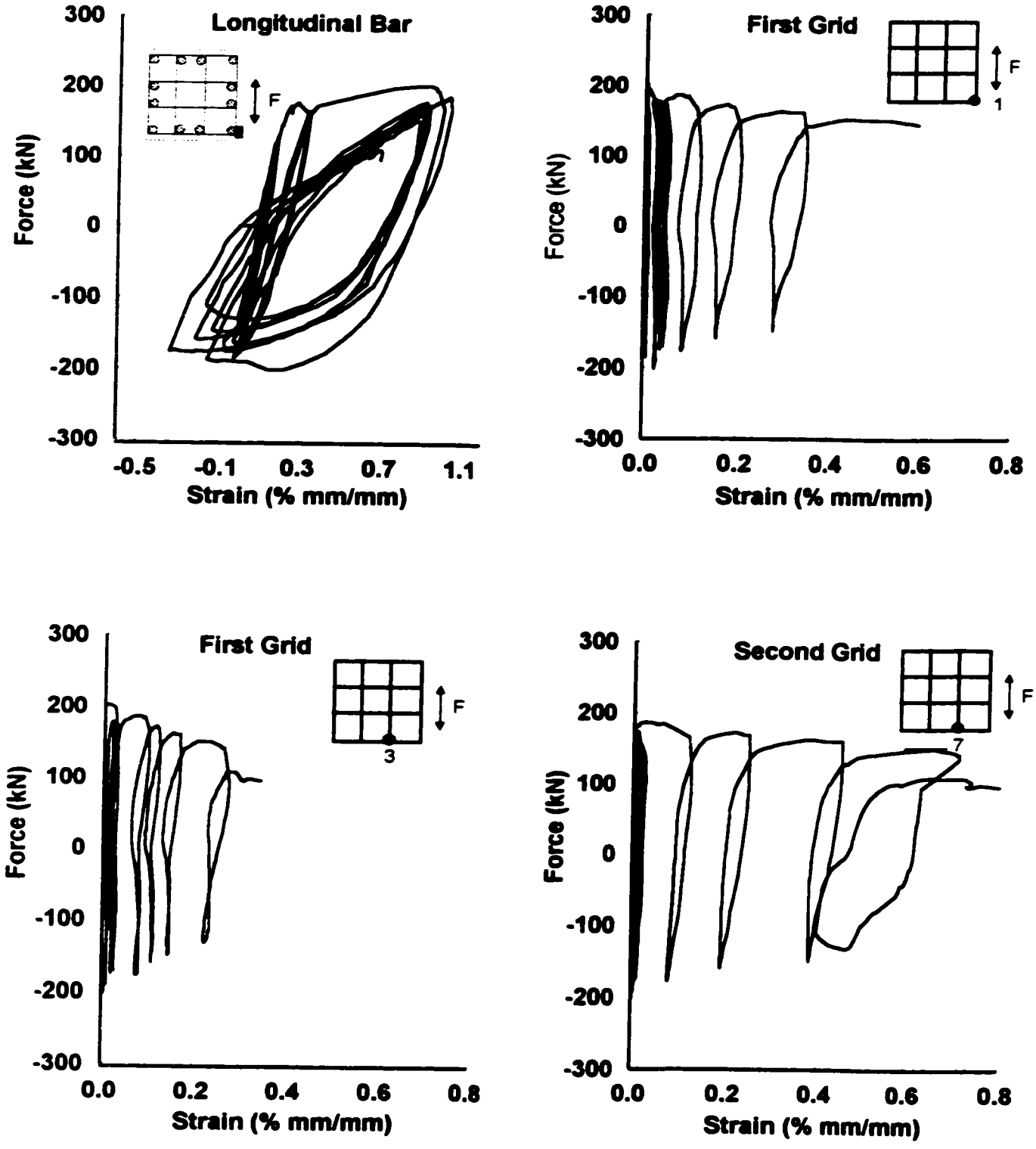

Figure 5-17: Reinforcement strain readings in Column BG-4

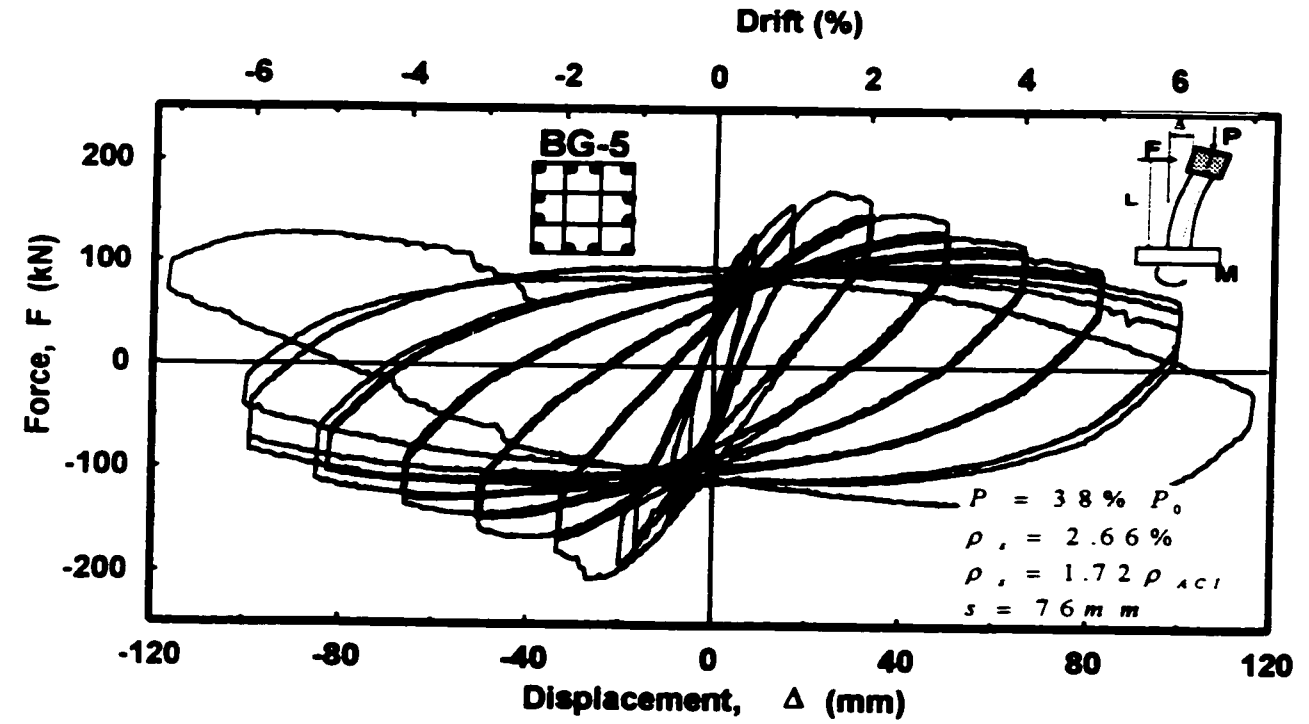

a) Hysteretic force-displacement relationship

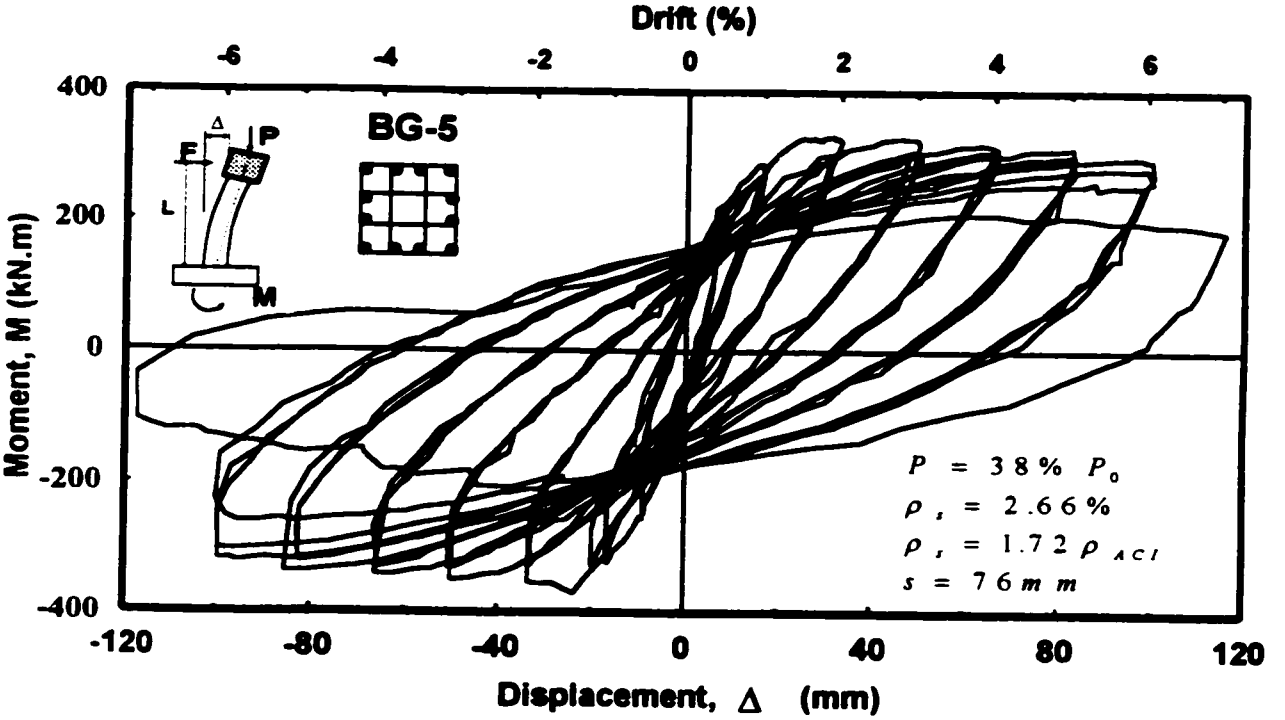

b) Hysteretic moment-displacement relationship

Figure 5-18: Hysteretic behavior of column BG-5

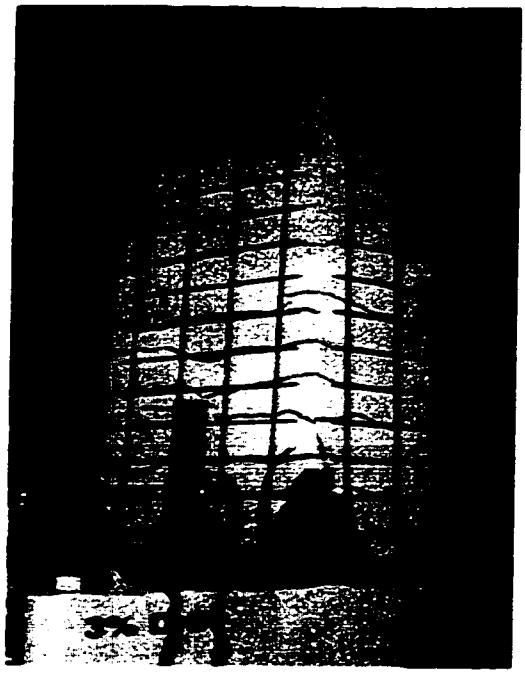

a) At 3% Drift

b) At 6% Drift

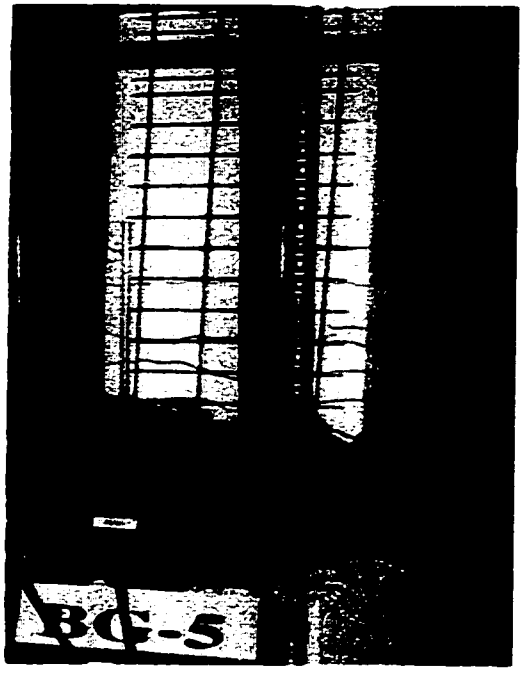

c) At 7% Drift

d) End of Test

Figure 5-19: Observed damage in column BG-5 at selected stages of loading

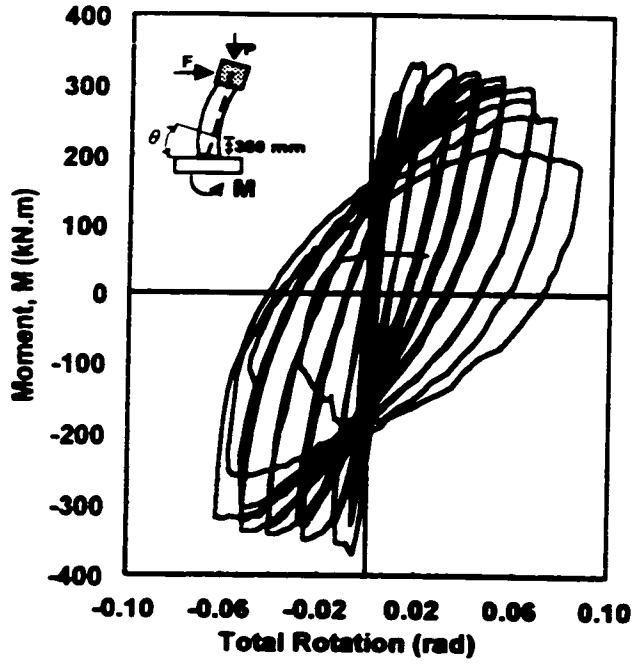

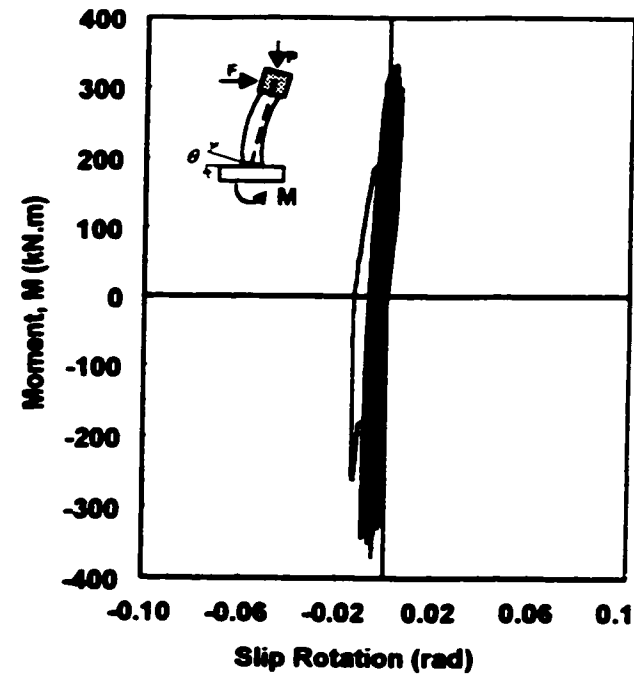

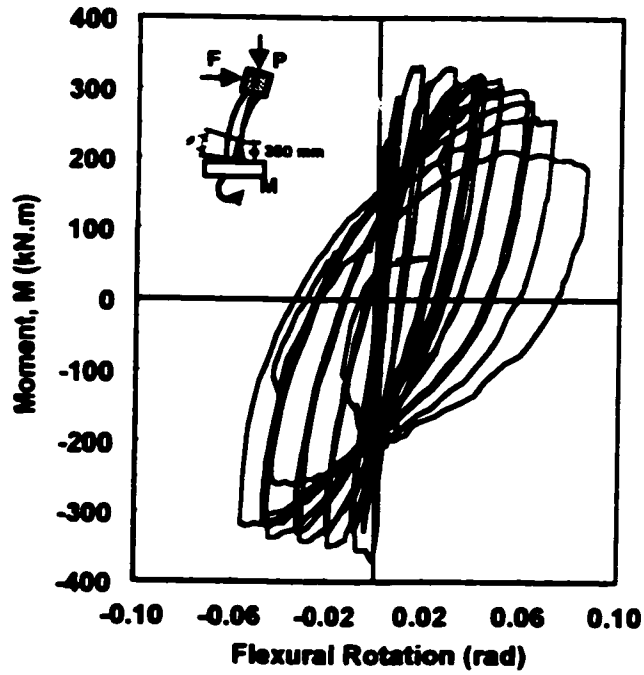

Figure 5-20: Moment-rotations relationships for column BG-5

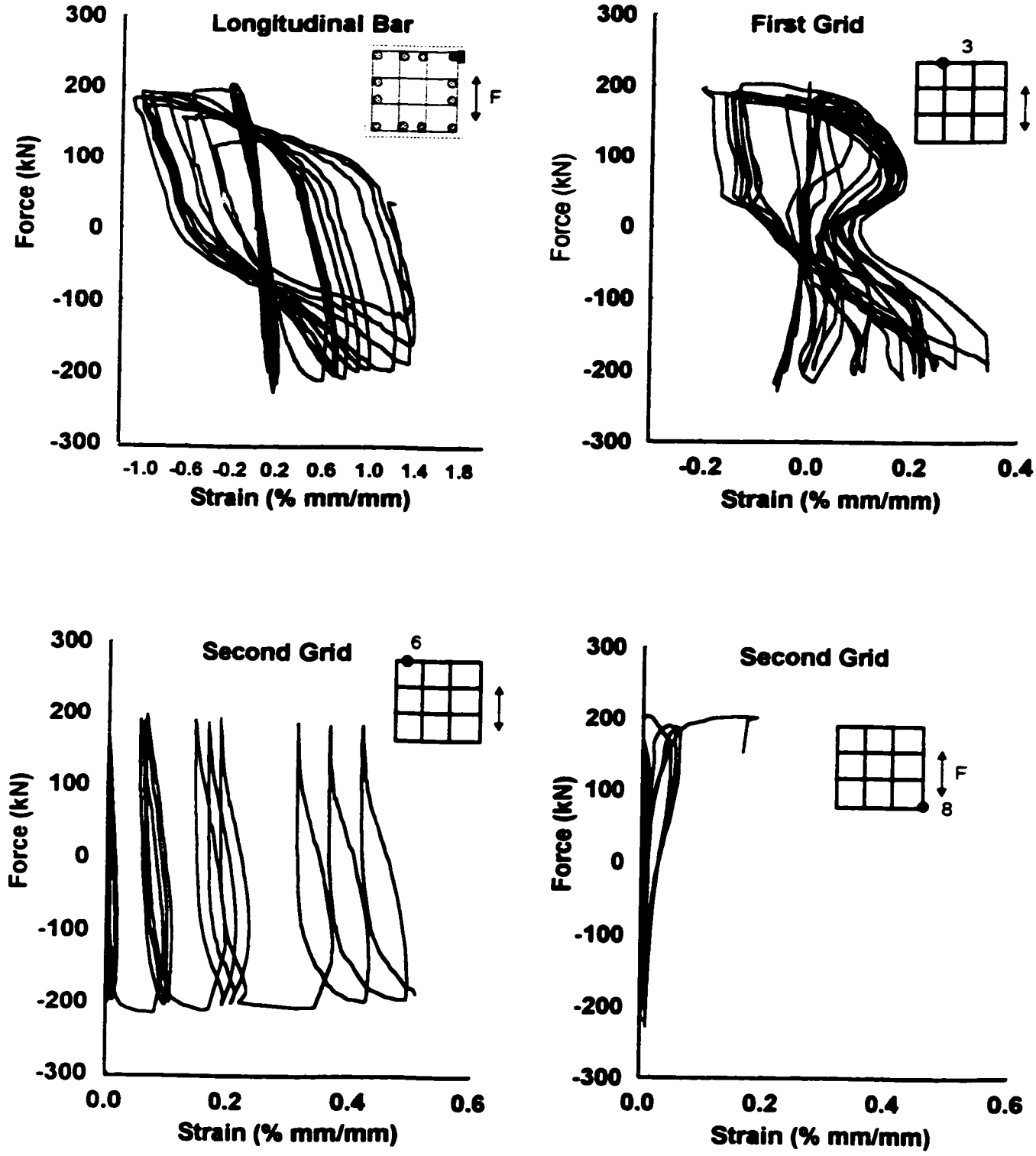

Figure 5-21: Reinforcement strain readings in Column BG-5

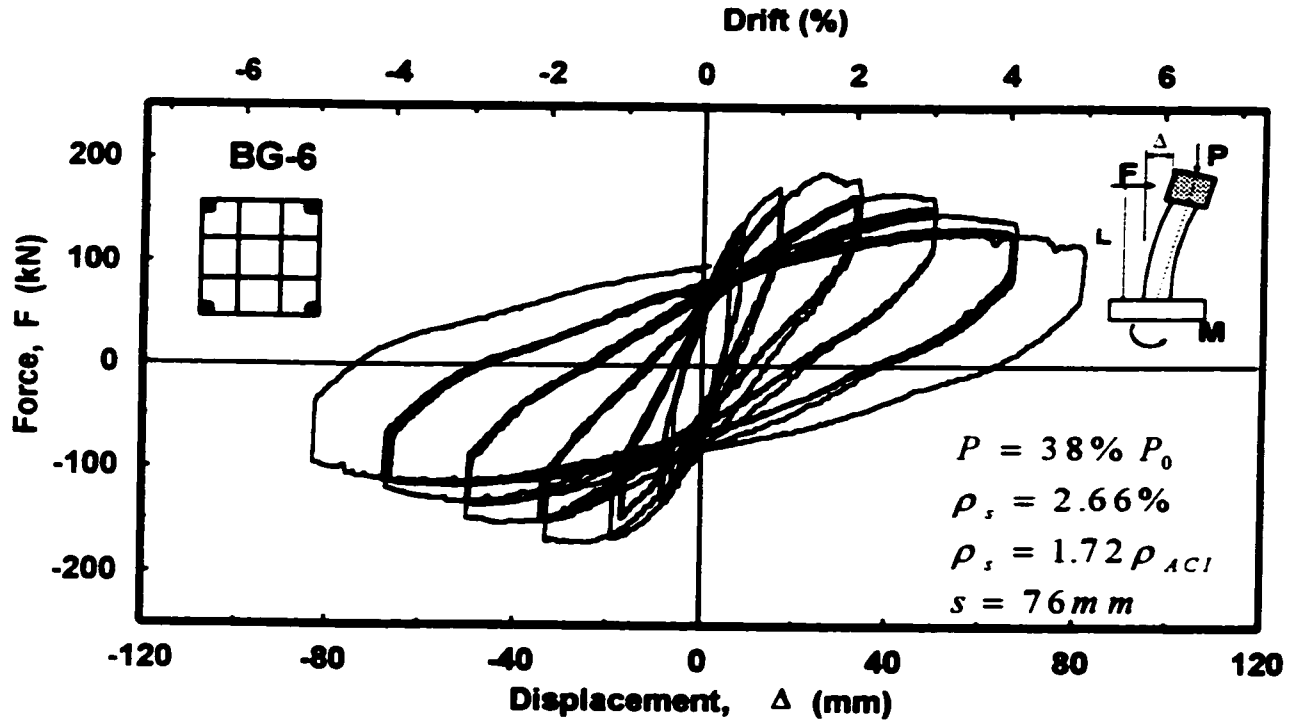

a) Hysteretic force-displacement relationship

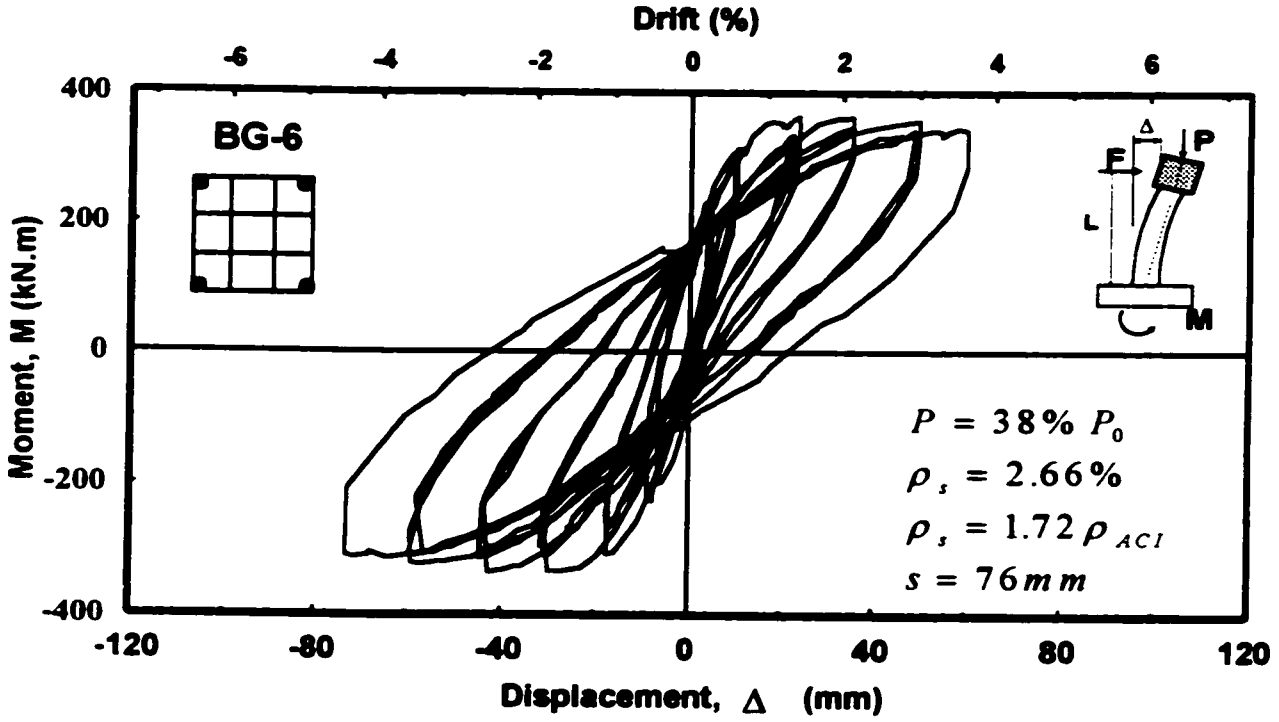

b) Hysteretic moment-displacement relationship

Figure 5-22: Hysteretic behavior of column BG-6

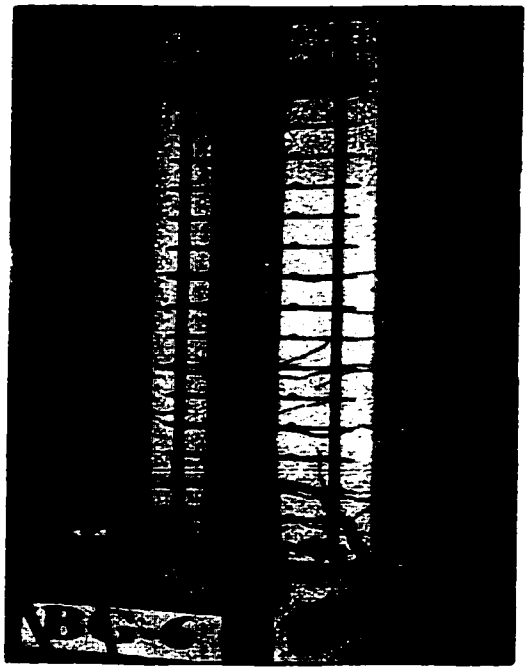

a) At 2% Drift

b) At 4% Drift

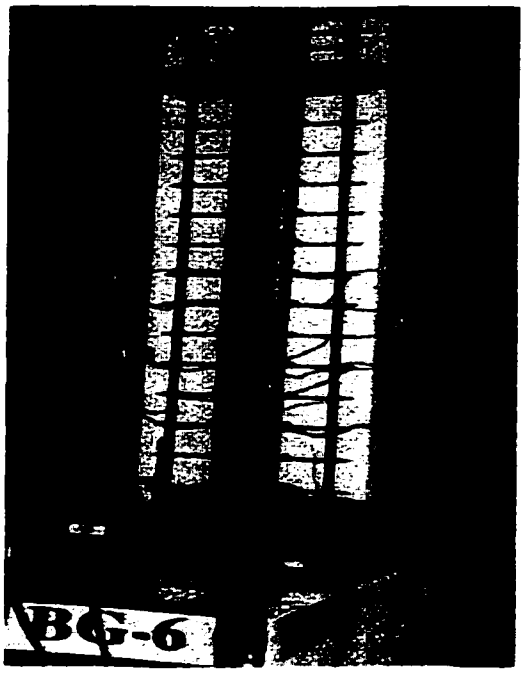

c) At 5% Drift

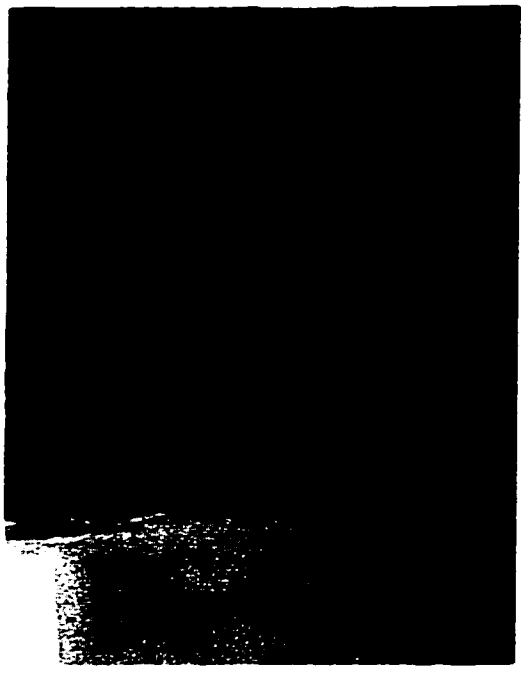

d) At 6% Drift Close-up

Figure 5-23: Observed damage in column BG-6 at selected stages of loading

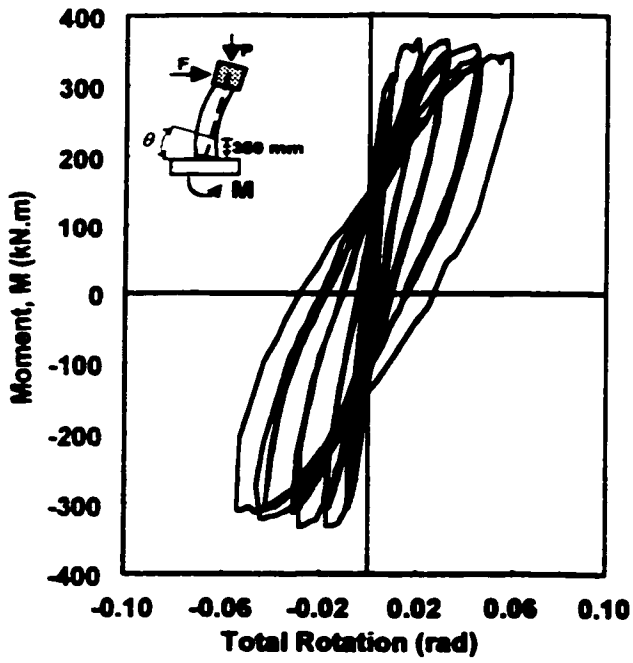

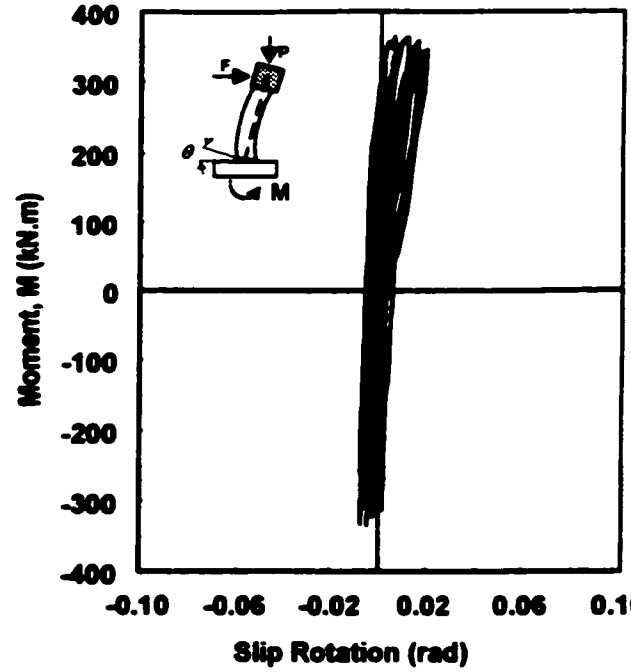

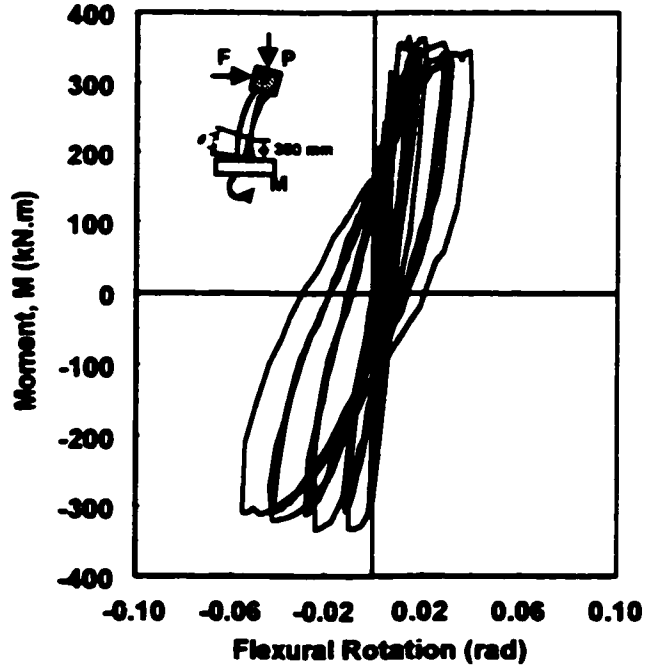

Figure 5-24: Moment-rotations relationships for column BG-6

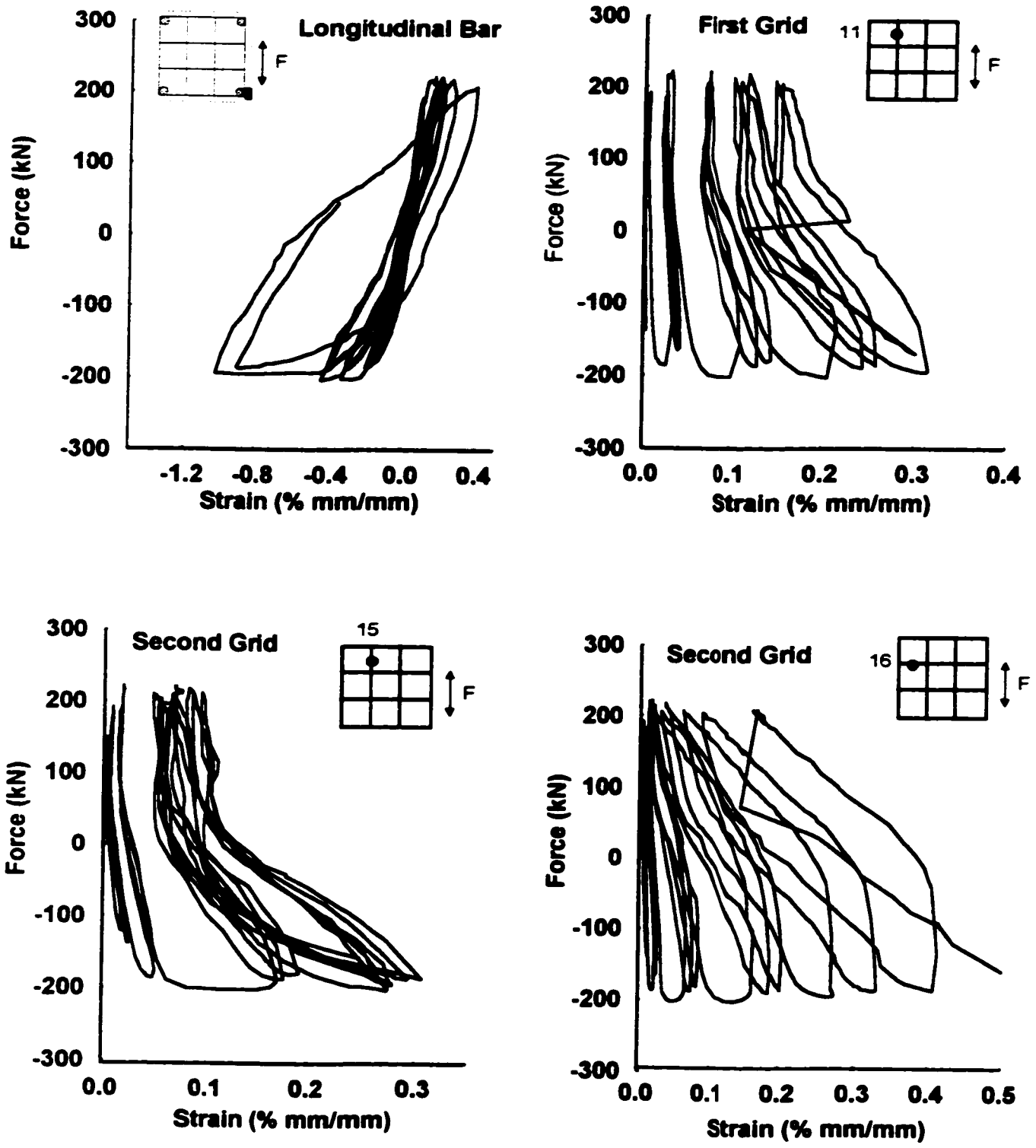

Figure 5-25: Reinforcement strain readings in Column BG-6

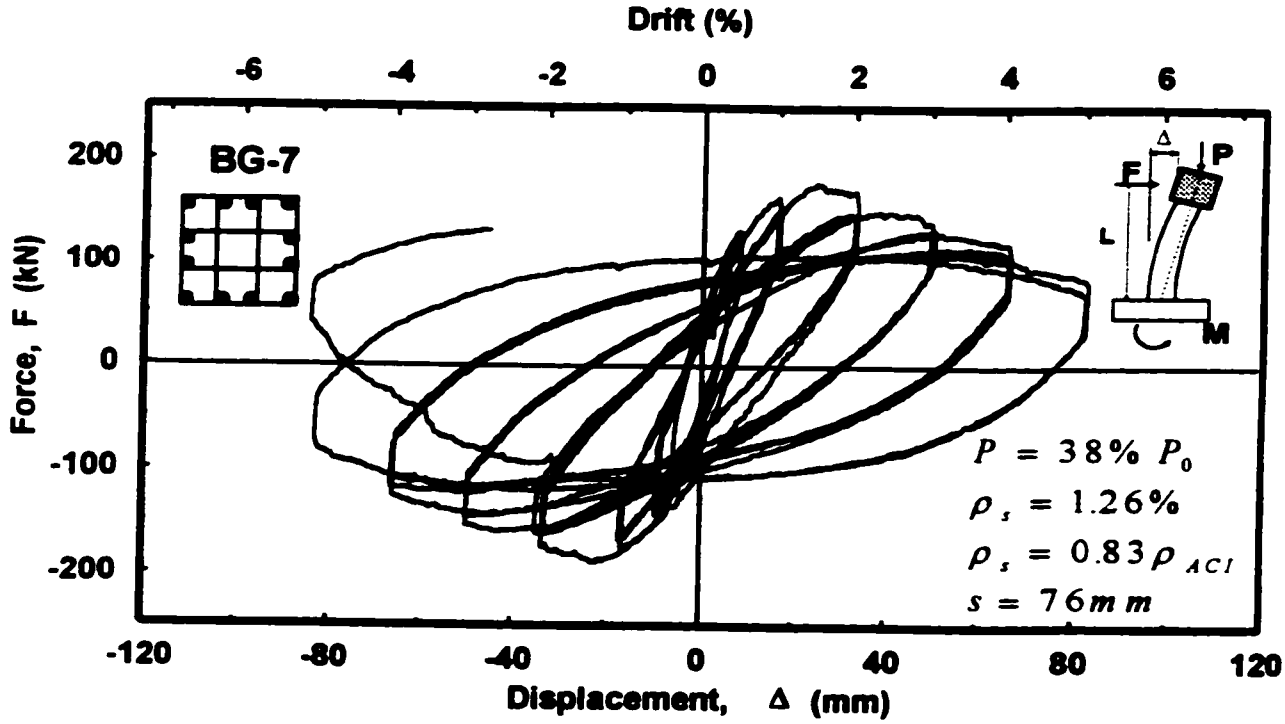

a) Hysteretic force-displacement relationship

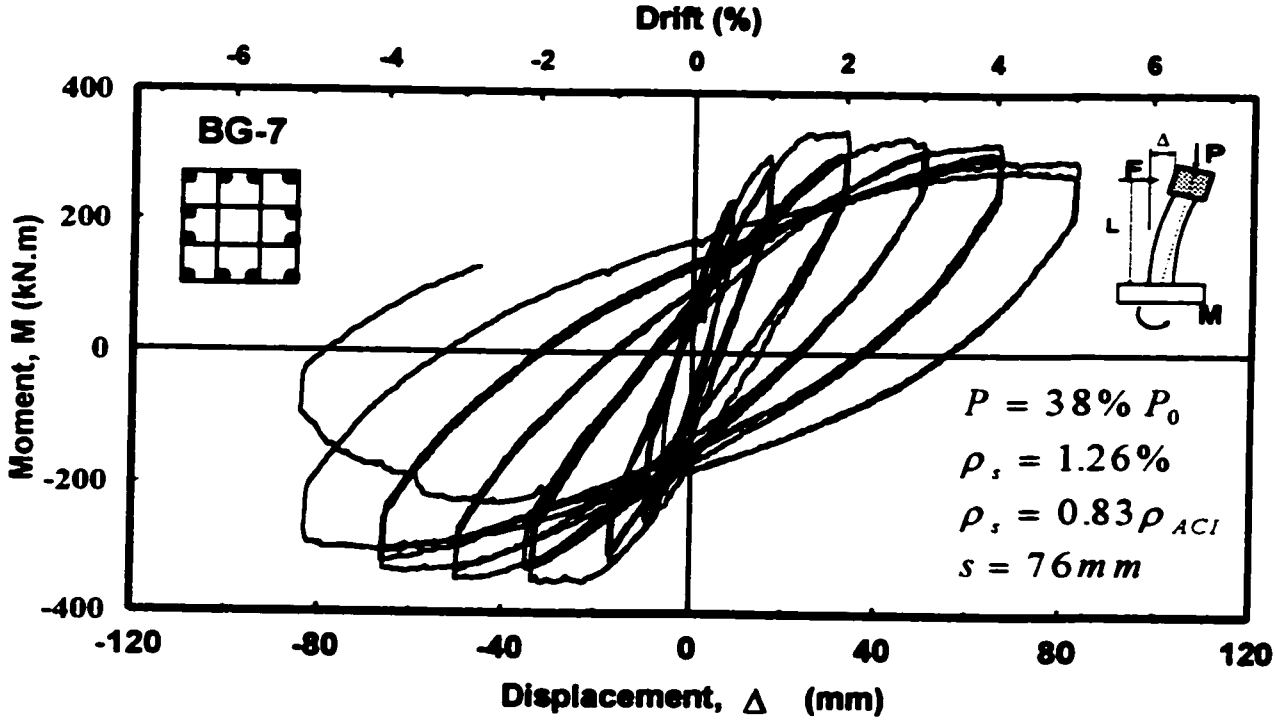

b) Hysteretic moment-displacement relationship

Figure 5-26: Hysteretic behavior of column BG-7

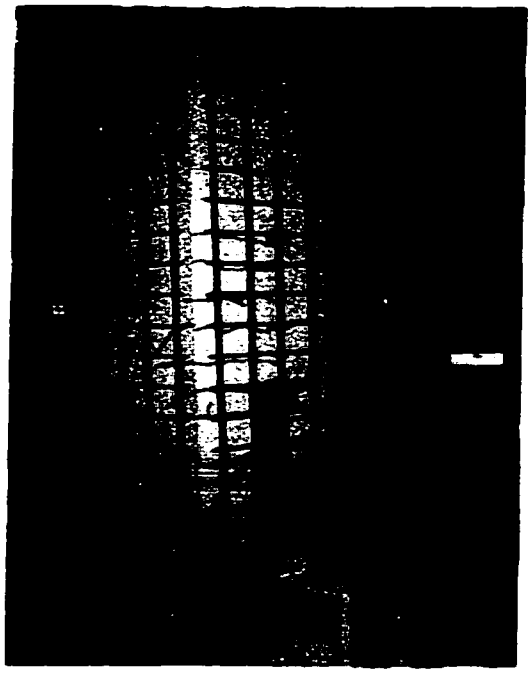

a) At 2% Drift

b) At 3% Drift

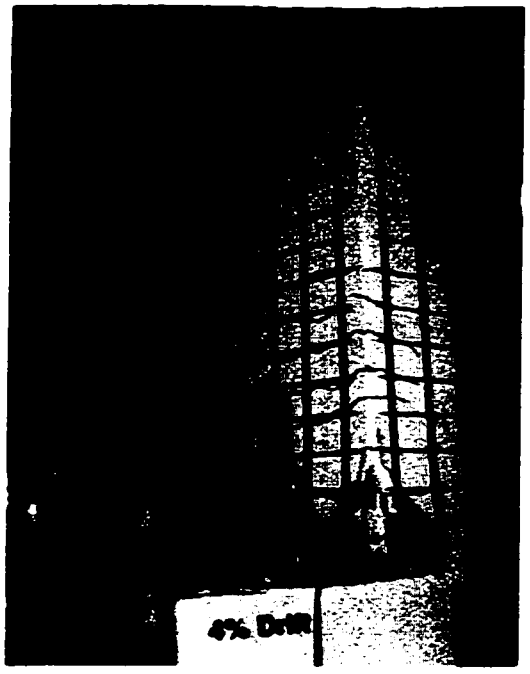

c) At 4% Drift

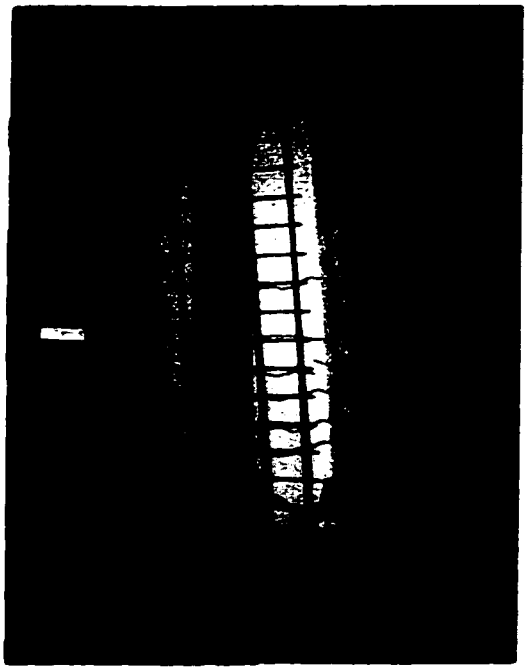

d) At 5% Drift Close-up

Figure 5-27: Observed damage in column BG-7 at selected stages of loading

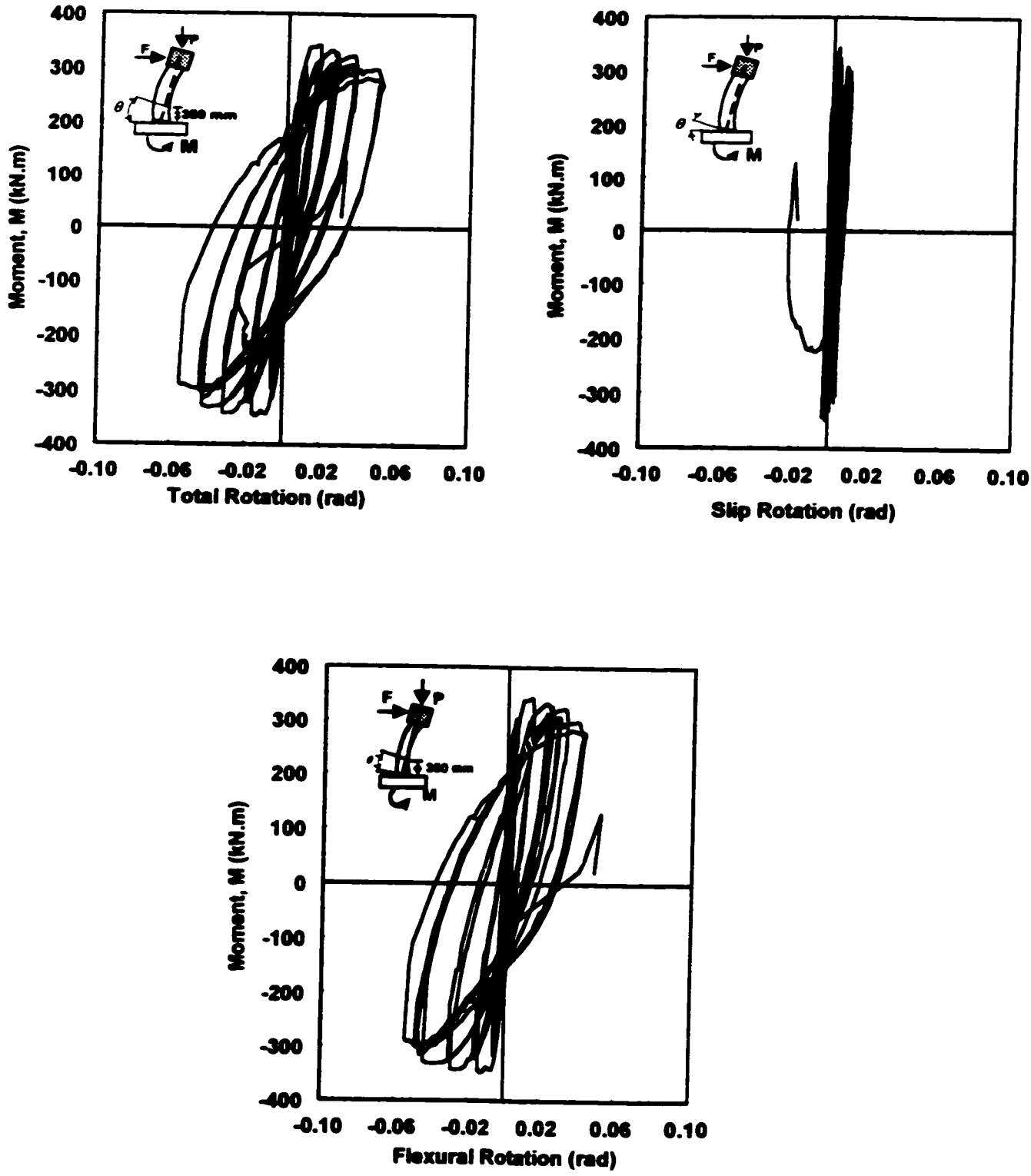

Figure 5-28: Moment-rotations relationships for column BG-7

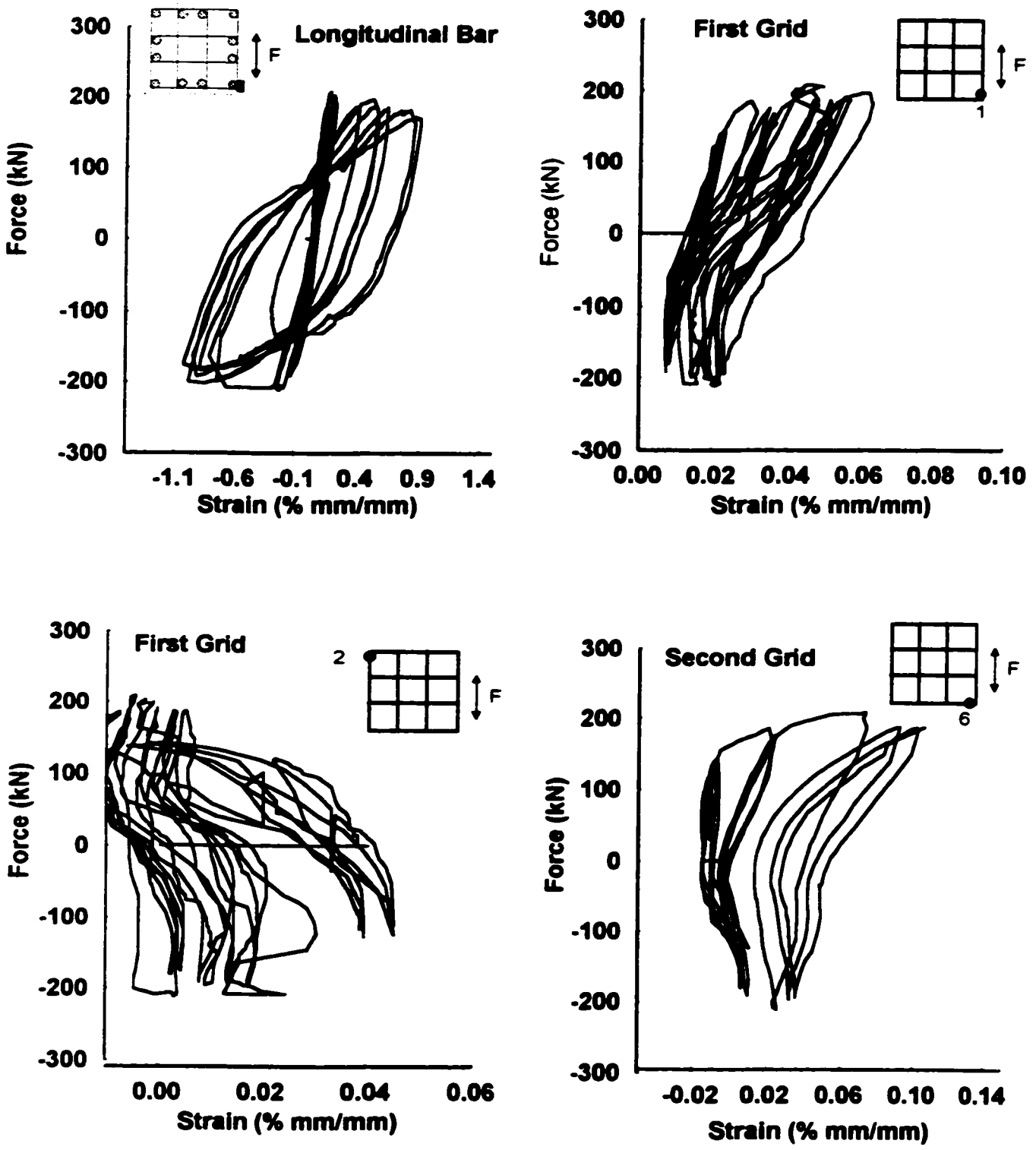

Figure 5-29: Reinforcement strain readings in Column BG-7

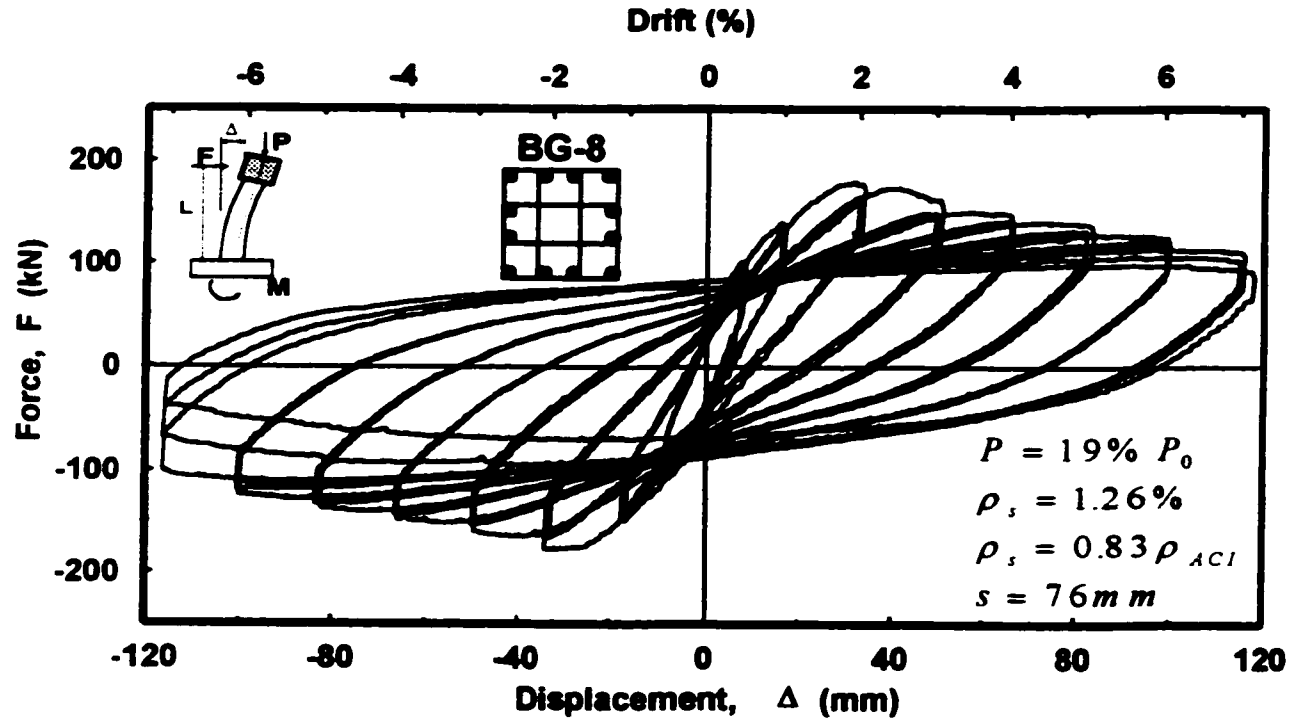

a) Hysteretic force-displacement relationship

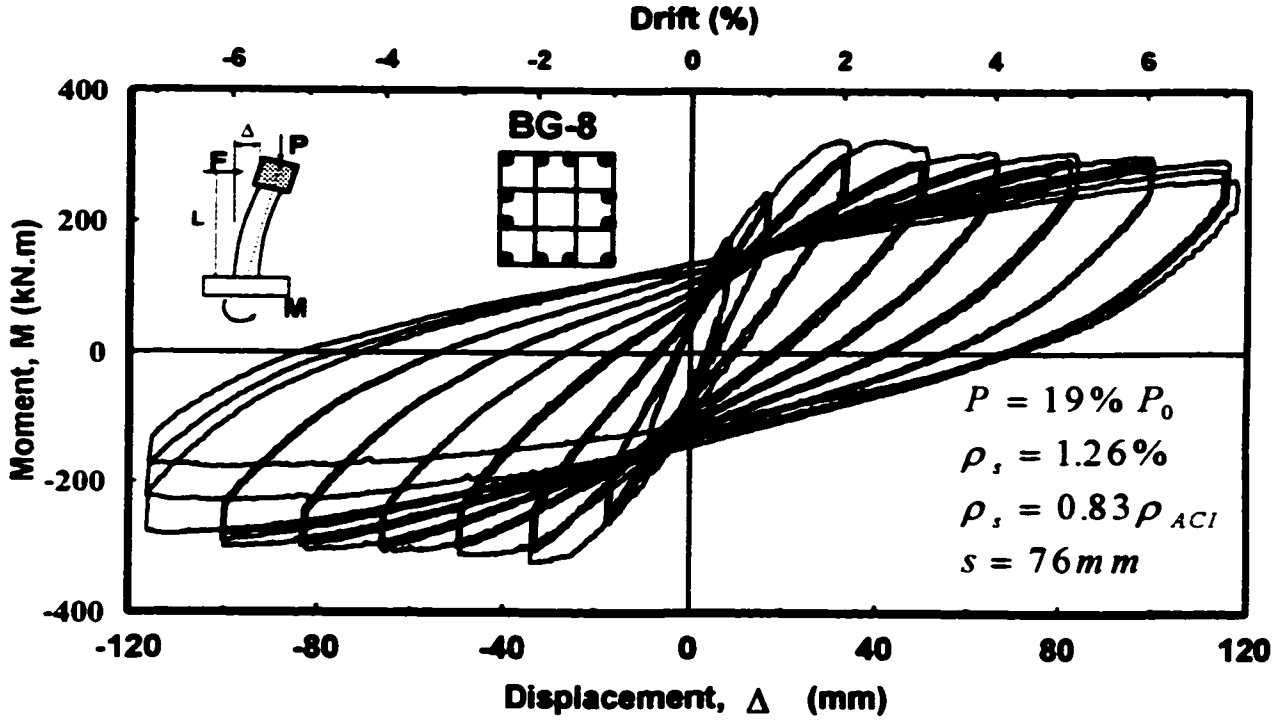

b) Hysteretic moment-displacement relationship

Figure 5-30: Hysteretic behavior of column BG-8

a) At 4% Drift

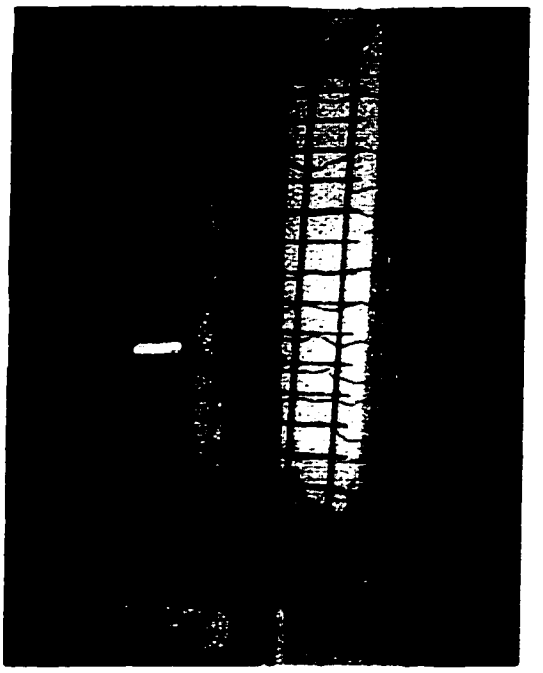

b) At 5% Drift

c) At 7% Drift

d) End of Test

Figure 5-31: Observed damage in column BG-8 at selected stages of loading

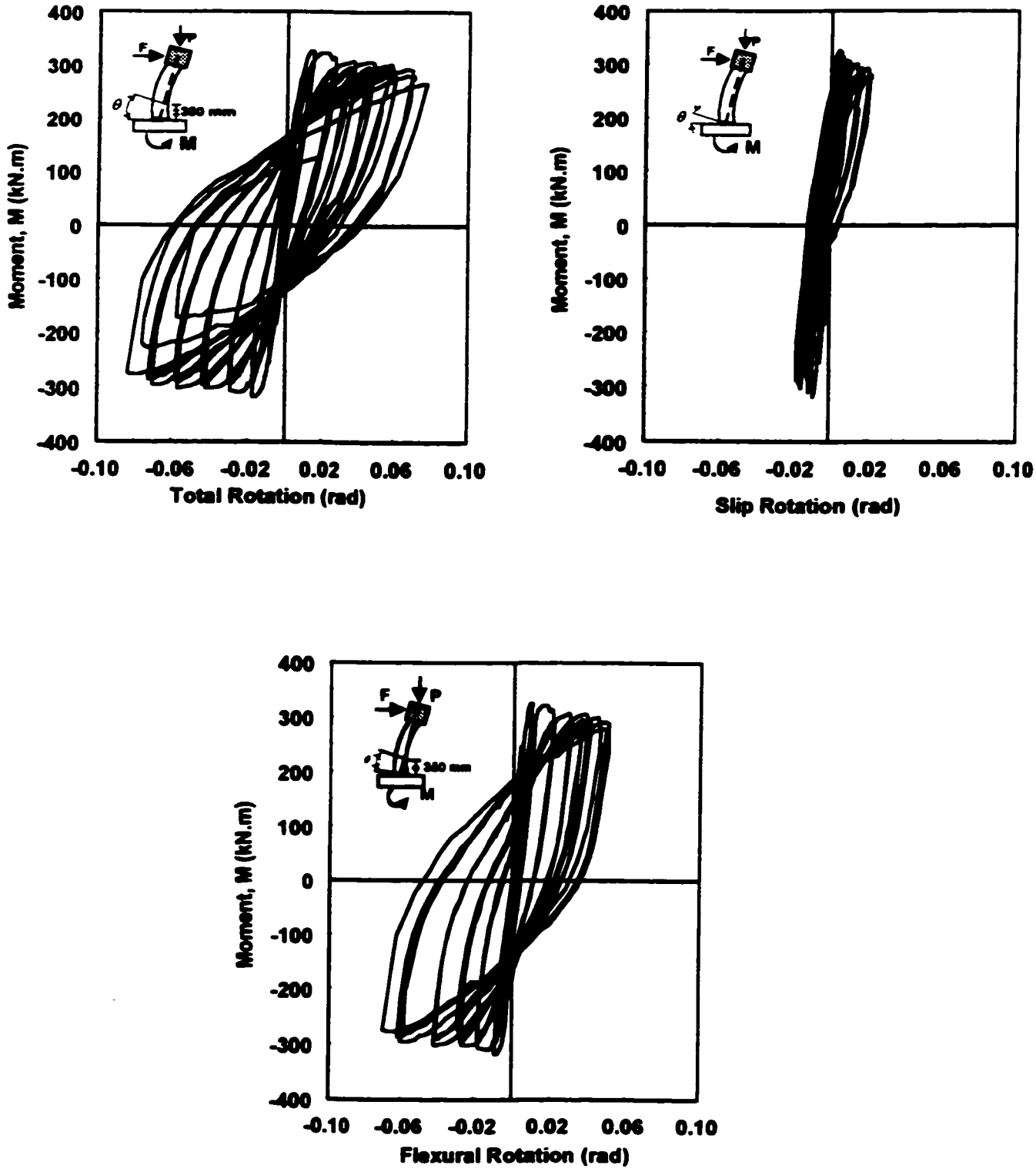

Figure 5-32: Moment-rotations relationships for column BG-8

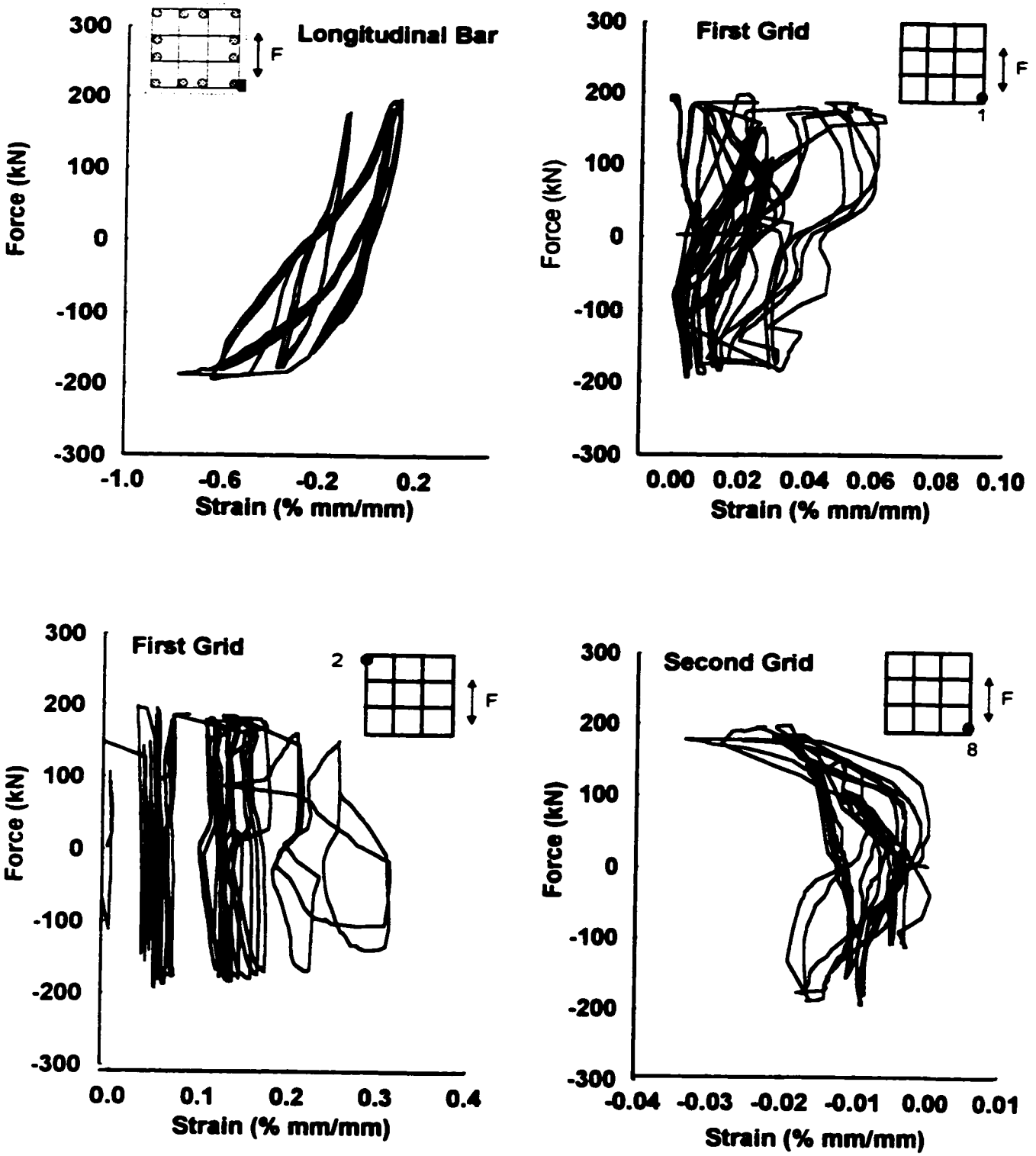

Figure 5-33: Reinforcement strain readings in Column BG-8

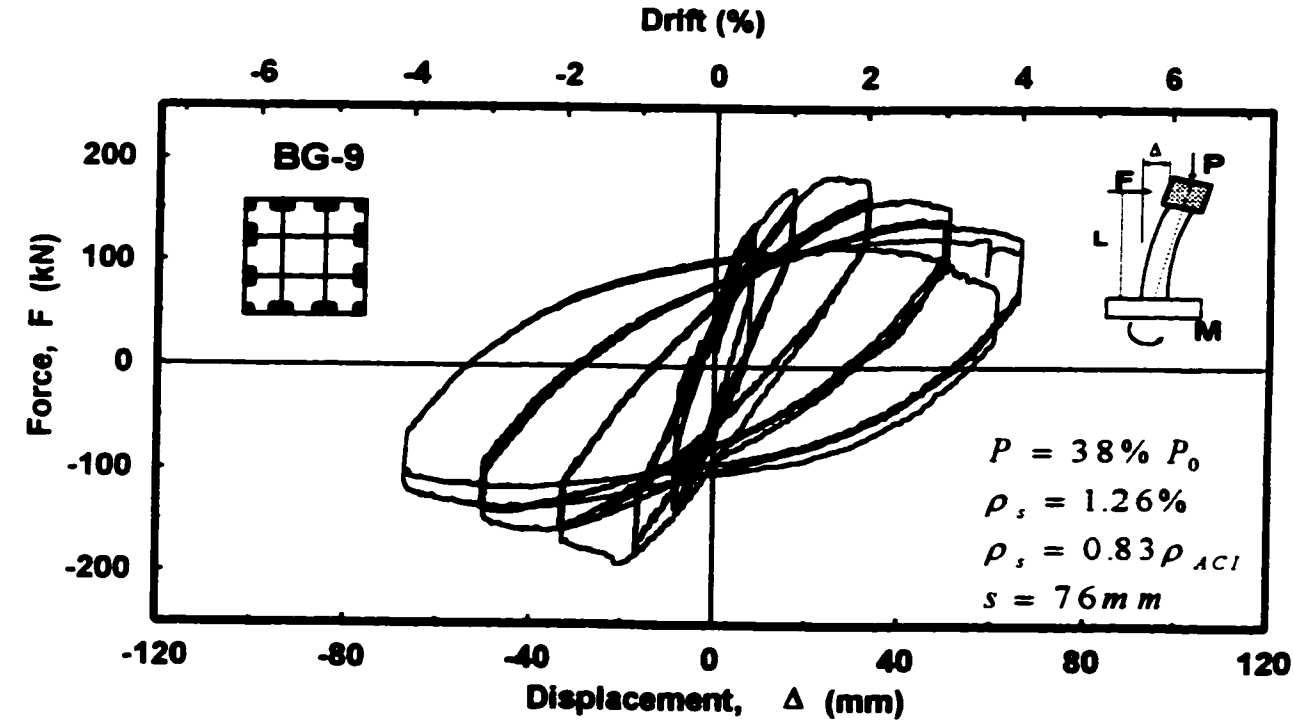

a) Hysteretic force-displacement relationship

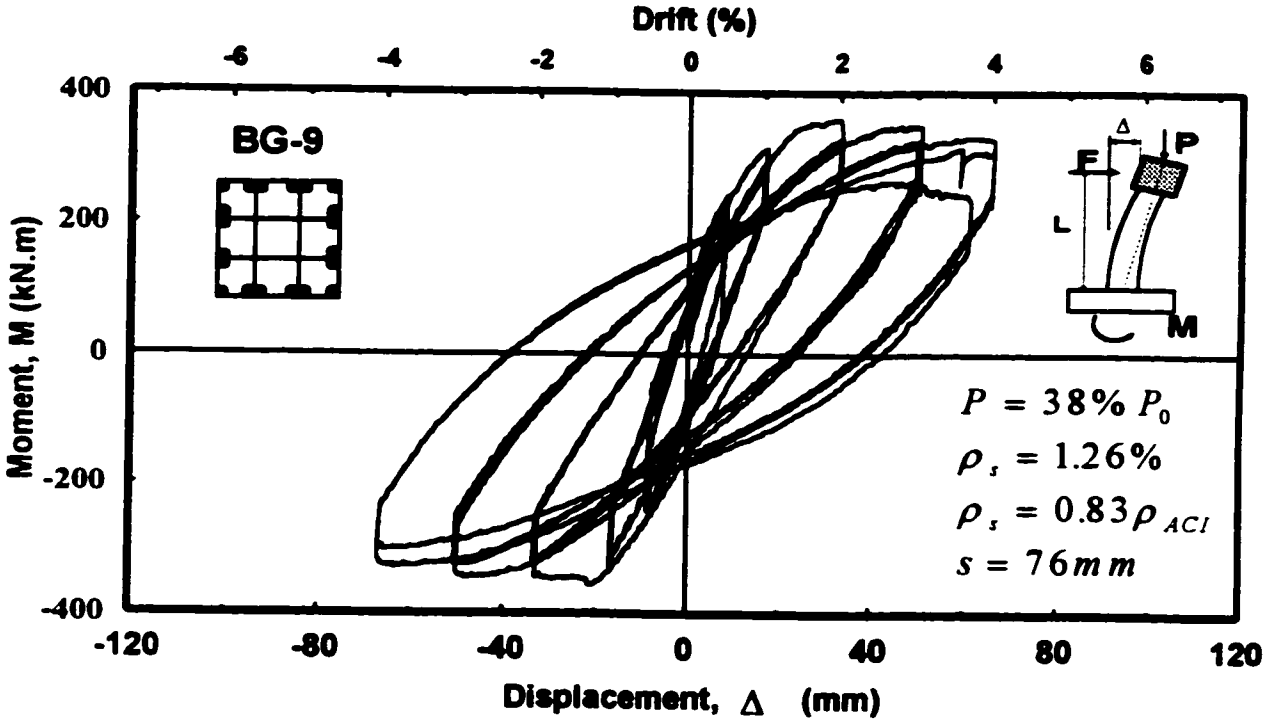

b) Hysteretic moment-displacement relationship

Figure 5-34: Hysteretic behavior of column BG-9

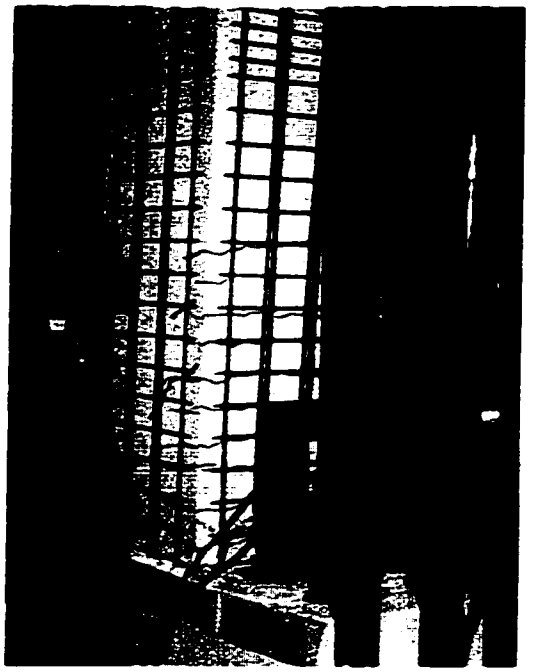

a) At 2% Drift

b) At 3% Drift

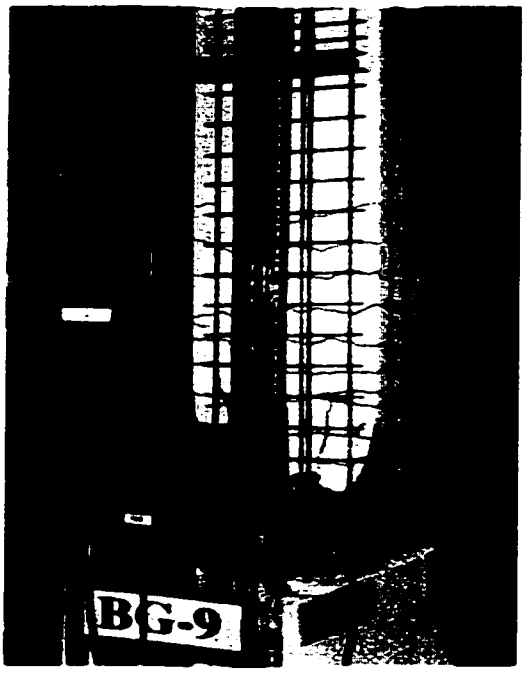

c) At 4% Drift

d) End of Test

Figure 5-35: Observed damage in column BG-9 at selected stages of loading

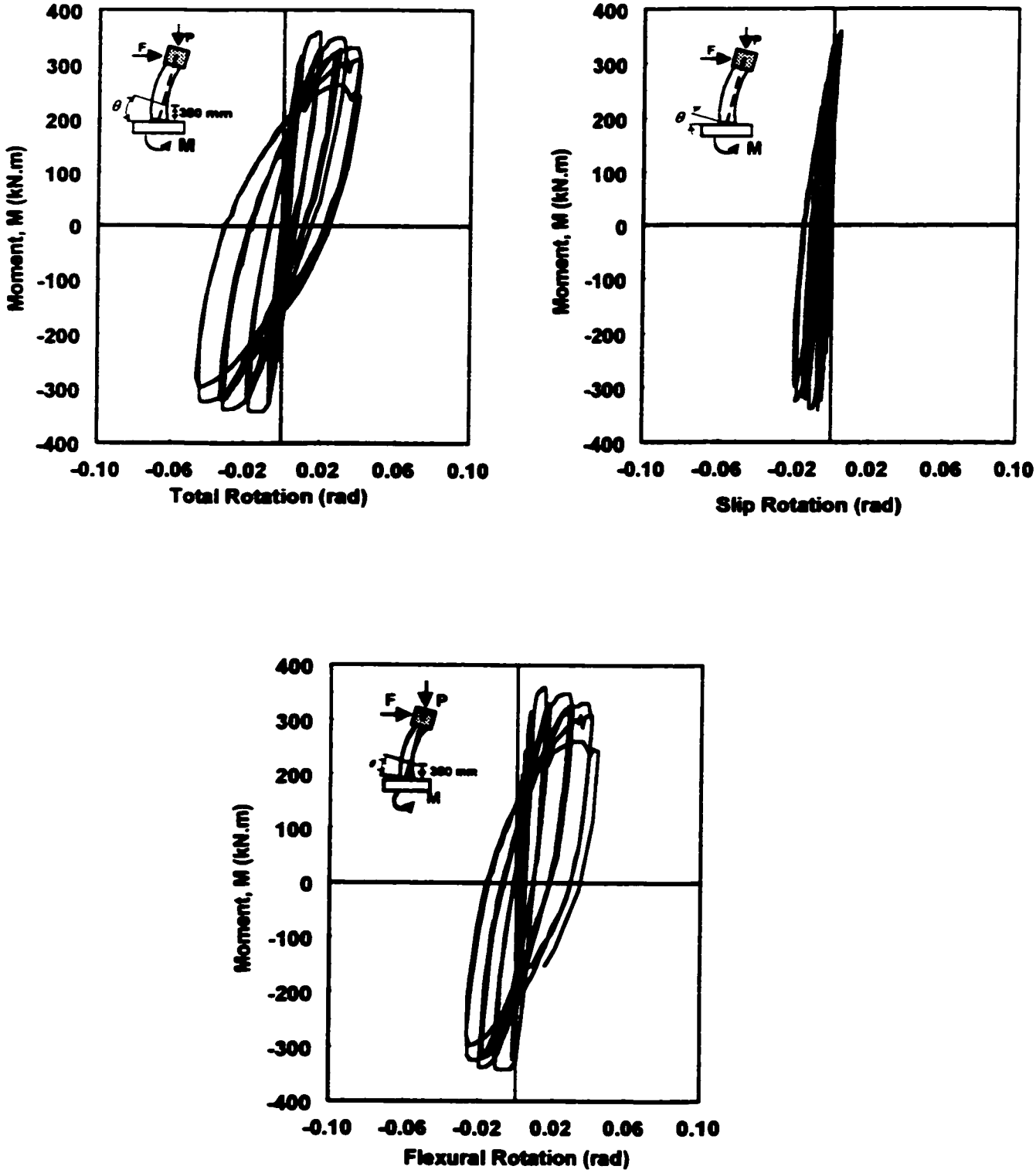

Figure 5-36: Moment-rotations relationships for column BG-9

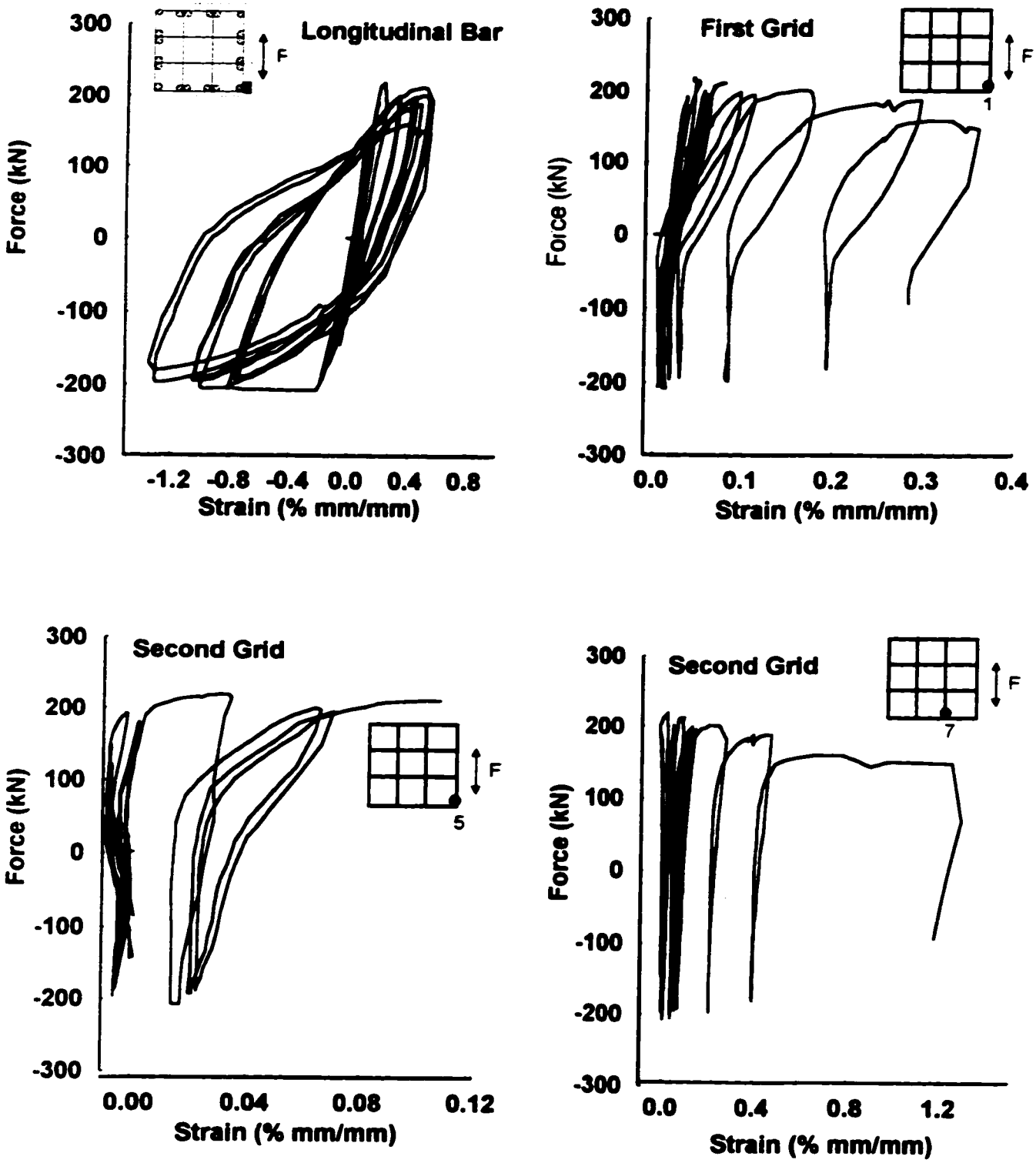

Figure 5-37: Reinforcement strain readings in Column BG-9

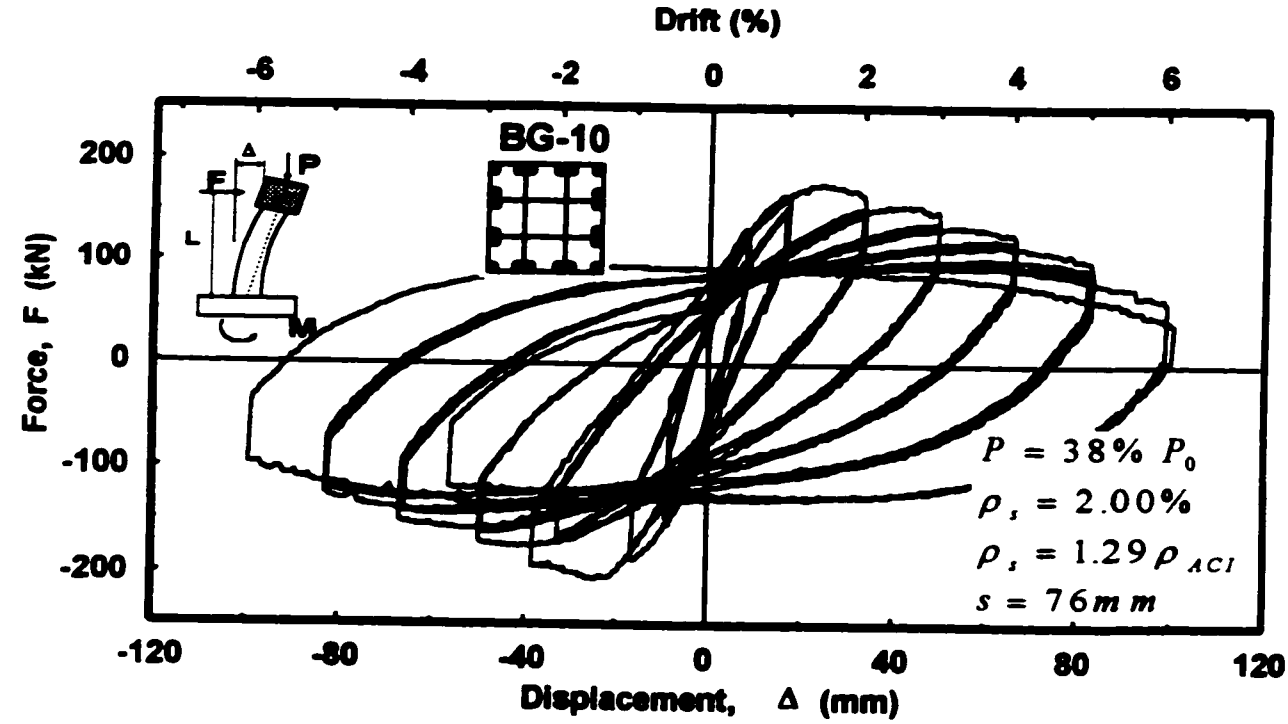

a) Hysteretic force-displacement relationship

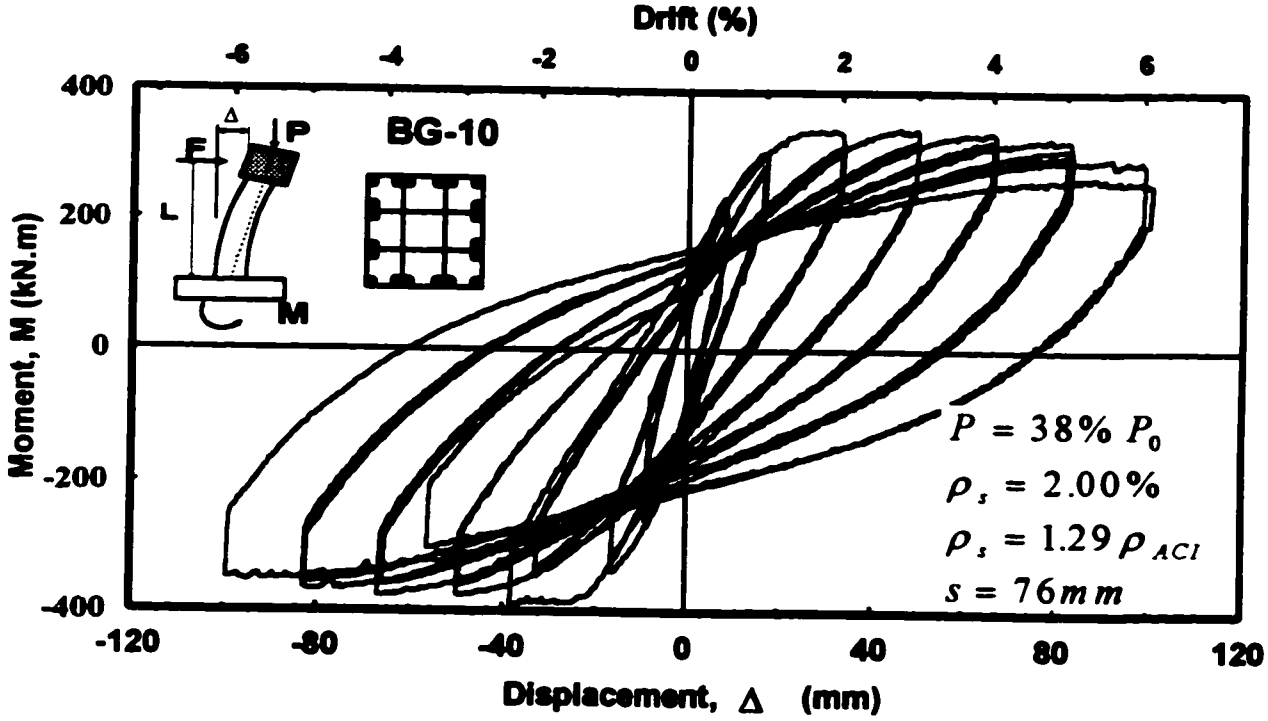

b) Hysteretic moment-displacement relationship

Figure 5-38: Hysteretic behavior of column BG-10

a) At 2% Drift

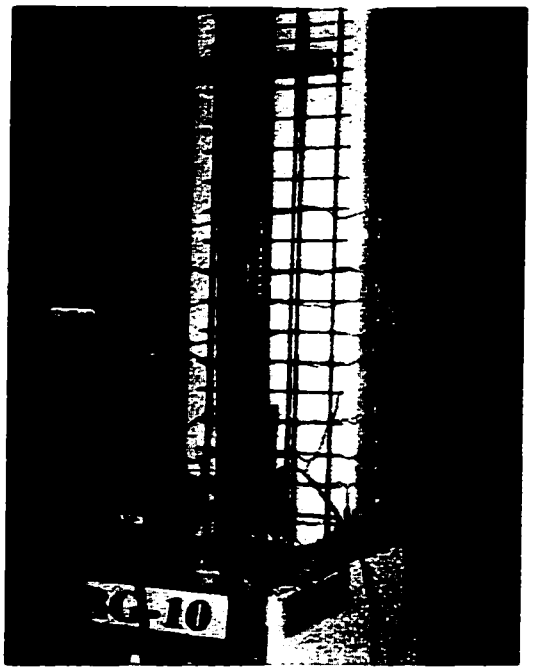

b) At 3% Drift

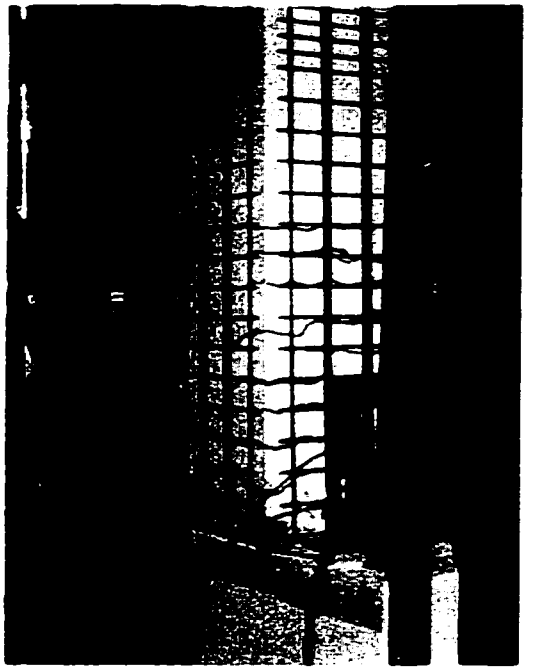

c) At 4% Drift

d) At 5% Drift

Figure 5-39: Observed damage in column BG-10 at selected stages of loading

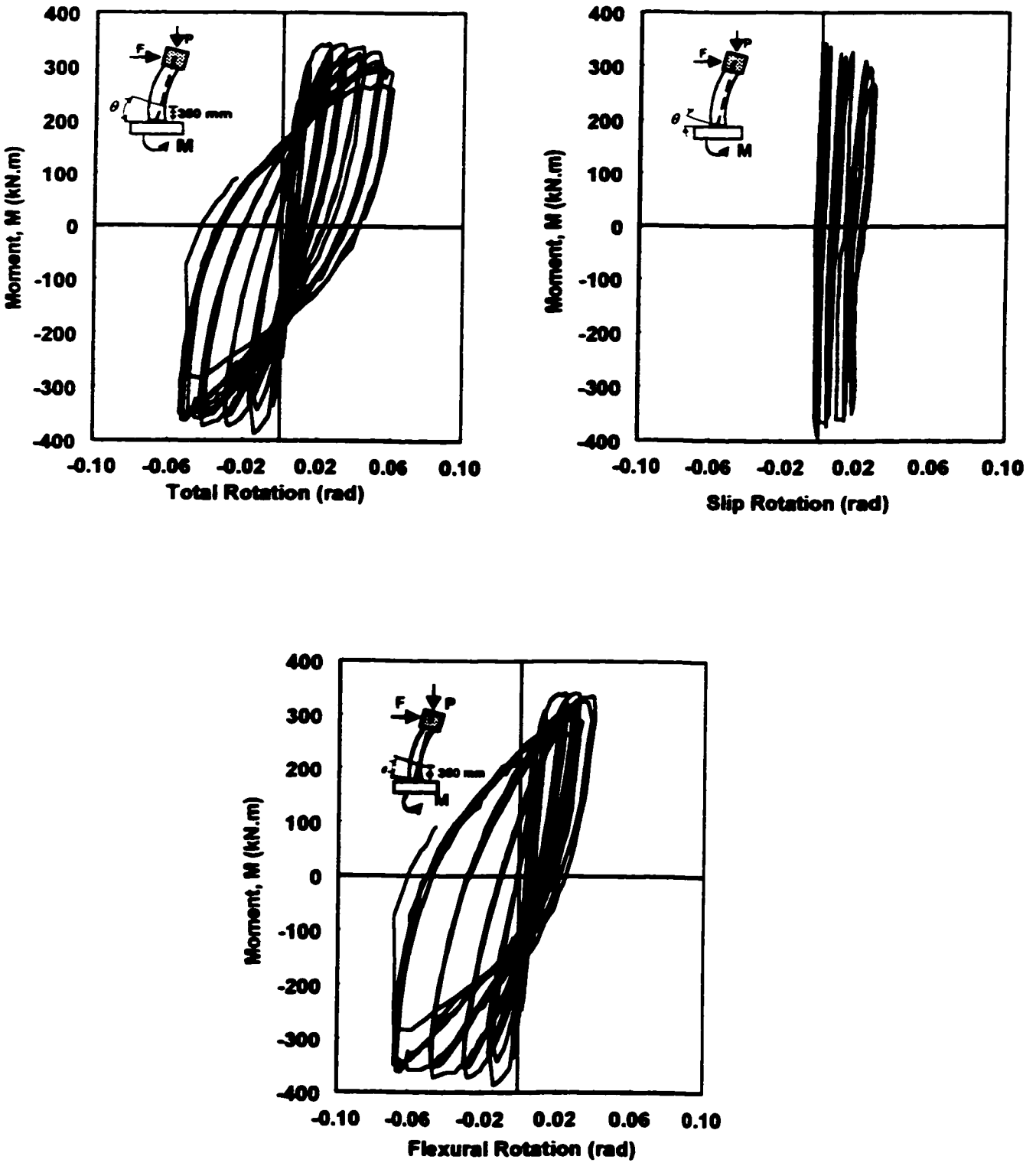

Figure 5-40: Moment-rotations relationships for column BG-10

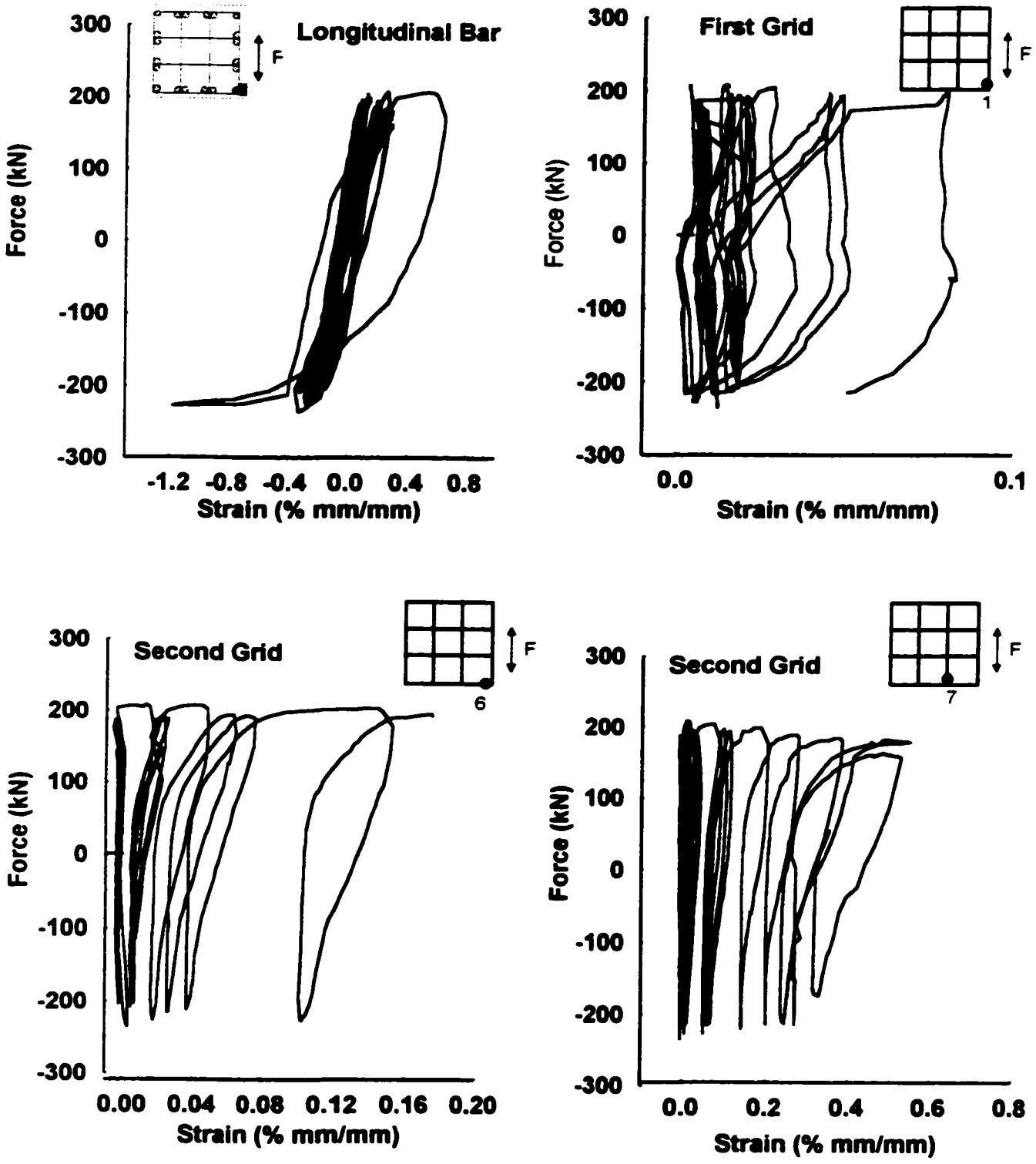

Figure 5-41: Reinforcement strain readings in Column BG-10

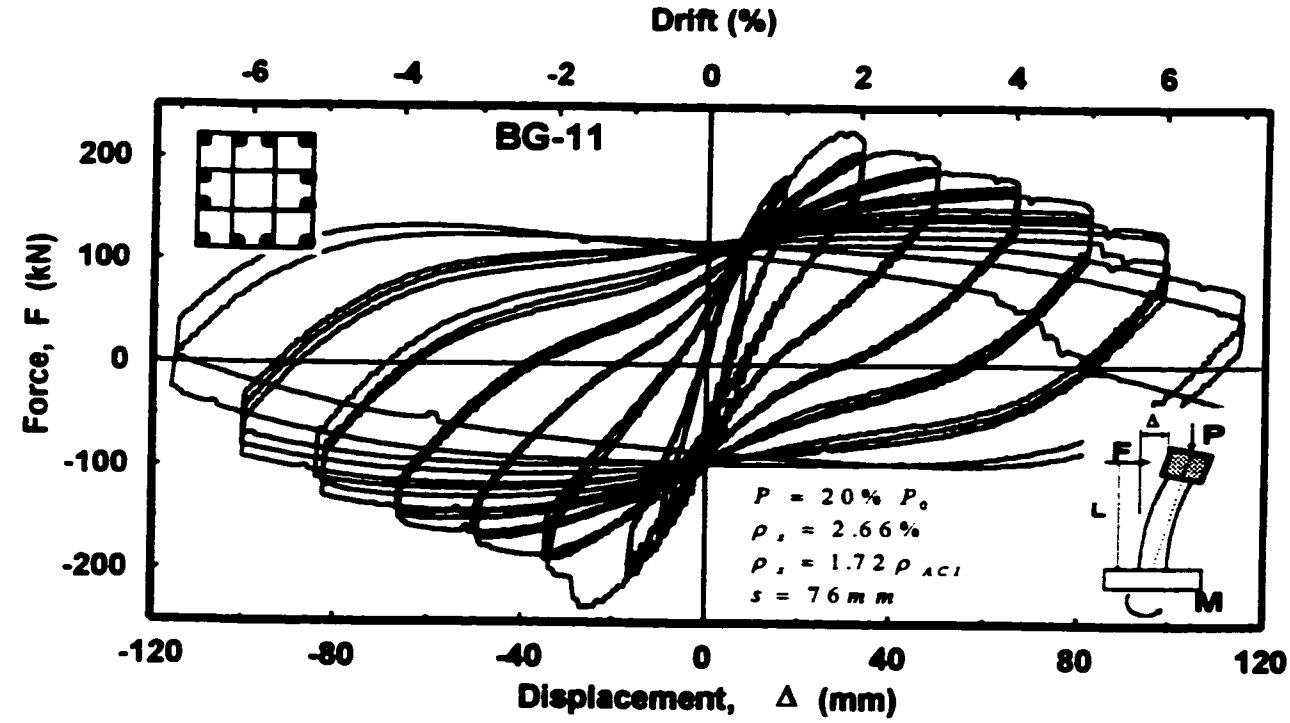

a) Hysteretic force-displacement relationship

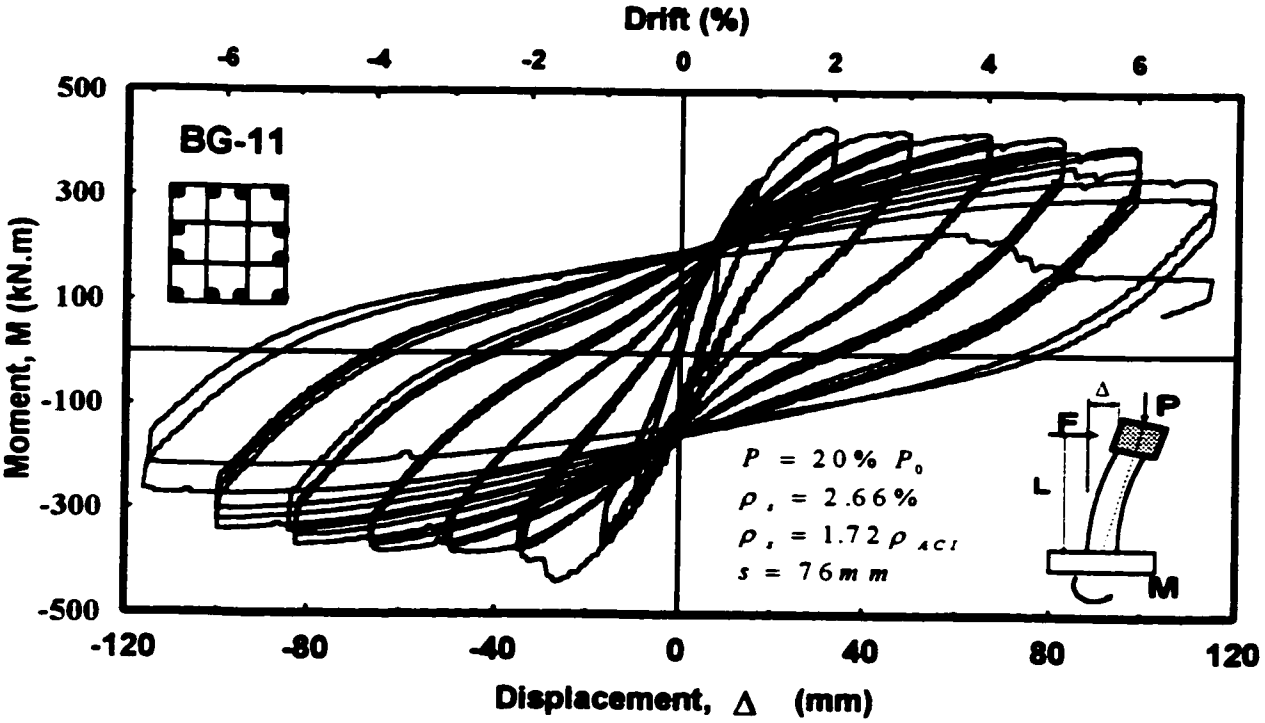

b) Hysteretic moment-displacement relationship

Figure 5-42: Hysteretic behavior of column BG-11

a) At 2% Drift

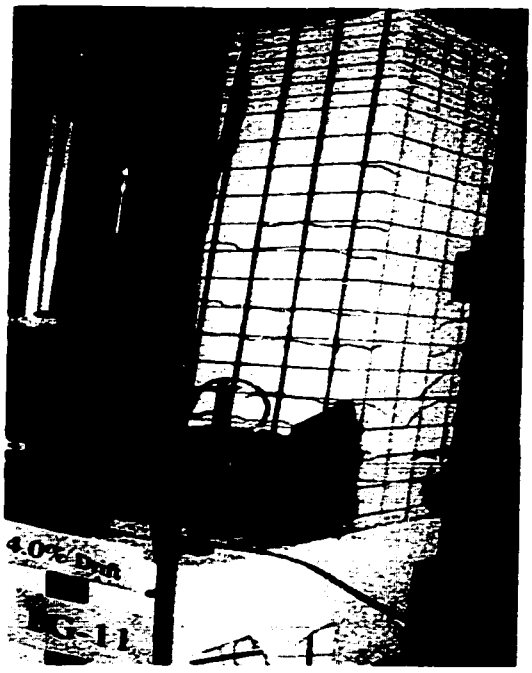

b) At 4% Drift

c) At 7% Drift

d) At End of Test

Figure 5-43: Observed damage in column BG-11 at selected stages of loading

d) Rupture of Longitudinal Steel in Tension

f) Buckling of Longitudinal Bars at the Compression Side

Figure 5-43: Cont.

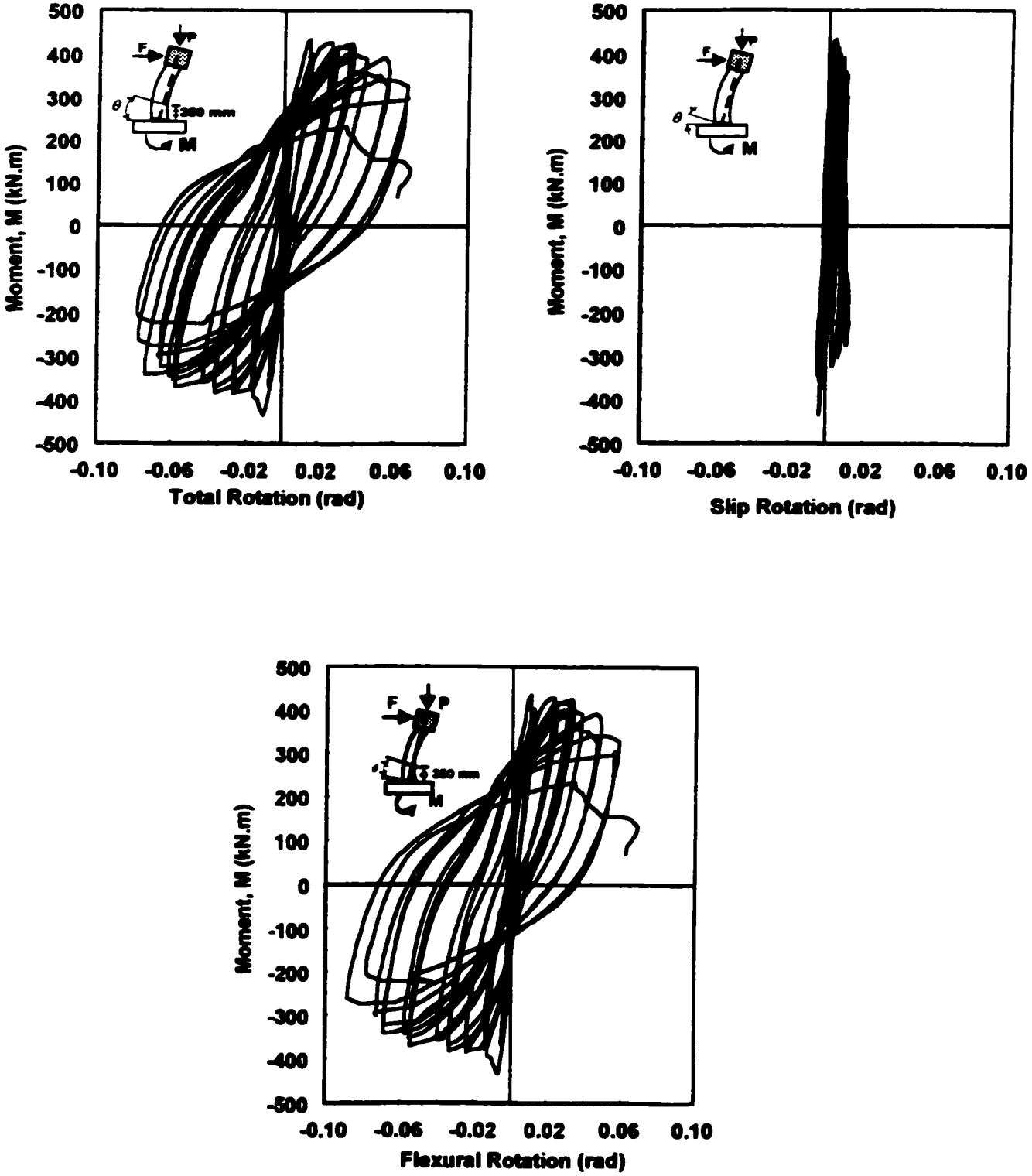

Figure 5-44: Moment-rotations relationships for column BG-11

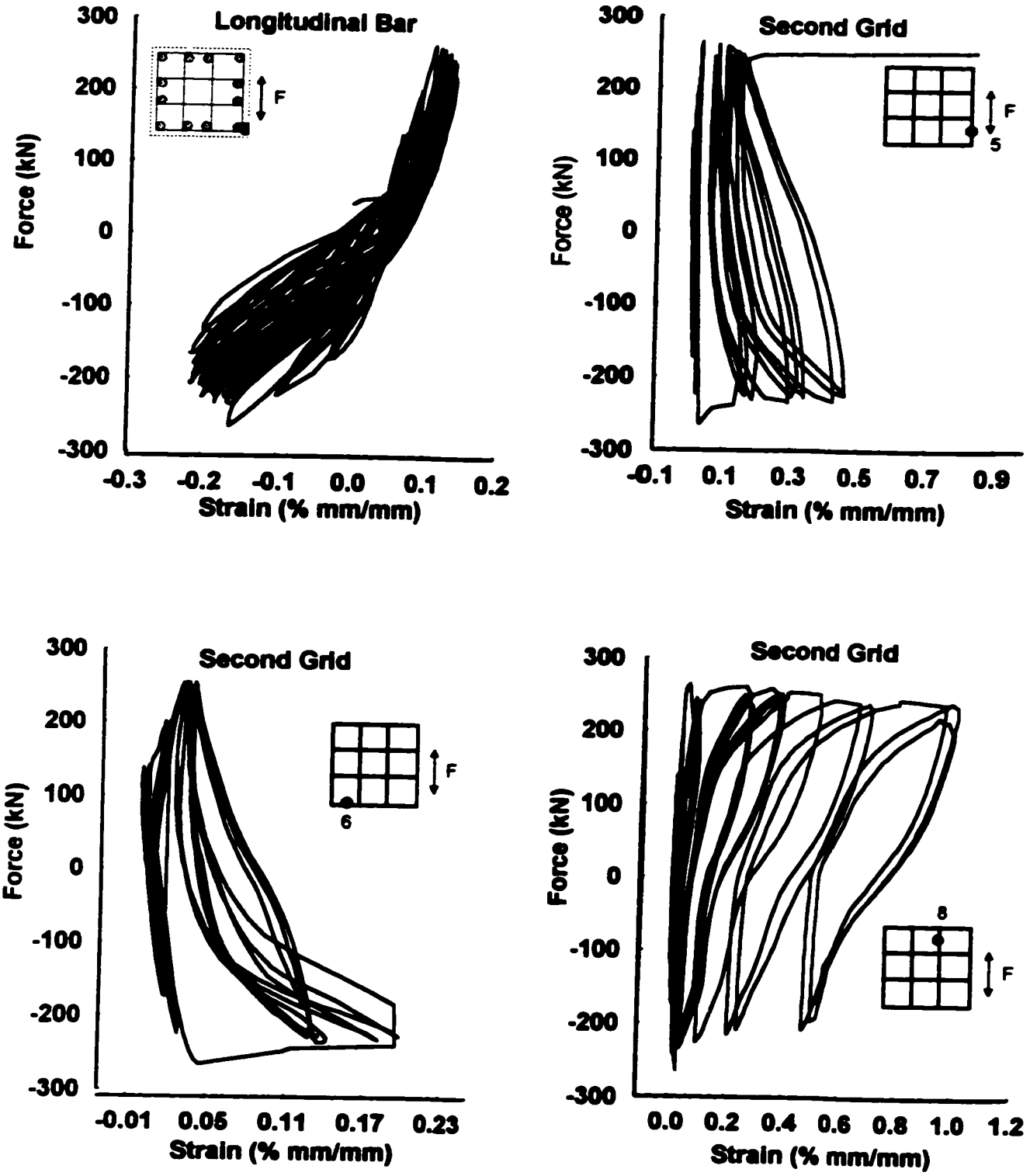

Figure 5-45: Reinforcement strain readings in Column BG-11

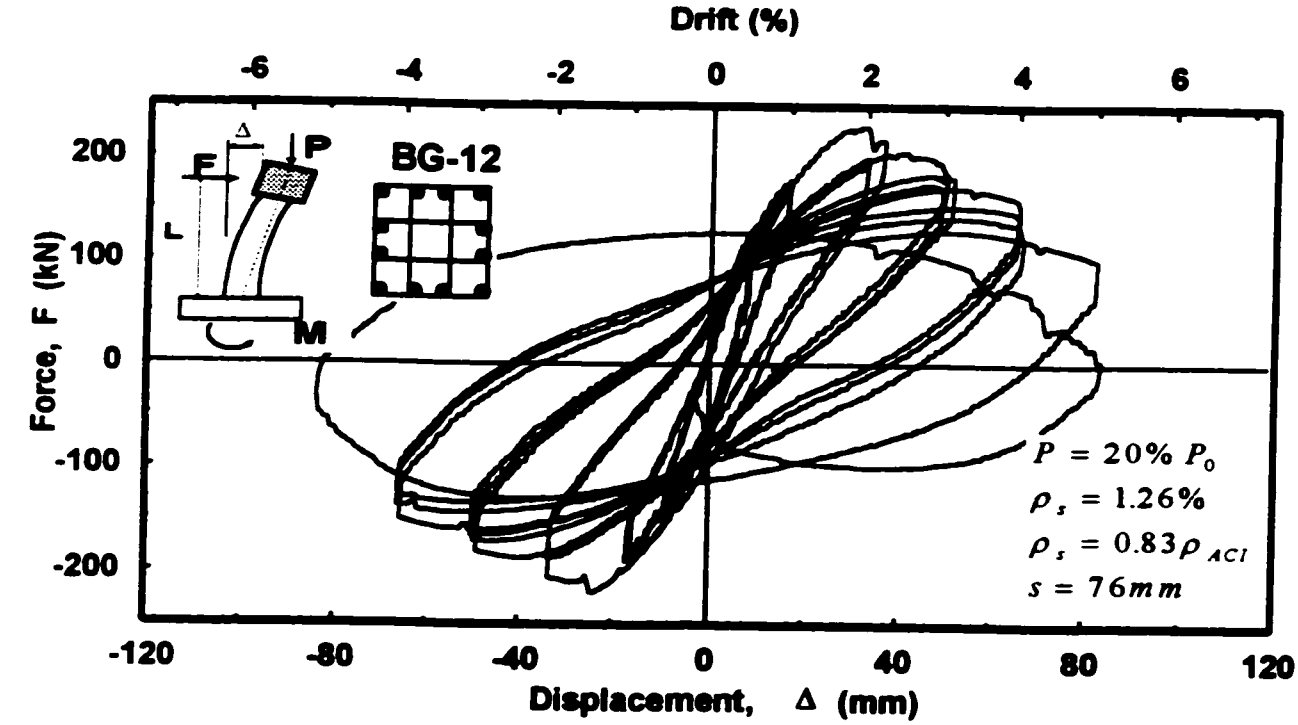

a) Hysteretic force-displacement relationship

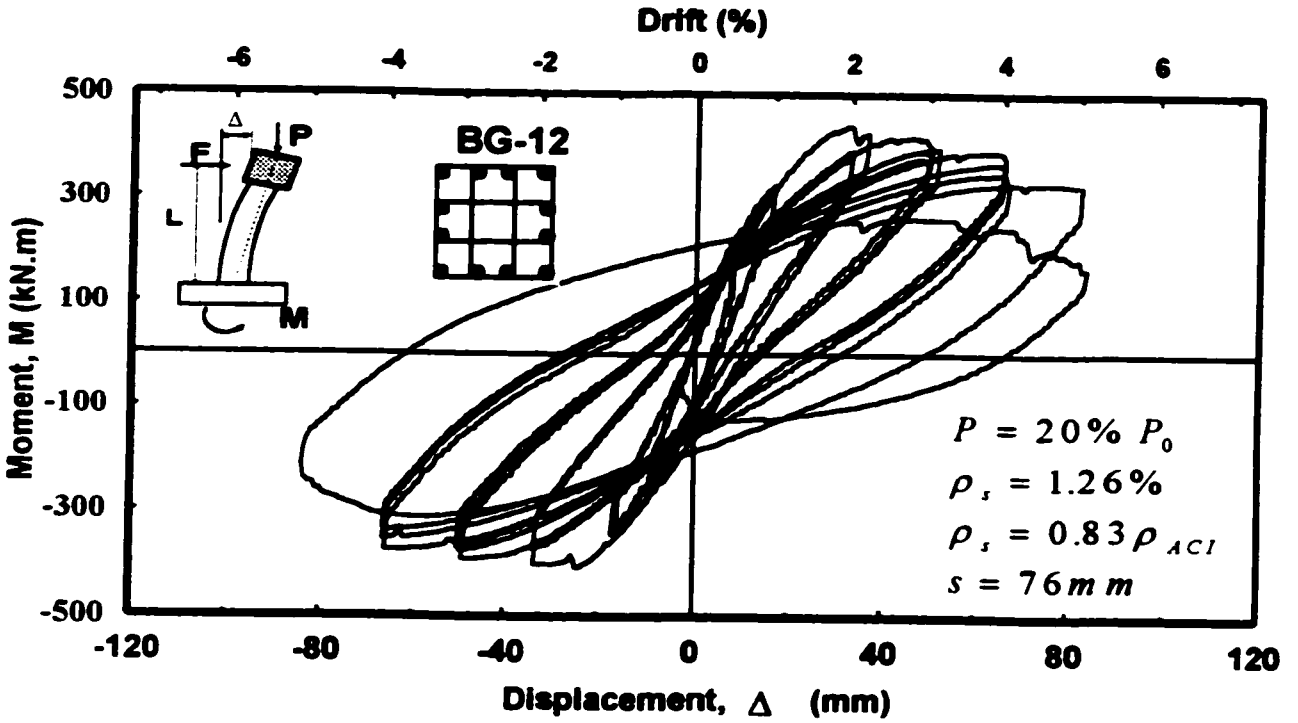

b) Hysteretic moment-displacement relationship

Figure 5-46: Hysteretic behavior of column BG-12

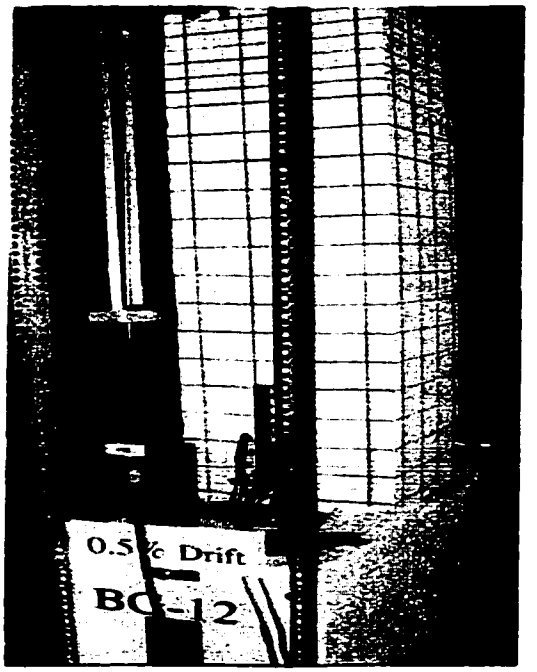

a) At 0.5% Drift

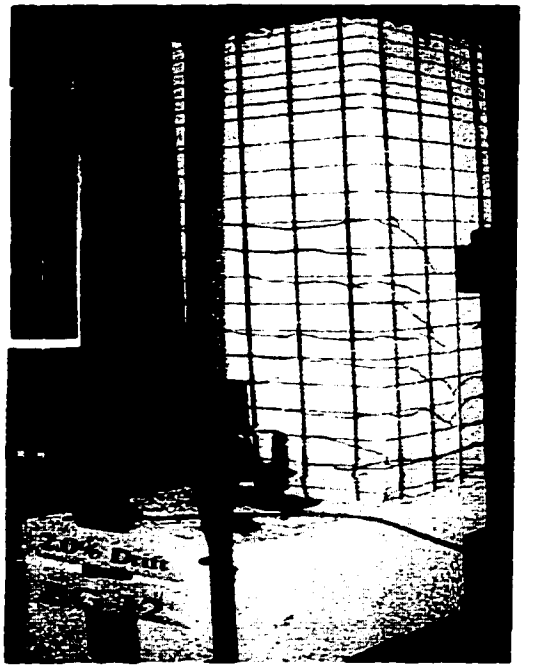

b) At 2% Drift

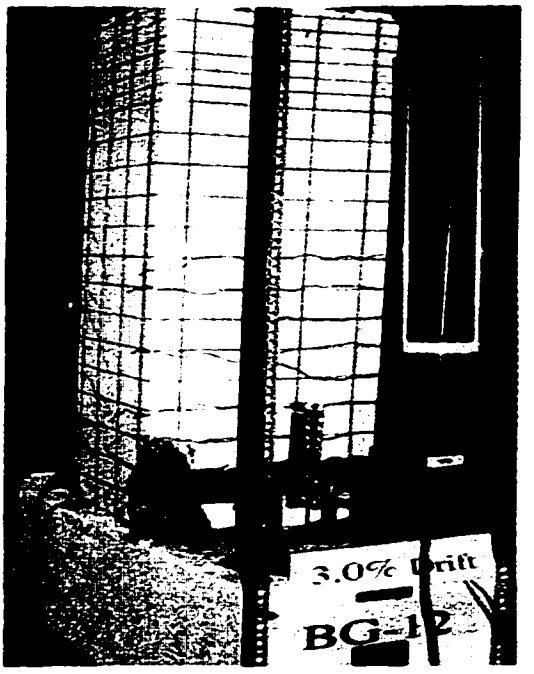

c) At 3% Drift

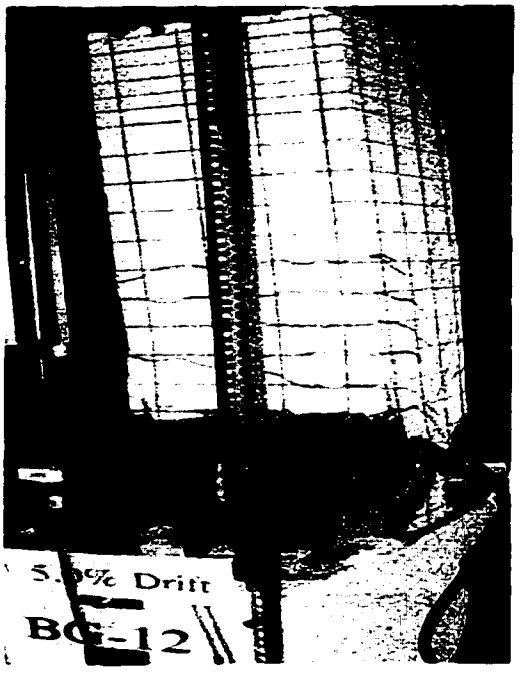

d) At 5% Drift

Figure 5-47: Observed damage in column BG-12 at selected stages of loading

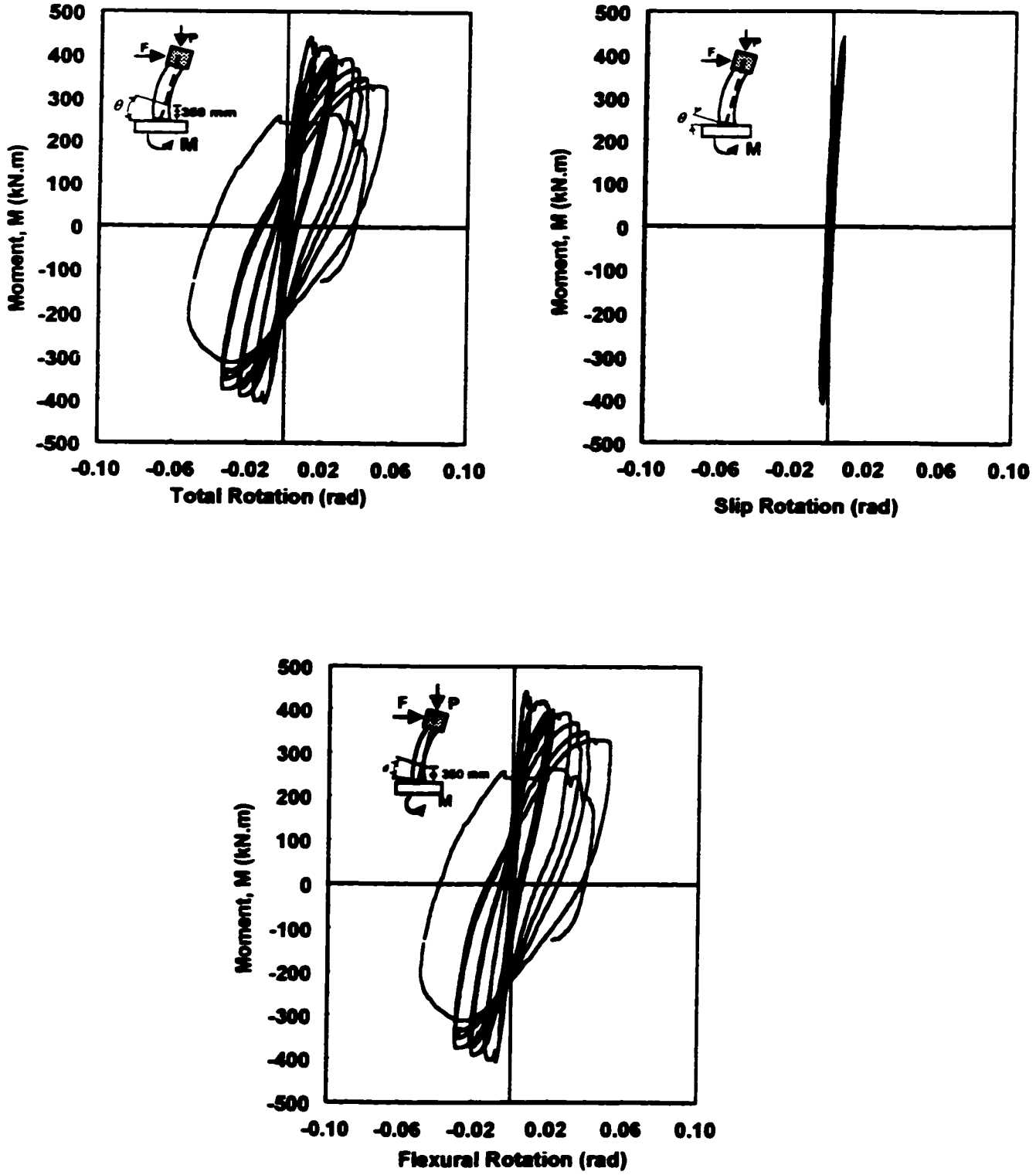

Figure 5-48: Moment-rotations relationships for column BG-12

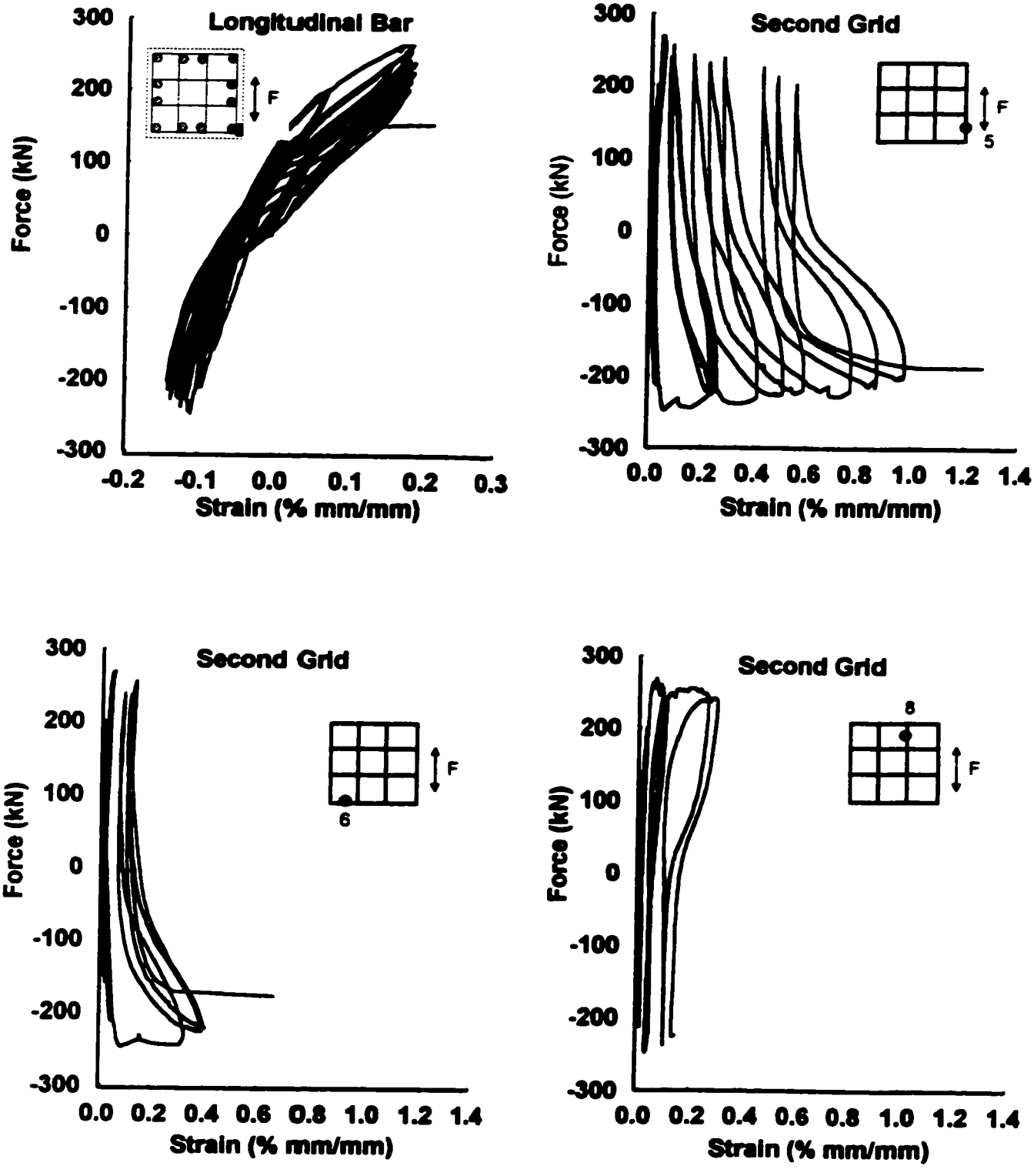

Figure 5-49: Reinforcement strain readings in Column BG-12

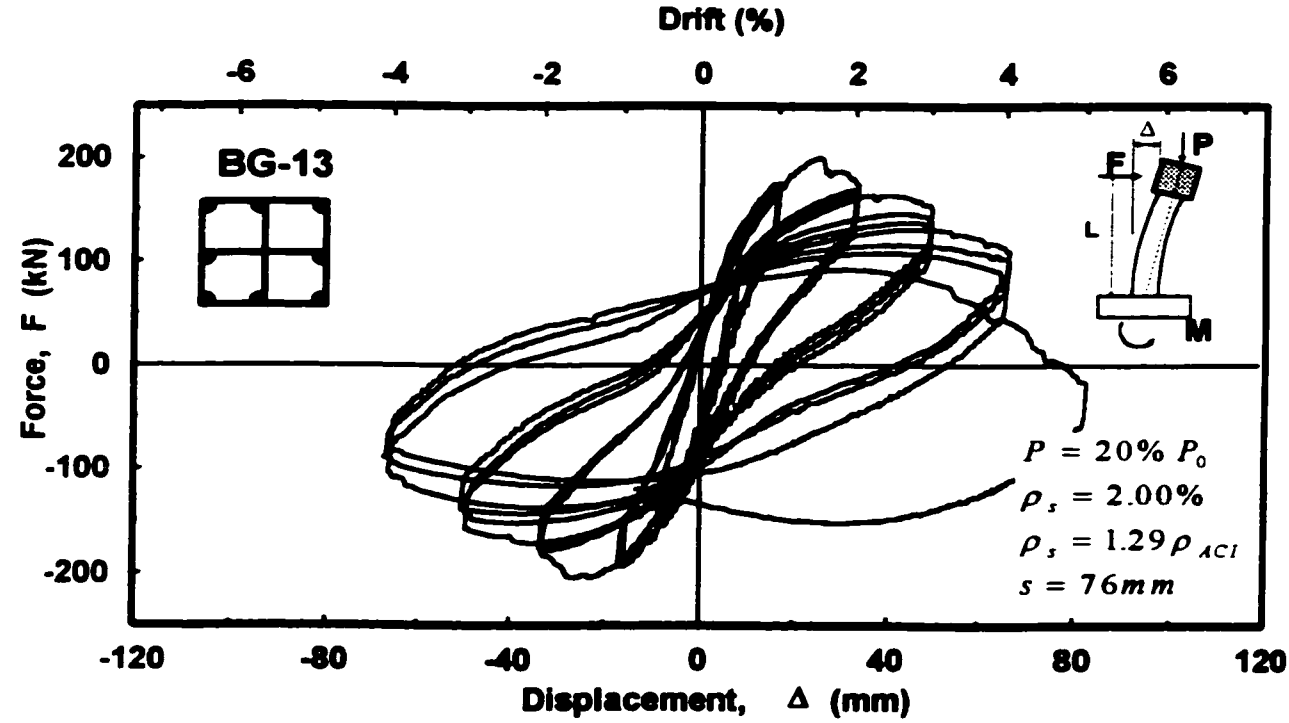

a) Hysteretic force-displacement relationship

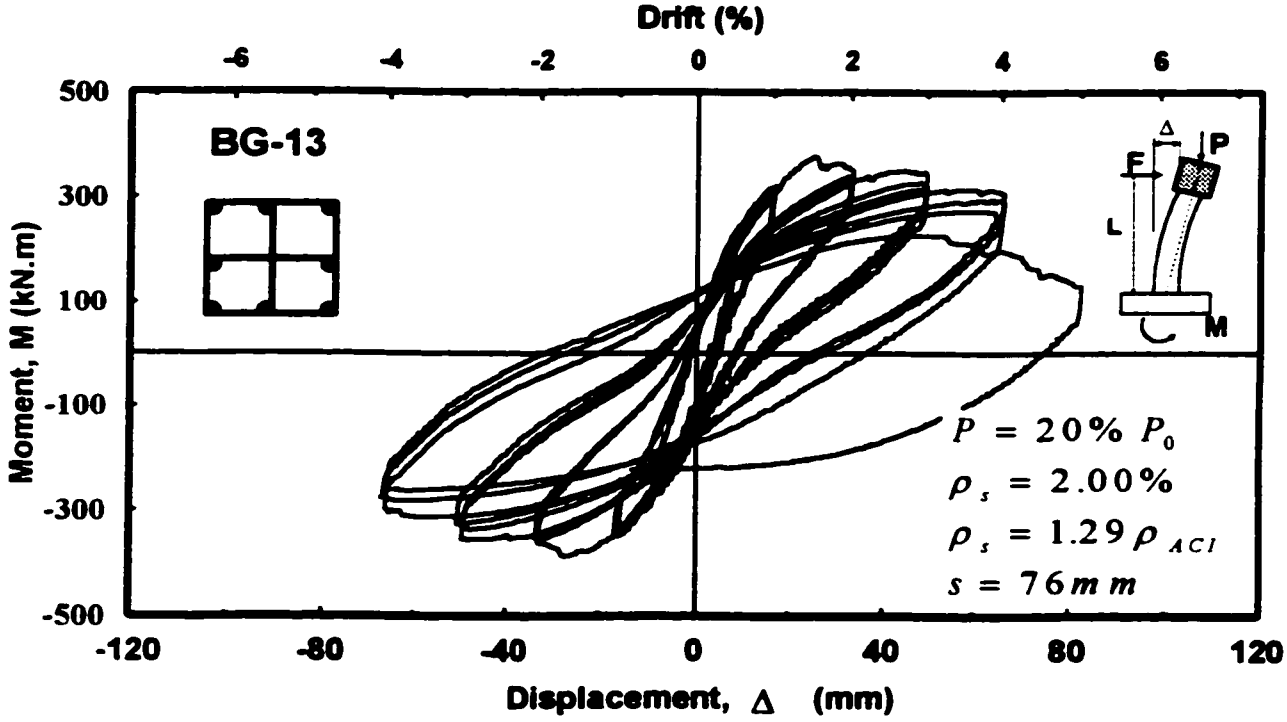

b) Hysteretic moment-displacement relationship

Figure 5-50: Hysteretic behavior of column BG-13

a) At 2% Drift

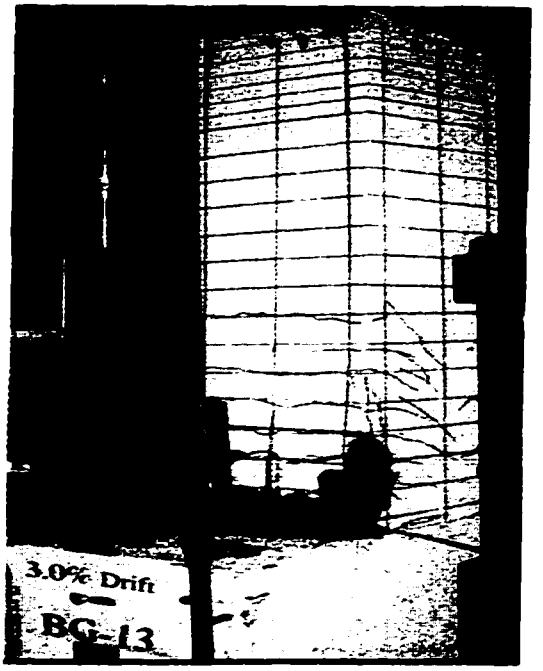

b) At 3% Drift

c) At 4% Drift

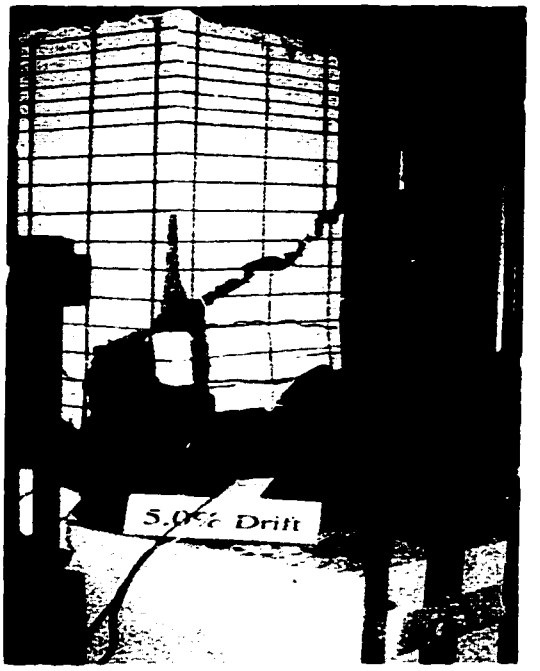

d) At 5% Drift

Figure 5-51: Observed damage in column BG-13 at selected stages of loading

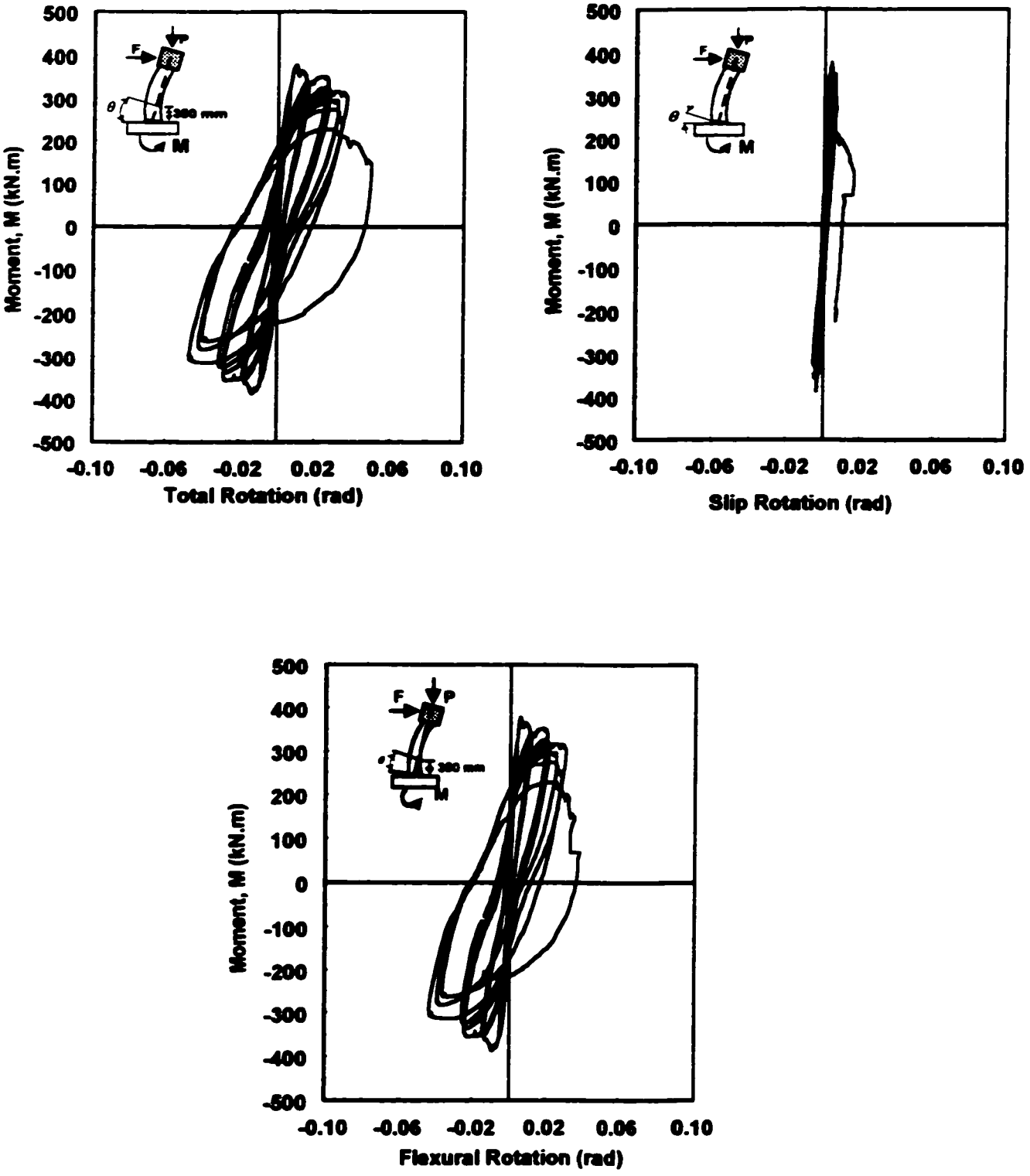

Figure 5-52: Moment-rotations relationships for column BG-13

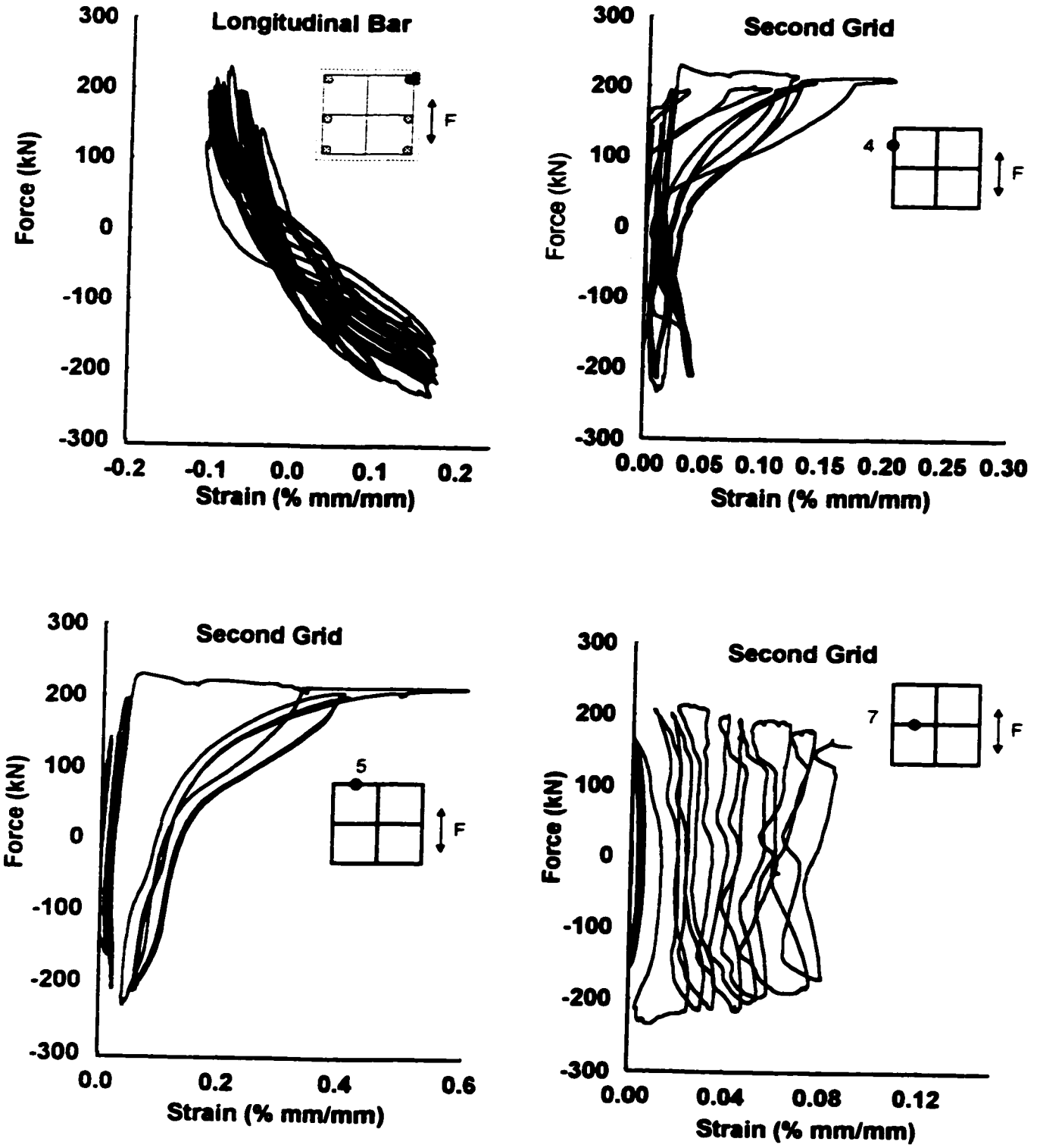

Figure 5-53: Reinforcement strain readings in Column BG-13

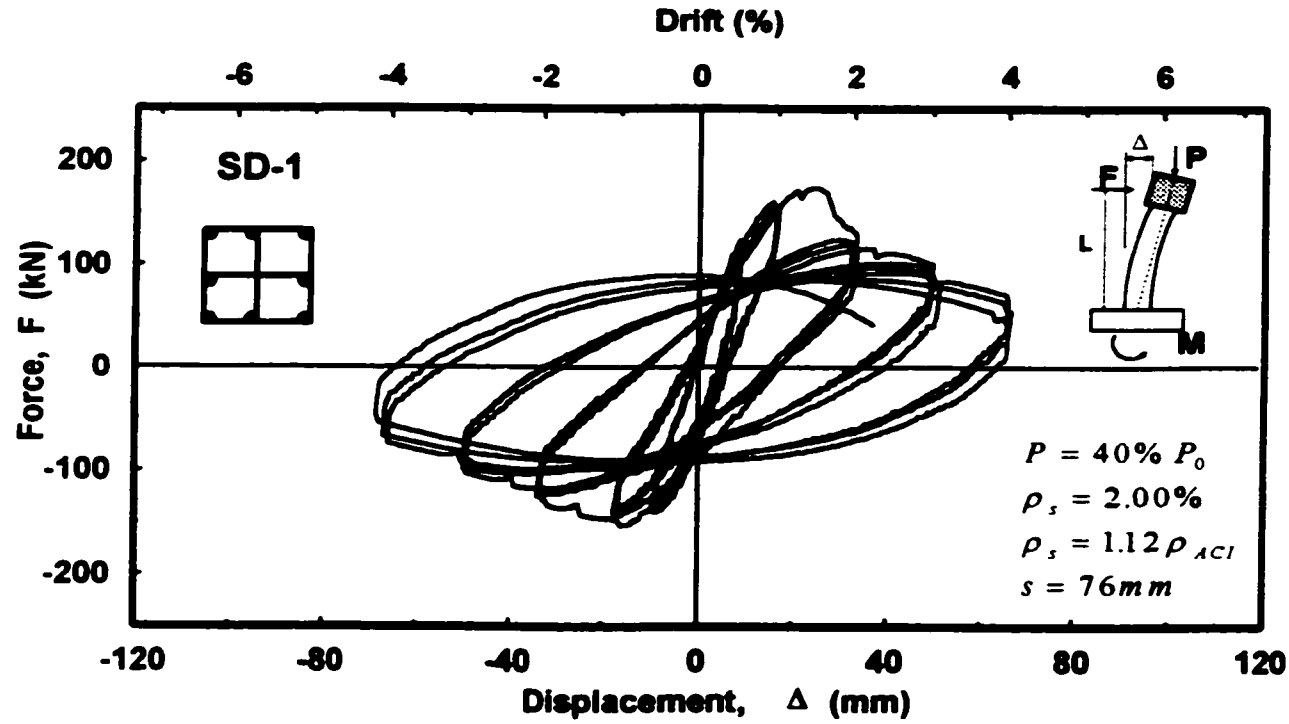

a) Hysteretic force-displacement relationship

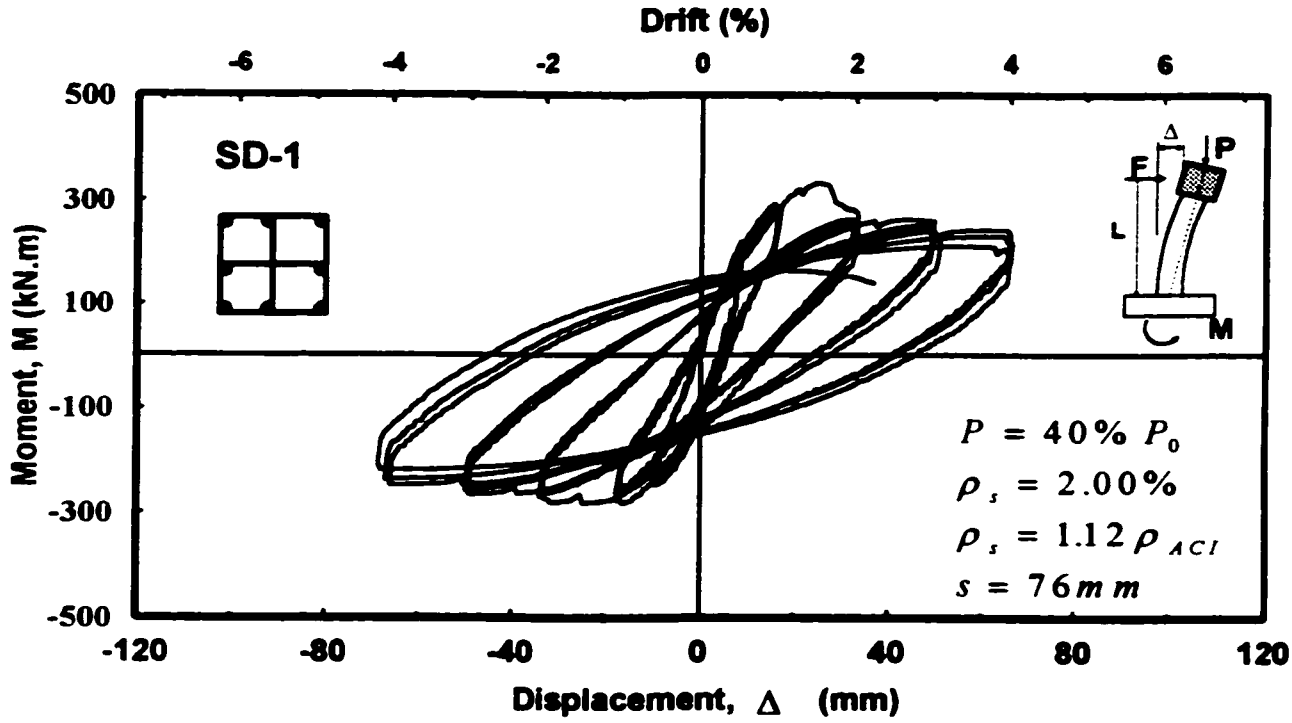

b) Hysteretic moment-displacement relationship

Figure 5-54: Hysteretic behavior of column SD-1

a) At 2% Drift

b) At 3% Drift

c) At 4% Drift

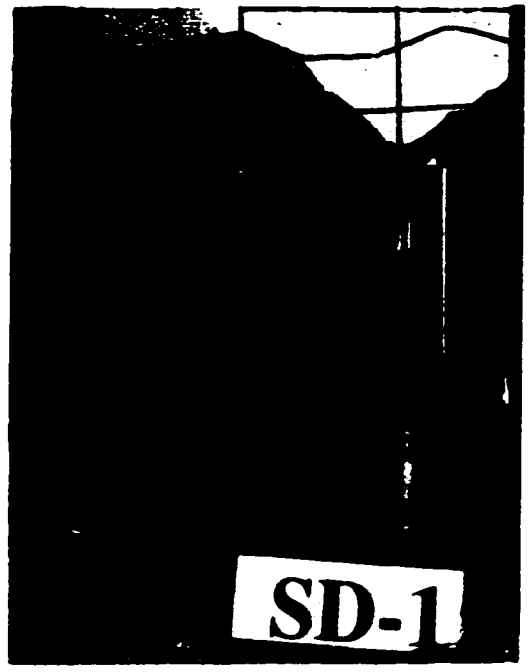

d) At end of test; Close-up

Figure 5-55: Observed damage in column SD-1 at selected stages of loading

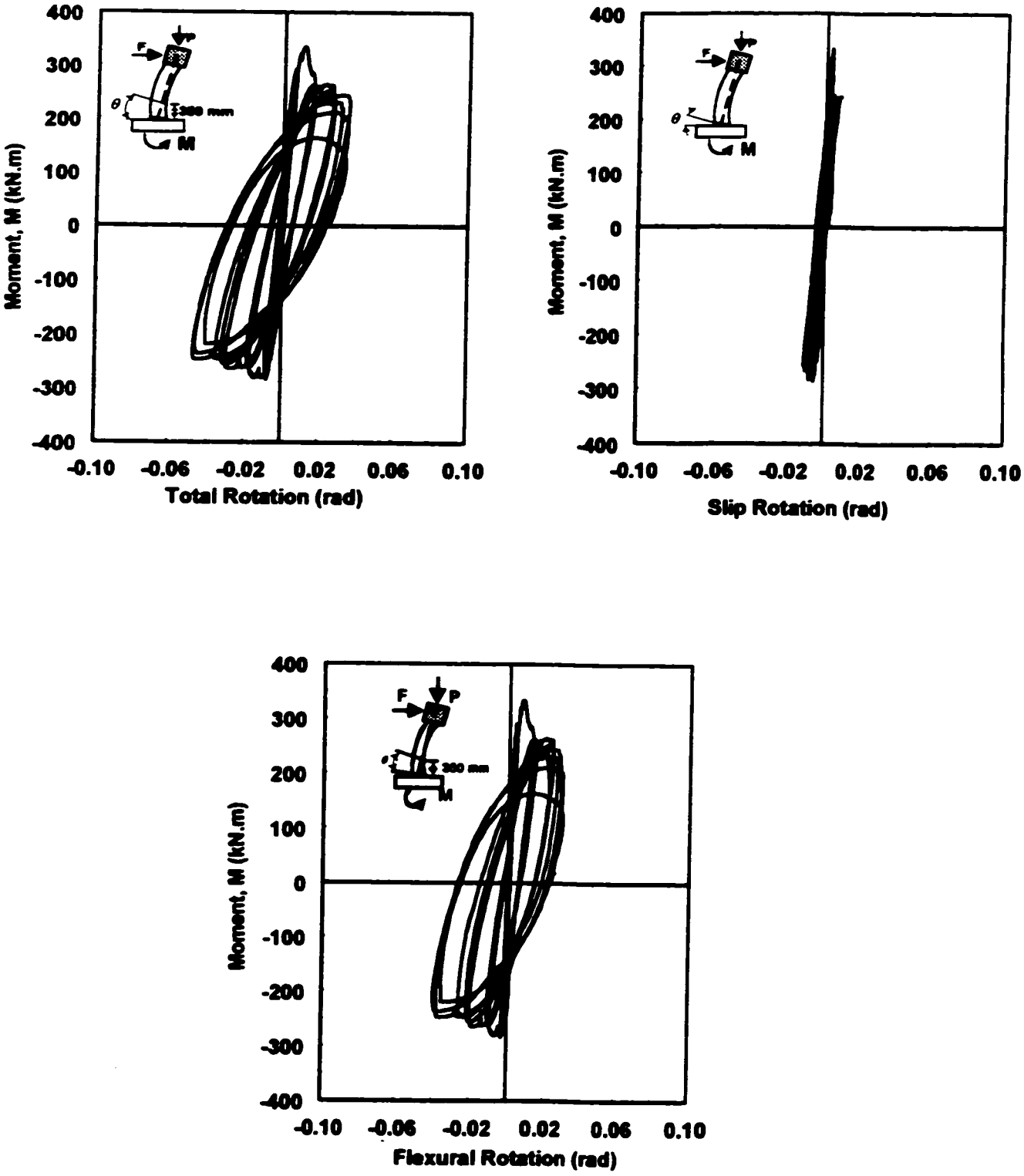

Figure 5-56: Moment-rotations relationships for column SD-1

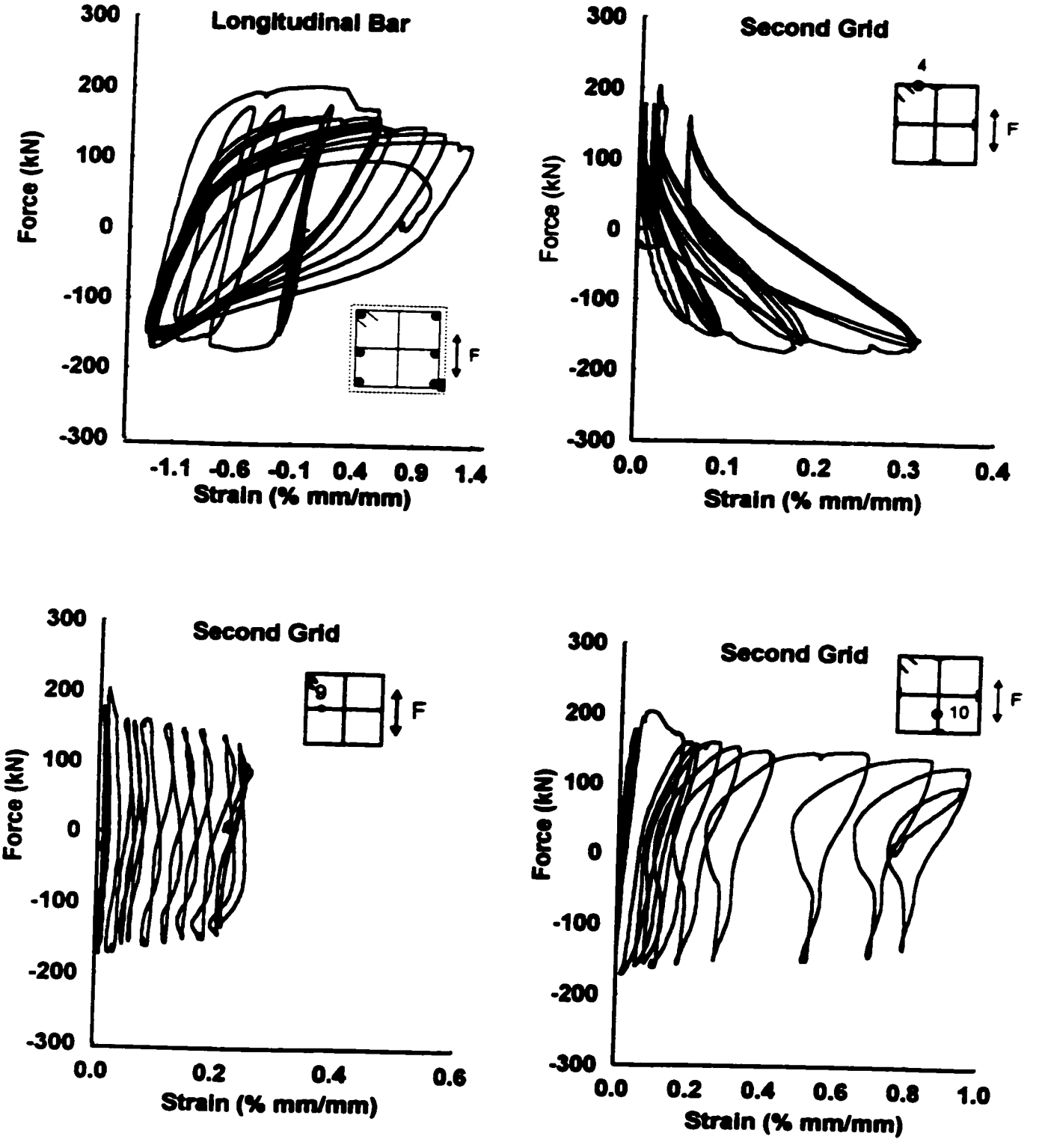

Figure 5-57: Reinforcement strain readings in Column SD-1

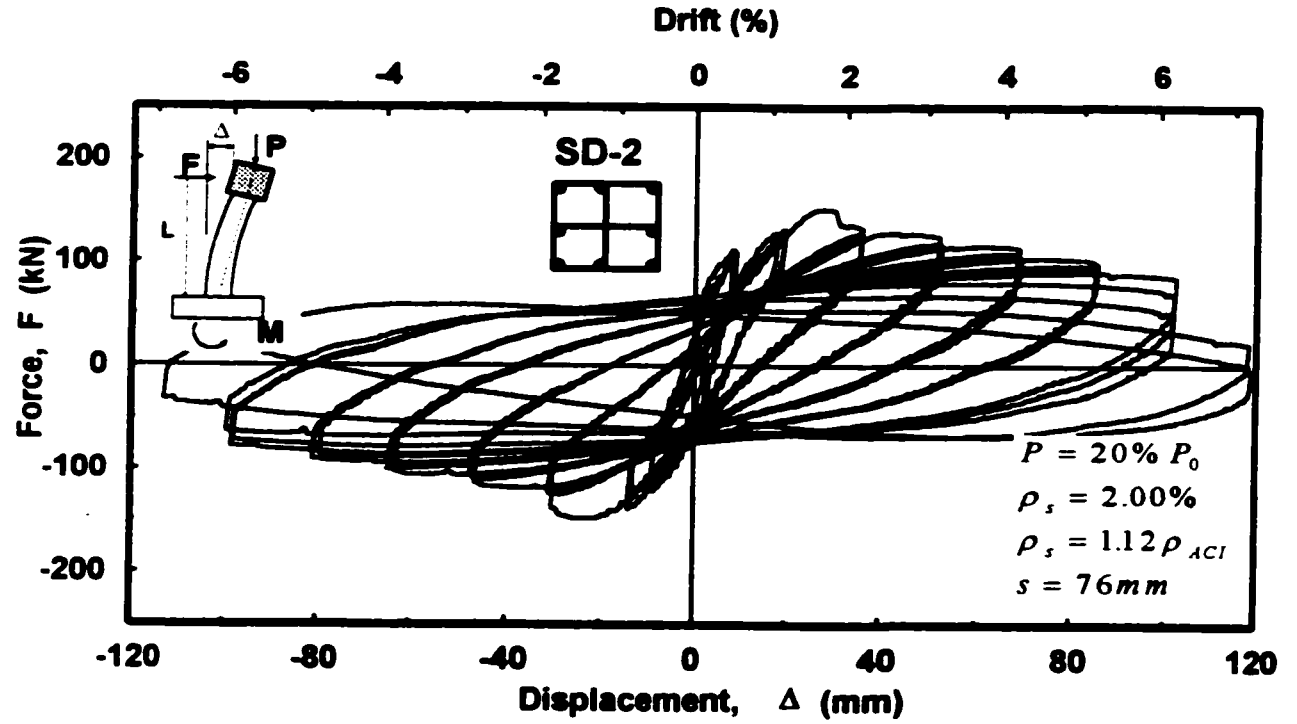

a) Hysteretic force-displacement relationship

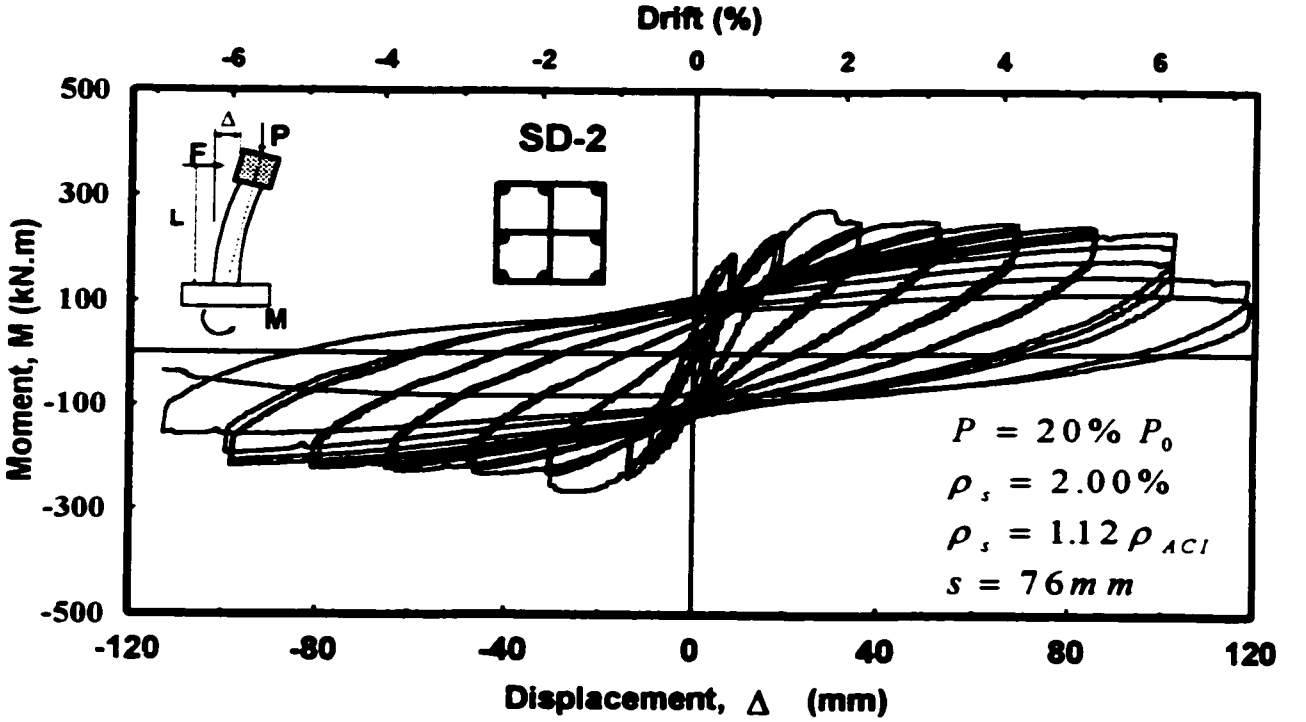

b) Hysteretic moment-displacement relationship

Figure 5-58: Hysteretic behavior of column SD-2

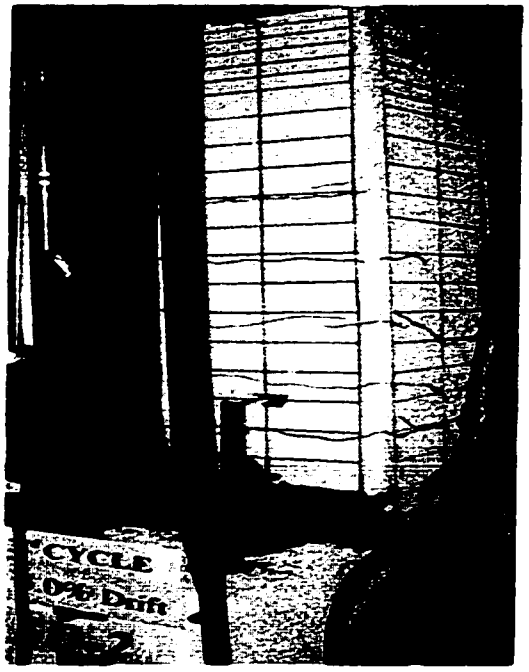

a) At 3% Drift

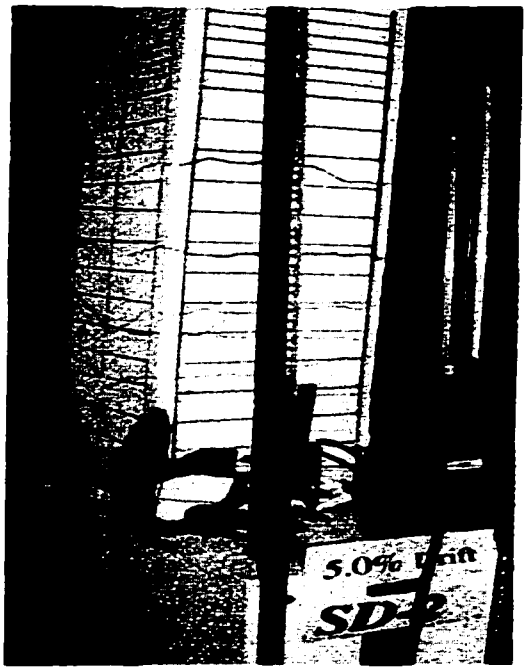

b) At 5% Drift

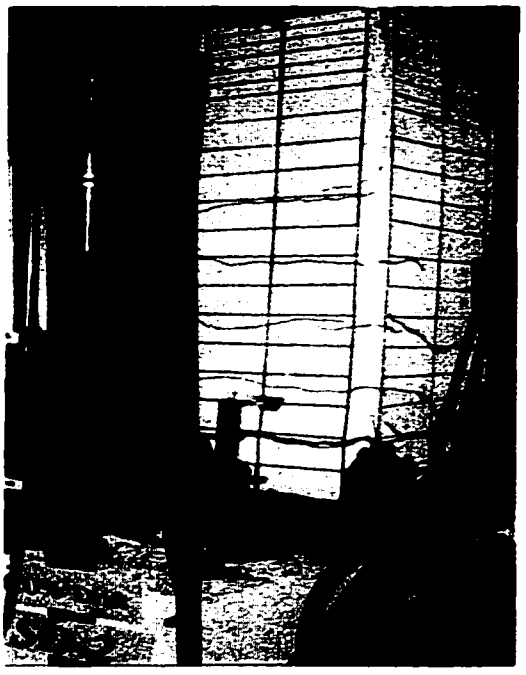

c) At 6% Drift

d) At 7% Drift

Figure 5-59: Observed damage in column SD-2 at selected stages of loading.

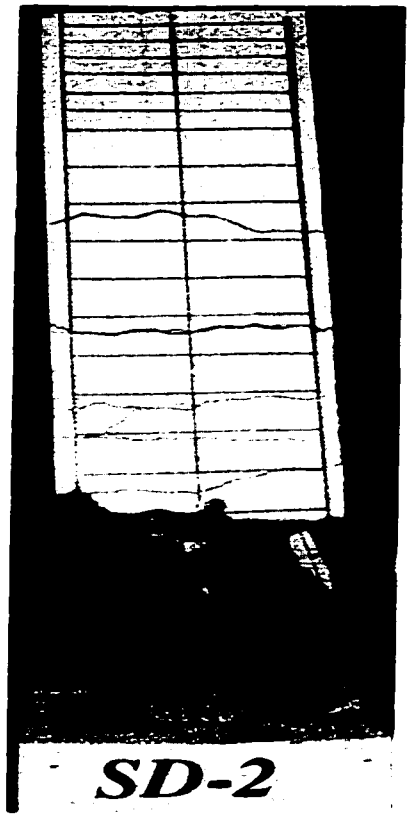

e) At End of Test

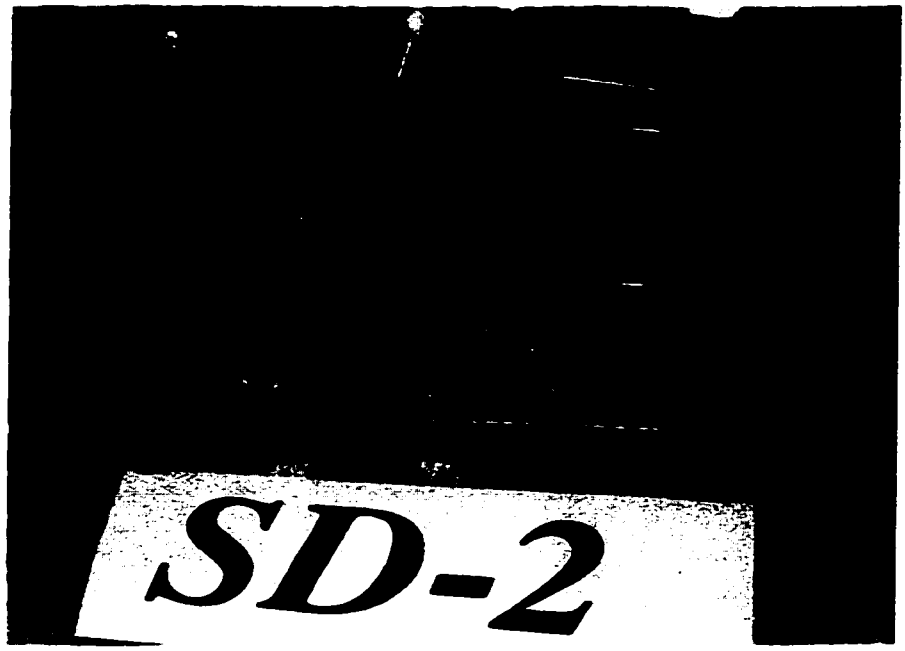

f) At End of Test; Close-up

Figure 5-59: Cont.

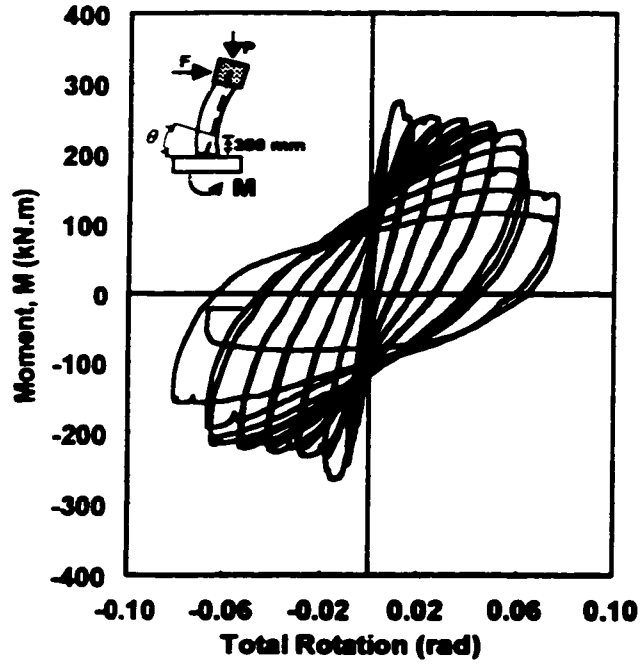

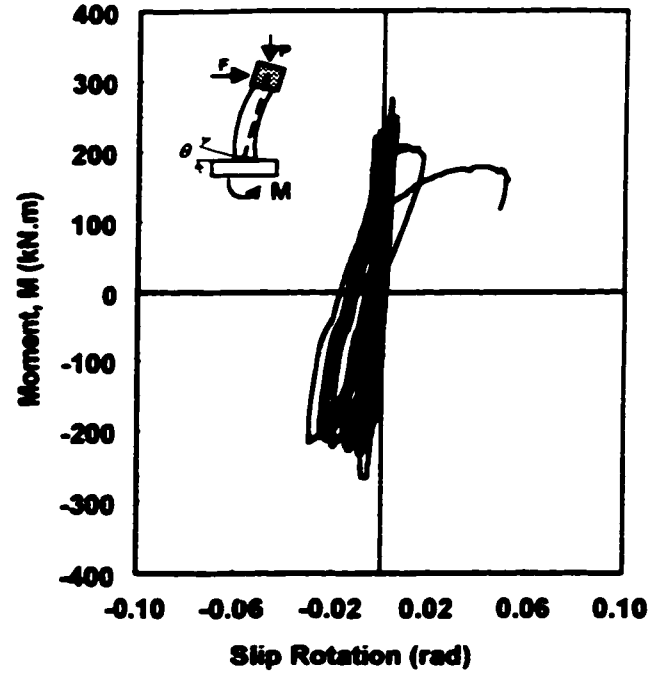

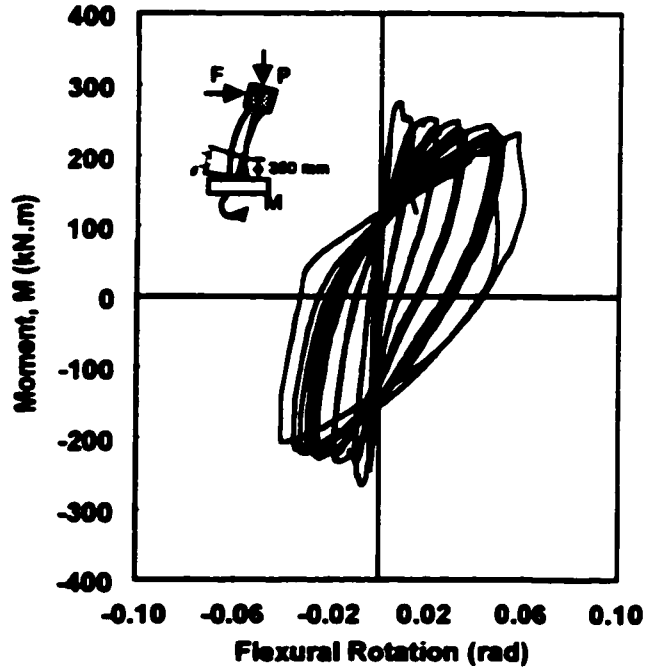

Figure 5-60: Moment-rotations relationships for column SD-2

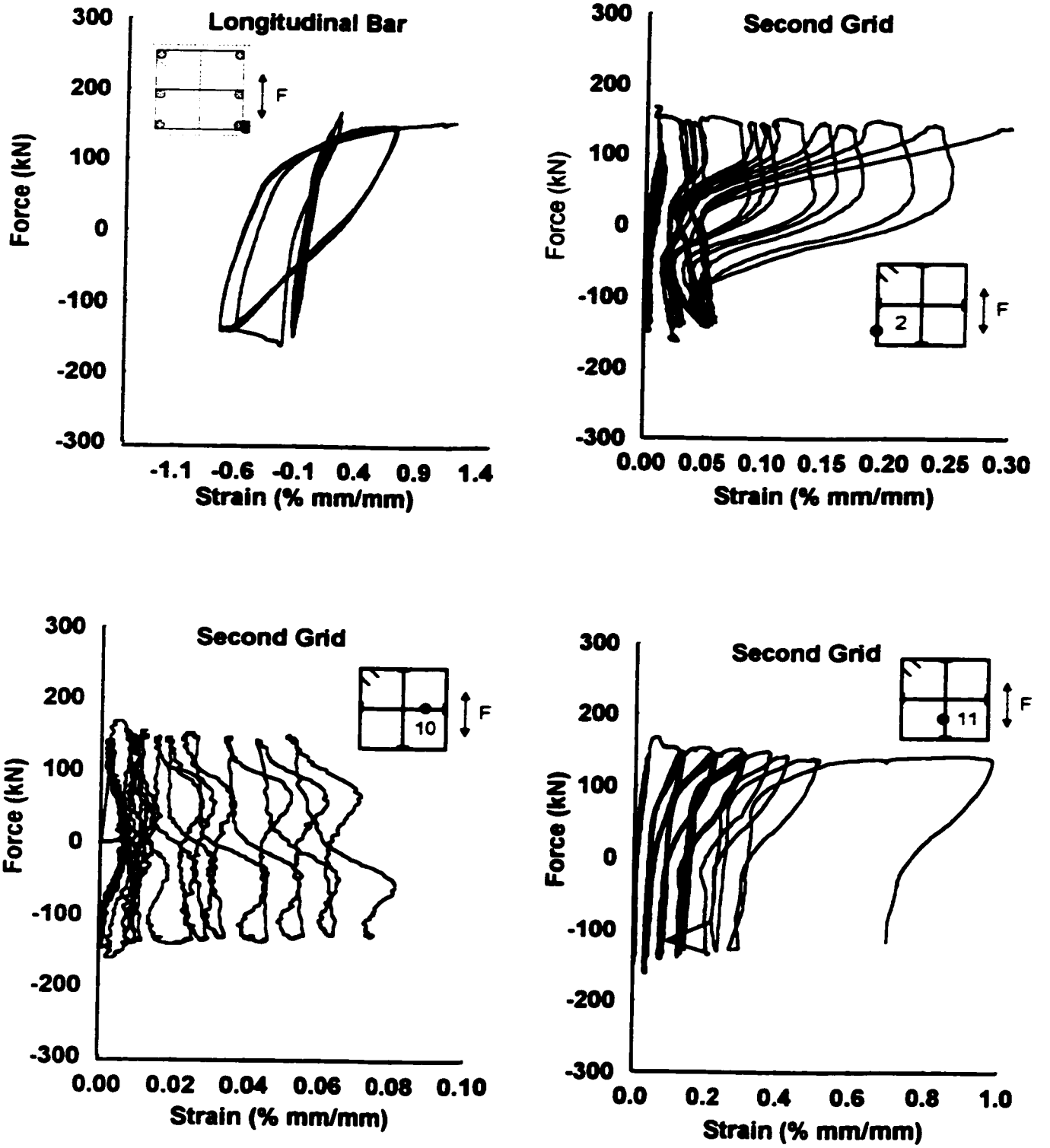

Figure 5-61: Reinforcement strain readings in Column SD-2

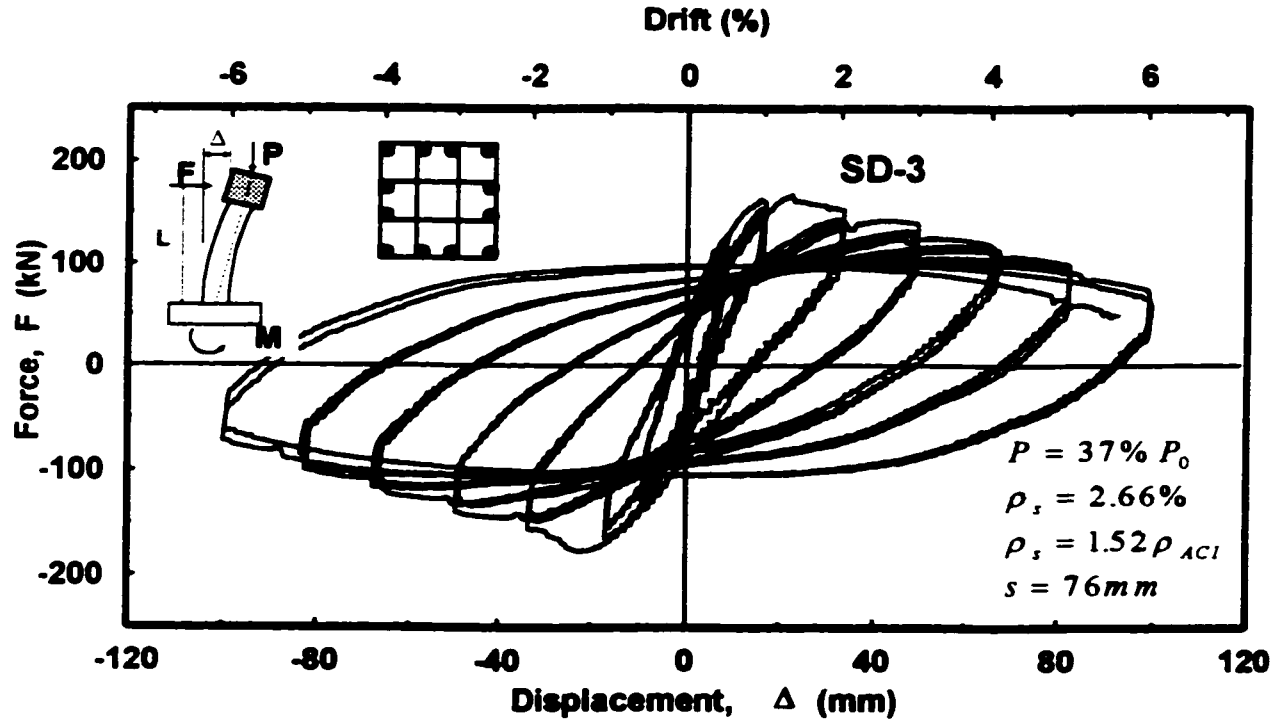

a) Hysteretic force-displacement relationship

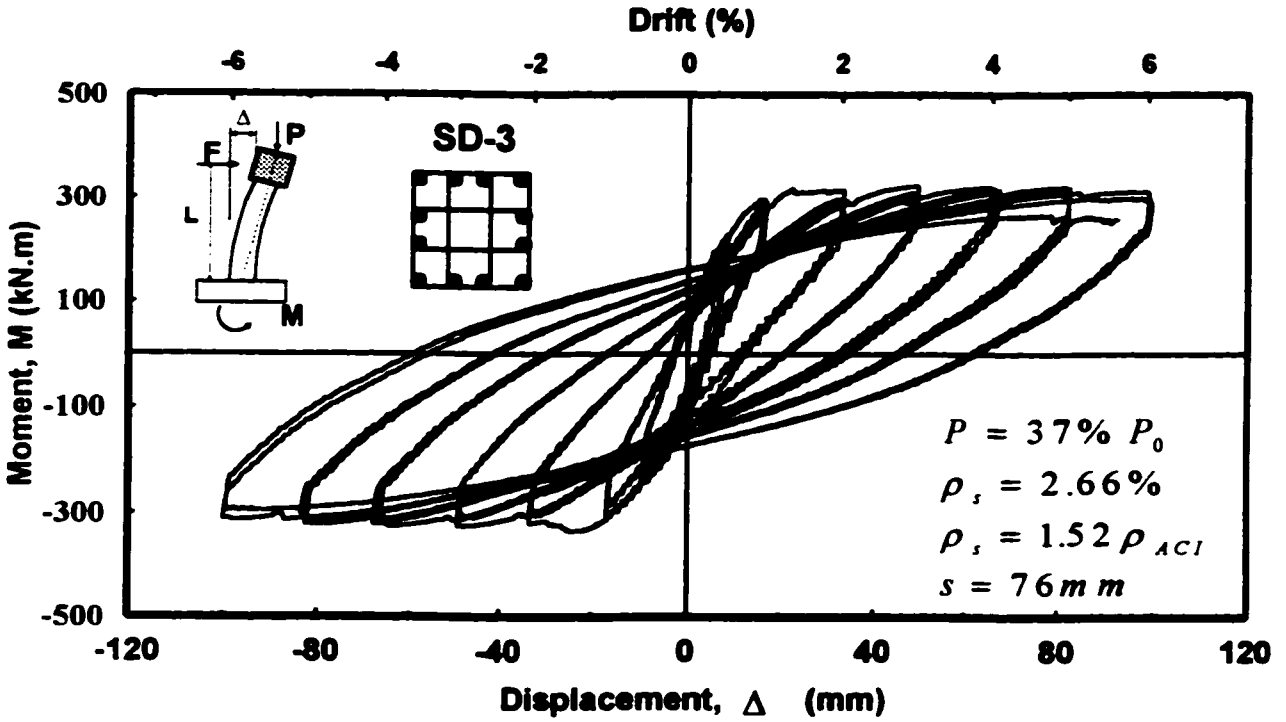

b) Hysteretic moment-displacement relationship

Figure 5-62: Hysteretic behavior of column SD-3

a) At 2% Drift

b) At 3% Drift

c) At 4% Drift

d) At 5% Drift

Figure 5-63: Observed damage in column SD-3 at selected stages of loading.

e) At 6% Drift

f) At End of Test; Close-up West Side

g) Buckling of Corner Bar

h) Slippage of Anchor Heads

Figure 5-63: Cont.

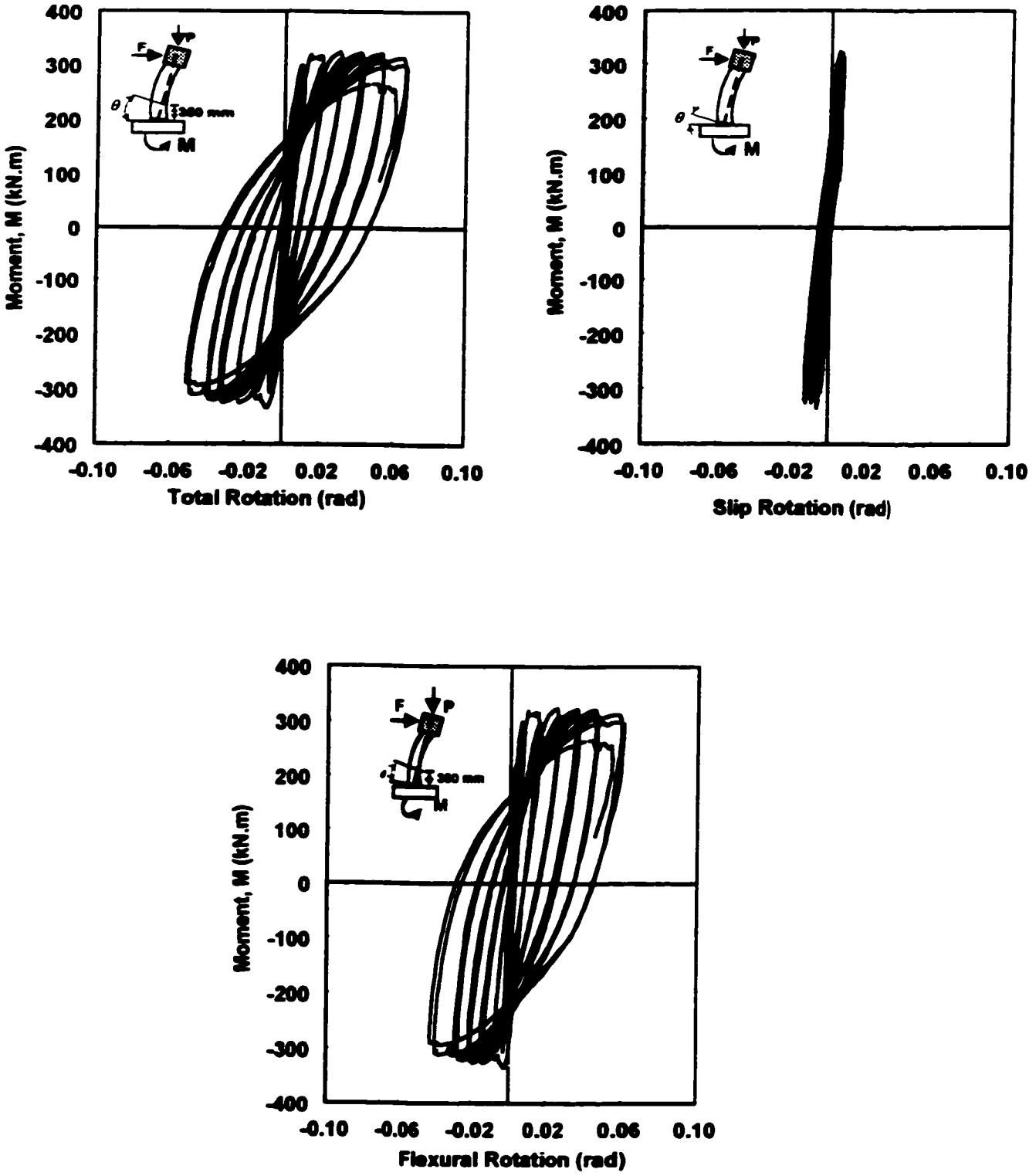

Figure 5-64: Moment-rotations relationships for column SD-3

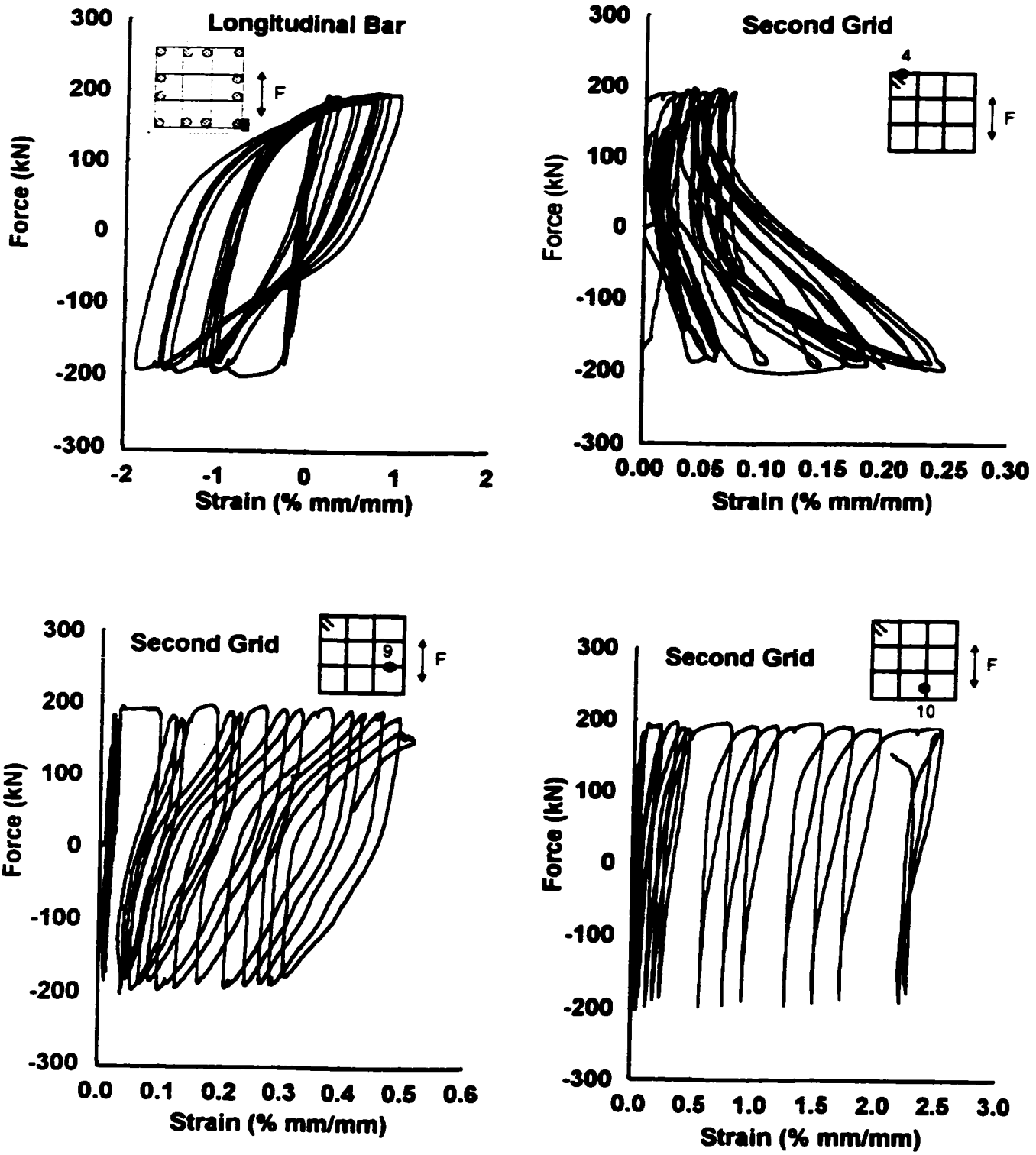

Figure 5-65: Reinforcement strain readings in Column SD-3

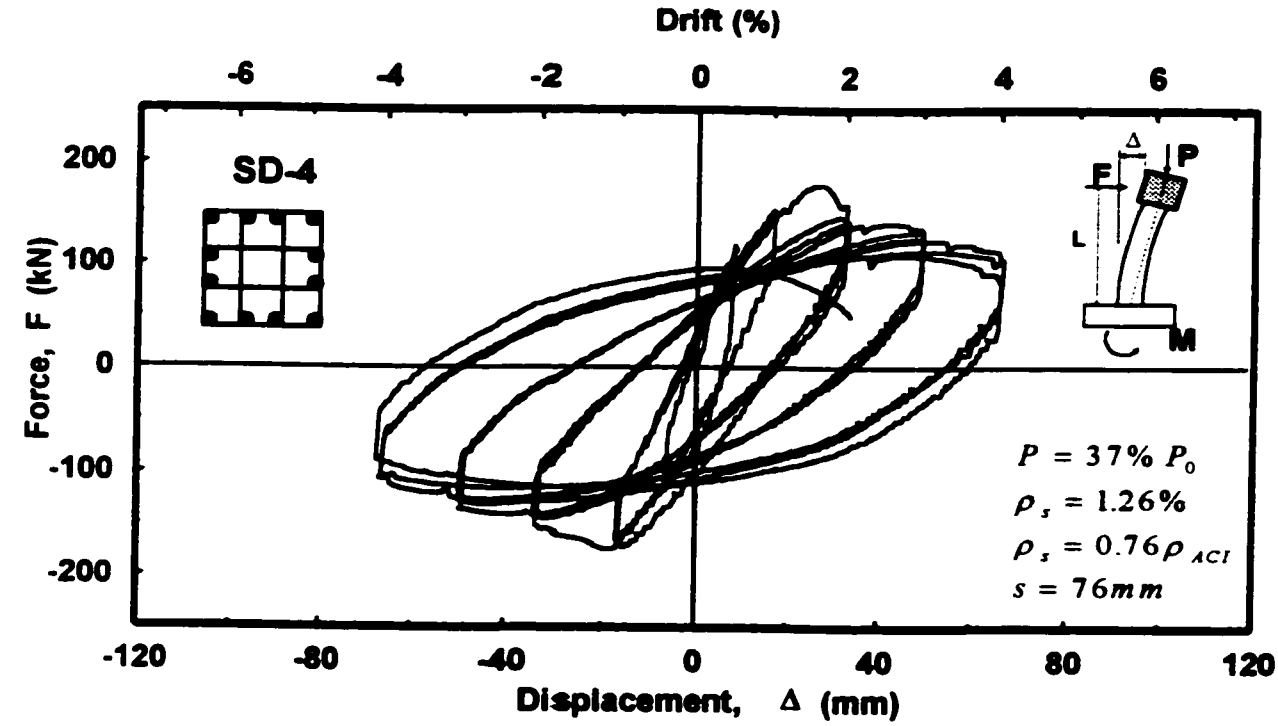

a) Hysteretic force-displacement relationship

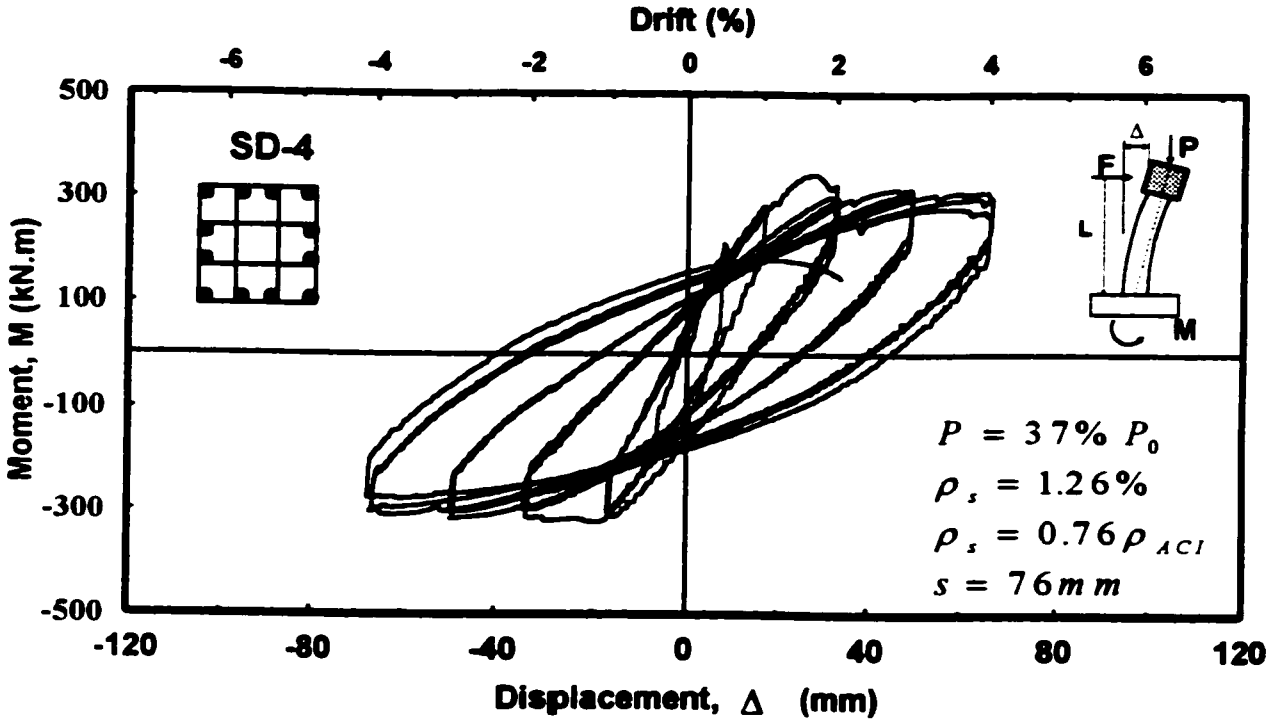

b) Hysteretic moment-displacement relationship

Figure 5-66: Hysteretic behavior of column SD-4

a) At 3% Drift

b) At 4% Drift

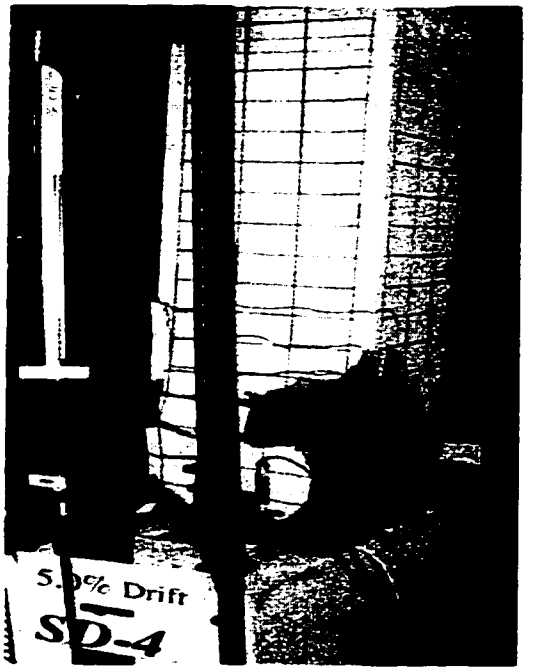

c) At 5% Drift

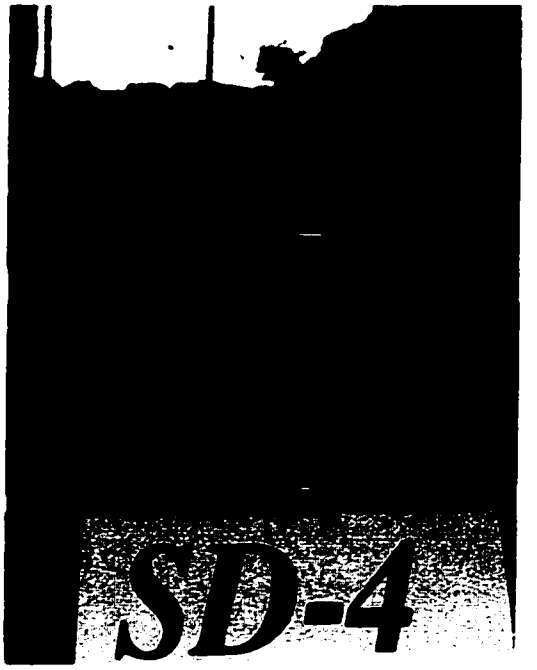

d) At end of test; Close-up

Figure 5-67: Observed damage in column SD-4 at selected stages of loading.

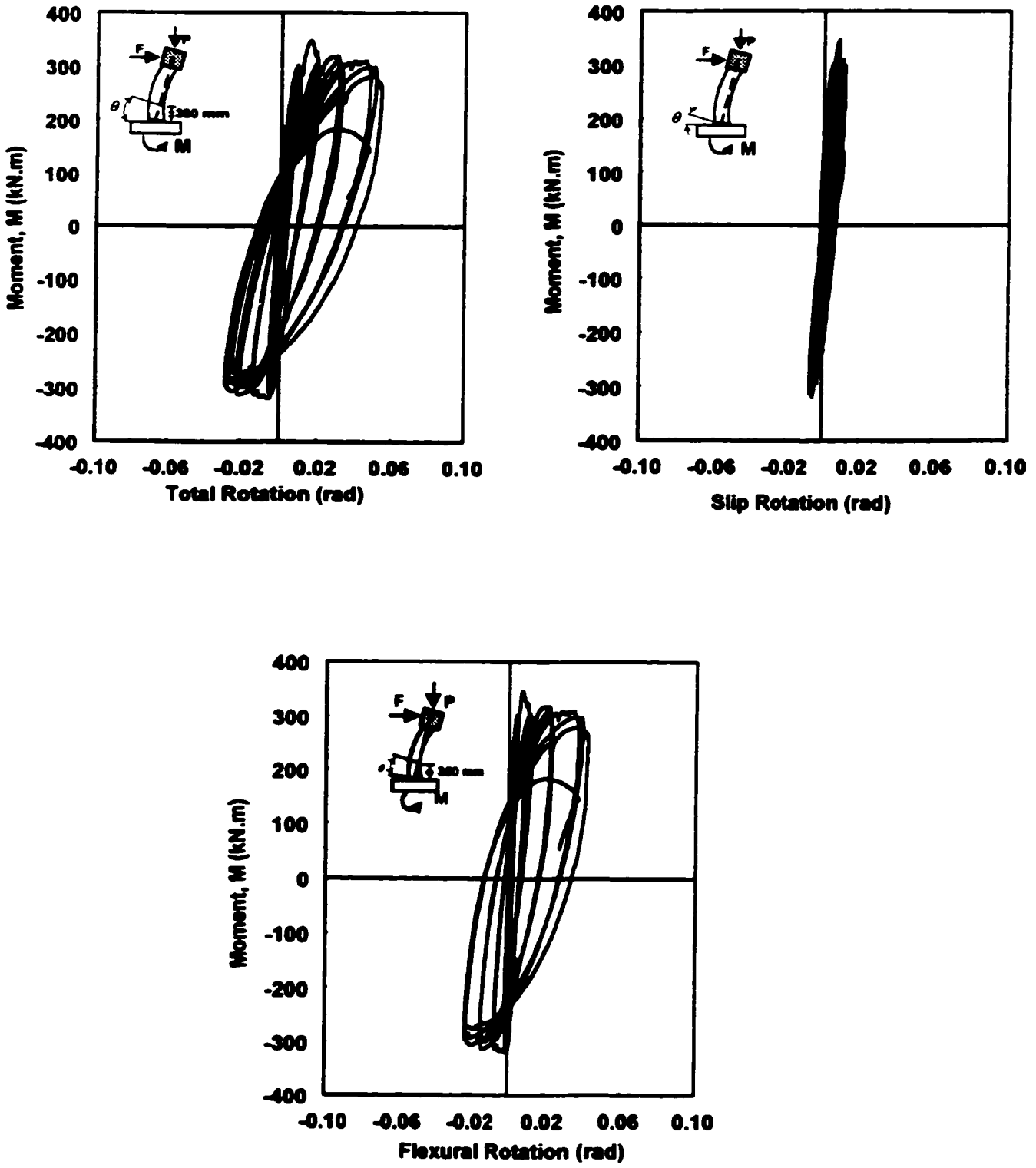

Figure 5-68: Moment-rotations relationships for column SD-4

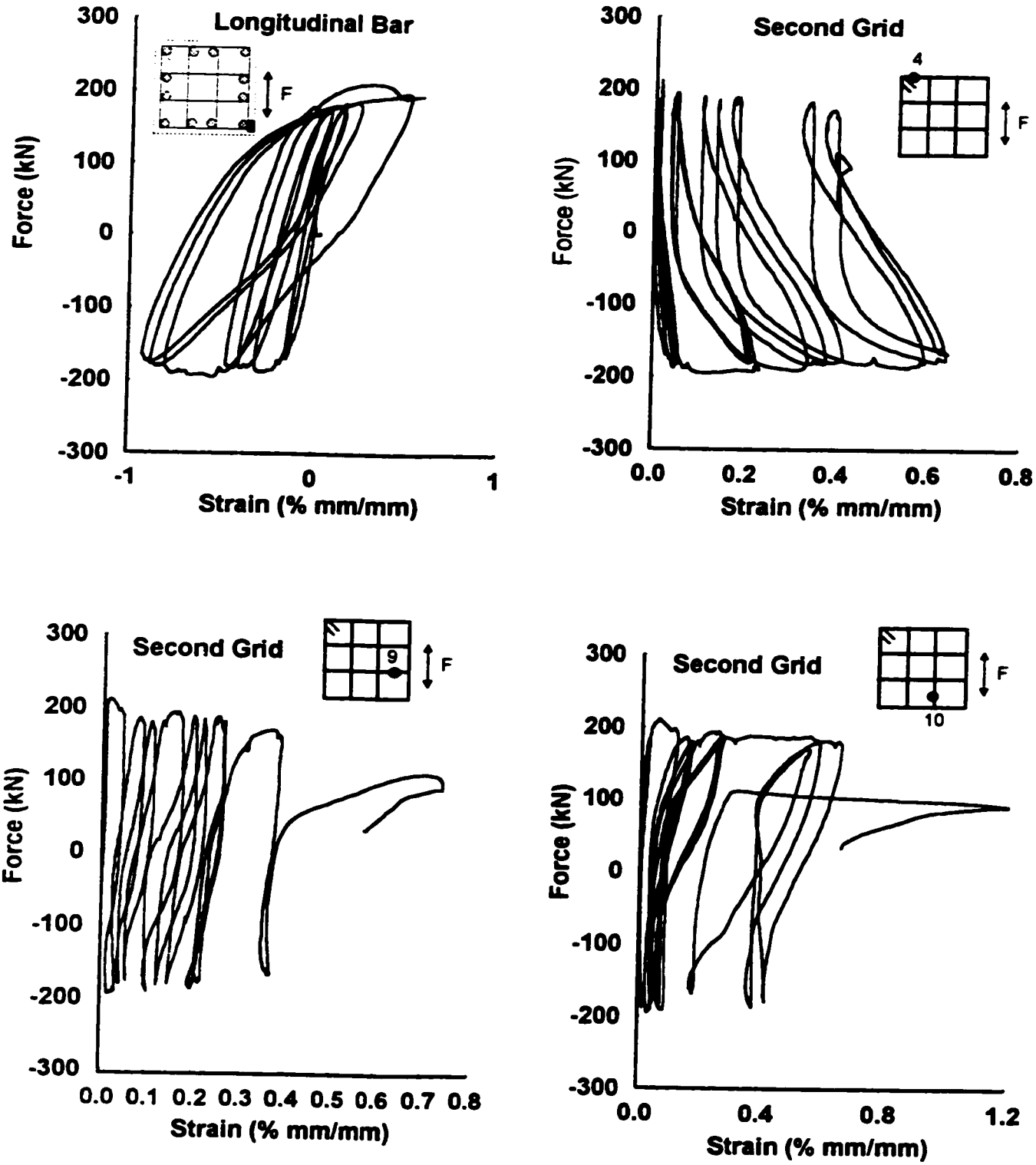

Figure 5-69: Reinforcement strain readings in Column SD-4

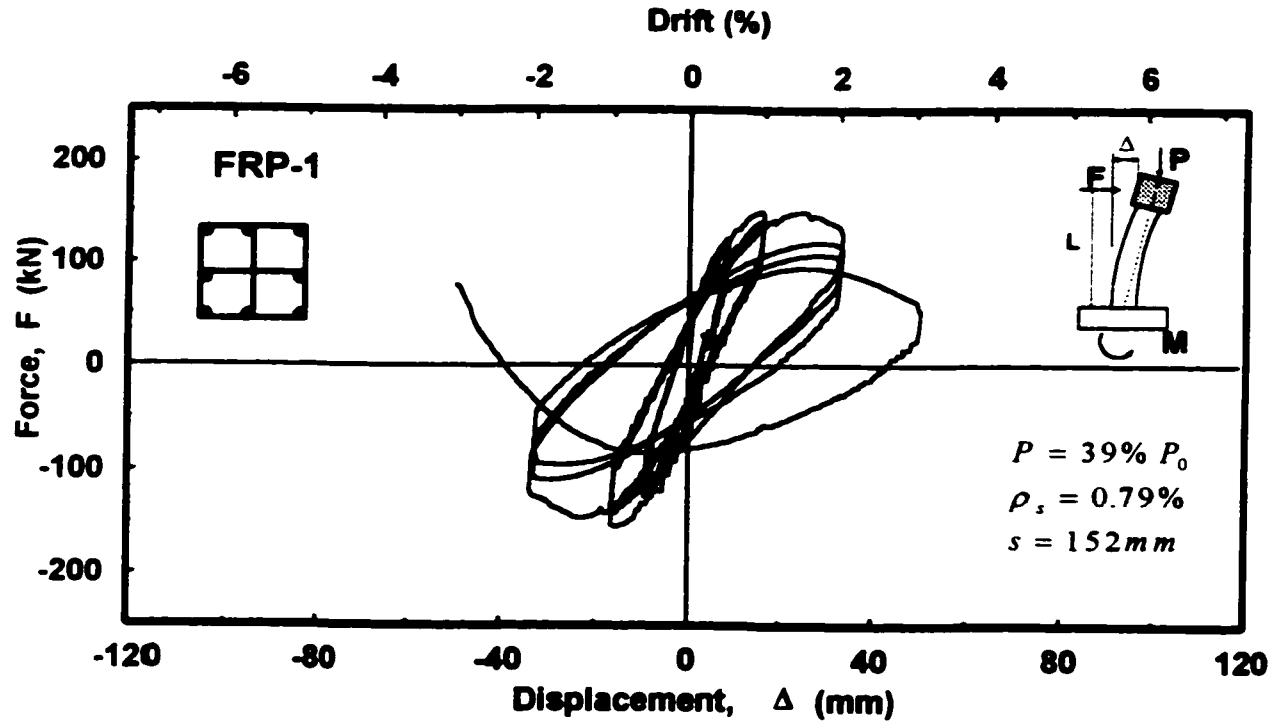

a) Hysteretic force-displacement relationship

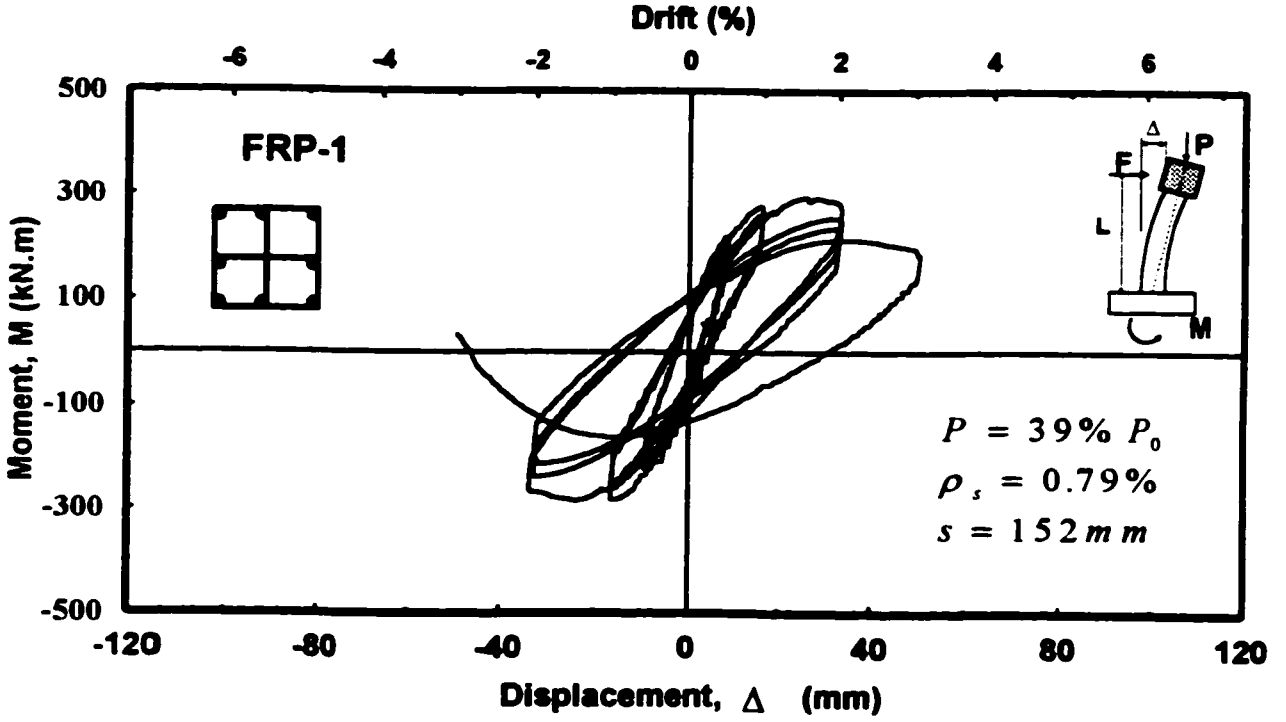

b) Hysteretic moment-displacement relationship

Figure 5-70: Hysteretic behavior of column FRP-1

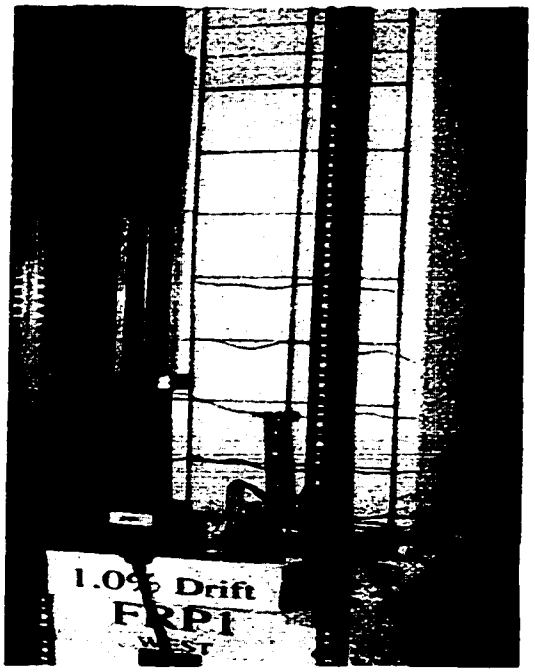

a) At 1% Drift

b) At 2% Drift

c) At 3% Drift

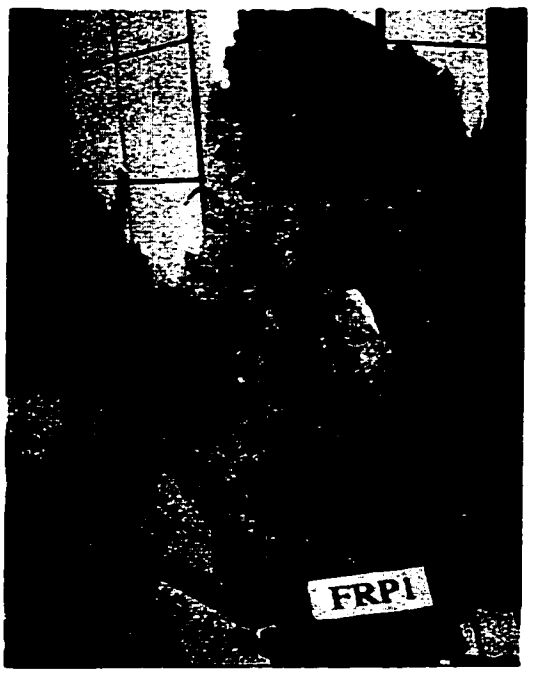

d) At end of test

Figure 5-71: Observed damage in column FRP-1 at selected stages of loading.

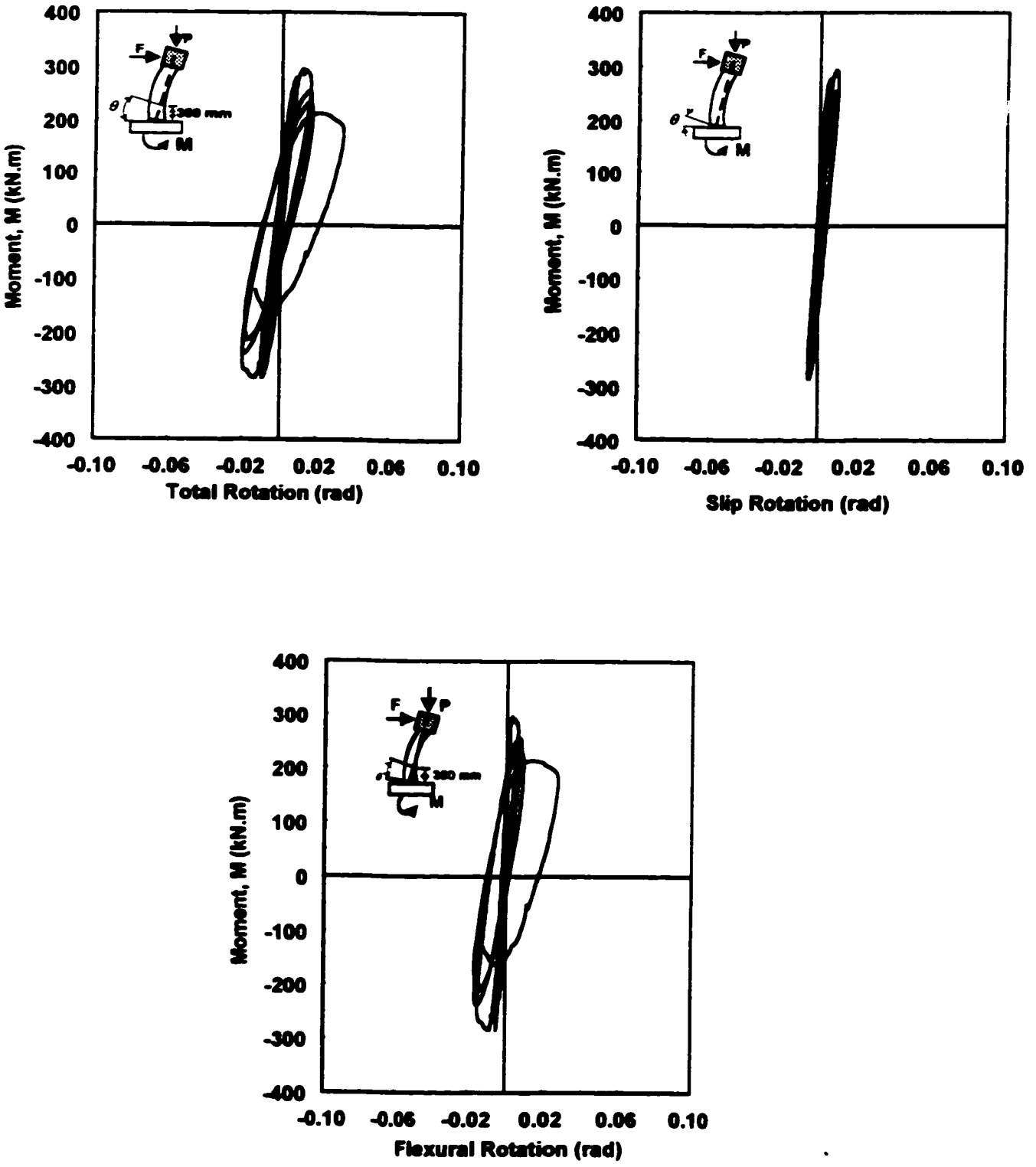

Figure 5-72: Moment-rotations relationships for column FRP-1

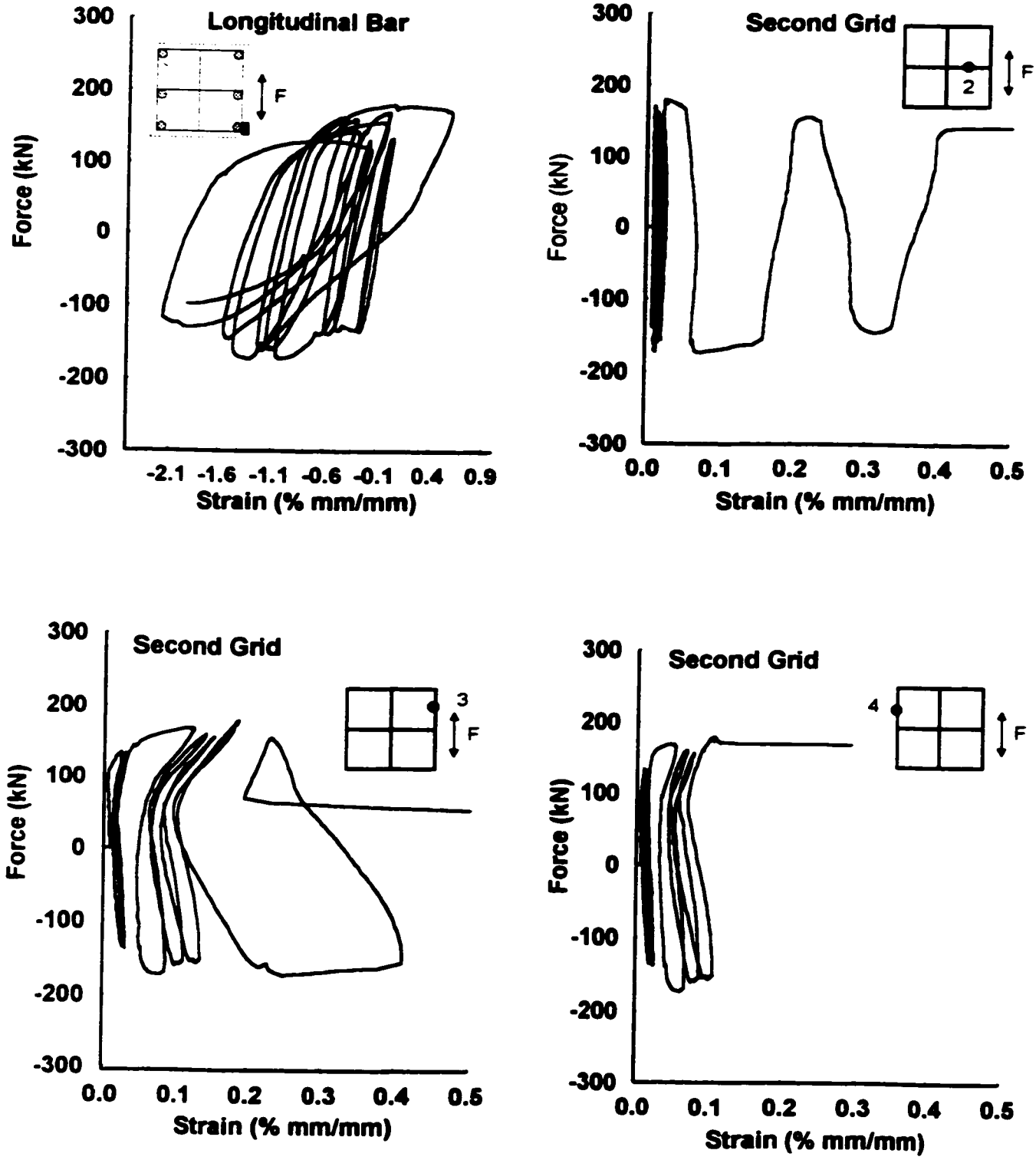

Figure 5-73: Reinforcement strain readings in Column FRP-1

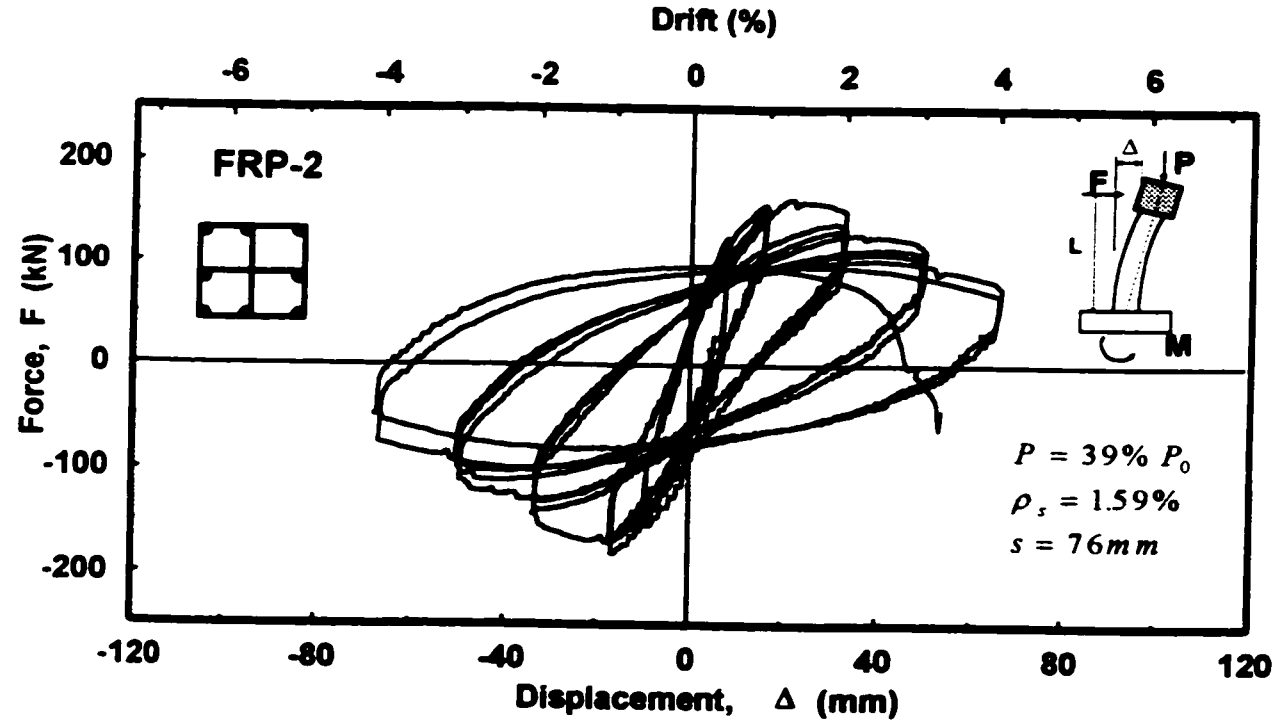

a) Hysteretic force-displacement relationship

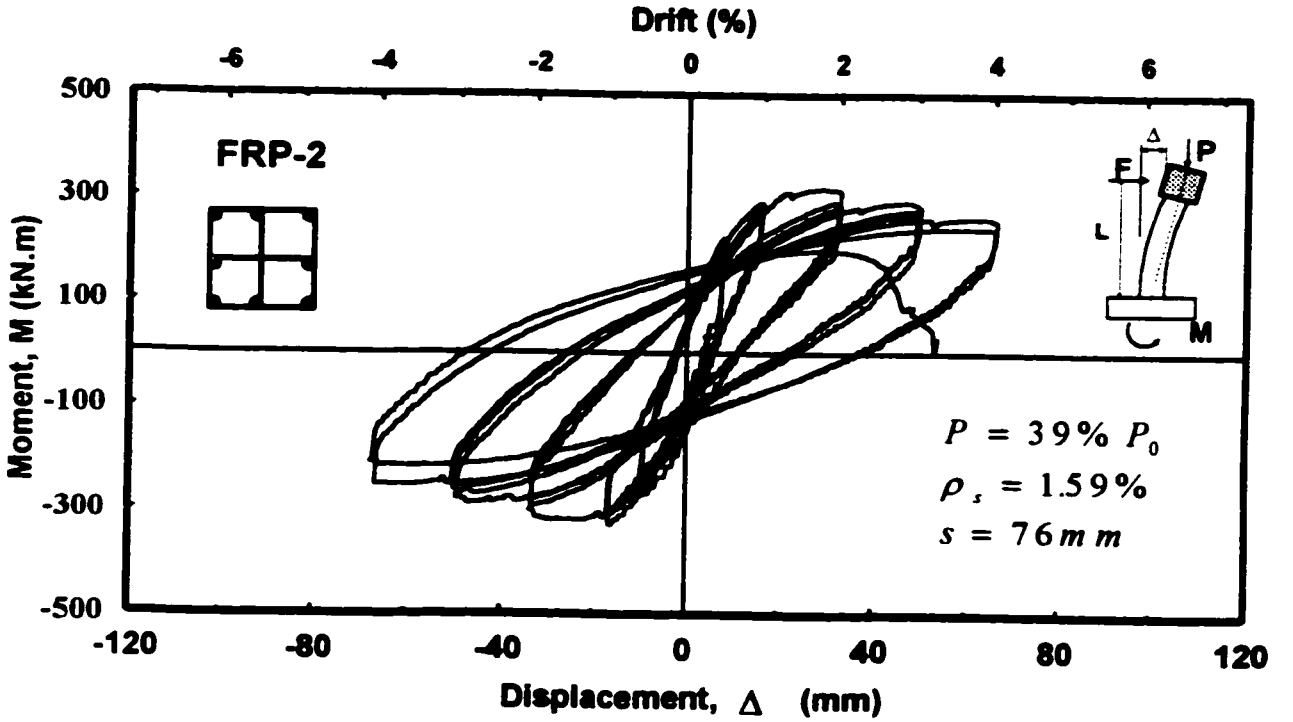

b) Hysteretic moment-displacement relationship

Figure 5-74: Hysteretic behavior of column FRP-2

a) At 1% Drift

b) At 2% Drift

c) At 3% Drift

d) At end of test

Figure 5-75: Observed damage in column FRP-2 at selected stages of loading.

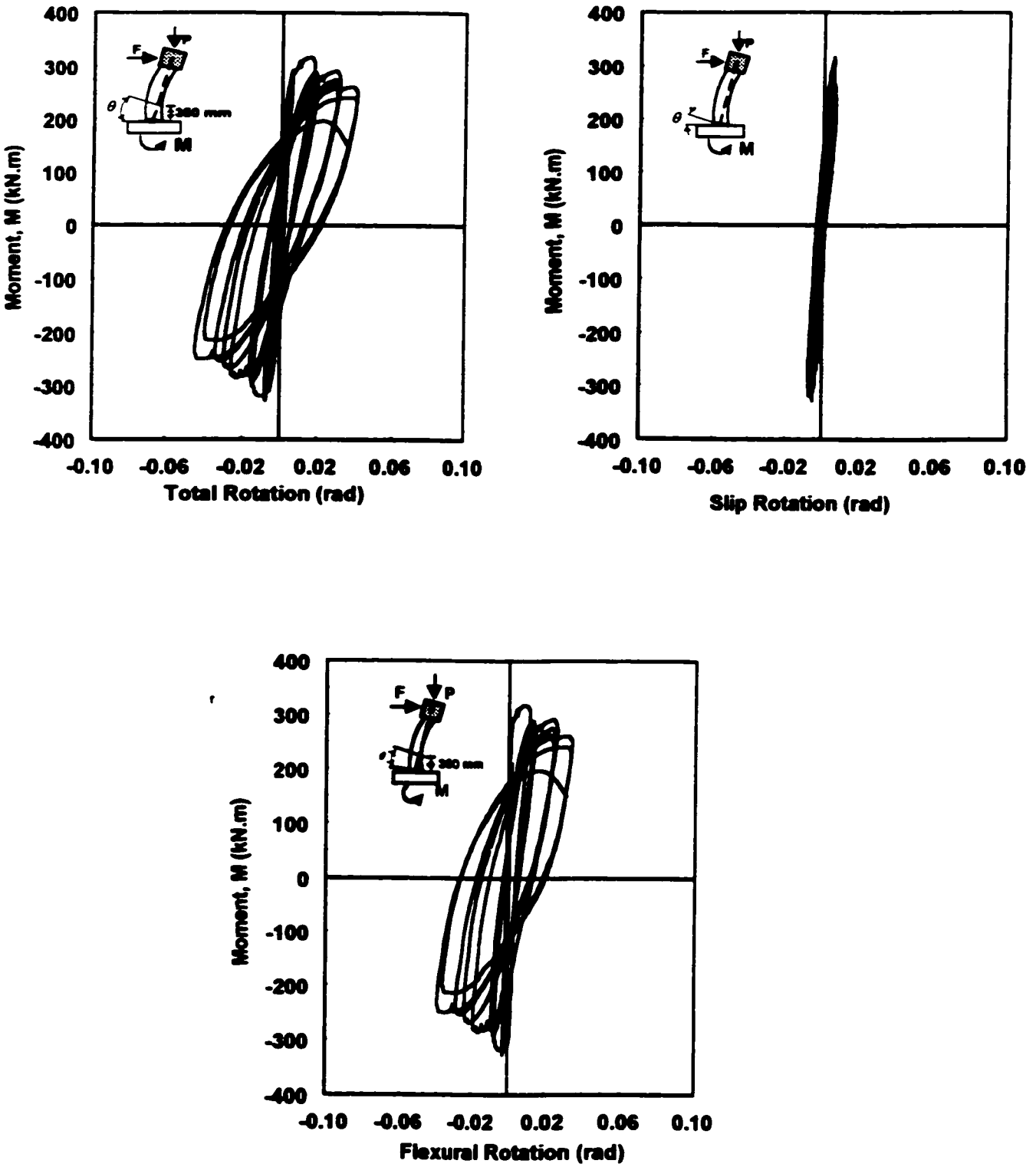

Figure 5-76: Moment-rotations relationships for column FRP-2

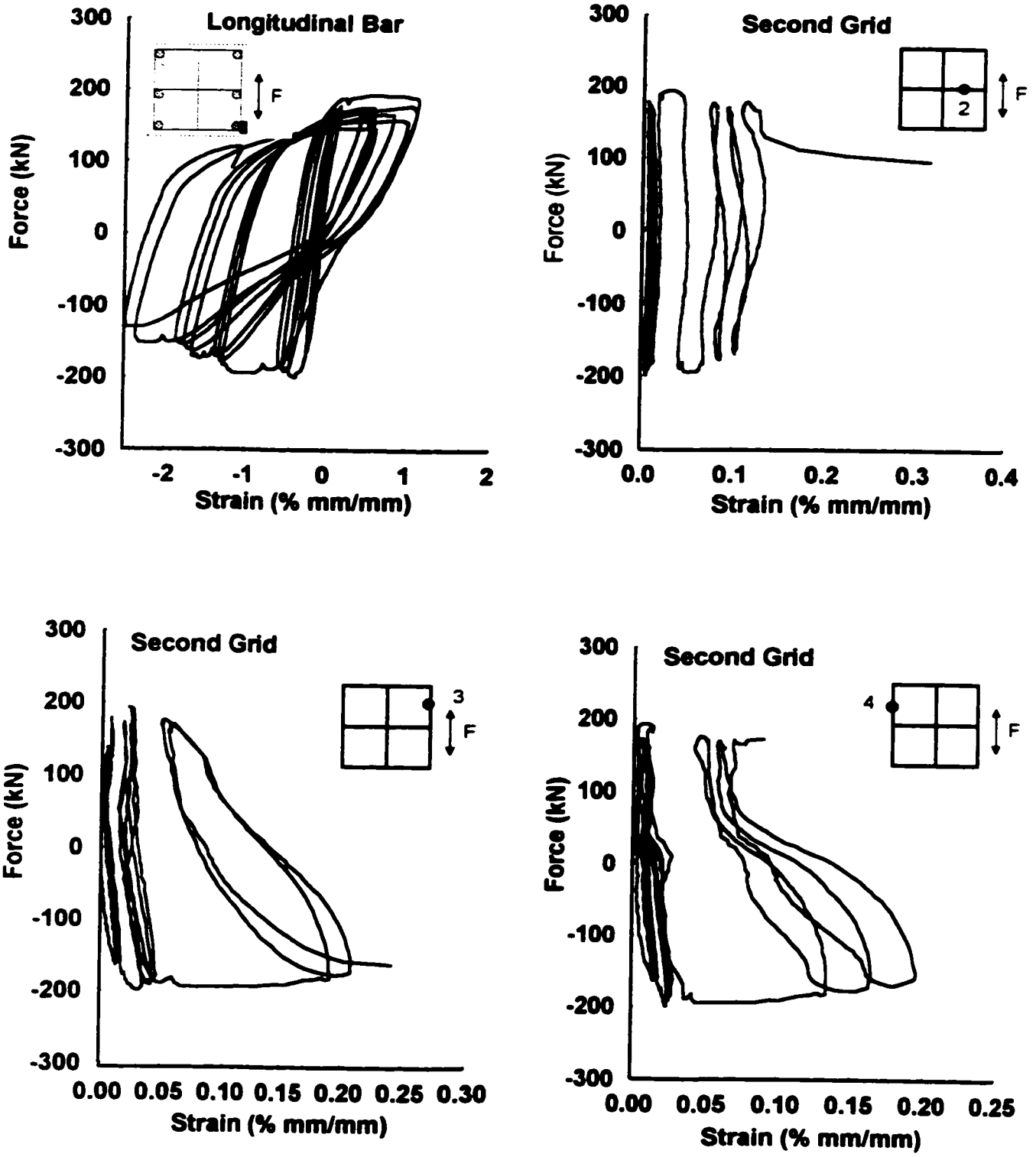

Figure 5-77: Reinforcement strain readings in Column FRP-2

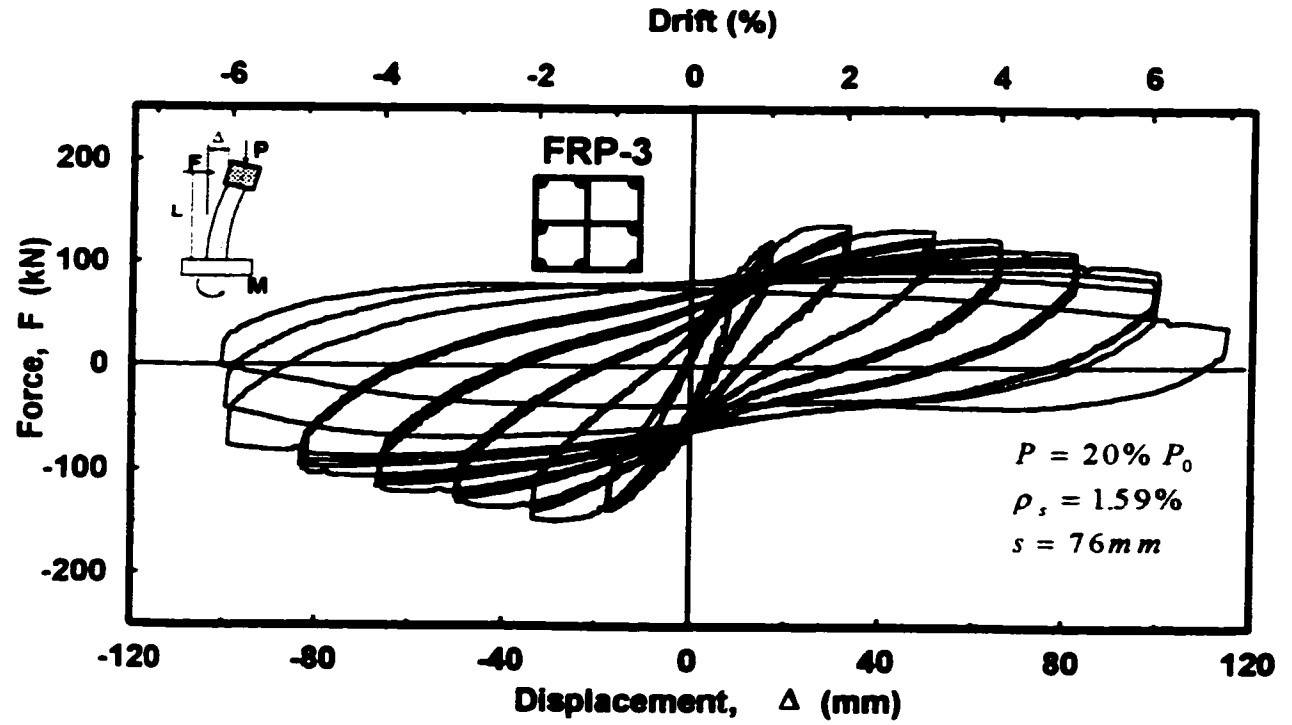

a) Hysteretic force-displacement relationship

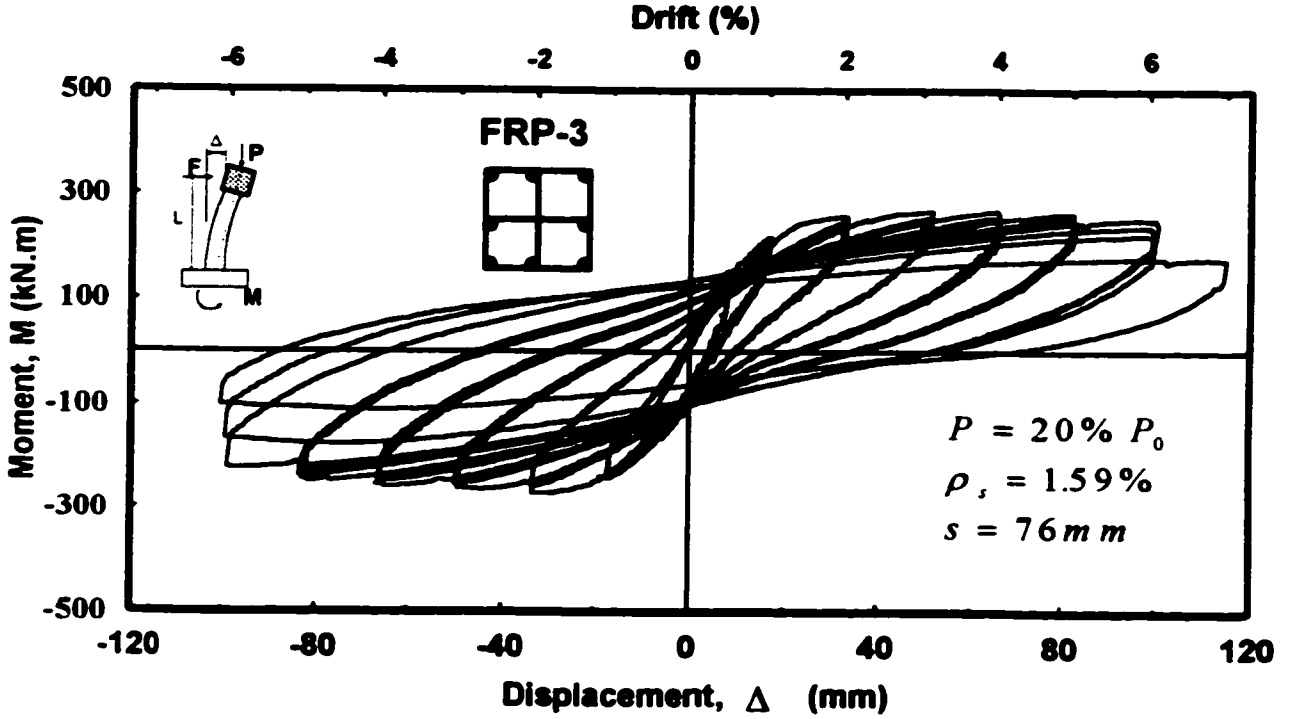

b) Hysteretic moment-displacement relationship

Figure 5-78: Hysteretic behavior of column FRP-3

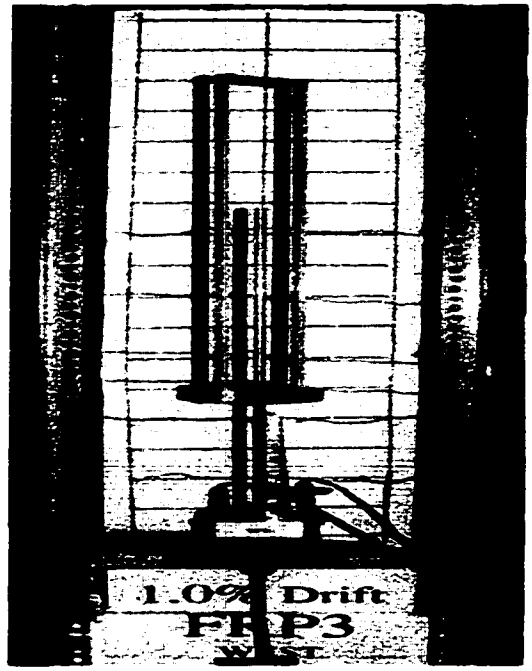

a) At 1% Drift

b) At 3% Drift

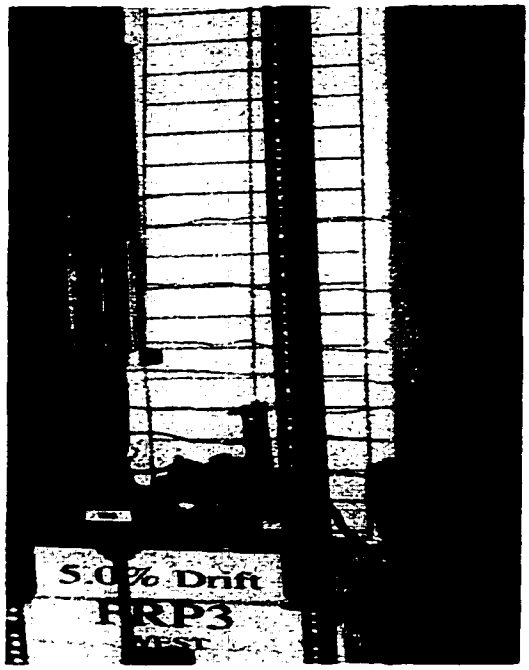

c) At 5% Drift

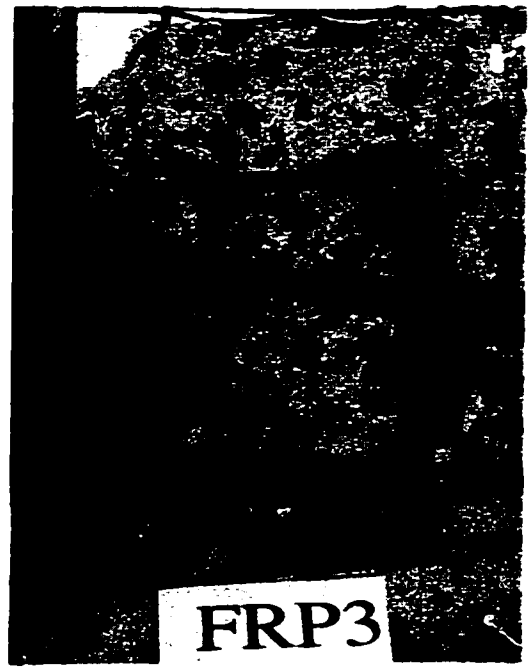

d) At end of test

Figure 5-79: Observed damage in column FRP-3 at selected stages of loading.

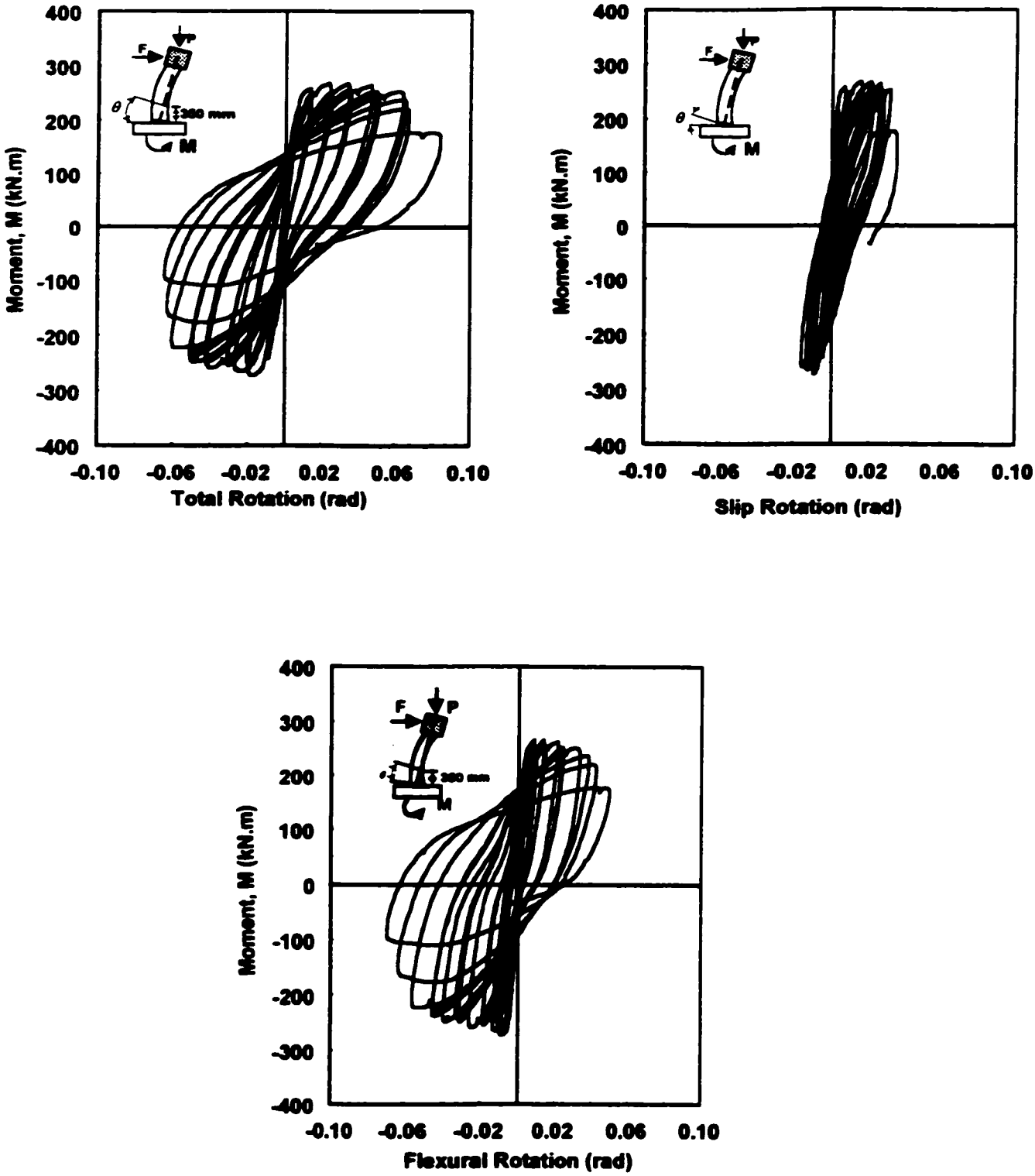

Figure 5-80: Moment-rotations relationships for column FRP-3

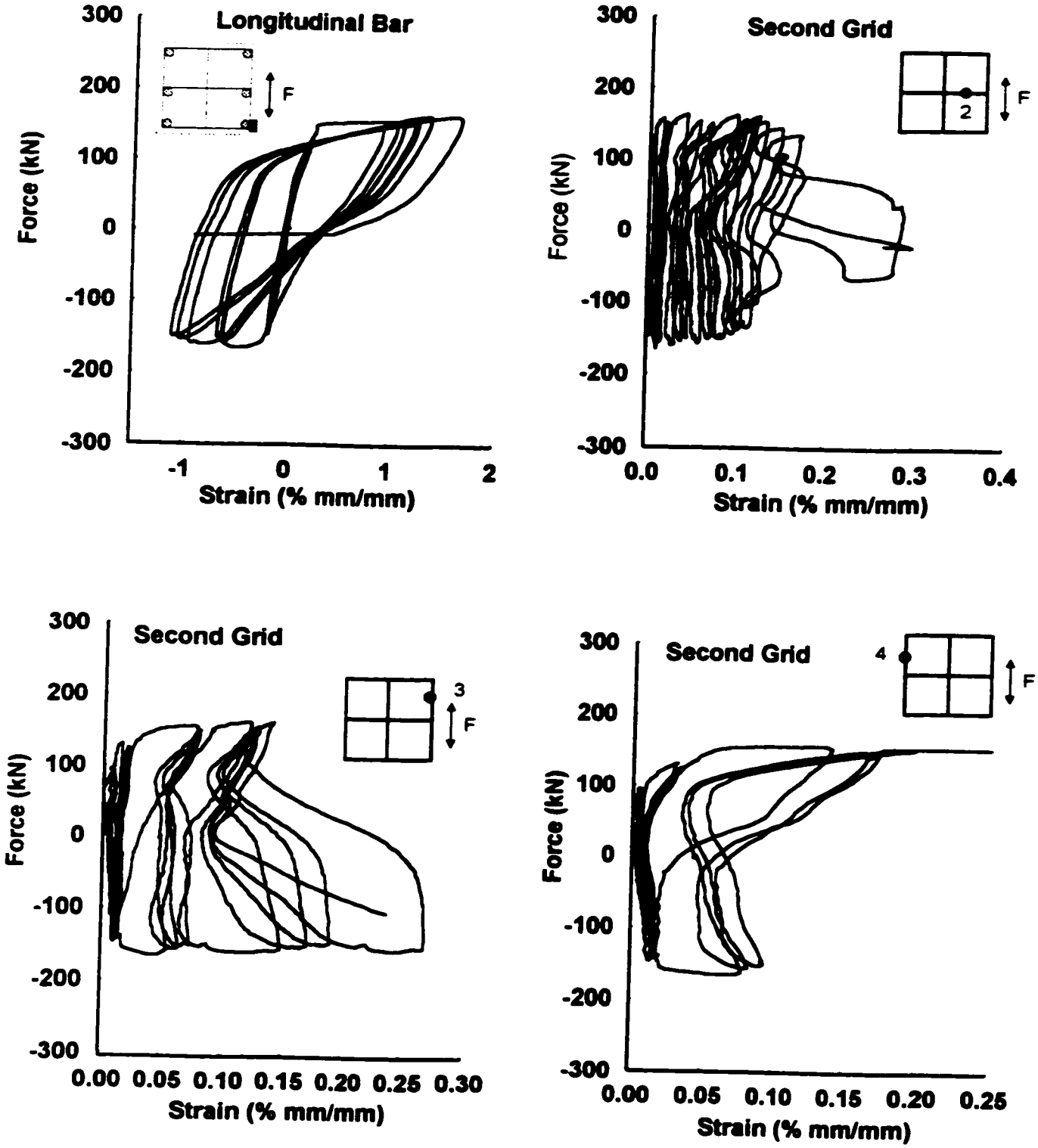

Figure 5-81: Reinforcement strain readings in Column FRP-3

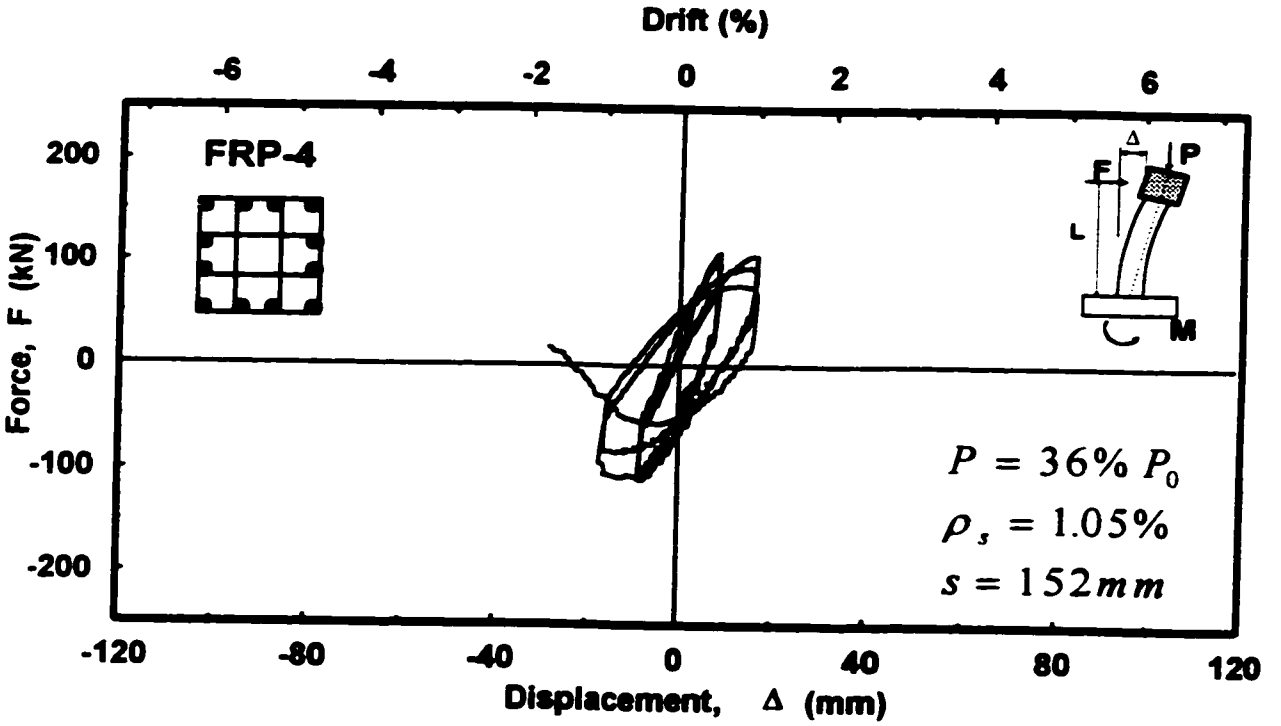

a) Hysteretic force-displacement relationship

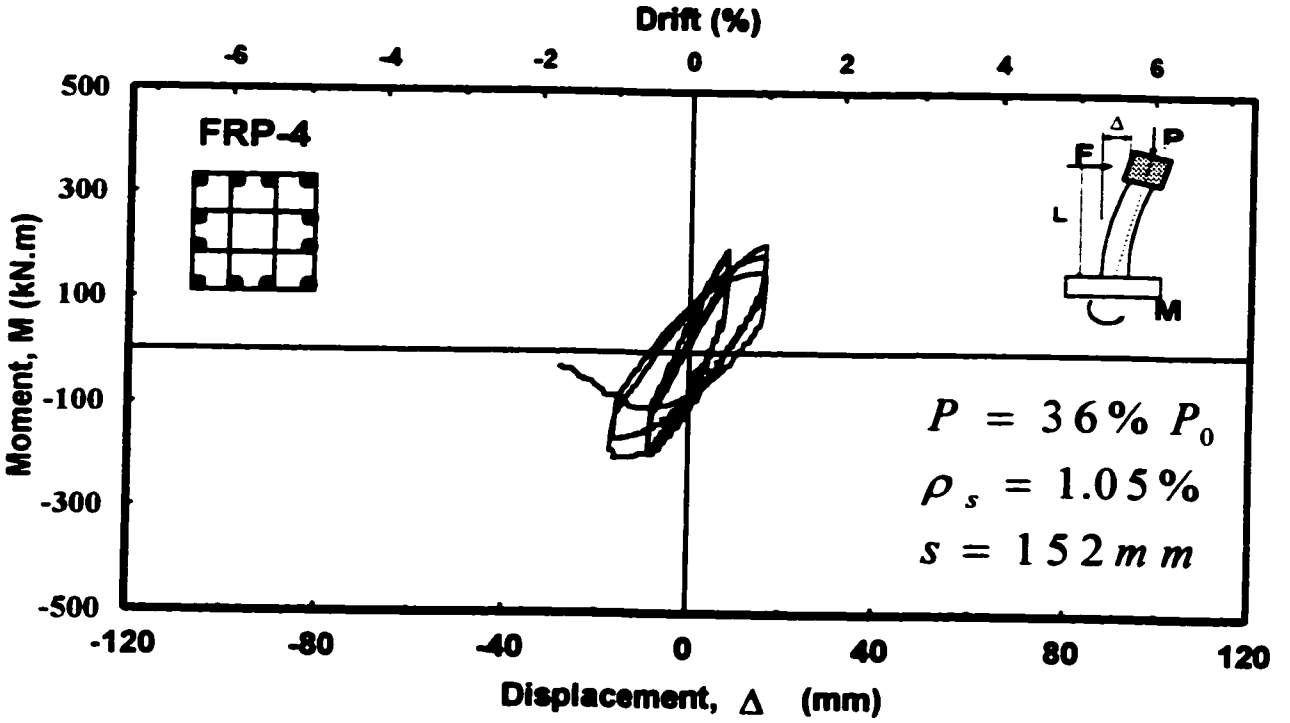

b) Hysteretic moment-displacement relationship

Figure 5-82: Hysteretic behavior of column FRP-4

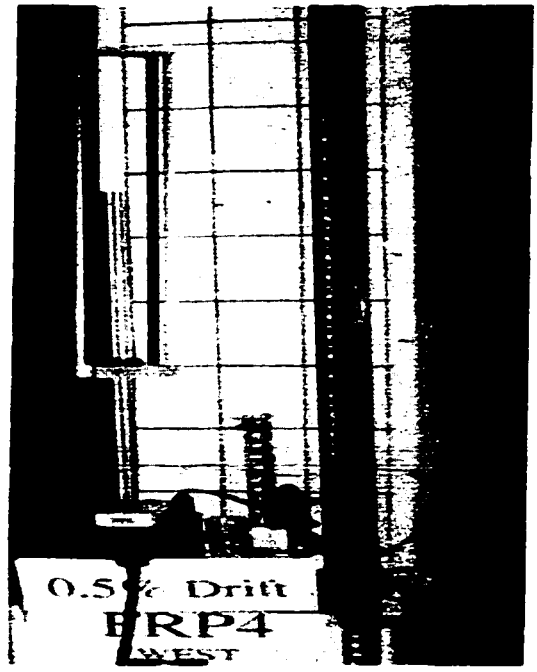

a) At 0.5% Drift

b) At 1% Drift (West Side)

c) At 1% Drift (East Side)

d) At end of test

Figure 5-83: Observed damage in column FRP-4 at selected stages of loading.

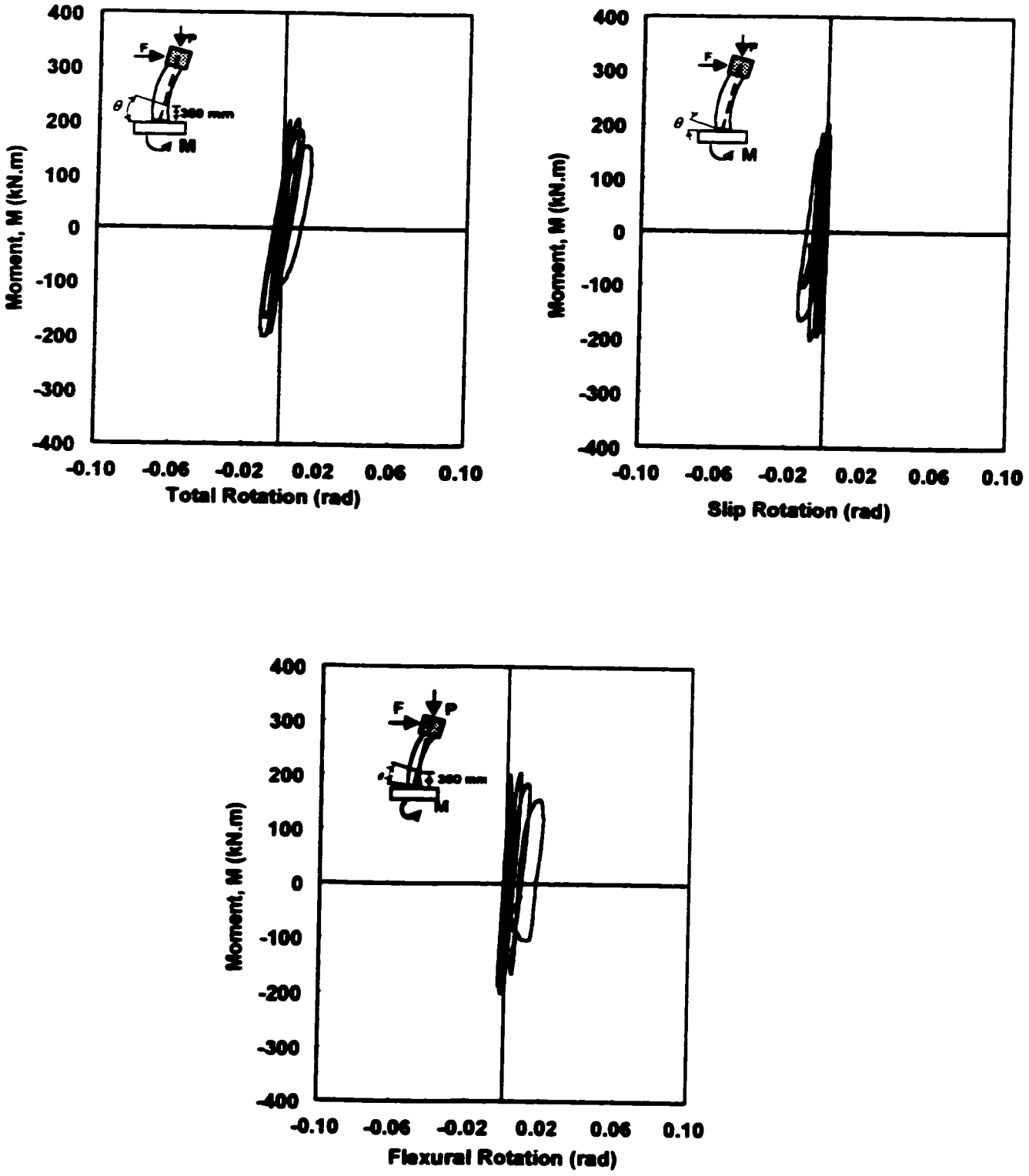

Figure 5-84: Moment-rotations relationships for column FRP-4

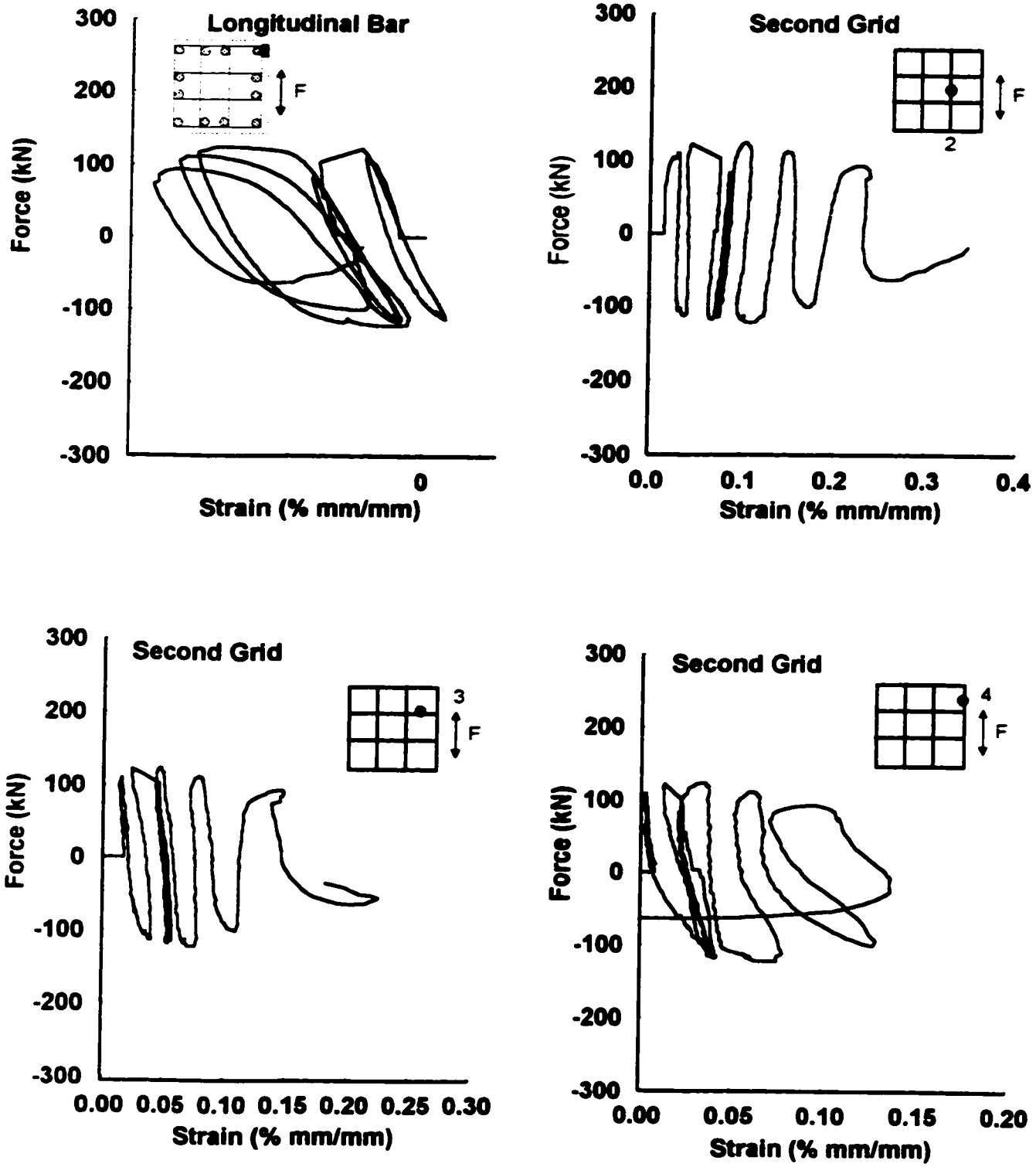

Figure 5-85: Reinforcement strain readings in Column FRP-4

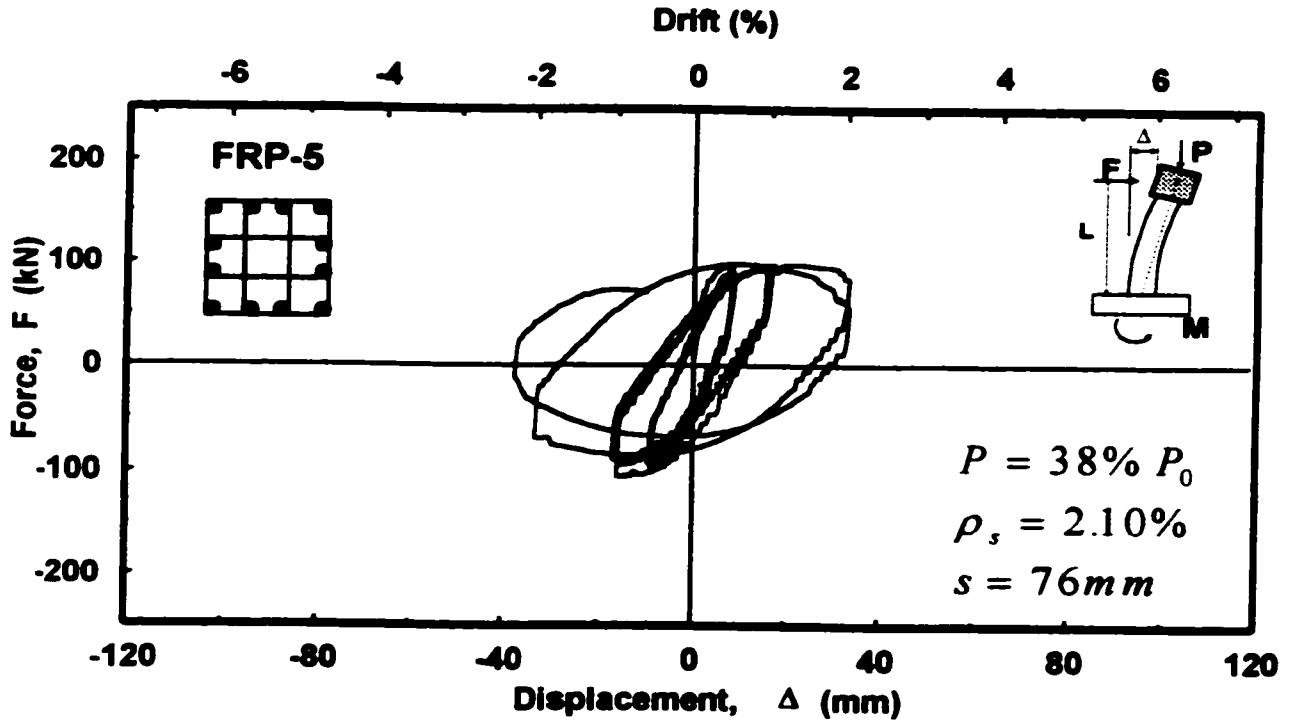

a) Hysteretic force-displacement relationship

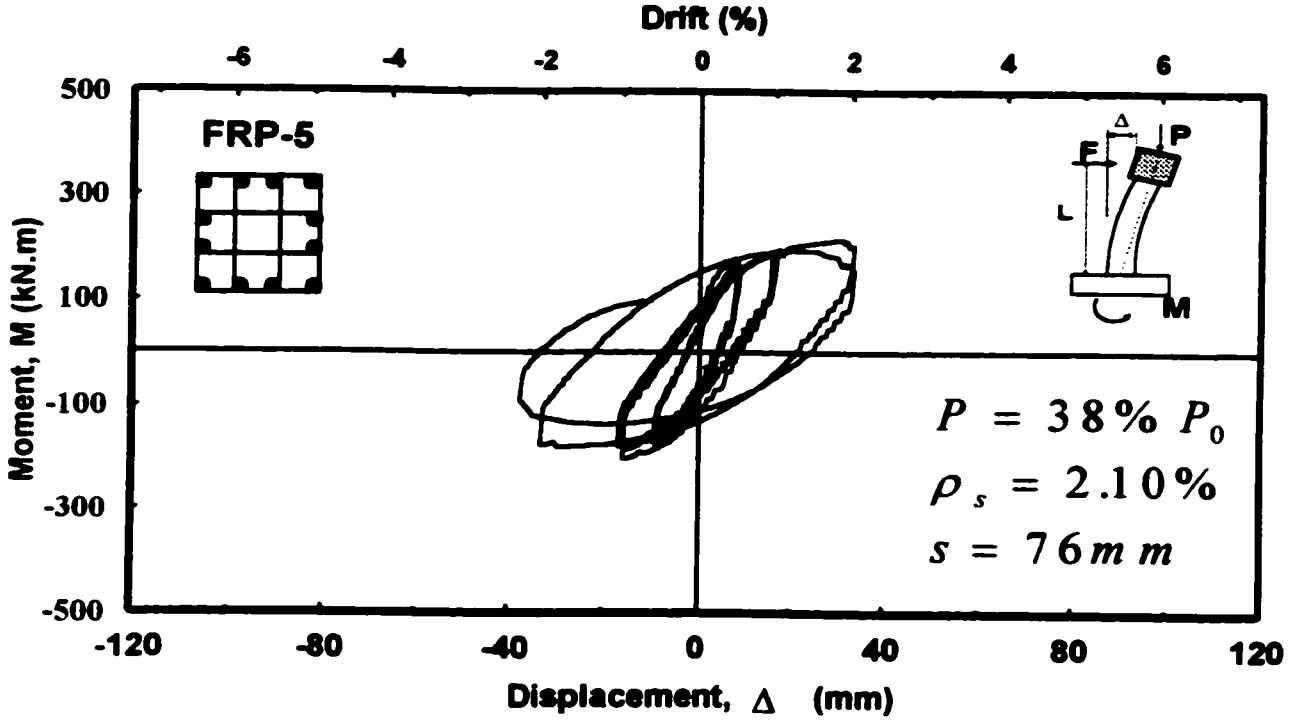

b) Hysteretic moment-displacement relationship

Figure 5-86: Hysteretic behavior of column FRP-5

a) At 1% Drift (West Side)

b) At 1% Drift (East Side)

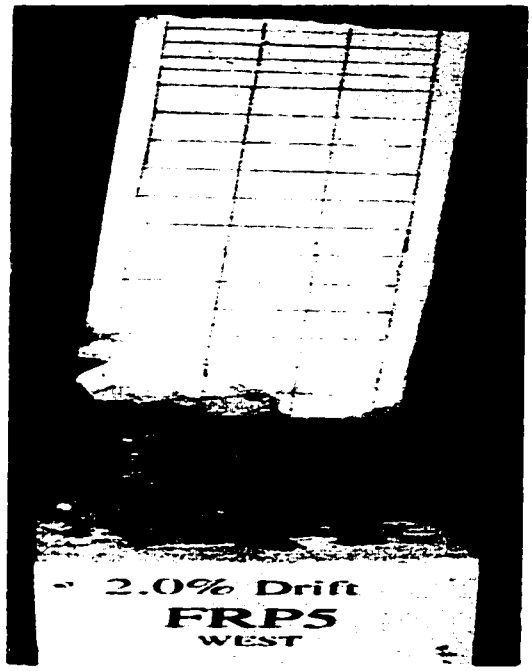

c) At 2% Drift (West Side)

d) At end of test

Figure 5-87: Observed damage in column FRP-5 at selected stages of loading.

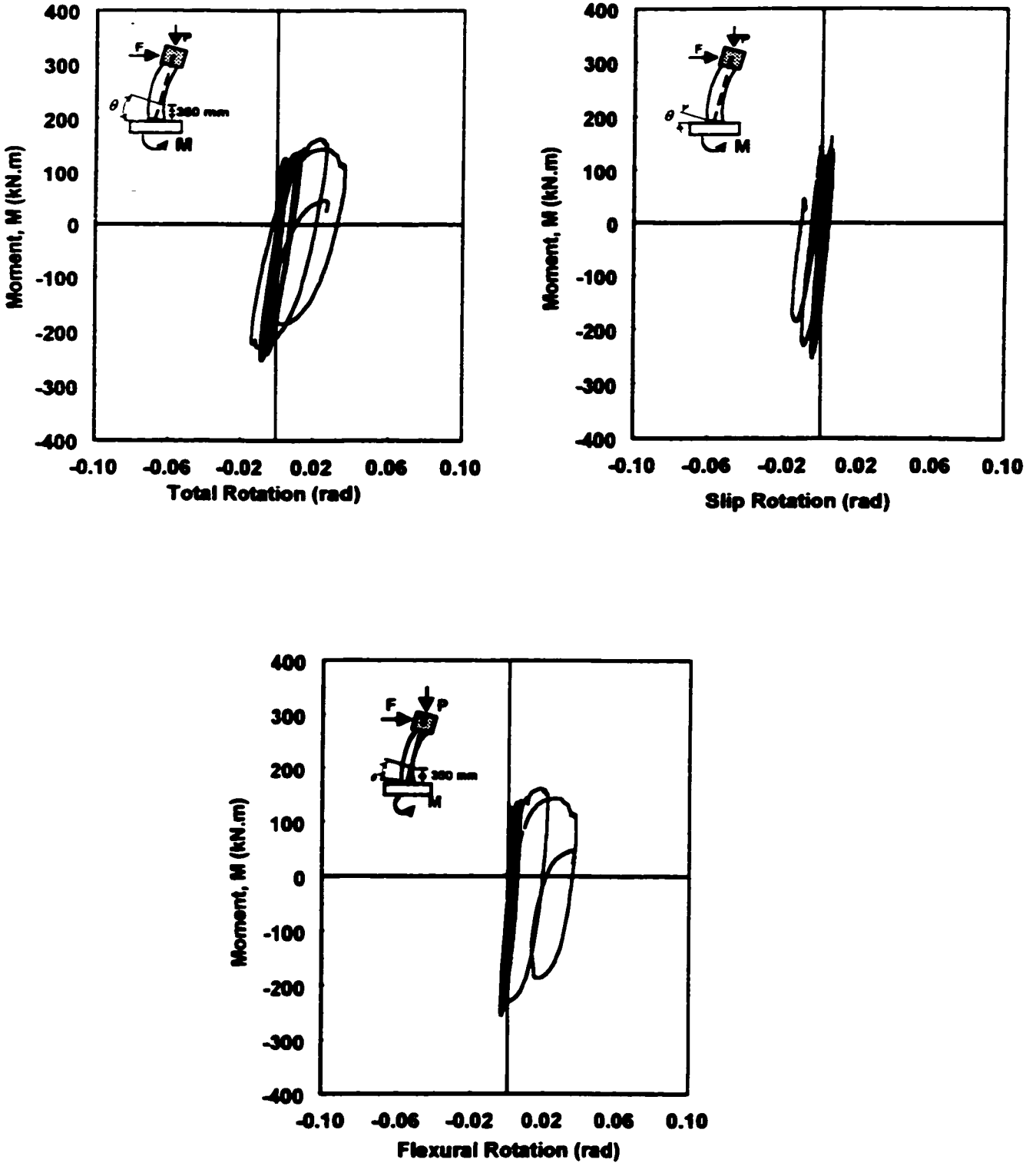

Figure 5-88: Moment-rotations relationships for column FRP-5

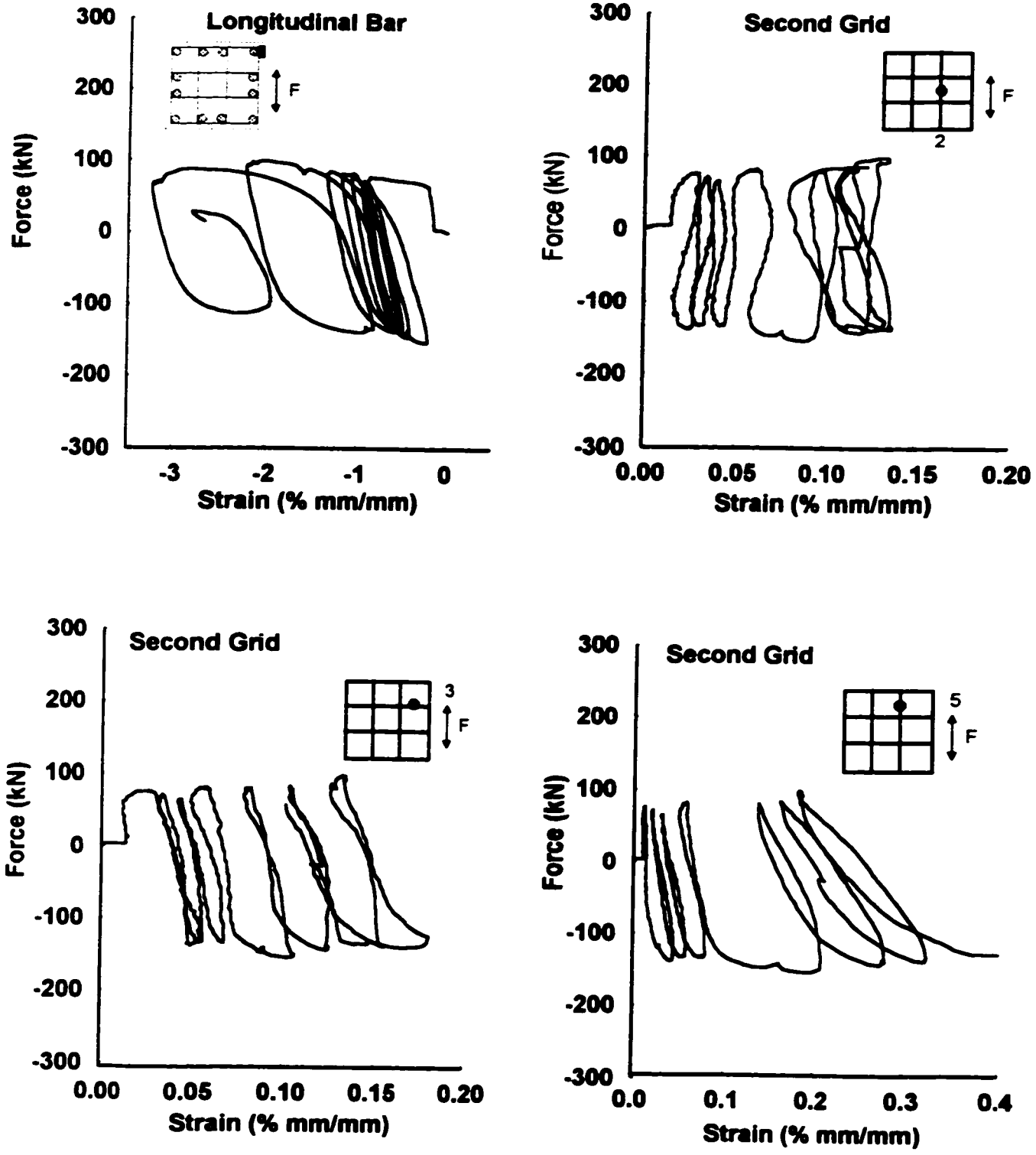

Figure 5-89: Reinforcement strain readings in Column FRP-5

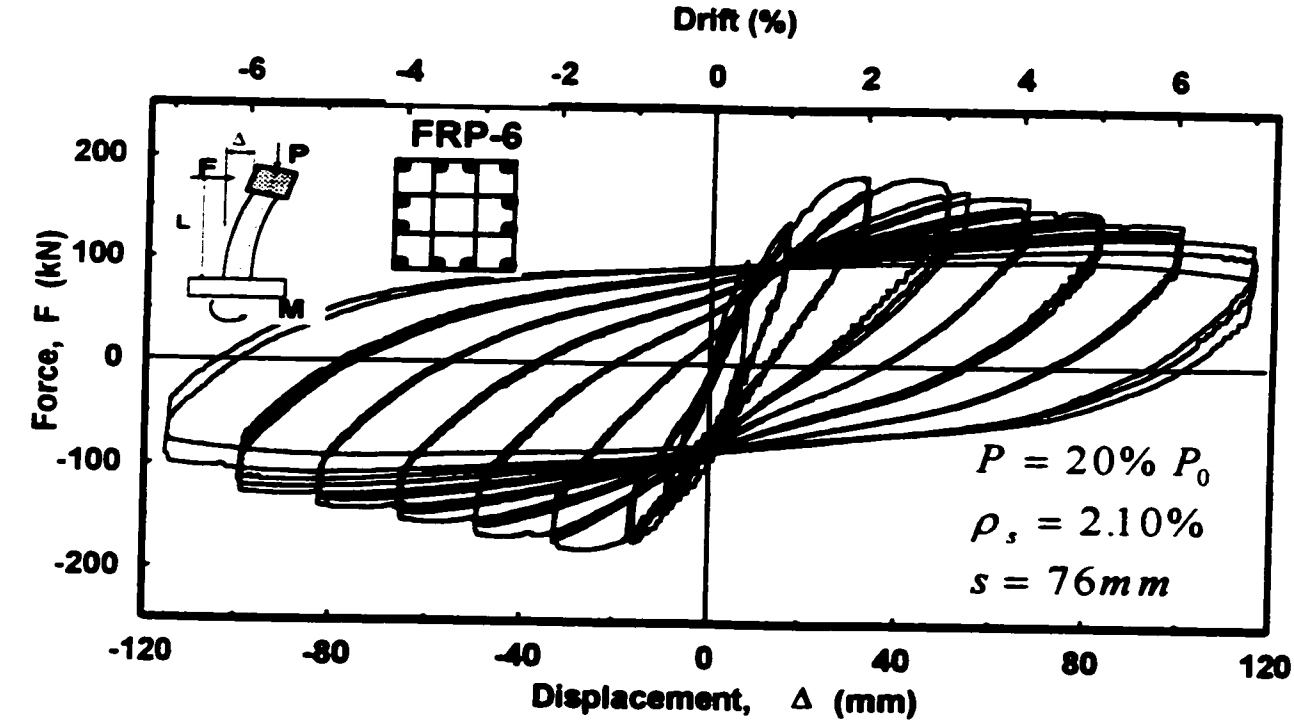

a) Hysteretic force-displacement relationship

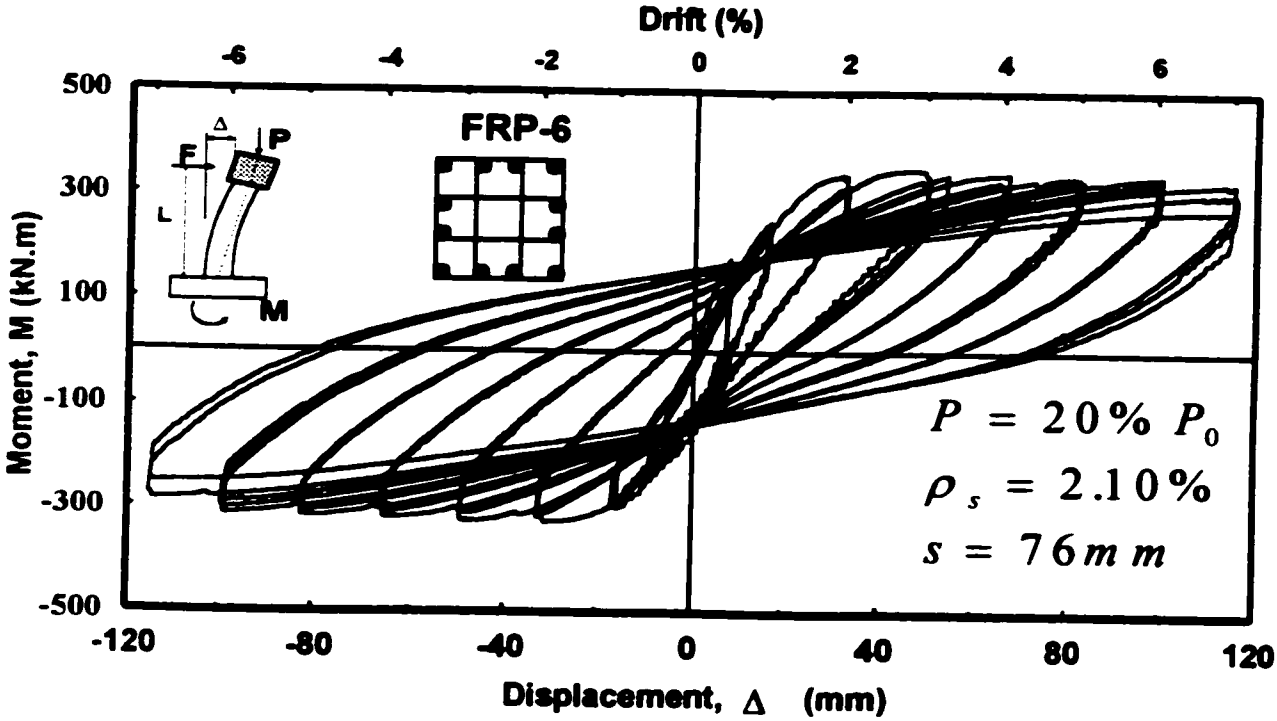

b) Hysteretic moment-displacement relationship

Figure 5-90: Hysteretic behavior of column FRP-6

a) At 1% Drift

b) At 3% Drift

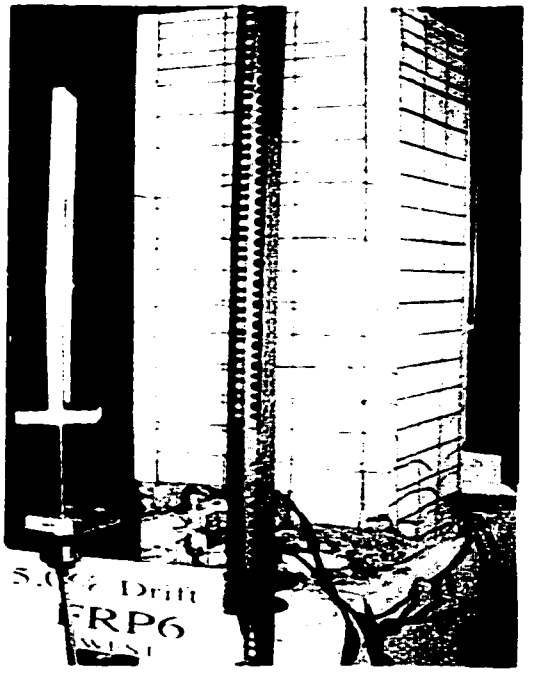

c) At 5% Drift

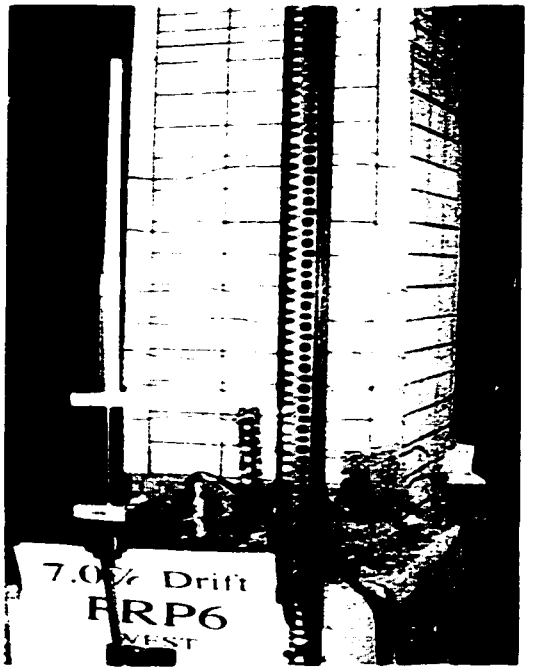

d) At 7% Drift

Figure 5-91: Observed damage in column FRP-6 at selected stages of loading.

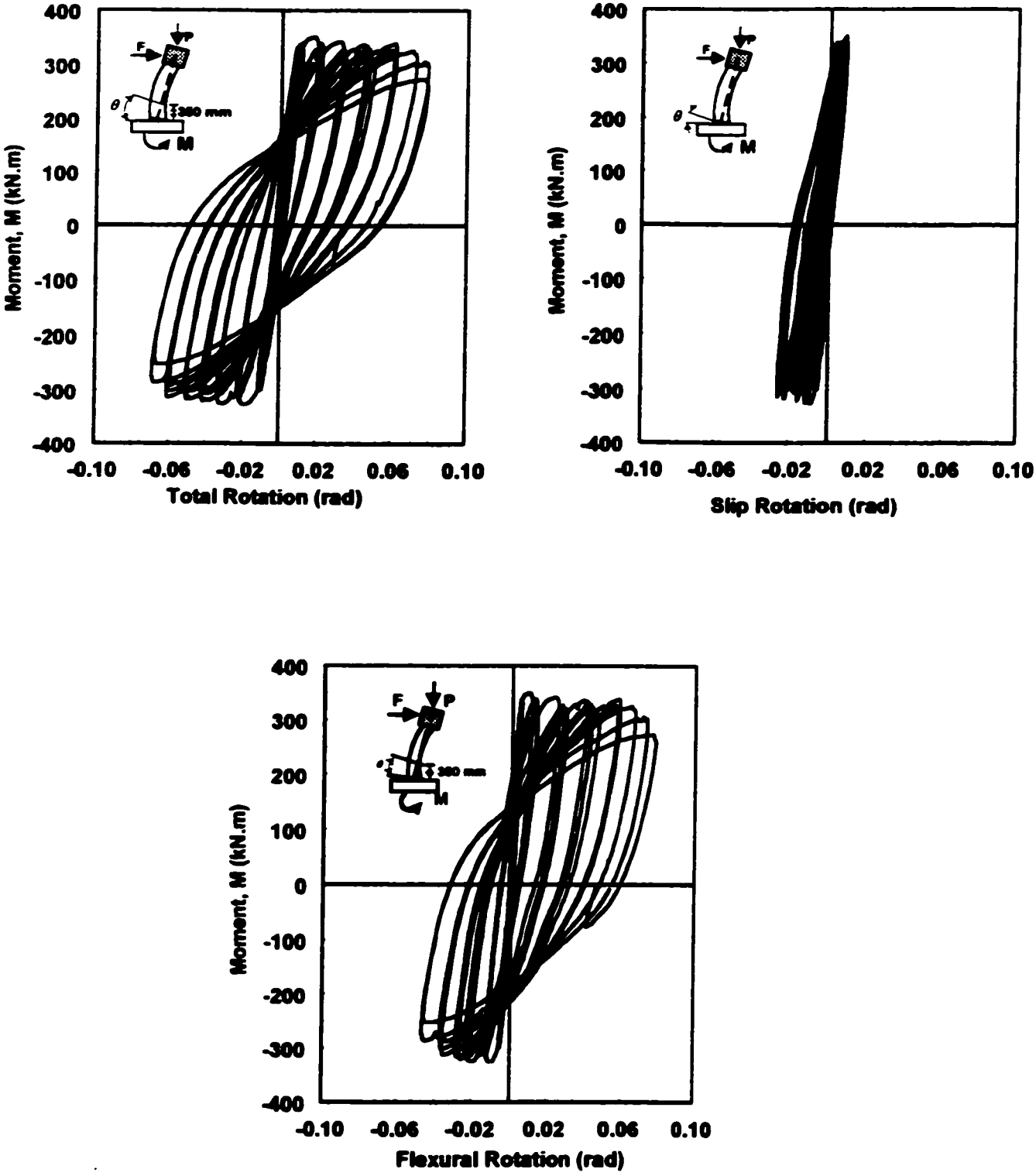

Figure 5-92: Moment-rotations relationships for column FRP-6

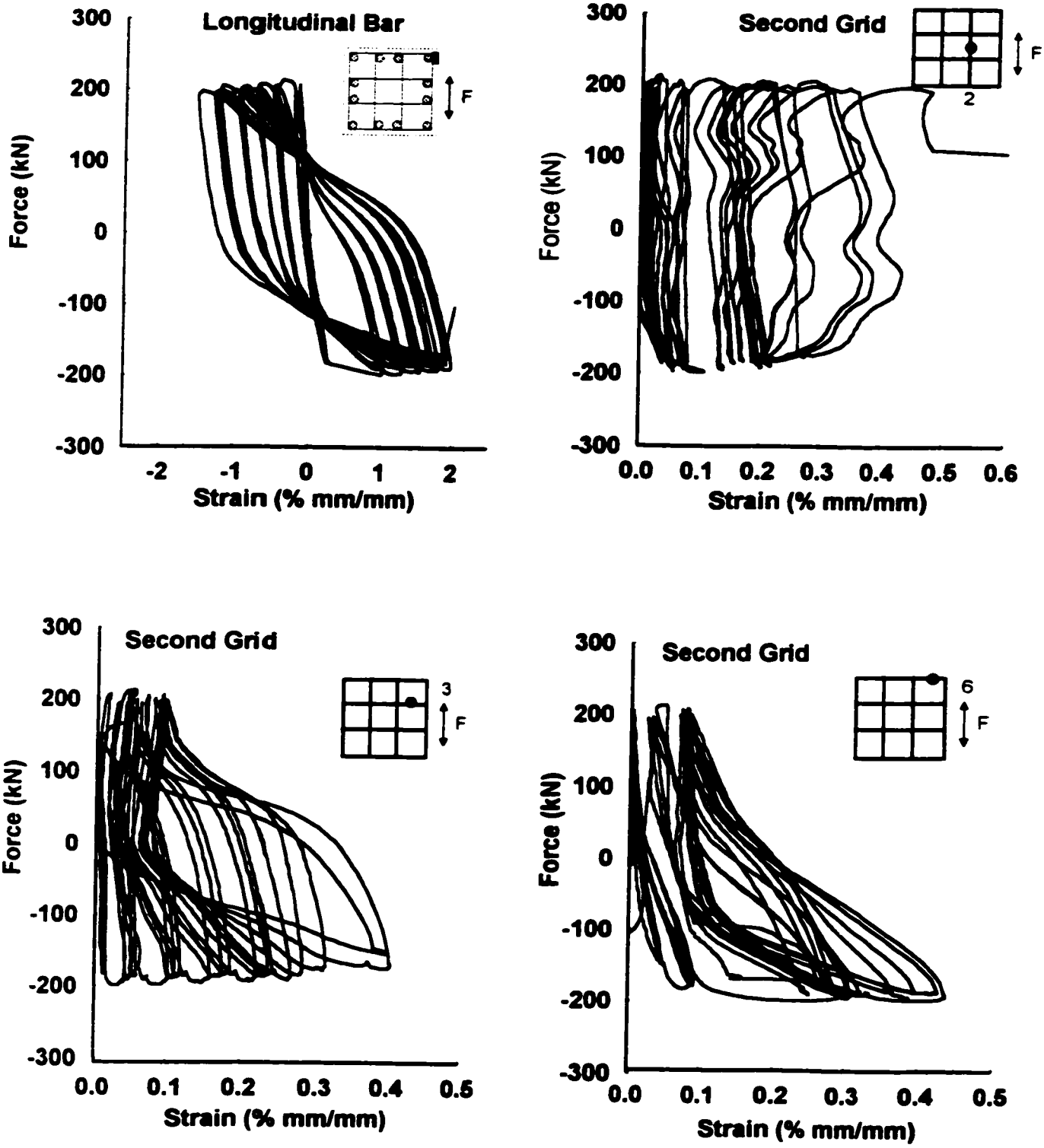

Figure 5-93: Reinforcement strain readings in Column FRP-6

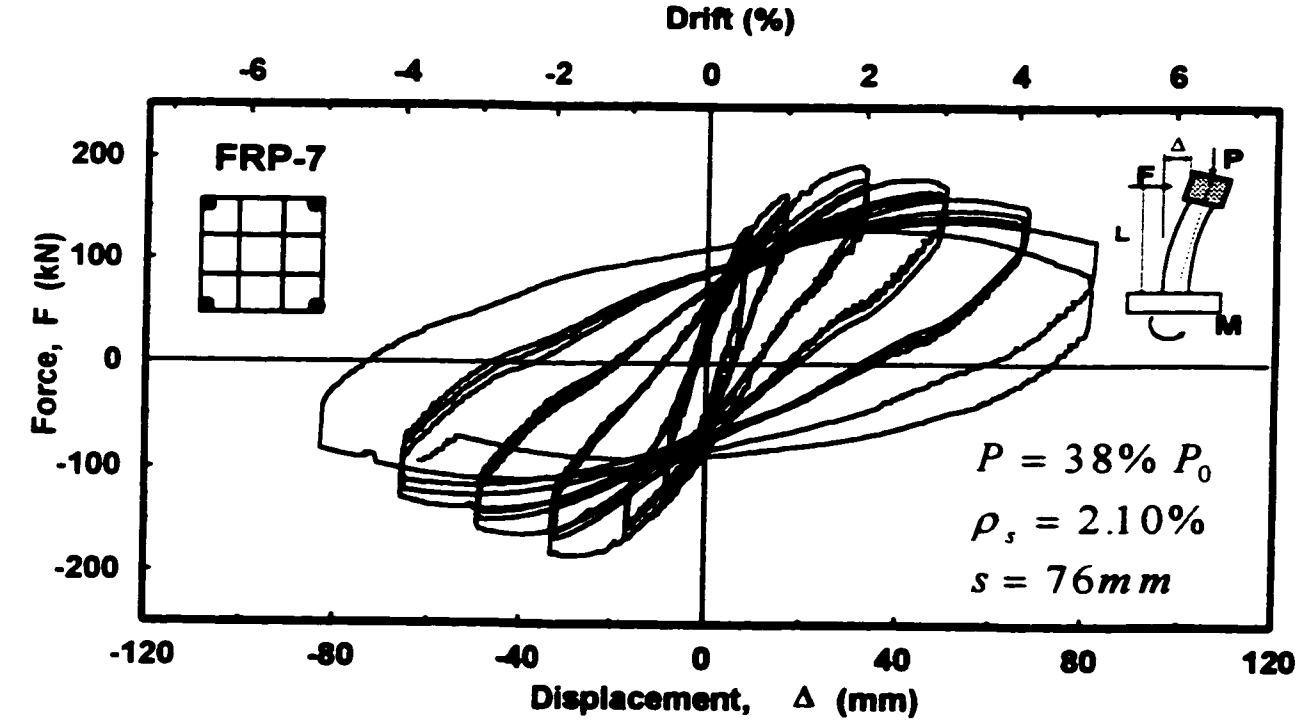

a) Hysteretic force-displacement relationship

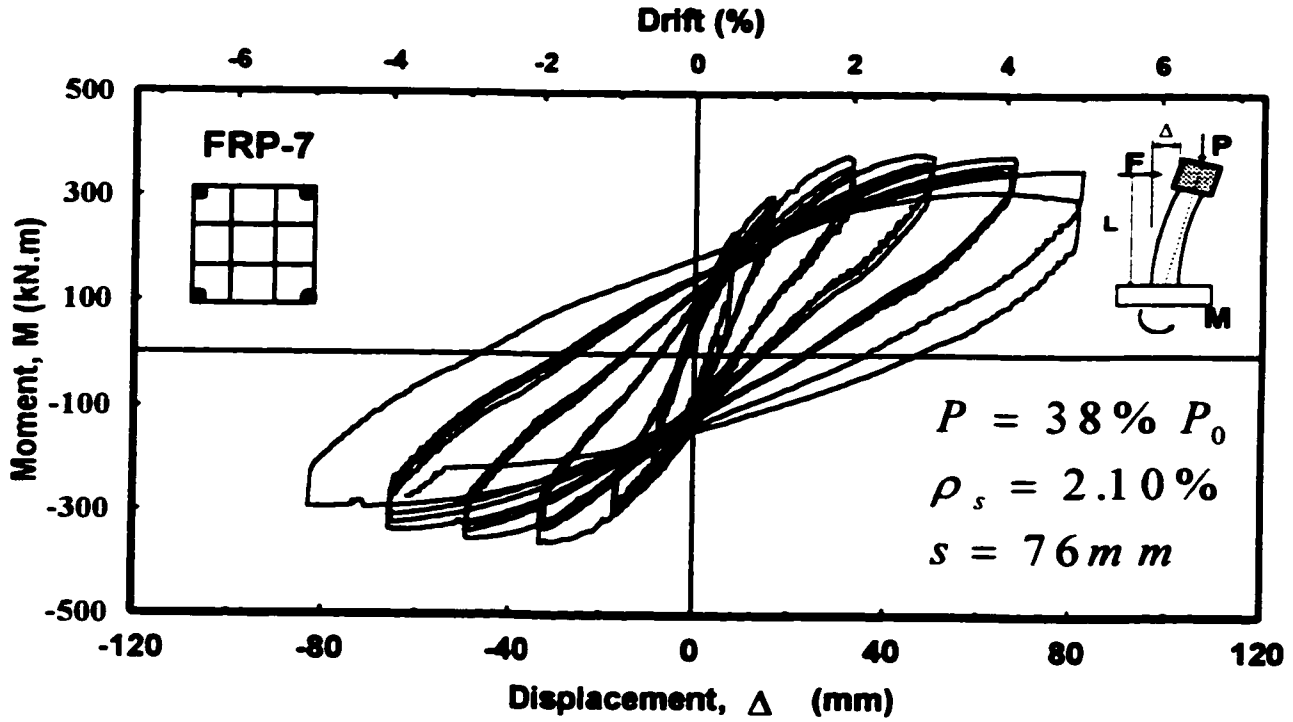

b) Hysteretic moment-displacement relationship

Figure 5-94: Hysteretic behavior of column FRP-7

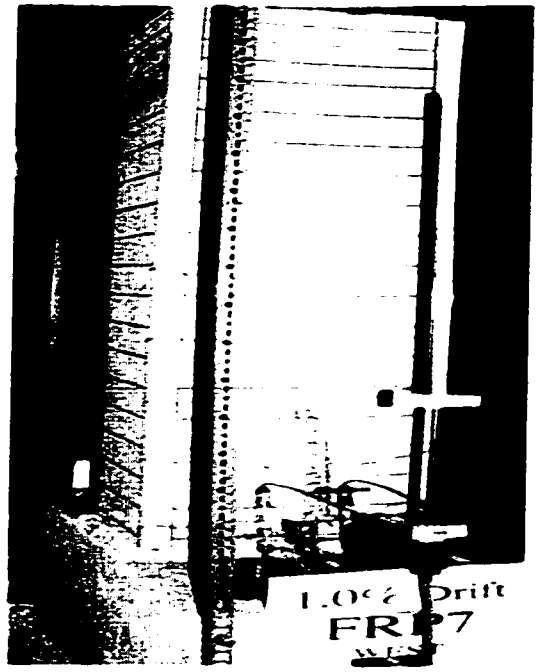

a) At 1% Drift

b) At 3% Drift

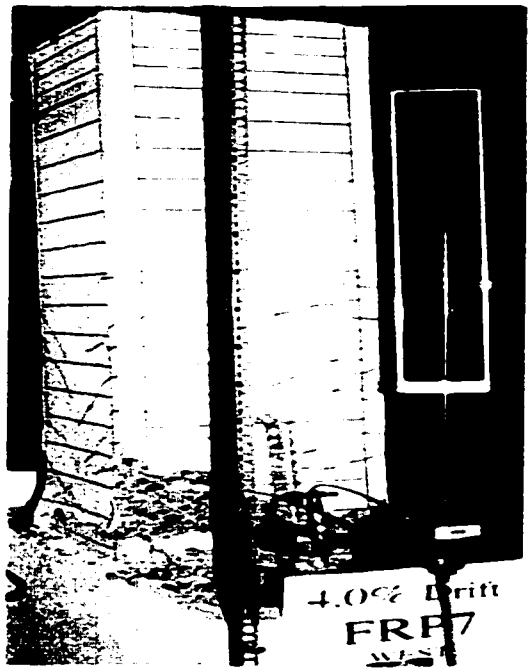

c) At 4% Drift

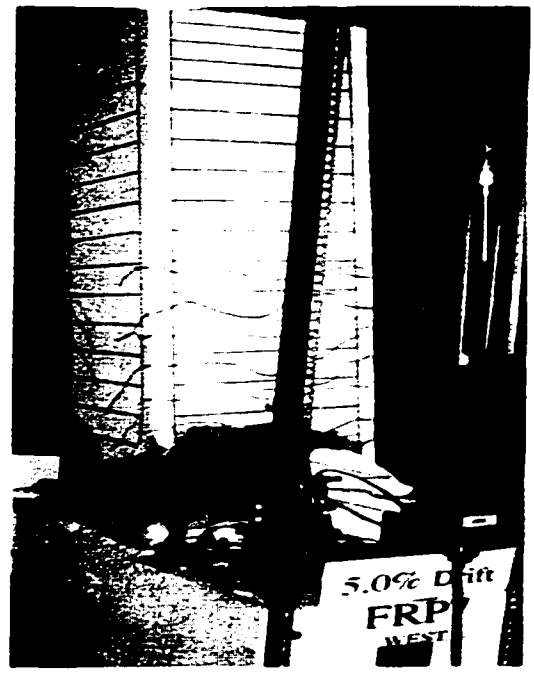

d) At 5% Drift

Figure 5-95: Observed damage in column FRP-7 at selected stages of loading.

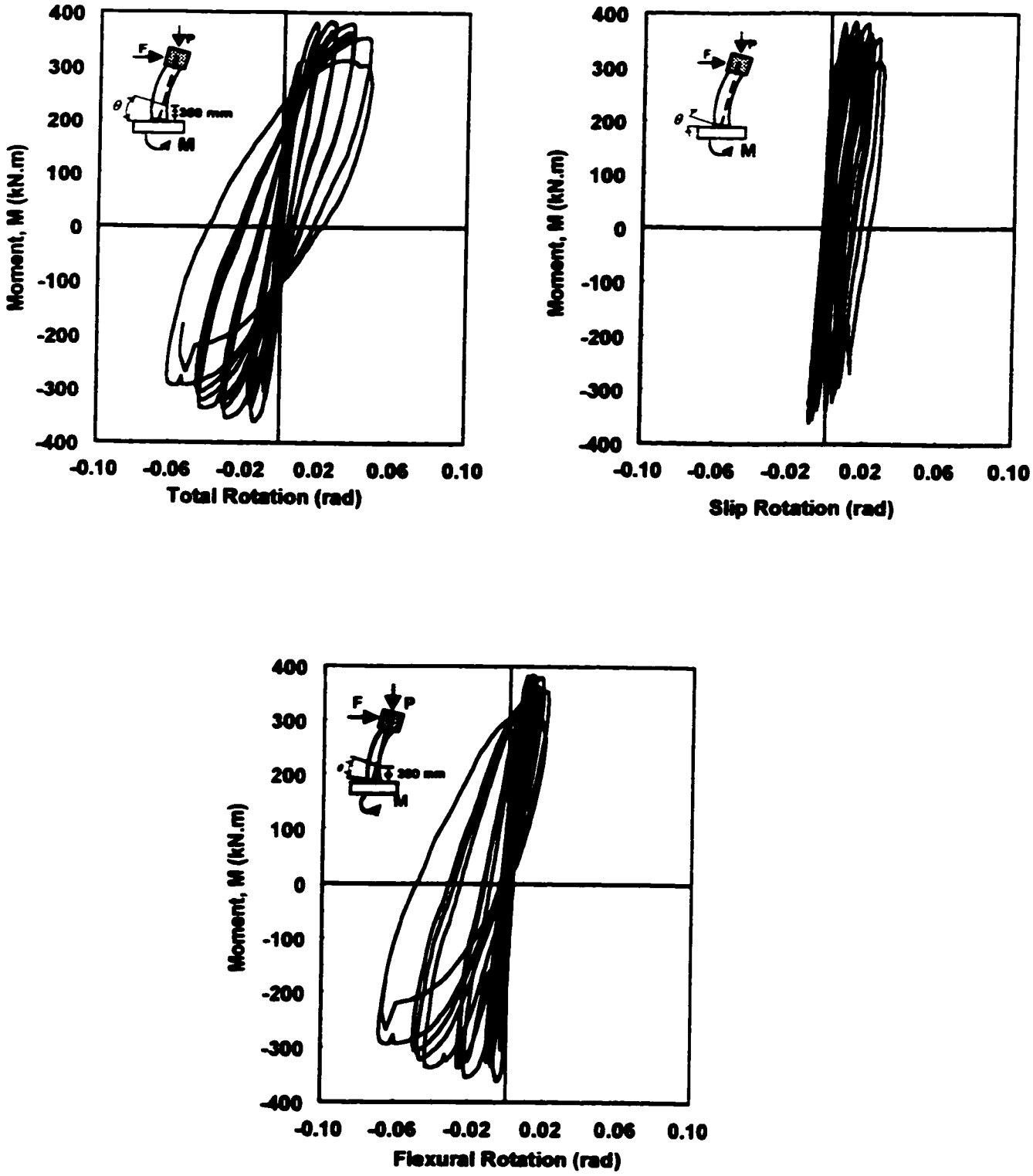

Figure 5-96: Moment-rotations relationships for column FRP-7

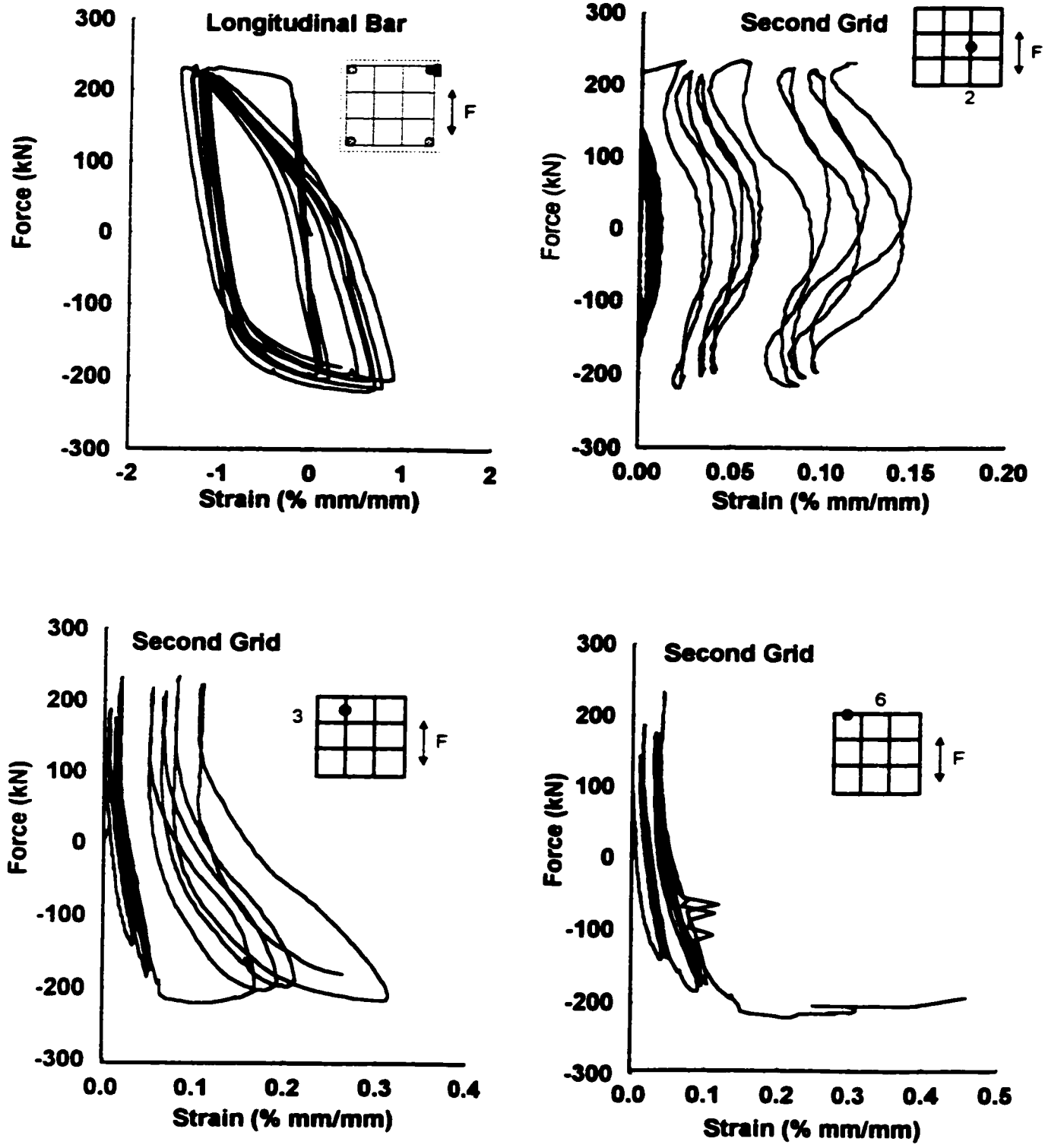

Figure 5-97: Reinforcement strain readings in Column FRP-7

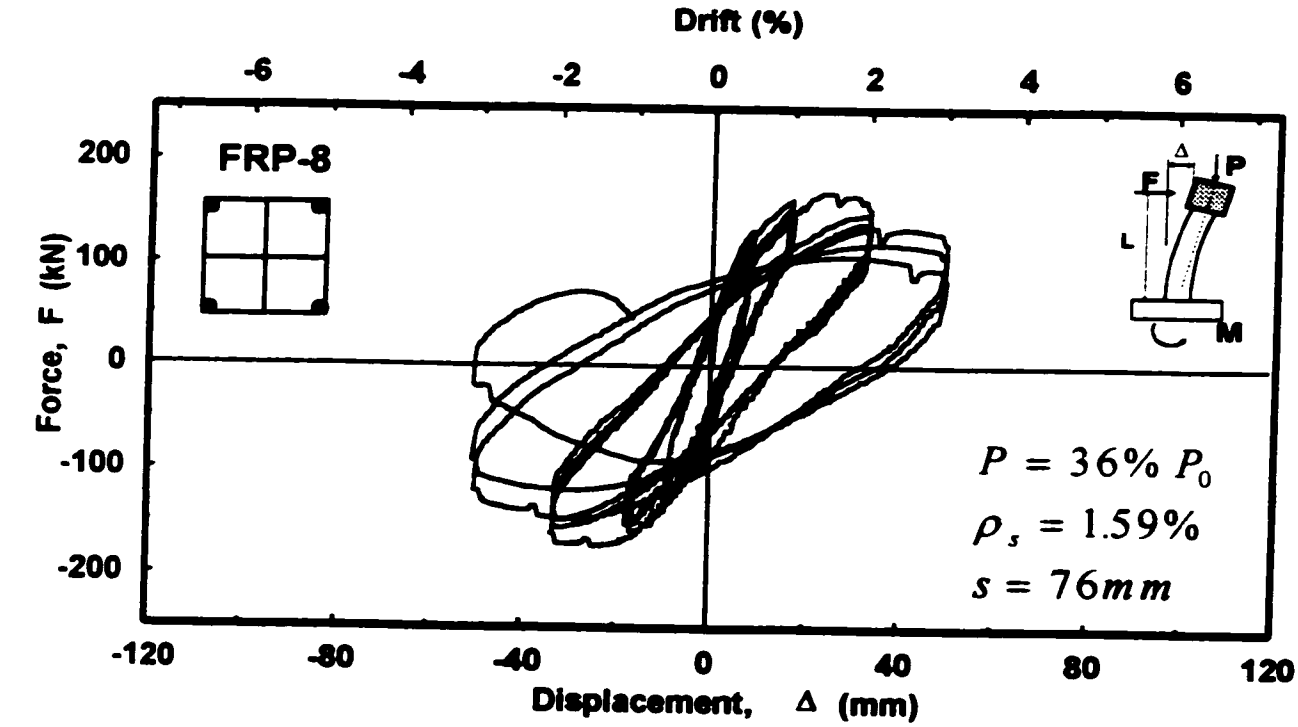

a) Hysteretic force-displacement relationship

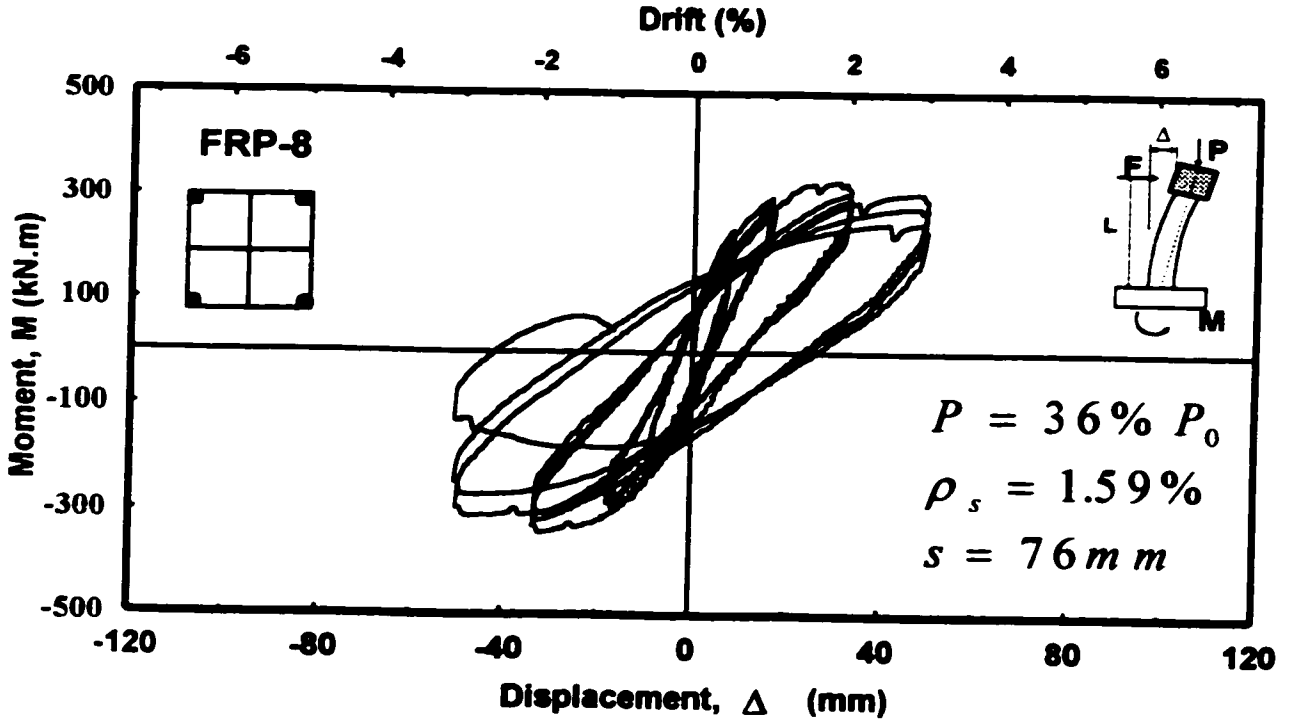

b) Hysteretic moment-displacement relationship

Figure 5-98: Hysteretic behavior of column FRP-8

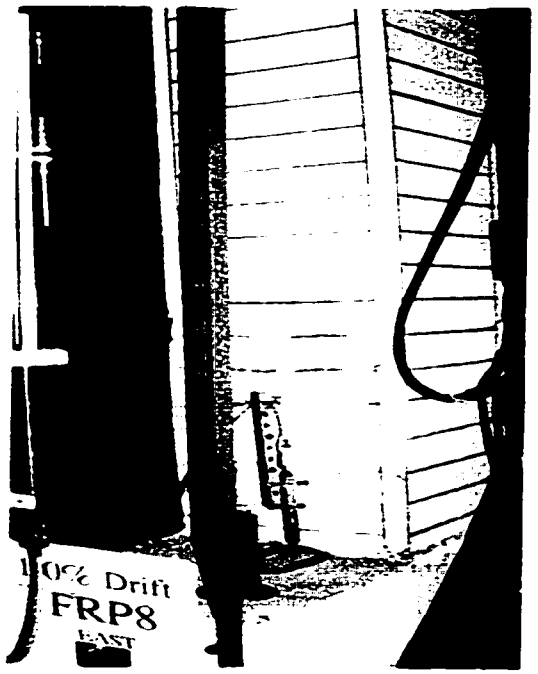

a) At 1% Drift

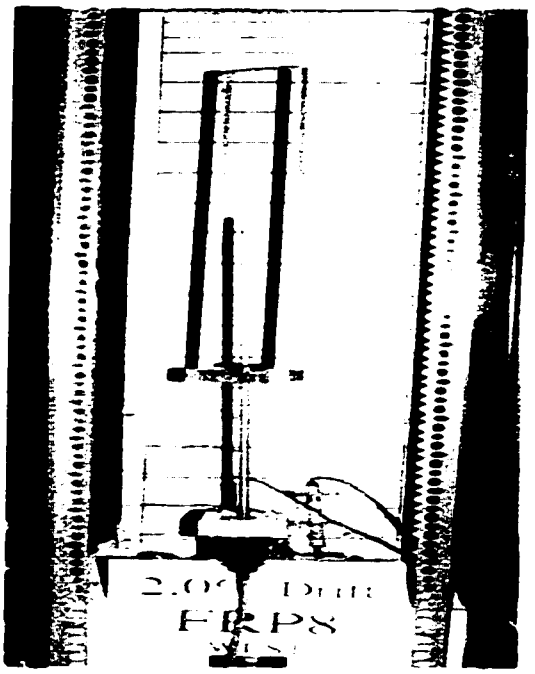

b) At 2% Drift

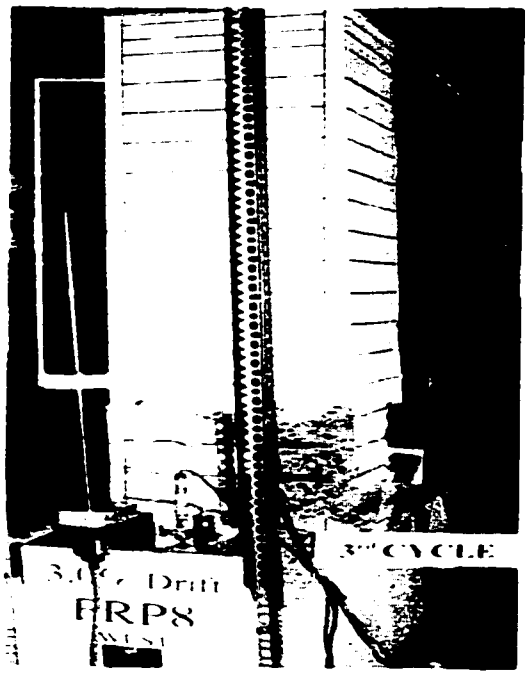

c) At 3% Drift

d) At end of test

Figure 5-99: Observed damage in column FRP-8 at selected stages of loading.

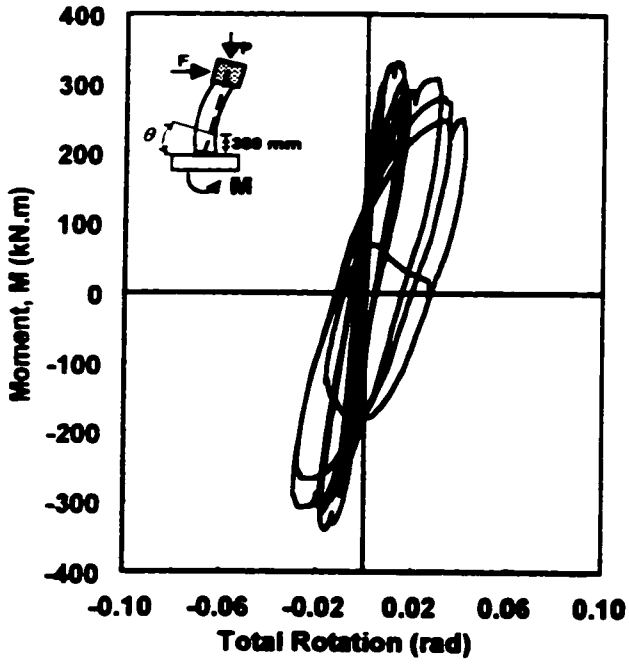

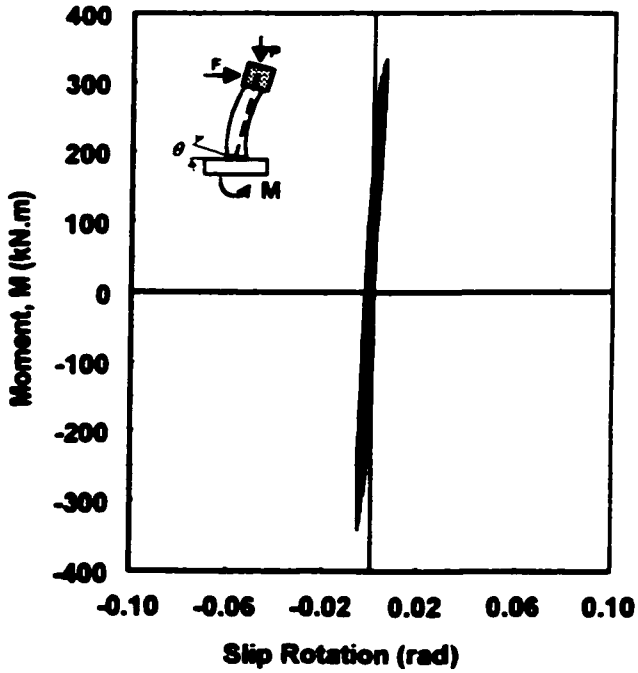

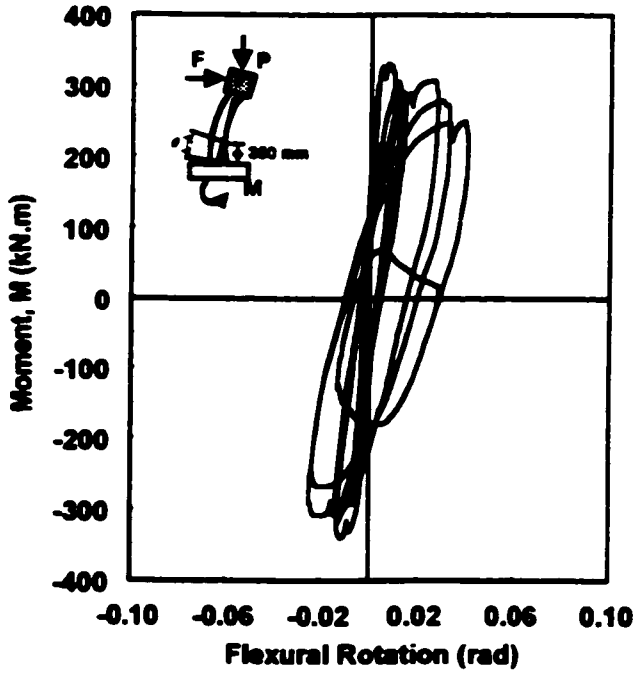

Figure 5-100: Moment-rotations relationships for column FRP-8

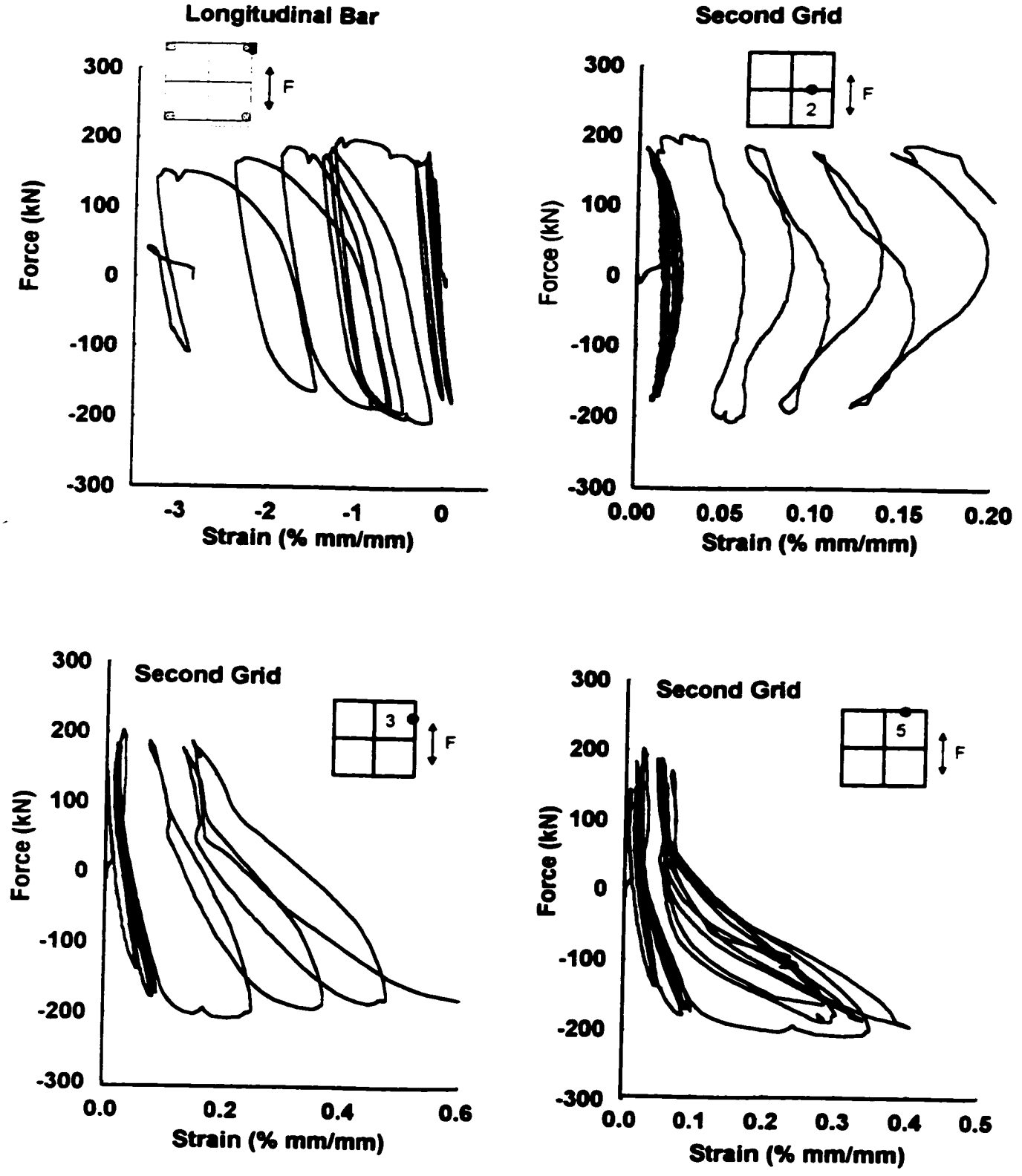

Figure 5-101: Reinforcement strain readings in Column FRP-8

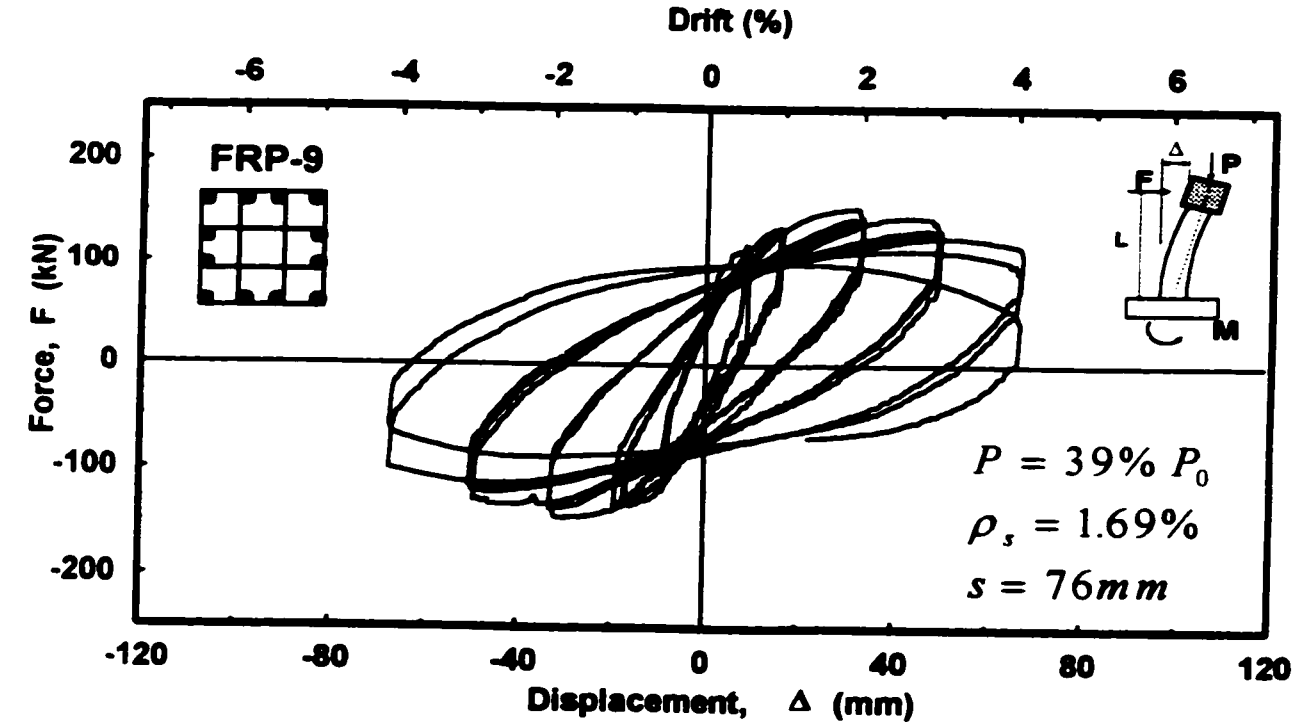

a) Hysteretic force-displacement relationship

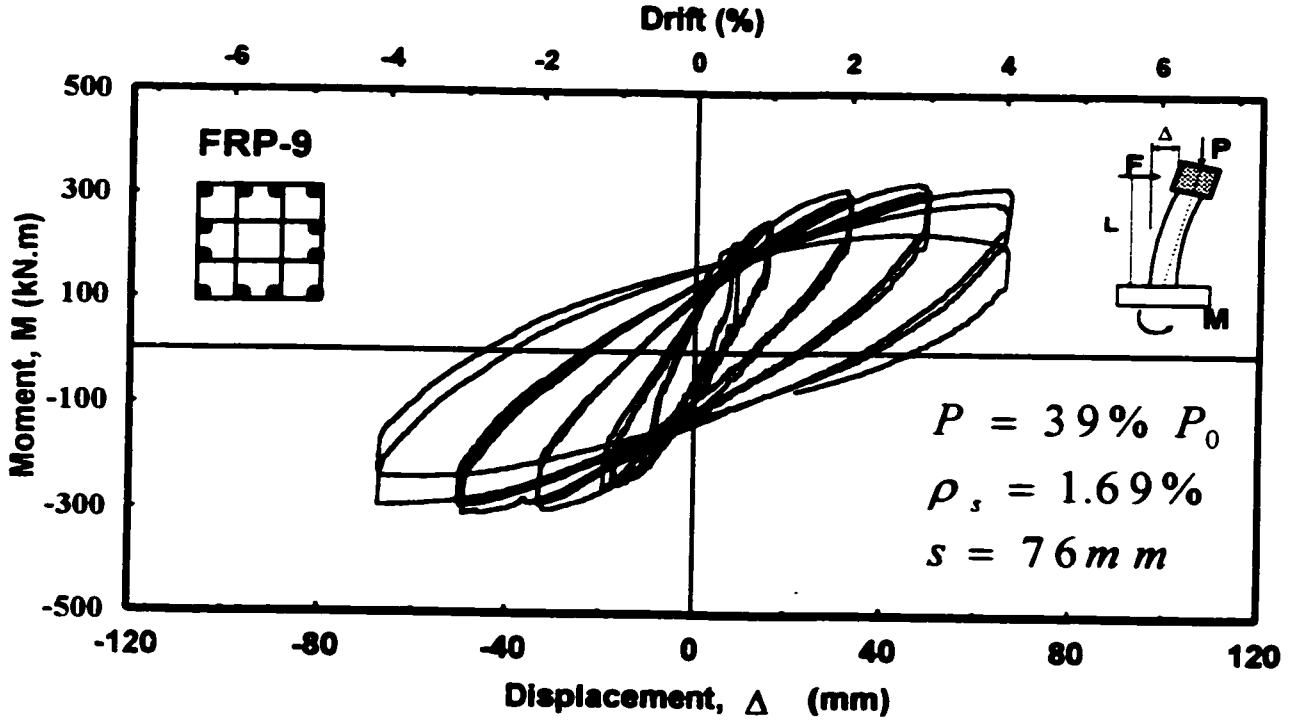

b) Hysteretic moment-displacement relationship

Figure 5-102: Hysteretic behavior of column FRP-9

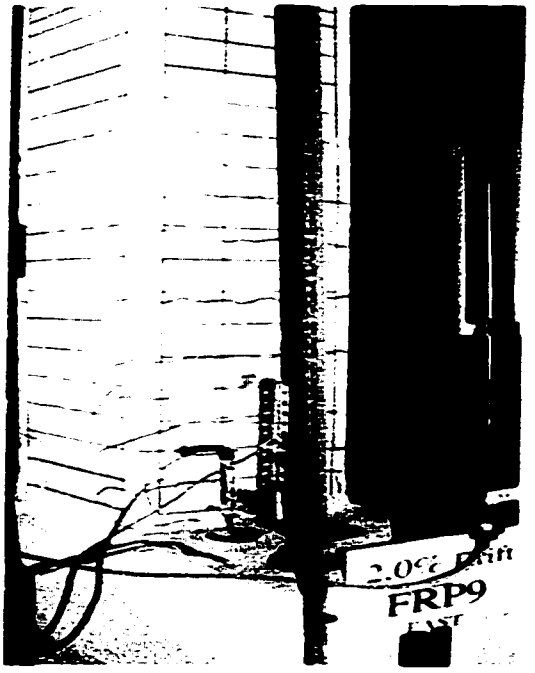

a) At 2% Drift

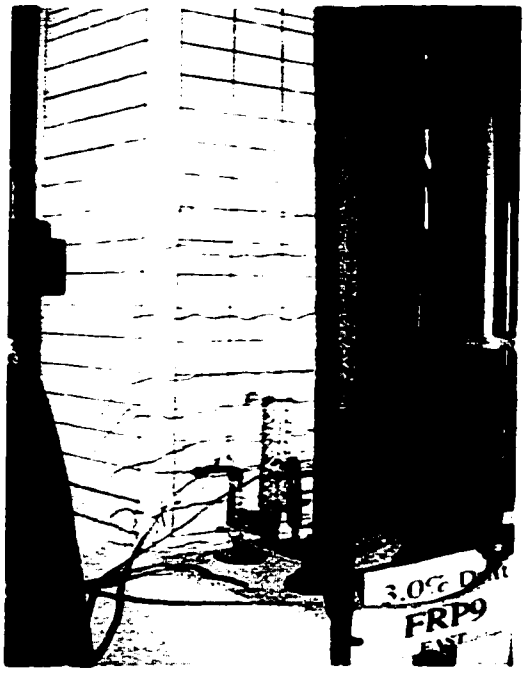

b) At 3% Drift

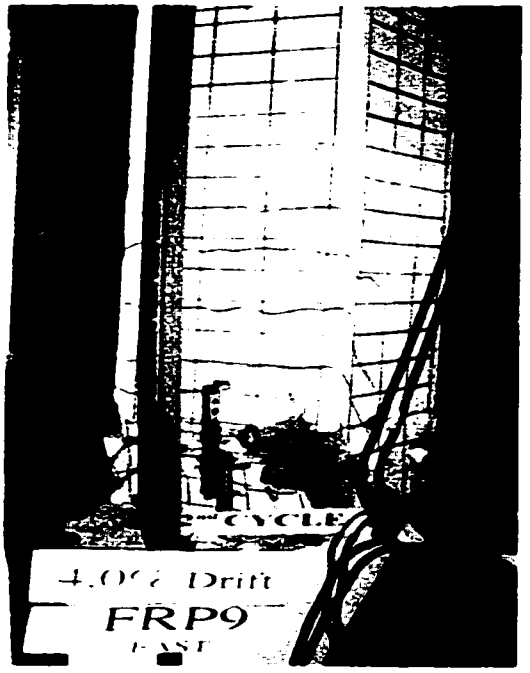

c) At 4% Drift (East Side)

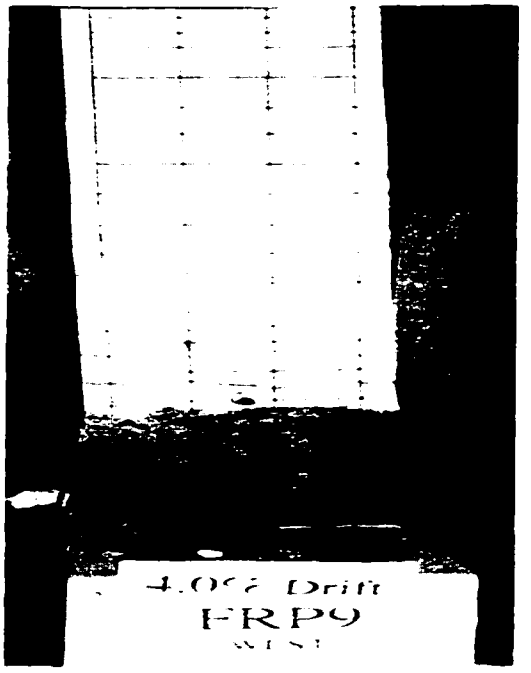

d) At 4% Drift (West Side)

Figure 5-103: Observed damage in column FRP-9 at selected stages of loading.

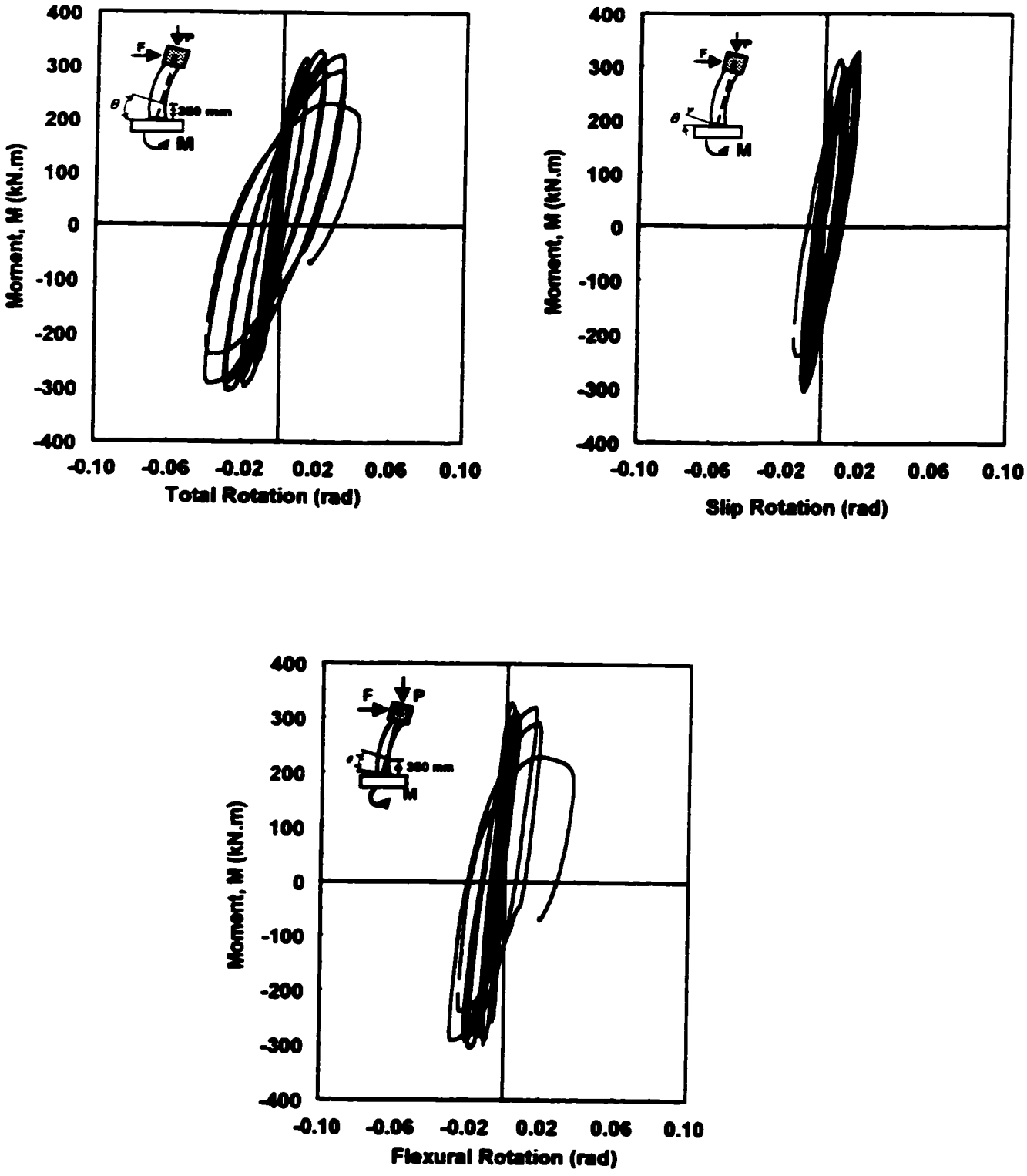

Figure 5-104: Moment-rotations relationships for column FRP-9

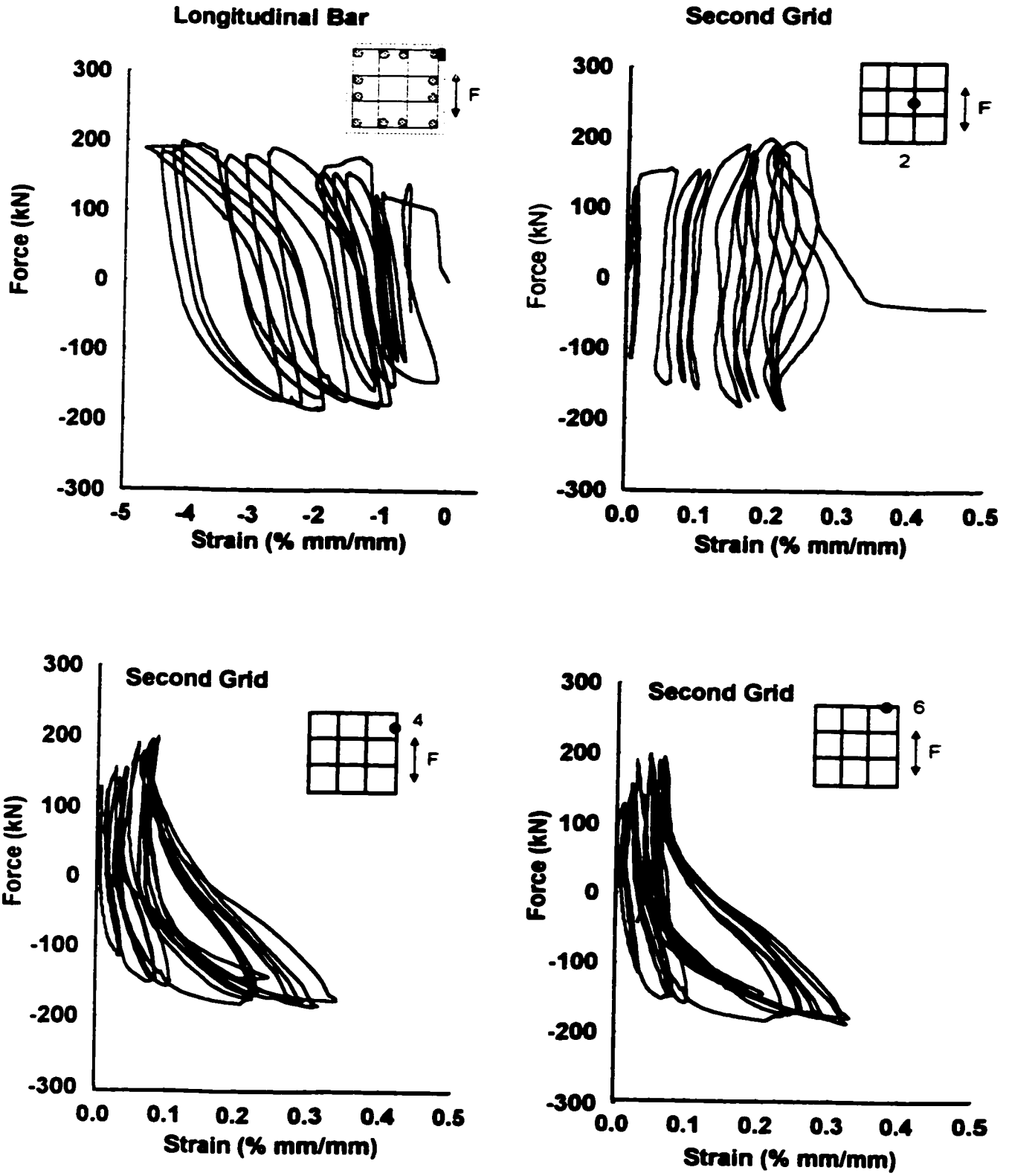

Figure 5-105: Reinforcement strain readings in Column FRP-9

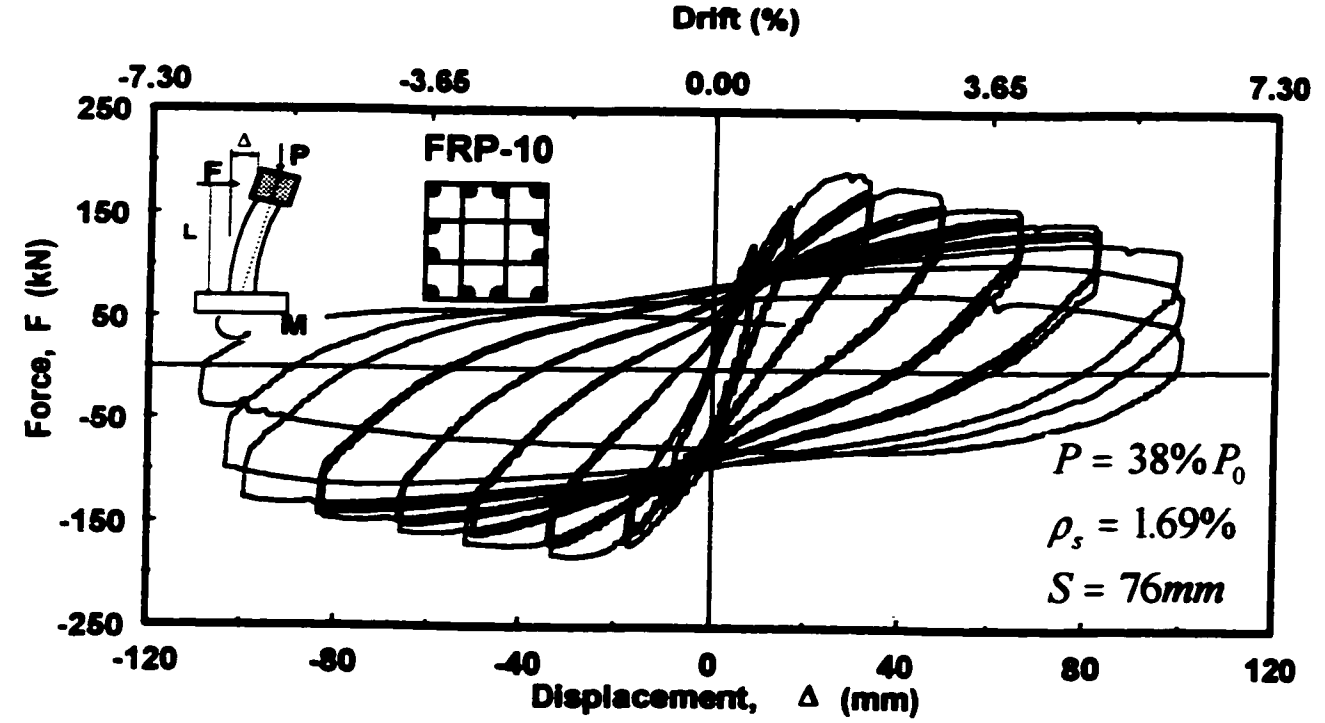

a) Hysteretic force-displacement relationship

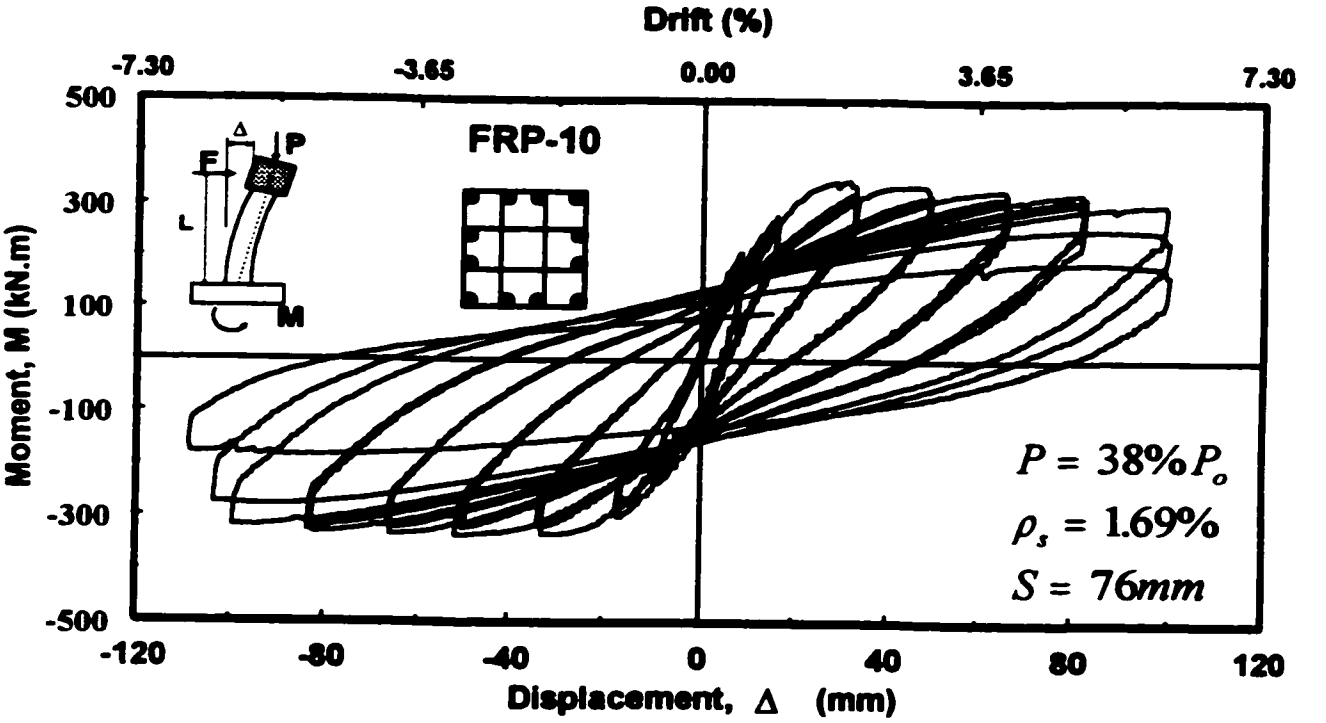

b) Hysteretic moment-displacement relationship

Figure 5-106: Hysteretic behavior of column FRP-10

a) At 3% Drift

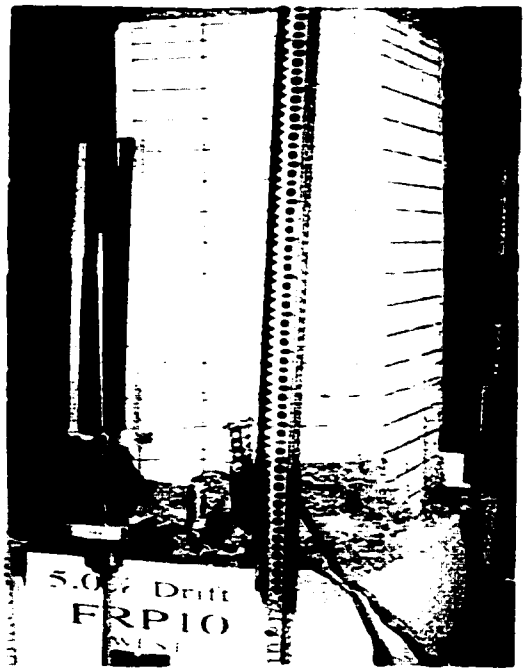

b) At 5% Drift

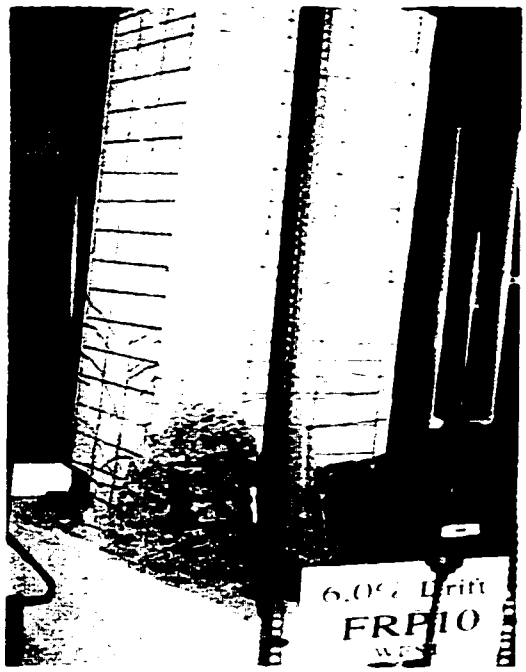

c) At 6% Drift

d) At end of test

Figure 5-107: Observed damage in column FRP-10 at selected stages of loading.

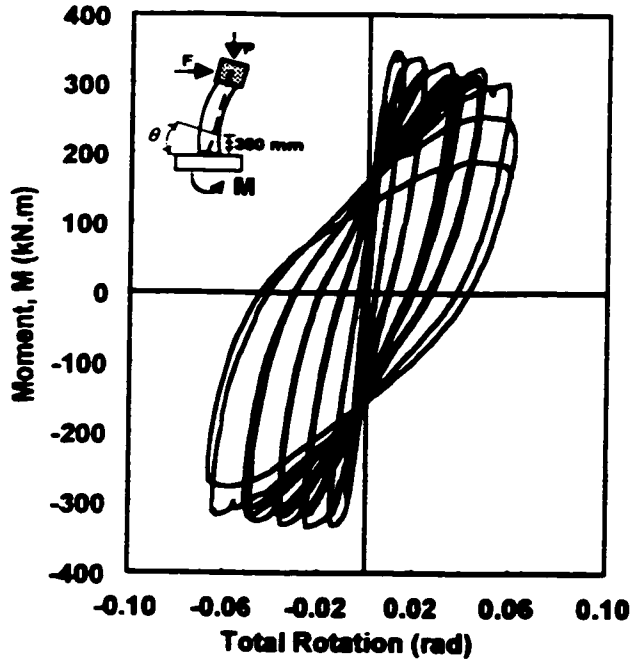

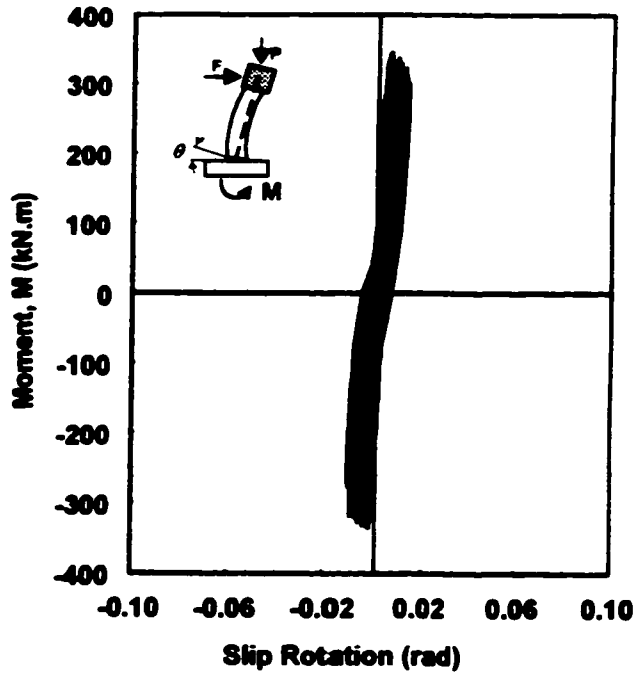

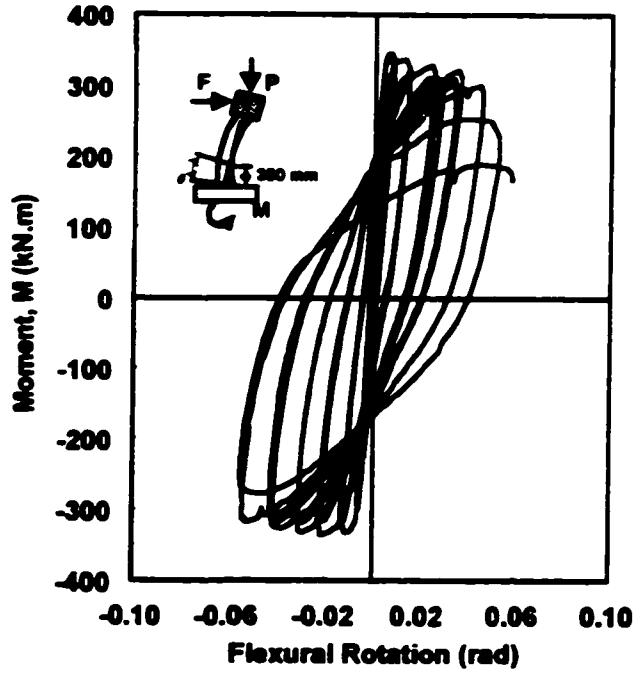

Figure 5-108: Moment-rotations relationships for column FRP-10

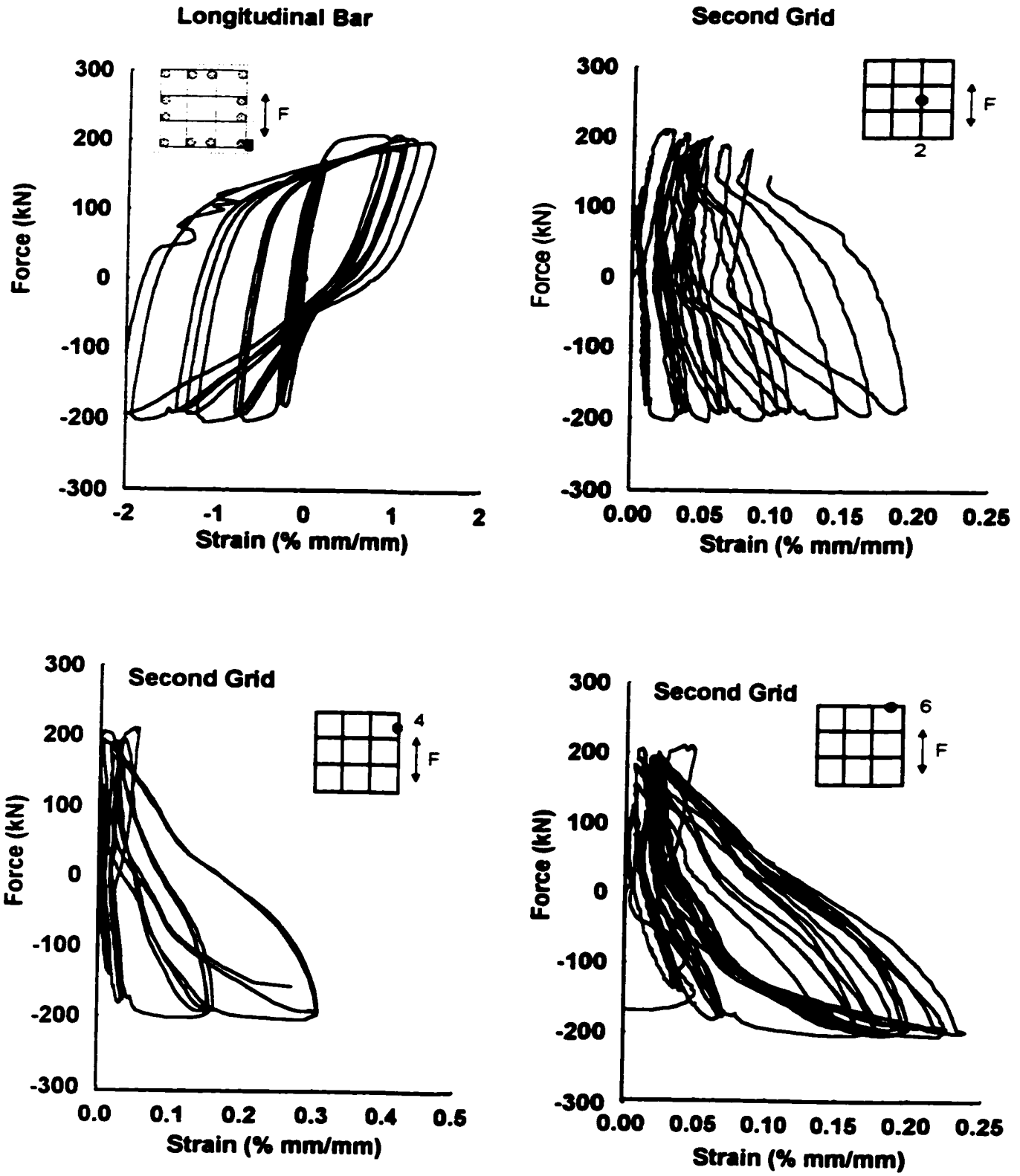

Figure 5-109: Reinforcement strain readings in Column FRP-10

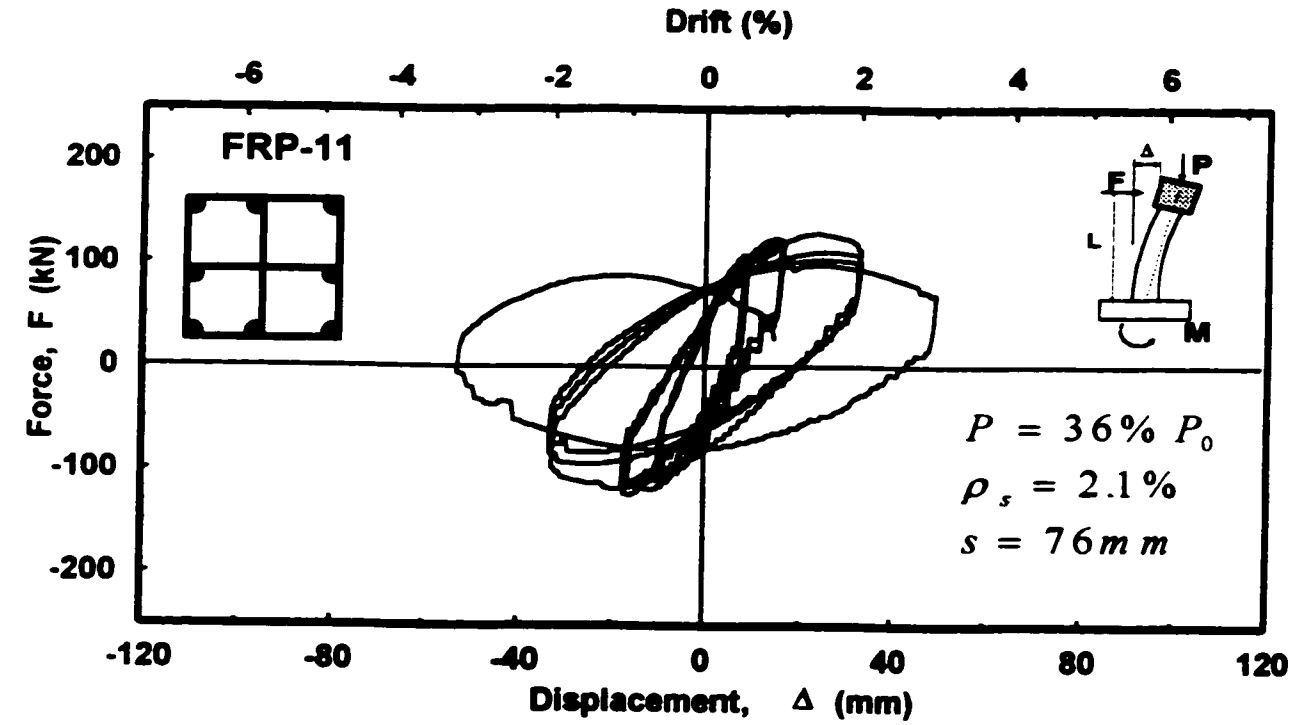

a) Hysteretic force-displacement relationship

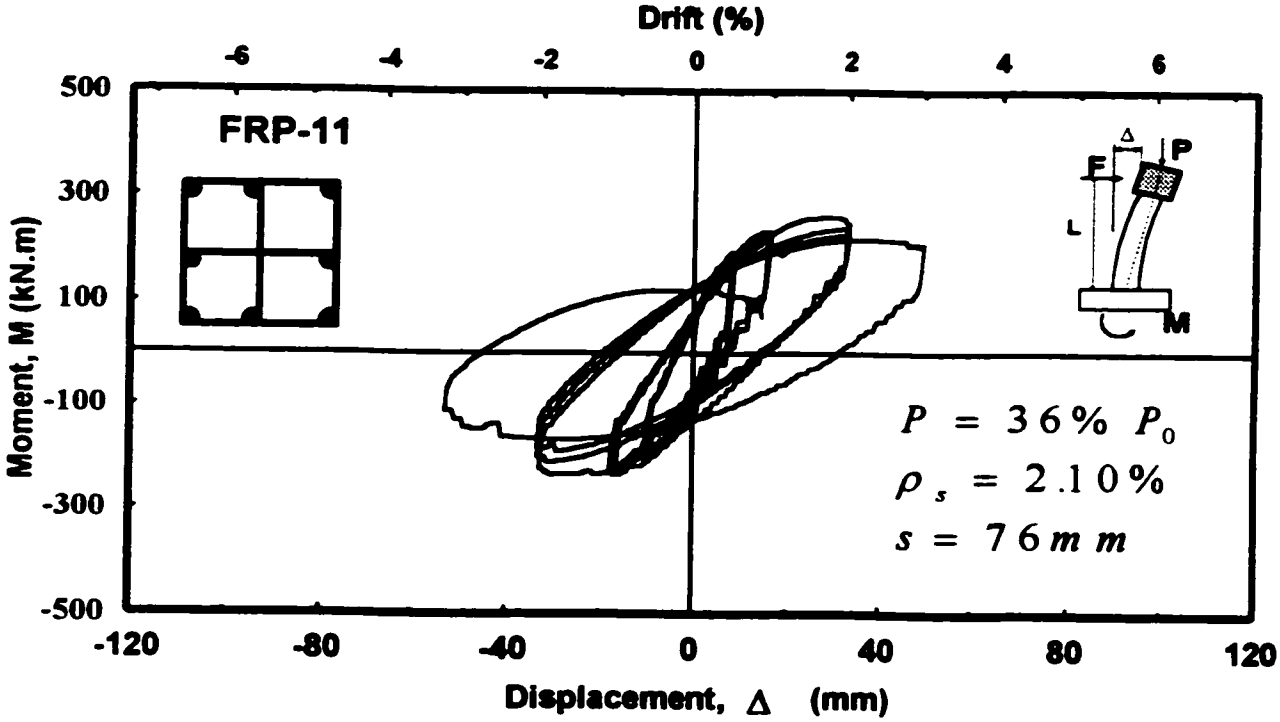

b) Hysteretic moment-displacement relationship

Figure 5-110: Hysteretic behavior of column FRP-11

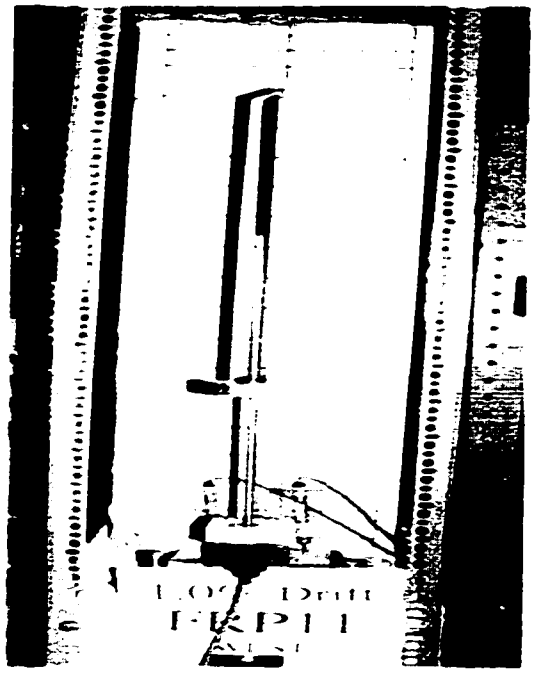

a) At 1% Drift

b) At 2% Drift

c) At 3% Drift

d) At end of test

Figure 5-111: Observed damage in column FRP-11 at selected stages of loading.

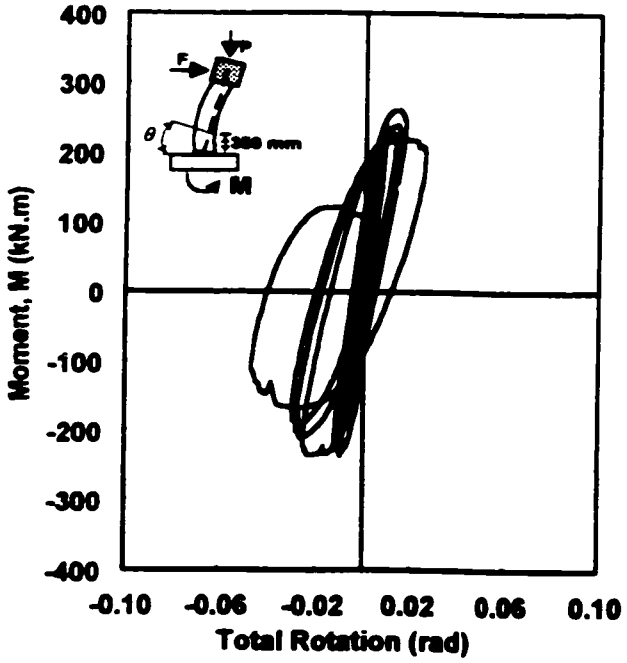

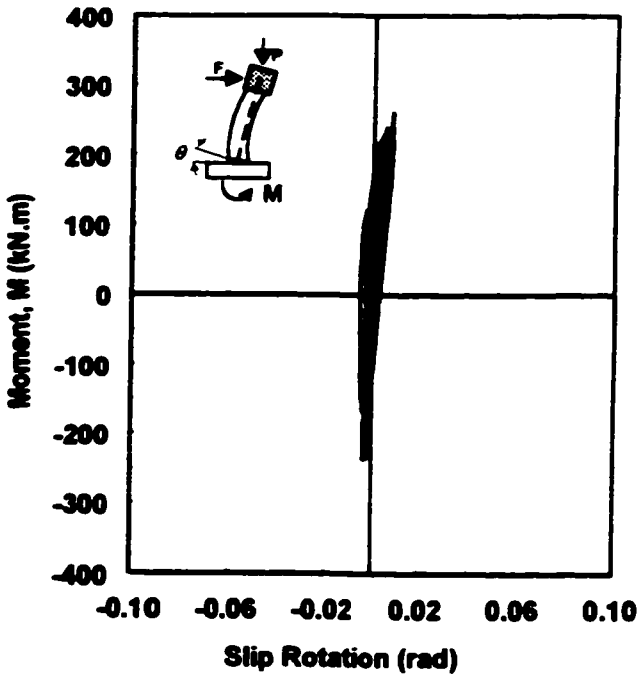

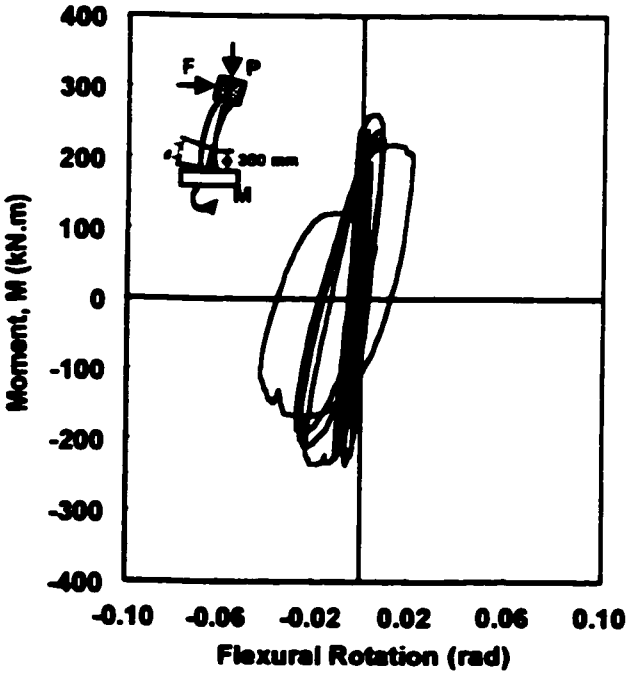

Figure 5-112: Moment-rotations relationships for column FRP-11

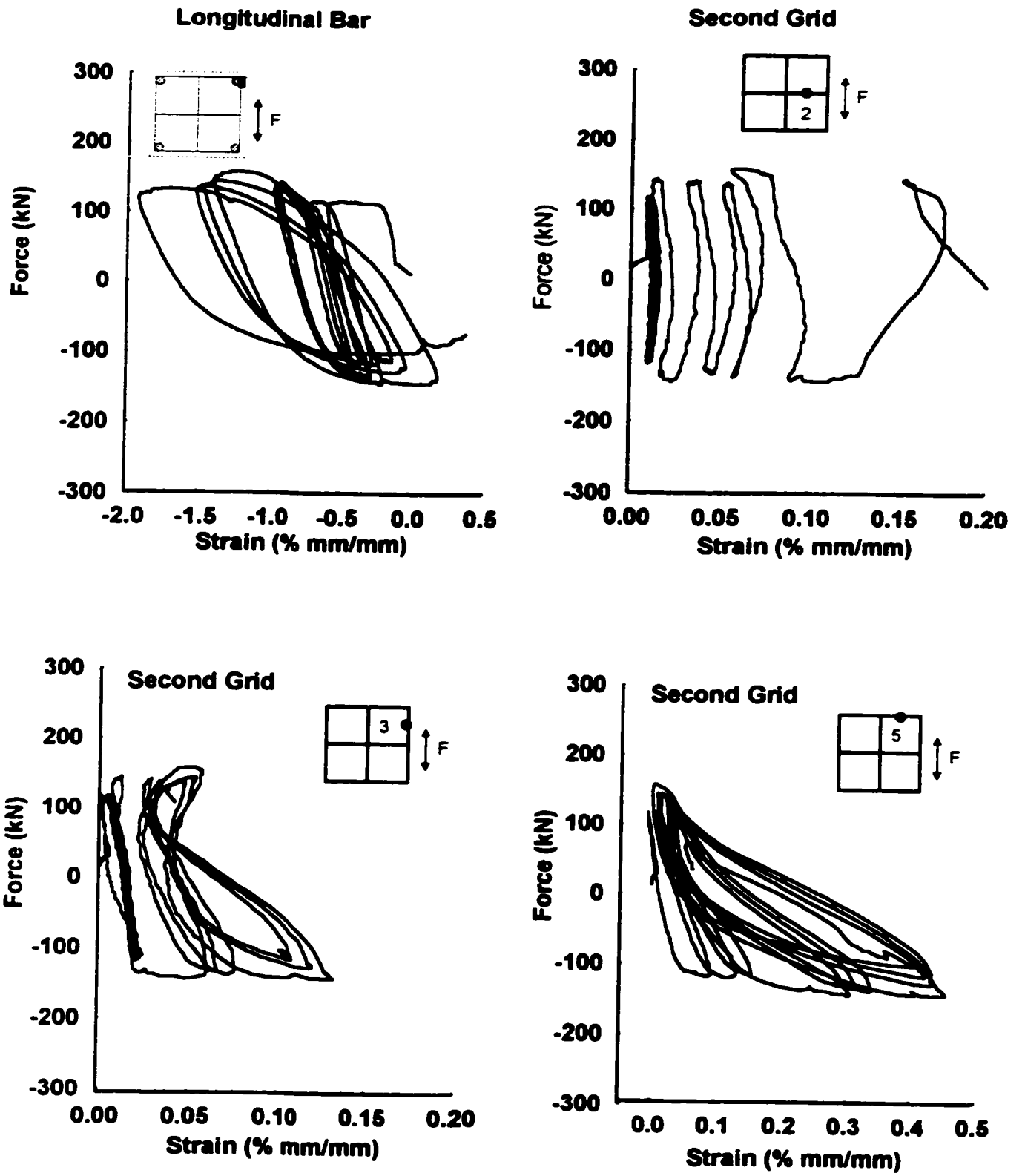

Figure 5-113: Reinforcement strain readings in Column FRP-11

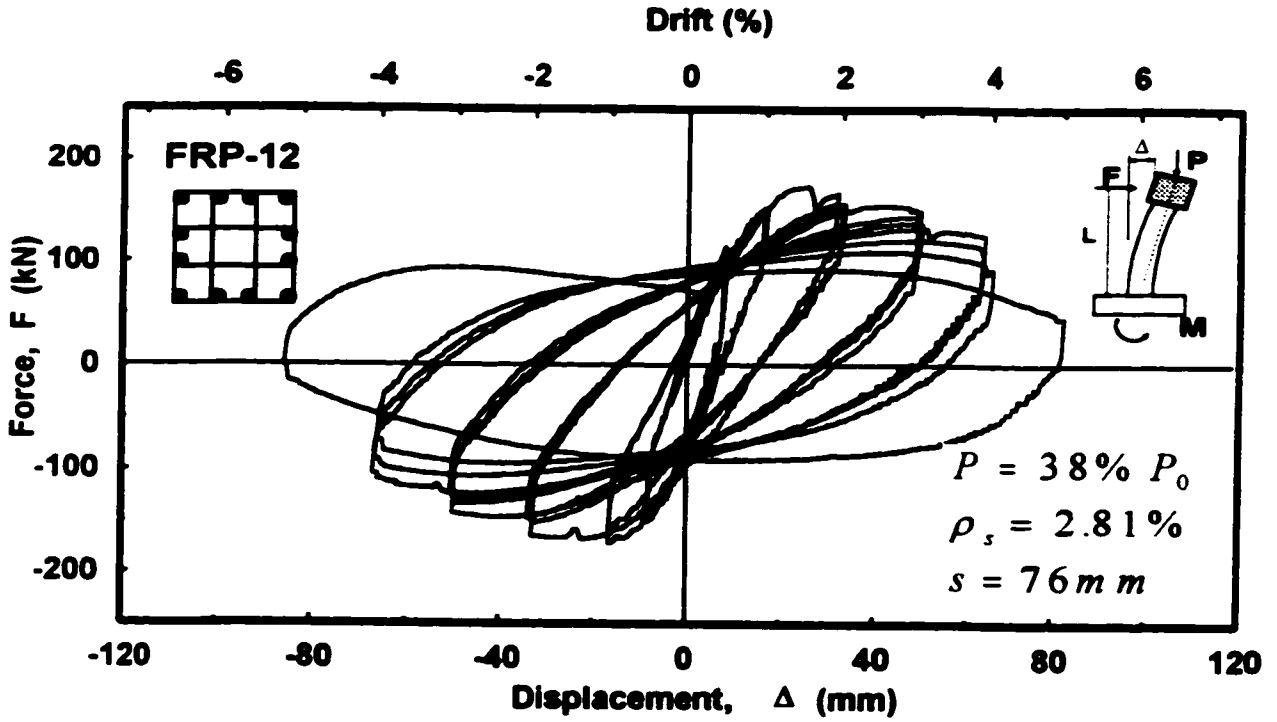

a) Hysteretic force-displacement relationship

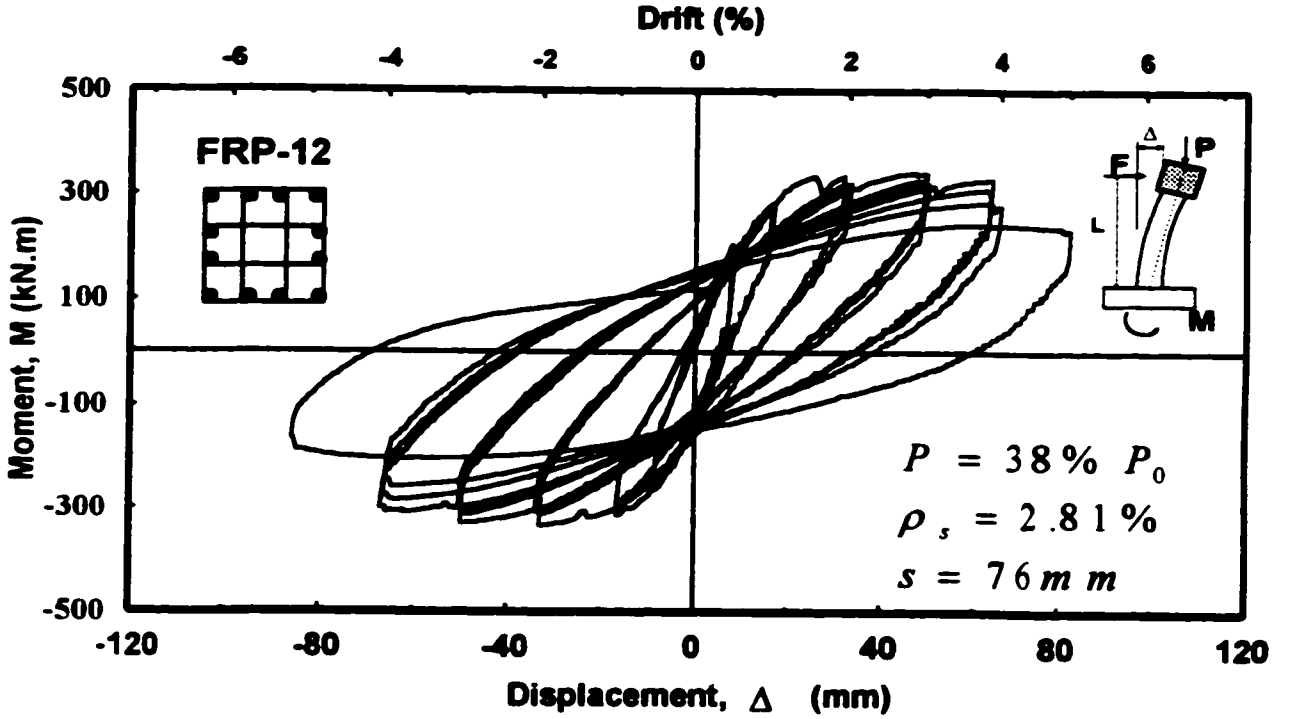

b) Hysteretic moment-displacement relationship

Figure 5-114: Hysteretic behavior of column FRP-12

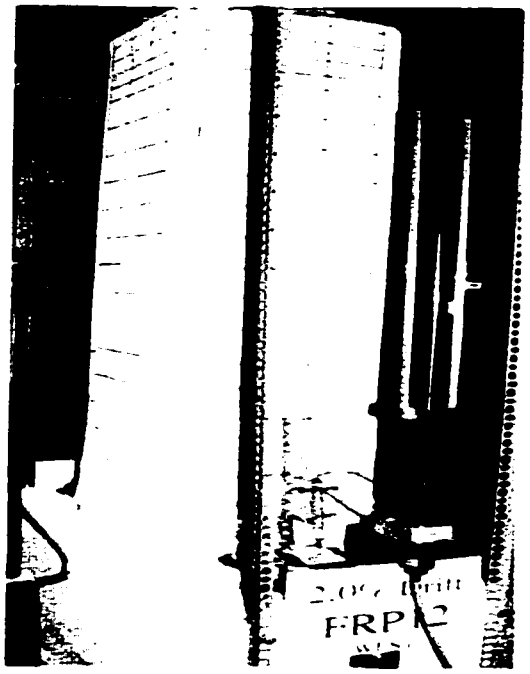

a) At 2% Drift

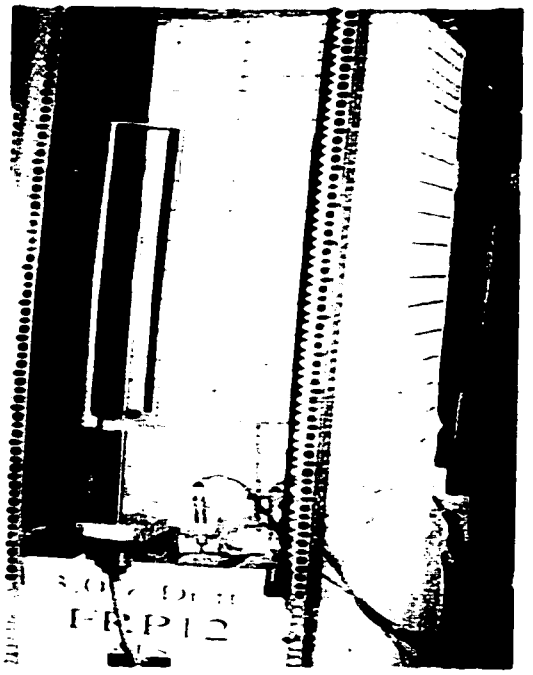

b) At 3% Drift

c) At 4% Drift

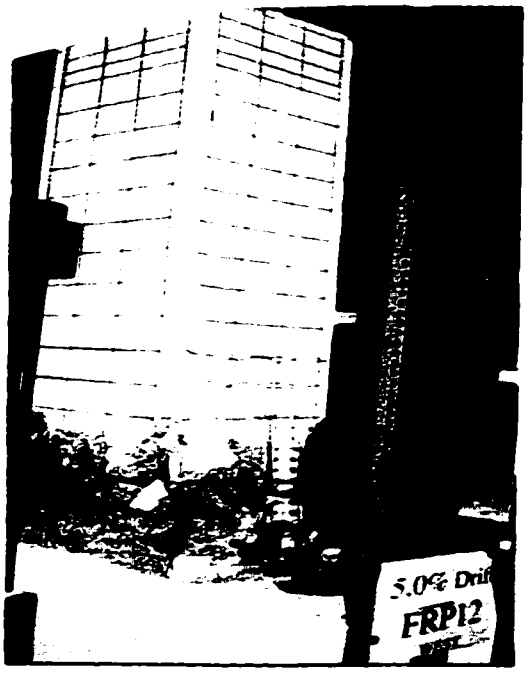

d) At 5% drift

Figure 5-115: Observed damage in column FRP-12 at selected stages of loading.

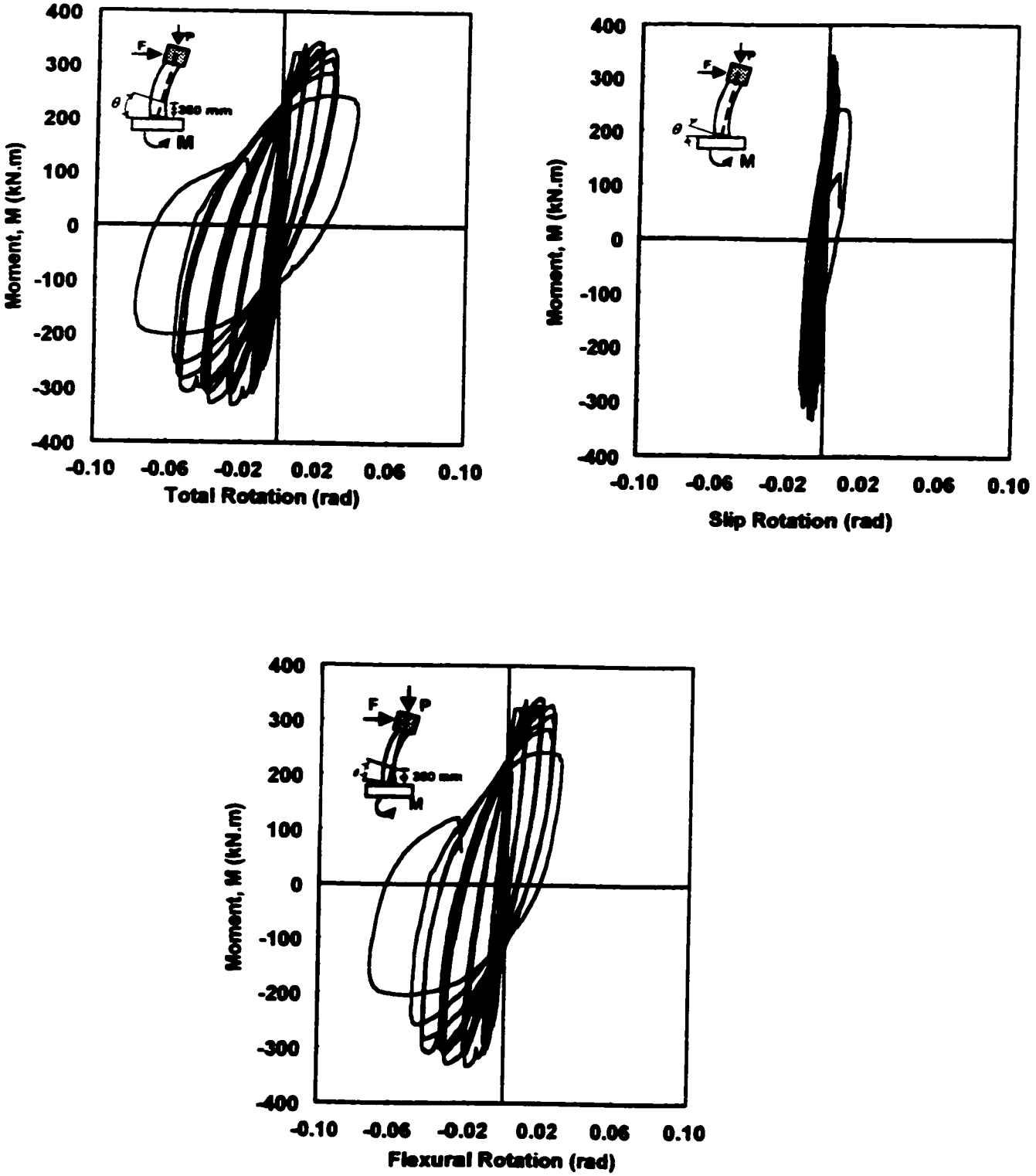

Figure 5-116: Moment-rotations relationships for column FRP-12

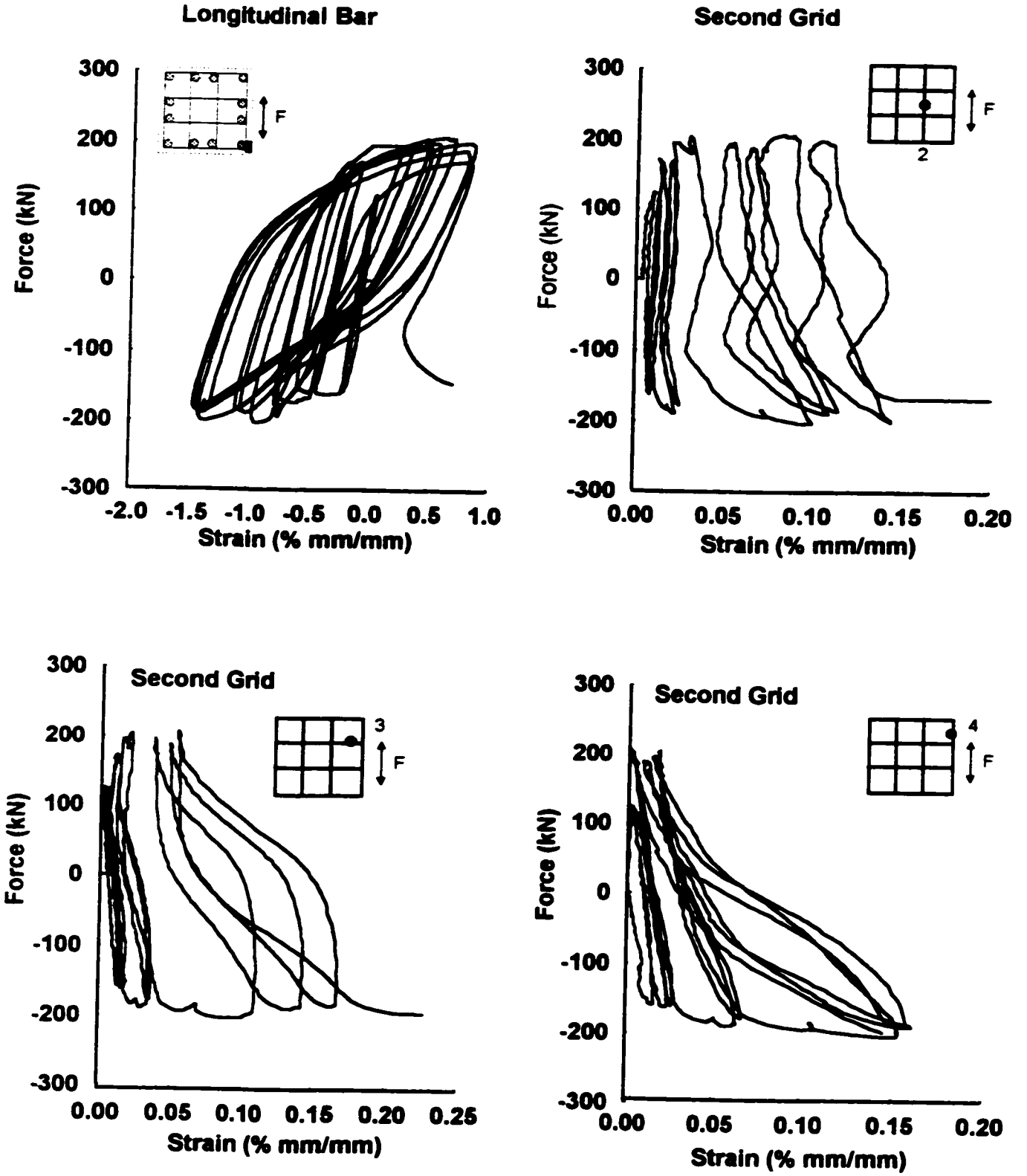

Figure 5-117: Reinforcement strain readings in Column FRP-12

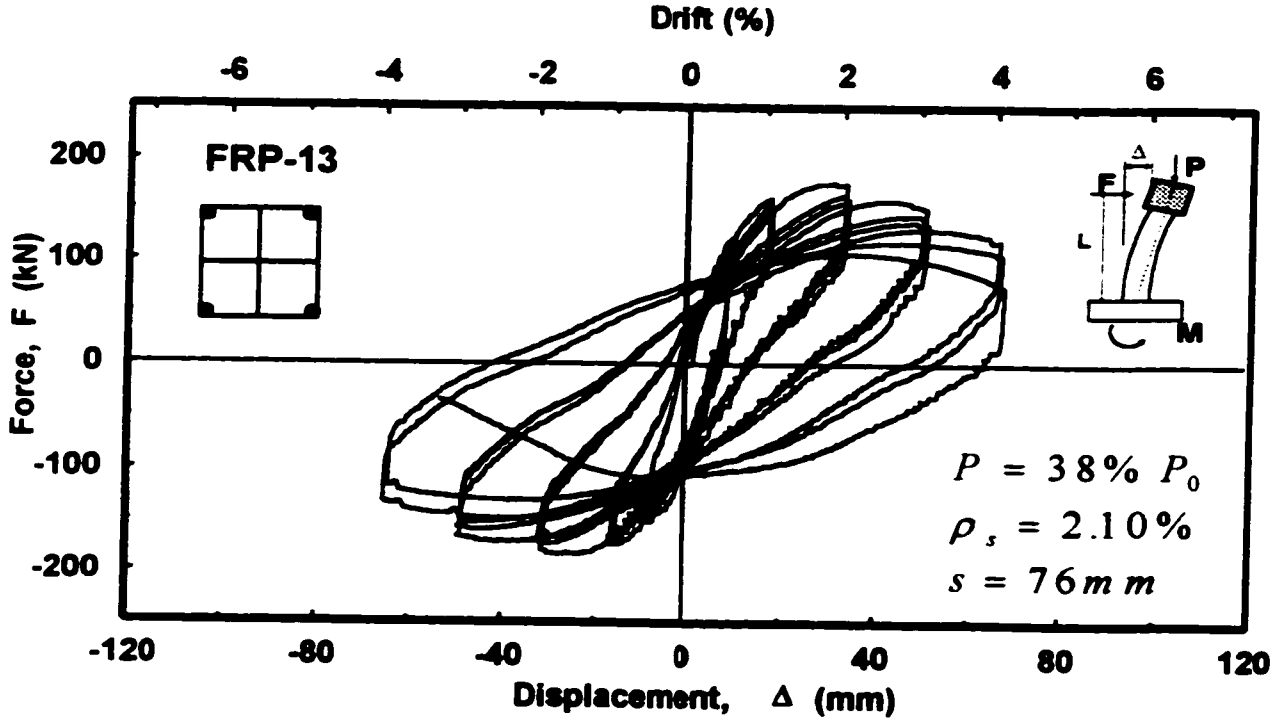

a) Hysteretic force-displacement relationship

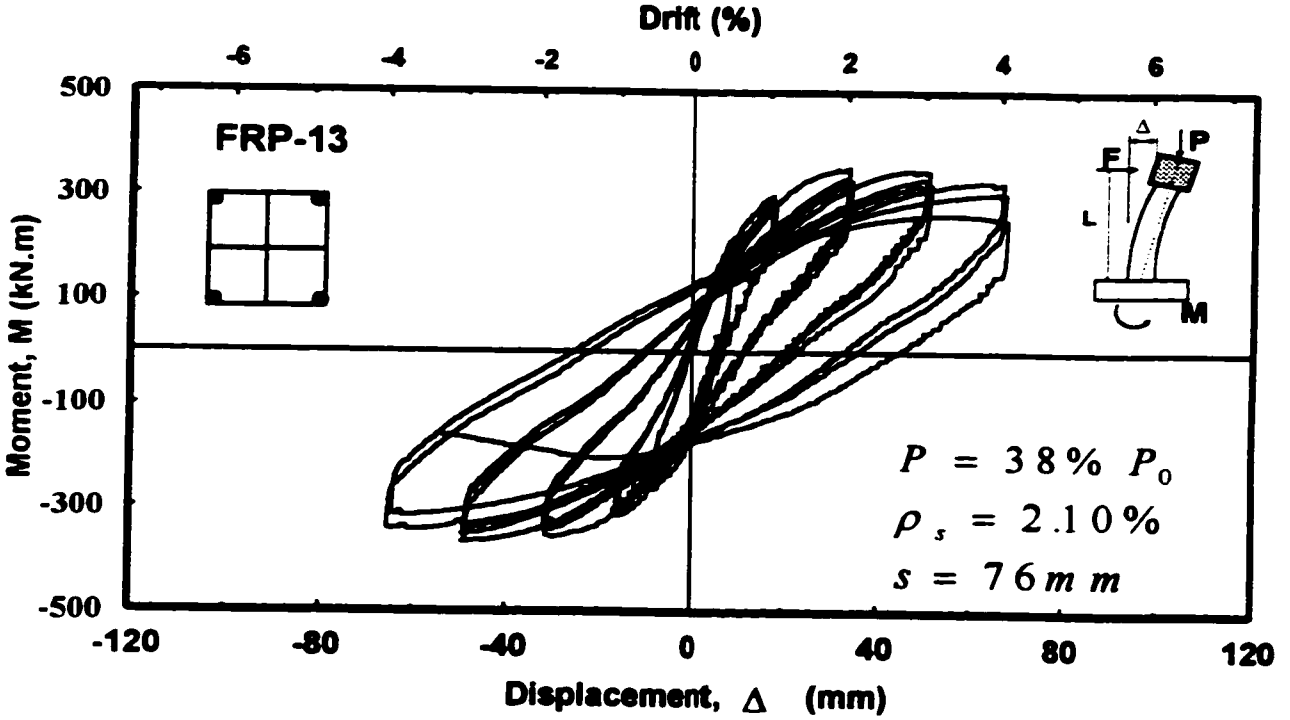

b) Hysteretic moment-displacement relationship

Figure 5-118: Hysteretic behavior of column FRP-13

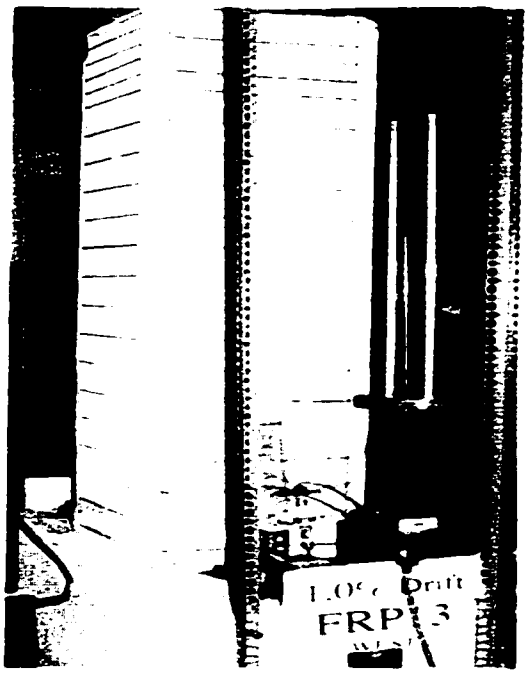

a) At 1% Drift

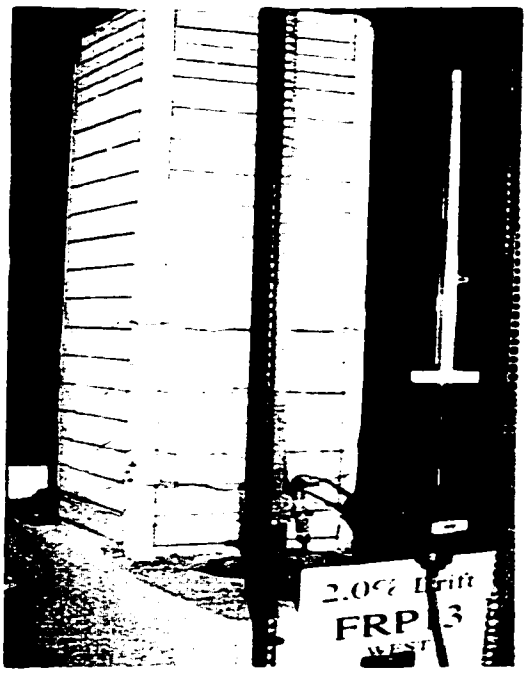

b) At 2% Drift

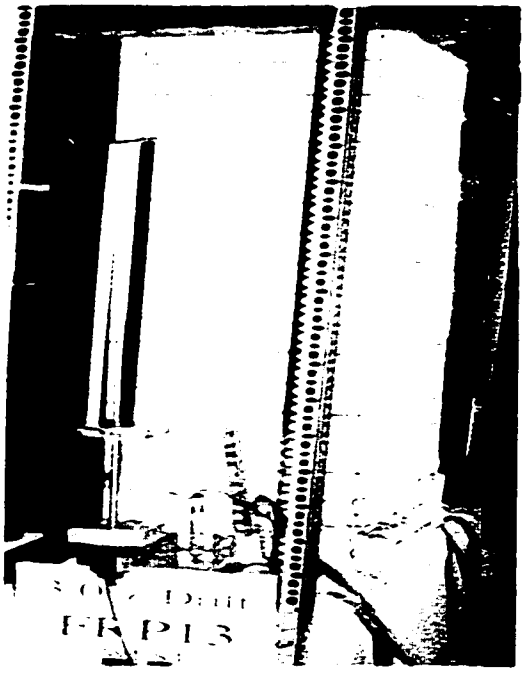

c) At 3% Drift

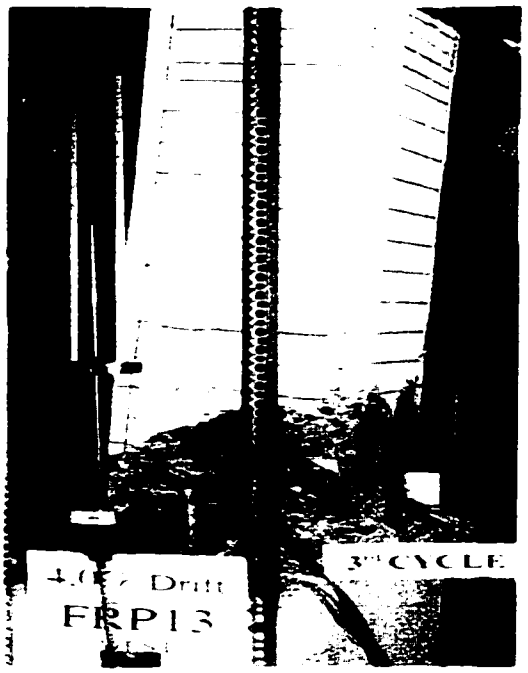

d) At 4% drift

Figure 5-119: Observed damage in column FRP-13 at selected stages of loading.

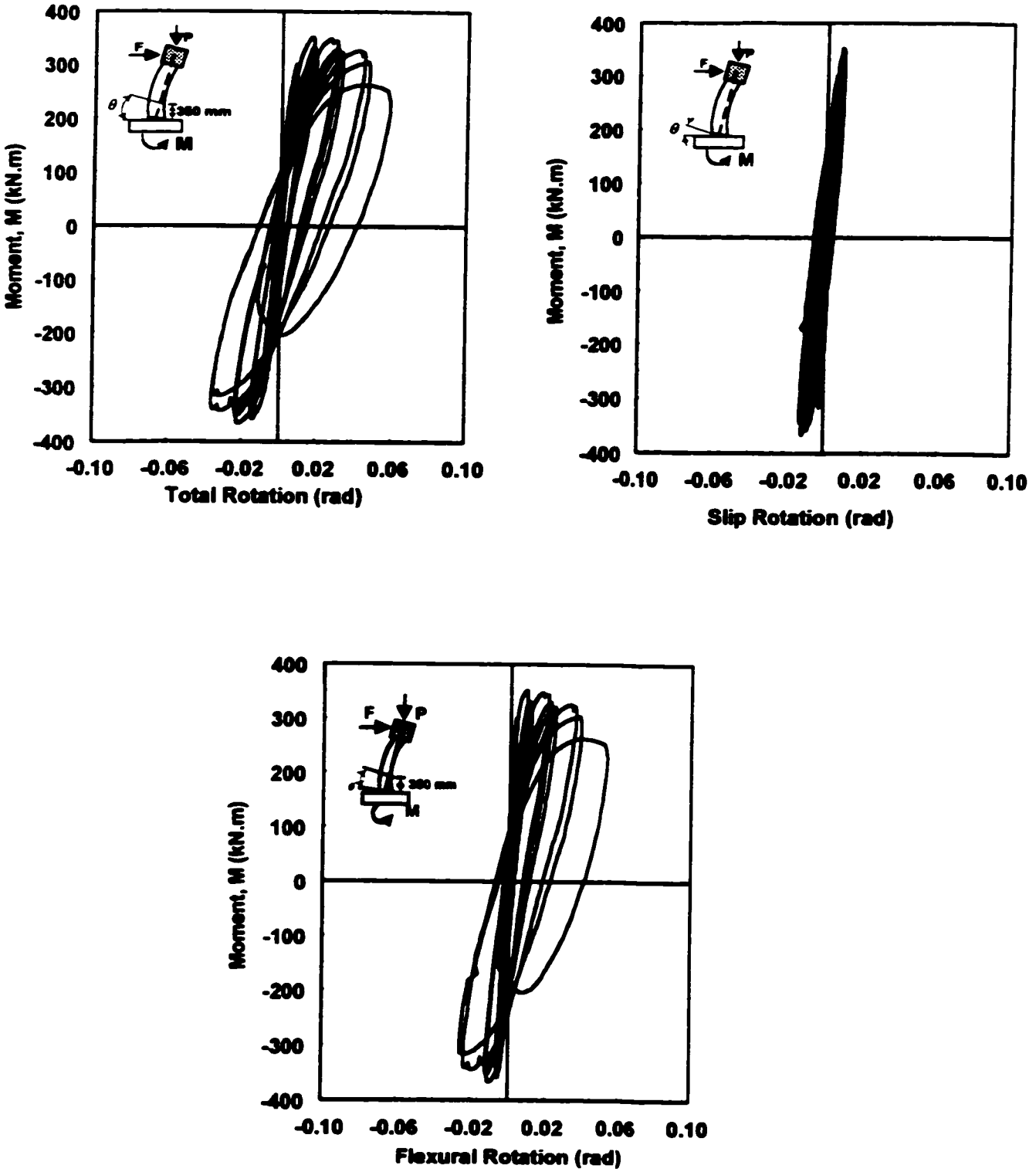

Figure 5-120: Moment-rotations relationships for column FRP-13

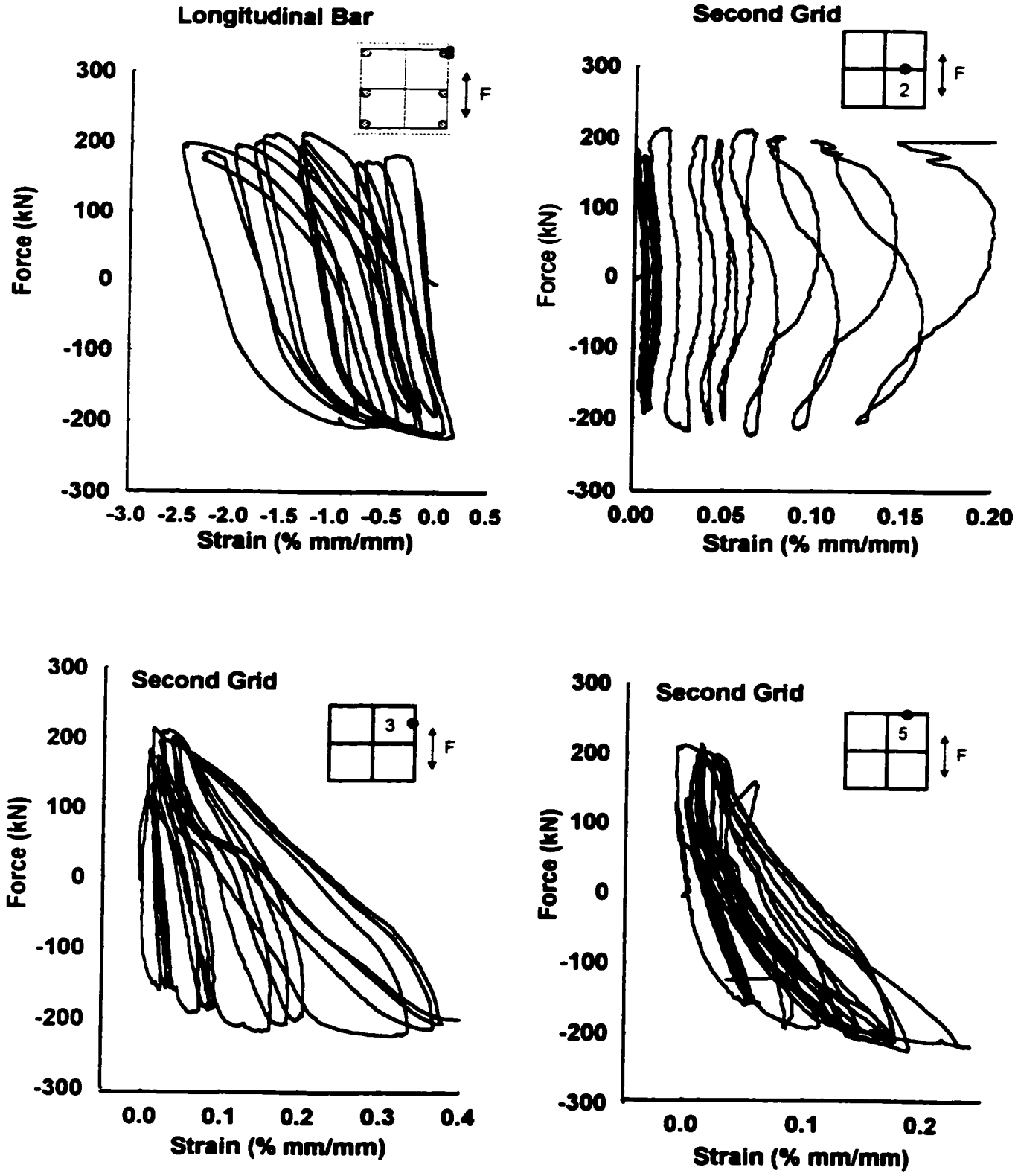

Figure 5-121: Reinforcement strain readings in Column FRP-13

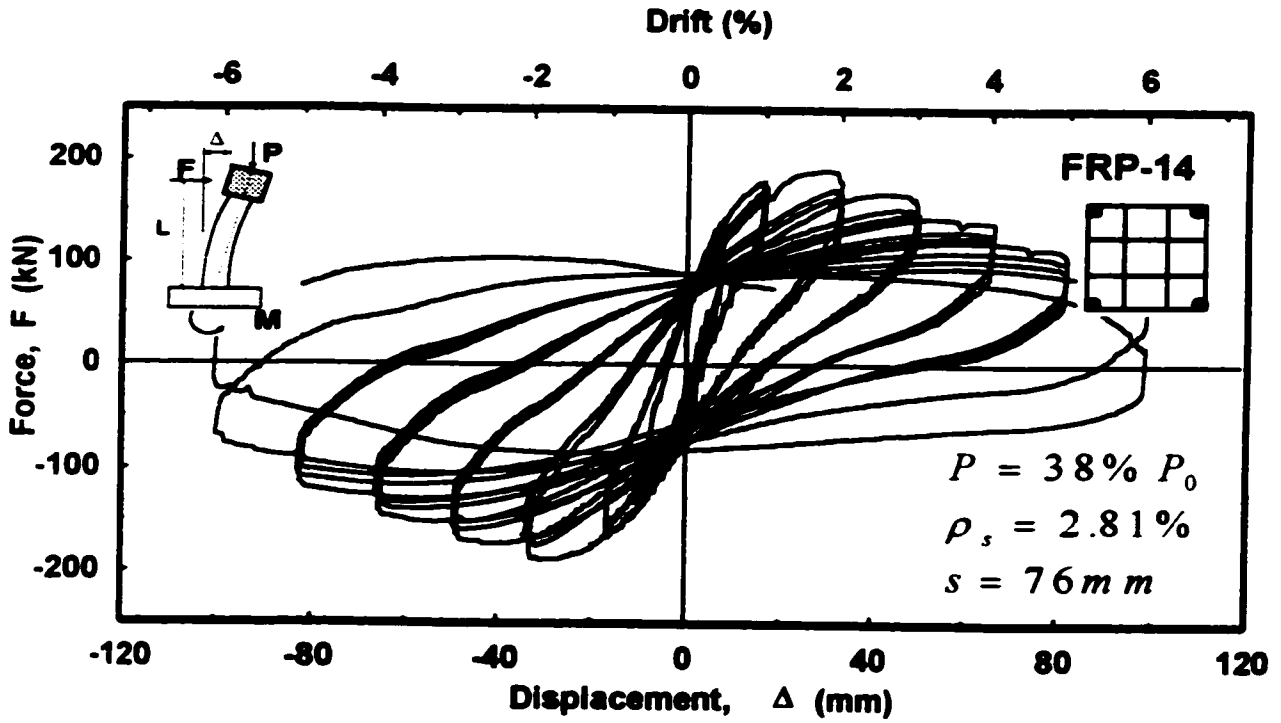

a) Hysteretic force-displacement relationship

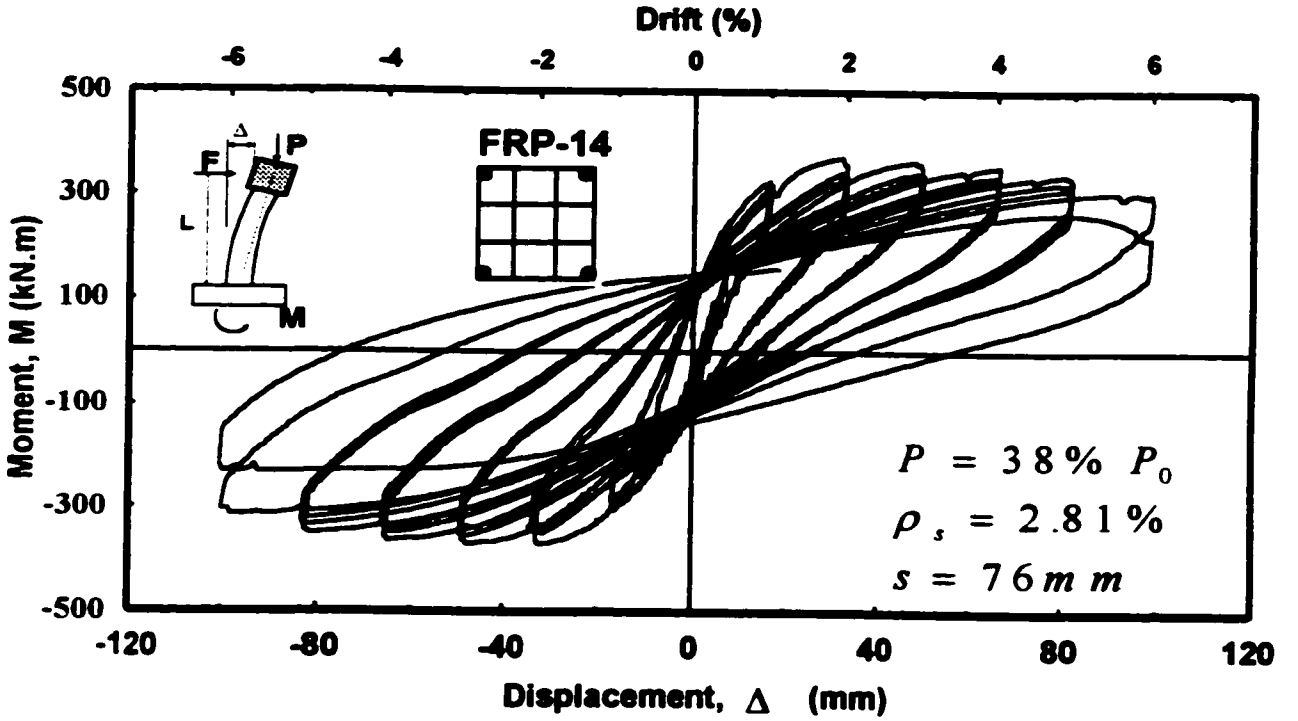

b) Hysteretic moment-displacement relationship

Figure 5-122: Hysteretic behavior of column FRP-14

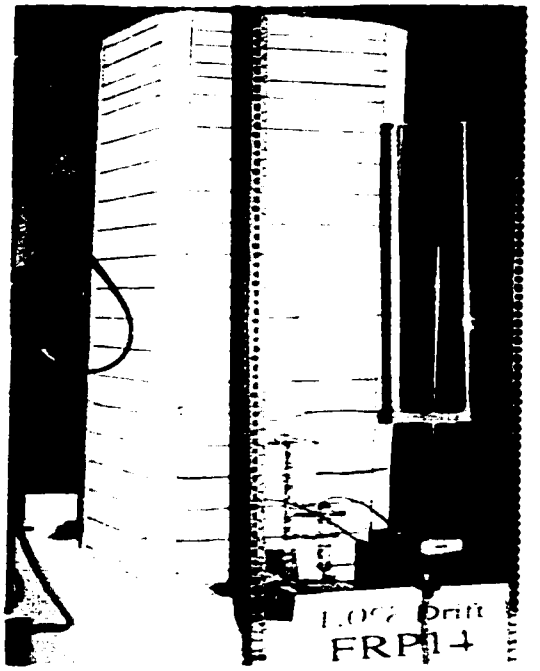

a) At 1% Drift

b) At 3% Drift

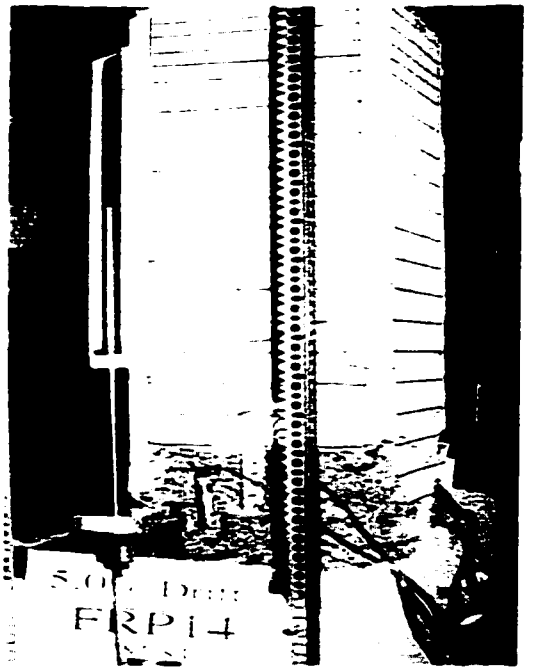

c) At 5% Drift

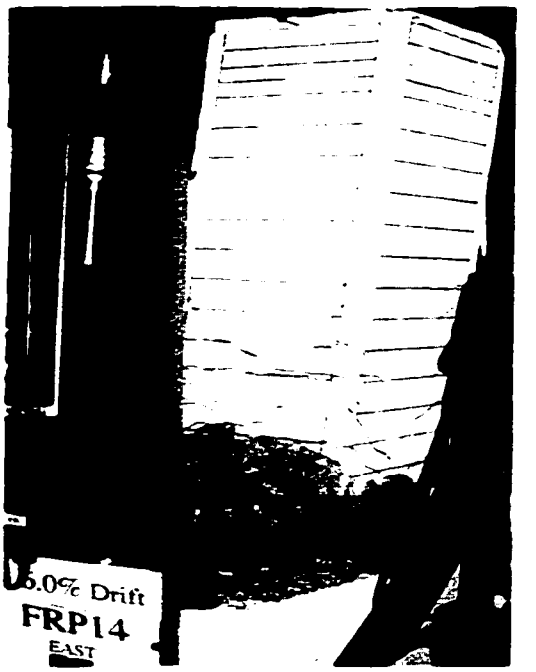

d) At 6% drift

Figure 5-123: Observed damage in column FRP-14 at selected stages of loading.

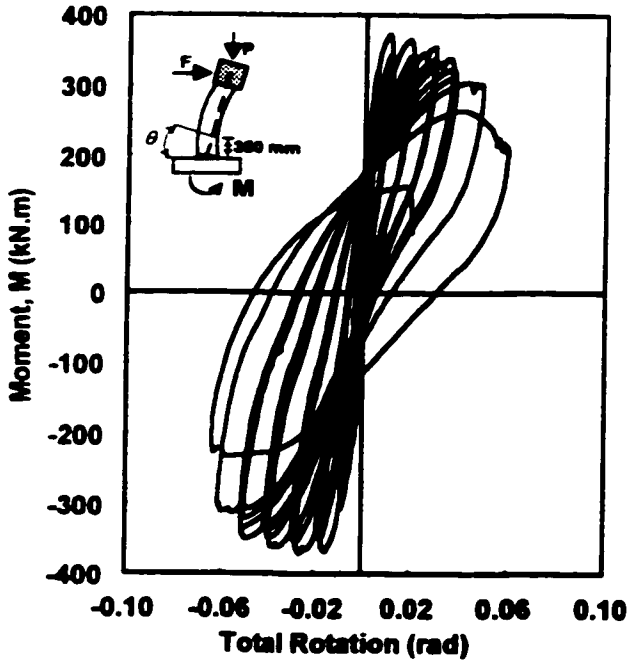

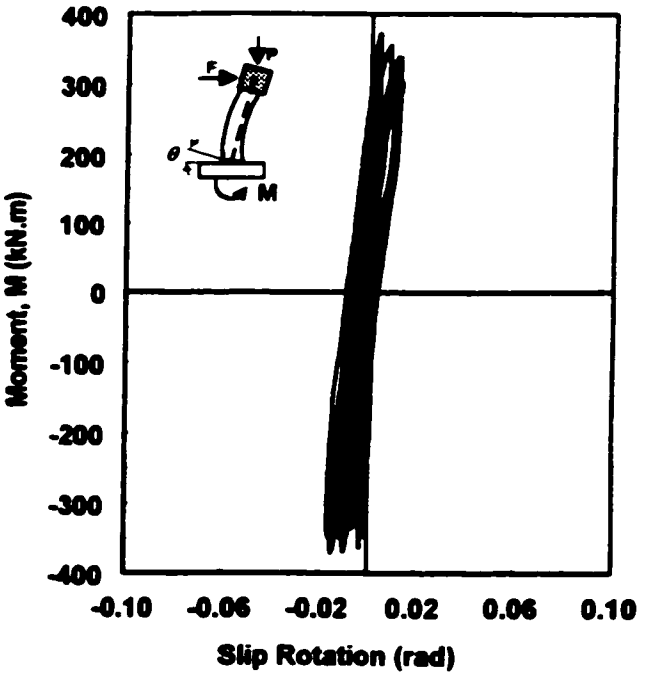

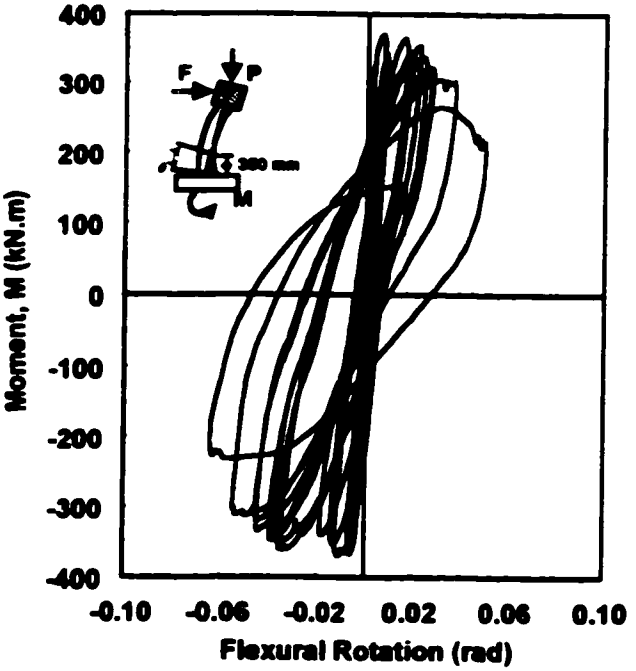

Figure 5-124: Moment-rotations relationships for column FRP-14

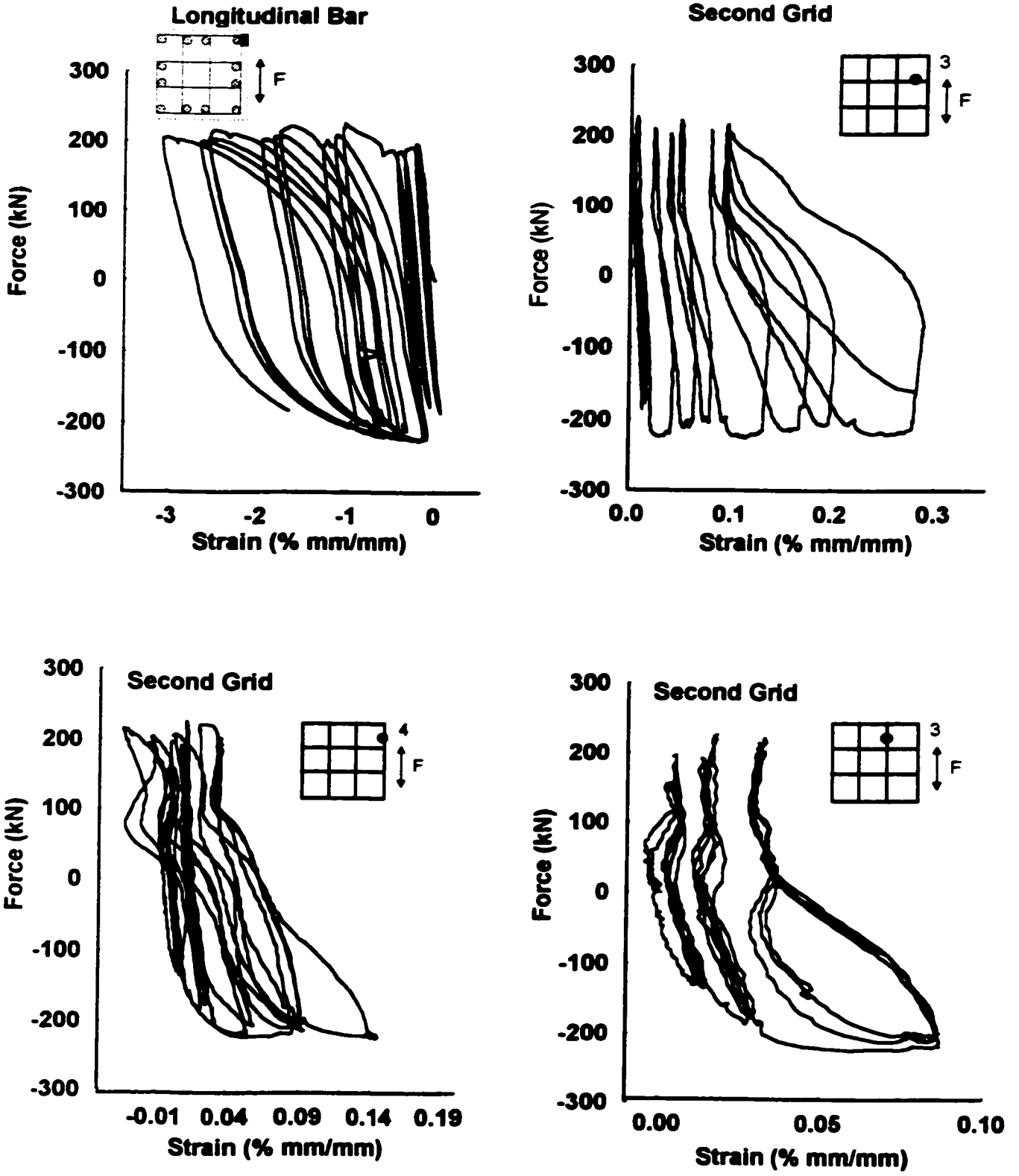

Figure 5-125: Reinforcement strain readings in Column FRP-14

Chapter 6

EFFECTS OF TEST PARAMETERS

6.1 Introduction

The significance of test variables is assessed in this Chapter by evaluating the test results presented in the previous Chapter. The effects of test parameters on strength and ductility of concrete columns were investigated by comparing the envelopes (backbone curves) of hysteretic force-displacement relationships of companion columns. The force-displacement and moment-rotation hysteretic relationships of individual column specimens were presented in Chapter 5.

6.2 Test Parameters

The experimental program was mainly designed to study the effects of confinement parameters with the objective of developing new and innovative techniques and materials for column confinement. Each test parameter was investigated by varying the parameter among companion columns while maintaining all other parameters approximately the same. The test parameters and associated companion columns were listed in Table 4-2 of Chapter 4. The test parameters considered in this experimental study are summarized below:

1. Concrete compressive strength.
2. Type of transverse reinforcement.
3. Volumetric ratio of transverse reinforcement.
4. Number of cells of transverse reinforcement grids.
5. Spacing of transverse reinforcement.

6. Arrangement of longitudinal reinforcement.

7. Axial load level.

The emphasis in evaluating the effects of test variables was placed on strength and deformability of columns.

6.2.1 Effect of Concrete Compressive Strength

It is known that strength and deformability of plain concrete are inversely proportional. Hence, high-strength concrete is more brittle than normal-strength concrete. The effect of concrete strength on seismic behavior of columns was studied by building three high-strength concrete columns, companion to three normal-strength concrete columns. All other parameters were maintained approximately constant. High-strength concrete columns BG-12 and BG-13 were companions to normal-strength concrete columns BG-8 and BG-3, respectively. Column BG-11 was also built using high-strength concrete and had the same reinforcement arrangement as normal-strength concrete column BG-5. However, these two columns were subjected to *1920 kN* axial compressive load, representing 20% and 38% of their concentric capacities, respectively. This was due to the restriction on the capacity of loading setup by which a maximum of *1920 kN* axial load could be applied. Therefore, when comparing these two columns, both the effect of concrete strength, as well as axial load, have to be considered.

Columns BG-3 and BG-13 were reinforced with 8#20 longitudinal bars and confined with 4-cell welded reinforcement grids. The grids were made out of *9.53-mm (3/8-in.)* high-strength steel reinforcement. The vertical spacing of the grids was *76-mm (3in.)*, resulting in 2.00 % volumetric ratio of transverse reinforcement. Both columns were subjected to axial compressive load, equal to about 20% of their concentric capacities. Force-displacement envelopes for the two columns are compared in Fig. 6-1. The test results indicate that both columns exhibited ductile behavior. Column BG-3, with lower strength concrete, developed 7% drift, while Column BG-13, with higher strength concrete, developed 5% drift. The ductile behavior observed in both columns can be attributed mainly to the favorable confinement characteristics of the high-strength steel grids used. An increase in concrete

strength by about 240% resulted in an increase in lateral load resistance by about 40%, and a reduction in column deformabilty by about 30%.

The second pair of columns consisted of BG-8 and BG-12 made out of 33.7 MPa and 81.6 MPa concrete respectively. These two columns were reinforced with 12#20 longitudinal bars and 9-cell welded reinforcement grids spaced at 76 mm (3 in). The diameter of the crossbars of the grid reinforcement was *6.60 mm (1/4 in.)*, resulting in 1.26% volumetric ratio. The columns were subjected to a constant axial compressive load approximately equal to 20% of their concentric capacities.

Force-displacement envelopes for specimens BG-8 and BG-12 are compared in Fig. 6-1. The test results indicate that the columns experienced similar characteristics as the previous pair of columns with different concrete strengths. They exhibited ductile behavior and showed maximum drifts of 7% and 5% in normal-strength and high-strength concrete columns, respectively. The increase in concrete strength resulted in a significant increase in lateral load resistance, and a decrease in column deformabilty.

The third pair of columns consisted of BG-5 and BG-11, built using 33.7 MPa and 81.6 MPa concrete, respectively. These two columns were reinforced with 12#20 longitudinal bars, and were confined with 9-cell welded grids made out of *9.53-mm (3/8-in.)* diameter steel reinforcement. The grids were placed at a vertical spacing of *76 mm (3 in.)* resulting in a volumetric ratio of 2.66%. Columns BG-5 and BG-11 were subjected to the same axial load, which corresponded to different levels of compression relative to their concentric capacities. These corresponded to 38% and 20% of concentric capacities for Columns BG-5 and BG-11, respectively. Force-displacement envelopes of the columns are compared in Fig. 6-1. The test results indicate that these columns exhibited ductile behavior and failed at about 7% drift. The reduction in column deformability associated with increased concrete strength was approximately the same as the reduction attributed to increased axial compression, resulting in similar column deformabilities.

6.2.2 Effect of Type of Transverse Reinforcement

Three different types of transverse reinforcement were investigated in this research program;

i) welded steel reinforcement grids (WRG), ii) double-head studs (DHS) used in combination with conventional perimeter hoops, and iii) fiber reinforced plastic grids (FRP). The BG columns were designed first, considering the requirements of *ACI318-95* as benchmark. The SD columns were designed to be companion to BG columns. The FRP columns were designed such that they could be compared with both SD and BG columns. The grids were assumed to develop their tension capacity while confining the columns. Because their tension capacity, as determined by tension coupon tests, was about twice the strength of steel used in other columns, they were provided with lower volumetric ratios of transverse reinforcement.

Comparisons of force displacement relationships of columns confined with different types of reinforcement are shown in Fig. 6-2. Test results indicate little difference in behavior among the columns confined with different types of non-conventional transverse reinforcement. The strength enhancement due to confinement was almost identical in all columns, except for repaired FRP columns, which are not included in this comparison. Column deformability depended highly on tension capacities of transverse reinforcement. Generally, the FRP columns developed lower deformabilities than the BG columns, because the majority of FRP grids failed prematurely at perimeter joints. A similar behavior was observed in SD columns when they were tested under increased axial compression. The premature failure of SD columns was caused mainly by the sideways slippage of stud-heads, causing sudden buckling of longitudinal bars. However, these failure modes occurred at a rather late stage of inelastic deformations, and hence did not jeopardize column deformability within the range typically expected during seismic response.

Examination of the plots presented in Fig. 6-2 indicates that both Columns BG-1 and FRP-1 experienced the same level of deformability and strength enhancement. Both columns failed due to the buckling of longitudinal reinforcement during the first cycle at 3% drift. Transverse reinforcements in both columns were vertically spaced at *152 mm (6 in.)*, which may be considered to be too wide for the column and reinforcement sizes considered. Therefore, the deformation capacity of these columns was governed by bar buckling.

Figure 6-2 shows a comparison between columns BG-2, SD-1, and FRP-2. These columns were reinforced with 8#20 longitudinal bars and confined with transverse reinforcement

having a 4-cell grid configuration. Columns BG-2 and SD-1 had higher volumetric ratios than Column FRP-2. The columns were subjected to 40% of their concentric compression capacities. The test results indicated no difference in strength between the three columns. However, Columns SD-1 and FRP-2 developed lower deformabilty than BG-2. This was due to the slippage of stud heads in SD-1 and premature rupture of the FRP grid joints in FRP-2.

The behavior of columns BG-3, SD-2, and FRP-3 are compared in Fig. 6-2. These columns were built and tested in much the same manner as BG-2, SD-1, and FRP-2, except for the level of axial load, which was reduced by one half. It can be seen in the same figure that these columns exhibited similar behavior both in term of deformation and strength. The reduction in the level of axial load, as compared to the previous three columns, resulted in reduced axial compression on core concrete and longitudinal bars. Hence, the longitudinal bars were able to maintain their stability until the end of the test with reduced demands for lateral restraint. In fact, strain gauges placed on second layers of transverse reinforcement within the plastic hinging regions of columns (BG-3, SD-2, FRP-3) recorded strain values below 0.3%.

Figure 6-2 also shows a comparison between columns BG-5, SD-3, FRP-9, and FRP-12 in terms of force-displacement relationships. These columns were reinforced with 12#20 longitudinal bars, and were confined with transverse reinforcement having a 9-cell grid configuration. Columns BG-5 and SD-3 had higher volumetric ratios than that of columns FRP-9 and FRP-12. The columns were tested under 40% of their concentric capacities. The results indicated that column BG-5 showed a superior behavior compared to the companion columns. The noticeable difference observed in peak lateral force resistance indicates the superiority of steel grids over the other types of reinforcement considered. The FRP columns showed lower deformability than the SD column, which had a lower drift capacity than the BG column. The deformation capacities of FRP-9 and FRP-12 columns were limited by the grid joint capacity. Many FRP grids failed prematurely during testing because of the delaminating of grid joints. The deformability of SD-3 was limited to 6% drift, by the slippage of stud heads from longitudinal bar being supported.

The comparison between column BG-6, FRP-7, and FRP-14 is shown in Fig. 6-2. Column

BG-6 was longitudinally reinforced with 4#30 bars and was laterally confined with 9-cell welded reinforcement grids placed at *76mm (3 in.)* spacing. Columns FRP-7 and FRP-14 were built similarly to BG-6 except that the transverse reinforcement was made out of fiber reinforcement plastic. The FRP grids in columns FRP-7 and FRP-14 had *6* x *10 mm* and *8* x *10 mm* cross sectional dimensions, respectively. These three columns were tested under approximately 40% of their concentric capacities. The plots in Fig 6-2 show no difference in behavior among the three columns, except for Column FRP-14, which resisted higher lateral deformations than others because of the high volumetric ratio of transverse reinforcement provided in this column.

Other comparisons of columns (BG-7, SD-4, and FRP-9), with low volumetric ratios of different types of transverse reinforcement, are shown in Fig 6-2. BG-7 was reinforced with 12#20 longitudinal bars and 9-cell welded reinforcement grids, made out of *6.6 mm (1/4 in.)* diameter steel reinforcement. SD-4 and FRP-9 had the same reinforcement configuration except for the type. These three columns were tested under constant compressive loads of 40% of their concentric capacities. Column FRP-9 recorded a lower lateral force capacity than the others. This could be attributed to the small cross-section and lower elastic modulus of FRP reinforcement. The SD-4 and FPR-9 columns showed lower deformability than BG-7, because of the premature failure of these transverse reinforcements.

Steel transverse reinforcement is also compared with FRP grids in Fig. 6-2. Here, the behavior of column BG-8 is compared with those of FRP-6 and FRP-10. Column BG-8 was reinforced with 12#20 longitudinal bars and 9-cell grids, made out of *6.6 mm (1/4 in.)* diameter steel reinforcement. The FRP-6 and FRP-10 columns had the same reinforcement configuration as Column BG-8. The grids were made out of *6* x *10 mm* and *6* x *8 mm* FRP reinforcement, respectively. The columns were tested under constant axial compression, equal to about 20% of their concentric capacities. The plots in Fig. 6-2 show no appreciable difference in behavior between the three columns. The lower axial load level used in these columns once again reduced the confinement demand on transverse reinforcement, eliminating possible differences in behavior that often arose at later stages of testing, and often caused by the instability of longitudinal reinforcement.

6.2.3 Effect of Volumetric Ratio of Transverse Reinforcement

The effect of volumetric ratio of transverse reinforcement was investigated by testing several companion columns confined with different types and amounts of transverse reinforcement. The envelopes of relevant force-displacement relationships are compared in Fig. 6-3. The test results indicate that the ductility of columns increased with increasing volumetric ratio of confinement reinforcement. However, no appreciable difference was observed in column strength, as affected by the volumetric ratio, within the range considered.

6.2.4 Effect of Number of Cells of Grids

The effect of number of reinforcement grid cells on strength and ductility of concrete columns was investigated by comparing Columns FRP-7 and FRP-13. Column FRP-7 was confined with 4-cell grids, as opposed to FRP-13 that had 9-cell grids. The grids used in these columns were made out of 8 x 10 mm and 6 x 10 mm FRP reinforcement for 4-cell and 9-cell grids, respectively to produce the same volumetric ratio of transverse reinforcement in both columns. Both columns were reinforced with four corner #30 longitudinal steel bars only, to minimize the effect of longitudinal reinforcement on concrete confinement. All other parameters were identical in both columns, including concrete strength *(37.2 MPa)*, vertical spacing of transverse reinforcement *(76 mm)*, and axial load level $(0.38P_0)$.

The force-displacement envelopes of these columns are compared in Fig. 6-4. The results showed no significant difference in peak lateral load resistance. However, Column FRP-7, confined with 9-cell grids developed higher deformability than Column FRP-13, which was confined with 4-cell grids. This implies that the 9-cell grids were able to provide superior confinement. The presence of closely spaced crossties, as in the case of 9-cell grids, improved the uniformity of passive lateral pressure around the core concrete. In addition, the FRP joints in Column FRP-7 were not as susceptible to failure as some of the others were, since the majority of grid joints in FRP-7 were not subjected to lateral forces exerted by longitudinal bars, and the corner joints that contained longitudinal bars had relatively stable #30 bars.

6.2.5 Effect of Spacing of Transverse Reinforcement

Spacing of transverse reinforcement is an important parameter that affects seismic behavior of reinforced concrete columns. Both the stability of longitudinal reinforcement and effectiveness of confinement improve by closer spacing of transverse reinforcement.

To vertical spacing of transverse reinforcement as a parameter was studied by testing two companion BG columns. Column BG-4 was reinforced with 12#20 (diameter $d_b = 19.5mm$) longitudinal bars and 9-cell welded steel grids, made out of *9.53 mm (3/8 in.)* diameter reinforcement. The grids were placed at a vertical spacing (s) of *152-mm (6-in.)*, resulting in volumetric ratio of transverse reinforcement of 1.33% and aspect ratio (S/d_b) of 7.5. The companion column BG-9 was reinforced with 20#15 ($d_b = 16.0mm$) longitudinal bars and 9-cell welded still grids, made out of *6.6 mm (1/4 in.)* diameter crossbars. BG-9 had slightly higher volumetric ratio than BG-4. The vertical spacing of transverse grids was *76 mm (3 in.)* resulting in aspect ratio (S/d_b) of 5.0 and volumetric ratio of 1.26%. Both columns were tested under constant axial compressive load of 1923 *kN*. The force-displacement envelopes of columns are compared in Fig. 6-5. The figure shows that column BG-9 with closely spaced grids developed lower strength degradation when compared with BG-4. In addition, the test results showed that the longitudinal bars buckled at about 4% drift. This demonstrated that decreasing the size of longitudinal bars would have a similar effect as increasing the vertical spacing of transverse reinforcement, although it is difficult to quantify the relationship between longitudinal bar size and the spacing of transverse reinforcement based on limited test data. As it will be discussed later in Chapter 8, the aspect ration (S/d_b) plays an important role in determining the stability of longitudinal bars and hence the ductility of column.

Four additional pairs of normal-strength concrete columns were also tested to investigate the effect of spacing of transverse reinforcement on column behavior. In this case, the vertical spacing of transverse reinforcement was doubled in one column of each pair, resulting in a decrease of one half in the volumetric ratio. Two pairs of BG columns were confined with welded reinforcement grids and the other two pairs were reinforced using fiber reinforced

plastic grids. Column BG-1 was companion to BG-2, which was reinforced with 8#20 longitudinal bars and 4-cell welded reinforcement grids. The grids were made out of *9.53 mm (3/8 in.)* diameter reinforcement. The vertical spacing of grids in columns BG-1 and BG-2 were *76 mm (3 in.)* and *152 mm (6 in.)* respectively. Column BG-4 was built companion to BG-5, which was reinforced with 12#20 longitudinal bars and 9-cell welded reinforcement grids made out of *9.53 mm (3/8 in.)* diameter steel bars. The vertical spacing of grids in columns BG-4 and BG-5 were *76 mm (3 in.)* and *152 mm (6 in.)* respectively. Column FRP-1 was companion to column FRP-2, whereas column FRP-4 was companion to column FRP-5. These FRP columns had the same reinforcement arrangement as BG-1 BG-2 and BG-4 BG-5 pairs, respectively, except that the transverse reinforcement consisted of fiber reinforced plastic grids instead of steel grids. During tests, all the aforementioned columns were subjected to axial compressive load equal to about 38% of their concentric capacity P_0. The effect of spacing on strength and ductility of columns is illustrated in Fig. 6-5. The results indicate that deformability of columns was reduced with an increase in vertical spacing of transverse reinforcement and a decrease in volumetric ratio. Columns with wider spacing of transverse reinforcement experienced rapid strength degradation. This confirms that vertical spacing of transverse reinforcement plays an important role in strength and ductility capacity of concrete columns.

It may be useful to compare the vertical spacing of transverse reinforcement relative to the diameter of longitudinal bars and their mechanical properties to those required by building codes and suggested by other researchers. The maximum spacing to prevent buckling of compression bars in the first mode (between two layers) depends on the compressive strain imposed on longitudinal bars as well as the effective modulus in strain hardening. A common spacing requirement to prevent inelastic bar buckling is not to exceed six times the diameter of longitudinal bar $(S/d_b) \leq 6.0$ for North American steel. This type of steel typically has ultimate to yield stress ratio (f_u/f_y) of about 1.5, which is higher than that of European steel. A lower value of (f_u/f_y) ratio results in a lower strain hardening modulus, and hence reduced resistance to compression. The columns with a vertical spacing of *152 mm (6 in.)*, tested in the current investigation, had an S/d_b ratio of 7.6 and did not satisfy the above

criterion. These columns failed prematurely due to bar buckling. Their ductility was lower than that attained by companion columns with reduced S/d_b ratio.

6.2.6 Effect of Arrangement of Longitudinal Reinforcement

The effect of arrangement of longitudinal reinforcement was investigated by testing several sets of columns, confined with four different arrangements of longitudinal bars. The reinforcement arrangements included 4, 8, 12, and 20 longitudinal bars, laterally supported by either 4-cell or 9-cell grids. The envelopes of force-displacement relationships are compared in Fig. 6-6. The results indicate that the grids were able to provide the required lateral restraint at perimeter grid joints, without the need to have longitudinal reinforcement between the corner bars. The close spacing of transverse reinforcement within the cross-sectional plane improved the distribution of lateral confinement pressure without the presence of longitudinal reinforcement.

Companion columns BG-5, BG-6, and BG-10 were confined with 9-cell welded reinforcement grids and were reinforced with 12#20, 4#30, and 20#15 longitudinal bars, respectively. All other parameters were identical, including concrete strength (*33.7 MPa)*, vertical spacing of transverse reinforcement (*76 mm)*, and axial load level $(0.38P_0)$. Comparisons of force-displacement envelopes of columns BG-5, BG-6, and BG-10 are shown in Fig. 6-6. No significant difference in behavior of the three columns was noticed, except that the deformability at later stages of loading was affected by bar buckling. Although, column BG-10 had a longitudinal reinforcement ratio of 3.26%, which was higher than that of BG-5, it showed earlier bar buckling, because #15 bars were more susceptible to buckling than #20 bars. BG-6 has the lowest longitudinal reinforcement ratio and the largest longitudinal bar size. The column maintained its strength up to about 5% drift, with potentials for higher drift capacity. However, Column BG-6 was one of the first columns tested, and the test was discontinued prematurely due to a safety concern at a high drift level of 5 %.

A comparison of force-displacement envelopes of Columns BG-7 and BG-9 is shown in Fig. 6-6. These columns were confined with 9-cell grids (6.6 mm diameter bar) and reinforced

with 12#20 and 20#15 longitudinal bars, respectively. All other parameters were identical, including concrete strength *(33.7 MPa)*, vertical spacing of transverse reinforcement *(76 mm)*, and axial load level $(0.38P_0)$. The results show that no significant difference in behavior was observed in strength. However, Column BG-9 suffered earlier bar buckling because of the small size of longitudinal reinforcement, although it had higher volumetric ratio of longitudinal steel.

Columns FRP-2 and FRP-8 were also built and tested similar to BG-7 and BG-9, except that the reinforcement grids were made out of fiber reinforced plastic. No significant difference in behavior was recorded as shown in Fig. 6-6. Similarly, Columns FRP-12 and FRP-14 were confined with 9-cell fiber reinforced plastic grids and reinforced with 12#20 and 4#30 longitudinal bars, respectively. All other parameters remained identical, including concrete strength *(37.2 MPa)*, vertical spacing of transverse reinforcement *(76 mm)*, and axial load level $(0.38P_0)$. The force-displacement envelopes of these columns are compared in Fig. 6-6. The results indicate that column FRP-14 showed slightly superior behavior compared to column FRP-12, providing further proof that grids with reasonable number of cells improve the uniformity of lateral confinement pressure without the presence of longitudinal reinforcement at intermediate perimeter joints. Using a fewer number of larger size bars not only simplifies cage fabrication, but also increases stability of bars.

6.2.7 Effect of Axial Load Level

The columns tested in this investigation were subjected to different levels of constant axial load to investigate the significance of axial compression. All normal-strength concrete columns were initially loaded to about 40% of their concentric load capacity, P_0, expect when the level of axial load was a parameter, in which case the compression force was reduced to about $20\%P_0$. Six pairs of columns were tested to investigate the effect the axial load on strength and deformability of columns. Each pair had otherwise identical characteristics.

The first pair consisted of columns BG-2 and BG-3, which were reinforced with 8#20 longitudinal bars and 4-cell welded reinforcement grids, resulting in a volumetric ratio of

2.00%. The second pair consisted of BG-7 and BG-8, which were reinforced with 12#20 longitudinal bars and 9-cell welded reinforcement grids, resulting in a volumetric ratio of 1.26%. The third pair consisted of SD-1 and SD-2, which were reinforced with 12#20 longitudinal bars and confined with perimeter hoops and double-head studs, forming a 9-cell grid configuration. The fourth pair consisted of FRP-2 and FRP-3, which had a similar reinforcement arrangement as BG-2 and BG-3, except the transverse reinforcement consisted of fiber reinforcement plastic grids. The fifth and sixth pairs consisted of FRP-5 and FRP-6, and FRP-9 and FRP-10, with the same reinforcement configuration as BG-7 and BG-8, except the transverse reinforcement was made out of fiber reinforcement grids having two different sizes (see Table 4-1).

The comparisons of force-displacement envelopes of each pair of columns are shown in Fig. 6-7. The figures indicate that all specimens resisted lateral deformations of 4% drift and higher with the exception of column FRP-5 that was a repaired column. While all columns showed ductile behavior due the proper confinement of core concrete and superior quality of transverse reinforcement, the deformability of the columns was reduced when the level of axial compression was high. In addition, the columns subjected to higher axial compression experienced rapid strength degradation. In fact, columns subjected to about 40% of P_0 experienced 1% lower lateral drift than those subjected to 20% P_0, at 20% strength decay in moment resistance. Furthermore, the *P-Delta* effect was more pronounced in columns with higher axial compression.

The final failure of columns under heavy axial compression was characterized by buckling of longitudinal reinforcement either between two layers of transverse reinforcement (first mode) or over a longer length (second mode or higher). Higher buckling modes involved yielding and rupture of one or more transverse reinforcement. This case was observed in column BG-7, which was reinforced with small size welded reinforcement steel. The tendency of longitudinal bars to become unstable, in BG-7, exerted high lateral pressure and stress concentration on corner grid joints, rupturing steel and releasing the lateral restraint on longitudinal bars and increasing their unsupported length. Fiber reinforced plastic materials had higher elastic deformation capacity and lower stiffness compared to steel. Therefore, these grids experienced higher deformation and lower restraint to longitudinal bars. The

longitudinal bars tended to buckle in the second mode or higher in FRP columns.

Another phenomenon that was observed during testing was that, columns subjected to higher axial compression experienced reduced yield penetration of longitudinal reinforcement into the footing, producing lower rotation due to anchorage slip. This observation is illustrated in Fig. 6.8 through Fig. 6-13 in companion columns. This phenomenon can be explained by reduced tension in longitudinal reinforcement during flexural action due to the presence of increased compression.

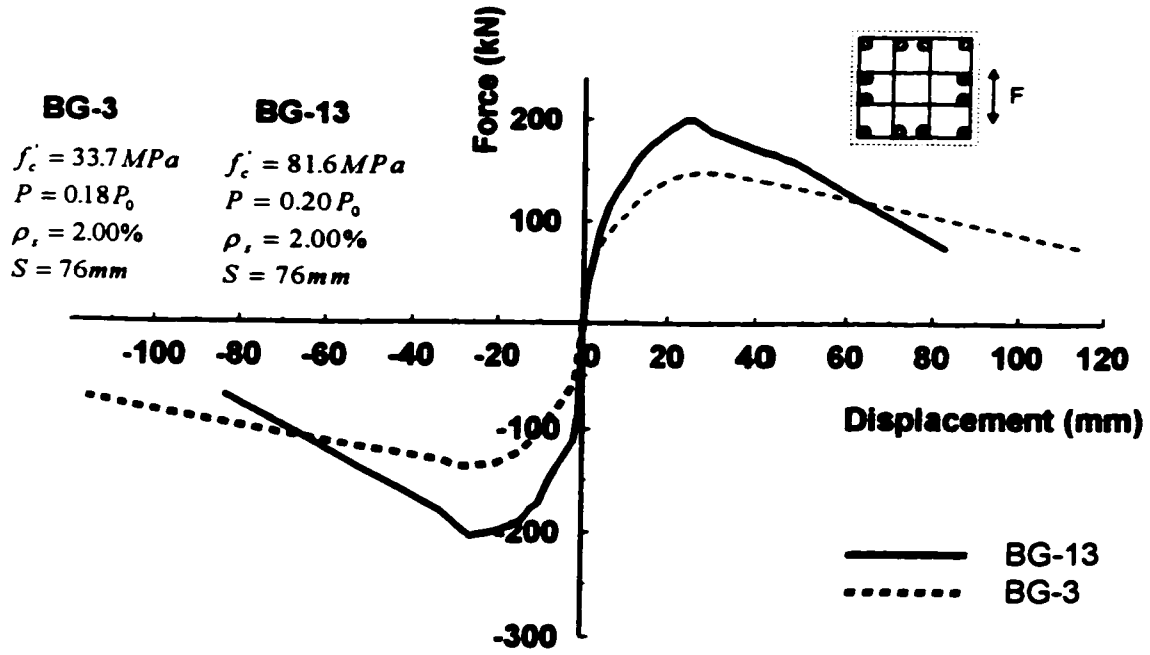

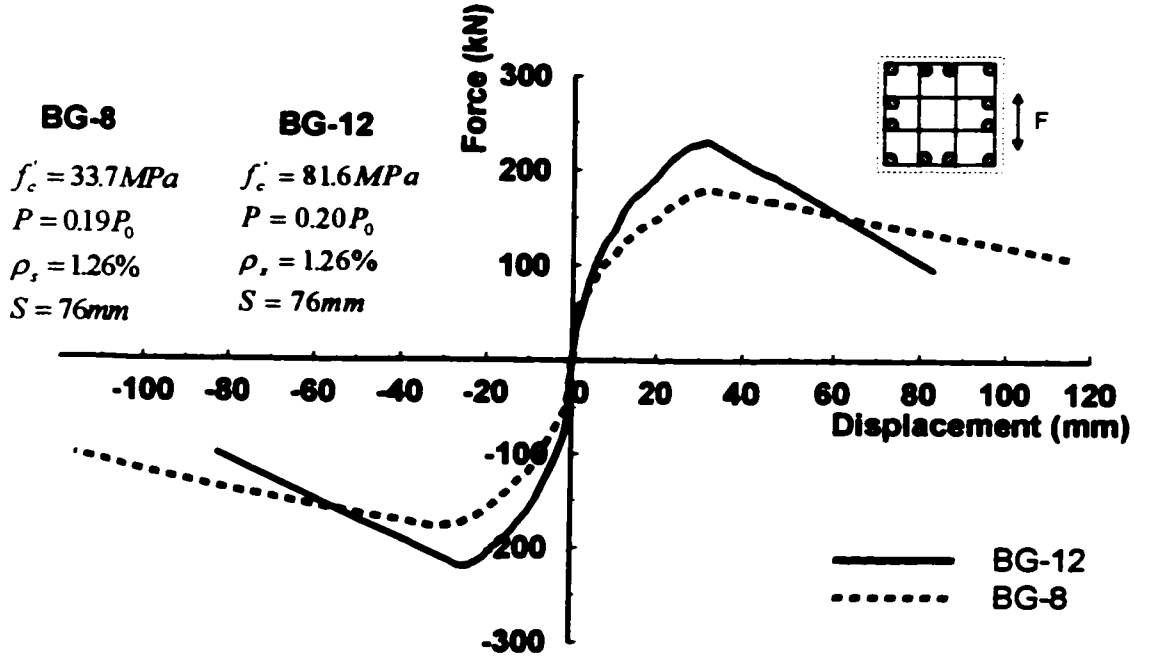

Figure 6-1: Effect of concrete compressive strength

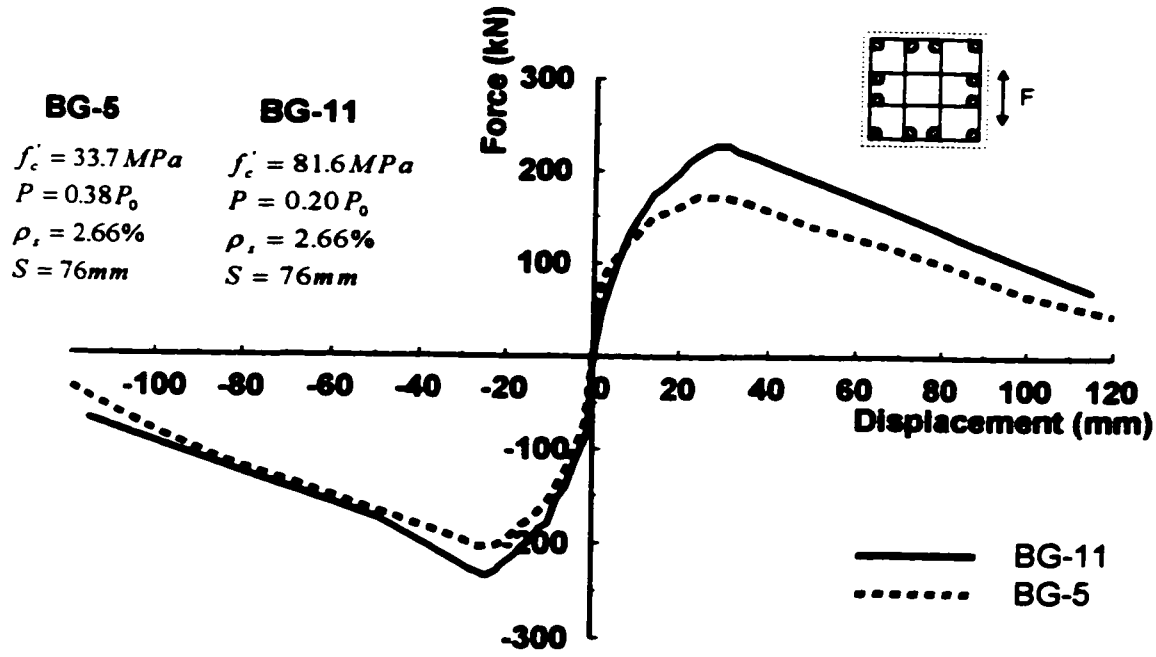

Figure 6-1: Cont.

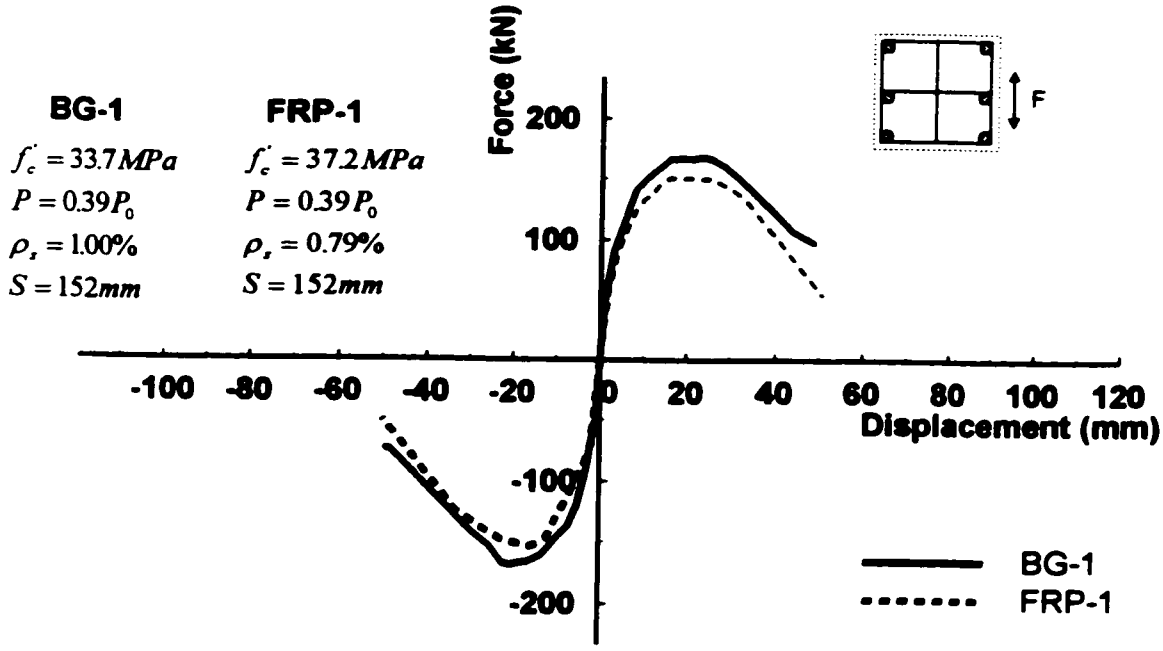

Figure 6-2: Effect of type of transverse reinforcement

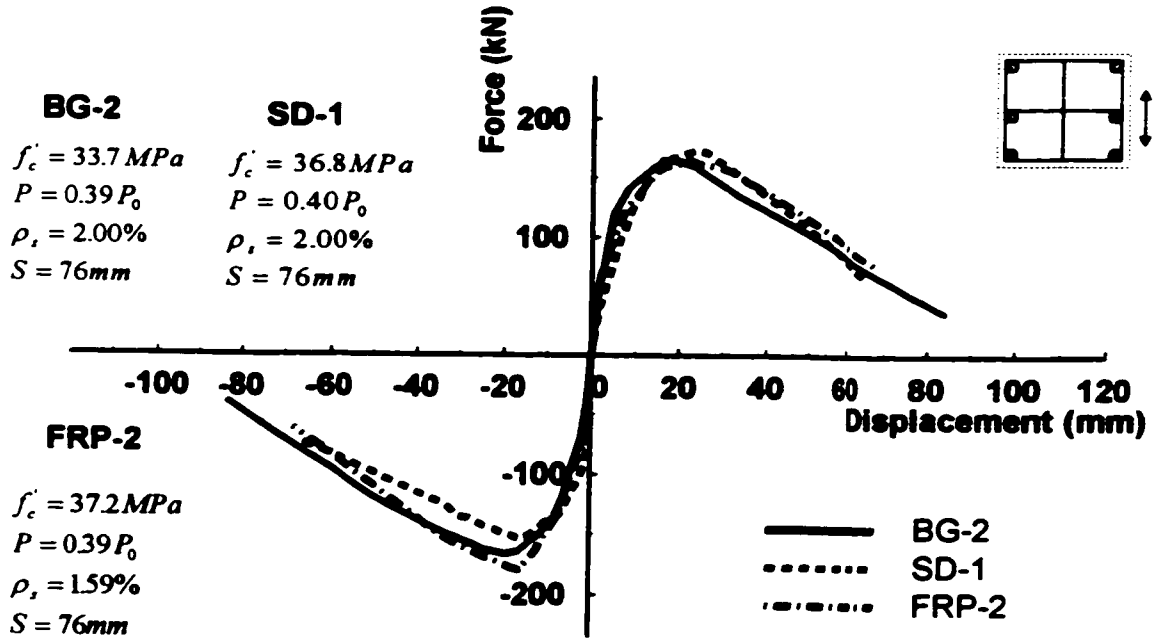

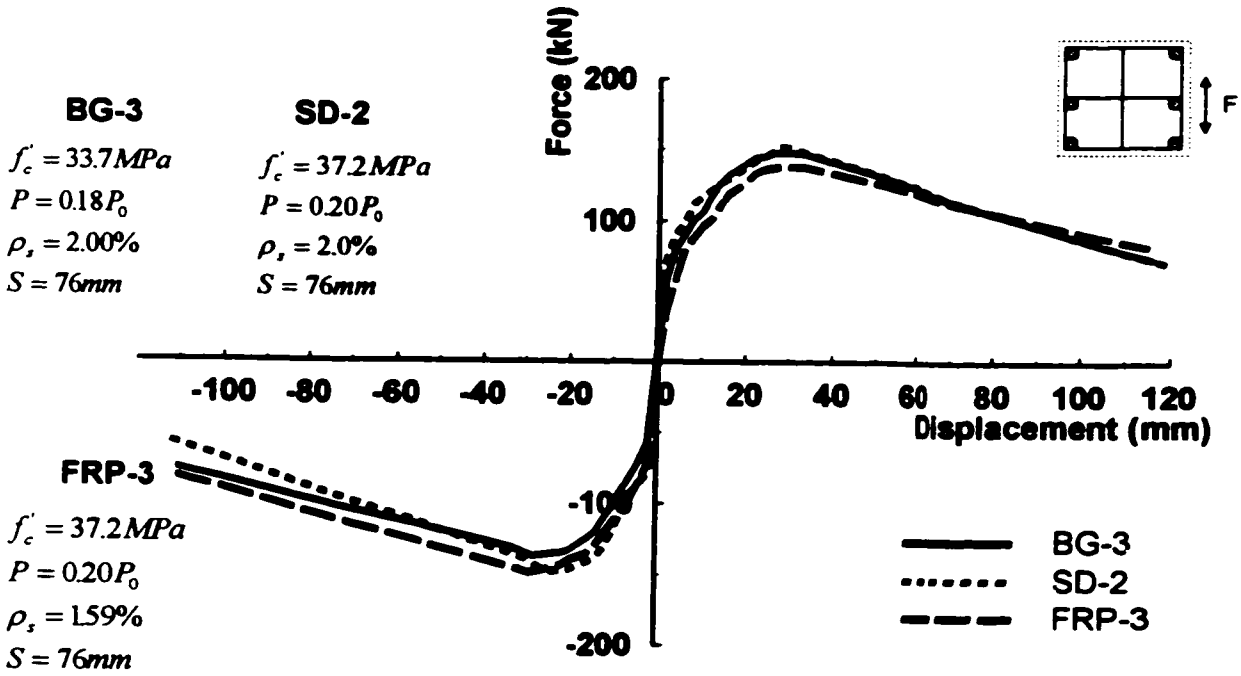

Figure 6-2: Cont.

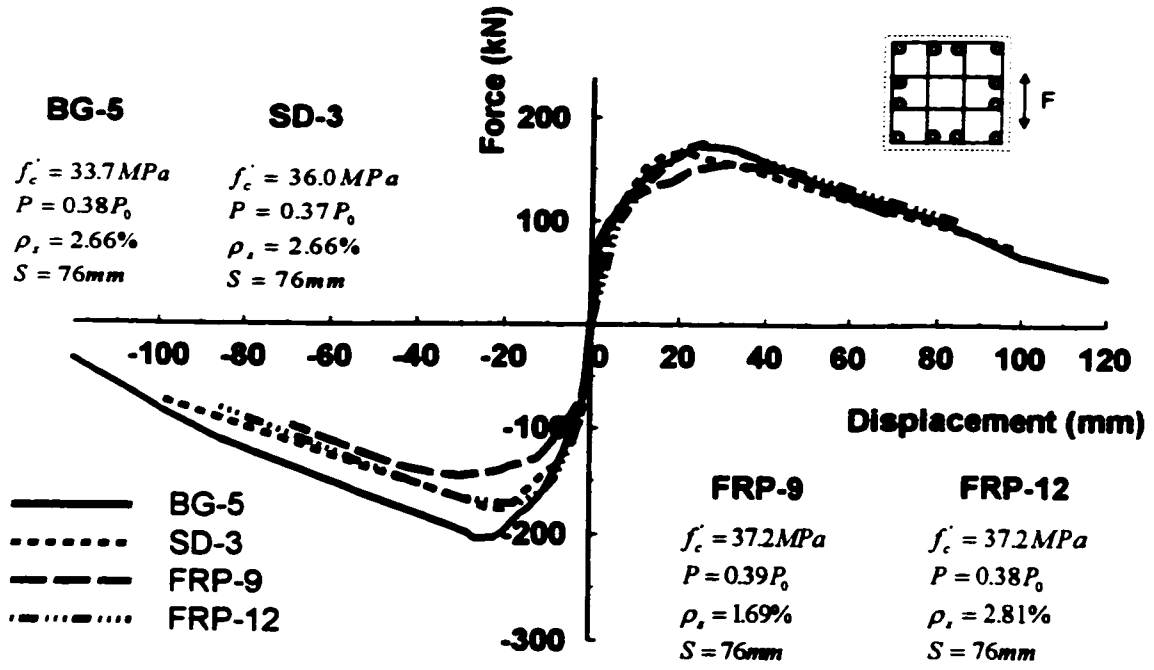

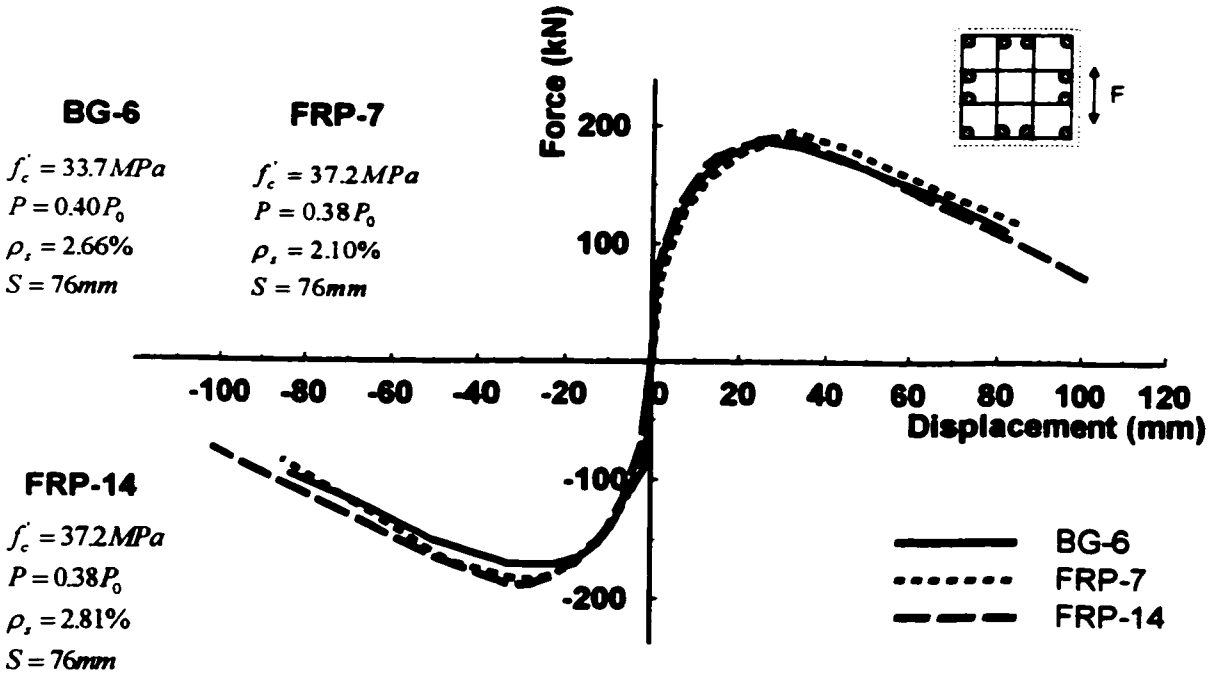

Figure 6-2: Cont.

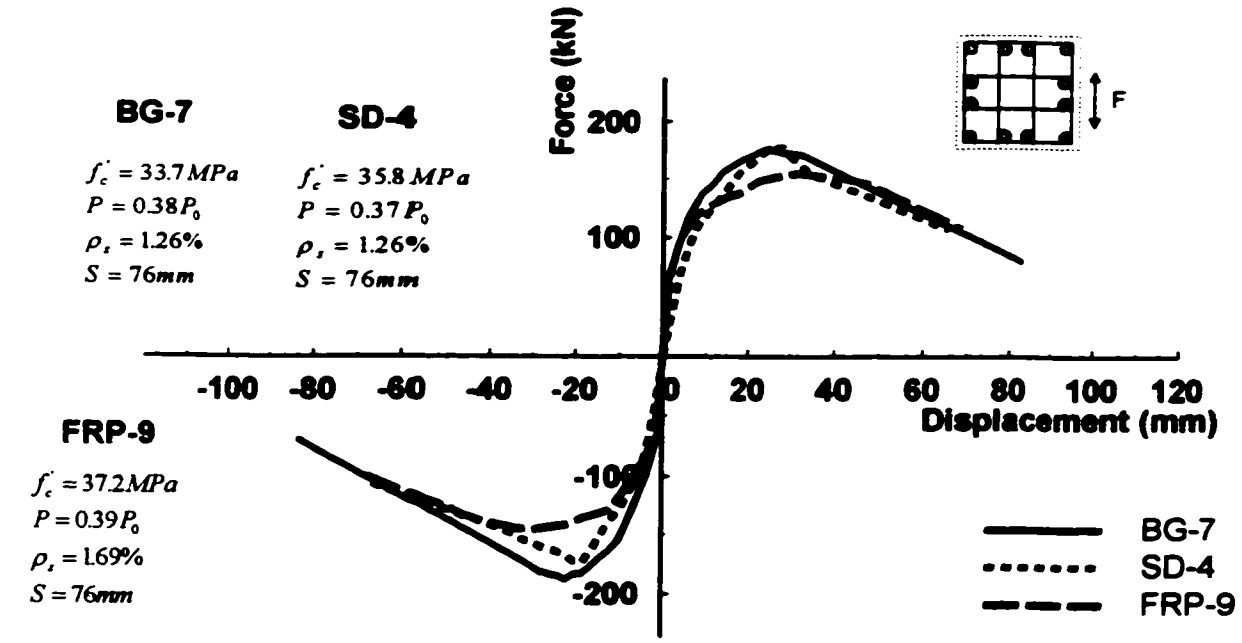

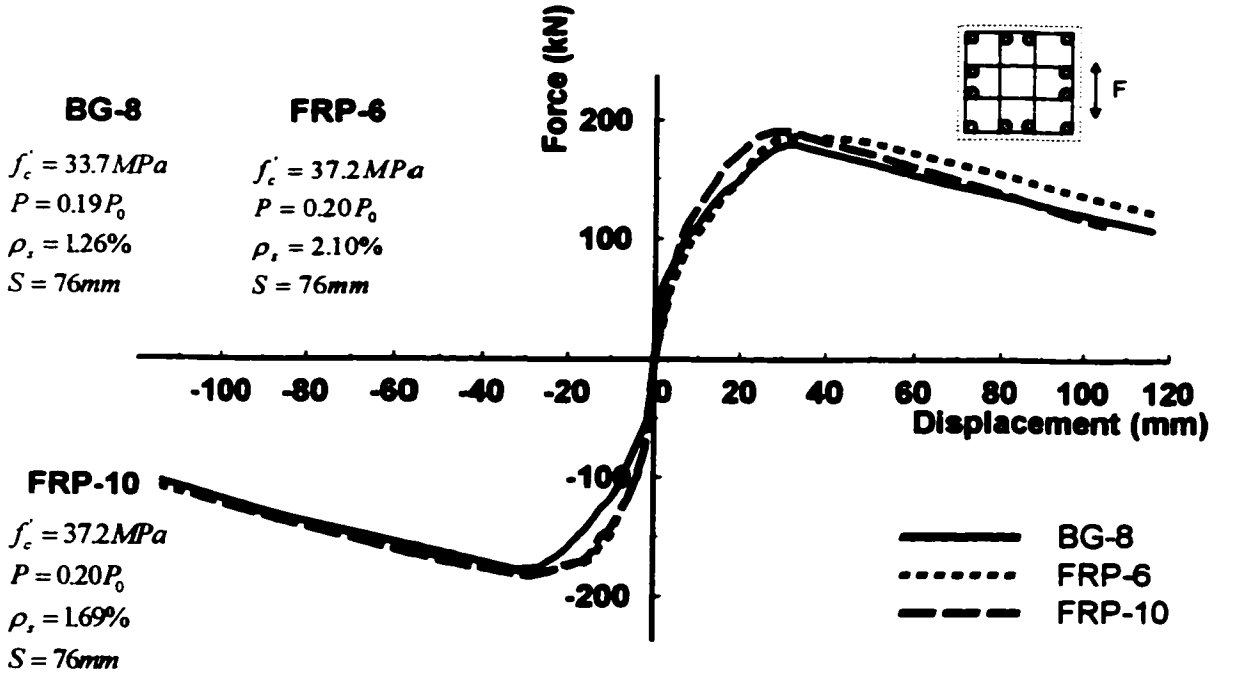

Figure 6-2: Cont.

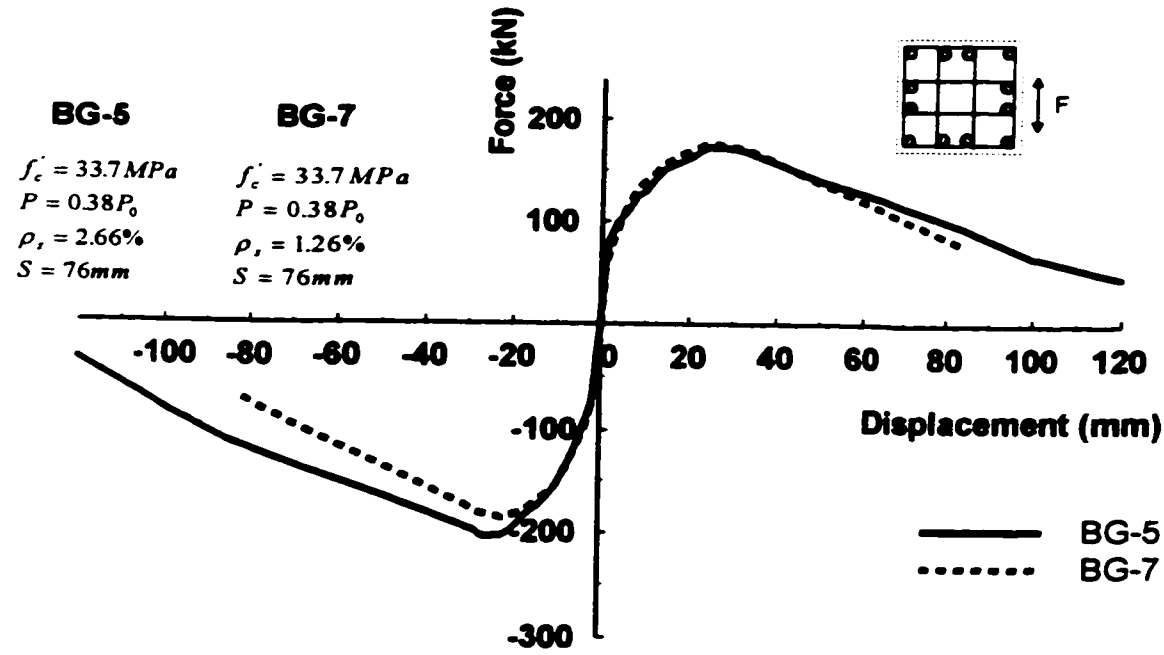

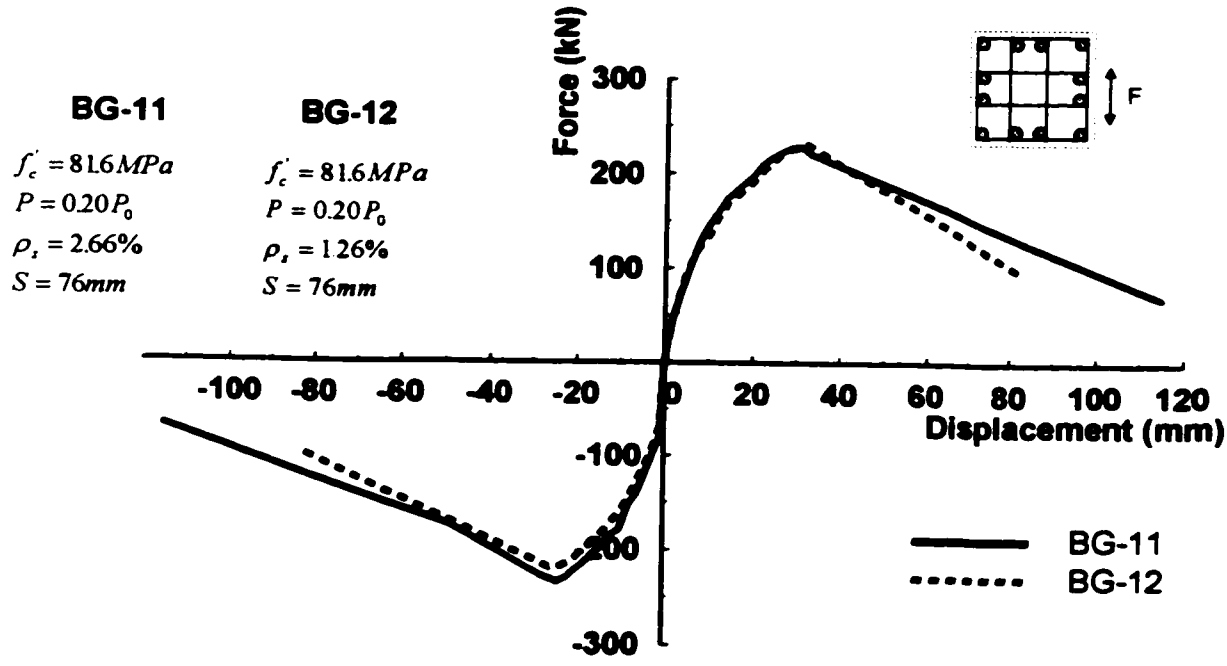

Figure 6-3: Effect of volumetric ratio of transverse reinforcement

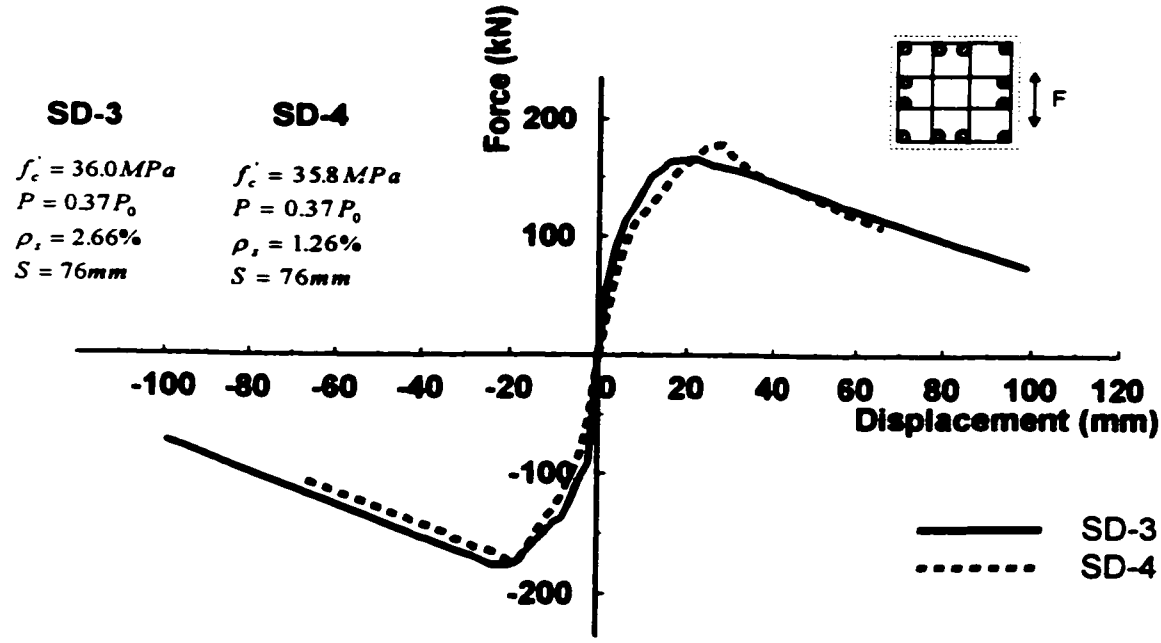

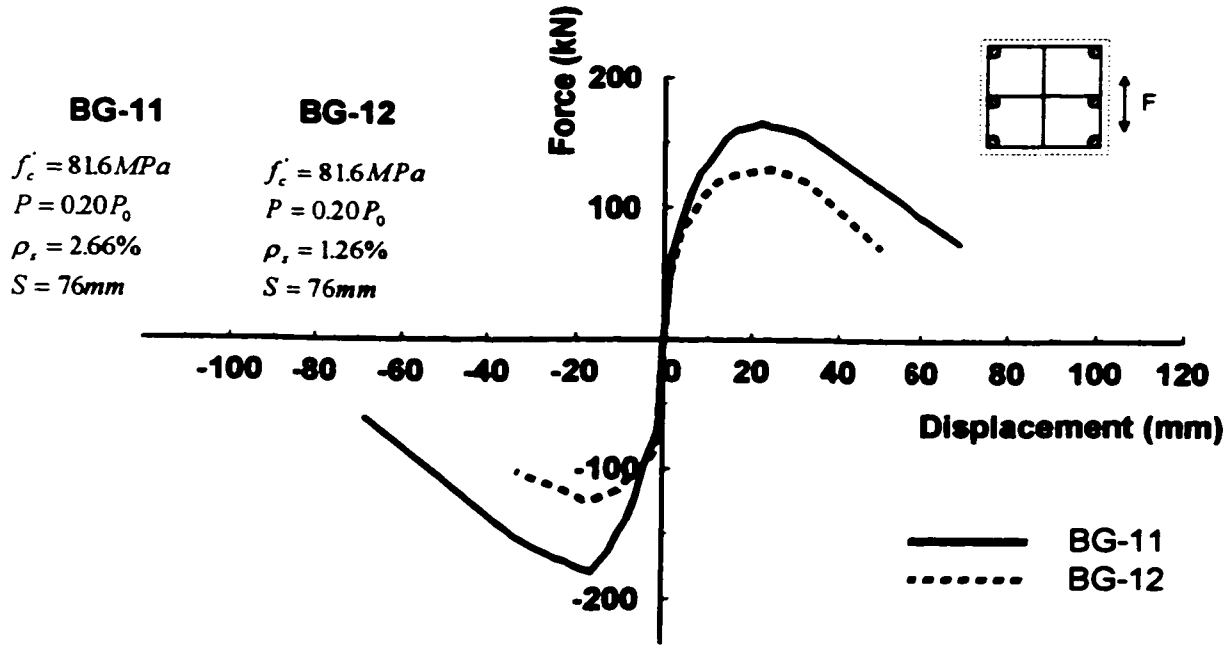

Figure 6-3: Cont.

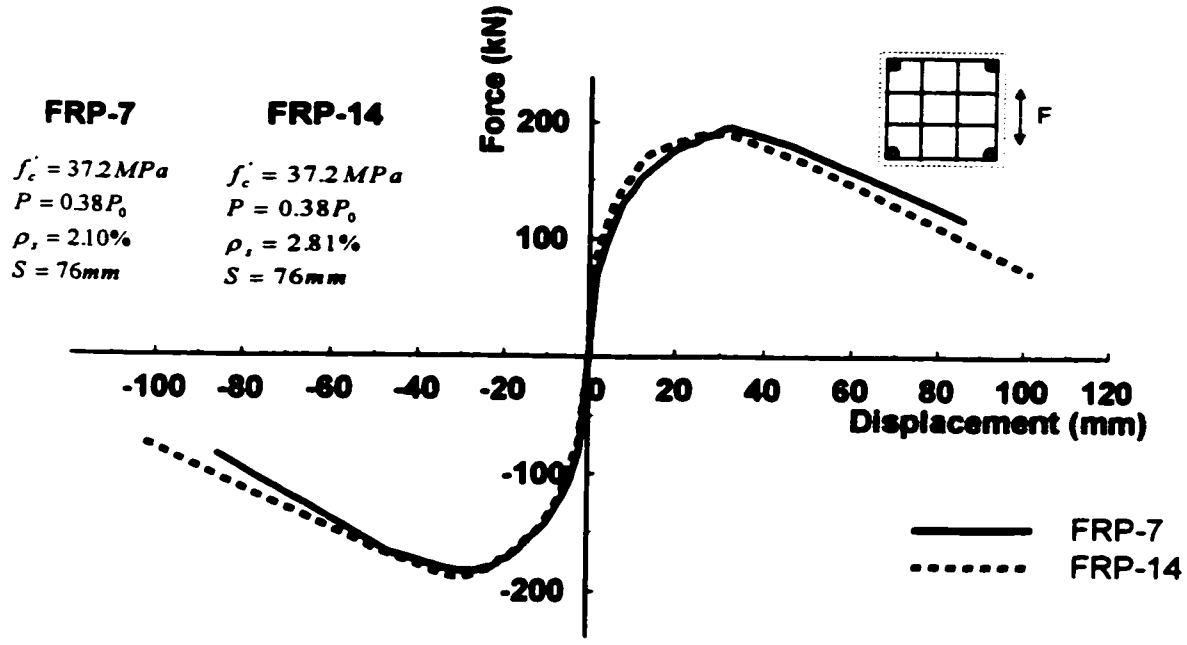

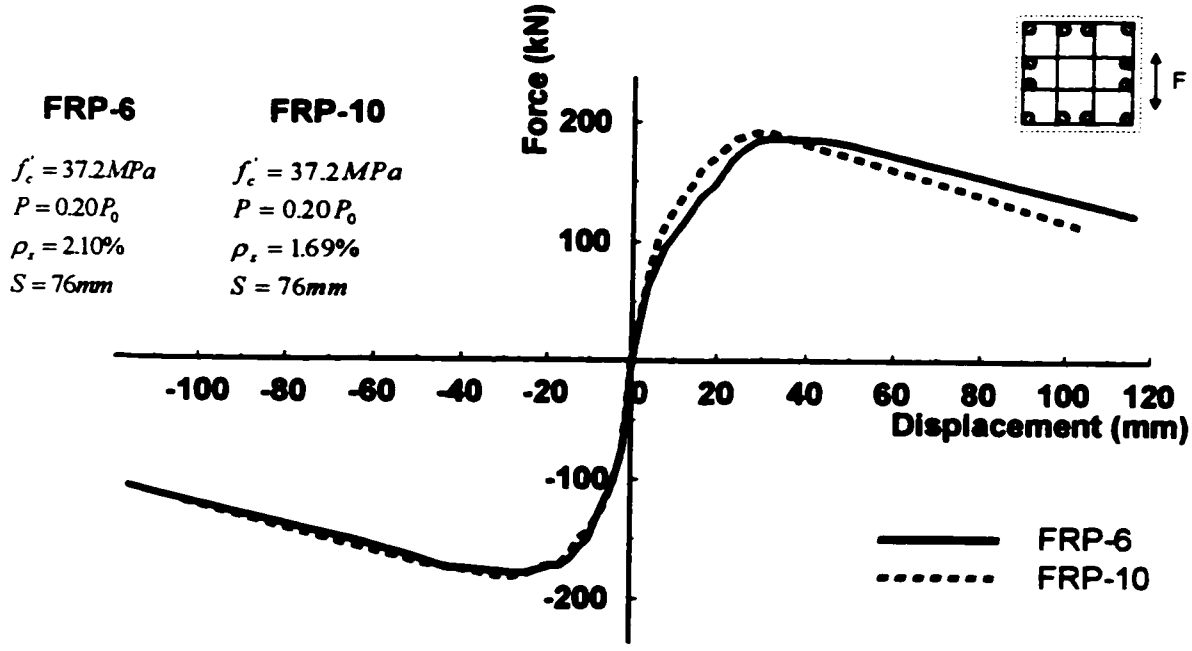

Figure 6-3: Cont.

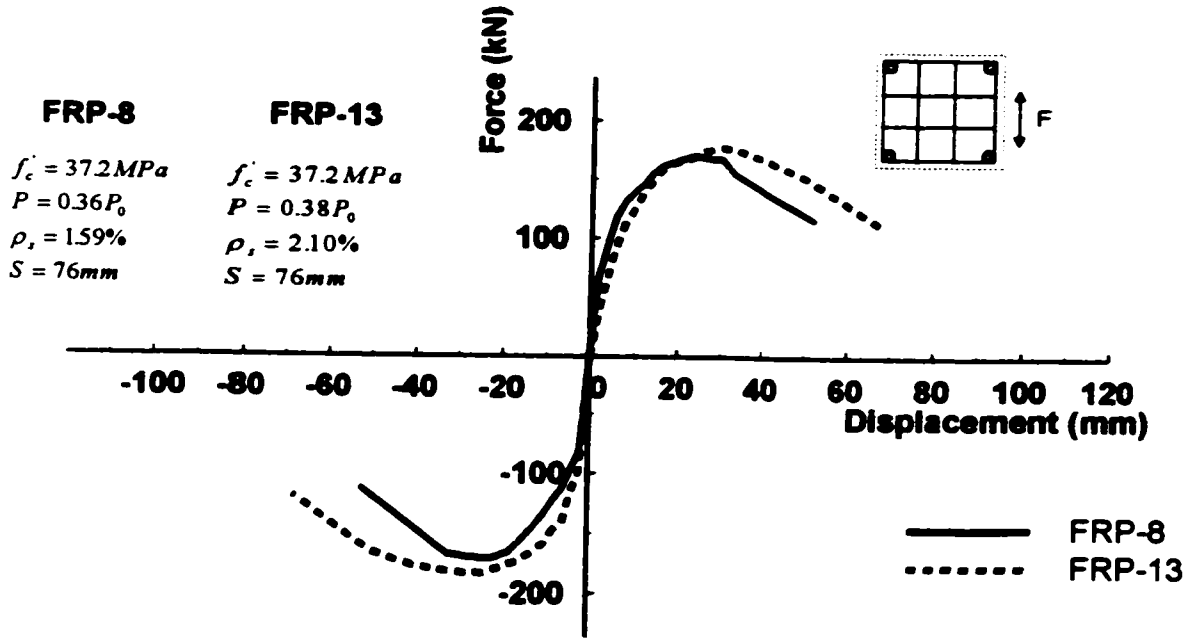

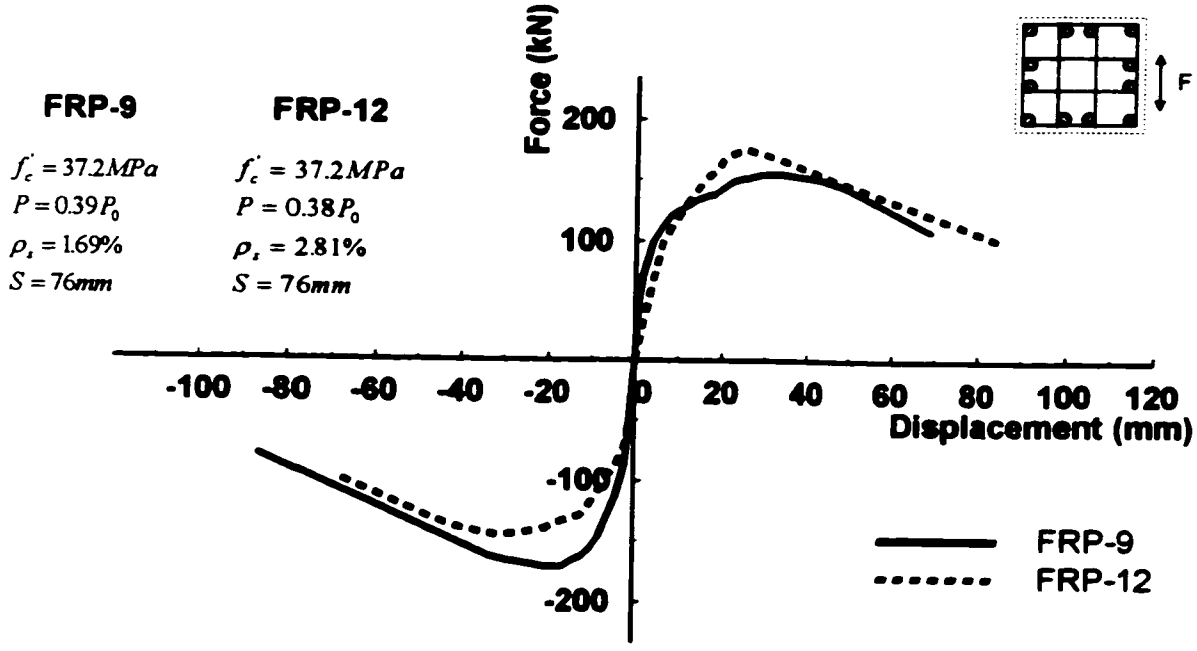

Figure 6-3: Cont.

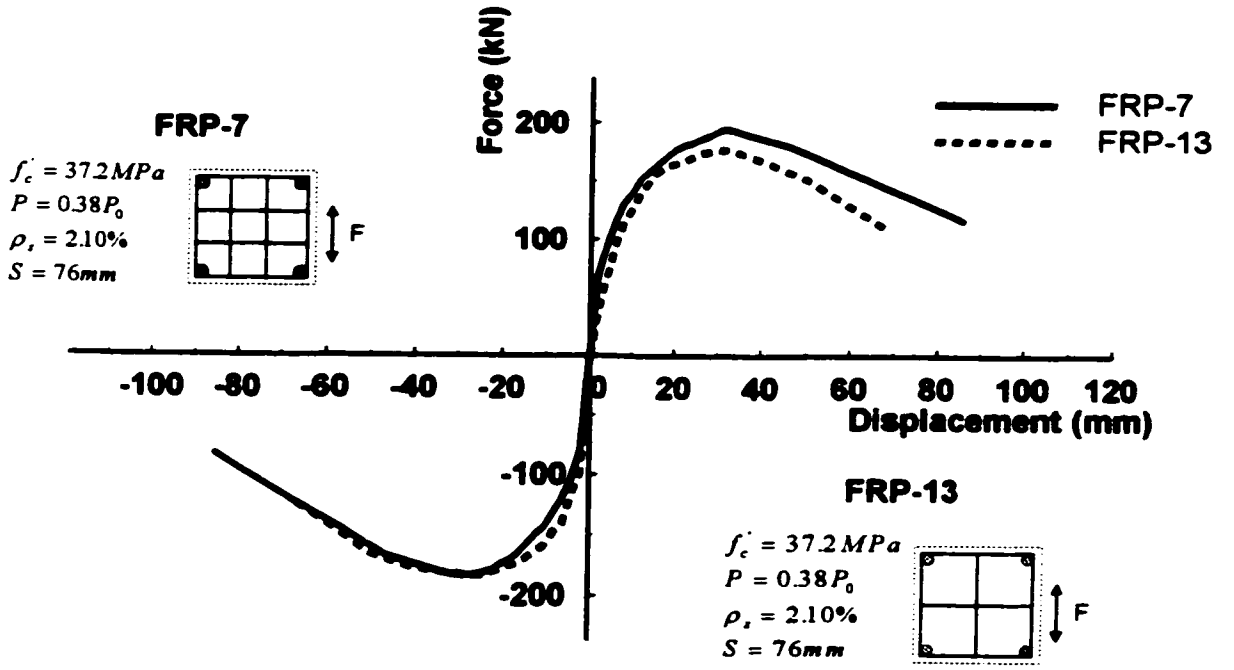

Figure 6-4: Effect of number of cells of transverse reinforcement grids

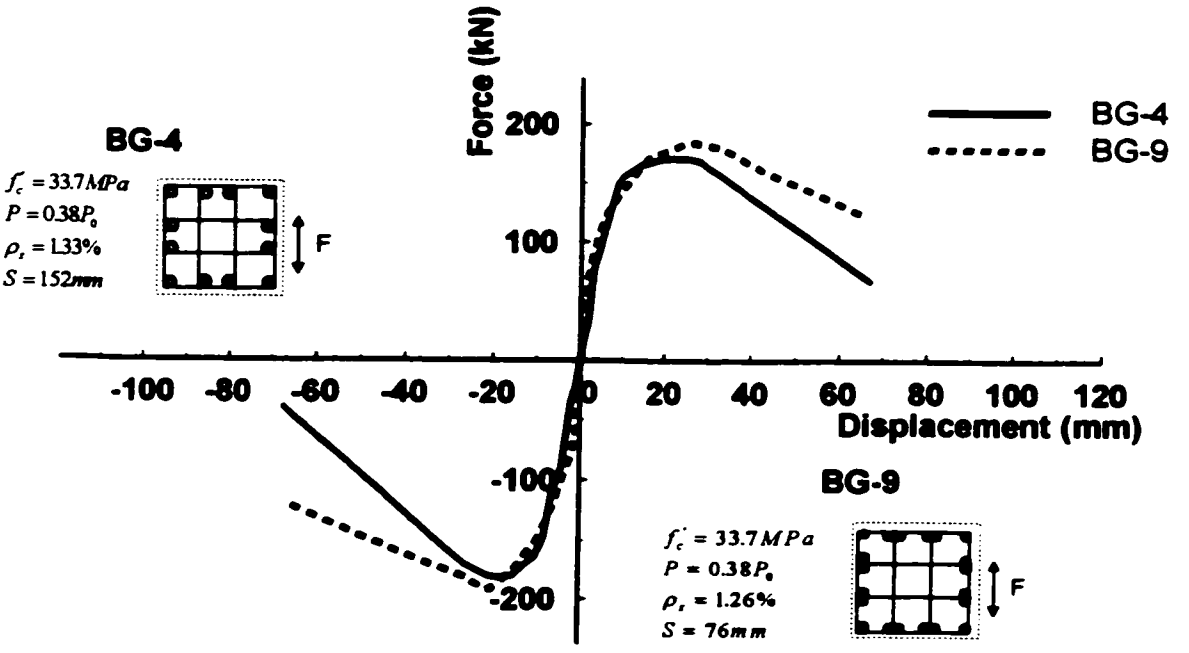

Figure 6-5: Effect of vertical spacing of transverse reinforcement

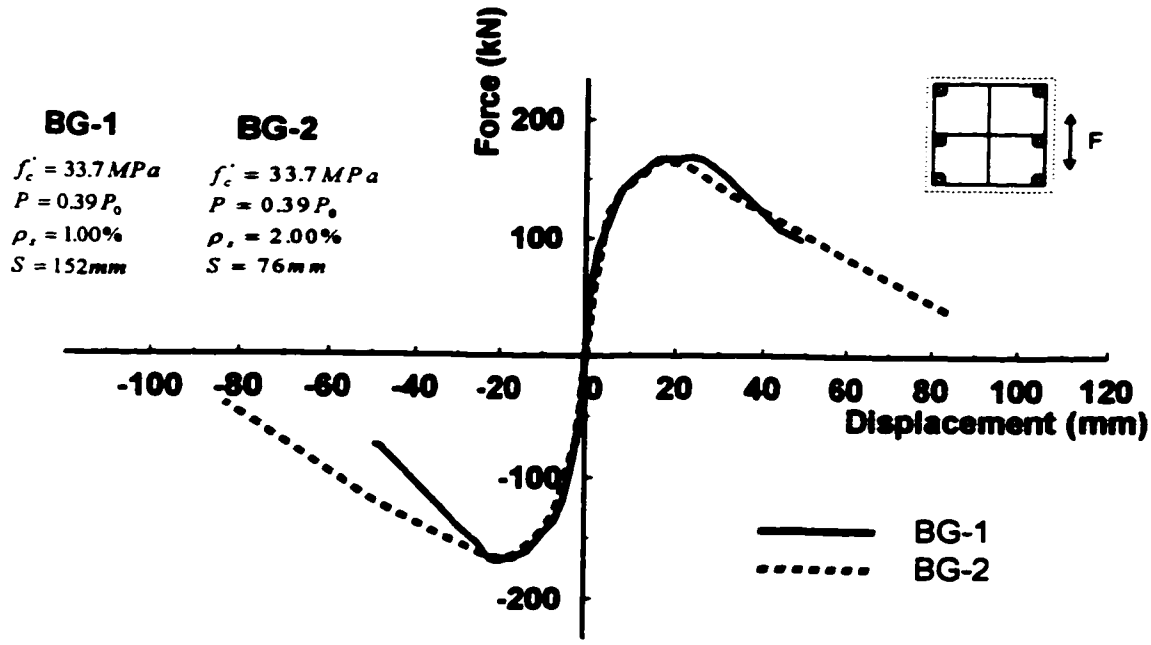

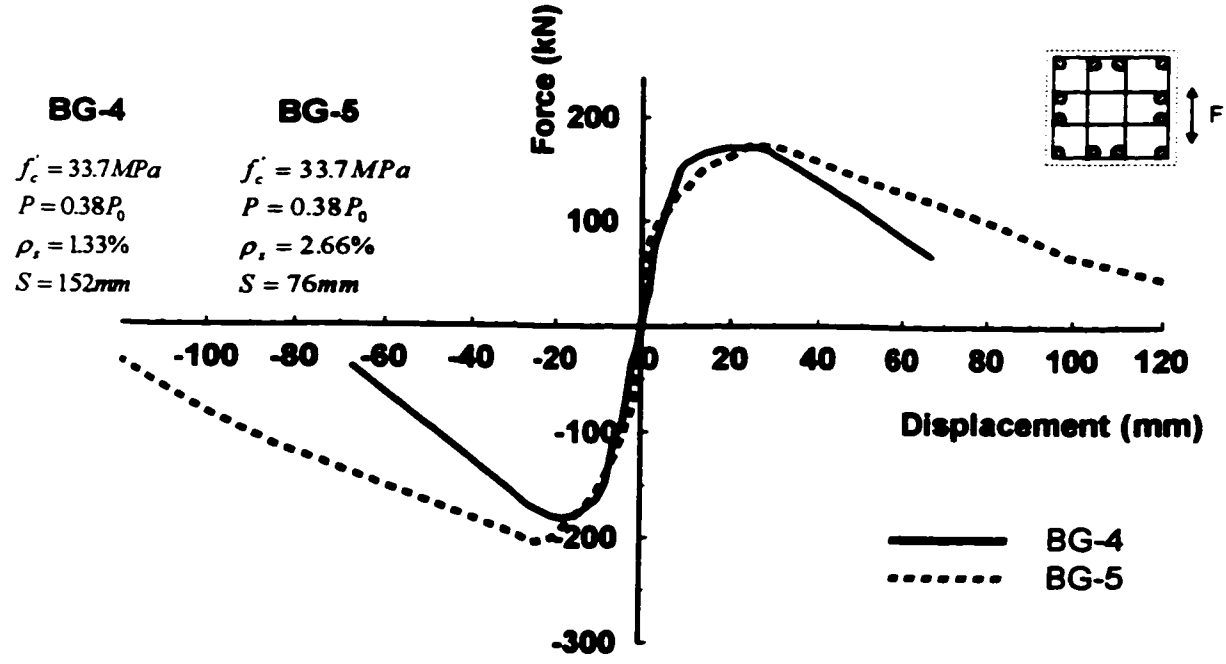

Figure 6-5: Cont.

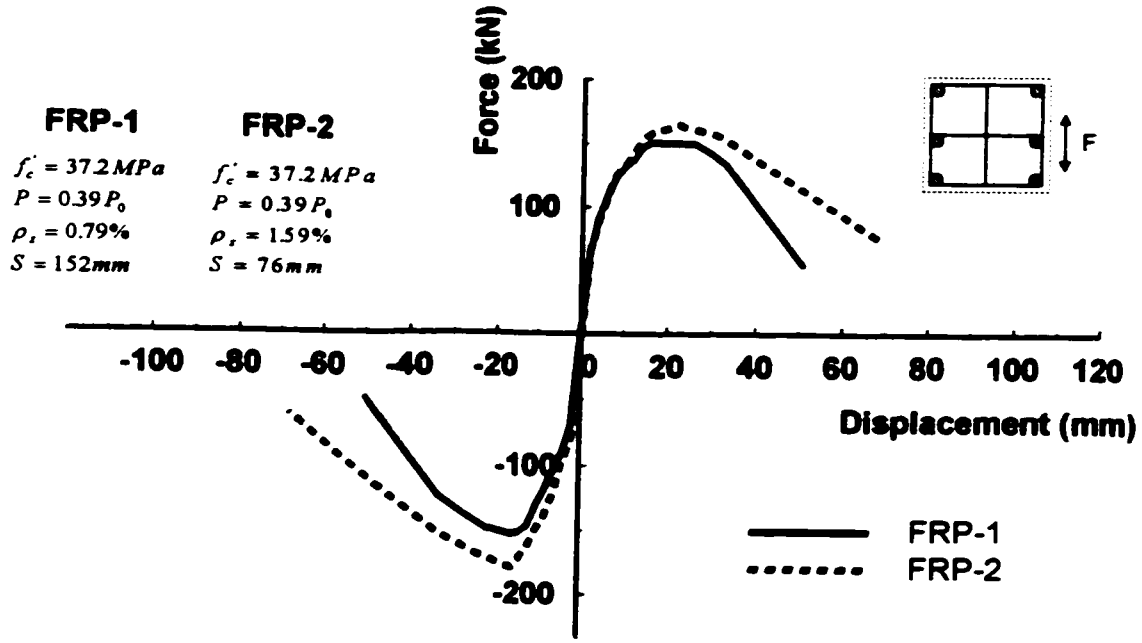

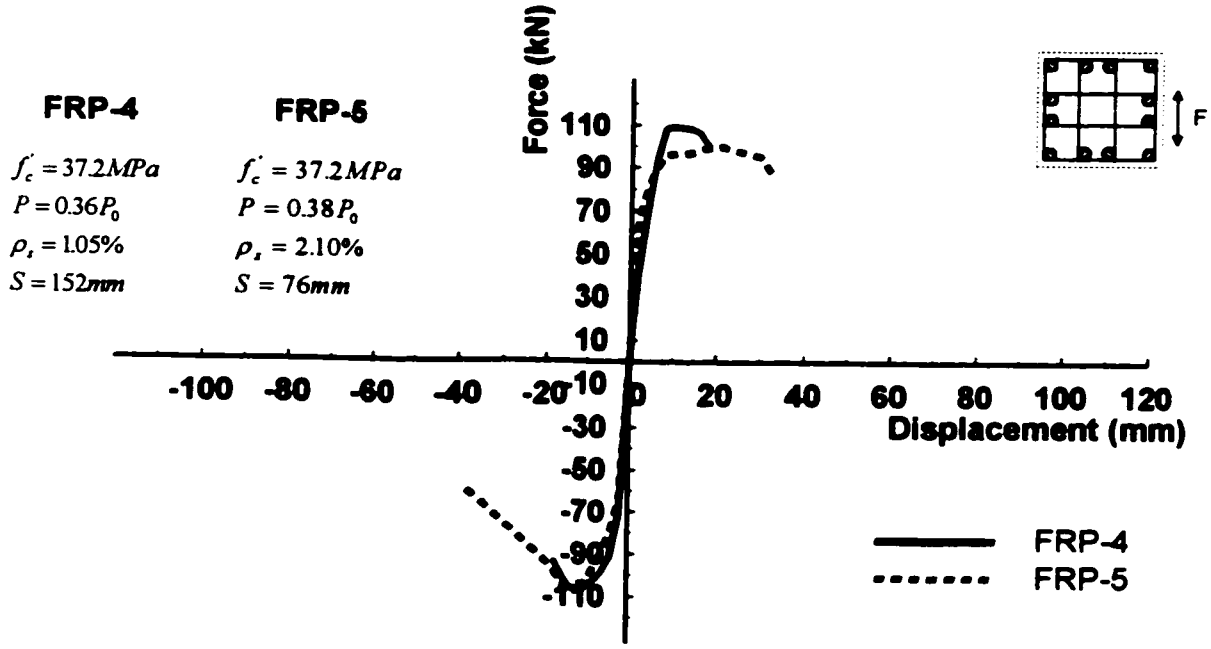

Figure 6-5: Cont.

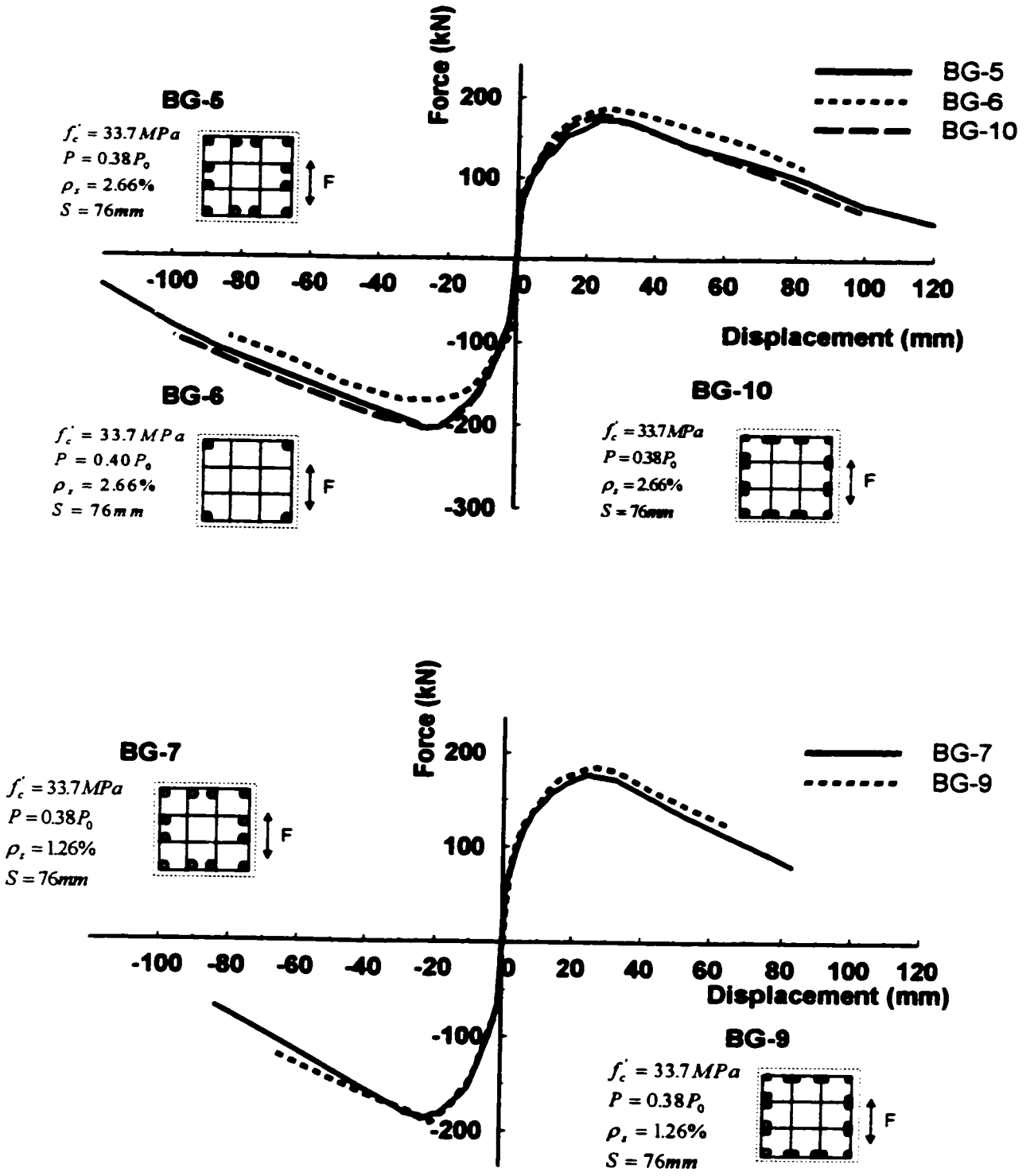

Figure 6-6: Effect of arrangement of longitudinal reinforcement

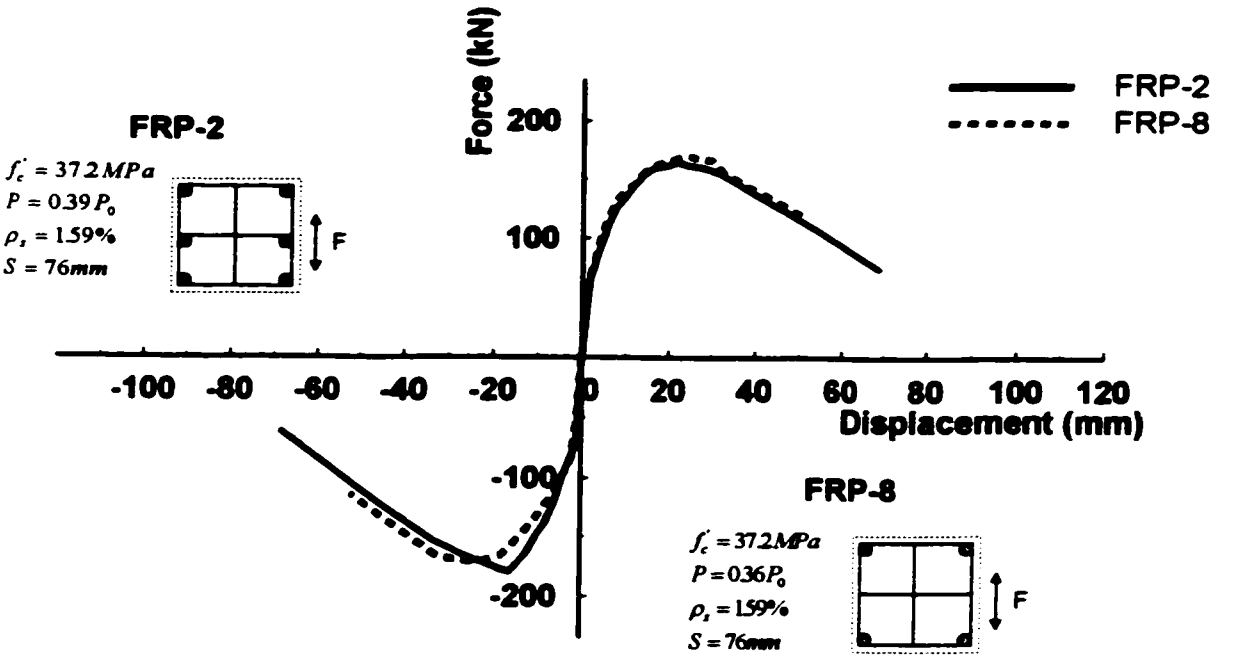

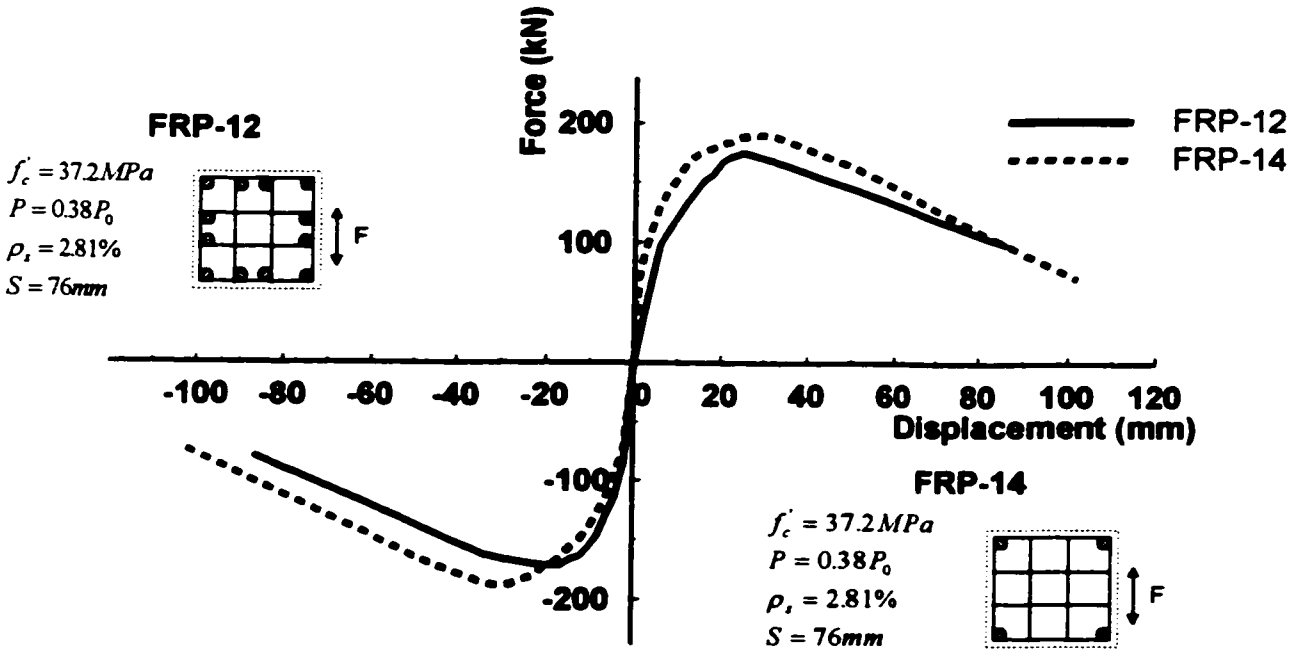

Figure 6-6: Cont.

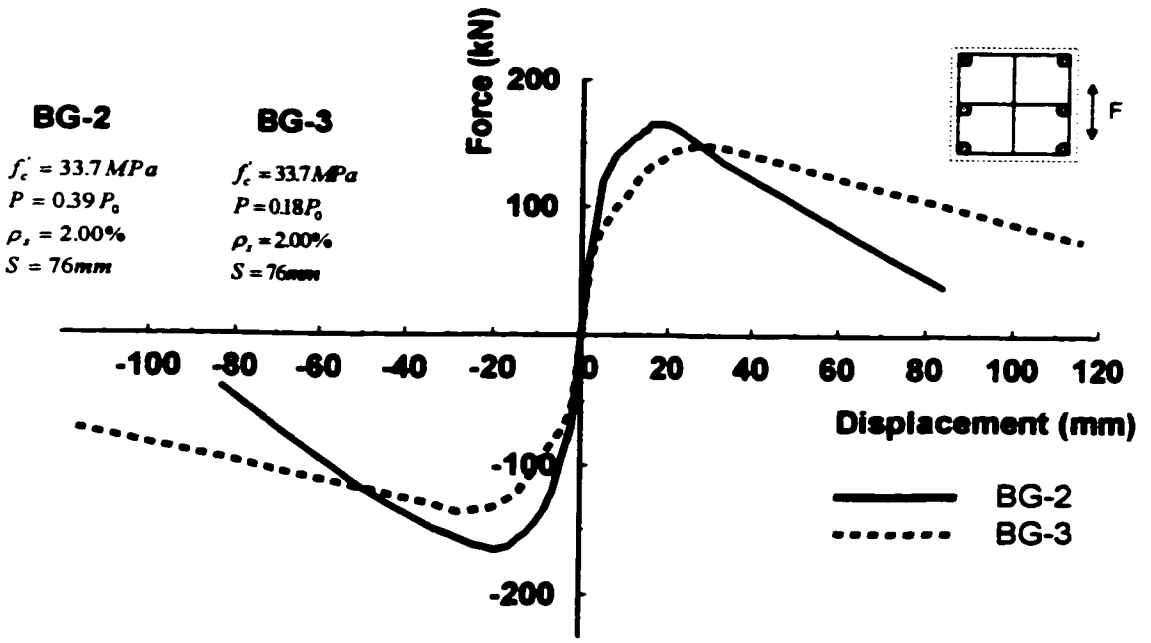

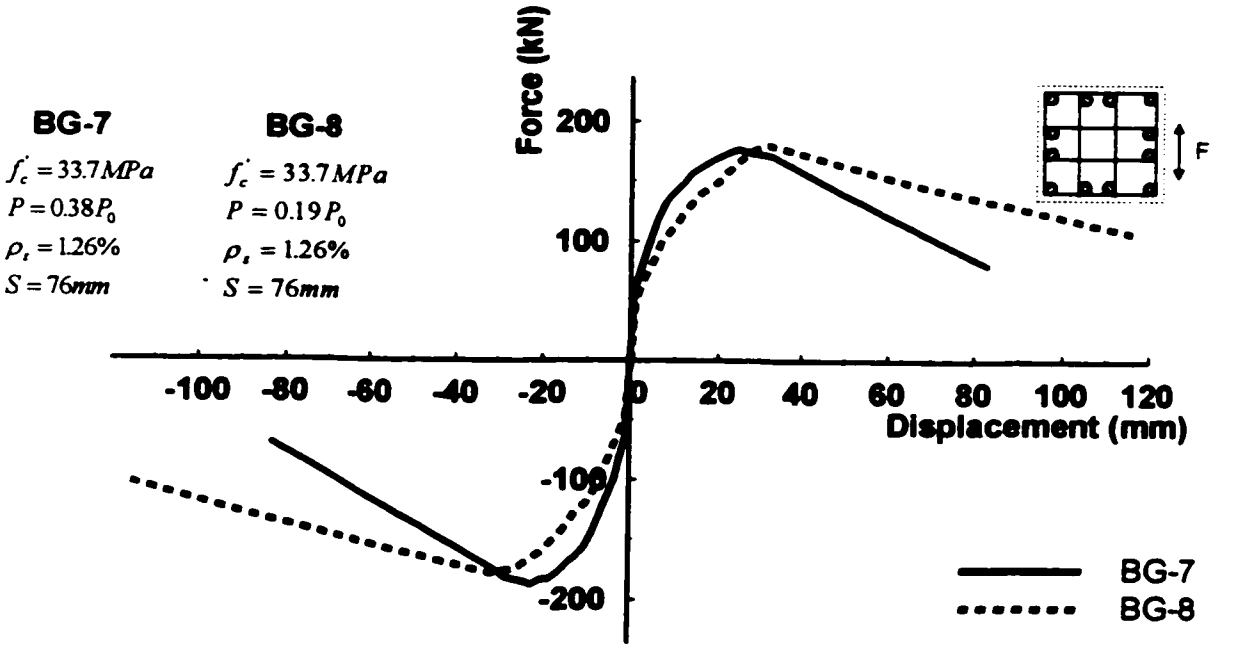

Figure 6-7: Effect of axial load

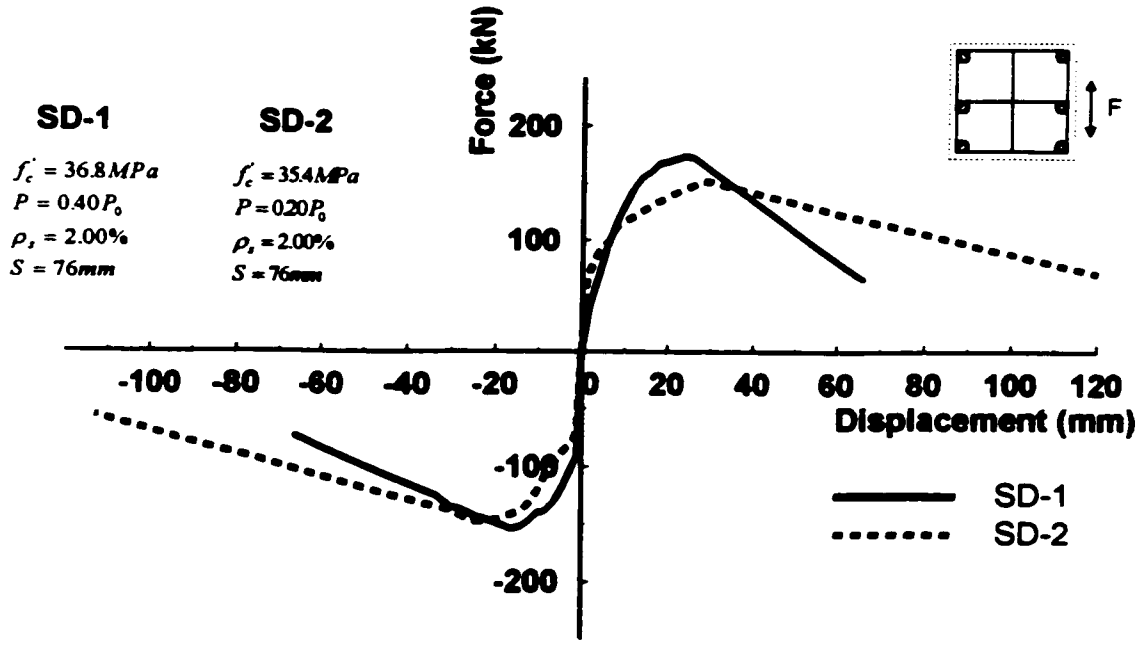

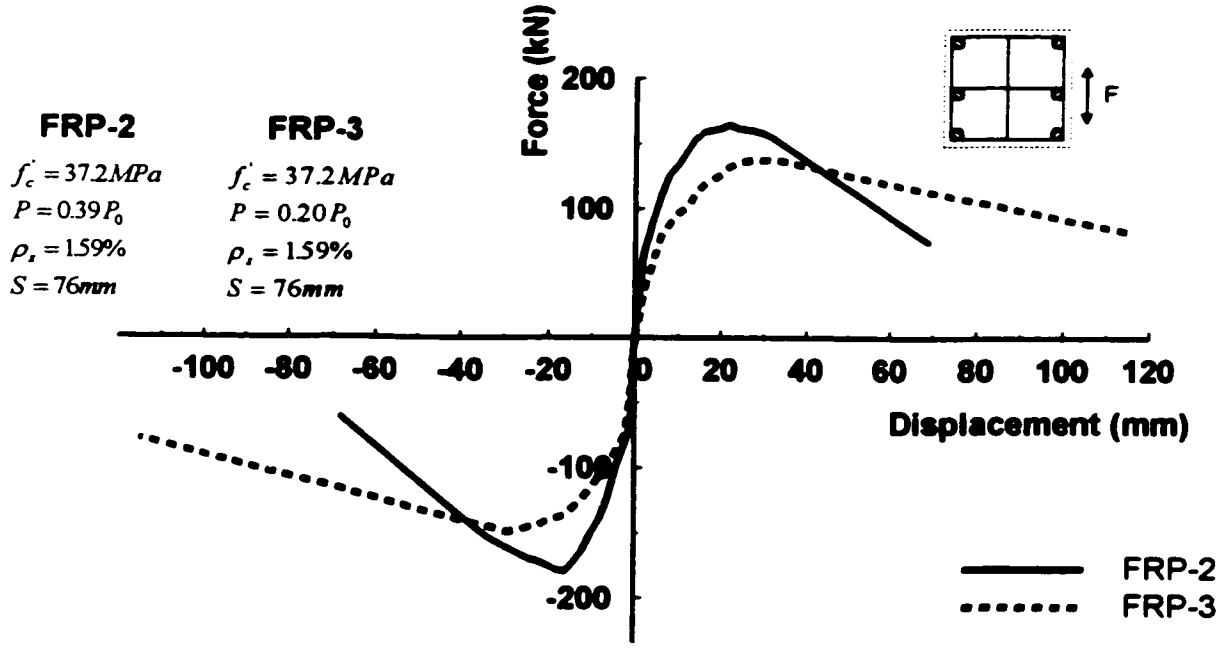

Figure 6-7: Cont.

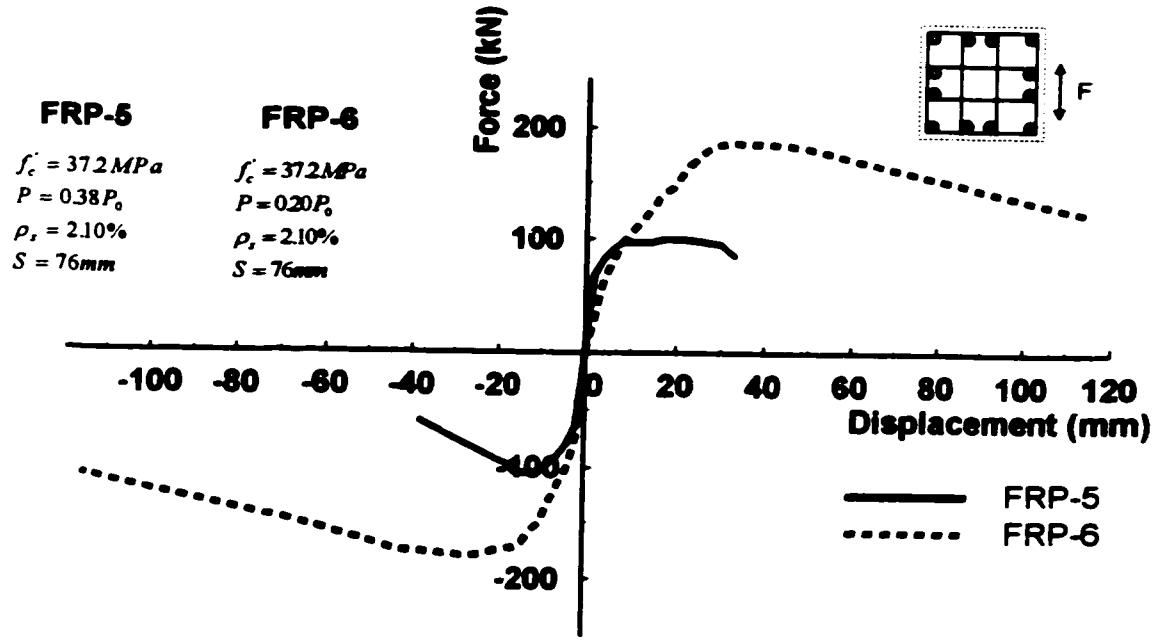

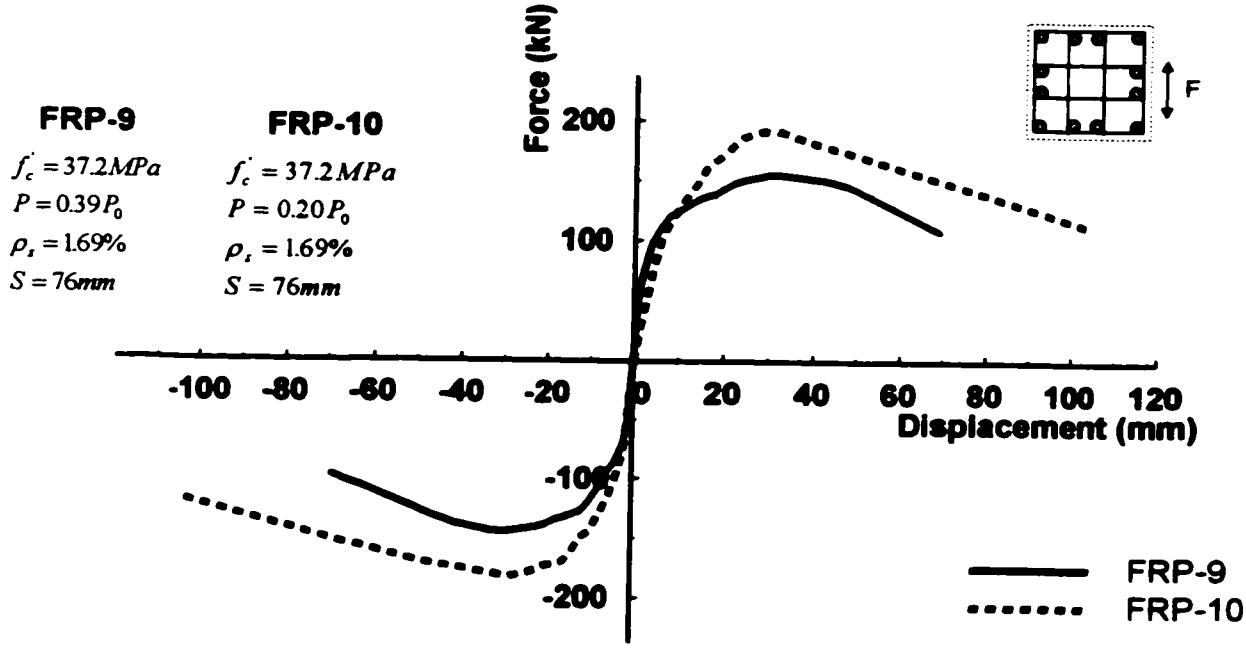

Figure 6-7: Cont.

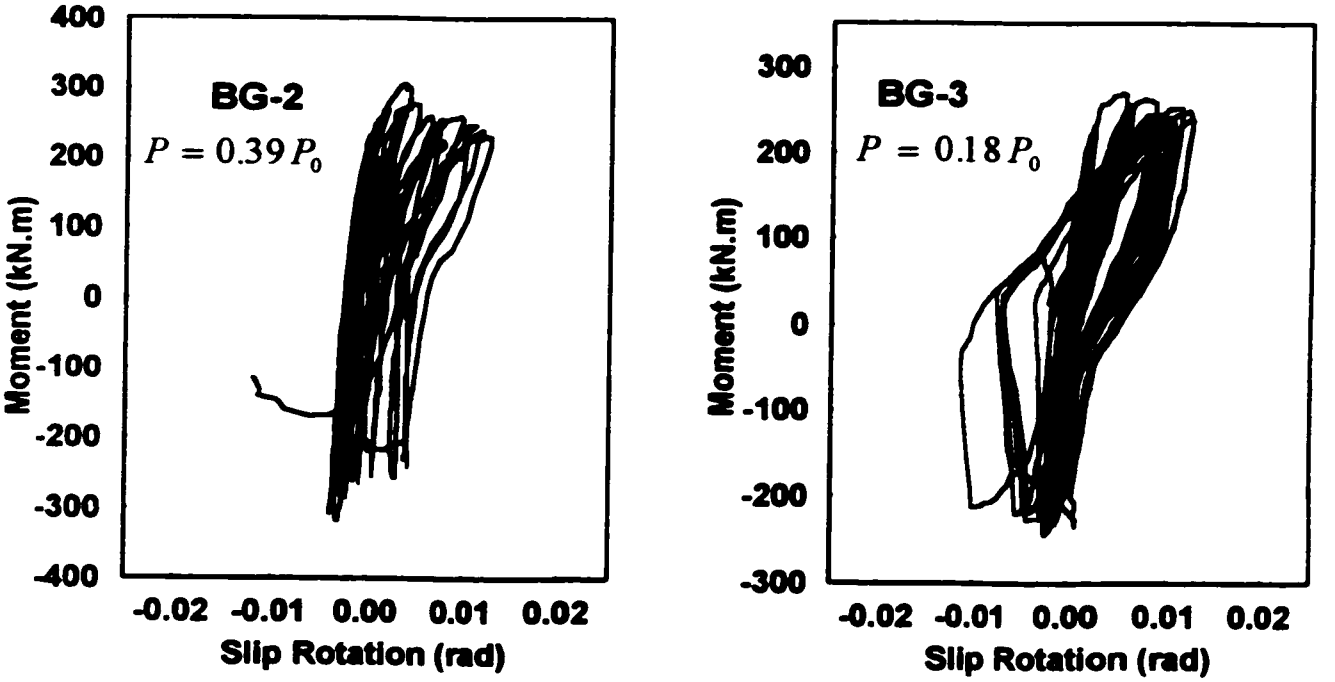

Figure 6-8: Effect of axial load on slip rotation (column BG-2 versus column BG-3)

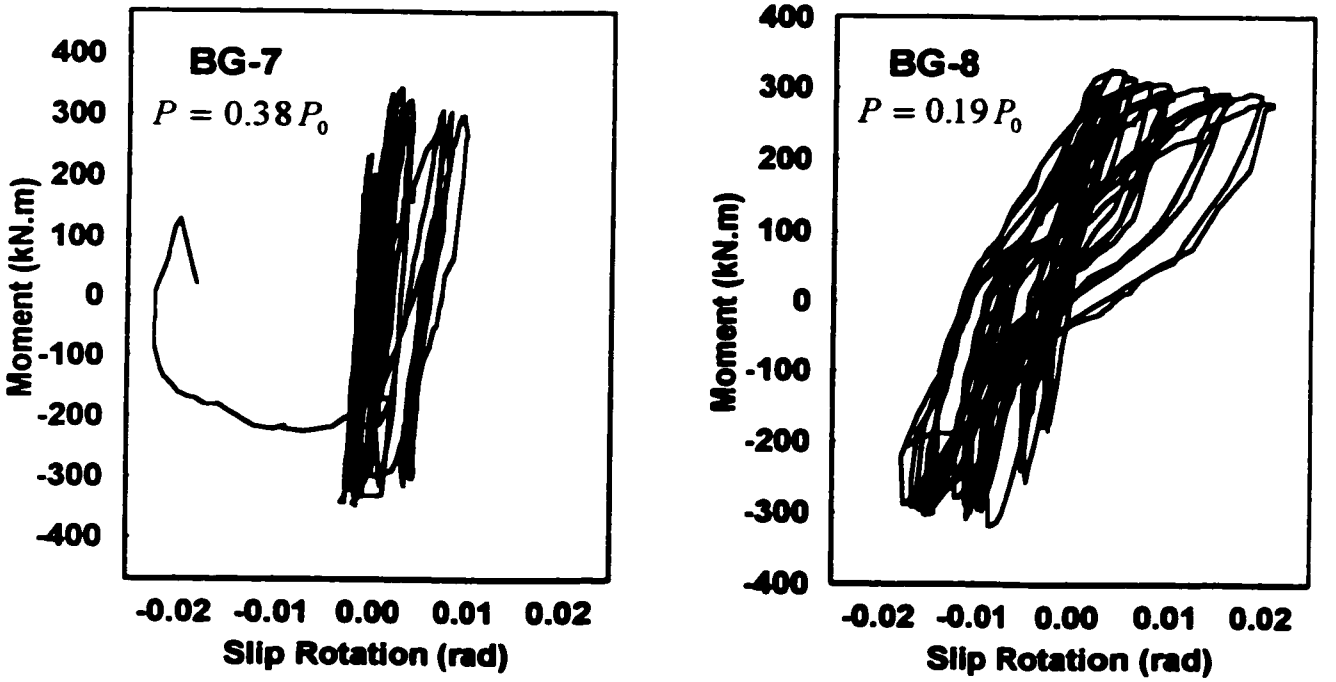

Figure 6-9: Effect of axial load on slip rotation (column BG-7 versus column BG-8)

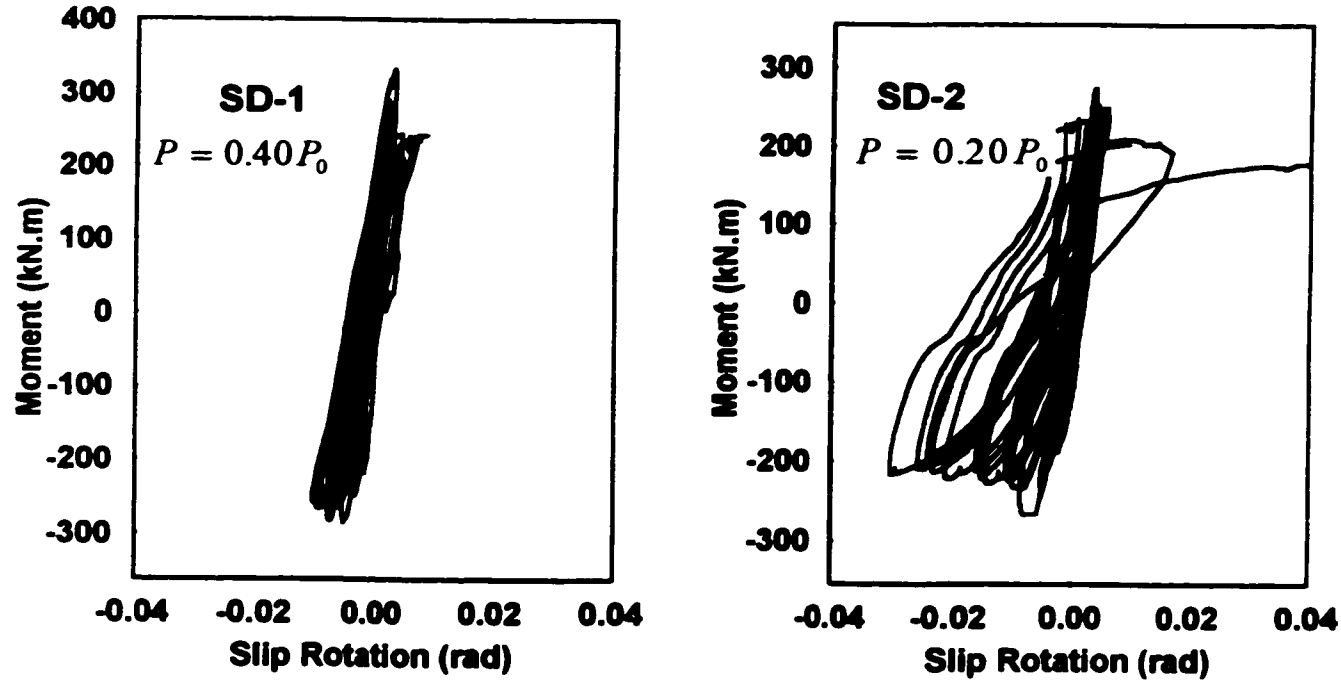

Figure 6-10: Effect of axial load on slip rotation (column SD-1 versus column SD-2)

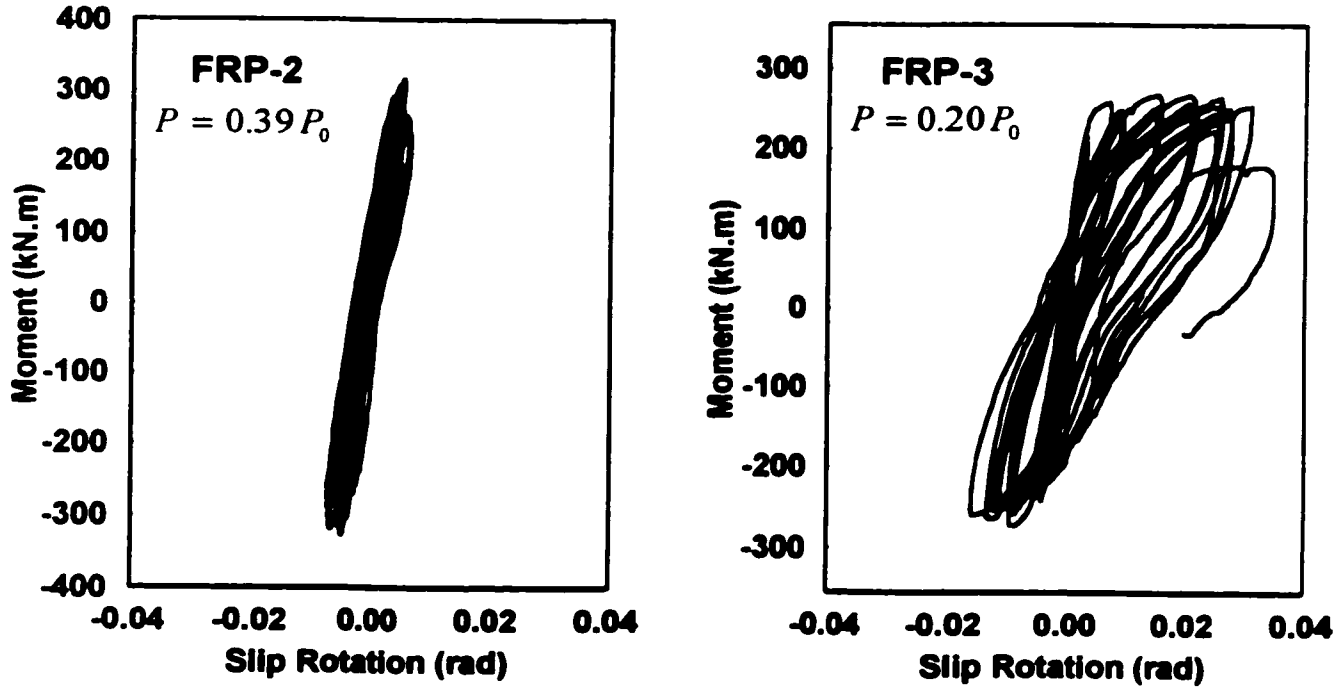

Figure 6-11: Effect of axial load on slip rotation (column FRP-2 versus column FRP-3)

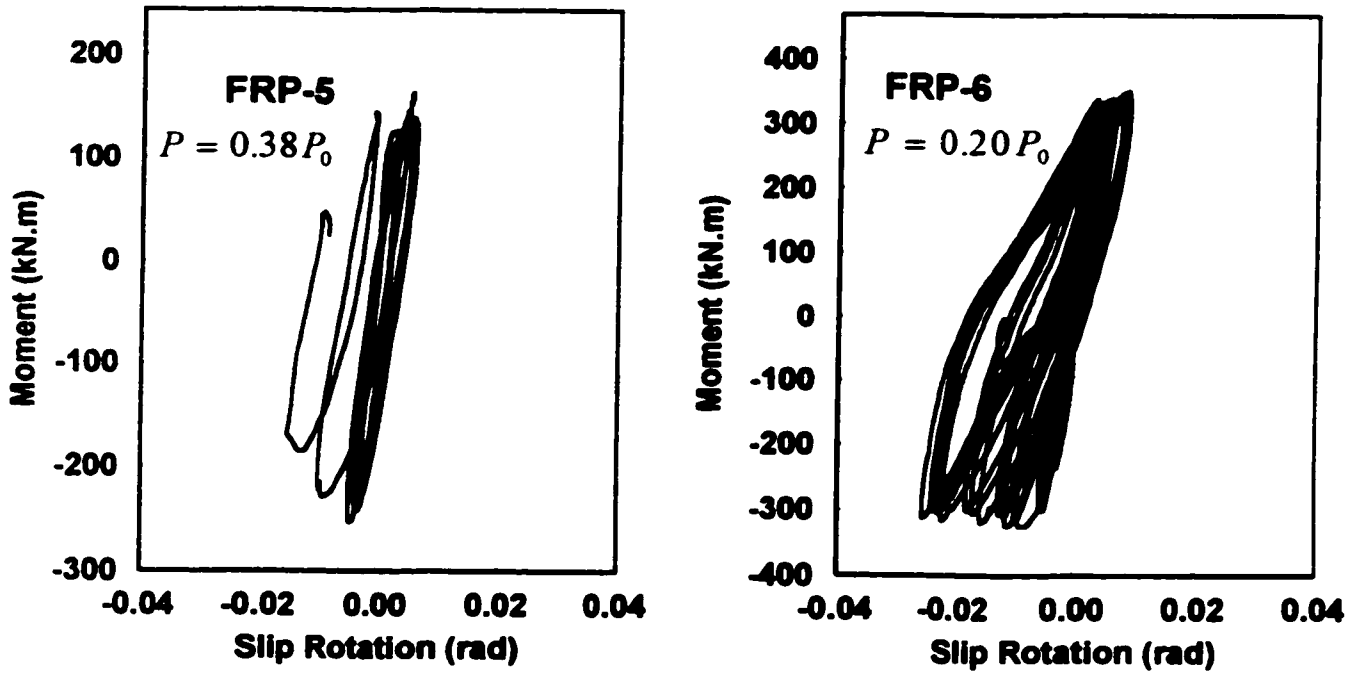

Figure 6-12: Effect of axial load on slip rotation (column FRP-5 versus column FRP-6)

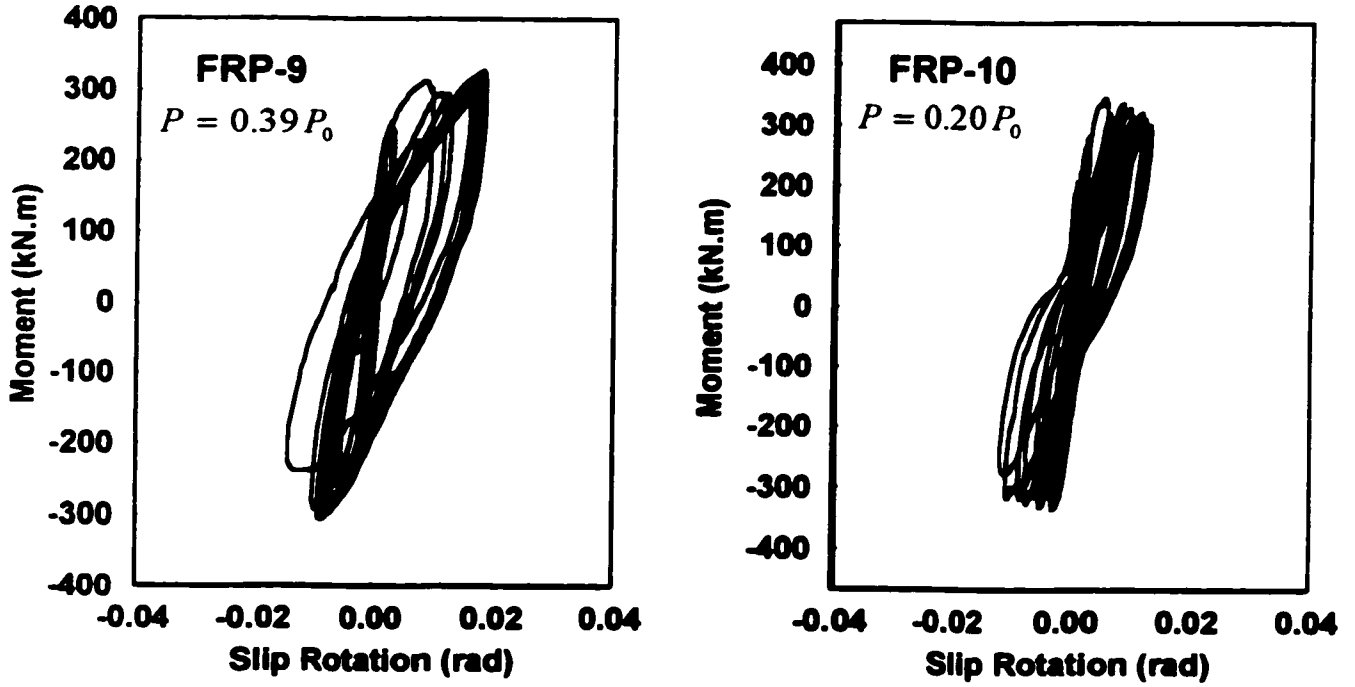

Figure 6-13: Effect of axial load on slip rotation (column FRP-9 versus column FRP-10)

Chapter 7

ANALYSIS OF COLUMNS

7.1 Introduction

Reinforced concrete columns may develop plastic hinges in their critical regions during strong earthquakes. Analysis of such columns requires modeling of the plastic hinge region, as well as nonlinear material characteristics. This becomes a challenging task in view of the nonlinearity of both steel and concrete. Furthermore, formation and progression of plasticity in the hinge is a difficult phenomena to simulate, especially under reversed cyclic loading and decaying strength conditions. This Chapter provides details of various analytical models employed in column analysis, including the analysis procedure for establishing inelastic force-deformation relationships. The analytical results are also compared with those obtained experimentally.

7.2 Constitutive Model for Unconfined Concrete Under Monotonic Compression

7.2.1 Normal Strength Versus High Strength Concrete

Recent advances in concrete technology over the last two decades made it possible to improve strength and performance of concrete. Concrete with a compressive strength greater than *50 MPa* is generally considered as high-strength concrete. Concrete strengths of up to *130 MPa* can now be attained with ordinary materials used in industry to manufacture concrete. Concrete with strengths as high as *120 MPa* has become available in large metropolitan centers of the world through local ready-mix companies. Extensive research is underway to establish fundamental and engineering properties of high-strength concrete, as well as structural elements cast from this material.

Concrete strengths, in the range of *25 MPa* to *45 MPa*, are commonly used in seismically active regions. Higher strength concrete is not employed in these regions because of inherent brittleness of the material. Strength and ductility of concrete is known to be inversely proportional. High-strength concrete behaves like a homogeneous material, while showing brittle mode of fracture and lower volumetric dilatation, as compared to normal-strength concrete. Typical stress-strain curves for concretes with different strengths are shown in Fig. 7.1. High-strength concrete exhibits higher elastic modulus, increased linear elastic range, and reduced ultimate strain. This is often attributed to reduced micro cracking in high-strength concrete.

While high strength concrete is considered to be a superior material, lack of ductility is a source of concern among structural engineers, especially in seismic applications where deformability of columns is relied up on, for dissipation of seismic induced energy. Therefore, some codes of practice place an upper limit on the specified strength of concrete, especially for use in earthquake prone areas. This is mainly due to the limited research that has been carried out on the use of high-strength concrete. However, recent experimental research (Razvi and Saatcioglu 1996, Lipien and Saatcioglu 1997, and Baingo and Saatcioglu 1997) suggests that one potential solution to the problem material brittleness is to provide confinement using sufficiently high volumetric ratio and/or grade of reinforcement.

7.2.2 Stress-Strain Relationship of Unconfined Concrete

Concrete is a highly non-linear material. The most important feature of concrete is its stress-strain relationship. Laboratory experiments show that concrete under compression exhibits initial hardening, followed by softening. Over the past few decades, a considerable volume of research has been directed toward generating stress strain curves for concrete in compression. However, though it appears to be a simple process, experimental determination of complete stress-strain curve is a highly demanding process, because the curve is highly sensitive to test conditions. These conditions include the stiffness of testing machine relative to that of the specimen, size, and shape of specimen, strain rate, gauge length, characteristics of strain gauge, and type of loading. There have been numerous attempts (Hognestad 1951, Wang et al. 1978, Carreira and Chu 1985, and Wee et al. 1996) to analytically model the observed

results to generate complete stress-strain curve from readily available concrete parameters, such as compressive strength and modulus of elasticity. The analytical models, which were developed primarily based on curve fitting, gave conflicting results, particularly for the descending branch of curve because of different testing conditions. Therefore, the selection of an appropriate model is of utmost importance for analysis of columns. Five concrete properties are often required to define a mathematical model for stress-strain curve. These include; i) compressive strength $f_{co}^{'}$, ii) initial modulus of elasticity E_c, iii) ascending branch, iv) strain at peak stress ε_{01}, and v) descending branch. These properties are discussed in detail in the following sections.

7.2.3 Compressive Strength of Concrete

The compressive strength of unconfined concrete can be considered as the most important property, since most other properties can be expresses as a function of concrete strength. The *specified* compressive strength is almost universally defined by the specified 28-day strength, which is often measured by loading a standard concrete cylinder (*150 mm* in diameter and *300 mm* in length). A standard cylinder test may not give an exact representation of the in-place strength of concrete in a structural element. The standard cylinder test often takes 2 to 3 minutes to complete, which may be different from the actual rate of loading applied on a structure. Furthermore, the size, shape, and concrete casting practice vary between a standard cylinder and a structural member. These differences should be kept in mind in modeling material behavior for the purpose of structural analysis. The unconfined strength of concrete used in the current experimental program was determined by testing standard cylinders on the day of respective column test.

7.2.4 Modulus of Elasticity of Concrete

There have been may attempts to formulate the relationship between concrete strength and modulus of elasticity E_c, since this is another important mechanical property to perform structural analysis. The modulus of elasticity E_c, used for analysis, is generally based on secant measurement under slowly applied compressive load to a maximum of $0.45f_{co}^{'}$. It is

generally agreed that the modulus of elasticity increases with strength. Different expressions were proposed by different codes and researchers for this purpose. The apparent disagreement among researchers is often explained by the differences in the modulus of elasticity of aggregates and the volumetric proportion of aggregate in concrete (Neville, 1997). High-strength concrete has high modulus of elasticity because of the particularly strong bond between aggregates and the hydrated cement paste. Chang and Mander (1994) studied several equations for E_c reported in the literature based on experimental data, and proposed an equation that fits both normal and high-strength concretes. This equation has been adopted here for the analysis of columns tested in this project. Accordingly, the modulus of elasticity of concrete can be expressed as a function of f'_{co} as follows:

$$E_c = 8200\left(f'_{co}\right)^{\frac{3}{8}} \tag{7.1}$$

7.2.5 Characteristic of Ascending Branch of Stress-Strain Curve for Unconfined Concrete

It has been reported in the literature by many researchers that the ascending branch shows a linear-elastic behavior up to about 45% of the ultimate strength f'_{co}. This can be explained by micro cracks in the transition zone (interfacial region between the particles of coarse aggregate and hydrated cement paste) that remain undisturbed within this stress range. For stresses above this point, the relationship shows a gradual increase up to $0.75f'_{co}$ to $0.9f'_{co}$, then it curves to become almost flat at the top. In other words, the rising portion of the stress-strain curve resembles to a parabola with its vertex at peak stress. This curve tends to become more linear as the concrete strength increases.

7.2.6 Strain at Peak Stress for Unconfined Concrete

The strain ε_{01}, corresponding to peak stress f'_{co}, is an essential parameter for modeling the stress-strain relationship. However, there is some controversy about the dependence of ε_{01} on concrete strength. Some researchers are convinced that the strain at peak stress is

independent of concrete strength, while others have published results that show heavy dependence of ε_{01} on $f_{co}^{'}$. Some authors have taken ε_{01} as a constant value (0.002) for unconfined normal-strength concrete (Park and Paulay, 1975). In addition, the CEB model code (1990) suggested ε_{01} being equal to 0.0022 for low and normal-strength concrete. However, test results showed that there is a relationship between ε_{01} and $f_{co}^{'}$. The peak strain ε_{01} increases with $f_{co}^{'}$. Therefore, it is advantageous to have a common expression for normal-strength and high-strength concrete. Chang and Mander (1994) proposed the following equation based on the data reported by Sulayfani and Lamirault (1991), and Muguruma et al. (1991):

$$\varepsilon_{01} = \frac{(f_{co}^{'})^{\frac{1}{4}}}{1153} \tag{7.2}$$

The above equation is used to analyze the columns tested in the present research program.

7.2.7 Characteristic of Descending Branch for Unconfined Concrete

The descending portion of the stress-strain curve of plain concrete beyond the peak is highly variable and strongly dependent on the test procedure. The slope of the descending branch of stress strain curve tends to be lower than that of the ascending branch. This slope increases with an increase in compressive strength. Although the descending branch looks like a spine curve, most researchers modeled it as a straight line, with a slope defined by the strain and stress values corresponding to certain percentage of the peak.

7.2.8 Complete Stress-Strain Curve for Unconfined Concrete

Many equations have been proposed in the past defining stress-strain curve of concrete under uniaxial compression. Probably the most widely accepted curve is the one proposed by Hognestad (1951). Hognestad's curve was obtained from tests on short eccentrically loaded columns with concrete strengths less than *30 MPa*. For high-strength concrete, it was proven by a number of researchers (Cusson and Paultre 1993, Razvi 1995, Wee et al. 1996) that

Hognestad's curve did not agree well with test results. Hence, researchers developed new analytical expression to describe the stress-strain relationship of normal and high-strength concretes. Recently, Wee et al. (1996) studied the expressions proposed by Wang et al. (1978), *CEB* (1990), and Carreira and Chu (1985); and proposed an improved expression. This resulted in a more accurate model to represent the complete stress-strain curve, particularly for high-strength concrete.

Chang and Mander (1994) listed other models for concrete and provided a critical review of these models. The equations for the stress-strain curve were classified in four categories; equations representing only the ascending branch, equations representing the ascending and descending branches without having control on the initial slope, equations representing the ascending and descending branches having control on the initial slope, and equations having control on both the initial slope of ascending branch and the descending branch. It was reported that the expression proposed by Tsai (1988) was the only one that gave reasonably accurate results under any one of the above scenarios considered. Furthermore, this expression was flexible and general, and hence it could be applied to both confined and unconfined concrete, as illustrated in the following sections. Therefore, this equation is adopted in the present analysis. Accordingly, the unconfined compressive stress f_c for normal or high-strength concrete at a given strain ε_c is expressed by the following continuous function;

$$f_c = f_{co}^{'} \frac{n\frac{\varepsilon_c}{\varepsilon_{01}}}{1+\left(n-\frac{r}{r-1}\right)\frac{\varepsilon_c}{\varepsilon_{01}}+\frac{\left(\frac{\varepsilon_c}{\varepsilon_{co}}\right)^r}{r-1}} \tag{7.3}$$

where, ε_{01} is the strain corresponding to the ultimate compressive stress $f_{co}^{'}$. The parameter n is defined as;

$$n = \frac{E_c \varepsilon_{01}}{f_{co}^{'}} \tag{7.4}$$

where, E_c is the initial modulus of elasticity of concrete defined by Eq. 7.1. The factor r is to control the descending branch of the stress-strain relationship and is defined as;

$$r = \frac{f'_{co}}{5.2} - 1.9 \tag{7.5}$$

The curve proposed earlier by Popovic (1973) is a special case of the above equation when $n = \frac{r}{r-1}$. Figures 7-2 and 7-3 show comparisons of the theoretical stress-strain curves with those obtained experimentally for unconfined normal and high-strength concretes, respectively.

7.3 Constitutive Model for Confined Concrete Under Monotonic Compression

Compressive strength of concrete is affected by lateral confining pressure. Numerous tests have shown that high level of strength enhancement can be achieved by confining concrete with spirals in circular columns, and by ties in rectangular or square members. The confining pressure results form the restraint that transverse reinforcement provides to the laterally expanding concrete. The Poisson's ratio can reach a value of about 0.2 when a concrete member is axially compressed up to 70 percent of control cylinder strength (Madas and Elnashai, 1992). At stresses above this level, extensive micro-cracks form in concrete, causing Poisson's ratio to increase rapidly. The lateral expansion of concrete is counteracted by the restraining transverse steel, creating a triaxial state of stress. The resulting confined concrete shows drastically different stress-strain characteristics than those of unconfined concrete. Therefore, confined concrete is modeled separately.

Stress-strain behavior of confined reinforced concrete columns has been extensively studied in recent years. Several models were proposed by Sargin (1971), Kent and Park (1971), Vallenas et al. (1977), Sheikh and Uzumeri (1982), Fafitis and Shah (1985), Yong et al. (1988), Mander et al. (1988a), Saatcioglu and Razvi (1992), Li (1994), and Cousson and Paultre (1995). A comprehensive bibliography and a critical review of available models for confined normal and high-strength concrete was presented in Chapter 2. These models are

applicable to either normal-strength or high-strength concrete. With the exception of those proposed by Mander et al., Li, and Saatcioglu and Razvi models, all other models are limited to a specific section geometry for which they were derived. Models proposed by Mander et al. and Li were developed on the basis of the effectively confined core area concept proposed by Sheikh and Uzumeri (1982), whereas Saatcioglu and Razvi model is based on equivalent lateral pressure. The latter model is relatively simple to use and general enough to cover wide range of cross-sectional shapes and reinforcement arrangements used in practice. It incorporates all the relevant parameters of confinement including the amount, spacing, grade and arrangement of transverse reinforcement. Some parameters of the model are adopted to the new confinement techniques and materials used in the experimental part of this investigation.

7.3.1 Confined Concrete Strength

Lateral confining pressure, when applied to concrete, has been found to increase both the compressive strength and the ultimate strain. Richart et al. (1928) showed that, under triaxial test conditions, the compressive strength was conservatively given by;

$$f'_{cc} = f'_{co} + 4.1 f_l \tag{7.6}$$

where, f_l is the confining pressure.

Saatcioglu and Razvi (1992) used the same concept as Richart et al. (1928), and expressed the confined concrete strength as;

$$f'_{cc} = f'_{co} + k_1 f_l \tag{7.7}$$

where, k_1 is a variable coefficient depending on the degree of confinement. The researchers used regression analysis of reported test data to express the variation of k_1 with lateral pressure.

$$k_1 = 6.7(f_l)^{-0.17} \tag{7.8}$$

When concrete is subjected to axial compression, deformations in lateral direction develop

owing to the Poisson's effect. In particular, the lateral expansion increases as the axial strain rises. Thus, for sections confined by transverse reinforcement, lateral-confining pressure develops with increasing axial strain. However, this increase of confinement is limited by the tensile strength of transverse reinforcement. As soon as the confining steel yields, irrespective of the lateral expansion of concrete, the confining pressure remains constant and only the strain hardening of steel will result in limited further increase.

The confining pressure f_l is computed from hoop tension in the case of circular reinforced concrete columns confined by closely spaced spirals. This passive pressure is considered to be uniform around the perimeter of circular columns, whereas the confining pressure exerted by hoops, ties or grids in a square column is variable and dependent on the restraining forces that develop in the confining material. High passive pressure is built up at locations of high lateral restraint, which occurs where there is transverse reinforcement joining the perimeter tie. Corners of the lateral reinforcement are used to support longitudinal bars and restraint them against buckling specially when columns are under heavy axial load or excessive lateral deformation. Effective confinement results from the presence of closely spaced transverse bar legs. The presence of a number of longitudinal bars well distributed around the perimeter of concrete section, tied across the section, will also add the confinement of concrete.

Saatcioglu and Razvi (1992) proposed a method of computing equivalent uniform pressure f_{le} that has the same effect as the actual non-uniform lateral pressure generated by nodal forces at lateral reinforcement joints. Figure 7-4 illustrates the actual and equivalent lateral pressures in a square column. The equivalent uniform pressure generated by rectilinear reinforcement is expressed below:

$$f_{le} = k_2 f_l \tag{7.9}$$

where

$$f_l = \frac{\sum A_s f_{st}}{Sb_c} \tag{7.10}$$

$$k_2 = 015\sqrt{\left(\frac{b_c}{S}\right)\left(\frac{b_c}{S_l}\right)} \leq 1.0 \tag{7.11}$$

A_s = Cross section area of lateral reinforcement.

f_{st} = Limiting stress of lateral reinforcement.

b_c = Core dimension measured center to center of the outside perimeter of the hoop.

S = Vertical spacing between lateral reinforcement.

S_l = Dimension of grid cells, or transversal dimension between longitudinal reinforcement.

The vertical spacing of transverse reinforcement S should be less than half of the cross-section dimension h of a column $S \leq \frac{h}{2}$. Furthermore, the spacing limits specified in *ACI-95* building code, for longitudinal reinforcement should be respected. The maximum value of k_2 is limited to 1.0 when the lateral pressure is relatively uniform in the case of square columns confined with closely spaced lateral reinforcement, and laterally supported longitudinal reinforcement, or circular columns with closely spaced spirals and/or circular hoops.

The limiting stress f_{st} depends on the mechanical and physical properties of lateral reinforcement and the characteristics of concrete. Although most of the existing confinement models assume f_{st} to be equal to the yield stress of transverse steel f_{yt}, experimental studies showed that the transverse steel might or might not yield. Sheikh and Uzumeri (1980) tested normal-strength concrete columns confined with normal-strength steel and reported that transverse steel did not yield at peak concrete stress in many cases. High-strength concrete columns tested under concentric axial compression by Razvi (1995) showed that 1000 MPa steel yielded shortly before crushing of core concrete and not at initial peak. Cusson and Paultre (1994) reported that high strength steel yielded at peak concrete stress only when high-strength concrete columns were well confined. Therefore, Razvi and Saatcioglu (1998) proposed an expression for the limiting stress depending on the reinforcement efficiency, amount of transverse steel, and concrete strength,

$$f_{st} = E_{st}\left(0.0025 + 0.04\left(\frac{k_2\rho_{st}}{f'_{co}}\right)^{\frac{1}{3}}\right) \leq f_{yt} \tag{7.12}$$

where, E_{st} is the modulus of elasticity of steel and ρ_{st} is the lateral reinforcement ratio.

The above equation was proven adequate for lateral steel reinforcement. Hence, a similar equation for fiber reinforced plastic (FRP) material is suggested here,

$$f_{st} = E_{FRP}\left(\frac{1}{7}\right)\left(\frac{k_2\rho_{st}}{f'_{co}}\right)^{\frac{1}{3}} \leq f_u \tag{7.13}$$

where, E_{FRP} and f_u are the modulus of elasticity and the ultimate stress of FRP material, respectively. The above-suggested equation was used to analyze the FRP columns tested during this experimental investigation. The results show good prediction of column capacity as discussed later in the Chapter.

7.3.2 Characteristic of Ascending Branch of Stress-Strain Curve for Confined Concrete

The stress-strain curves for plain and confined concretes are similar up to the cylinder compressive strength. The initial behavior of confined concrete is not different from the unconfined concrete behavior, because at low levels of axial load the stresses in lateral reinforcement and confining pressure are low. Since the confined concrete has higher compressive strength, the ascending strain-curve continues to rise beyond the unconfined peak, in a parabolic manner, up to the maximum stress f'_{cc}. While the ascending curve for unconfined concrete tends to become straighter as the concrete strength increases, this is not usually the case for confined concrete. Although the stress-strain curve for confined concrete initially follows the same shape as that for unconfined concrete, its concave shape at the vertex depends on the degree of confinement and the value of strain at peak stress, ε_1. The higher the value of ε_1 is, the less steep the ascending curve becomes.

7.3.3 Strain at Peak Stress of Confined Concrete

The strain at peak stress of confined concrete ε_1 is dependent on the degree of confinement, unlike unconfined concrete where it is dependent on the compressive strength of concrete. Many expressions were proposed by various researchers for normal strength concrete confined with ordinary hoops and ties (Saatcioglu and Razvi 1992, Mander et al. 1988). Richart et al. (1929) suggested an expression in the form of,

$$\varepsilon_1 = \varepsilon_{01}(1 + \lambda K) \tag{7.14}$$

where,

$$K = \frac{k_1 f_{le}}{f'_{co}} \tag{7.15}$$

The coefficient λ depends on the type of lateral reinforcement used and the effectiveness of confinement. It is traditionally chosen to be equal to 5.0 for normal strength steel. The above expression has been confirmed by many researchers (Balmer 1949, Mander et al. 1988, and Saatcioglu et al. 1992). For high-strength transverse steel, Zahn et al. (1990) found that the value of λ varies between 1.7 and 5.0 when concrete members were subjected to flexural deformations. Therefore, an average value of 3.0 was chosen for the analysis of columns tested in the experimental investigation. This value ($\lambda = 3.0$) resulted in good predictions of column behavior. However, it gave poor predictions for columns confined by FRP reinforcement. Hence, a value of 5.0 was chosen for these columns.

7.3.4 Characteristic of Descending Branch of Stress-Strain Curve for Confined Concrete

The strength and ductility of concrete increase with the degree of confinement, in contrast to plain concrete that behaves in brittle manner. The amount of confinement is the essential parameter in determining the shape and slope of the descending branch for confined concrete. Some researchers defined the descending branch as a straight line having a slope defined by the strain at peak stress and at 85% of strength beyond the peak. However, most tests showed

that the descending branch is not linear. The slope of the descending branch becomes flatter as confinement increases. Chang and Mander (1994) proposed the following points to define the descending curve;

$$\varepsilon_f = 3\varepsilon_1 \tag{7.16}$$

$$f_f = f_{cc} - \Delta f_{cc} \tag{7.17}$$

$$\Delta f_{cc} = \Gamma \Delta f_{co}\left(\frac{0.8}{\Gamma^5} + 0.2\right) \tag{7.18}$$

$$\Gamma = \frac{f_{cc}}{f_{co}} \tag{7.19}$$

where, Δf_{co} is the stress drop in unconfined concrete for a strain $\varepsilon_c = 3\varepsilon_{01}$, as shown in Fig. 7-5.

7.3.5 Complete Stress-Strain Curve for Confined Concrete

A reliable stress-strain model is needed to determine the compressive resistance of concrete at any given strain, preferably following a continuous function. Using the above-defined parameters and equations, the compressive stress f_{cc} of confined concrete may be expressed as a function of strain ε_c by following a continuous function.

$$f_{cc} = f'_{cc}\frac{n_c\dfrac{\varepsilon_c}{\varepsilon_1}}{1+\left(n_c - \dfrac{r_c}{r_c-1}\right)\dfrac{\varepsilon_c}{\varepsilon_1} + \dfrac{\left(\dfrac{\varepsilon_c}{\varepsilon_1}\right)^{r_c}}{r_c-1}} \tag{7.20}$$

where, $n_c = \dfrac{E_c\varepsilon_1}{f'_{cc}}$ and r_c are parameters to control the shape of the descending branch.

7.4 Behavior of Concrete in Tension

Cracking of concrete in tension affects the overall behavior of a structural element. Hence, the tensile characteristics of concrete become important for accurate assessment of member behavior. The contribution of tension concrete to member capacity under seismic loading is always ignored by design engineers, because of its variable nature and limited contribution. However under controlled laboratory conditions, it can be estimated with good degree of accuracy and used in analyses for improved accuracy.

7.4.1 Ultimate Tensile Strength of Concrete

The tensile strength of concrete varies between 8% and 15% of its compressive strength. Its actual value is strongly affected by the type of test carried out, curing age, the type of aggregate, water/cement ratio, the presence of admixture, the compressive strength of concrete, and the presence of transverse stresses (Raphael, 1984). The tensile stress can be determined using three different methods: i) direct tension test, ii) three point beam test, or iii)splitting test. These tests give different strengths. The modulus of rupture determined from a 150-*mm* (6-*in.*) square prism test is about 50% higher than that established by a splitting tensile strength. A 150 *mm* (6 *in.*) square prism, tested in pure tension, gives a direct tensile strength that average about 86% of the splitting strength (Neville, 1995). Since the beam and the split tests are based on the elastic theory, and can not be used to determine the complete stress-strain curve, only the direct tension test is of interest here.

The strength of concrete in direct tension can be estimated using the equations proposed by Carreira and Chu (1986);

$$f_t' = 0.62\sqrt{f_{co}'} \text{ for uncracked sections} \tag{7.21}$$

$$f_t' = 0.37\sqrt{f_{co}'} \text{ for cracked sections} \tag{7.22}$$

7.4.2 Strain at Peak Tensile Stress of Concrete

It has been shown experimentally that the strain at peak tensile strength ε_{to} varies between

0.00015 to 0.00025 for light-weight concrete and is approximately equal to 0.00018 for normal-weight concrete (Carreira and Chu 1986). Carreira and Chu (1986) suggested that ε_{to} should be assumed such that the initial slopes of the tension and compression stress-strain curves are the same. This implies that the modulus of elasticity of concrete in tension and in compression should be the same. Hence, the strain at peak tensile strength can be expressed as;

$$\varepsilon_{to} = \frac{f_t' \varepsilon_{01}}{f_{co}'} \tag{7.23}$$

7.4.3 Complete Stress-Strain Curve for Concrete in Tension

Many researchers assumed a linear stress-strain relationship of concrete in tension up to peak stress, for design purpose (MacGregor, 1988). This assumption is conservative. Stress-strain curve in tension may be considered similar in shape to that in compression (Carreira and Chu 1986, Gopalaratnam and Shah 1985). Hence, the tensile stress of concrete can be expressed as follows;

$$f_t = f_t' \frac{n_t \left(\frac{\varepsilon_t}{\varepsilon_{to}}\right)}{1 + \left(n_t - \frac{r_t}{r_t - 1}\right)\left(\frac{\varepsilon_t}{\varepsilon_{to}}\right) + \frac{\left(\frac{\varepsilon_t}{\varepsilon_{to}}\right)^{r_t}}{r_t - 1}} \tag{7.24}$$

where, ε_t and ε_{to} are strains corresponding to f_t and peak tensile stress f_t', respectively, $n_t = \frac{E_c \varepsilon_{to}}{f_t'}$, and r_t is a parameter to control the shape of the descending branch.

7.5 Effect of Strain Rate on Behavior of Concrete

Stress-strain relationship of concrete is established by standard cylinder tests, conducted under slow strain rates. During seismic excitations, strain rates can be significantly higher than those commonly used to determine stress-strain characteristics of concrete. Strain rates

of up to 0.02 /sec may be expected in multistory buildings. Higher values usually occur in structures with short periods (Bertero, 1972). Effect of strain rates on the behavior of concrete has received much attention by some researchers in the past (Bertero, 1972, Fu et al. 1991, Li 1994). The behavior of plain and confined concretes under dynamic loading is discussed separately in the following sections, since they show different characteristics under high strain rates.

7.5.1 Plain Concrete

It is generally reported that the observed strength of plain concrete is higher under high strain rates. The increase in strength can be as high as 1.8 times the value obtained for plain normal-strength concrete under typical structural testing rates (Neville 1995). However, the strength enhancement is lower in high-strength concrete. Li (1994) reported that under high strain rates of loading, the compressive strength of 58 MPa concrete increased by 58%, whereas the increase in 74 MPa concrete was only 13%. This indicates that high-strength concrete is less sensitive to strain rate effects than normal-strength concrete. Li (1994) reviewed tests reported by Dodd and Cooke (1992) and suggested that strength enhancement due to dynamic loading could be ignored, and if considered, it could be taken as a constant value of 1.2 for strain rates of 0.002 to 0.01/sec.

7.5.2 Confined Concrete

Experimental research conducted by Ahmad and Shah (1985) indicated that strength enhancement due to increased strain rate could be observed in confined concrete as well. The strength enhancement observed in confined high-strength concrete was found to be less profound than that observed in confined normal-strength concrete. Tests carried out by Scott et al. (1982) on confined normal-strength concrete columns showed that an increase in strain rate from 0.0000033 to 0.0167/ sec resulted in a 25% strength enhancement. However, Li (1994) reported that high strain rates resulted in only 11% strength increase in confined high-strength concrete columns. It was also reported in the literature that high strain rate had no significant effect on modulus of elasticity and ultimate strain of confined concrete. However, high strain rates resulted in an increase in the slope of the descending branch of confined

concrete stress-strain curve. In addition, a significant decrease in strain at peak stress was reported in high-strength concrete columns confined with high-strength steel, when it was tested under high strain rates. During this experimental investigation, the columns were tested under slowly increasing lateral deformations (~ *1.0 mm/sec*). Hence, their actual dynamic capacities were higher than those measured.

7.6 Effect of Cyclic Loading on Behavior of Concrete

Concrete columns under earthquake loading experience load reversals as the structure sways back and forth during a seismic excitation. Hence, concrete on one side of a column provides compression resistance during sway in one direction and cracks in tension during the sway in the opposite direction. The effect of repeated loading at high strain levels on concrete was examined by a number of researchers (Gopalaratnam and Shah 1985, Mander et al. 1988, Otter and Naaman 1989, Li 1994). It was reported that the behavior did not change significantly due to load reversals. When a compression specimen is loaded, unloaded, and reloaded again, the envelope of the cyclic loading stress-strain curves is very close to the stress-strain curve established under monotonic loading. The two curves are generally accepted as the same. This is illustrated in Fig. 3-45 – 3.47 for plain concrete cylinders tested in the experimental part of this investigation. The large residual strains that remain after unloading is indicative of damage to the internal structure of concrete. Concrete strength and stiffness degrade, under cyclic loading, at high levels of inelastic strains. For stress levels below 50 and 75 percent of peak stress, a gradual degradation occurs in both the elastic modulus and compressive strength. As the number of cycles increases, the unloading curves show non-linearity, followed by stiffness degrading reloading branches. For stress levels below 50% of peak stress, the unloading-reloading curves exhibit strong non-linearity.

7.7 Constitutive Model for Reinforcing Steel

Axial tension behavior of a typical steel reinforcement is characterized by an initial linear elastic portion, with modulus of elasticity of approximately 200,000 MPa. This segment continues up to yield stress f_y, followed by a strain plateau of variable length. The steel then develops the subsequent region of strain hardening. Ultimate tensile stress is reached at about

$f_{su} = 1.5 f_y$ for typical North American reinforcement steel, although this ratio decreases for higher-strength steels. The following equation, proposed by Mander et al. (1984) defines the complete curve of the stress-strain relationship of steel re-bars under pure axial tension.

$$f_s = f_u + (f_{sh} - f_u)\left(\frac{\varepsilon_u - \varepsilon_s}{\varepsilon_u - \varepsilon_{sh}}\right)^{p_t} \le f_u \tag{7.25}$$

The power index p_t is defined by the initial slope of the hardening curve E_h and the two end-points of the hardening portion, as expressed below:

$$p_t = E_h \frac{\varepsilon_u - \varepsilon_{sh}}{f_u - f_{sh}} \tag{7.26}$$

Analytically established stress-strain relationship of reinforcing steel in tension is compared with experimental results in Fig. 7-6.

When longitudinal steel reinforcement in columns is subjected to monotonic axial compression, its stress-strain relationship could be different than that obtained by standard tension coupon tests. The difference in behavior is caused by potential instability of reinforcement in compression. The stress-strain relationship is then affected by the diameter (d_b) of compression bar, the end conditions, and the vertical spacing (S) of lateral restraining ties. Yalcin (1997) derived empirical equations to express the stress-strain relationship of compression reinforcement as a function of aspect ratio (S/d_b). These equations are used in present analytical analysis with some modifications. When the aspect ratio is below 4.5, the longitudinal bars are considered stable and the stress-strain relationship is identical to that in tension. However, when the aspect ratio is greater than 4.5, the ultimate compressive stress and the ultimate strain are lower than the previous case. Two cases are presented below:

- **4.5≤ aspect ratio ≤8.0**

The compression bars exhibit lower strain hardening than tension coupons. As the aspect ratio increases, the slope of strain hardening curve decreases and becomes zero at an aspect ratio of 8.0. The stress f_s, the limiting value of stress $f_{S/Du}$, and the limiting value of strain

$\varepsilon_{S/Du}$ are established from the following expressions:

$$f_s = f_{S/Du} + (f_{sh} - f_{S/Du})\left(\frac{\varepsilon_{S/Du} - \varepsilon_s}{\varepsilon_{SDu} - \varepsilon_{sh}}\right)^{pc} \qquad \text{for} \qquad \varepsilon_s \succ \varepsilon_{sh} \tag{7.27}$$

$$f_{S/Du} = f_{sh} + (f_u - f_{sh})\left[47.98e^{-0.8782\left(\frac{s}{d_b}\right)}\right] \tag{7.28}$$

$$\varepsilon_{s/Du} = \varepsilon_{sh} + (\varepsilon_u - \varepsilon_{sh})\left[6.07e^{-0.4369\left(\frac{s}{d_b}\right)}\right] \tag{7.29}$$

$$p_c = E_h \frac{\varepsilon_{S/Du} - \varepsilon_{sh}}{f_{S/Du} - f_{sh}} \tag{7.30}$$

Stresses and strains in the above equations are expressed in *MPa* and mm/mm, respectively.

- **Aspect ratio ≥8.0**

Aspect ratios in this range represent a special case where the mid-height cross-section of a steel bar exhibits strain reversal. The stability of the bar is maintained with a limiting stress equal to the yield stress. When the aspect ratio is greater than 8.0, the bar becomes unstable as soon as the yield point is reached. The following expressions can be used within this range of aspect ratio.

$$f_s = f_y - (\varepsilon_s - \varepsilon_y)\left[-23140 + 11130\ln\left(\frac{S}{d_b}\right)\right] \qquad \text{for} \qquad \varepsilon_y \le \varepsilon_s \le \varepsilon_{S/Du} \tag{7.31}$$

$$f_{S/Du} = 27.95 f_y \left(\frac{S}{d_b}\right)^{-1.743} \tag{7.32}$$

$$\varepsilon_{S/Du} = \left[40.47 - 5.94\ln\left(\frac{S}{d_b}\right)\right]\varepsilon_y \tag{7.33}$$

Figure 7-6 illustrates stress-strain relationships for tension and compression reinforcement as a function of bar aspect ratio.

7.8 Effect of Cyclic Loading on Reinforcing Steel

When a reinforcing bar yields in tension or compression and the direction of the stress is reversed, the distinct yield point is lost and the stress-strain relationship takes a curvilinear form. This change in stress-strain relationship is known as the Beauschinger effect. Under these conditions, stress is no longer uniquely related to strain and it depends on the strain history. Many factors have been found to influence the stress-strain behavior of reinforcement under inelastic load cycles. The principal factors, as outlined by MacGreror (1988), are the stress-strain characteristics under monotonic loading, magnitude of the maximum strain that has been previously applied to the bar, strain aging, chemical composition of the material, temperature, and strain rate. Paulay and Priestley (1992) indicated that the yield plateau is also suppressed when the cyclic inelastic excursions are predominately in tensile strain range. A similar behavior is also possible when the cyclic inelastic excursions are predominately in compression strain range. This case is typical of reinforcement in a plastic hinge region of a concrete column subjected to heavy axial load and large inelastic lateral deformations. Cyclic behavior of reinforcing steel may be important in computing hysteretic load-deformation relationships of columns and the buckling capacity of compression reinforcement. In the column analyses conducted as part of the current investigation, the envelope of hysteric behavior was constructed using the characteristics of reinforcing steel under monotonic loading. This may result in small inaccuracies, however, especially in predicting the buckling capacity of reinforcing steel because of the suppression of yield point. The buckling phenomenon of longitudinal reinforcing steel is presented in the following Chapter.

7.9 Behavior of Columns Under Combined Axial Force and Flexure

7.9.1 Plane Section Analysis

Behavior of a reinforced concrete column in flexure can be established by first conducting sectional analysis. This is done by constructing moment-curvature relationship. The moment-curvature relationship prior to cracking can be determined from the elastic beam theory.

However, beyond cracking, especially beyond yielding of reinforcement, the materials of reinforced concrete exhibit non-linearity, and the elastic beam theory is no longer applicable. Sectional response within this range is determined by performing plane-section analysis. The details and the assumptions involved in the plane-section analysis are described in the following sections.

7.9.1.1 Basic Assumptions for Plane-Section Analysis

Analysis of reinforced concrete columns under combined flexure and axial load is based on the following assumptions:

- Strain in reinforcement and concrete is assumed to be directly proportional from the neutral axis.
- Strain in reinforcement is equal to the strain in concrete at the same level. This assumption implies perfect bond between concrete and steel.
- Plain sections perpendicular to member axis before bending remain plain after bending. Although this assumption may not be entirely true in regions of high shear and resulting diagonal cracks, these regions with sufficiently high shear capacities do not affect the behavior in flexure of a typical flexure dominant member.
- Cover concrete has the same stress-strain curve as unconfined concrete in the member.
- Stress-strain relationship for confined concrete developed based on concentricity loaded specimens is applicable to members under strain gradient.
- The contribution of shear is negligible.

7.9.1.2 Computation Procedure

The procedure of analyzing a reinforced concrete column section in flexure consists primarily on assuming a strain value on the extreme compression side, and iterating on the depth of the neutral axis, c, until the equilibrium of internal forces is attained. The process is

continued by incrementing the strain value until the ultimate capacity of section is reached.

The compressive strain ε_{cu} of cover concrete at the extreme fiber of section is first computed. The compressive strain of core concrete is then computed using strain compatibility. This is illustrated below,

$$\varepsilon_{cc} = (c - cover)\left(\frac{\varepsilon_{cu}}{c}\right) \tag{7.34}$$

where, *"cover"* is the thickness of the cover concrete. From similar triangles formed by strain diagrams, the strain at each layer of longitudinal reinforcement is computed as shown below;

$$\varepsilon_{si} = \left(\frac{c - d_i}{c}\right)\varepsilon_{cu} \tag{7.35}$$

where, ε_{si} is the strain in the *ith* layer of steel and d_i is the depth to the *ith* layer of steel. Once the values of "c" and ε_{si} are known, stresses in concrete and in each layer of longitudinal reinforcement are computed. The stresses on each steel layer are computed using either compression or tension stress-strain relationships. The stresses in the cover and core concrete are computed separately using the unconfined and confined concrete stress-strain models, respectively. Internal compressive resistance provided by core concrete is then expressed as,

$$C_{cc} = (b - 2cover)\int_0^{\varepsilon_{cc}} f_{cc}\, d\varepsilon_c \tag{7.36}$$

where, b is the width of the concrete section and f_{cc} is the confining stress at a given strain value ε_c.

The location of point of application of the core concrete force from neutral axis (moment arm) is defined by:

$$x_c = \frac{\int_0^{\varepsilon_{cc}} f_{cc}\varepsilon_c d\varepsilon_c}{\int_0^{\varepsilon_{cc}} f_{cc} d\varepsilon_c} \tag{7.37}$$

The compressive force resisted by cover concrete is computed using unconfined stress-strain relationship, and is defined as follows;

$$C_{cover} = C_{side} + C_{end} \tag{7.38}$$

where,

$$C_{side} = 2cover\left(\int_0^{\varepsilon_{co}} f_{co} d\varepsilon_c\right) \tag{7.39}$$

$$C_{end} = (b - 2cover)\left(\int_0^{\varepsilon_{co}} f_{co} d\varepsilon_c - \int_0^{\varepsilon_{cc}} f_{co} d\varepsilon_c\right) \tag{7.40}$$

The locations of the above forces (moment arms) are defined respectively by:

$$x_{side} = \frac{\int_0^{\varepsilon_{co}} f_{co}\varepsilon_c d\varepsilon_c}{\int_0^{\varepsilon_{co}} f_{co} d\varepsilon_c} \tag{7.41}$$

$$x_{end} = c - \frac{cover}{2} \tag{7.42}$$

The Simpson's rule is used to evaluate the above integrals. Total compressive force resisted by concrete is,

$$C_c = C_{cc} + C_{side} + C_{end} \tag{7.43}$$

Concrete tension resistance is considered by first calculating the strain ε_{tu} at the extreme tension fiber;

$$\varepsilon_{tu} = \left(\frac{h-c}{c}\right)\varepsilon_{cu} \tag{7.44}$$

where, h is the section height. Total tension force T_c is determined using the stress-strain model for concrete in tension, presented earlier in this Chapter.

$$T_c = b\int_0^{\varepsilon_{tu}} f_t d\varepsilon_t \tag{7.45}$$

The location of point of application from the neutral axis of the above force is:

$$x_t = \frac{\int_0^{\varepsilon_{tu}} f_t \varepsilon_t d\varepsilon_t}{\int_0^{\varepsilon_{tu}} f_t d\varepsilon_t} \tag{7.46}$$

If the distance "c" form the extreme compressive fiber to the neutral axis is greater than d_i for a particular layer of steel, then the reinforcement is in compression. The area of concrete occupied by reinforcement in that layer is included in the concrete area used to compute C_c. Therefore, it is necessary to subtract the concrete stress f_{csi} at the *ith* location of the steel layer from the steel stress f_{si} before computing the compressive force resisted by longitudinal reinforcement, C_{si};

$$C_{si} = (f_{si} - f_{csi})A_{si} \tag{7.47}$$

where, A_{si} is the area of steel in the *ith* layer

The forces resisted by longitudinal reinforcement in tension are expressed below.

$$T_{si} = f_{si}A_{si} \tag{7.48}$$

The axial capacity, P, of the column for a specific strain distribution is the summation of all the resisting forces:

$$P = C_c + \sum C_{st} - \sum T_{st} \tag{7.49}$$

The moment capacity M for a specific strain distribution is computed about section centroid by summing bending moments caused by internal forces.

$$M = C_{cc}\left(\frac{b}{2} - c + x_{cc}\right) + C_{end}\left(\frac{b}{2} - c + x_{end}\right) + C_{side}\left(\frac{b}{2} - c + x_{side}\right) \tag{7.50}$$
$$+ \sum C_{st}\left(\frac{b}{2} - d_i\right) - \sum T_{st}\left(\frac{b}{2} - d_i\right) - T_c\left(\frac{b}{2} - x_i - c\right)$$

Curvature corresponding to the computed moment is then determined as the ratio between the extreme compressive fiber strain divided by the distance to neutral axis

$$\phi = \frac{\varepsilon_{cu}}{c} \tag{7.51}$$

7.9.2 Axial Force - Moment Interaction

Capacity of a short reinforced-concrete column is established through axial force-moment interaction diagrams. These diagrams provide for the interaction of axial load and bending moment capacity, and give the failure surface of a column section. They can be constructed by conducting sectional analyses with different profiles of strains at ultimate. Either the material models used in preceding sections or simplified models as recommended by Building Codes (ACI 318-1995, CSA A23.3-1994) can be employed in such analyses. The following sections provide the details of axial force-moment interaction calculations.

7.9.2.1 Maximum axial Load Capacity of Columns

Columns under concentric axial load develop uniformly longitudinal strains across the section. The concentric capacity of a reinforced concrete column can be computed using the following equation.

$$P_0 = K_3 f'_{co}\left(A_g - A_{st}\right) + f_{st} A_{st} \tag{7.52}$$

where,

A_g = Cross-section area of column.

f_{sy} = Strength of longitudinal reinforcing bars.

A_{st} = Cross-sectional area of total longitudinal reinforcing bars.

K_3 = Constant relating the in-place stress-strain relationship for the column concrete to the stress-strain relationship determined by testing a concrete cylinder.

The exact value of K_3 is a source of controversy among researchers. However, it is a common practice to take $K_3 = 0.85$. The in-place strength of concrete in a column is slightly lower than that determined by a cylinder test. The difference is believed to come from differences in shape, size and casting practice between a full size column and a standard cylinder. The value of K_3 may approach 1.00 under strain gradient. Collins et al. (1992) reported that K_3 varied with compressive strength of concrete, and its values could be taken between 0.7 and 0.75. There was wide scatter of data, especially in the case of high-strength concrete columns. This wide scatter was attributed to instability of cover concrete in high-strength concrete columns by Razvi and Saatcioglu (1994). They suggested that the concentric capacity of confined high-strength concrete columns should be based on the core area rather than the total cross-section area of the column. This was explained by the fact that the cover concrete may fail prematurely due to instability of shell under high compressive stresses. In the present analytical study, the following expressions for the axial capacity of concrete columns are used;

$$P_0 = 0.85 f'_{co}\left(A_g - A_{st}\right) + f_{st} A_{st} \quad \text{for normal-strength concrete} \tag{7.53}$$

$$P_0 = 0.85 f'_{co}\left(A_c - A_{st}\right) + f_{st} A_{st} \quad \text{for high-strength concrete}$$

where, A_c is the core concrete area.

7.9.2.2 Computation Methods for Generating Interaction Diagrams

Combination of axial force and corresponding bending moment capacities can be computed by conducting plane section analyses with the material models described earlier in the Chapter. The analyses are conducted for strain profiles with the ultimate compressive strain of concrete assigned to the extreme compression fiber. Though the *ACI* code recommends the use of 0.003 strain for design purposes, the actual recorded values of ultimate strain may be as high as 0.02, especially in well confined concrete. Priestly et al (1996) recommend $\varepsilon_c = 0.004$ for design purposes, instead of 0.003. Although this recommended value is still conservative, it is used here to generate the interaction diagrams of columns.

The ACI code procedure involves the assumption of $\varepsilon_c = 0.003$ as the maximum usable compressive strain in concrete. In addition, the concrete stress-strain relationship is simplified by a rectangular stress block. Tension resistance of concrete, as well as the strain hardening of reinforcing steel are ignored. Otherwise, the procedure remains the same as that described earlier, essentially involving plane section analysis for different profiles of ultimate strain with different strain gradients.

7.9.3 Member Analysis

Tests of reinforced concrete columns under simulated earthquake loading indicate that lateral deflection of a column consists of components due to flexure, shear, and anchorage slip. Figure 7.8 shows experimentally recorded displacement components in a typical test column. While the components due to flexure and anchorage slip may be equally significant, shear deformation in a typical column is negligibly small, forming less than 10% of total displacement. Therefore, the effects of inelastic shear deformation on lateral drift capacity of a flexure dominant column can be ignored for simplicity.

The rotation of a reinforced concrete column at the plastic hinge due to flexure is defined as the integration of curvatures along its height L_c.

$$\theta_f = \int_0^{L_c} \phi(x)dx \tag{7.54}$$

The expression for the curvature ϕ is defined by Eq. 7.51 and determined from the moment-curvature analysis outlined previously. The deflection of a reinforced concrete column due to flexure, at a height of L_c, is defined as;

$$\Delta_f = \int_0^{L_c} \phi(x)xdx \tag{7.55}$$

Because of the nature of reinforced concrete, the variation of the curvature along the height of the column is difficult to establish. The moment curvature relationship does not have a unique shape. Razvi and Saatcioglu (1996) developed an iterative procedure to model the progression of hinging during the initial ascending, descending and subsequent ascending branches of the moment-curvature relationship. The procedure is suitable for computer use. The proposed algorithm is illustrated graphically in Fig. 7.9, and is outlined in a report published by the researchers (Razvi and Saatcioglu 1996). The procedure is adopted here to predict the force-displacement relationships of columns.

7.10 Anchorage Slip

7.10.1 Extension and Slippage of Reinforcement

The extension and/or slip of longitudinal bars within the adjoining member may have significant contribution to the overall lateral displacement of a column, especially under low levels of axial compression. Alsiwat and Saatcioglu (1992) presented a simplified procedure to compute the amount of slip under monotonic loading. This procedure is adopted here to compute the anchorage slip rotation of a column. In well-anchored reinforcement, which is the case of the columns tested, the slippage of reinforcement is prevented and hence not considered in the analysis. In the present experimental investigation, the longitudinal bars embedded in the foundation had 90-degree hooks extended to prevent slippage. However, the extension of reinforcement caused by yield penetration does occur whenever the critical

section is located at column-footing interface. The extension of reinforcement in the adjoining member is defined as the area under the strain diagram. Therefore, it is essential to establish the strain distribution along the embedded length of the hooked bars. The embedded region consists of four segments as shown in Fig. 7.7. The length of each segment is evaluated as follows.

7.10.1.1 Elastic Region

This portion of the bar is stressed elastically. The bond stress in this region may be assumed to remain constant, and may be defined as elastic bond stress,

$$u_e = \frac{f_y d_b}{4 l_d} \tag{7.56}$$

The development length is defined as,

$$l_d = \frac{440 A_b}{K\sqrt{f'_{co}}} \frac{f_y}{400} \geq 300 \tag{7.57}$$

where,

A_b = area of longitudinal bar in mm^2.

K = Smaller of $(C_c + K_{tr})$, $\left(C_s + \sum \frac{K_{tr}}{n}\right)$, $3d_b$.

$K_{tr} = \frac{A_{tr} f_{yt}}{10.34 s} \leq d_b$.

n = Number of bars in the layer

A_{tr} = Area of transverse steel crossing the plane of splitting, adjacent to a single anchored bar.

Once the bond stress over the elastic region is known, the length of this region is determined

from equilibrium of forces, as follows:

$$L_e = \frac{\Delta f_s d_b}{4u_e} \tag{7.58}$$

7.10.1.2 Yield Plateau region

In this region, the bar is stressed beyond its yield point without reaching strain hardening. The local bond at this region is approximated by the frictional bond stress defined below,

$$u_f = \left(5.5 - 0.07\frac{S_l}{H_l}\right)\sqrt{\frac{f'_{co}}{27.6}} \tag{7.59}$$

where, S_l and H_l are clear spacing and height of lugs on the bar, respectively. Thus, the length of the yield plateau region is,

$$L_{yp} = \frac{\Delta f_s d_b}{4u_f} \tag{7.60}$$

where, Δf_s is the increment of steel stress between the stress value at yield and its value at the beginning of strain hardening. Since there is a small change between the yield and strain hardening stresses, if any, L_{yp} becomes insignificant, and is equal to zero in most cases.

7.10.1.3 Strain Hardening Region

This region represents the portion of the bar that is stressed into the strain hardening range. The same principles that apply to the yield plateau region also apply to this region. The bond stress is assumed equal to the frictional bond stress given in Eq. 5.59. The length of the strain-hardening region is determined from equilibrium as expressed below.

$$L_{yp} = \frac{\Delta f_s d_b}{4u_f} \tag{7.61}$$

7.10.1.4 Pullout Cone Region

The pullout cone forms when the concrete near the pulled end of the bar breaks away in the form of a cone. This usually takes place when the bar yields in tension within unreinforced concrete. However, when the embedment length of reinforcing bar is not sufficiently long, the bond stress near the loaded end may exceed the critical value of bond associated with pull-out cone, and it may occur even when the bar is in the elastic range. The pullout cone can be prevented by reinforcing the potential cone region with transverse steel, which happens to be the case for the columns tested in this investigation. Therefore, the pullout cone is ignored in the present analysis.

7.10.1.5 Hooked bars

The resistance of a hooked bar consists of two parts; resistance of the lead-in length, and the resistance of hook. The lead-in length is treated as in the case of a straight bar. If the lead-in length is not sufficiently long to resist the applied force, the excess force is taken by the hook. The extension of the hook is determined from the following empirical relationship, based on the model given in Fig. 7.7.

$$P_h = P_{hu}\left(\frac{\delta_h}{2.54}\right)^{0.2} \tag{7.62}$$

$$P_{hu} = 271(0.05d_b - 0.25) \tag{7.63}$$

$$P_{hf} = 0.54P_{hu} \tag{7.64}$$

The hook displacement δ_h and bar diameter b_b are in *mm*, and the force terms are in *kN*.

The hook force is calculated first by subtracting the force resisted by the elastic region of the straight lead length from the total steel force;

$$P_h = \pi d_b\left(\frac{d_b f_s}{4} - L_e u_e\right) \tag{7.65}$$

where, f_s is the maximum steel stress in the elastic region and it is limited by the yield stress. Once the hook force is determined, the force-deformation relationship defined in Eq. 7.62 – Eq. 7.64 can be used to obtain the hook deformation δ_h. This can be added to the extension of straight lead length to find total displacement.

Once all the stressed lengths in different regions are calculated, the total extension of the bar, δ_{ext}, can be determined as the area under the strain diagram;

$$\delta_{ext} = 0.5(\varepsilon_s + \varepsilon_{sh})L_{sh} + 0.5(\varepsilon_{sh} + \varepsilon_y)L_{yp} + 0.5(\varepsilon_y)L_e + \delta_h \tag{7.66}$$

7.10.2 Rotation and Deflection due to Anchorage Slip

The rotation due to bar extension is expressed as;

$$\theta_s = \frac{\delta_{ext}}{d_i - c} \tag{7.67}$$

where, d_i is the effective depth of column cross section from the extreme concrete fiber to the center of the bar for which δ_{ext} is evaluated, c is the position of the neutral axis from the cover concrete. The tip deflection of column due anchorage slip is defined as shown below.

$$\Delta_{slip} = L_c\theta_s \tag{7.68}$$

The total lateral displacement of reinforced concrete column is determined by superposing displacement components due to flexure and anchorage slip.

$$\Delta_{tp} = \Delta_f + \Delta_{slip} \tag{7.69}$$

7.11 Comparisons of Analytical and Experimental Force-Displacement Relationships

Lateral drift capacities of columns tested in the experimental part can be established using the procedures and material models described in the above sections. The computation of all

major components of column response requires the use of computer. It was decided to develop a FORTRAN program for this purpose, rather than using other researcher's programs. Previously developed programs had many limitations and it was hard to modify them because of their complexity or the language used. The developed software consists of both sectional and member analyses. The flowchart of the program is illustrated in Fig. 7-10. A selection of confinement models was incorporated in the program. The program was extensively verified against COLA software developed by Yalcin (1997).

The force-displacement relationship was established for each column and compared with the experimentally recorded hysteretic relationship. The analytical force-displacement curves were established for constant axial compression and monotonically increasing lateral loads. Although the columns were subjected to axial compression and lateral cyclic deformations, the envelopes (backbone curves) of the hysteretic force-deformation relationships were compared with the analytical relationships. It is generally agreed that force deformation relationships under monotonically increasing forces provide good estimates of the envelopes for hysteretic relationships (Fafitis and Shah 1982, Saatcioglu et al., 1995).

The recommended confinement model is also compared to other existing models by analytically predicting the force-deformation relationships for the columns confined with high-strength steel grids or studs (BG and SD columns). The selected existing models include Sheikh and Uzemeri (1982) and Mander et al. (1988) models for normal strength concrete, and Saatcioglu and Razvi (1992, 1995) models for normal and high strength concretes. These models are illustrated graphically in Fig. 7-11 and detailed descriptions of them can be found in the literature. The aforementioned analytical models for confined concrete were developed for conventional ties, consisting of perimeter hoops, overlapping hoops and/or crossties. In addition, the lateral reinforcement was made of normal strength steel. Figure 7-12 shows the comparisons of the analytically predicted force-displacement curves for the tested columns, using different confinement models. The comparisons indicate that the suggested model consistently showed approximately 5 to 10% higher peak lateral force. The increase in strength reflects the improved confinement characteristics of grids associated with high strength steel and increased rigidity of welded ties. The inelastic deformabilities beyond the peak, as indicated by the slope of the curves, were almost identical.

The strength interactions diagrams using the *ACI* code and the proposed analytical procedures for the tested columns are illustrated in Fig. 7- 13. The actual stress distribution of concrete and an ultimate concrete strain of 0.004 were used in the analytical predictions. The theoretical predictions are compared to the results obtained during this experimental investigation. The results show that the ACI code is very conservative, and the assumed strain of 0.004 still underestimate capacities of reinforced concrete columns under combined bending and axial loads.

In addition, deformation capacities of all tested columns were predicted using the recommended procedures in the above section. The analytically predicted force-displacement relationships for the tested columns are compared with those recorded experimentally in Fig. 7-14. The analytical results show good correlation with experimental data. The employed procedure with the adopted analytical models can be used to compute inelastic displacements of reinforced concrete columns confined with high strength steel grid, double headed studs, or fiber reinforced plastic grids.

7.12 Column Limit States

A reinforced concrete column under constant axial compression and lateral load reversals may experience different modes of failure. Depending on the axial load and deformation level, a column may be declared failed if any one or a combination of the following events occur; i) core concrete crushes under compression, ii) longitudinal steel ruptures under tension, iii) anchored reinforcement pulls out, iv) *P-Delta* moment becomes excessive, v) lateral reinforcement ruptures, or vi) longitudinal steel buckles under compression. Occurrence of any one of these failure modes is governed by geometric and material properties of columns.

The maximum (crushing) concrete strain that a reinforced concrete column can sustain is a limiting parameter for column capacity. Flexural strength calculations for reinforced concrete members are generally conducted by assuming extreme fiber compressive strain of 0.003 (ACI 318-95). Moehle (1985) assumed that maximum core strain in a confined column was 0.005. Other researchers (Baker and Amarakone 1965, Corley 1966) proposed empirical

equations for the limiting strain of concrete, depending on the volumetric ratio and yield strength of transverse reinforcement. Recently Priestly et al. (1996) suggested the following expression;

$$\varepsilon_{cu} = 0.004 + 1.4\frac{\rho_s f_{yt} \varepsilon_{su}}{f'_{cc}} \tag{7.70}$$

where, ρ_s, f_{yt}, and ε_{su} are the volumetric ratio, yield stress, and strain at maximum stress of transverse reinforcement. The equation was derived for concentric compression. The resulting strain limit was reported to provide conservative values up to 50 % under strain gradient (Priestley et al., 1996). Typical values for ε_{cu} range from 0.012 to 0.05 when the above equation is used for combined bending and axial compression.

The reinforcement fracture point is governed by ultimate elongation of steel. Typical fracturing strains for re-bars range between 8% and 12%. However, cold-drawn wires sometimes used as transverse reinforcement may have reduced elongation capacity, especially for small size wires.

The limit states indicated above result in degradation of column strength during response. Confined concrete columns of multistory frame systems do not fail immediately after attaining their peak loads. Instead, they continue carrying loads while deforming and dissipating energy. Hence, the limiting displacement should not be taken as the one corresponding to the peak load. Usually a 20% strength decay is tolerated before the column is considered to have failed.

A common measure of column deformability is drift ratio. Drift ratio is determined by dividing the maximum usable displacement by the unsupported column height. It is usually expressed in percentage. Drift capacity of reinforced concrete columns may be limited by sudden buckling of longitudinal compression reinforcement. In properly designed columns the transverse reinforcement within the plastic hinge is designed to restrain compression bars against buckling, while also confining the core concrete.

Two possible buckling phenomena may occur in short concrete columns. These include the

buckling of longitudinal bars between two layers of transverse reinforcement, and buckling over multiple layers of transverse reinforcement. Codes of practice limit tie spacing and the minimum size of tie legs to ensure adequate confinement of the core concrete and stability of longitudinal reinforcement. These limits are not always adequate and may lead to unsafe column capacities (Priestly et al., 1996). A rational model is needed for bar buckling to establish this limit state reasonably accurately. Development of such a model forms one of the main objectives of the current research project, as discussed in the following Chapter.

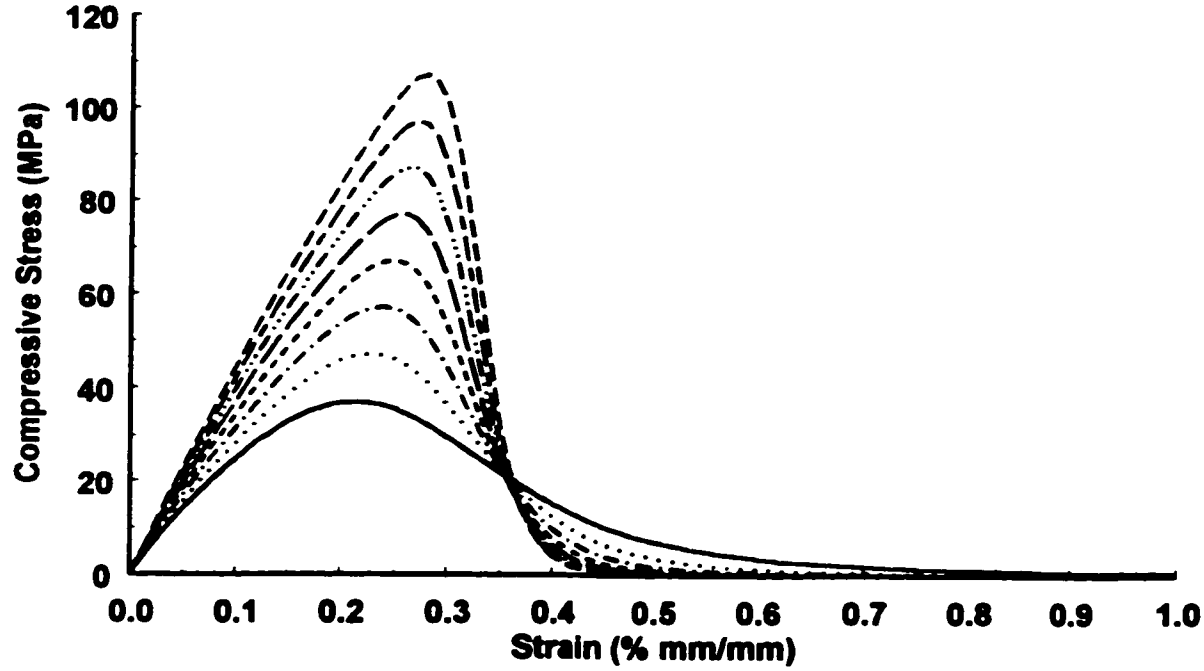

Figure 7-1: Analytical prediction of compressive stress-strain curves for unconfined concrete based on Eq. 7.3.

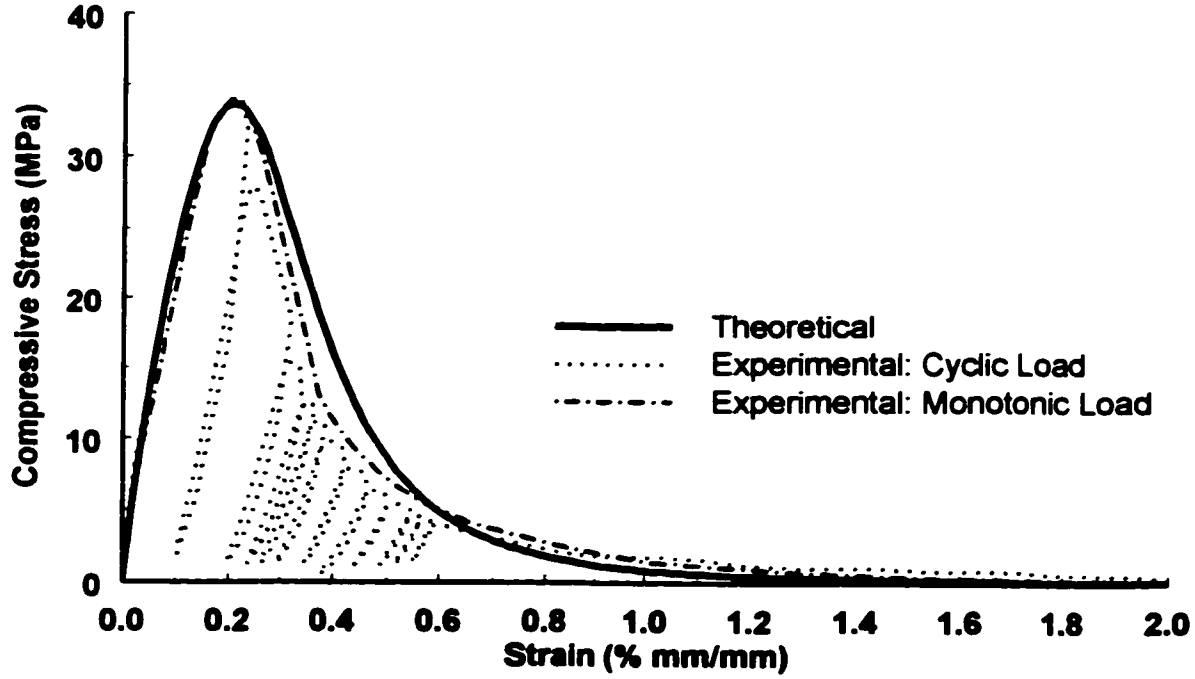

Figure 7-2: Comparison of predicted normal strength concrete stress-strain curve (Eq. 7.3) with results of tests conducted in present investigation

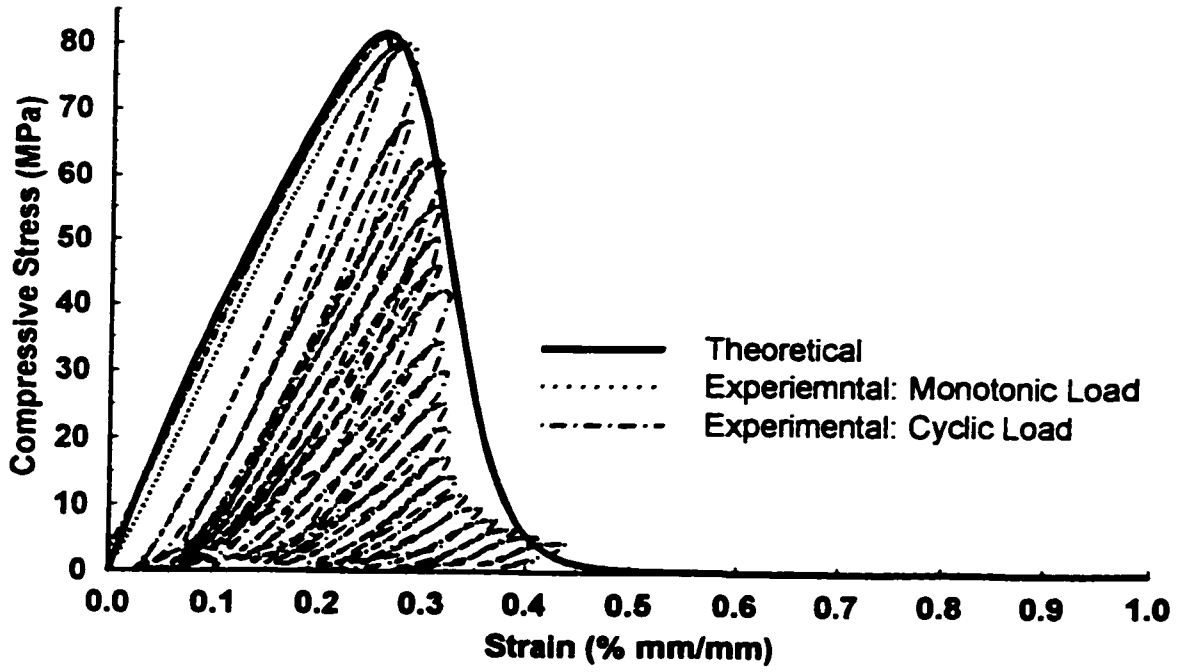

Figure 7-3: Comparison of predicted HSC stress-strain curve with test results

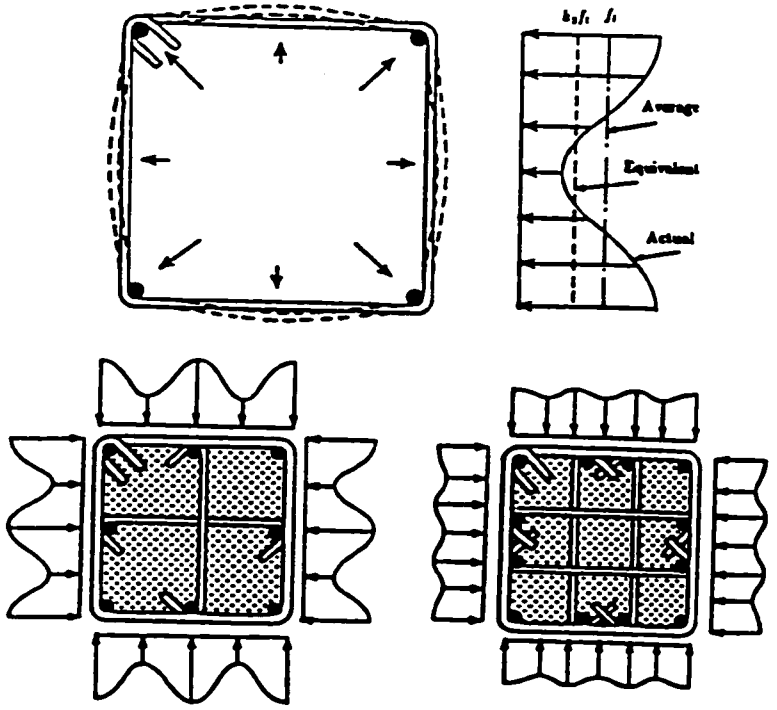

Figure 7-4: Lateral pressure built-up in square columns (Saatcioglu and Razvi, 1992)

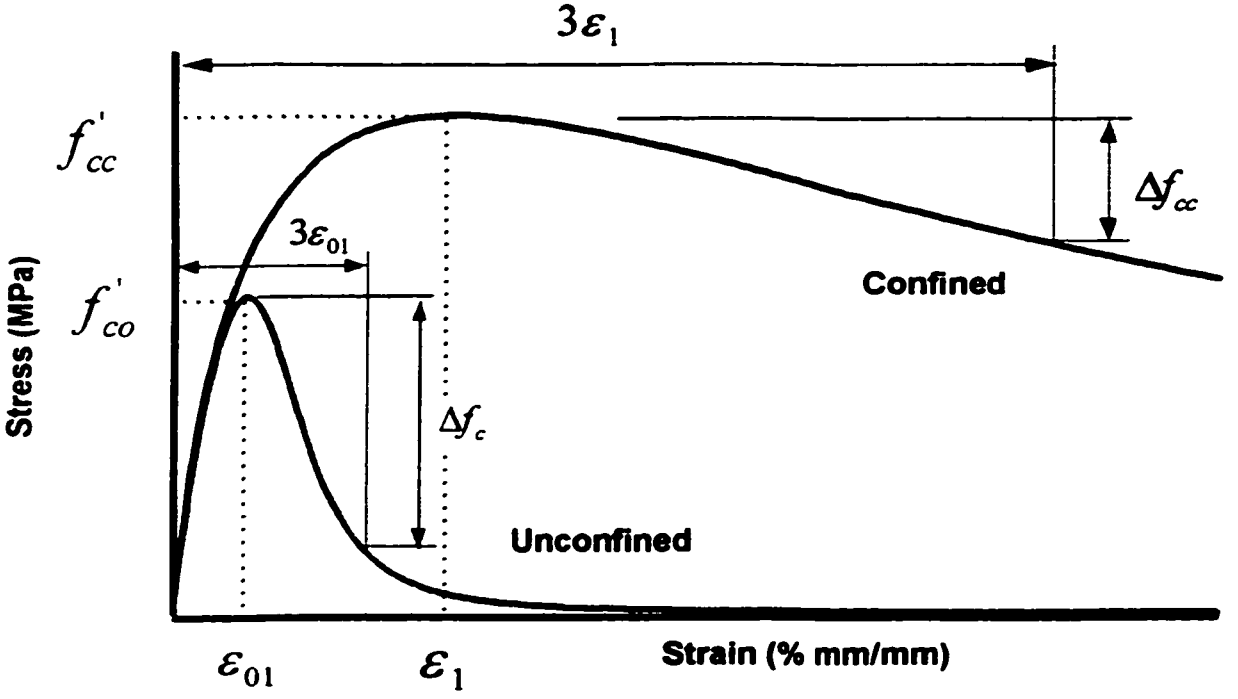

Figure 7-5: Theoretical stress-strain relationship for unconfined and confined concretes

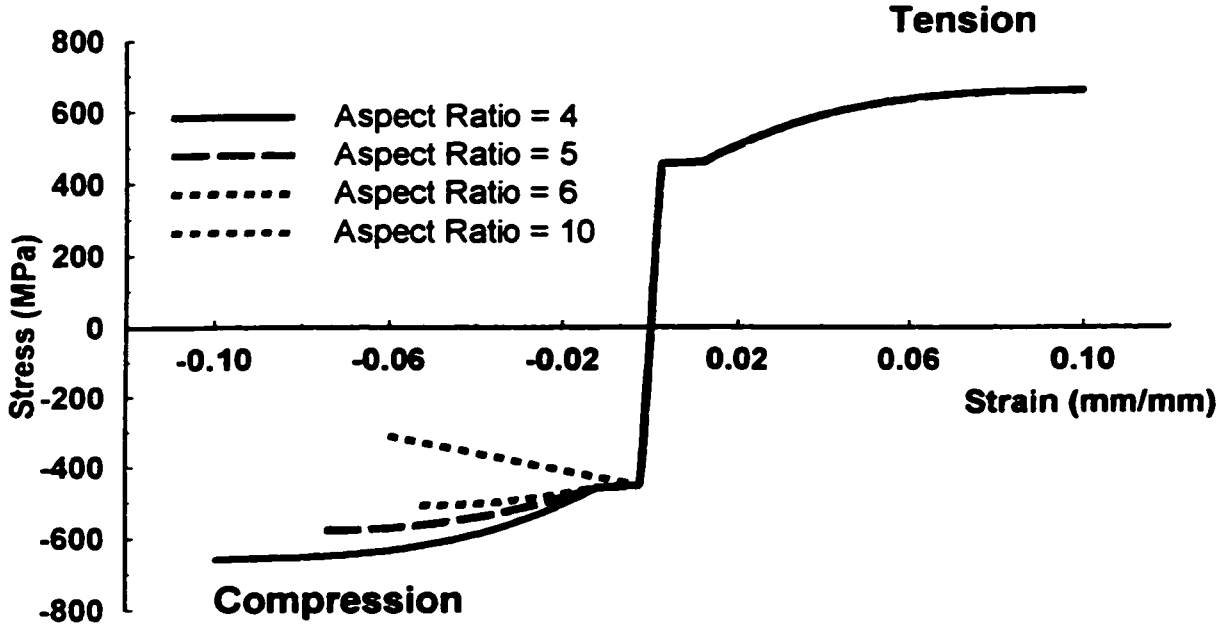

Figure 7-6: Analytical prediction of stress-strain curves for longitudinal reinforcing steel bars

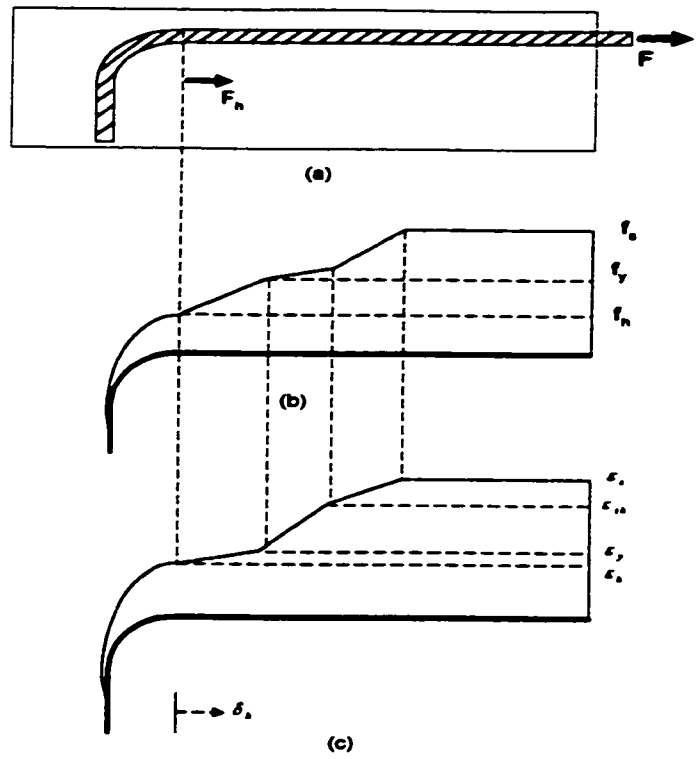

Figure 7-7: a) Hooked bar embedded in concrete; b) Stress distribution; c) Strain distribution

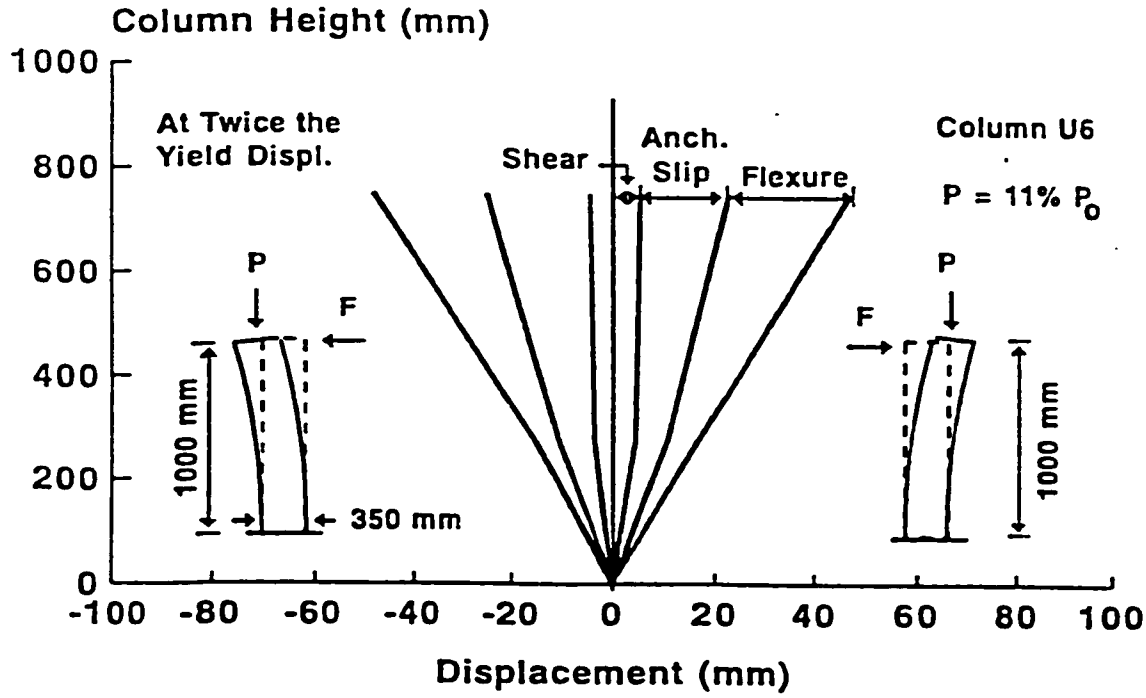

Figure 7-8: Displacement components recorded during a column test (Saatcioglu and Ozcebe, 1989)

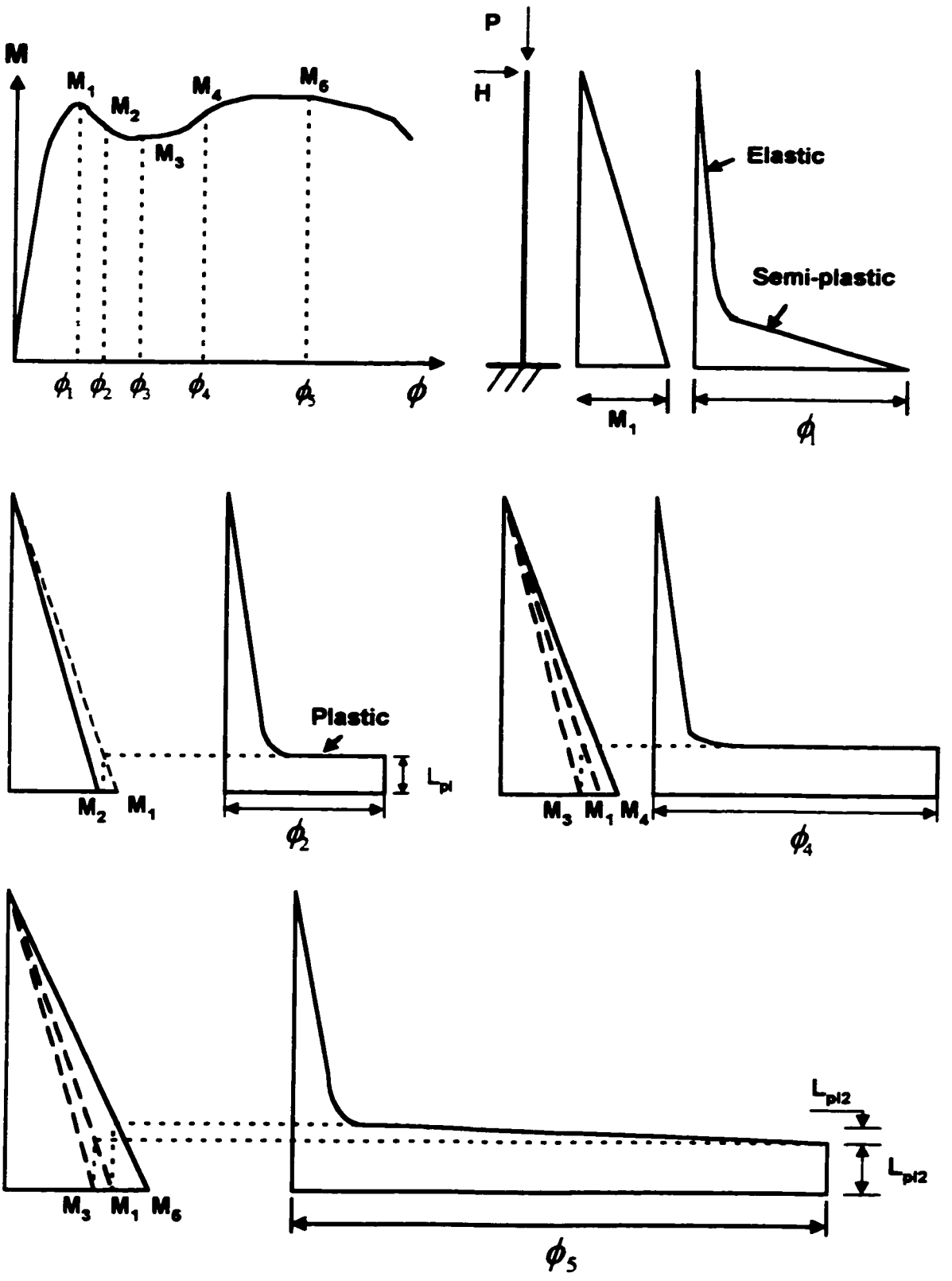

Figure 7-9: Formation and progression of plastic hinges due to flexure

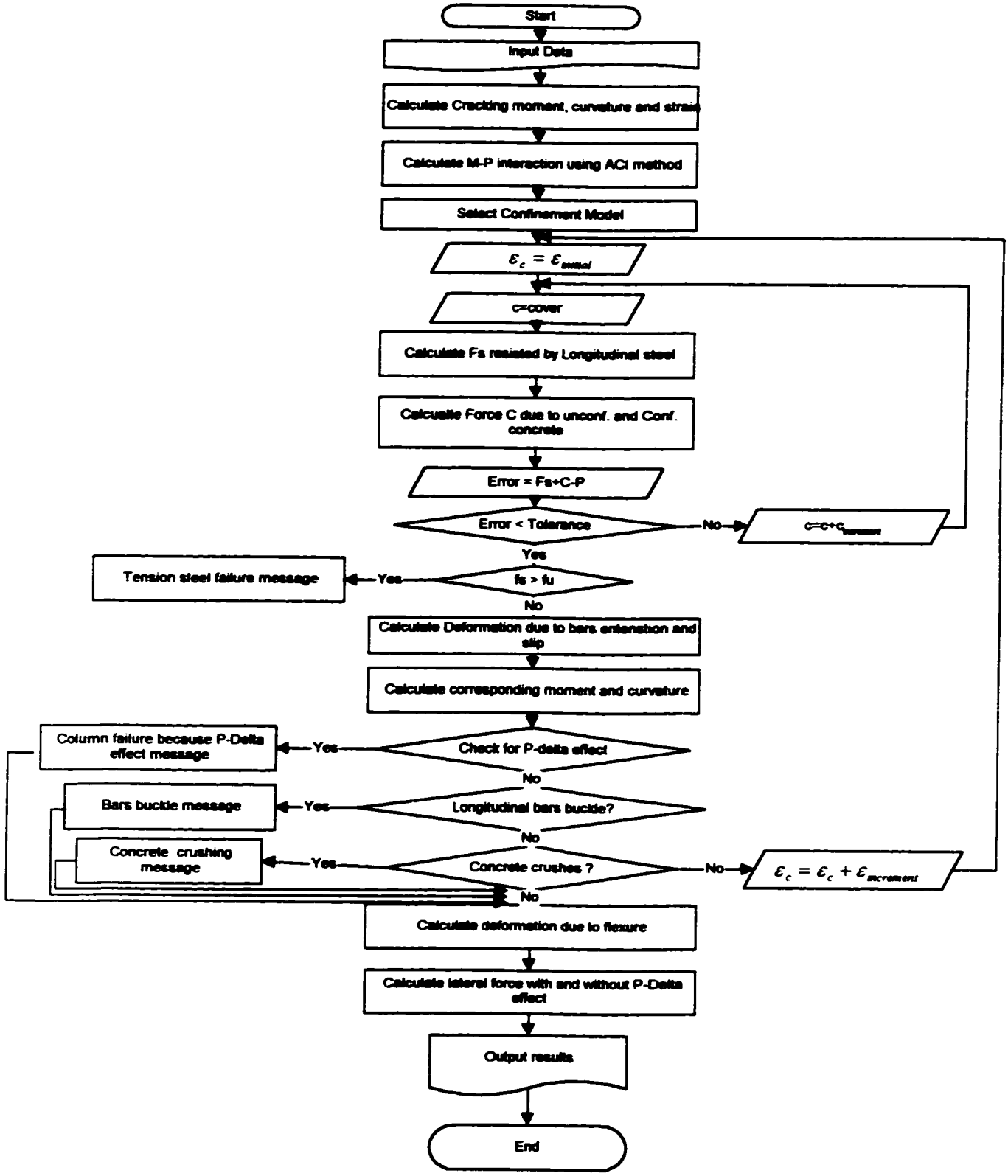

Figure 7-10: Flowchart of sectional analysis program

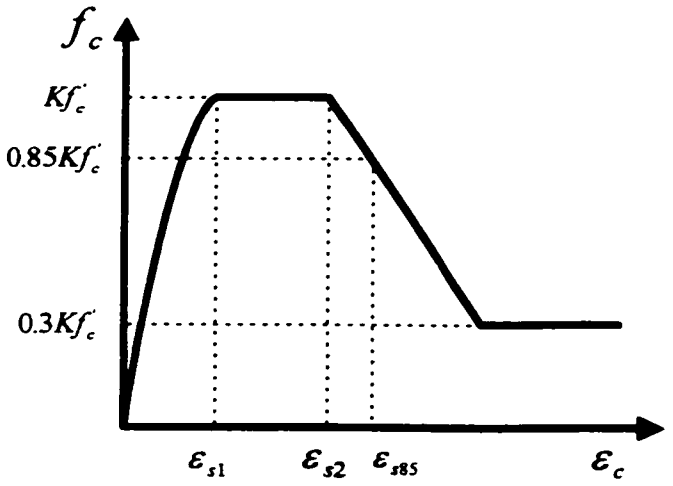

Sheikh and Uzumeri
(1982)

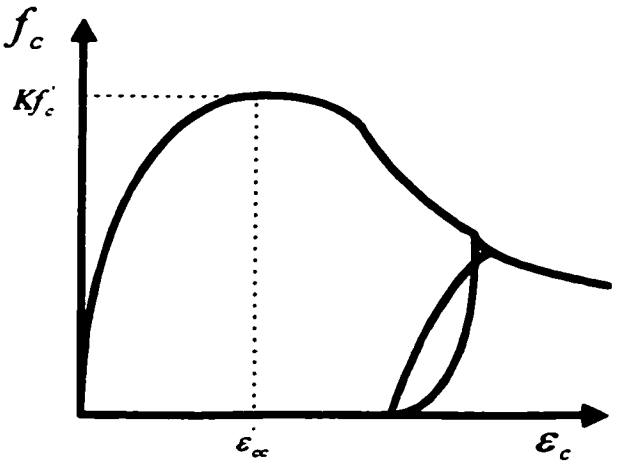

Mander, Priestly and Park
(1988)

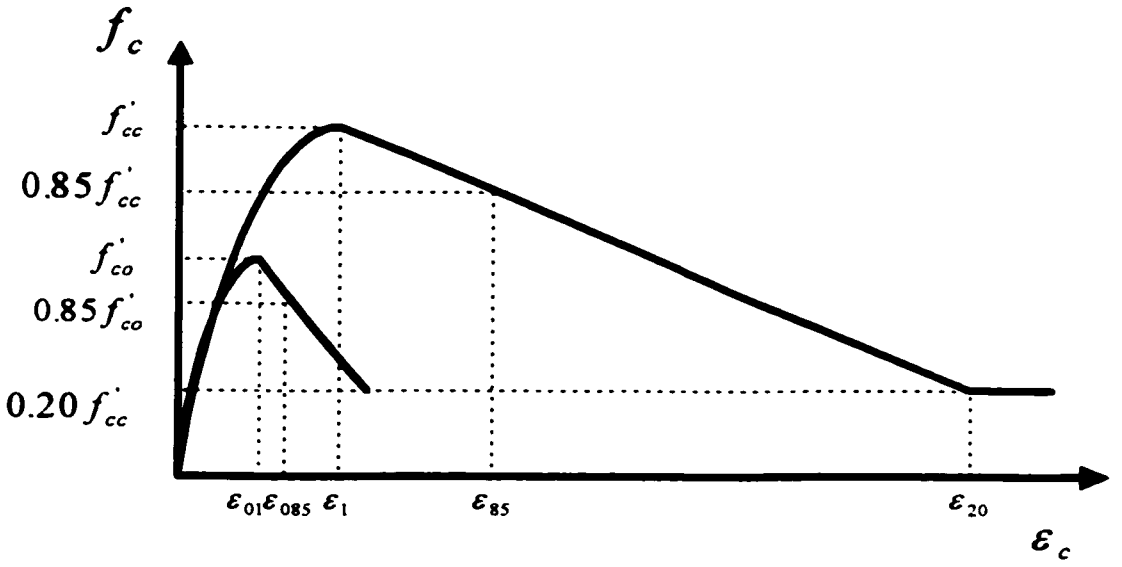

Saatcioglu and Razvi
(1992)

Figure 7-11: Some proposed stress-strain curves for confined concrete

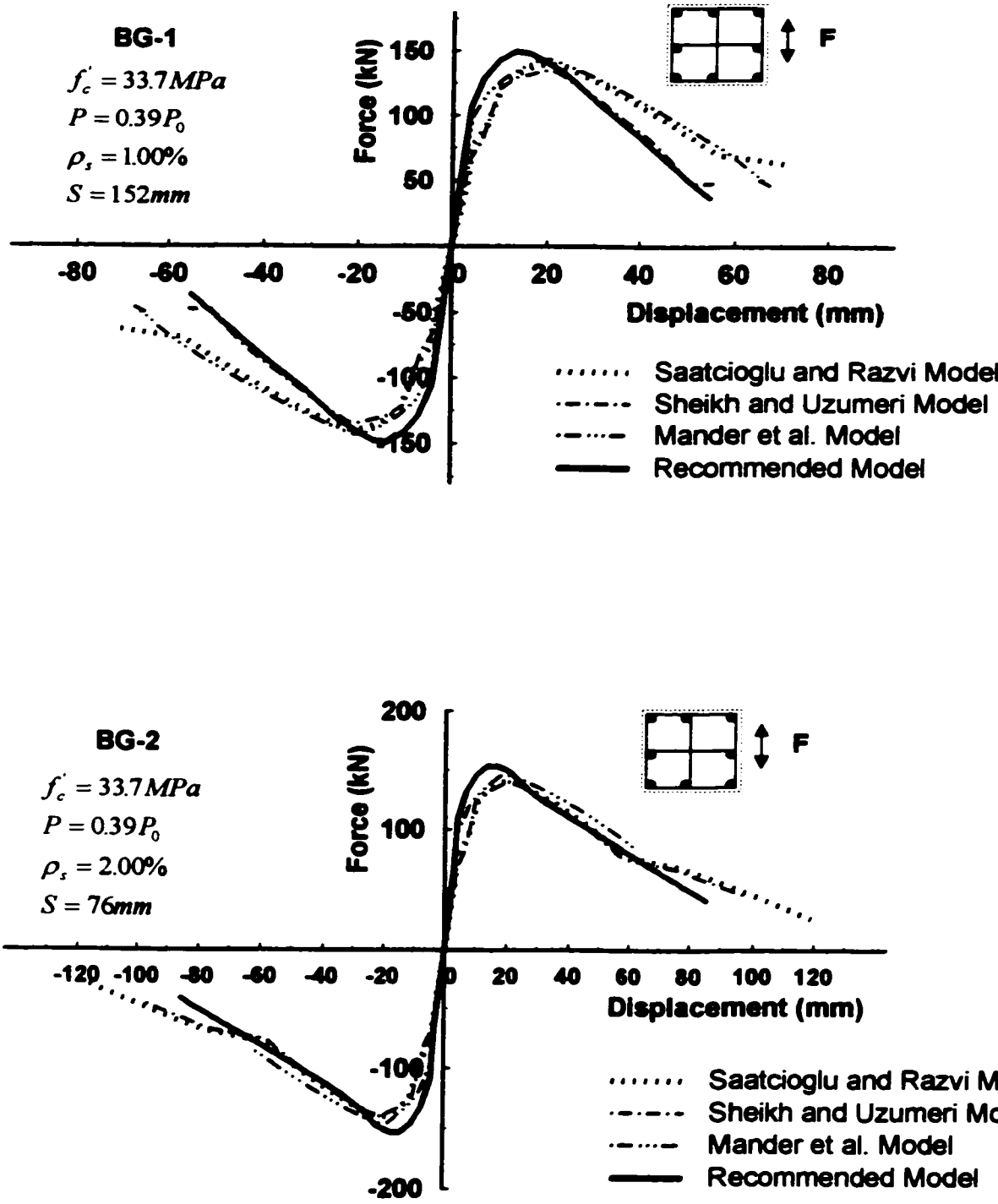

Figure 7-12: Comparisons of some proposed models with the recommended model

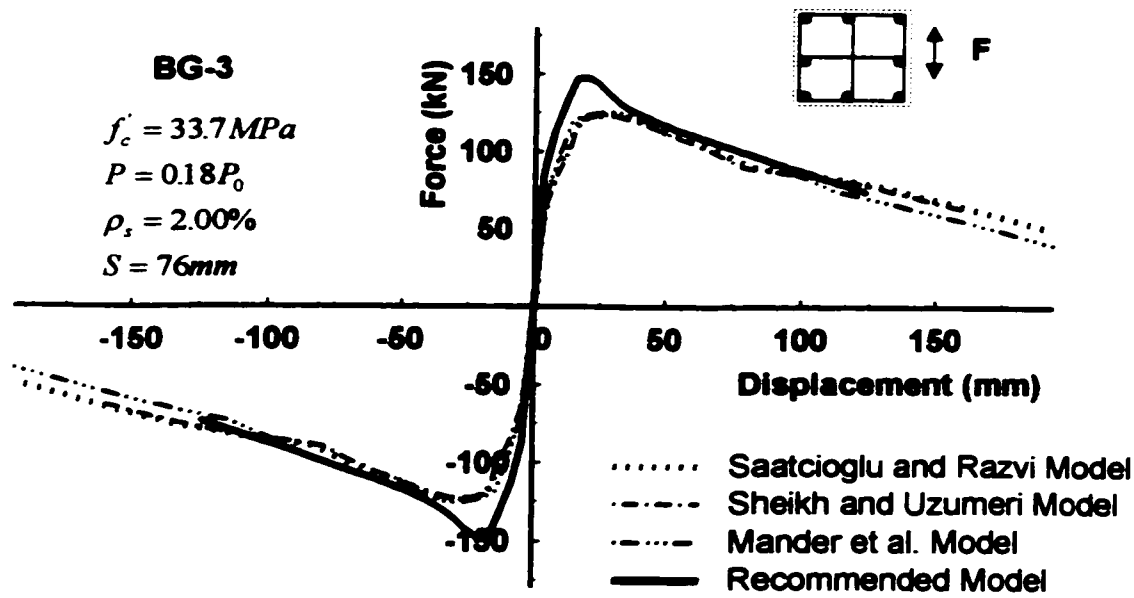

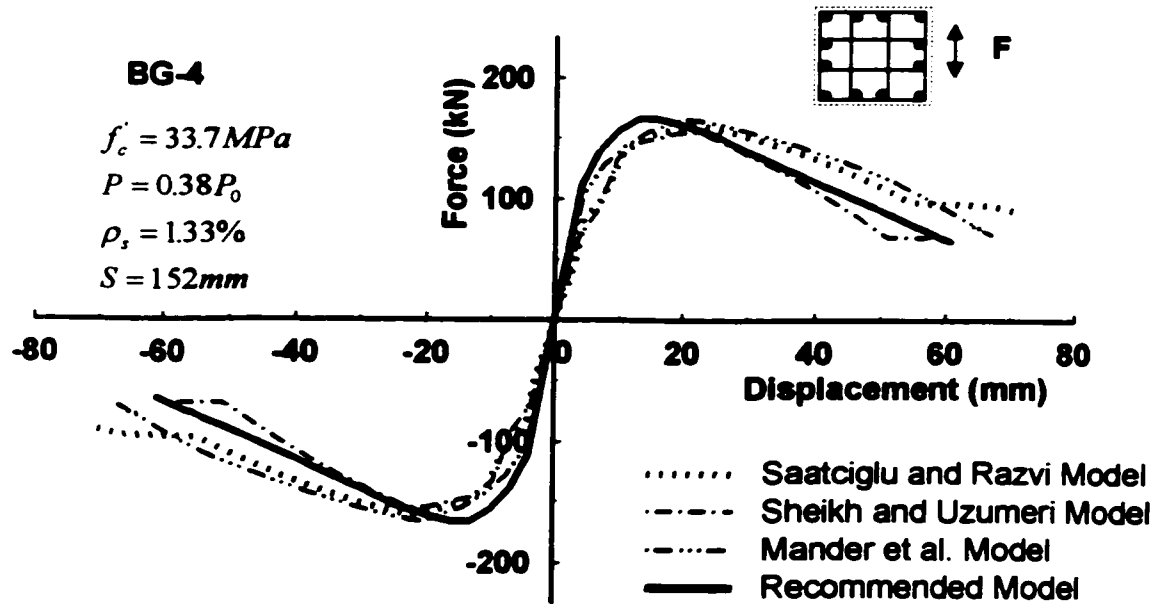

Figure 7-12: Continued

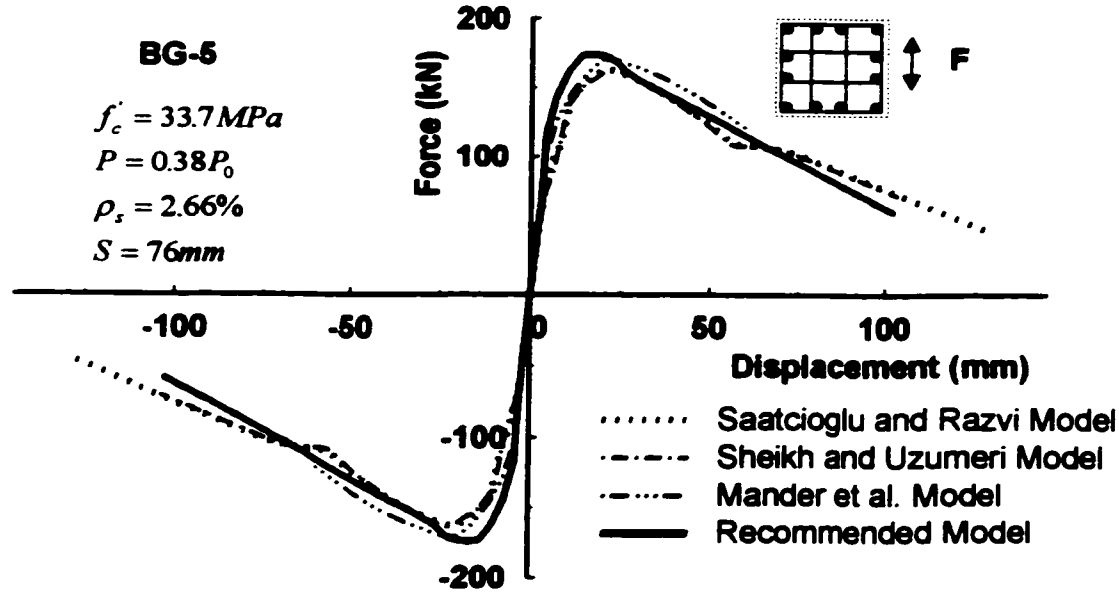

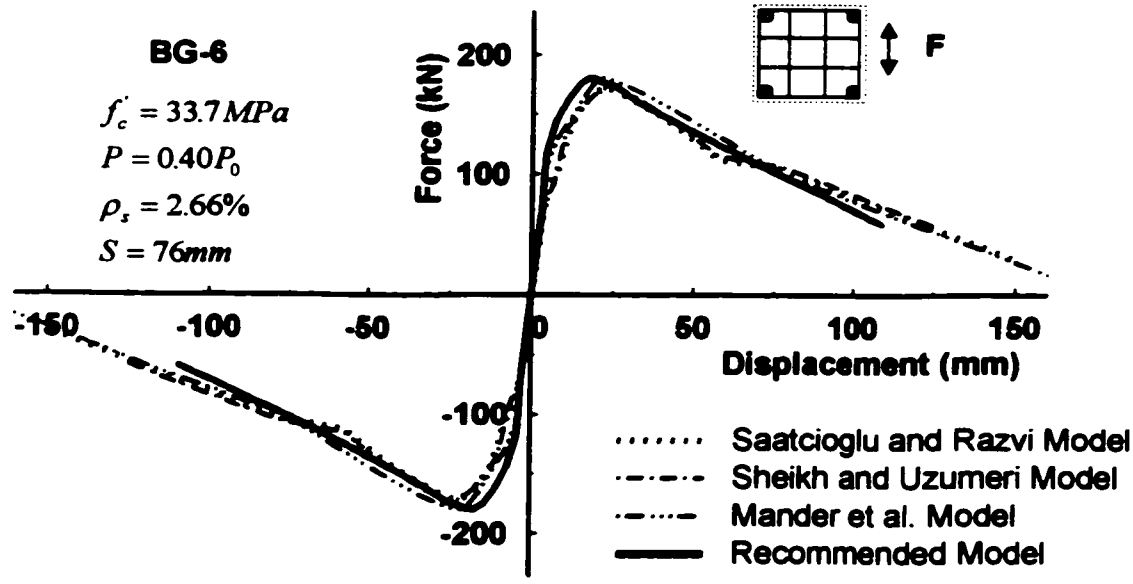

Figure 7-12: Continued

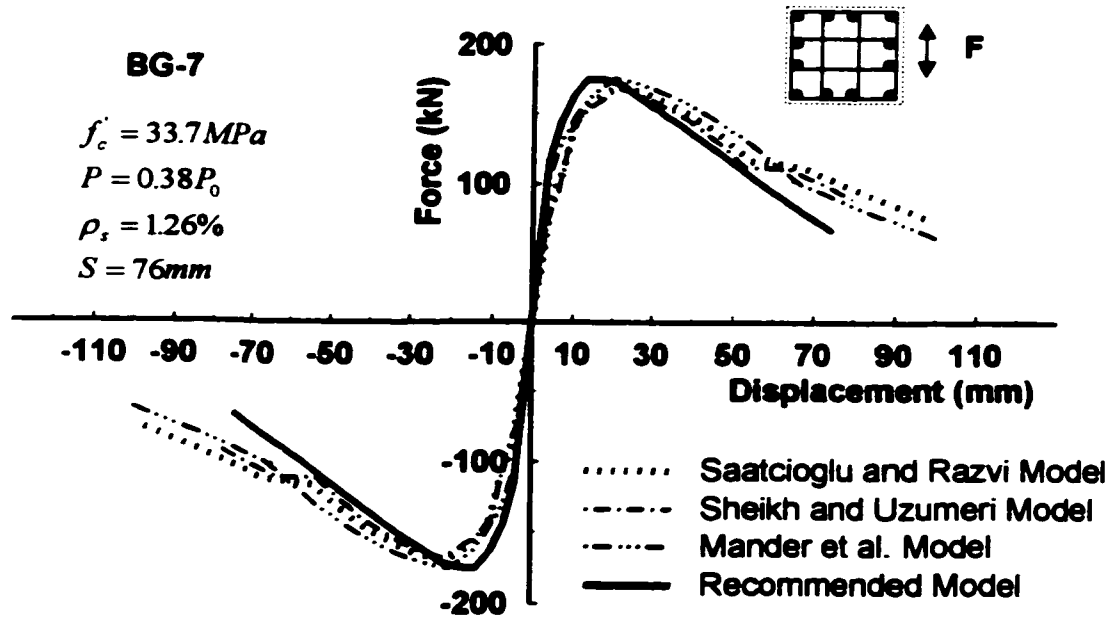

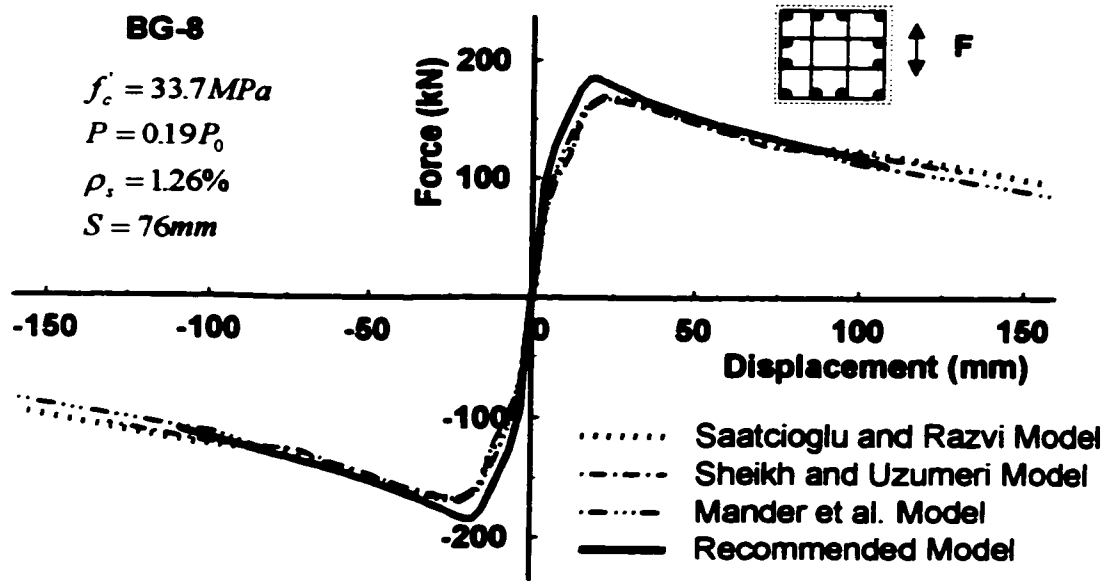

Figure 7-12: Continued

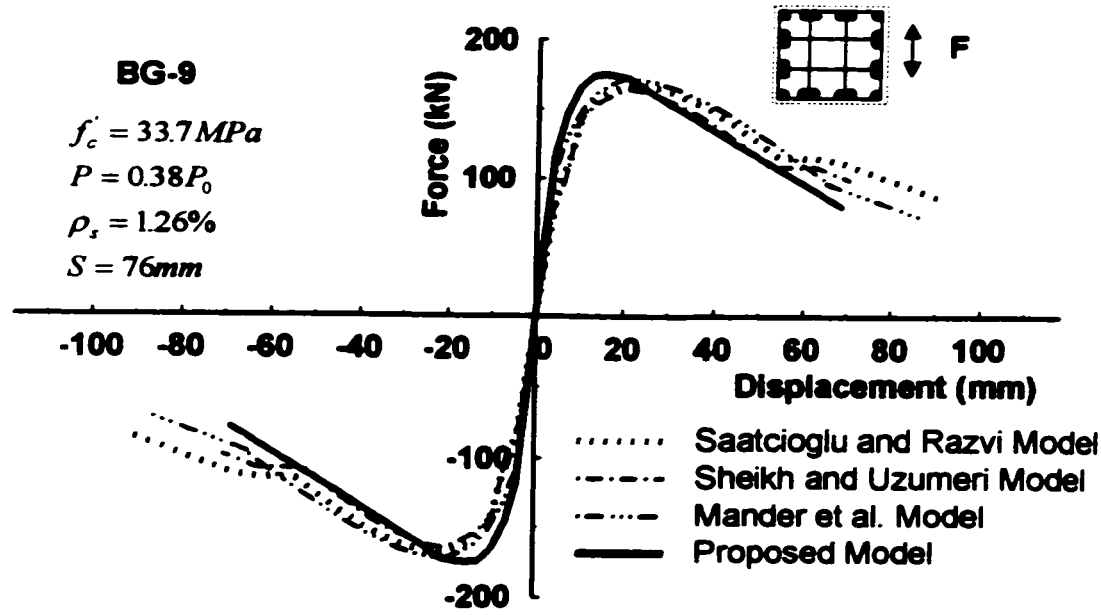

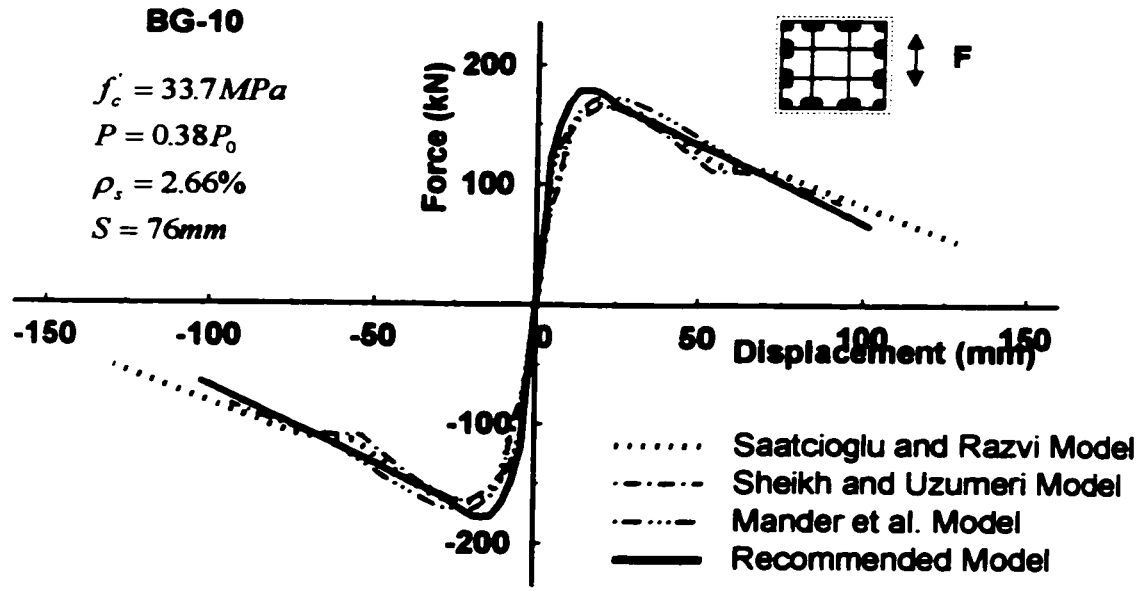

Figure 7-12: Continued

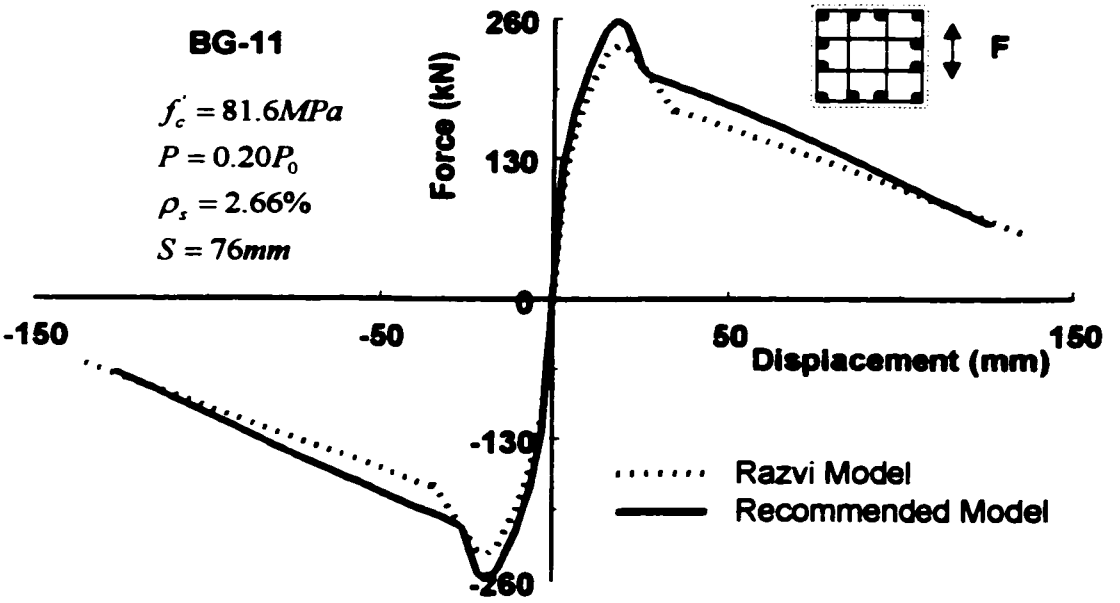

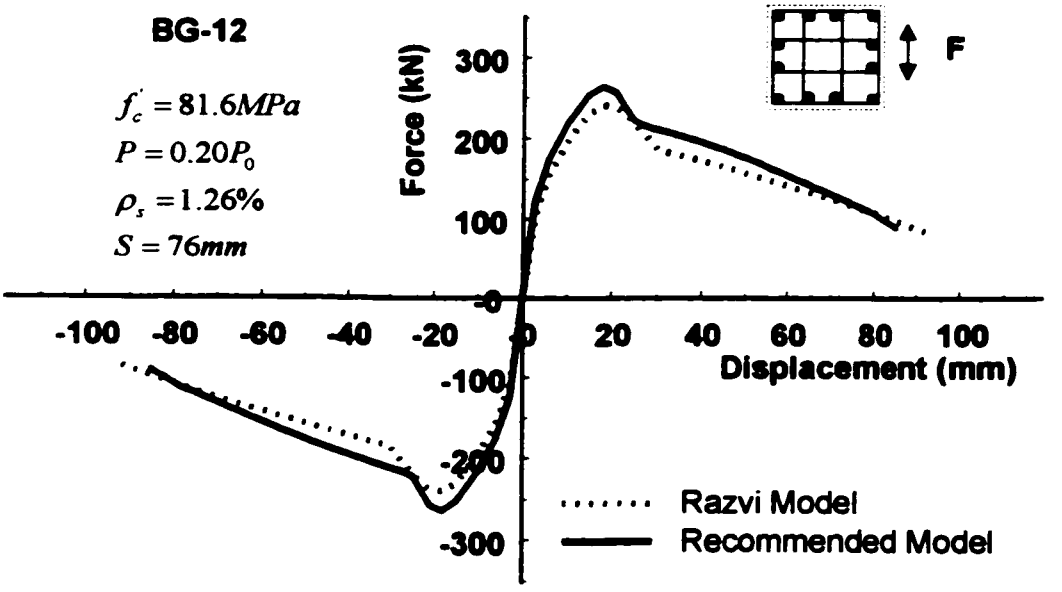

Figure 7-12: Continued

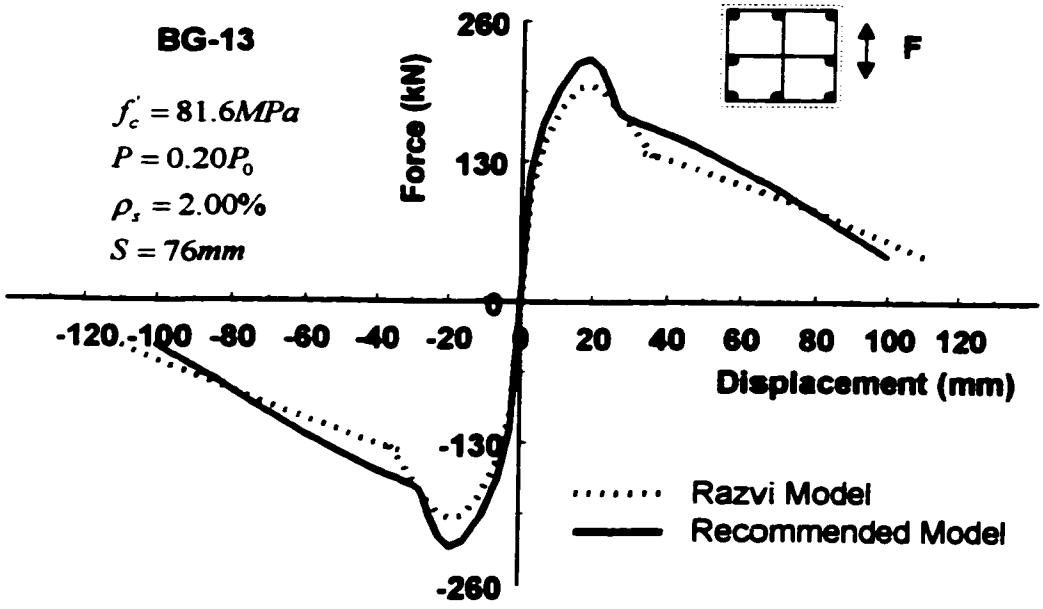

Figure 7-12: Continued

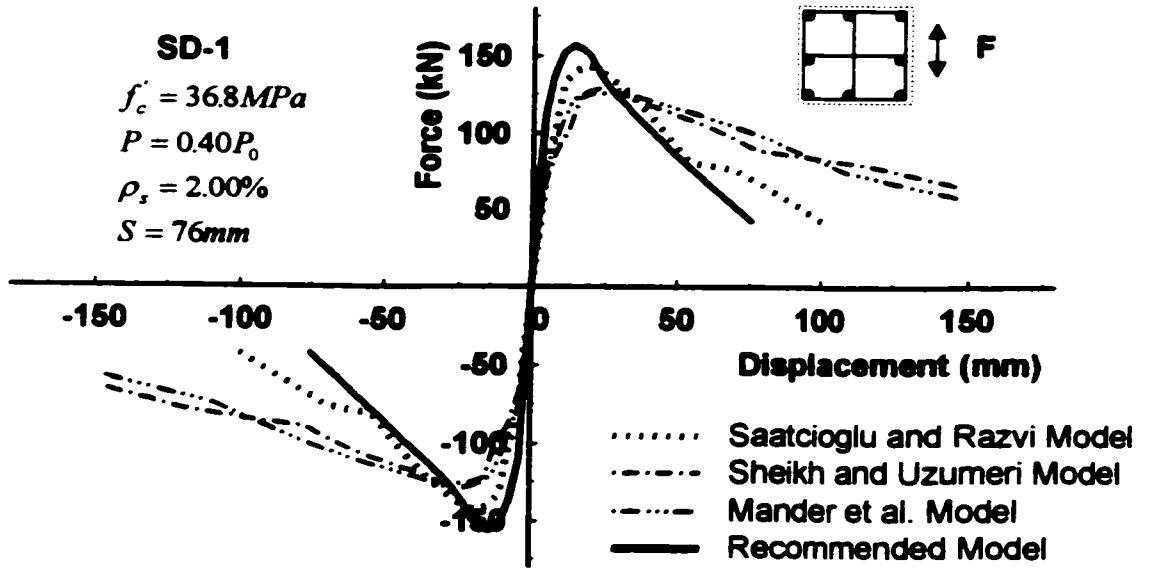

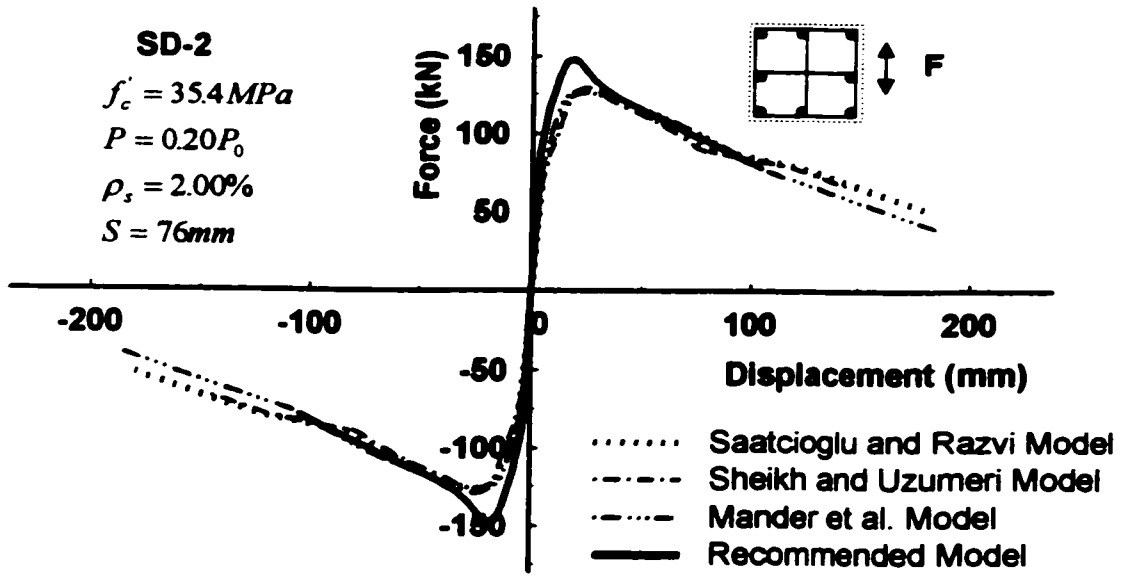

Figure 7-12: Continued

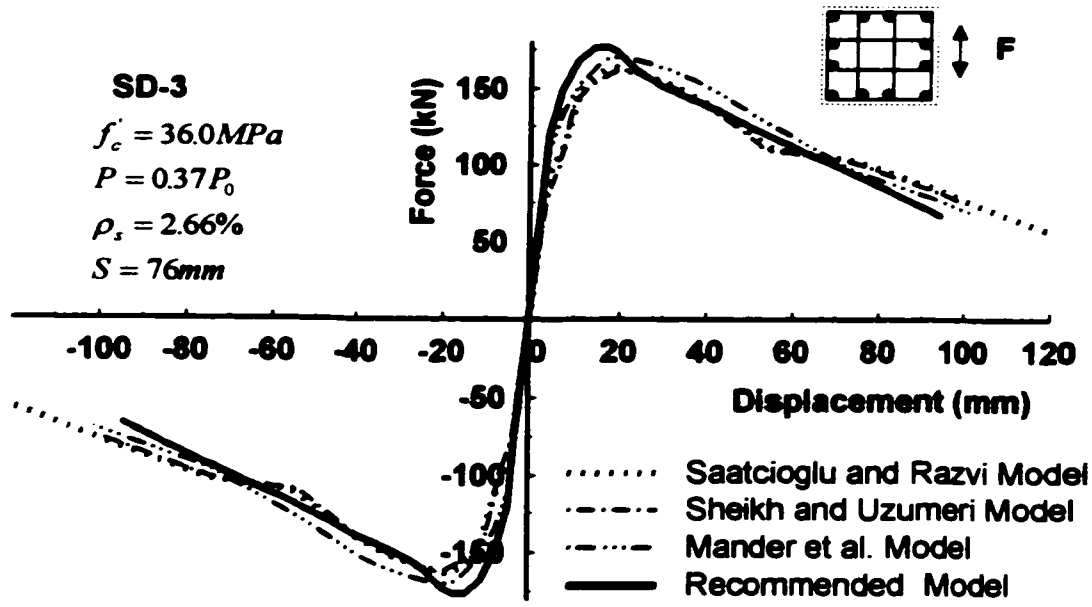

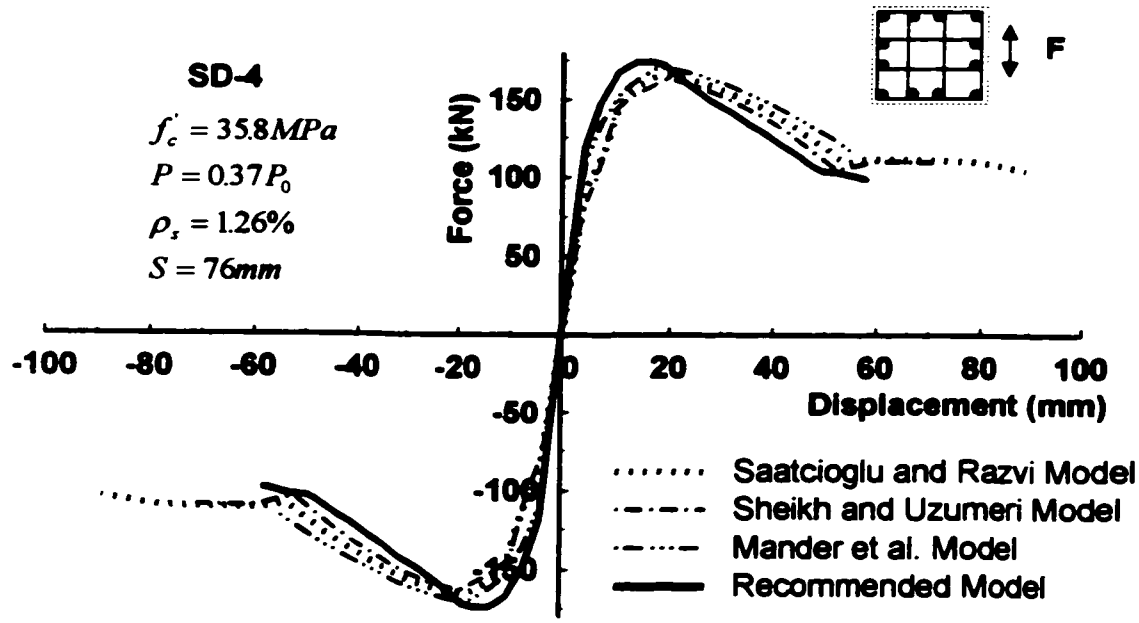

Figure 7-12: Continued

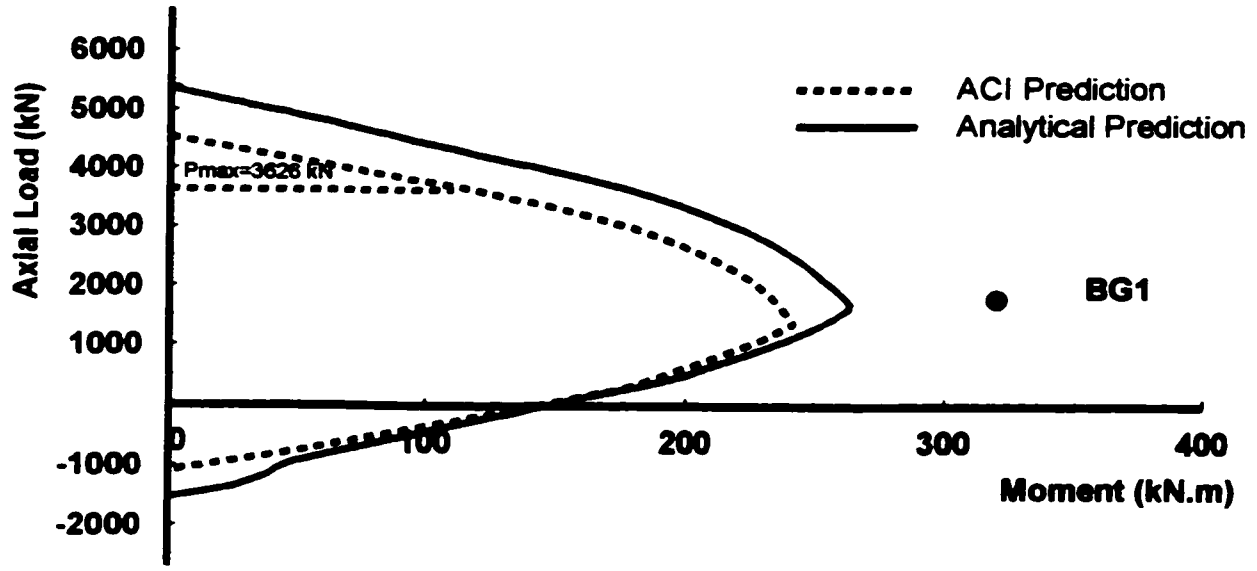

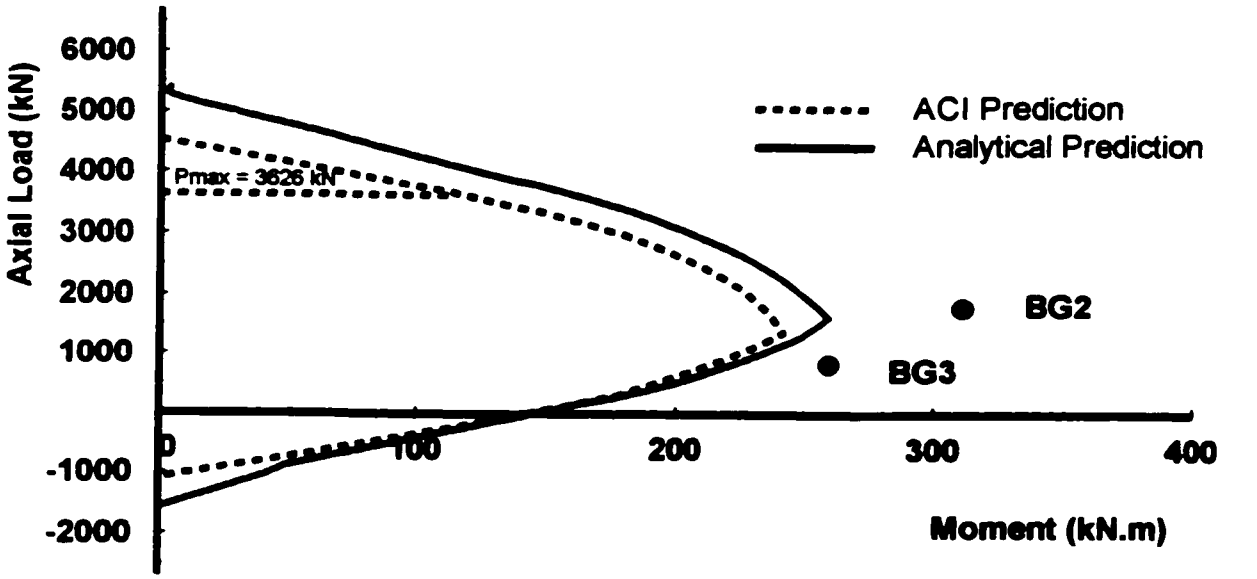

Figure 7-13: Load-moment interaction diagrams of tested columns

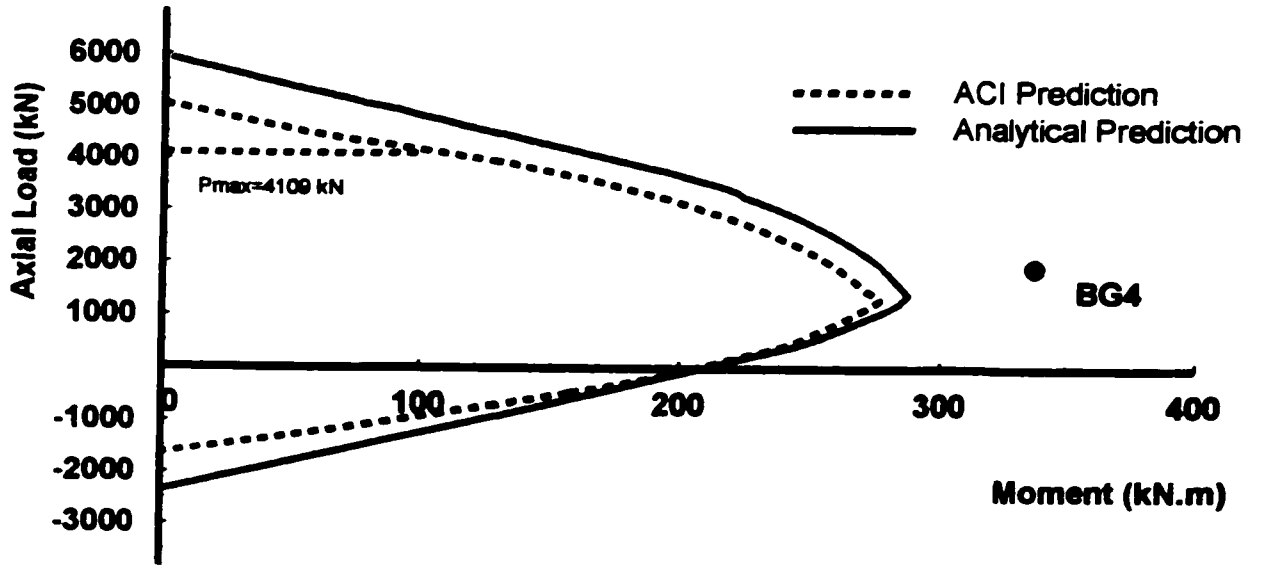

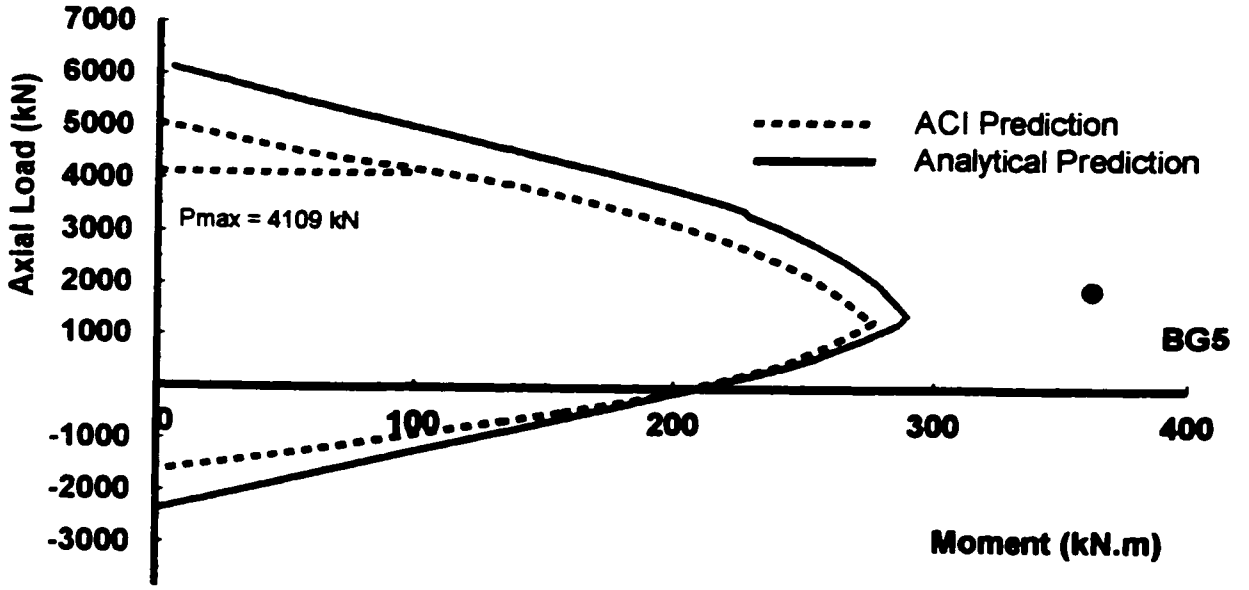

Figure 7-13: Continued

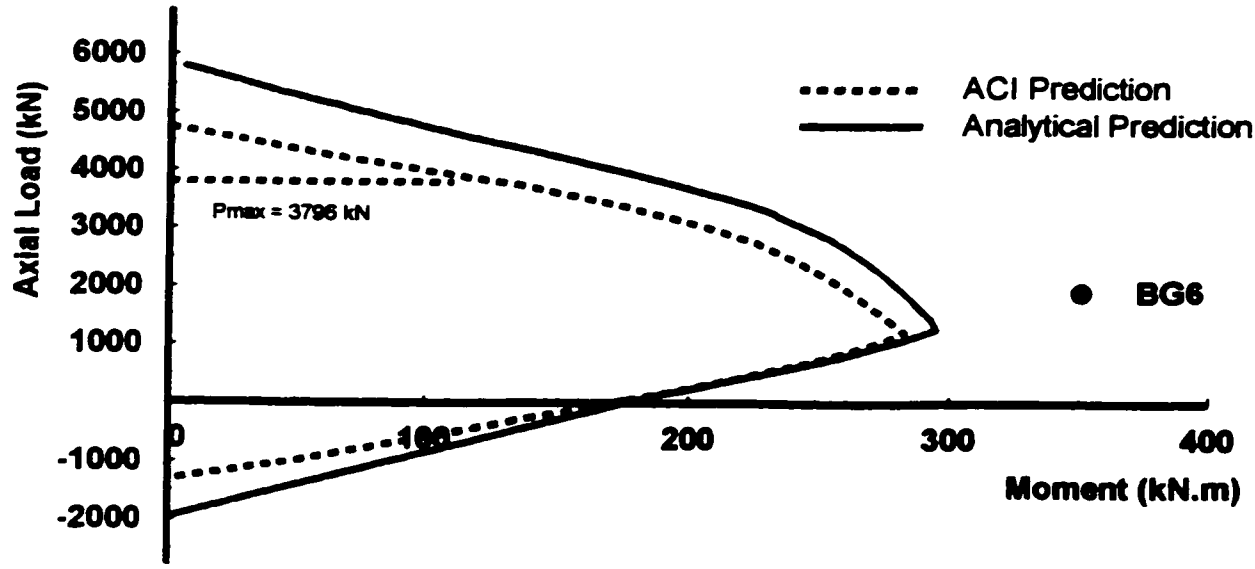

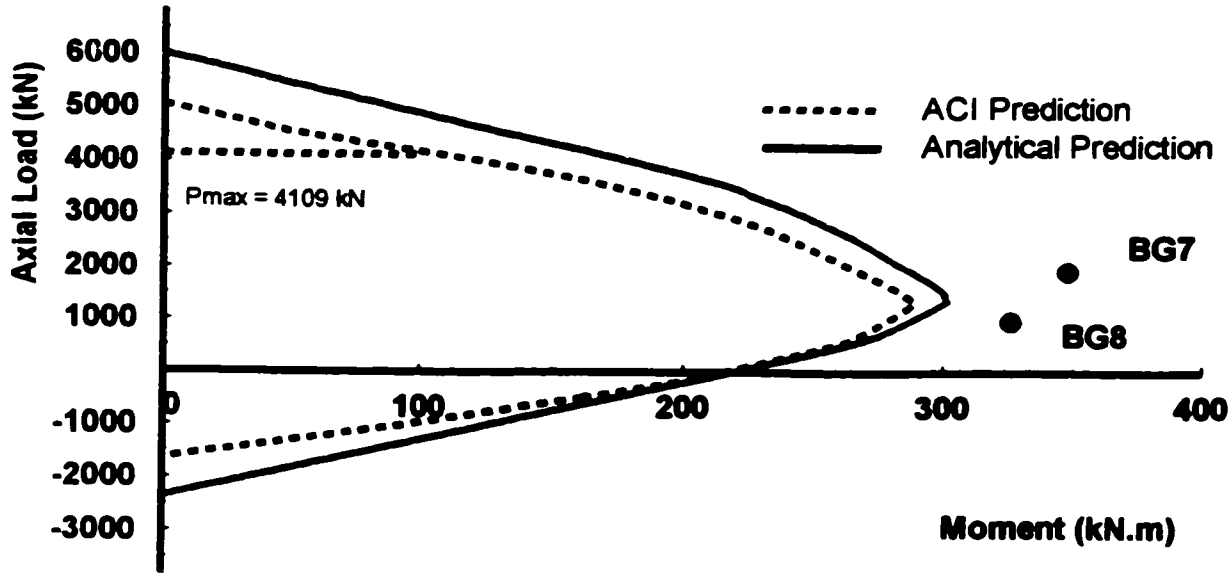

Figure 7-13: Continued

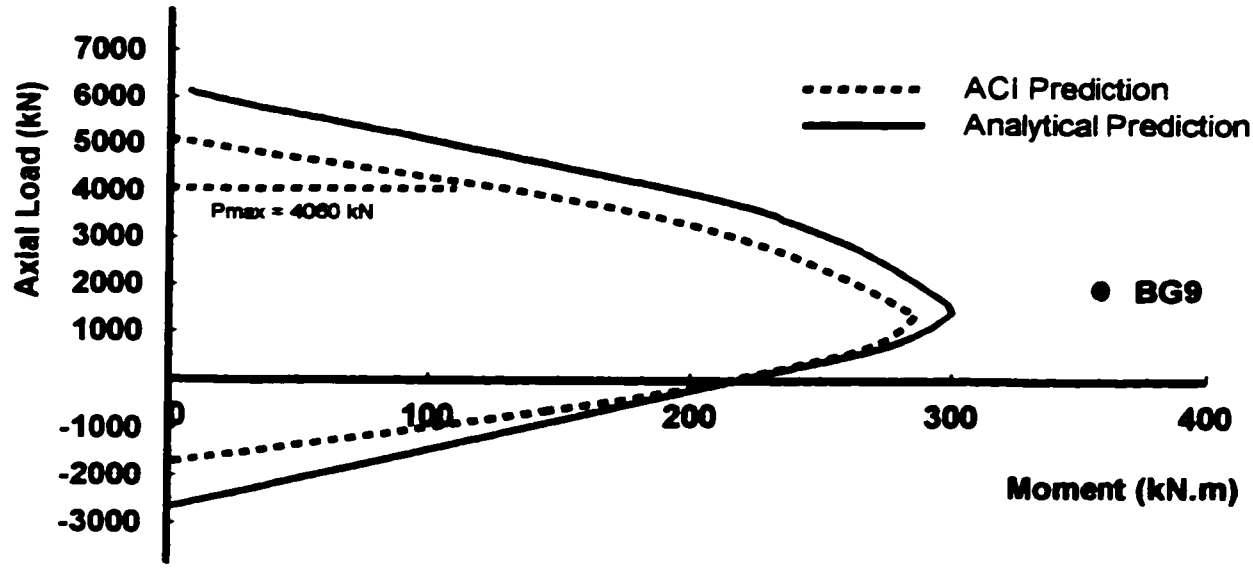

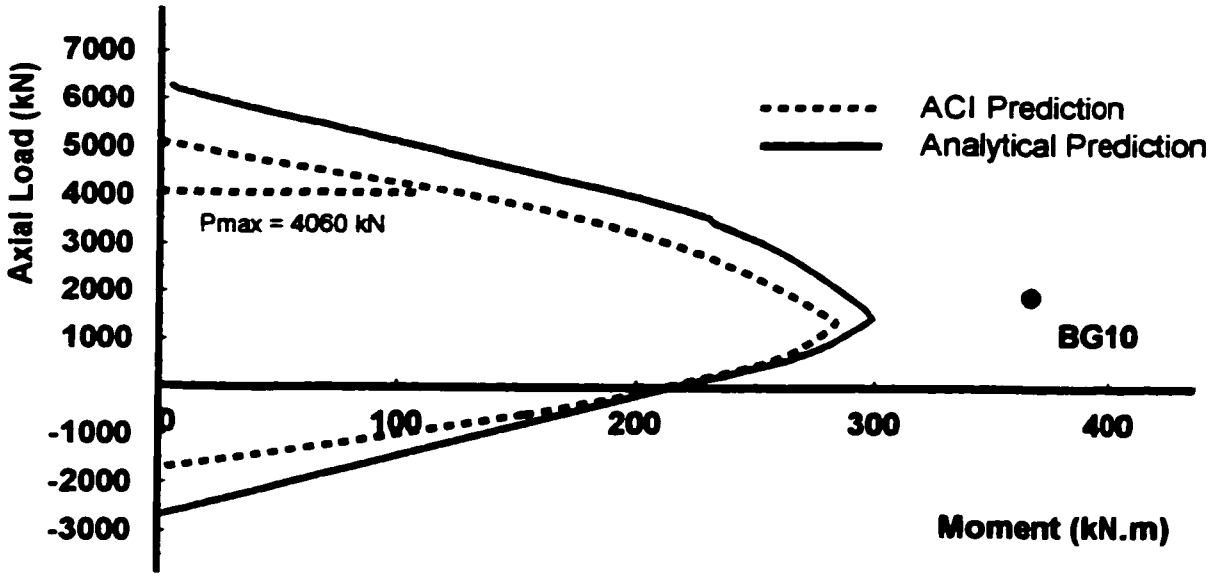

Figure 7-13: Continued

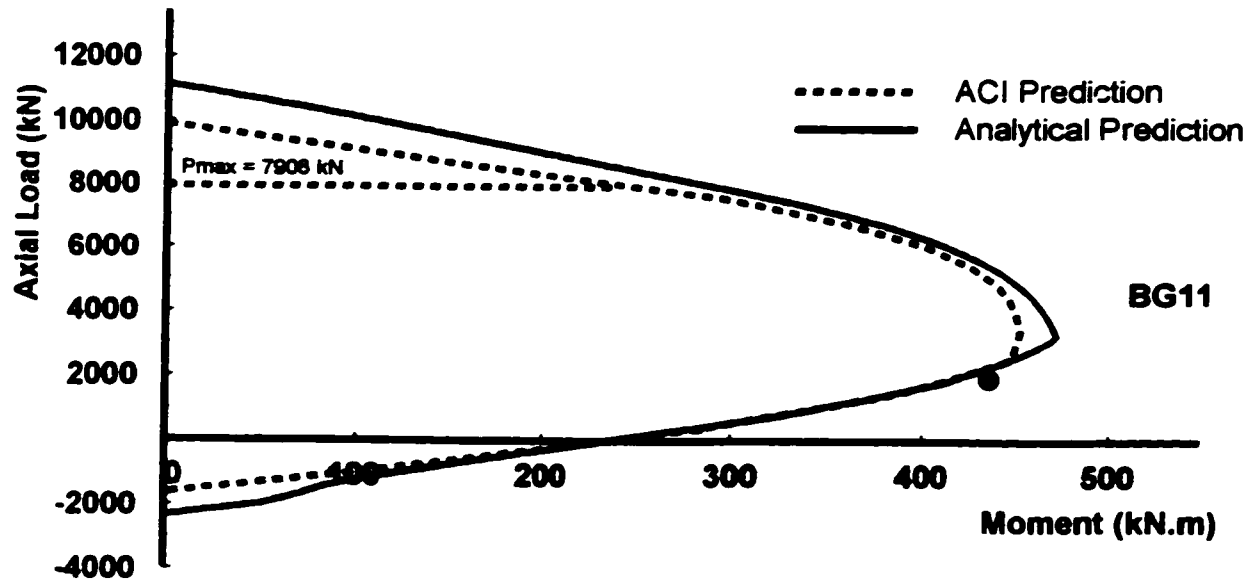

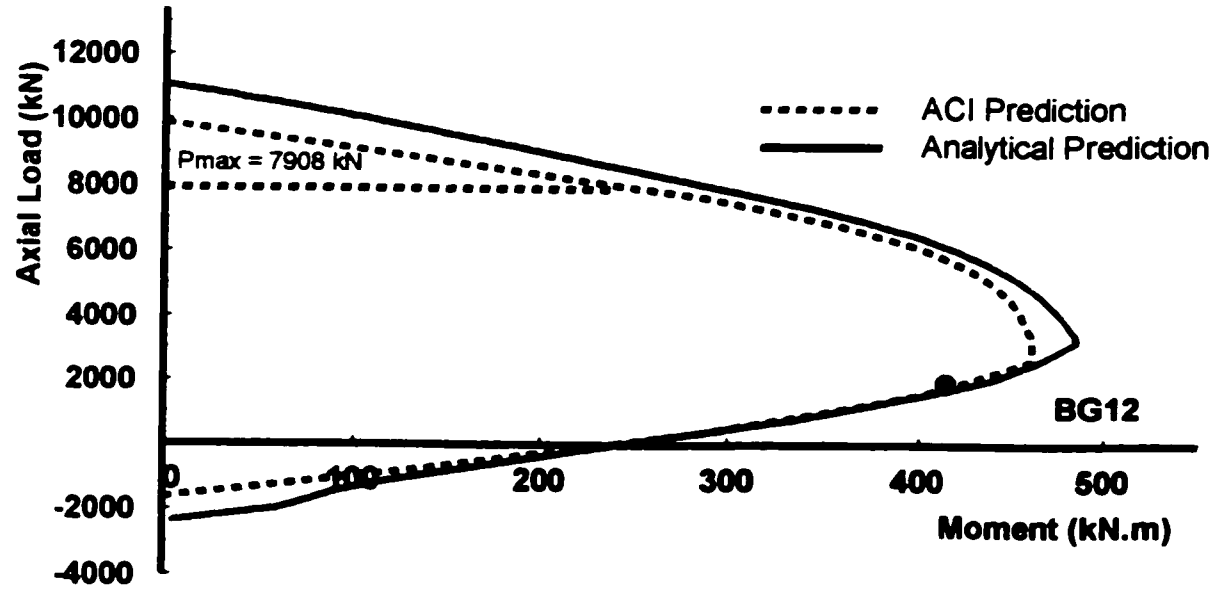

Figure 7-13: Continued

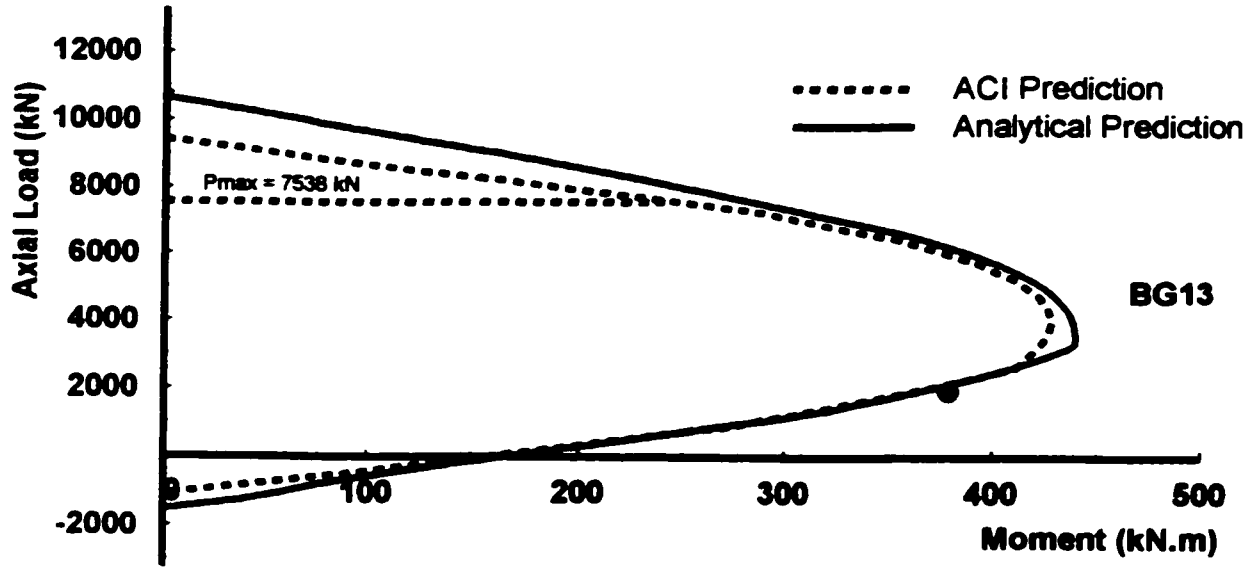

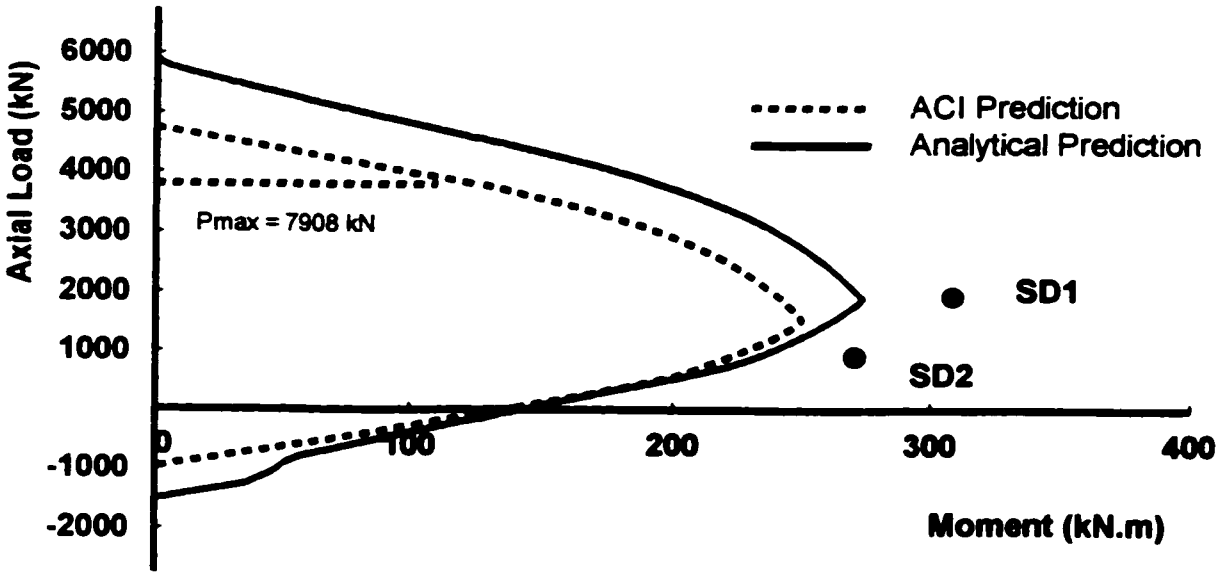

Figure 7-13: Continued

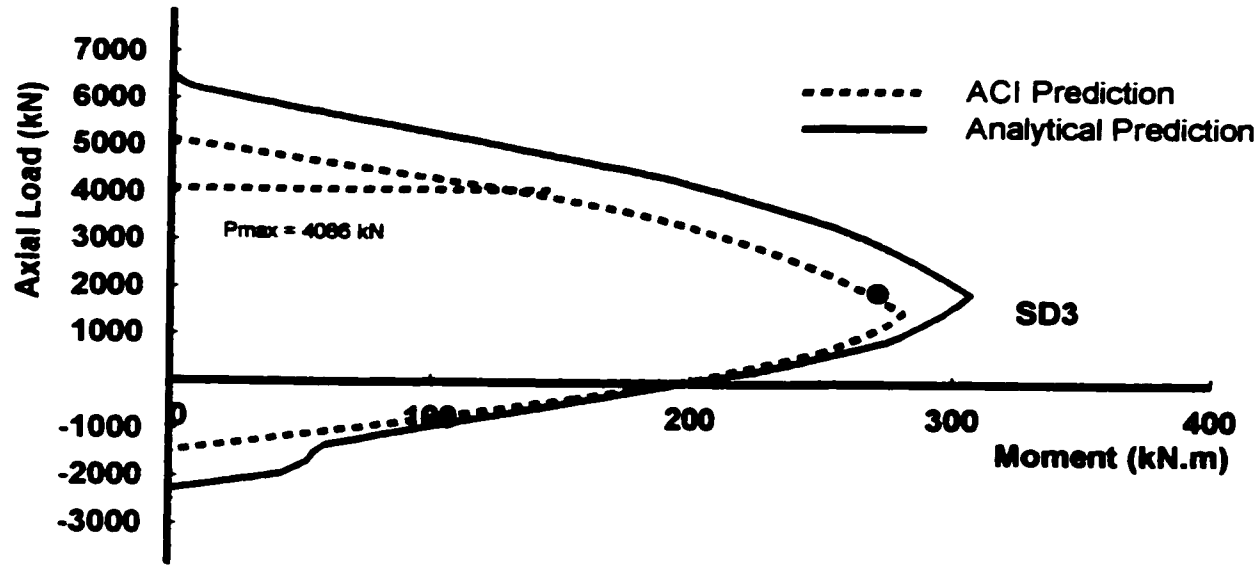

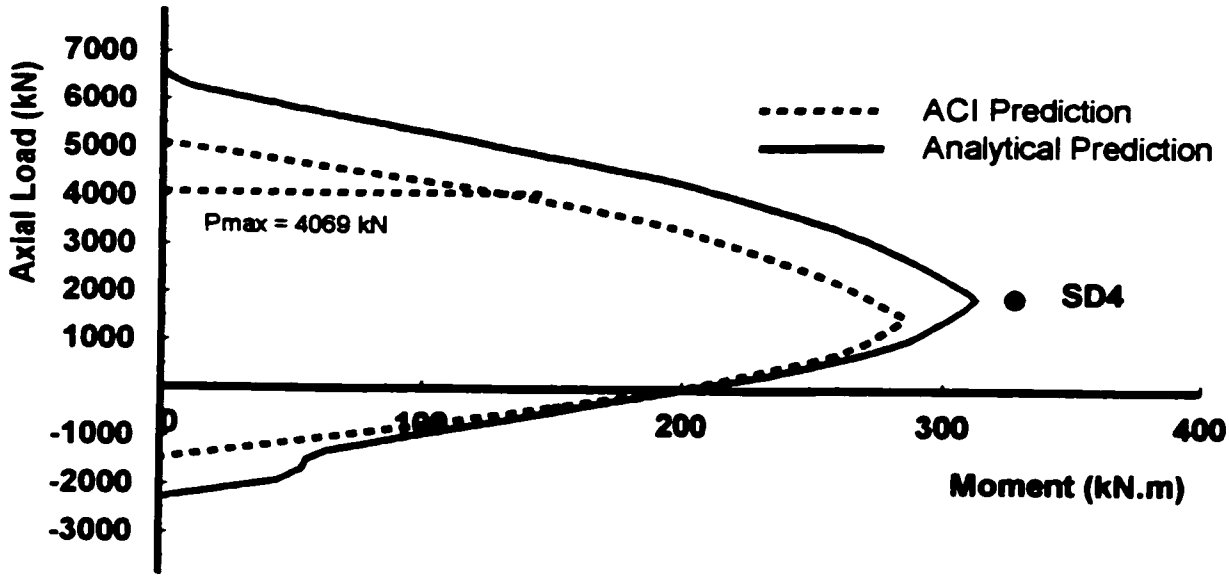

Figure 7-13: Continued

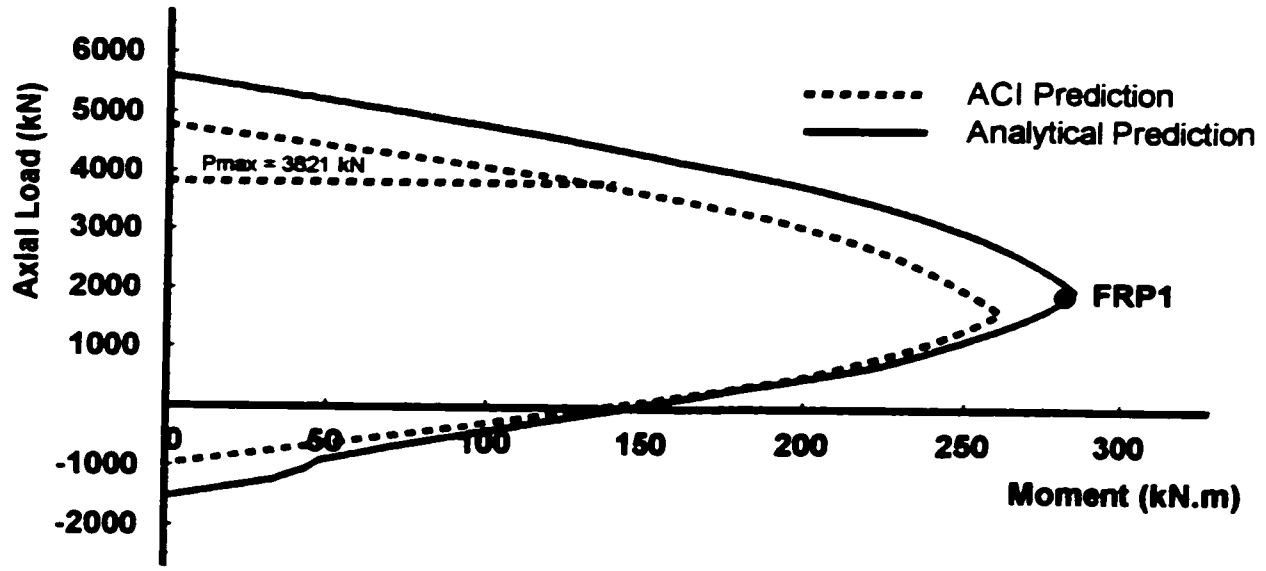

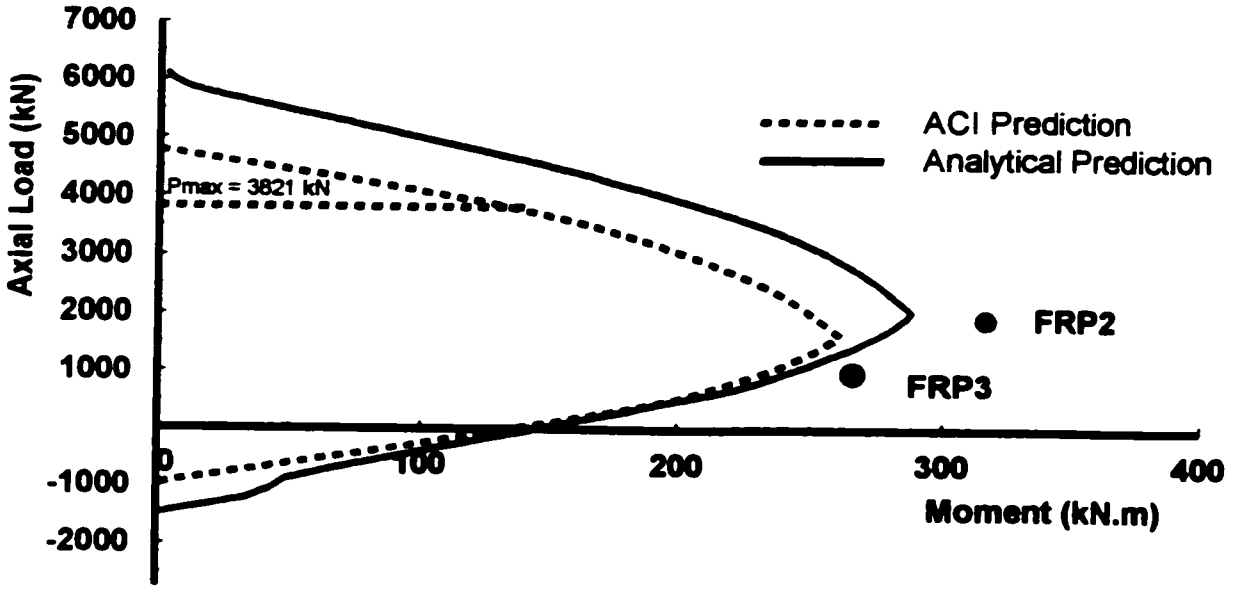

Figure 7-13: Continued

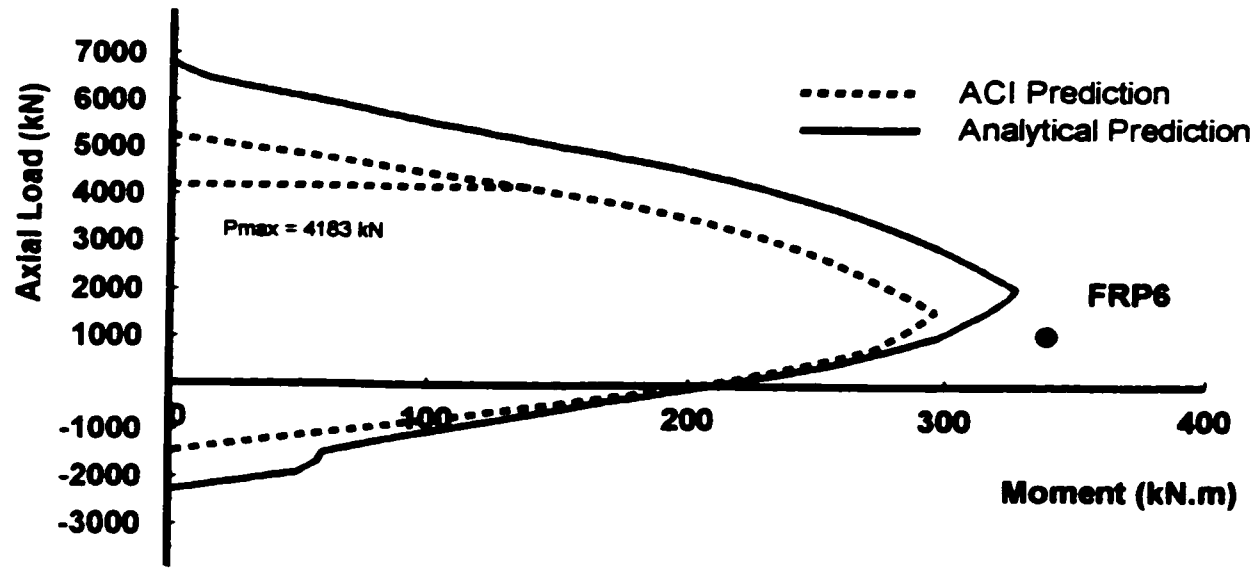

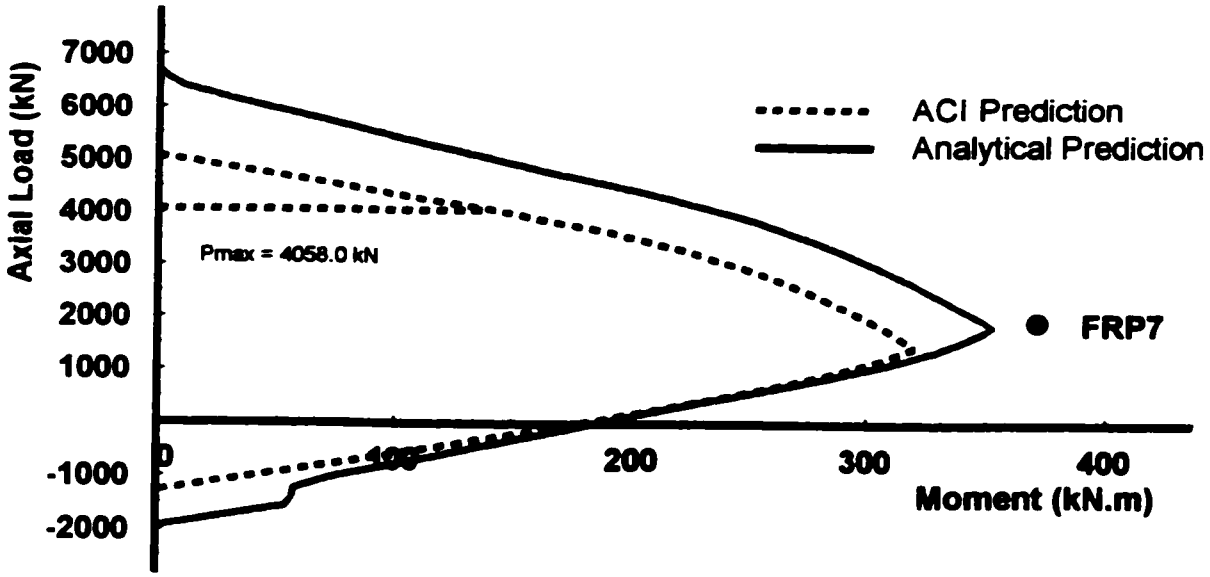

Figure 7-13: Continued

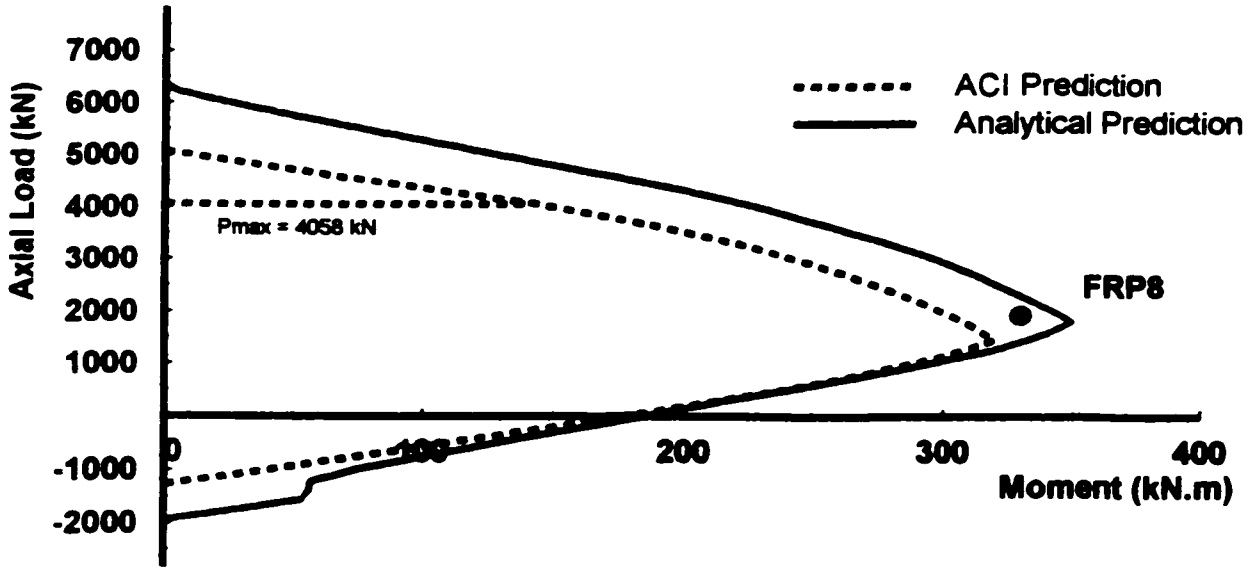

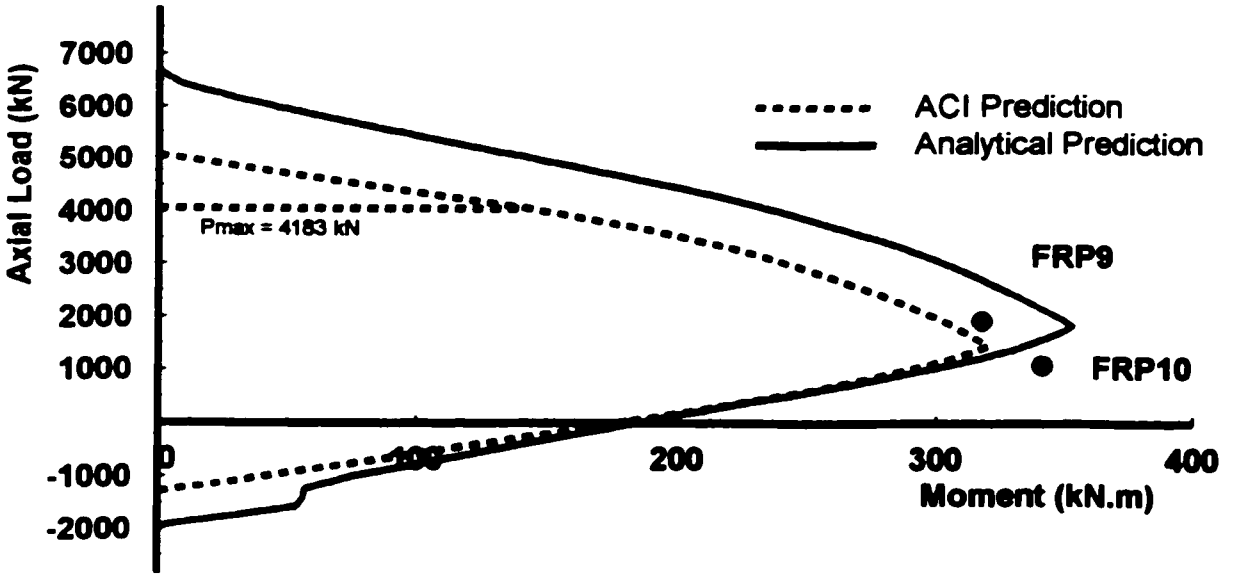

Figure 7-13: Continued

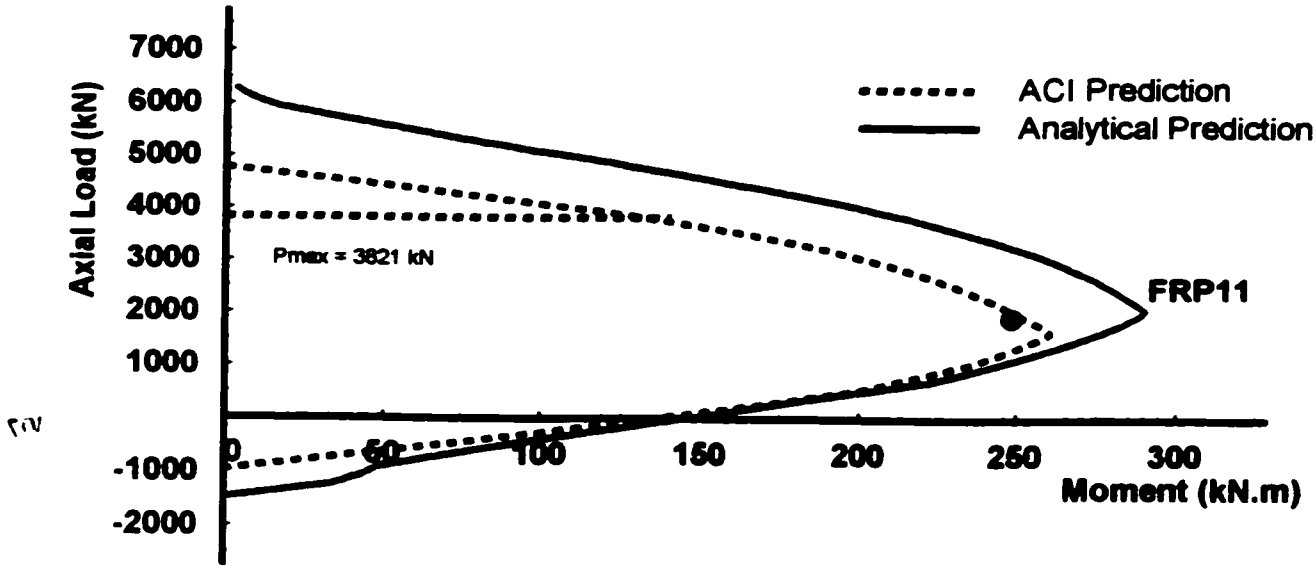

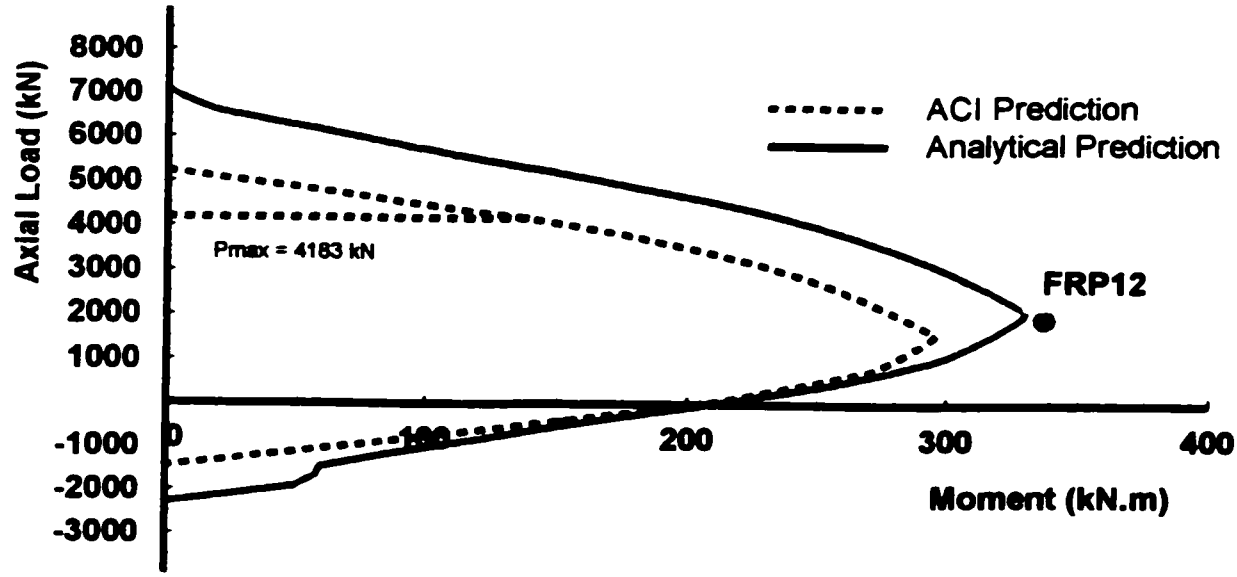

Figure 7-13: Continued

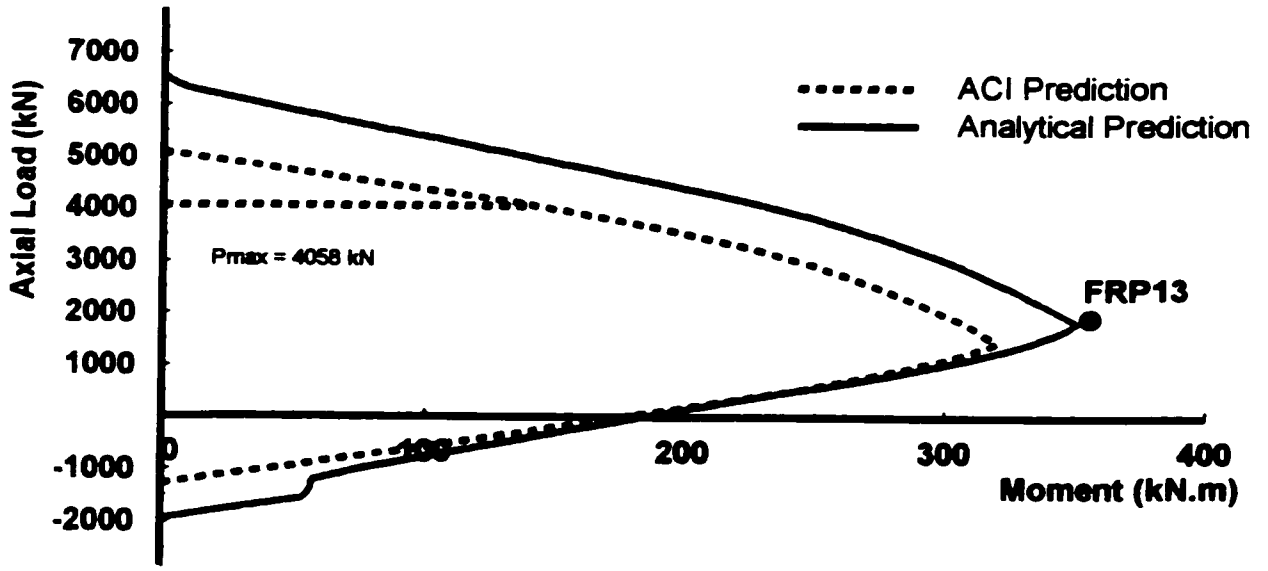

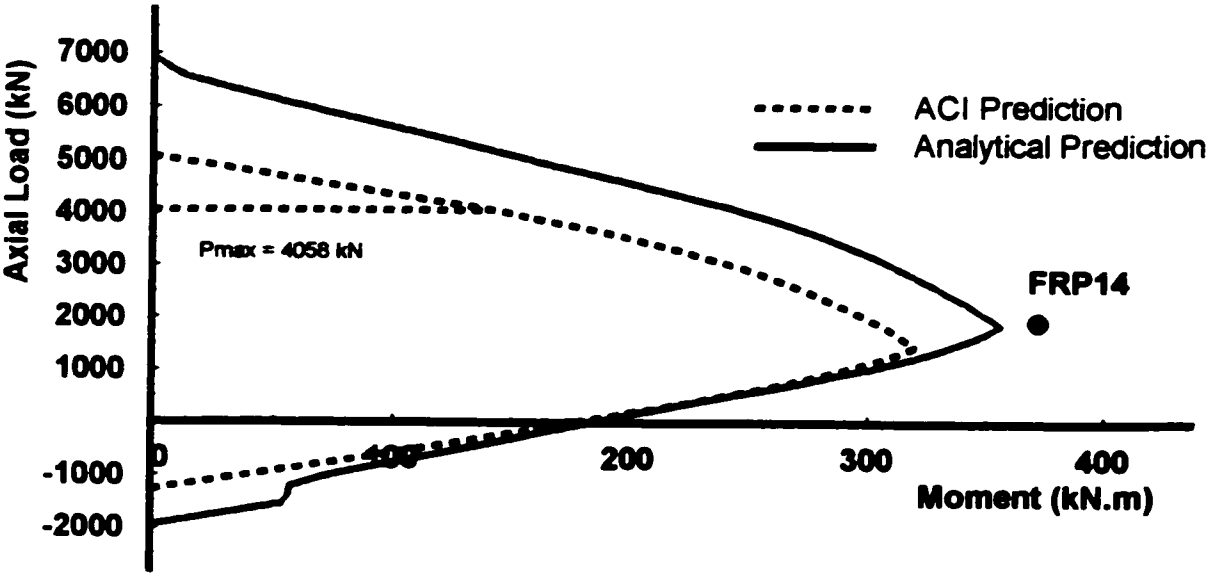

Figure 7-13: Continued

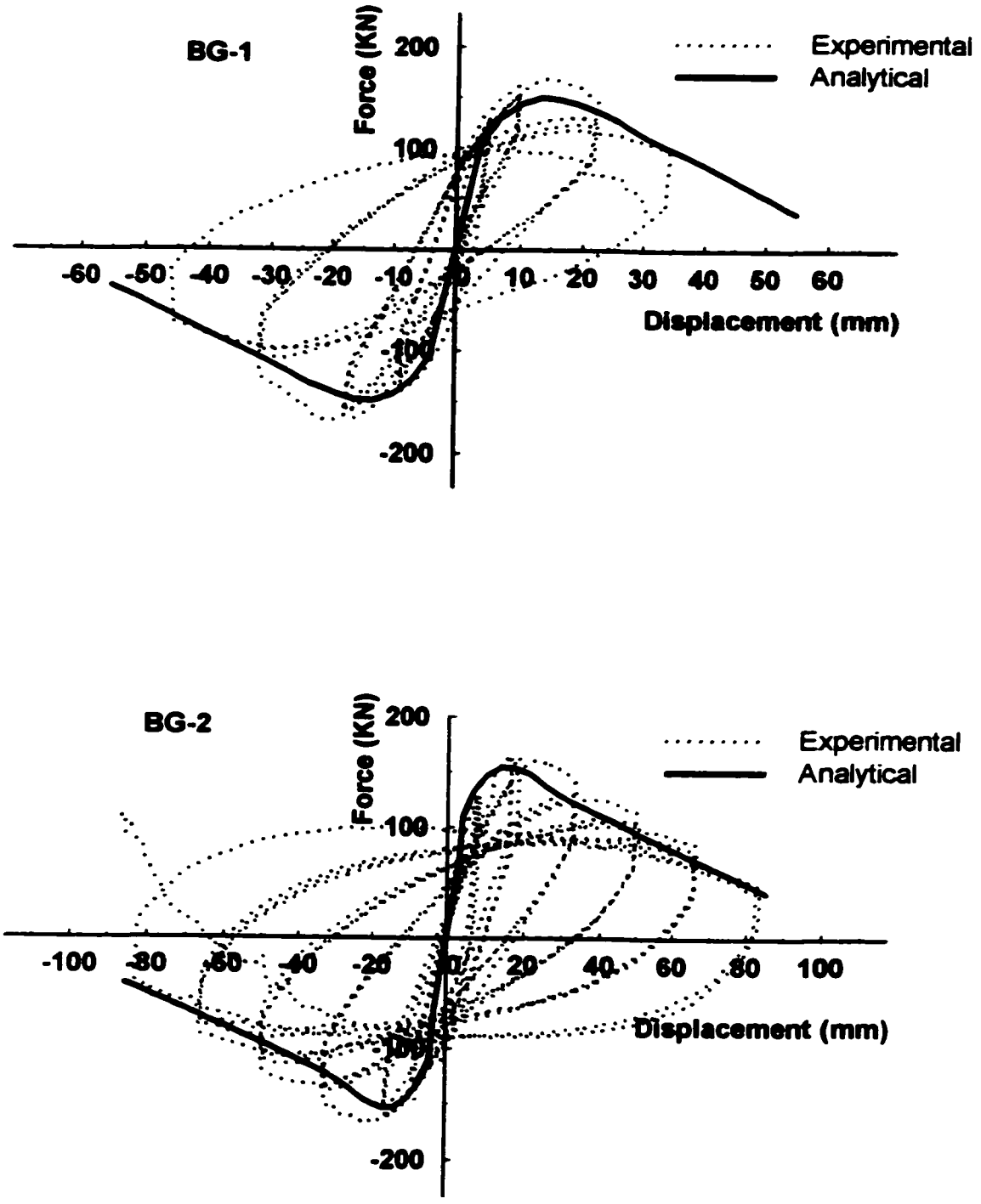

Figure 7-14: Comparisons of predicted force-displacement curves with experimental results

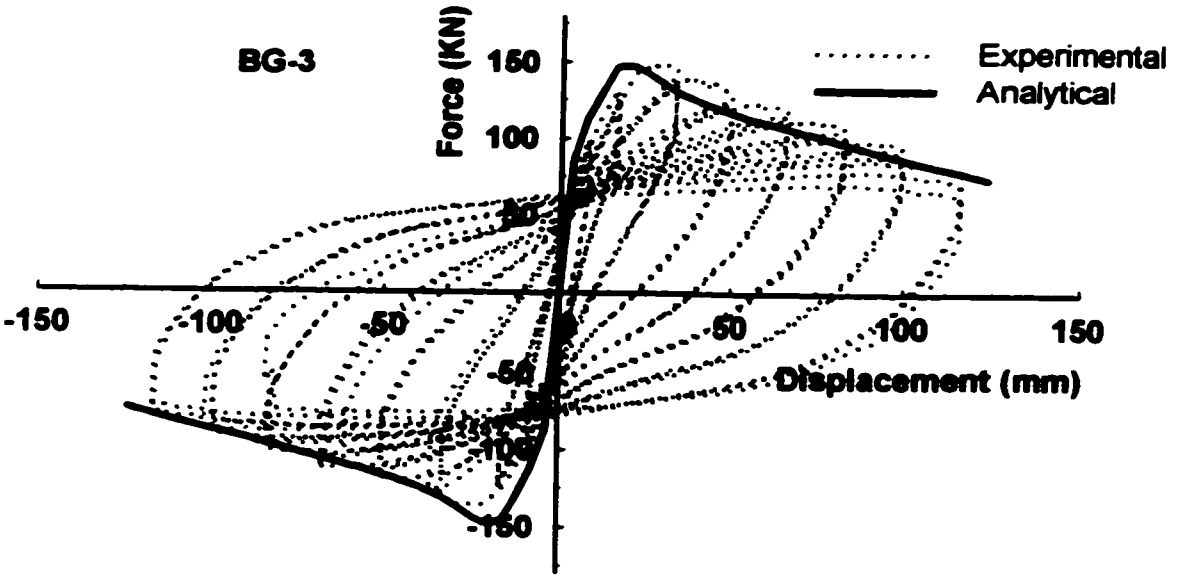

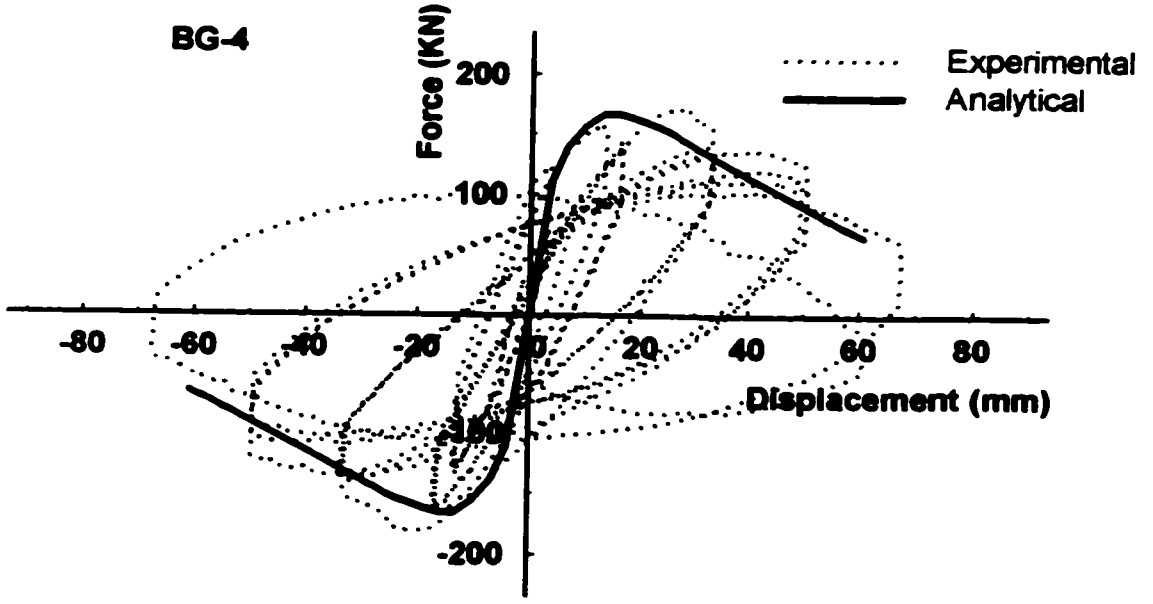

Figure 7-14: Continued

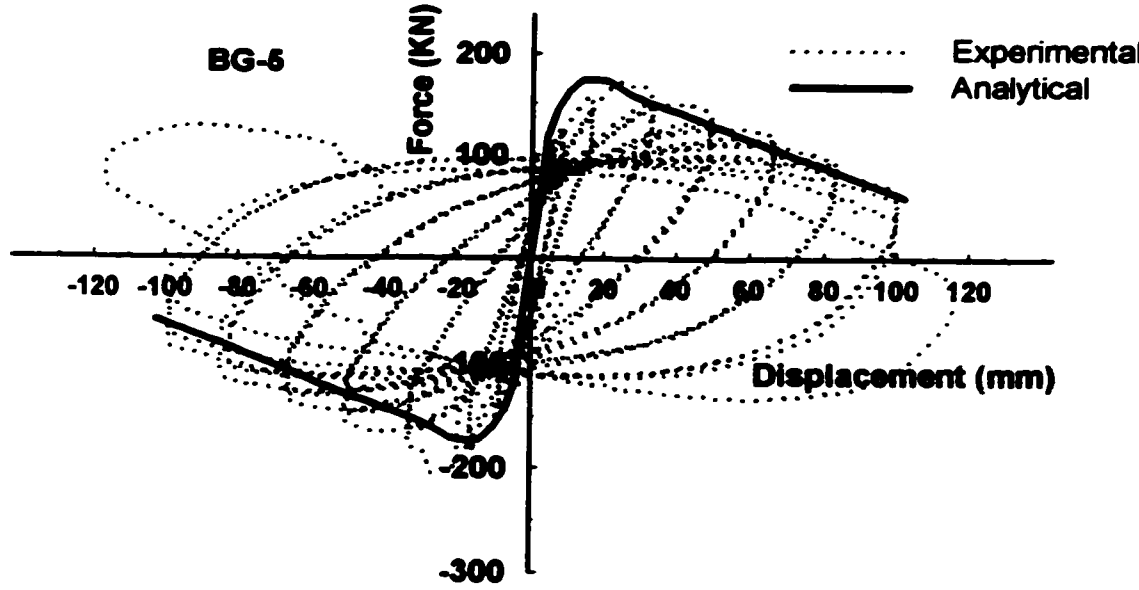

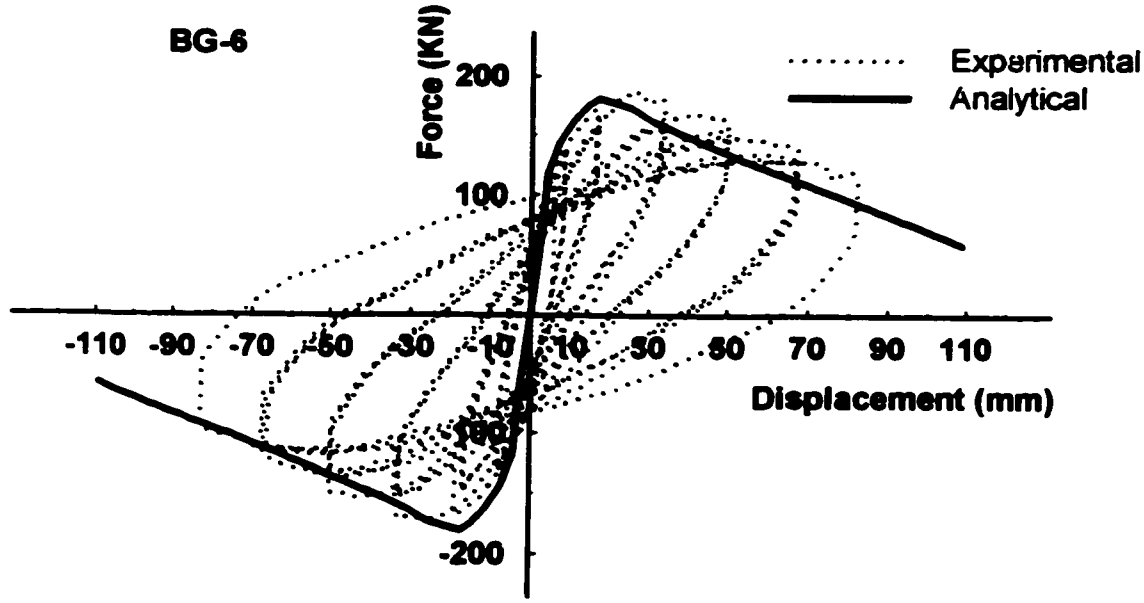

Figure 7-14: Continued

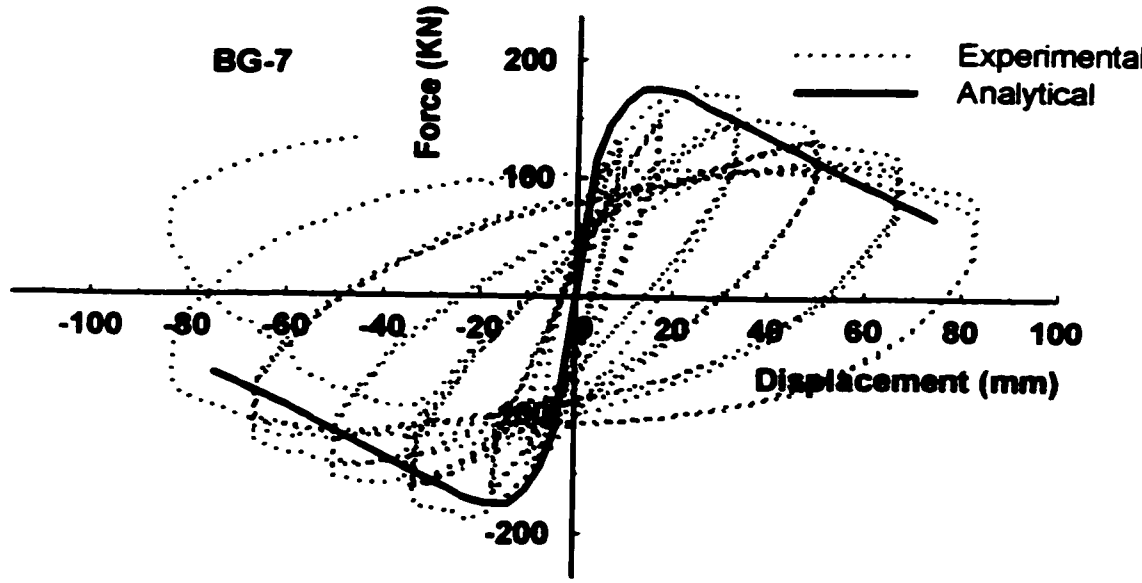

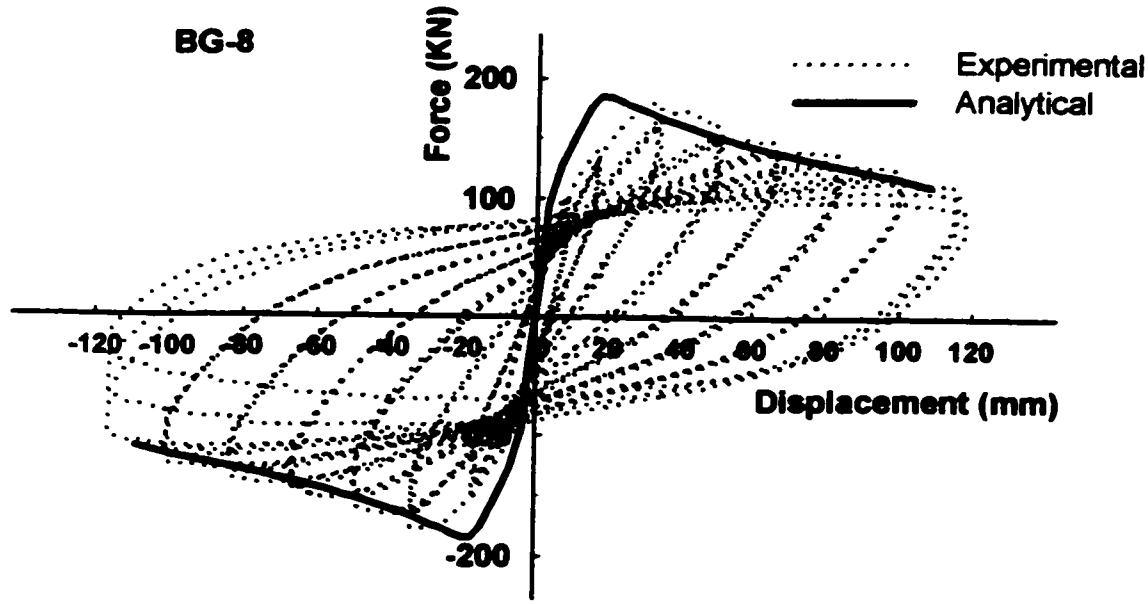

Figure 7-14: Continued

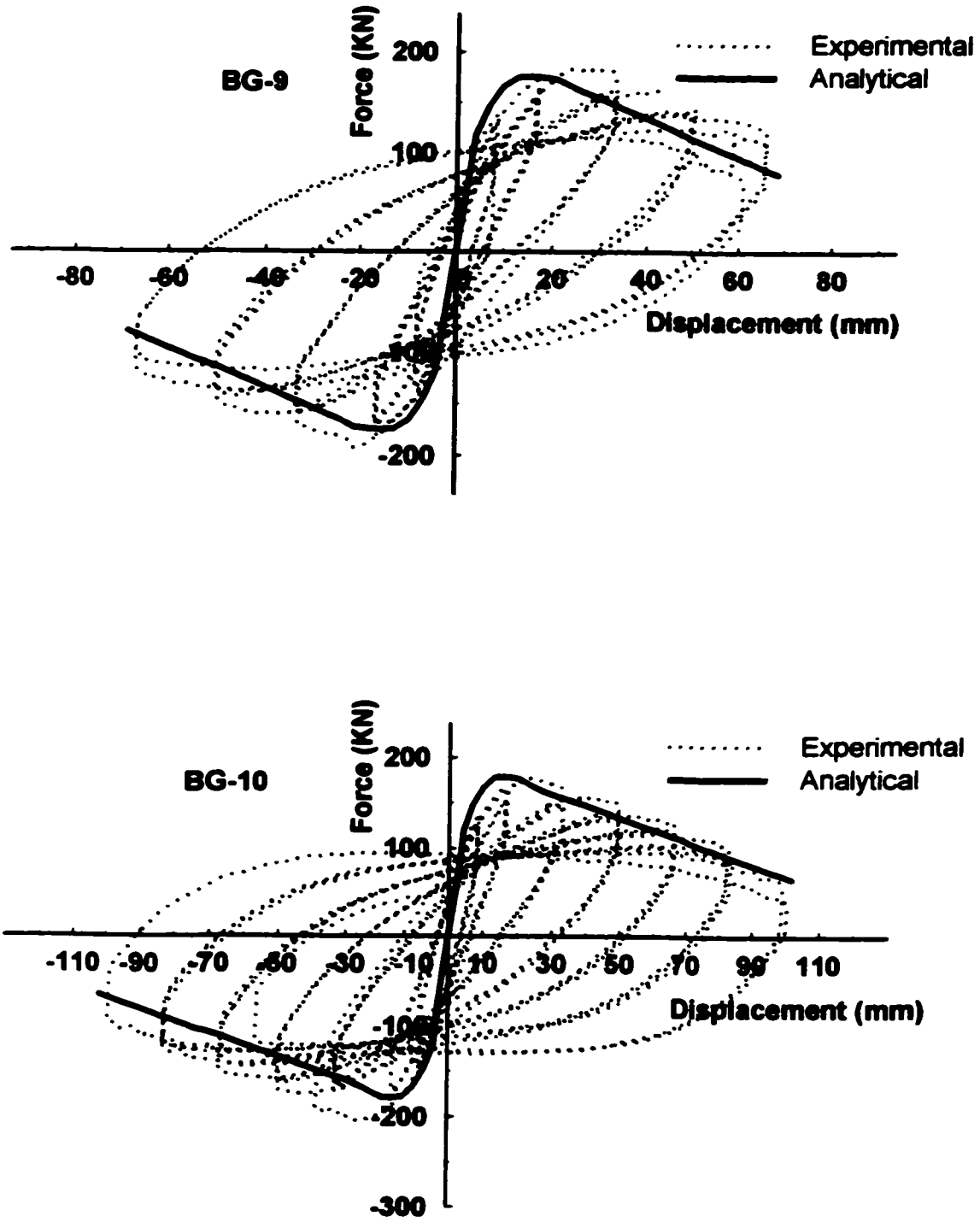

Figure 7-14: Continued

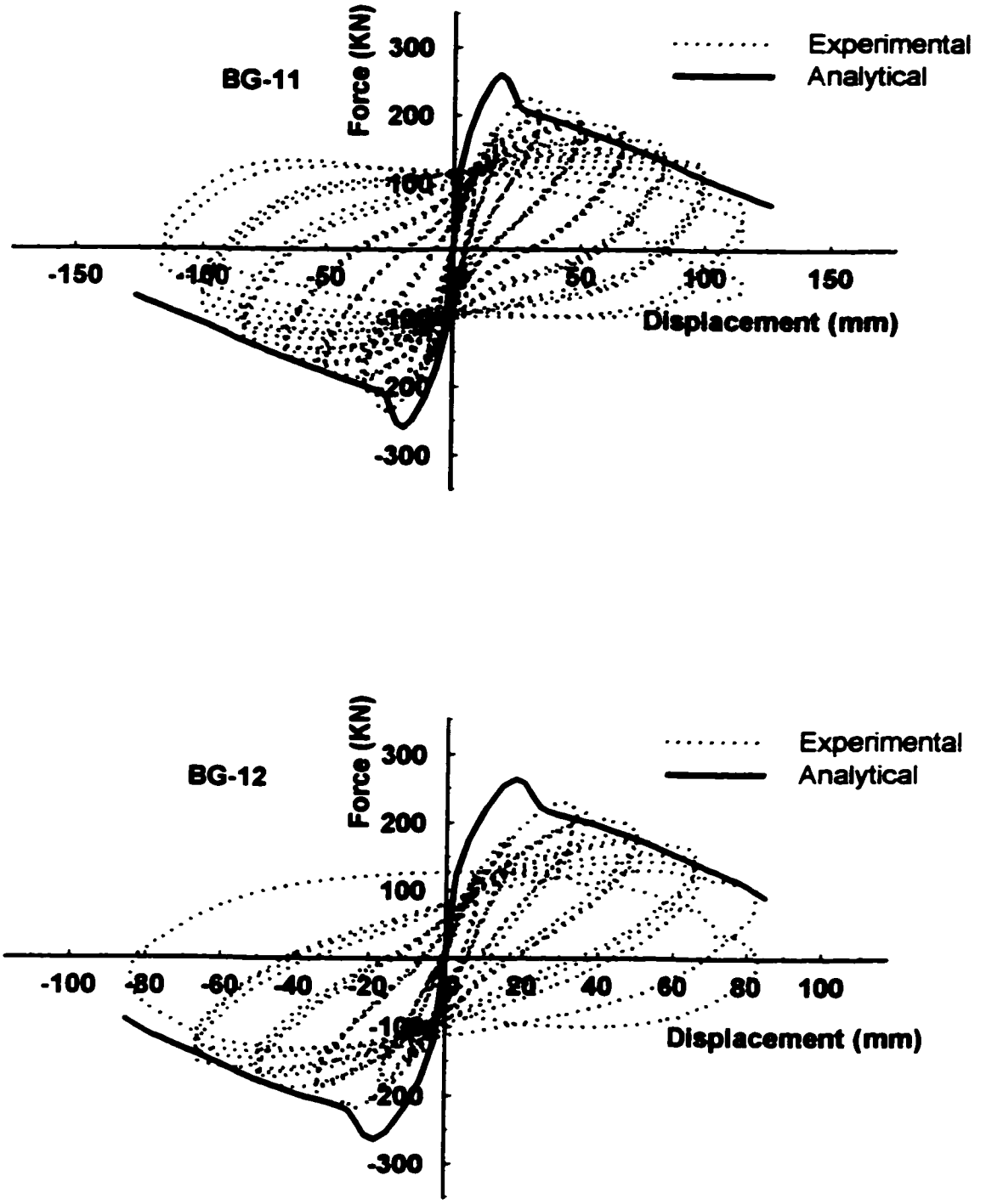

Figure 7-14: Continued

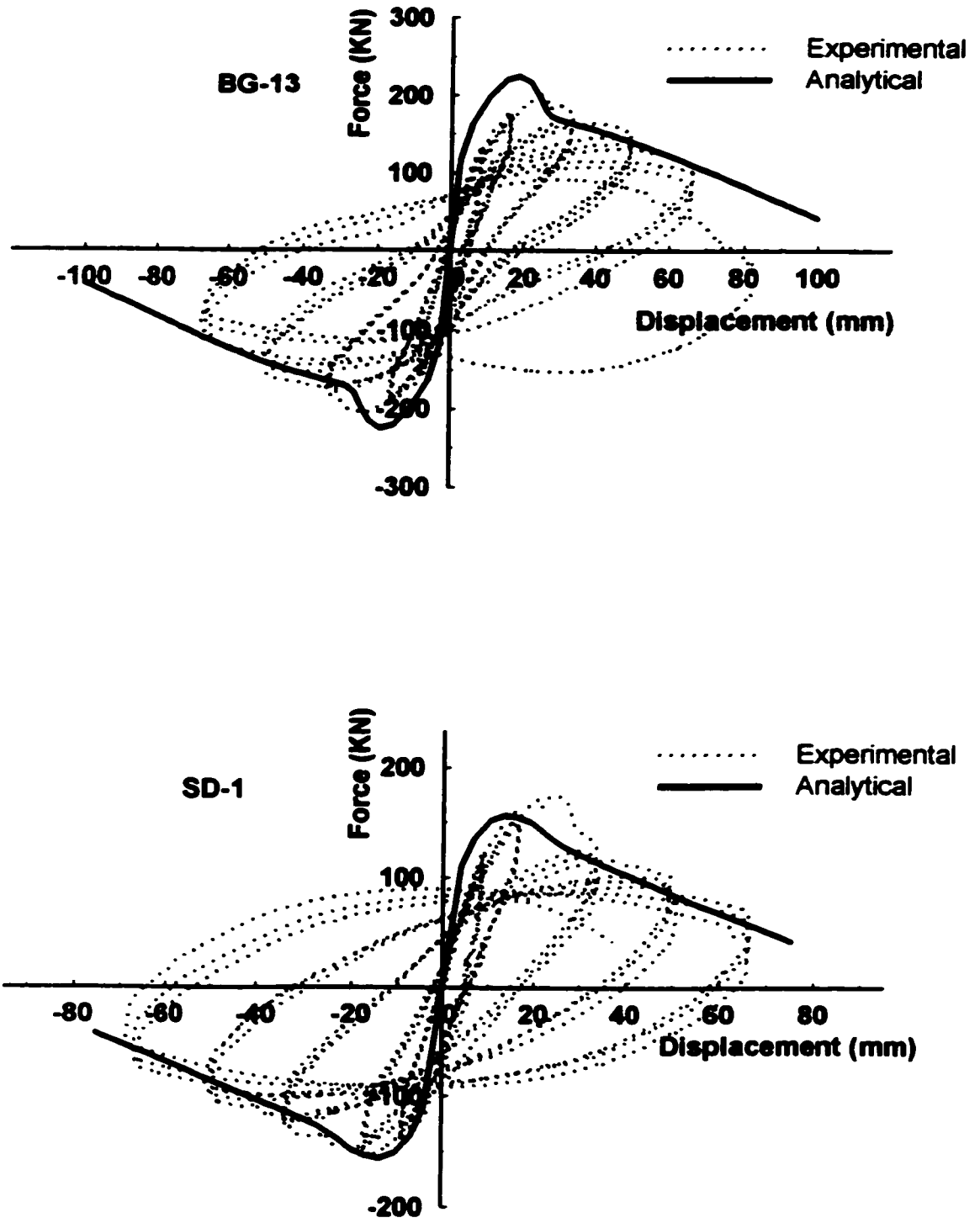

Figure 7-14: Continued

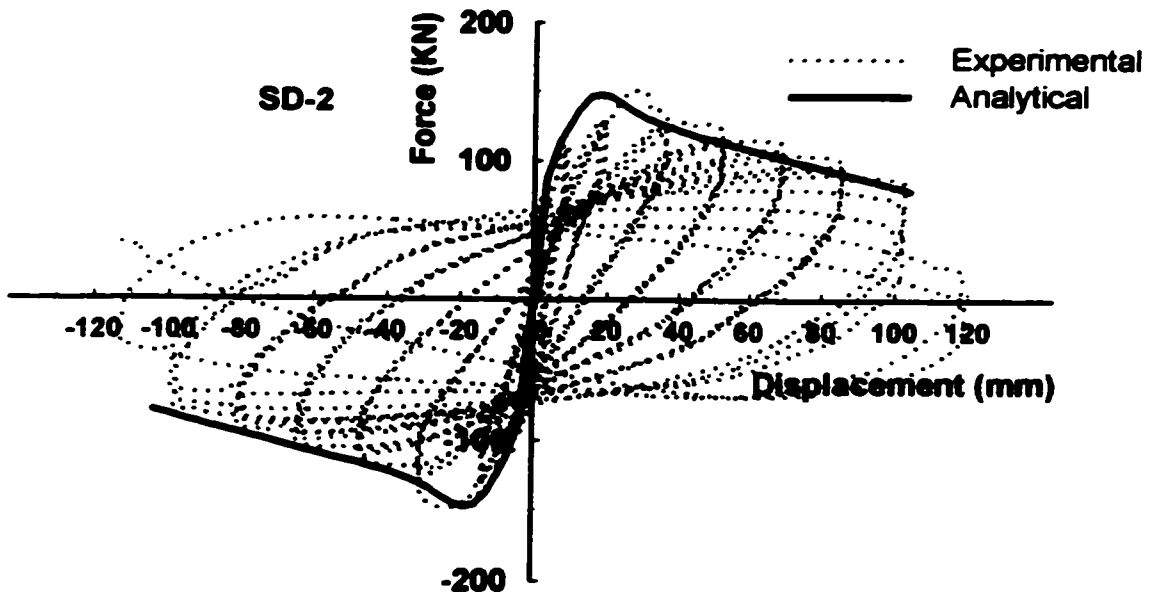

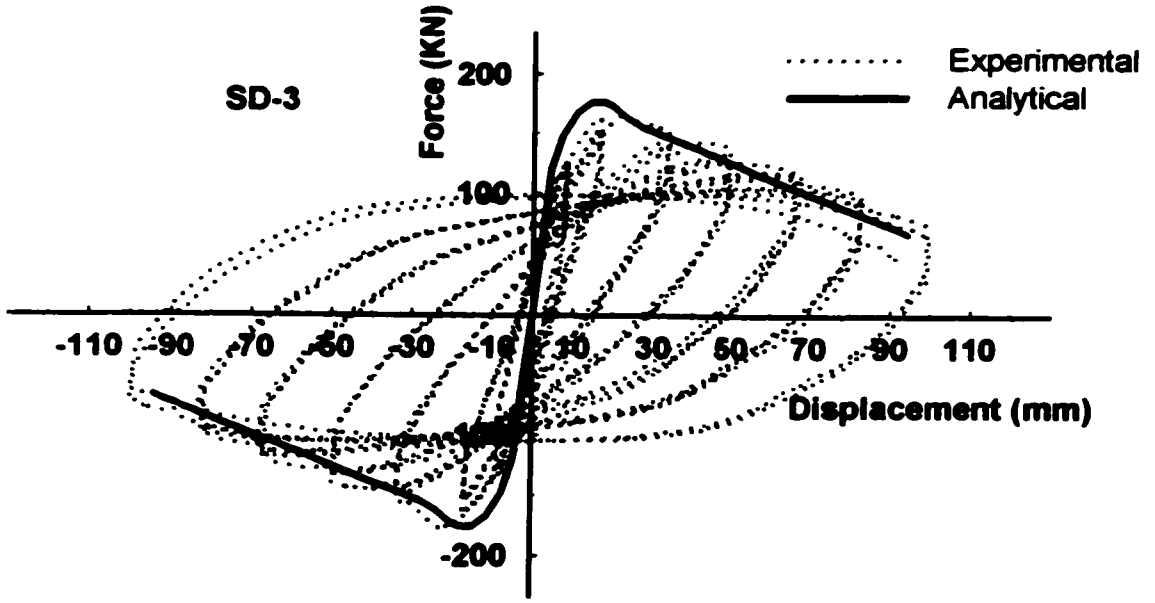

Figure 7-14: Continued

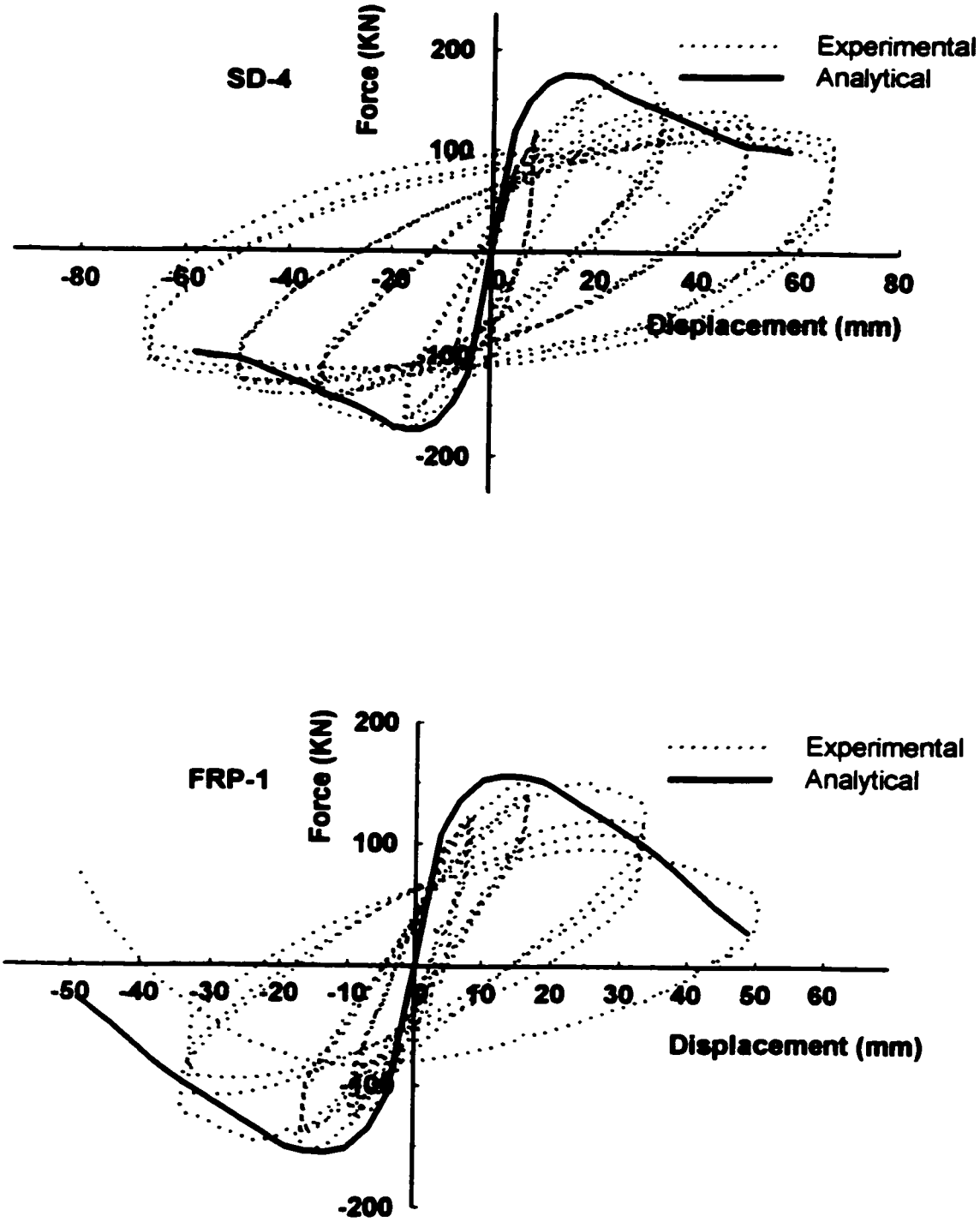

Figure 7-14: Continued

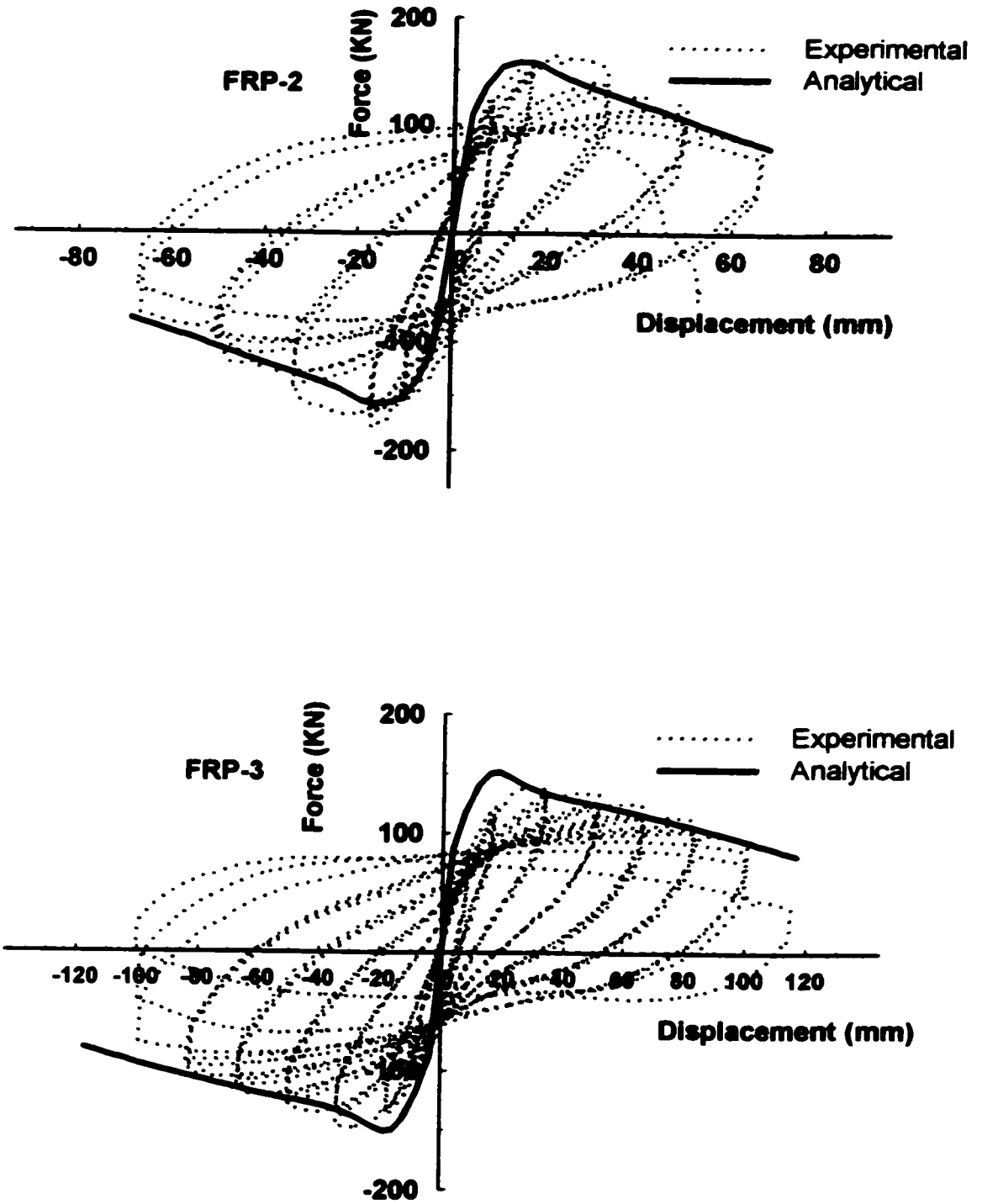

Figure 7-14: Continued

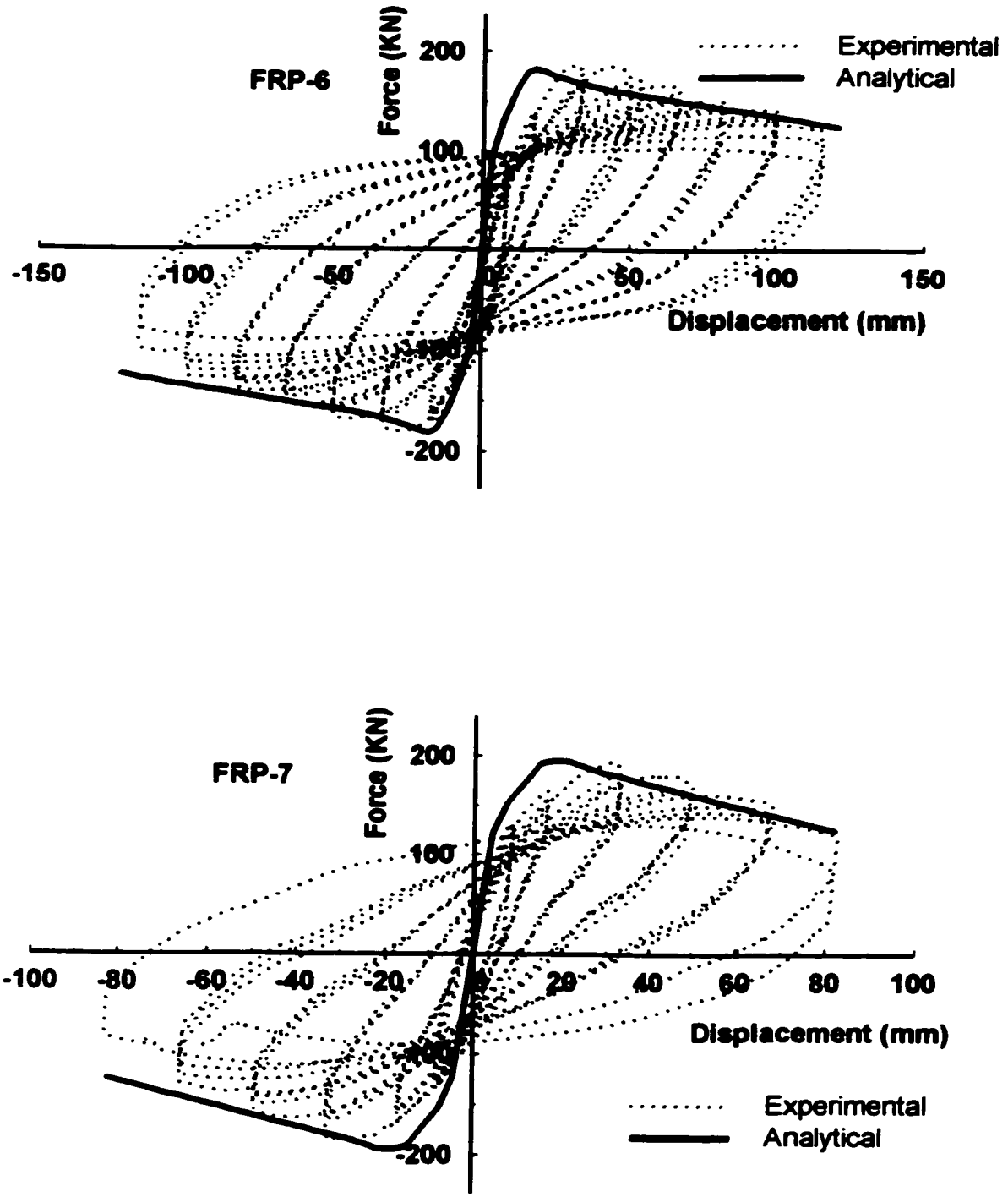

Figure 7-14: Continued

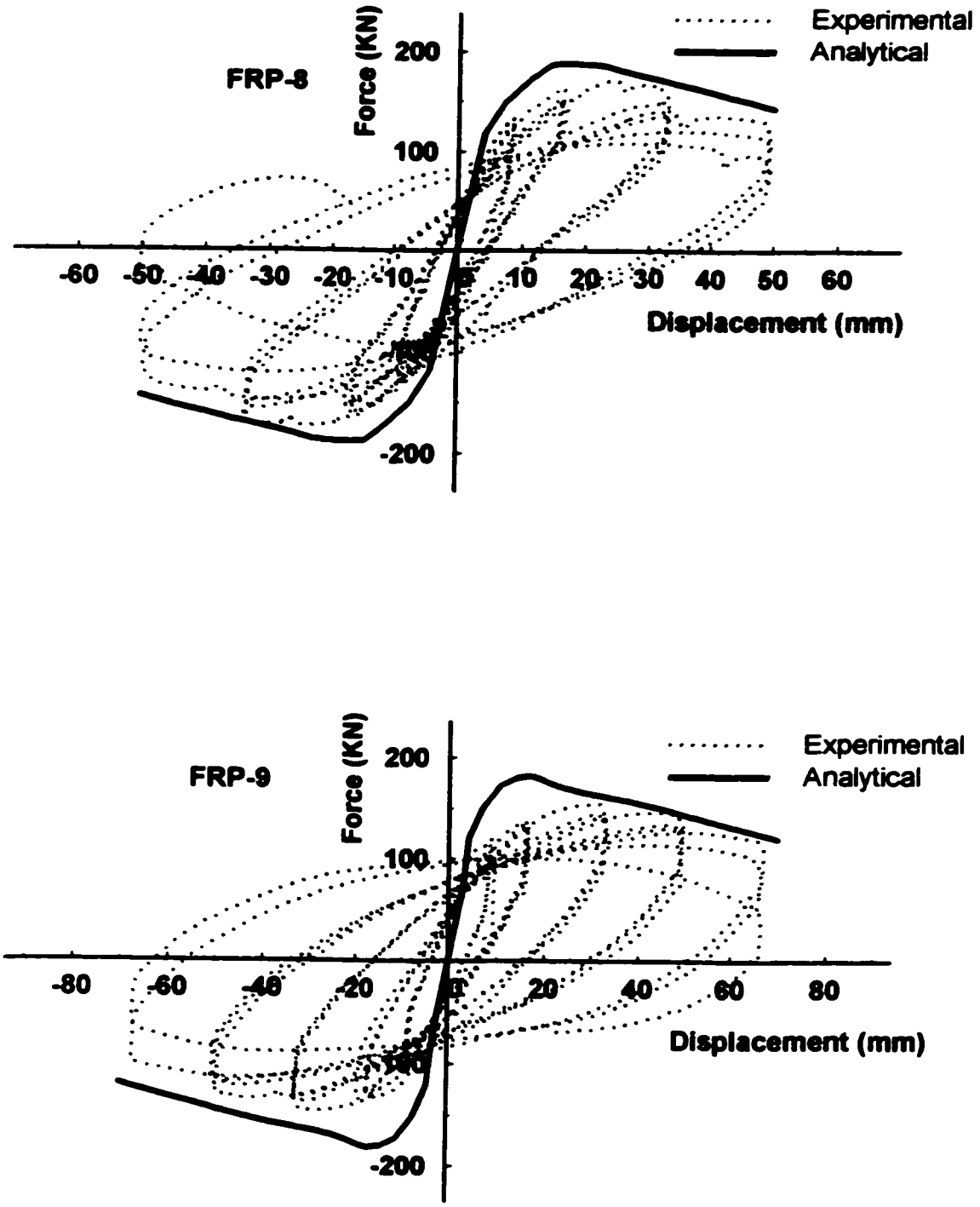

Figure 7-14: Continued

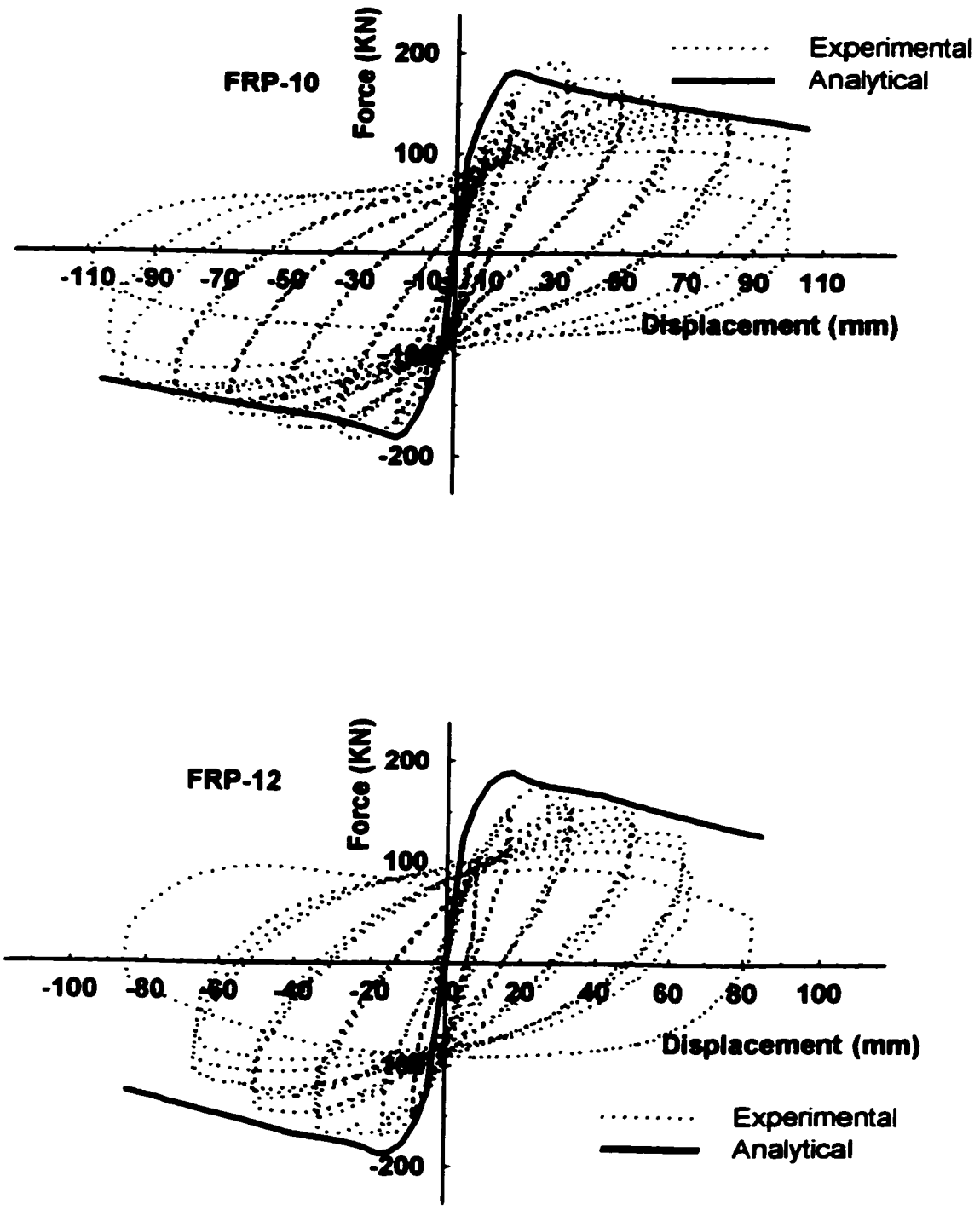

Figure 7-14: Continued

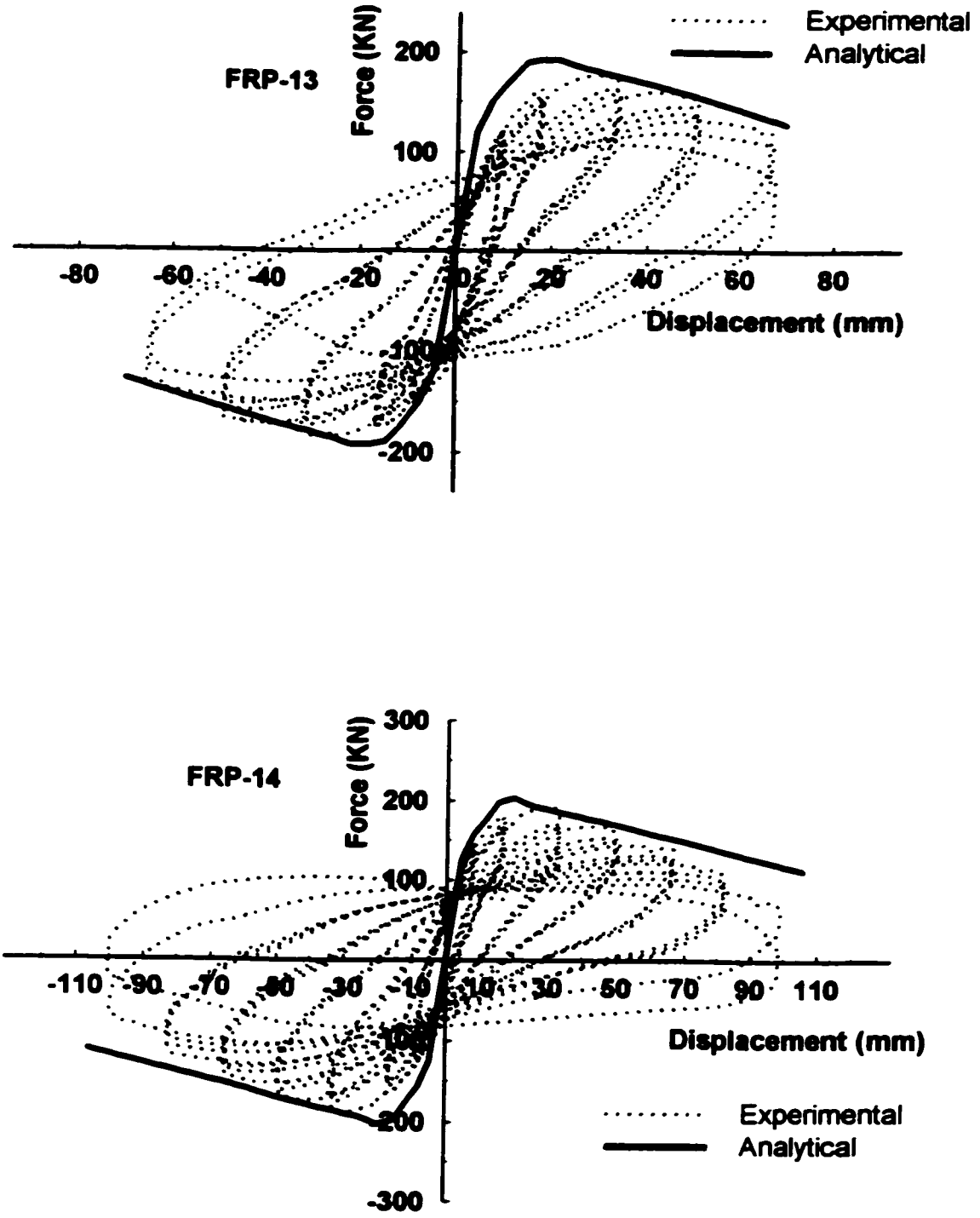

Figure 7-14: Continued

Chapter 8

BUCKLING OF LONGITUDINAL REINFORCEMENT IN CONCRETE COLUMNS

8.1 Introduction

Tests of reinforced concrete columns under concentric loading show spalling of cover concrete at longitudinal strain values ranging approximately between 0.003 and 0.004 (Park and Pauley 1975, Bertero 1979, Sheikh and Uzumeri 1980), though smaller strain values were also recorded in high-strength concrete columns (Razvi and Saatcioglu 1996). Beyond the spalling of cover concrete, the stability of longitudinal reinforcement is maintained by transverse reinforcement. The transverse reinforcement may develop high tensile strains due to the lateral pressure exerted by the laterally expanding core concrete and instability of the longitudinal reinforcement. The instability of longitudinal bars within plastic hinge regions of columns has been considered by some researchers in the past, though the complexity of the problem continue to provide challenges in providing proper analytical solutions to the problem. This complexity may be attributed partly to the peculiarities of the buckling phenomenon in steel and associated ambiguities related to lateral restraints against buckling, and partly to the peculiarities of the stress-strain relationship of steel in terms of yielding and subsequent strain hardening. The lack of experimental data in the field was another factor that slowed the progress in research related to bar buckling.

The stress-strain relationship of column reinforcement in compression does not necessary follow the behavior in tension (Monti and Nuti 1993, Mau and El-Mabsout 1989). The difference in behavior is triggered by potential instability of steel in compression, which is dependent on the effective length of reinforcement in concrete between lateral supports. In reinforced concrete columns, the lateral supports to longitudinal bars are provided by transverse steel. While the transverse steel remains elastic in most applications, it may experience inelasticity in certain locations. Inelasticity in transverse reinforcement changes

the support conditions significantly. This behavior has not been modeled accurately in the past, and therefore, has been adopted as one of the objectives of the current research program. As a result, an analytical procedure has been developed to incorporate bar buckling in stress-strain relationship of compression reinforcement. This Chapter provides a summary of the approach followed.

8.2 Behavior of Longitudinal Reinforcement in Concrete under Compression

Cover concrete in reinforced concrete columns often spalls at or shortly after peak load resistance. This leaves the longitudinal reinforcement exposed without the lateral support provided by cover concrete. The core concrete remains essentially intact if it is well confined by transverse reinforcement. The core prevents compression bars from buckling inward, making them prone to buckling outward. Generally, it is assumed that compression reinforcement becomes unstable between two consecutive levels of transverse reinforcement where the longitudinal reinforcement is laterally restrained. However, it has been observed experimentally in well-confined reinforced concrete columns that the buckling of longitudinal bars may occur within a length greater than the spacing between transverse reinforcement. Longitudinal bars tend to exert high enough lateral forces on transverse reinforcement, causing yielding and sometimes fracturing the ties in tension. Clearly, the transverse reinforcement may not remain elastic when the spacing is small enough to prevent bar buckling between the two consecutive column ties. The strain in transverse reinforcement is proportional to the lateral expansion of core concrete and the deflection of compression bars to satisfy compatibility. Thus, the buckling phenomenon is also affected, among other parameters, by the lateral expansion of column concrete and stiffness of lateral reinforcement. The stiffness of transverse reinforcement has to be computed properly with due considerations given to potential yielding and subsequent softening in lateral restraint.

The critical buckling load of a reinforcing bar can be computed through Euler's theory for slender beam-columns. Euler's theory is only applicable to members in the elastic range of deformations. The theory is widely discussed in many textbooks. Typical intermediate and short prismatic columns experience yielding in compression prior to the onset of instability.

Longitudinal reinforcement in concrete columns falls into this category. Hence, the theory of inelastic buckling is needed to calculate the critical load of a longitudinal bar in a reinforced concrete column.

It has been observed experimentally that the instability of longitudinal compression bars in reinforced concrete columns occurs in plastic hinge regions, while elsewhere in the column they maintain their stability. The plastic hinge length is approximately equal to the column cross-sectional dimension (h). Column ties in this region act as intermediate lateral restraints against buckling. Therefore, a longitudinal bar can be modeled as a beam-column member fixed at both ends while being restrained by intermediate lateral supports. The bar is subjected to axial compression and lateral concrete pressure.

The steel bar can be assumed to have perfectly circular shape with diameter d_b. Hence, its moment of inertia can be defined as shown below.

$$I_b = \frac{\pi d_b^4}{64} \tag{8.1}$$

Furthermore, the deflection of a prismatic bar can conveniently be expressed by a trigonometric function. Since the assumed beam-column member is fixed at both ends, the shape of the deflection curve is best approximated by the following trigonometric function,

$$y = \frac{a_m}{2}\left(1 - \cos\frac{2\pi x}{S}\right) \tag{8.2}$$

where, a_m is the maximum deflection of the bar, considered to occur in the middle of its unsupported length S (also referred as the vertical spacing of transverse reinforcement), and x is distance measured from one of the fixed ends (Fig. 8.1). This expression satisfies the geometric boundary conditions of zero deflection and zero slopes at the ends of the bar, and the natural boundary conditions of non-zero moments at the ends of the bar.

The buckling load may be computed by using different approaches. Usually the behavior of axially loaded bars is investigated by formulating the governing differential equation and obtaining the exact solution. While it is relatively straight forward to express the critical load

for an elastic bar buckling in the first mode, by means of Euler's theory, an energy approach may be more appropriate for bar buckling in higher modes due to the change in lateral stiffness of the supporting ties. For instability in higher modes, an energy approach is proposed here for the computation of the critical load. This permits a systematic consideration of the variation in stiffness of intermediate supports during different stages of inelastic loading.

8.3 Energy Expressions

The concept of strain energy is of fundamental importance in applied mechanics. The principles of strain energy are widely used in determining the response of structures to both static and dynamic loads. Total energy of the complete system is required to determine the buckling load of a longitudinal bar in concrete. This includes the internal work, which is stored in the system in the form of strain energy, the external work caused by applied axial and lateral loads, and the elastic energy of the supporting spring system. These concepts are discussed separately in the following sections.

8.3.1 Bending

The problem of determining the critical load of a typical prismatic column may be solved by considering the equilibrium of column in a slightly deformed form. The equilibrium is established by satisfying the law of conservation of energy. The strain energy (some times referred to as internal work) in bending may be written as;

$$U_s = \int_0^S \frac{E_b I_b}{2} \left(\frac{d^2 y}{x^2} \right)^2 dx \tag{8.3}$$

where, E_b is the material modulus of elasticity of the member. Replacing the displacement term y by its trigonometric function as expressed in Eq. 8.2, and evaluating the above expression, the strain energy due to bending can be written as:

$$U_s = \frac{E_b I_b}{2}\int_0^S \left(\frac{d^2y}{x^2}\right)dx = \frac{E_b I_b}{2}\int_0^S \frac{4a_m^2\pi^4}{S^4}\cos^2\left(\frac{2\pi x}{S}\right) = \frac{a_m^2\pi^4}{S^3}E_b I_b \tag{8.4}$$

8.3.2 Axial Load

The work done by an external axial load consists of the negative product of the axial load and the vertical distance that the load moves as the member bends. If the column is considered axially rigid, the axial shortening can be determined as the difference between the length of the deflected curve and the length of chord AB between the ends, as illustrated in Fig. 8.2. The difference between the length of an element *ds* of the curve and the corresponding element *dx* of the chord can be expressed as shown below:

$$ds - dx = \sqrt{dx^2 + dy^2} - dx \tag{8.5}$$

Using the power series theorem, the above expression can be written as

$$ds - dx = dx\left[1 + \frac{1}{2}\left(\frac{dy}{dx}\right)^2 - \frac{1}{4}\left(\frac{dy}{dx}\right)^4 + \cdots\right] - dx \tag{8.6}$$

The value of the slope (dy/dx) is expressed in radians and its fourth order is too small to be included in the above equation. Therefore, Eq. 8.6 can be simplified as:

$$ds - dx = \frac{1}{2}\left(\frac{dy}{dx}\right)^2 dx \tag{8.7}$$

Thus, the axial shortening Δ_s of the column due to bending is the integration of $(ds - dx)$ throughout the entire column height.

$$\Delta_s = \frac{1}{2}\int_0^S \left(\frac{dy}{dx}\right)^2 dx \tag{8.9}$$

The potential energy is the work done by the axial force P due to the displacement of end B. This is illustrated below.

$$U_p = -\int_0^S \frac{P}{2}\left(\frac{dy}{dx}\right)^2 dx \tag{8.10}$$

The axial load P does not vary along the length. Substituting deformation expression, the above equation can be rewritten as:

$$U_p = -\frac{P}{2}\int_0^S \left(\frac{dy}{dx}\right)^2 dx = -\frac{P}{2}\int_0^S \frac{a_m^2\pi^2}{S^2}\sin^2\left(\frac{2\pi x}{S}\right)dx = -\frac{a_m^2\pi^2}{4S}P \tag{8.11}$$

8.3.3 Uniformly Distributed Load

In addition to axial force, longitudinal reinforcement in columns is also subjected to lateral pressure caused by the expansion of core concrete. Hence, a compression bar can be modeled as a beam-column subjected to uniformly distributed load W along its entire length. It should be noted that the contribution of the distributed load to instability of reinforcing bars in concrete is very small. The lateral pressure of concrete initiates the bending of longitudinal reinforcement and prevents it from buckling inward (towards the core concrete). The potential energy of laterally distributed load is defined as follows:

$$U_w = -\int_0^S Wy dx \tag{8.12}$$

Assuming that the distributed load is constant over the column length, and replacing the displacement term y by its trigonometric function, the above equation can be rewritten as;

$$U_w = -W\int_0^S y dx = -W\int_0^S \frac{a_m}{2}\left(1-\cos\frac{2\pi x}{S}\right)dx = \frac{a_m S}{2}W \tag{8.13}$$

8.3.4 Elastic Support System

Longitudinal reinforcement in concrete columns is supported by lateral ties. The ties can be modeled as elastic springs, proving supports to the longitudinal bar which is modeled as a beam-column. These elastic supports are characterized by their variable bending and axial

stiffnesses. The ties can undergo plastic behavior beyond their yield points. Therefore, it is essential to properly model the ties under axial tension as springs with different linear stiffnesses at different deformation stages. This can be done by establishing their load-deformation characteristics. In addition, the perimeter bars have variable bending stiffness. Total potential energy U_e of a typical elastic system can then be expressed as:

$$U_e = \int (k_{st} + b_{mi}) y dy \tag{8.14}$$

where, k_{st} and b_{mi} are the axial and bending stiffnesses of transverse reinforcement, respectively, at a given displacement level of δ_i.

8.3.5 Total Energy

Total energy U in the beam-column element modeled is the summation of all the work done by internal and external forces:

$$U = \frac{a_m^2 \pi^4}{S^3} E_b I_b - \frac{a_m^2 \pi^2}{4S} P - \frac{a_m S}{2} W + \int (k_{st} + b_{mi}) y dy \tag{8.15}$$

The deflected shape assumes an equilibrium configuration if the total energy has a stationary value. In this case, U is a function of the variable a_m. The partial derivative of U with respect to a_m must therefore vanish for the energy to have a stationary value. In a beam-column, bending and axial compression usually proceed simultaneously. However, bending deformations can be assumed to be independent of axial deformations as long as the deformations remain small.

8.4 Buckling Modes of Longitudinal Bars in Concrete Columns

Transverse reinforcements in columns provide concrete confinement, shear resistance, and stability of longitudinal reinforcement. Depending on the vertical spacing and rigidity of these transverse reinforcements, two modes of buckling are likely to occur; i) buckling

between two consecutive layers of transverse reinforcement, or ii) buckling over a longer segment. This is illustrated in Fig. 8.3. In the latter case, the transverse steel yields. It may develop high enough strains to enter into the strain hardening range. It may even fracture in tension. In the former mode, the bar buckles between the ties, while the ties remain elastic and continue providing sufficient lateral restrain to maintain the unsupported length at tie spacing. The vertical spacing required to avoid the first mode of buckling depends on the level of strain and associated modulus of elasticity of the longitudinal reinforcement. A common suggestion to avoid this kind of bar buckling (first mode) is to reduce tie spacing to approximately six times the longitudinal bar diameter.

When inelasticity is experienced in transverse reinforcement, second, third, or higher modes of buckling may develop. Three potential modes are considered in this research program, because it was observed during laboratory experiments that the plastic hinge length is limited to the cross sectional width (h), within which no more than four layers of transverse reinforcement are likely to be used. If the first and second modes of buckling are prevented by close spacing of ties, as in the case of h/4 spacing, buckling occurs over a length equal to three times the spacing. The buckling mode depends on the vertical spacing and stiffness of transversal reinforcement, in addition to the material properties of longitudinal bars. Therefore, the critical load is the lowest calculated among all possible modes. For small diameter ties, the third buckling mode is likely to govern, whereas for very stiff ties, the first mode may provide the lowest buckling load.

8.5 Computation of Buckling Load

8.5.1 First Mode Shape

In the case of large vertical spacing or very stiff lateral reinforcement, longitudinal bars may buckle between the two consecutive tie layers (Fig. 8.4). Hence, there is no intermediate support and the unsupported length of the bar (beam-column) is equal to the vertical spacing of ties S. The maximum deflection y_{m1} is in the middle of the beam-column. Thus, the expression for the total energy can be written as follows;

$$U = \frac{y_{m1}^2 \pi^4}{S^3} E_b I_b - \frac{y_{m1}^2 \pi^2}{4S} P - \frac{y_{m1} S}{2} W \tag{8.16}$$

where, y_{m1} is the mid-height deflection of the bar between the end supports. For the system to be in equilibrium, the derivative of U with respect of y_{m1} must vanish. Thus;

$$\frac{\partial U}{\partial y_{m1}} = \frac{2 y_{m1} \pi^4}{S^3} E_b I_b - \frac{y_{m1} \pi^2}{2S} P - \frac{WS}{2} = 0 \tag{8.17}$$

From the above equation, the maximum deflection can be determined as follows:

$$y_{m1} = \frac{WS}{\frac{4\pi^4}{S^3} E_b I_b - \frac{\pi^2}{S} P} \tag{8.18}$$

When buckling occurs, the mid-deflection of the beam column approaches infinity. That is, the denominator approaches zero since the numerator is almost constant and never vanishes. Therefore, the critical buckling load is expressed as;

$$P_{cr1} = 4 E_b I_b \frac{\pi^2}{S^2} \tag{8.19}$$

Where, E_b and I_b are instantaneous modulus of elasticity and moment of inertia of longitudinal bar, respectively. The above expression is referred to as the Euler's buckling load when the column axial stress remains elastic.

8.5.2 Second Mode Shape

When columns are confined with closer vertical spacing of ties, the longitudinal reinforcement may buckle in the second mode, involving a single layer of transverse reinforcement between the fixed ends. Hence, the critical load depends highly on the axial and bending stiffnesses of transverse reinforcement. The arrangement of the crossties and the reinforcement configuration determine the overall stiffness of transverse reinforcement. During the present experimental investigation, only 4-cell and 9-cell grids were used to

confine concrete columns. Therefore, the buckling load of longitudinal reinforcement is calculated based on these two configurations only, though the same analogy can be easily applied to other reinforcement arrangements. Since the buckling phenomenon occurs in inelastic stages of longitudinal and transverse reinforcement, a step-by-step solution is proposed. This method is suitable for computer solution.

4-Cell Grids

During laboratory experiments, it was observed that buckling was limited to the bars at the ends of column section (bars positioned on a line perpendicular to the applied load near the extreme compression fiber. This is illustrated in Fig. 8.4. Hence, the 4-cell grid reinforcement arrangement can be modeled as shown in Fig. 8.5. Referring to the aforementioned figure, the joint forces in the y direction are related to lateral deformations as follows;

$$\begin{Bmatrix} V_{c1} \\ V_m \\ V_{c2} \end{Bmatrix} = \begin{bmatrix} b_m + k_{c1} & -b_m & 0 \\ -b_m & 2b_m + 2k_m & -b_m \\ 0 & -b_m & b_m + k_{c2} \end{bmatrix} \begin{Bmatrix} y_{c1} \\ y_m \\ y_{c2} \end{Bmatrix} \tag{8.20}$$

where, V_{c1}, V_{c2}, and V_m are forces at corner joints *c1*, *c2* and the middle joint m, respectively. b_m is the bending stiffness of ties, k_{c1}, k_{c2}, and k_m are the axial stiffnesses of perimeter bars and the middle cross bar, respectively. y_{c1}, y_{c2}, and y_m are displacements at corner joints c1, c2 and middle joint m, respectively.

Since $y_{c1} = y_{c2} = y_c$, $V_{c1} = V_{c2} = V_c$, and $k_c = k_{c1} = k_{c2}$, then the above matrix can be reduced to:

$$\begin{Bmatrix} V_c \\ V_m \end{Bmatrix} = \begin{bmatrix} b_m + k_c & -b_m \\ -2b_m & 2(b_m + k_m) \end{bmatrix} \begin{Bmatrix} y_c \\ y_m \end{Bmatrix} \tag{8.21}$$

The energy equations for both corner and middle longitudinal bars are defined as:

$$\begin{cases} U_c = \dfrac{y_c^2\pi^2}{8S^3}E_bI_b - \dfrac{y_c^2\pi^2}{8S}P - y_cSW_c + U_{ec} \\ U_m = \dfrac{y_c^2\pi^2}{8S^3}E_bI_b - \dfrac{y_m^2\pi^2}{8S}P - y_mSW_m + U_{em} \end{cases} \tag{8.22}$$

The subscripts c and m in the above equations refer to corner and middle joints, respectively. Minimizing the energy equations with respect to y_c and y_m leads to;

$$\begin{cases} \dfrac{\partial U_c}{\partial y_c} = \dfrac{y_c\pi^2}{4S^3}E_bI_b - \dfrac{y_c\pi^2}{4S}P - SW_c + \dfrac{\partial U_{ec}}{\partial y_c} = 0 \\ \dfrac{\partial U_m}{\partial y_m} = \dfrac{y_m\pi^2}{4S^3}E_bI_b - \dfrac{y_m^2\pi^2}{4S}P - SW_m + \dfrac{\partial U_{em}}{\partial y_m} = 0 \end{cases} \tag{8.23}$$

Knowing that,

$$\begin{cases} \dfrac{\partial U_{ec}}{\partial y_c} = (b_m + k_c)y_c - b_m y_m = V_c \\ \dfrac{\partial U_{em}}{\partial y_m} = -2b_m y_c + 2(b_m + k_m)y_m = V_m \end{cases} \tag{8.24}$$

Then equation (8.24) can be rewritten as:

$$\begin{cases} \dfrac{\partial U_c}{\partial y_c} = \dfrac{y_c\pi^2}{4S^3}E_bI_b - \dfrac{y_c\pi^2}{4S}P - SW_c + (b_m + k_c)y_c - b_m y_m = 0 \\ \dfrac{\partial U_m}{\partial y_m} = \dfrac{y_m\pi^2}{4S^3}E_bI_b - \dfrac{y_m\pi^2}{4S}P - SW_m - 2b_m y_c + 2(b_m + k_m)y_m = 0 \end{cases} \tag{8.25}$$

However, the axial and bending stiffnesses of transverse and lateral reinforcement change in every step of calculation in sectional analysis. Hence, the above equations can be written as follows;

$$\begin{cases} \dfrac{\partial U_c}{\partial y_c} = \dfrac{y_{cn}\pi^2}{4S^3}E_bI_b - \dfrac{y_{cn}\pi^2}{4S}P - SW_c + \sum_{i=1}^{n}(b_{mi} + k_{ci})(y_{ci} - y_{ci-1}) - \sum_{i=1}^{n} b_{mi}(y_{mi} - y_{mi-1}) = 0 \\ \dfrac{\partial U_m}{\partial y_m} = \dfrac{y_{mn}\pi^2}{4S^3}E_bI_b - \dfrac{y_{mn}\pi^2}{4S}P - SW_m - 2\sum_{i=1}^{n} b_{mi}(y_{ci} - y_{ci-1}) + 2\sum_{i=1}^{n}(b_{mi} + k_{mi})(y_{mi} - y_{mi-1}) = 0 \end{cases} \tag{8.26}$$

where, the terms *i* and *n* define the *ith* and the last step in calculations, respectively. The only unknowns in each step of calculation are y_{cn} and y_{mn}. Rearranging the above system of equations in a matrix form yields;

$$\begin{bmatrix} \frac{\pi^2}{4S^3}E_bI_b - \frac{\pi^2}{4S}P + (b_{mn} + k_{mn}) & -b_{mn} \\ -2b_{mn} & \frac{\pi^2}{4S^3}E_bI_b - \frac{\pi^2}{4S}P + 2(b_{mn} + k_{mn}) \end{bmatrix} \begin{Bmatrix} y_{cn} \\ y_{mn} \end{Bmatrix} = \begin{Bmatrix} SW_c + \sum_{i=1}^{n-1} y_{ci}\left[(b_{mi+1} - b_{mi}) + (k_{ci+1} - k_{ci})\right] - \sum_{i=1}^{n-1} y_{mi}\left[b_{mi+1} - b_{mi}\right] \\ SW_m - 2\sum_{i=1}^{n-1} y_{ci}(b_{mi+1} - b_{mi}) + 2\sum_{i=1}^{n-1} y_{mi}\left[(b_{mi+1} - b_{mi}) + (k_{mi+1} - k_{mi})\right] \end{Bmatrix} \quad (8.27)$$

The buckling phenomenon occurs when the deflections y_{cn} and y_{mn} are very large, approaching infinity. Thus, the determinant of the above matrix should be equal to zero. Setting the determinant equal to zero results in a quadratic equation with two solutions for buckling loads. The critical buckling load is the smaller of the two;

$$P_{cr2} = \frac{\pi^2}{S^2}E_bI_b + \frac{2S}{\pi^2}\left(3b_{mn} + 2k_{mn} + k_{cn} \pm \sqrt{(3b_{mn} + 2k_{mn} + k_{cn})^2 - 8(b_mk_c + b_mk_m + k_ck_m)}\right) \quad (8.28)$$

If the transverse reinforcement does not yield, then b_{mn} is very small compared to axial stiffnesses k_{mn} and k_{cn}. Hence b_{mn} can be neglected and the expression for critical loads can be written as follows:

$$\begin{cases} P_{cr2} = \dfrac{\pi^2 E_b I_b}{S^2} + \dfrac{4Sk_{cn}}{\pi^2} \\ P_{cr2} = \dfrac{\pi^2 E_b I_b}{S^2} + \dfrac{8Sk_{mn}}{\pi^2} \end{cases} \quad \text{or} \quad (8.29)$$

If k_{mn} and k_{cn} are equal, then the above equation proves that corner bars are more susceptible to buckling than those in the middle. When the transverse reinforcement yields and develops

high inelastic strains into the strain hardening range, k_{mn} and k_{cn} become small, and almost equal to each other. In this case b_{mn} becomes significant. The buckling load then becomes;

$$P_{cr2} = \frac{\pi^2}{S^2} E_b I_b + \frac{2S}{\pi^2}\left(3b_{mn} + 3k_s - \sqrt{9b_{mn}^2 + k_s^2 + 2b_m k_s}\right) \tag{8.30}$$

9-Cell Grid

The forces resisted by 9-cell grids are modeled as shown in Fig. 8.6. The joint forces resisted by the ties can be related to the lateral joint deformations as follows:

$$\begin{Bmatrix} V_{c1} \\ V_{m1} \\ V_{m2} \\ V_{c2} \end{Bmatrix} = \begin{bmatrix} b_m + k_{c1} & b_m & 0 & 0 \\ b_m & 2b_m + 2k_{m1} & -b_m & 0 \\ 0 & -b_m & 2b_m + 2k_{m2} & -b_m \\ 0 & 0 & -b_m & b_m + k_{c2} \end{bmatrix} \begin{Bmatrix} y_{c1} \\ y_{m1} \\ y_{m2} \\ y_{c2} \end{Bmatrix} \tag{8.31}$$

All terms are self explanatory as illustrated in Fig. 8.6. Let $y_{c1} = y_{c2} = y_c$, $y_{m1} = y_{m2} = y_m$, $V_{c1} = V_{c2} = V_c$, $V_{m1} = V_{m2} = V_m$, $k_c = k_{c1} = k_{c2}$, and $k_{m1} = k_{m2} = k_m$ then the above matrix is reduces to

$$\begin{Bmatrix} V_c \\ V_m \end{Bmatrix} = \begin{bmatrix} b_m + k_c & -b_m \\ -b_m & b_m + 2k_m \end{bmatrix} \begin{Bmatrix} y_c \\ y_m \end{Bmatrix} \tag{8.32}$$

Using the same analogy as above, the solution can be written in a matrix form as follows:

$$\begin{bmatrix} \frac{\pi^2}{4S^3} E_b I_b - \frac{\pi^2}{4S} P + (b_{mn} + k_{mn}) & -b_m \\ -b_m & \frac{\pi^2}{4S^3} E_b I_b - \frac{\pi^2}{4S} P + (b_{mn} + 2k_{mn}) \end{bmatrix} \begin{Bmatrix} y_{cn} \\ y_{mn} \end{Bmatrix} =$$

$$\begin{Bmatrix} SW_c + \sum_{i=1}^{n-1} y_{ci}\left[(b_{mi+1} - b_{mi}) + (k_{ci+1} - k_{ci})\right] - \sum_{i=1}^{n-1} y_{mi}\left[b_{mi+1} - b_{mi}\right] \\ SW_m - \sum_{i=1}^{n-1} y_{ci}(b_{mi+1} - b_{mi}) + \sum_{i=1}^{n-1} y_{mi}\left[(b_{mi+1} - b_{mi}) + 2(k_{mi+1} - k_{mi})\right] \end{Bmatrix} \tag{8.33}$$

The buckling phenomenon occurs when the deflections are very large and approach infinity, that is the determinant of the above matrix becomes zero. The equation obtained by setting

the determinant equal to zero has two solutions, and the critical buckling load is the smaller of the two.

$$P_{cr2} = \frac{\pi^2}{S^2} E_b I_b + \frac{2S}{\pi^2}\left(2b_{mn} + 2k_{mn} + k_{cn} \pm \sqrt{4b_{mn}^2 + (2k_{mn} - k_{cn})^2}\right) \tag{8.34}$$

If b_{mn} is very small compared to axial stiffness k_{mn} and k_{cn}, then it can be neglected and the expression for critical loads can be written as follows:

$$\begin{cases} P_{cr2} = \dfrac{\pi^2 E_b I_b}{S^2} + \dfrac{4Sk_{cn}}{\pi^2} \\ P_{cr2} = \dfrac{\pi^2 E_b I_b}{S^2} + \dfrac{8Sk_{mn}}{\pi^2} \end{cases} \quad \text{or} \tag{8.35}$$

The above expressions are the same as those for 4-cell grids (Eq. 8.29), since increasing the number of cells and hence the crossties affect only the bending stiffness of the transverse reinforcement system.

When the transverse reinforcement is stressed to the strain hardening region, the axial stiffness k_{mn} and k_{cn} are small and almost equal to each other. In this case, b_{mn} becomes significant. The critical buckling load is then expressed as follows;

$$P_{cr2} = \frac{\pi^2}{S^2} E_b I_b + \frac{2S}{\pi^2}\left(2b_{mn} + 3k_s - \sqrt{4b_{mn}^2 + k_s^2}\right) \tag{8.36}$$

8.5.3 Third Mode Shape

During the experimental investigation, it was observed that most columns failed due to the buckling of longitudinal bars in the third mode. Figure 8.7 shows the buckling phenomenon in two columns. In this case, a longitudinal reinforcing steel bar within a plastic hinge of a concrete column can be modeled as a beam-column fixed at both ends and supported by two intermediate elastic supports. The total length of the beam-column model is equal to three times the vertical spacing of the transverse reinforcement (3S). Lateral deflections of the longitudinal bar at support locations are equal to ¾ of its middle deflection.

4-Cell grids

The 4-cell grid reinforcement arrangement can be modeled as shown in Fig. 8.8. Referring to this figure and following the same analogy as above, the derivative of the elastic energy with respect to joint displacement is expressed as;

$$\begin{cases} \dfrac{\partial U_{ec}}{\partial y_c} = \dfrac{9}{8}(b_m + k_c)y_c - \dfrac{9}{16}y_m b_m \\ \dfrac{\partial U_{em}}{\partial y_m} = -\dfrac{9}{8}b_m y_c + \dfrac{9}{4}(b_m + k_m)y_m \end{cases} \tag{8.37}$$

Knowing that two layers of transverse reinforcement are involved in the buckling mode, the total energy equations of the whole system can be easily constructed. Minimizing the energy equations with respect to y_c and y_m results in the following system of equations, expressed in matrix form;

$$\begin{bmatrix} \dfrac{2\pi^4}{27S^3}E_b I_b - \dfrac{\pi^2}{6S}P + \dfrac{9}{8}(b_{mn} + k_{mn}) & -\dfrac{9}{16}b_m \\ -\dfrac{9}{8}b_m & \dfrac{2\pi^4}{27S^3}E_b I_b - \dfrac{\pi^2}{6S}P + \dfrac{9}{4}(b_{mn} + k_{mn}) \end{bmatrix} \begin{Bmatrix} y_{cn} \\ y_{mn} \end{Bmatrix} =$$

$$\begin{Bmatrix} \dfrac{3}{2}SW_c + \dfrac{9}{8}\sum_{i=1}^{n-1} y_{ci}\left[(b_{mi+1} - b_{mi}) + (k_{ci+1} - k_{ci})\right] - \dfrac{9}{16}\sum_{i=1}^{n-1} y_{mi}\left[b_{mi+1} - b_{mi}\right] \\ \dfrac{3}{2}SW_m - \dfrac{9}{4}\sum_{i=1}^{n-1} y_{ci}(b_{mi+1} - b_{mi}) + \dfrac{9}{8}\sum_{i=1}^{n-1} y_{mi}\left[(b_{mi+1} - b_{mi}) + (k_{mi+1} - k_{mi})\right] \end{Bmatrix} \tag{8.38}$$

By setting the determinant of the above matrix to zero, the critical buckling load can be expressed as;

$$P_{cr3} = \frac{4}{9}\frac{\pi^2}{S^2}E_b I_b + \frac{27S}{8\pi^2}\left(3b_{mn} + 2k_{mn} + k_{cn} \pm \frac{9}{8}\sqrt{3b_{mn}^2 + 4k_{mn}^2 + k_{cn}^2 - 4k_{mn}k_{cn} + b_{mn}k_{mn} - 2b_{mn}k_{cn}}\right) \tag{8.39}$$

If b_{mn} is equal to zero, then,

$$\begin{cases} P_{cr3} = \dfrac{4}{9}\dfrac{\pi^2 E_b I_b}{S^2} + \dfrac{27Sk_{cn}}{4\pi^2} \\ P_{cr3} = \dfrac{4}{9}\dfrac{\pi^2 E_b I_b}{S^2} + \dfrac{27Sk_{mn}}{2\pi^2} \end{cases} \quad \text{or} \tag{8.40}$$

If k_{mn} and k_{cn} are small and almost equal to each other, and b_{mn} is significant, then the critical buckling load is expressed as follows;

$$P_{cr3} = \frac{4\pi^2}{9S^2} E_b I_b + \frac{27S}{8\pi^2}\left(3b_{mn} + 3k_s - \frac{9}{8}\sqrt{3b_{mn}^2 + k_s^2 - b_{mn}k_s}\right) \tag{8.41}$$

9-Cell Grid

Referring to Fig. 8.9 and applying the same principle as that for the previous 9-cell grid system, a system of equations relating joint deformations, applied loads, and stiffnesses can be established in matrix form. This is shown below.

$$\begin{bmatrix} \frac{\pi^2}{27S^3}E_bI_b - \frac{\pi^2}{6S}P + \frac{9}{8}(b_{mn} + k_{mn}) & -\frac{9}{16}b_m \\ -\frac{9}{16}b_m & \frac{2\pi^2}{27S^3}E_bI_b - \frac{\pi^2}{6S}P + \frac{9}{8}(b_{mn} + 2k_{mn}) \end{bmatrix} \begin{Bmatrix} y_{cn} \\ y_{mn} \end{Bmatrix} = \tag{8.42}$$

$$\begin{Bmatrix} \frac{3}{2}SW_c + \frac{9}{8}\sum_{i=1}^{n-1} y_{ci}\left[(b_{mi+1} - b_{mi}) + (k_{mi+1} - k_{mi})\right] - \frac{9}{16}\sum_{i=1}^{n-1} y_{mi}(b_{mi+1} - b_{mi}) \\ \frac{3}{2}SW_m - \frac{9}{8}\sum_{i=1}^{n-1} y_{ci}(b_{mi+1} - b_{mi}) + \frac{9}{16}\sum_{i=1}^{n-1} y_{mi}\left[(b_{mi+1} - b_{mi}) + 2(k_{mi+1} - k_{mi})\right] \end{Bmatrix}$$

The critical buckling load is determined by setting the determinant of the above matrix equal to zero. The system of equations has two solutions, with the smaller of the two giving the critical buckling load.

$$P_{cr3} = \frac{4}{9}\frac{\pi^2}{S^2}E_bI_b + \frac{27S}{8\pi^2}\left(2b_{mn} + 2k_{mn} + k_{cn} \pm \frac{9}{8}\sqrt{b_{mn}^2 + 4k_{mn}^2 + k_{cn}^2 - 4k_{cn}k_{mn}}\right) \tag{8.43}$$

If b_{mn} is equal to zero, then;

$$\begin{cases} P_{cr3} = \frac{4}{9}\frac{\pi^2 E_b I_b}{S^2} + \frac{27Sk_{cn}}{4\pi^2} \\ P_{cr3} = \frac{4}{9}\frac{\pi^2 E_b I_b}{S^2} + \frac{27Sk_{mn}}{2\pi^2} \end{cases} \quad \text{or} \tag{8.44}$$

If k_{mn} and k_{cn} are small and almost equal to each other, and b_{mn} is significant, then the critical buckling load is expressed as follows:

$$P_{cr3} = \frac{4\pi^2}{9S^2} E_b I_b + \frac{27S}{8\pi^2}\left(2b_{mn} + 3k_s - \sqrt{b_{mn}^2 + k_s^2}\right) \tag{8.45}$$

8.6 Reduced Modulus for Longitudinal Bars

The buckling load of a beam-column depends on the modulus of elasticity of steel. If the critical stress ($f_{cr} = 4P_{cr}/\pi d^2$) remains within the elastic range, the material behaves according to the Hooke's law. This, however, is true for slender beam-columns only. The column reinforcement is modeled as a short beam-column. Thus the elastic limit is exceeded before the initiation of the buckling phenomenon in most cases. Hence, the modulus of elasticity E_b, becomes a function of the stress within the strain-hardening region. Consequently, the results of elastic analysis are not valid, and the buckling load must be determined by due considerations given to inelastic properties of steel.

Two theories were presented on selection of appropriate modulus within the inelastic range, early in this century. The first theory was the double-modulus theory, which had been first proposed by Considere in late 18th century, and was also presented by Karman in 1910 and Sowthwell in 1912. The second theory was the tangent modulus theory. This theory was first presented by Engesser in 1889, and then subsequently developed by other researchers. Both theories were well discussed by Timoshenko in 1961. The major difference between the two theories can be summarized as follows.

The double modulus theory assumes that the axial load remains constant as the column moves from a straight to a slightly bent position under the critical load (Timoshenko and Gere, 1961). Hence, the compressive stress increases according to the tangential modulus of elasticity E_t on the concave side of the member, and decreases according to the Young's modulus of elasticity E_s on the convex side. In the tangent modulus theory, the axial load is assumed to increase during the transition to the bent position. Hence, there is no strain reversal anywhere in the member and the increase in stress is governed by E_t at all points in

the cross section. The value of the tangential modulus can be obtained from the compression stress-strain curve. The double modulus load has the dubious advantage of satisfying the classical criterion of stability, whereas, the tangent modulus load is somewhat conservative in predicting test results. Figure 8- 10 illustrates the variation of stress with respect to aspect ratio (S/d_b) of a typical loaded steel rebar using tangent, double, and elastic moduli of elasticity.

The double modulus approach is considered in this research program because it takes into account the stress reversal and subsequent stiffening of longitudinal bars (Papia et al. 1988). The double modulus of a typical axially loaded steel column depends on the member cross-sectional shape. Hence, the first principles are applied to locate the neutral axis of the generic section of longitudinal reinforcing bar and the resisting bending moment. The stress distribution is illustrated in Fig. 8.11. The resultant forces acting on the cross section about the neutral axis is zero. Maximum stresses on tension and compression sides are expressed as follows;

$$\sigma_t = -\frac{E_s y_1}{\rho_o} \tag{8.46}$$

$$\sigma_c = \frac{E_h y_2}{\rho_o} \tag{8.47}$$

The variables y_1 and y_2 are distances from the neutral axis to tension and compression extreme fibers, respectively, and ρ_o is the radius of curvature. The position of the neutral axis can be found by using the condition that the resultant axial force action on the cross-section is zero. Therefore

$$\int_0^{y_1} \sigma_t dA + \int_0^{y_2} \sigma_c dA = 0 \tag{8.48}$$

Replacing σ_t and σ_c in the above equation by their corresponding expressions from Eqs. 8.46 and 8.47, and transferring into the polar coordinates, a relationship between E_h and E_s can be established as;

$$\frac{E_h}{E_s} = \frac{\sin\theta - \frac{1}{3}\sin^3\theta - \theta\cos\theta}{\sin\theta - \frac{1}{3}\sin^3\theta + (\pi - \theta)\cos\theta} \tag{8.49}$$

Hence, the angle θ can be determined using the above equation. The external bending moment is expressed in terms of stresses as follows;

$$M = -\int_0^{y_1} \sigma_t y dA + \int_0^{y_2} \sigma_c y dA = \frac{E_b I}{\rho_o} \tag{8.50}$$

Evaluating the above integrals results in the following equations;

$$E_b = \frac{1}{\pi}(E_s\Theta(\theta) + E_h\Theta(\pi - \theta)) \tag{8.51}$$

$$\Theta(\theta) = \theta - \left(\frac{5}{2} - \frac{1}{3}\sin^2\theta\right)\sin 2\theta + 4\theta\cos^2\theta \tag{8.52}$$

The modulus of elasticity E_s of typical reinforcing steel represents the slope of the elastic curve of the stress-strain relationship, and it is approximately equal to 200,000 MPa. The tangent modulus E_h represents the instant tangential slope of the compression stress-strain curve within the strain-hardening region. An analytical model for stress-strain relationship of rebars under compression was presented on the preceding chapter. The tangent modulus E_h is determined as a differential of the equation representing the stress-strain curve for the selected (S/d_b) ratio. In addition to the aspect ratio of rebars, the presence of intermediate lateral support may also have an effect on stress-strain behavior of members under compression. Although there is no experimental evidence, the problem can be solved analytically. The compression stress of laterally supported members can be calculated as follows;

$$f_s = f_{so} + \frac{4Sk_s}{\pi A_b} \qquad \text{for one intermediate spring} \tag{8.53}$$

$$f_s = f_{so} + \frac{27Sk_s}{4\pi A_b} \qquad \text{for two intermediate springs} \tag{8.54}$$

where, f_{so} is the compression stress without intermediate supports, S is vertical spacing between lateral elastic supports, k_s is the instant stiffness of lateral support, and A_b is cross-sectional area of longitudinal reinforcing bar. The second terms of the above equations are determined based on an assumed deflected shape of longitudinal bars (Eq. 8.2). Once the compression stress f_s is calculated for a given strain value, it should be compared to the closest stress-strain curve as shown in Fig. 8.12. The tangent modulus E_h is determined based only on the suggested four curves for now. More experimental and analytical work is needed to generate more accurate and wide range of curves. However, the proposed method proved to be satisfactory for the present column analysis, as it will be shown later in the Chapter.

8.7 Bending and Axial Stiffness of Transverse Reinforcement

Longitudinal reinforcing steel bars in concrete columns are restrained against buckling by transverse reinforcement with variable bending and axial stiffnesses. A typical segment of perimeter reinforcement having a length S_g, modulus of elasticity E_s, and moment of inertia I_s is modeled as shown in Fig. 8.13. The joint force F_1 is highly affected by the tension force T on the bar element and it is related to the joint displacement d_1 as follows;

$$F_1 = \left(\frac{2(m+n)}{S_g^2} + \frac{T}{S_g} \right) d_1 \tag{8.55}$$

where,

$$m = \frac{u(u\cosh u - \sinh u)}{2 - 2\cosh u + u\sinh} \frac{E_s I_s}{S_g} \tag{8.56}$$

$$n = \frac{u(\sinh u - u)}{2 - 2\cosh u + u\sinh u} \frac{E_s I_s}{S_g} \tag{8.57}$$

$$u = S_g \sqrt{\frac{T}{E_s I_s}} \tag{8.58}$$

The axial tension force T on the perimeter ties is mainly caused by the variable lateral pressure exerted by concrete in compression. In the sectional analysis of reinforced concrete members under compression, the analysis is usually done step-by-step, as the compressive strain in concrete is increased. This leads to a variation in height of the compressed concrete in section "c". This also leads to a variation of tension force in the ties. Therefore, the flexural stiffness of the ties vary since it depends on the "m" and "n" values as defined in Eq. 8.55. Assuming uniform lateral concrete pressure, the tension force T can be easily determined from static equilibrium, as shown in Fig. 8.14.

When lateral stirrups are stiff enough to reach the yield point, a longitudinal reinforcing bar becomes prone to buckling between two ties (first mode). However, laboratory tests of reinforced concrete columns showed that in most cases lateral reinforcement yielded and buckling of longitudinal bars involved one or more ties. The crossbars of transverse reinforcement can undergo plastic behavior when their axial deformation passes the yield point. Therefore, it is essential to properly model a tie under axial tension as a spring with different stiffnesses corresponding to different stages of deformation. The deformation of ties in confined concrete column is caused primarily by lateral expansion of core concrete, which in turn is affected by the axial compression. Madas and Elnashai (1992) proposed a cubic polynomial to determine the variation of Poisson's ratio with axial strain for plain concrete only, and used to compute confining pressure using an iteration process. However, experimental evidence showed that Poisson's ratio is also highly affected by lateral confining pressure (Imran and Pantazopoulou, 1996). Hence, lateral strain of confined concrete is

proportional to concrete axial strain. Pantazopoulou (1998) proposed a simple expression relating the lateral strain ε_2 to axial strain of concrete ε_c based on experimental data.

$$\varepsilon_2 = \nu\varepsilon_c - (1-2\nu)\frac{k_2\rho_{st}f_{st}}{E_c} + \varepsilon_1\frac{(1-2\nu)}{2}\left(\frac{\varepsilon_c - \dfrac{0.00015}{\nu}}{\varepsilon_1 - \dfrac{0.00015}{\nu}}\right)^2 \tag{8.59}$$

where ν is initial Poisson's ratio of concrete (~0.2), k_2 is confining effectiveness of transverse reinforcement as defined by Eq. 7.11, ρ_{st} is volumetric ratio, f_{st} is limiting stress of transverse reinforcement as defined by Eq. 7.12, and ε_1 is the axial strain corresponding to peak stress of confined concrete. Figure 8.15 illustrates the variation of the lateral strain with respect to confined concrete strain. Using the above computed strain value of ε_2 and the material stress strain relationship of transverse reinforcement stress, the instant modulus $E_{st}^{'}$ can be determined. Hence, the axial stiffness of transverse reinforcement is expressed as;

$$k_s = \frac{E_{st}^{'}A_{bs}}{L_s} \tag{8.60}$$

where, A_{bs} is the cross-sectional area of transverse reinforcement and L_s is the length of crosstie. When the lateral strain is less than the yield, the instant modulus is equal to the elastic modulus of elasticity (~200,000 MPa) and axial stiffness is very high compared to that for bending. However, when the transverse reinforcement yields and goes into the strain-hardening region, the instant modulus degrades rapidly and approaches zero. Then, the bending stiffness becomes significant. Figure 8.16 illustrates the variation of both stiffnesses with respect to lateral strain.

8.8 Results of Column Tests

A systematic computation is required to determine the inelastic behavior of longitudinal reinforcement in concrete columns subjected to axial load and lateral seismic deformations. A computer subroutine was written in FORTRAN language to be called by the main program

used for sectional analysis in Chapter 7. For each strain increment, the main program calls this subroutine. Based on given information, the subroutine calculates the lateral strain of concrete then the axial and bending stiffnesses of lateral reinforcement. The program checks for the governing mode shape and calculates the critical buckling load. Only columns confined with welded reinforcement steel grids or double head studs are analyzed here, because the Fiber Reinforcement Grids failed prematurely at joints as discussed in Chapters 3 and 4. Analytical predictions of the ultimate deformations of columns tested in this investigation and their modes of failure are presented and compared with experimental results in Table 8.1. A good agreement between the two is obtained, indicating that the proposed buckling model can be used with confidence in predicting inelastic deformation capacity of a reinforced concrete column confined with transverse steel.

Table 8-1: Comparisons of experimental and analytical predictions of deformation capacities for the tested Columns

Column Label	Experimental		Analytical	
	Maximum Def. (mm)	Mode of Failure	Maximum Def. (mm)	Mode of Failure
BG-1	50.0	Buckling 1st ,2nd Mode	55.0	Buckling 2nd Mode
BG-2	82.5	Buckling 3rd Mode	85.4	Buckling 3rd Mode
BG-3	100.0	Buckling 3rd Mode	123.5	Buckling 3rd Mode
BG-4	66.0	Buckling 1st Mode	60.7	Buckling 1st Mode
BG-5	100.0	Buckling 3rd Mode	102.0	Buckling 3rd Mode
BG-6	82.5	Test stopped prematurely	109.0	Buckling 3rd Mode
BG-7	82.5	Buckling 3rd Mode	74.5	Buckling 3rd Mode
BG-8	100.0	Buckling 3rd Mode	108.6	Buckling 3rd Mode
BG-9	66.0	Buckling 3rd Mode	68.6	Buckling 3rd Mode
BG-10	100.0	Buckling 2nd Mode and Overall Instability	101.9	P-Delta effect
BG-11	116.0	Buckling 3rd Mode	126.0	Buckling 3rd Mode
BG-12	82.5	Core concrete crushes	85.0	Core concrete crushes
BG-13	82.5	Test stopped prematurely	99.8	Buckling 3rd Mode
SD-1	66.0	Buckling 3rd Mode	75.2	Buckling 3rd Mode
SD-2	120.0	Buckling 3rd Mode	104.0	Buckling 3rd Mode
SD-3	100.0	Buckling 3rd Mode	94.2	Buckling 3rd Mode
SD-4	66.0	Overall Instability	58.0	P-Delta effect

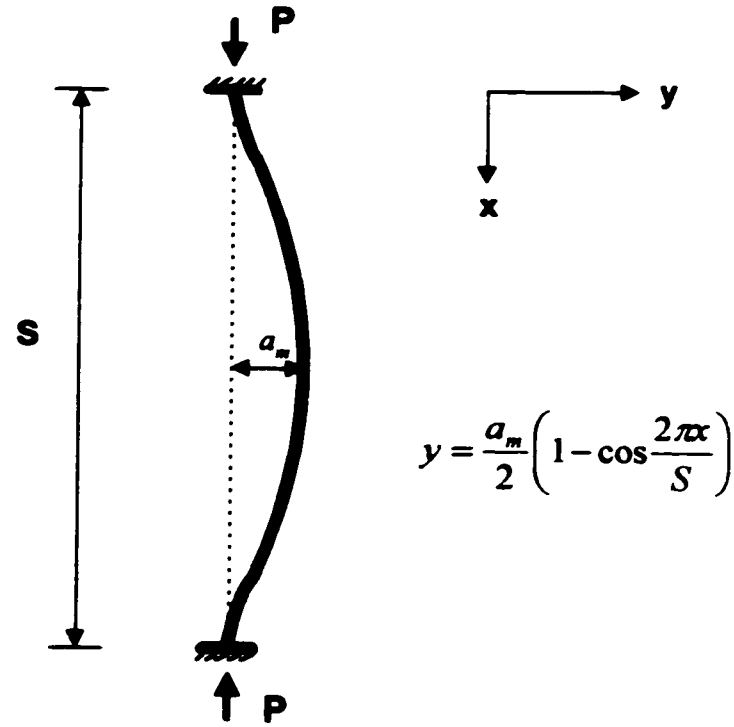

Fig. 8- 1: Deflection of fixed end column under axial load.

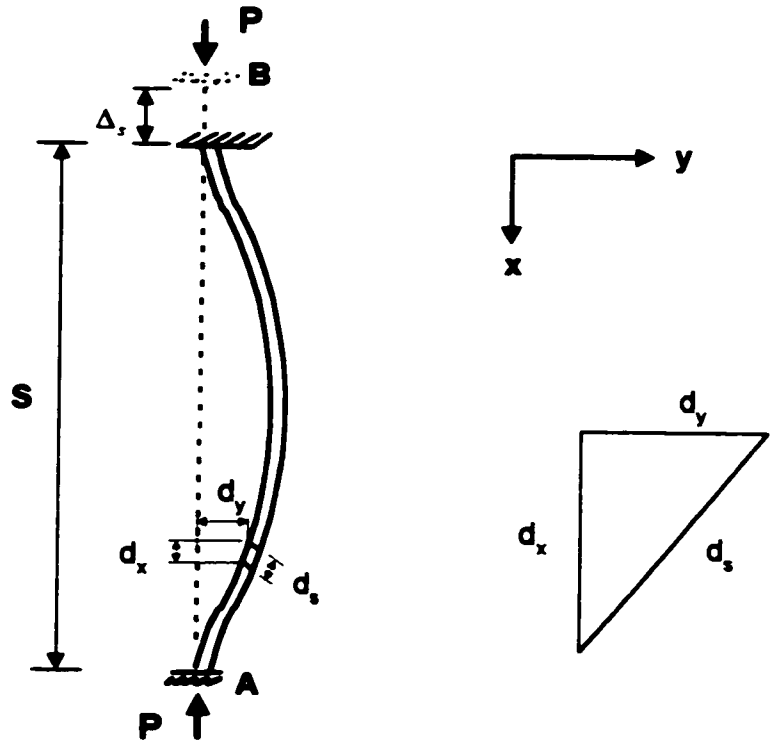

Fig. 8- 2: Axial shortening of column.

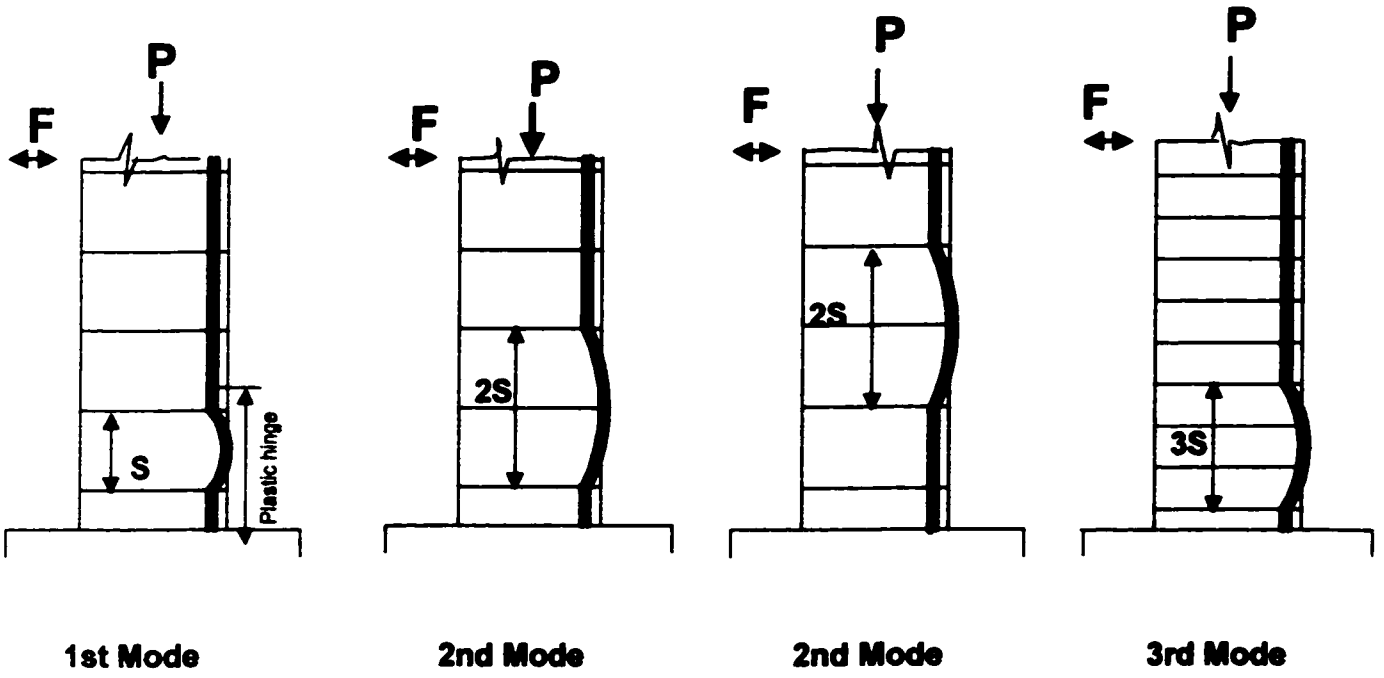

Fig. 8- 3: Different buckling mode shapes of longitudinal steel bars in concrete columns.

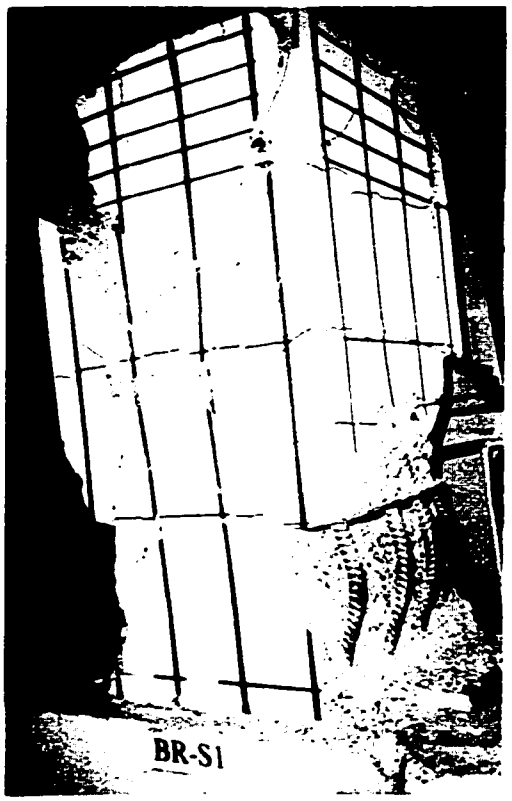

Fig. 8- 4: Buckling of longitudinal bars in 1st mode (Yalcin 1997).

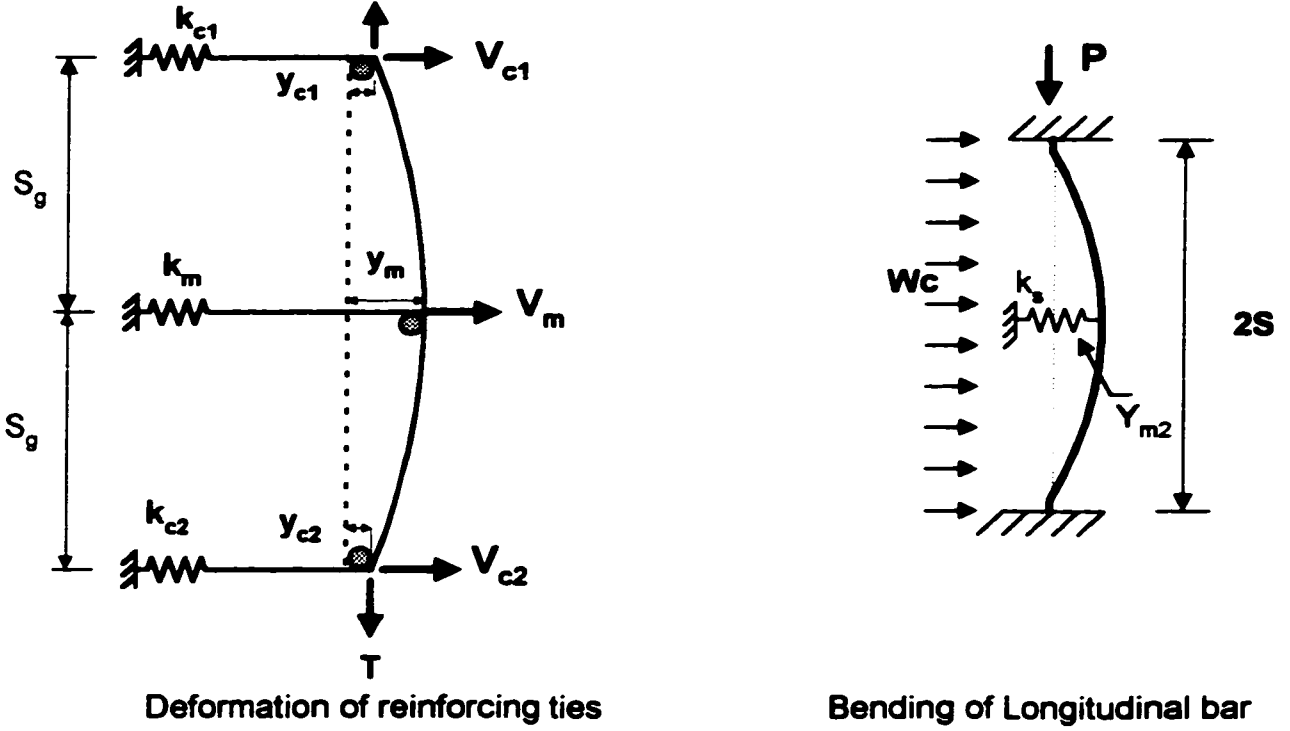

Fig. 8- 5: Modeling of 4-cell grids and buckling of longitudinal bar in 2nd mode shape.

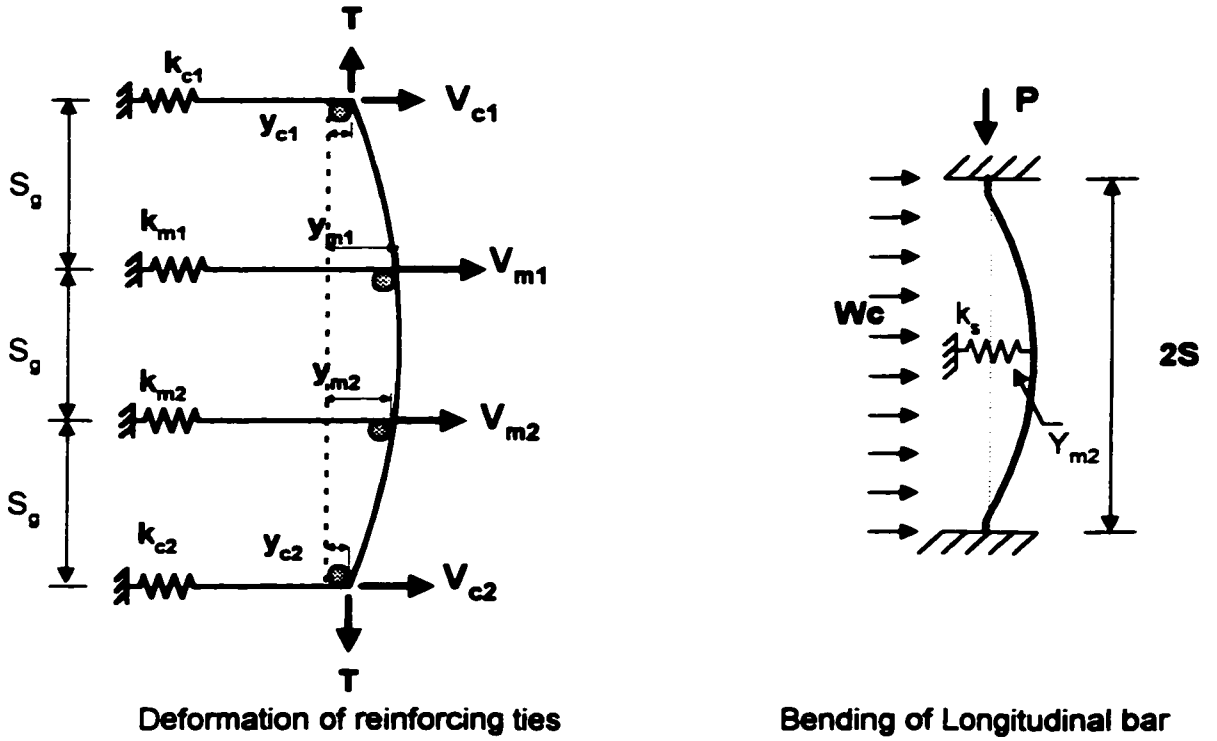

Fig. 8- 6: Modeling of 9-cell grids and buckling of longitudinal bars in 2nd mode shape.

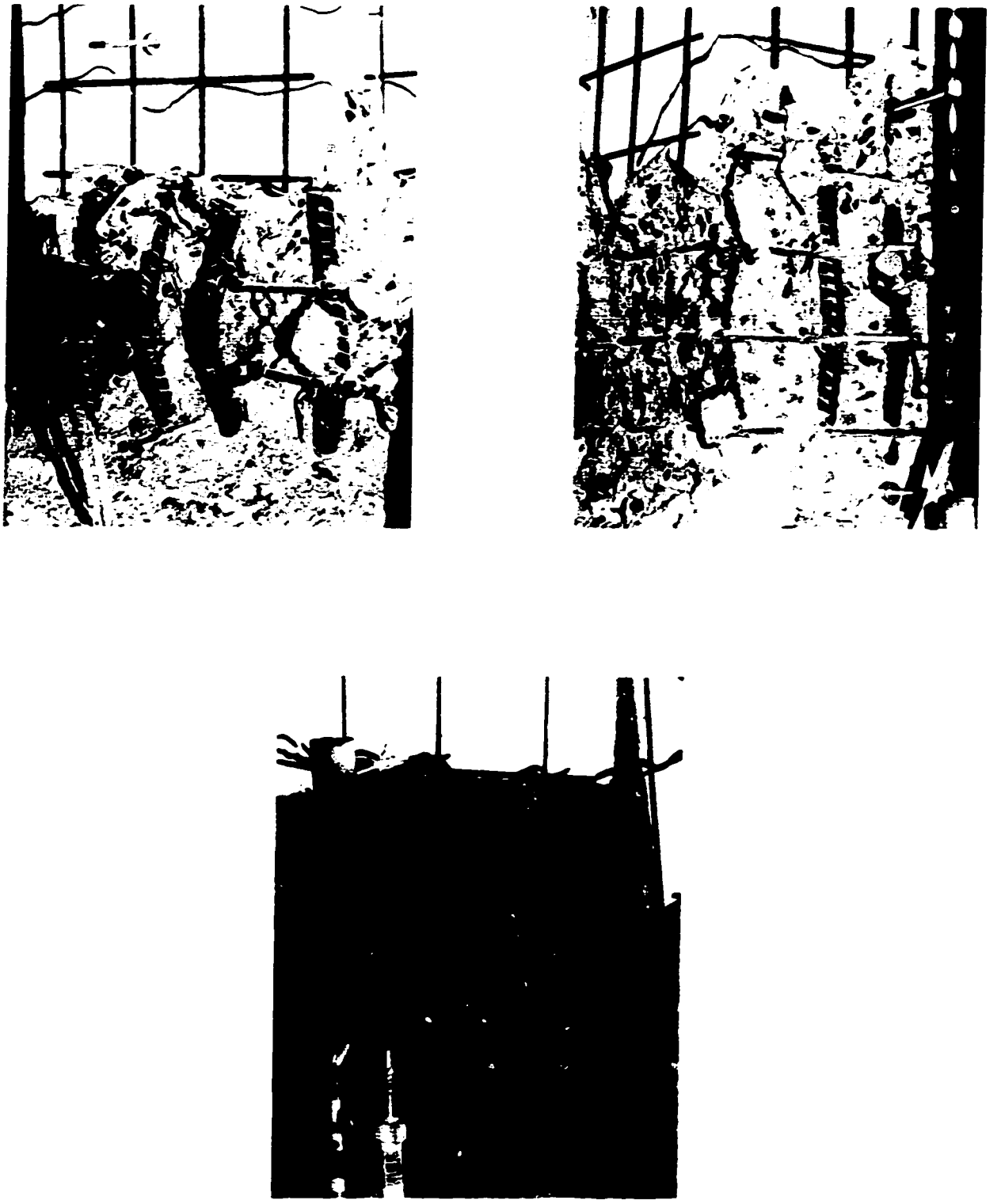

Fig. 8- 7: Buckling of longitudinal bars in third mode shape as observed during tests.

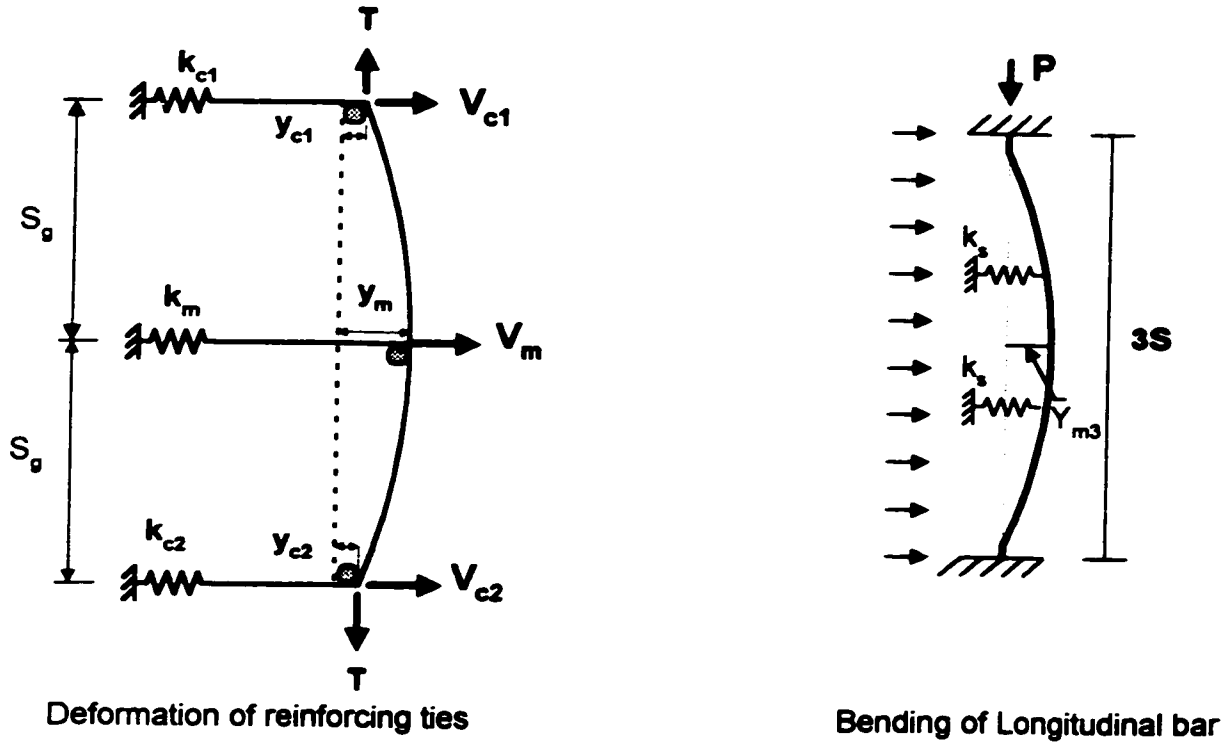

Fig. 8- 8: Modeling of 4-cell grids and buckling of longitudinal bars in third mode shape.

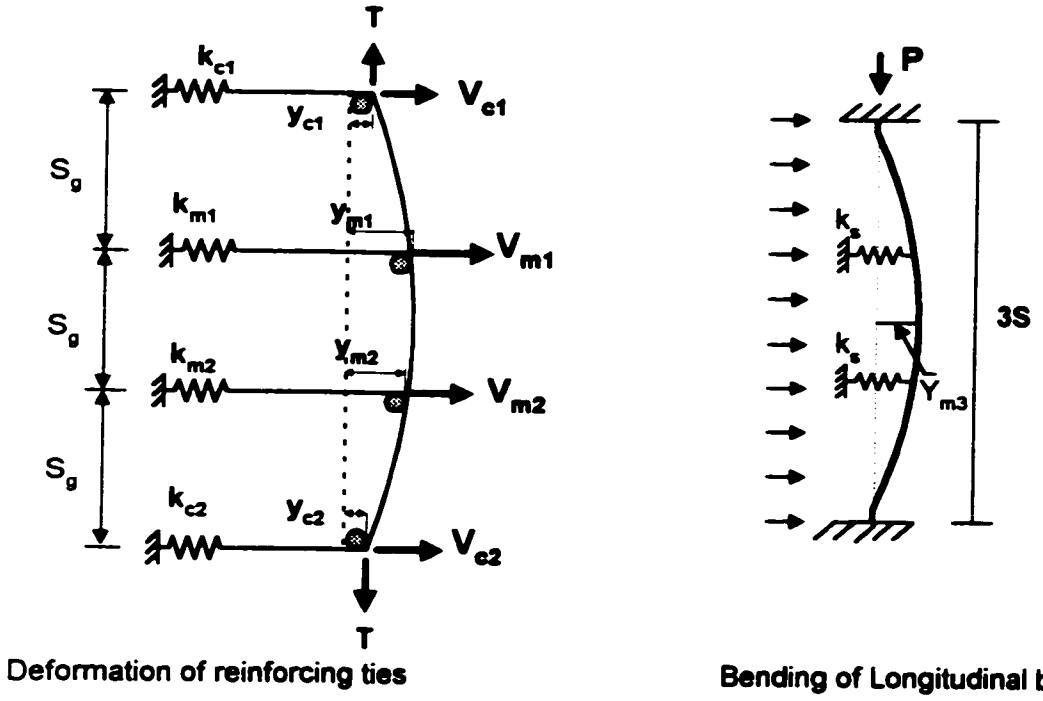

Fig. 8- 9: Modeling of 9-cell grids and buckling of longitudinal bars in third mode shape.

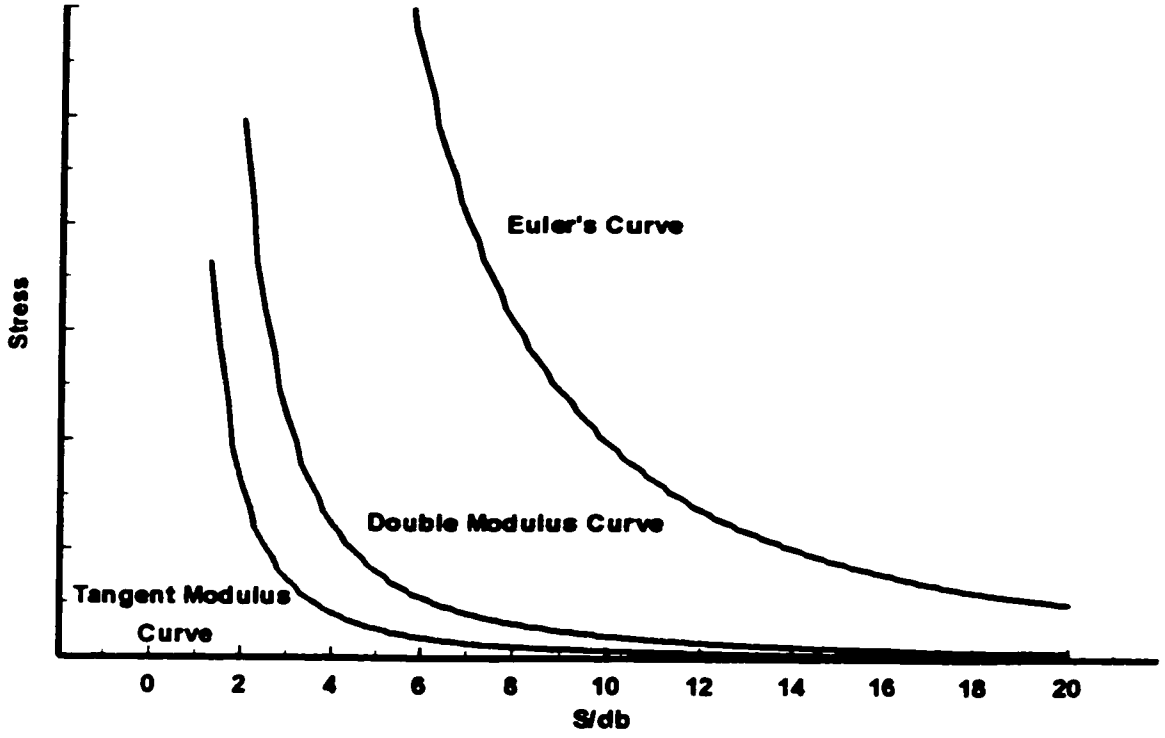

Fig. 8- 10: Variation of stress with respect to aspect ratio.

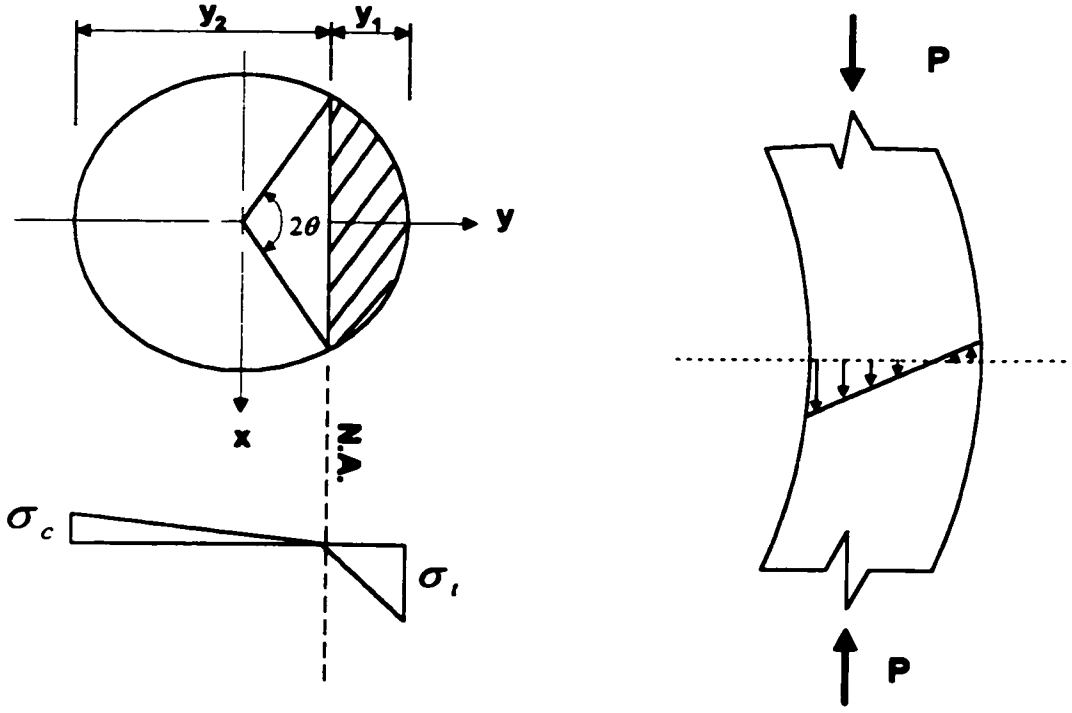

Fig. 8- 11: Bending stress distribution in longitudinal bar.

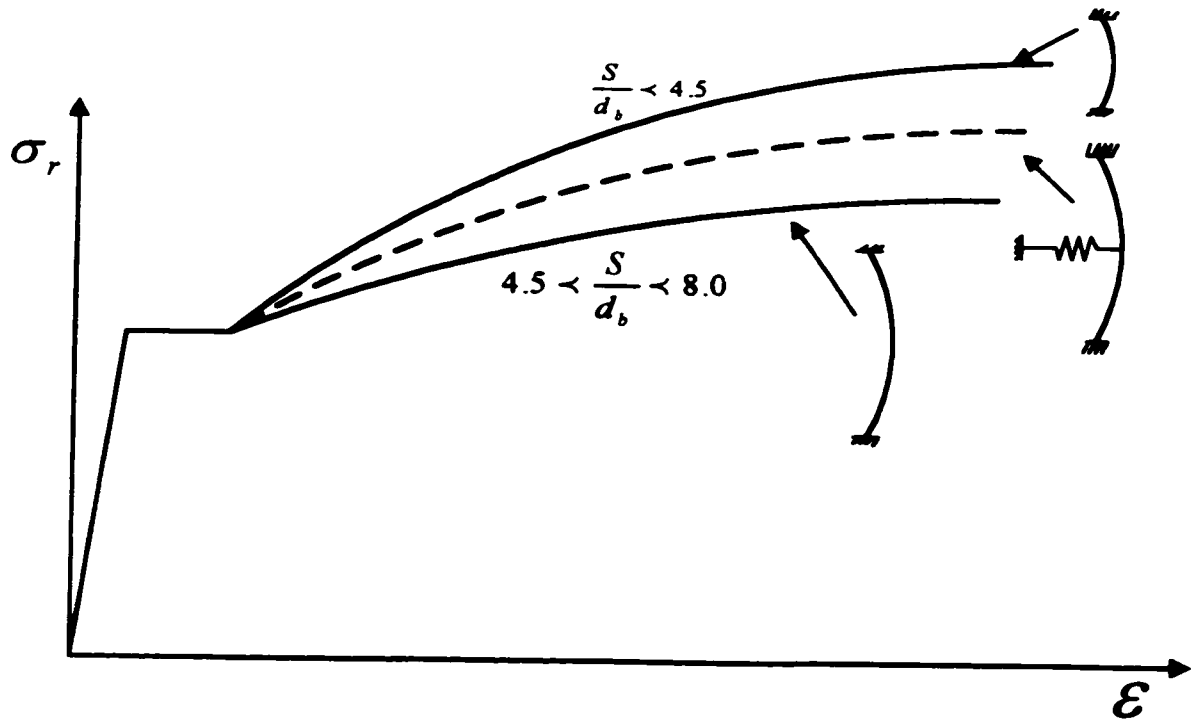

Fig. 8- 12: Effect of intermediate elastic supports on the stress-strain relationship of longitudinal bars.

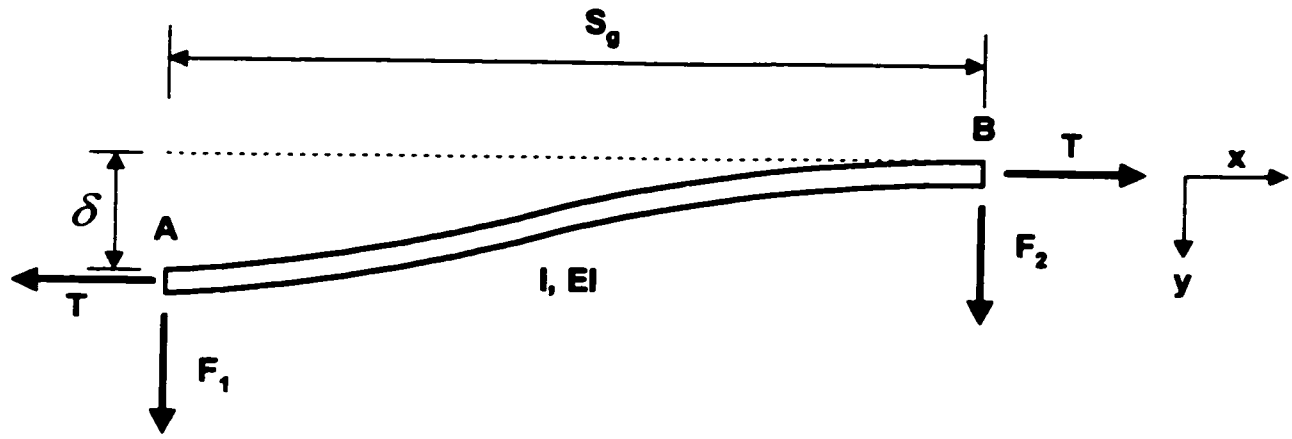

Fig. 8- 13: Beam element under tension and subjected to joint displacement.

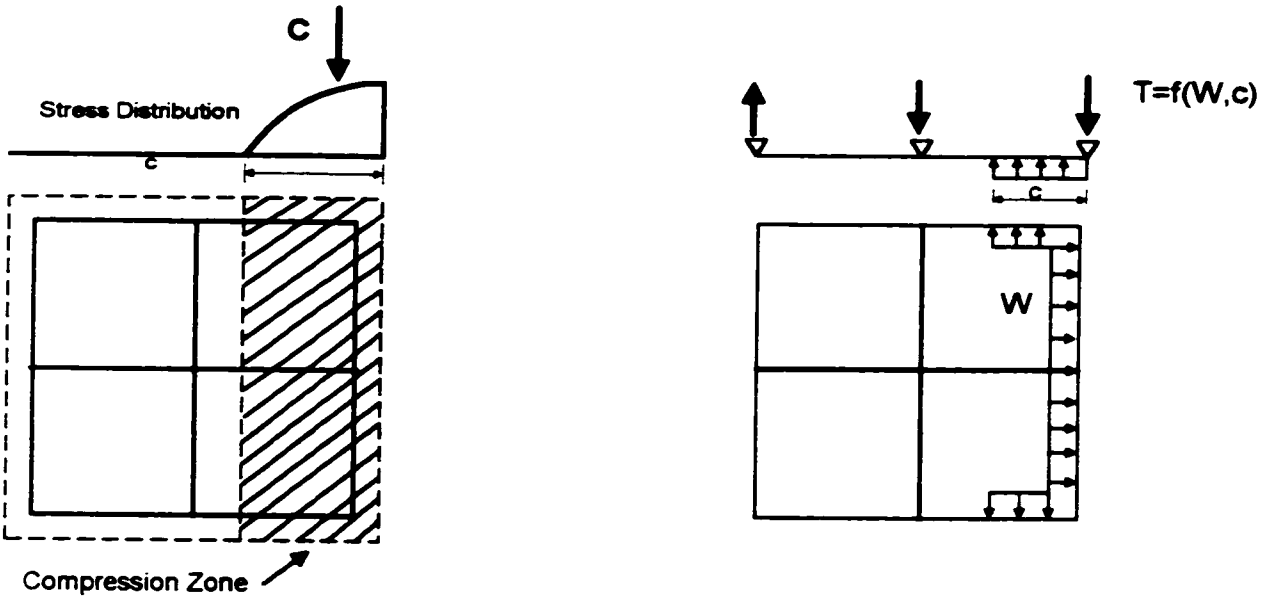

Fig. 8- 14: Tension on tie joints caused by concrete pressure.

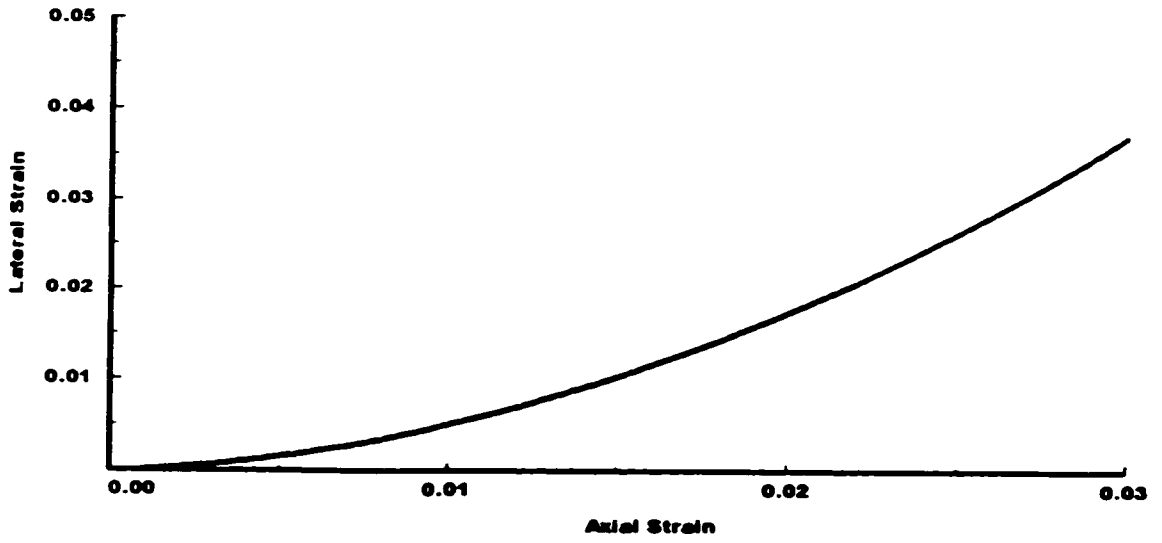

Fig. 8- 15 : Variation of lateral strain with respect to axial compression strain of concrete.

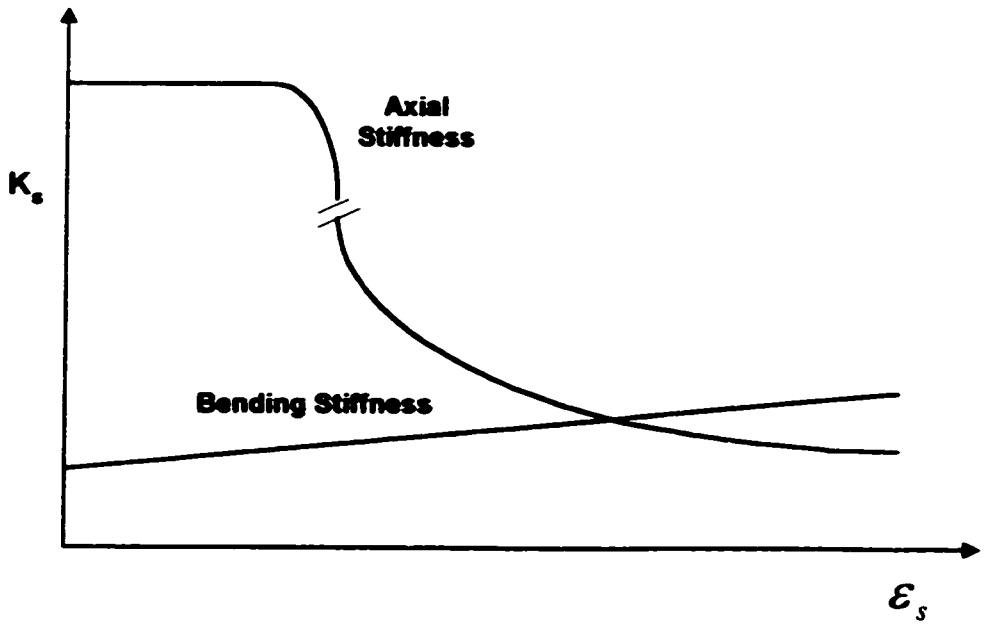

Fig. 8- 16: variation of bending and axial stiffness with lateral strain of ties

Chapter 9

CONCLUSIONS AND RECOMMANDATIONS

9.1 Conclusions

The following conclusions may be drawn from this research project:

- Welded reinforcement grids can be used as transverse confinement reinforcement provided that the welding process does not adversely affect strength and ductility of reinforcement and the steel has sufficient elongation. The steel grids used in this research program met these requirements. While the coupon tests indicated approximately 7% to 10% tensile strains at rupture, maximum tensile strains recorded during column tests were below 1.00% at 4% lateral drift when the steel grade ranged between 570 MPa and 580 MPa. This implies that the maximum elongation requirement for the grids may be significantly lower than the rupturing strain recorded during coupon tests. No grid failure was observed during column tests prior to either a longitudinal bar buckling in compression or a longitudinal bar fracture in tension. Only two BG columns exhibited grid fracture beyond these limiting load conditions.

- Columns confined with reinforcement grids showed ductile response, developing lateral drifts equal or greater than those expected in columns confined with conventional ties of equal volumetric ratio, grade, arrangement, and spacing. With the exception of column BG-1, which had a grid spacing equal to one half the cross-sectional dimension and the volumetric ratio equal to 65% of that required by *ACI 318-95* and hence developed 1% lateral drift, all others showed drift capacities of 2% and higher, even when the *P-Delta* effect was considered. Columns conforming the spacing requirements of *ACI 318-95* with volumetric ratios ranging between 83% and 129% of that required by the code showed ductile response even under high axial compression of approximately 40% of nominal concentric capacity, developing drifts of 3% to 6% prior to 20% degradation in moment

resistance. The same columns developed 2% to 4% drift prior to similar degradation in lateral force resistance. Companion columns tested under 20% of nominal concentric capacity showed significantly higher deformabilities, developing 6% to 7% drift prior 20% degradation in moment resistance and 4% drift at 20% decay in lateral force resistance.

- Columns reinforced with double head studs showed ductile behavior developing approximately the same drift capacities as those developed by companion BG columns. Their failure was characterized by sudden opening of the 135-degree hooks of perimeter hoops followed by core concrete crushing and instability of longitudinal bars. The double head studs performed satisfactorily when compared with welded reinforcement grids, and superior when compared with conventional reinforcement.

- Properly confined FRP columns showed ductile responses and behaved as well as companion BG-columns. The failure of FRP columns was characterized by premature failure of FRP grids at the joints. With the exception of columns FRP-1 and FRP-2, which had a grid spacing equal to approximately one half the cross-sectional dimension and a volumetric ratio equal to 39% and 52% of that required by *ACI 318-95*, respectively, and hence developed 1% lateral drift, all other columns showed drift capacities of 2% and higher, even when *P-Delta* effect was considered. Columns conforming the spacing requirements of ACI 318-95, with volumetric ratios ranging between 79% and 140% of that required by the code showed ductile response even under high axial compression of approximately 40% of nominal concentric capacity, developing drifts of 2% to 6% prior to 20% degradation in moment resistance. Companion columns tested under 20% of nominal concentric capacity showed significantly higher deformabilities, developing 5% to 7% drift prior 20% degradation in moment resistance and 4% to 5% drift at 20% decay in lateral force resistance.

- Concrete columns confined with different types of non-conventional transverse reinforcement (WRG, DHS, or FRP grids), subjected to axial compression and lateral deformation reversals, behaved similar to each other. The concrete strength enhancement was almost identical in companion columns. However, their lateral deformation

capacities depended highly on tension capacity of transverse reinforcement. Generally FRP columns experienced less lateral displacement compared to BG columns because of premature failure of FRP grid joints.

- Ductility of confined columns is highly affected by the volumetric ratio of confinement reinforcement. Columns with low volumetric ratio showed higher rate of strength decay immediately after the peak lateral load. On the other hand, columns with increased confining reinforcement were able to deform significantly with very small drop in lateral load capacity.

- Columns confined with 9-cell grids (WRG or FRP grids) showed higher deformability than those confined with 4-cell grids having the same volumetric ratio and spacing. The presence of cross reinforcement resulted in improved uniformity of confinement pressure and produced superior behavior.

- Columns confined with only 4-corner longitudinal reinforcement and either 4 or 9-cell FRP grids showed ductile response similar to that of 8 or 12-bar arrangements. This indicates that grids with closely spaced reinforcement in the cross-sectional plane can be used to get the beneficial effects of well-distributed and laterally supported reinforcement with four corner bars.

- Deformability of concrete columns is reduced with an increase in vertical spacing of transverse reinforcement and a decrease in volumetric ratio. Columns with high vertical spacing of transverse reinforcement experience rapid strength degradation and longitudinal bar buckling.

- Deformability of reinforced concrete columns decreases with increasing concrete strength. However, the reduction in deformability associated with increase in concrete strength can be compensated by the use of high-strength welded steel grids.

- Column deformability reduces with increased axial compression. Furthermore, increased axial compression results in rapid strength degradation due to P-Delta effect. In addition, columns subjected to increased axial compression developed lower yield penetration into

the footing. This resulted in reduced rotations due to anchorage slip.

- Columns with longitudinal bars placed on both sides of a perimeter grid joint perform as good as those with single longitudinal bar placed at each perimeter grid joint. This indicates that in cases where the use of bundled bars is considered, or a large number of smaller size bars are preferred, welded grids may be used with longitudinal bars on both sides of grid joints. However, small size longitudinal bars are more susceptible to buckling.

- The analytical material models and the stress-strain relationship of confined concrete employed in this investigation proved to be adequate to generate force-displacement relationships. The analytical procedure can be used for normal-strength and high-strength concrete columns, confined by reinforcements of different types and arrangements.

- The proposed analytical model for bar buckling produces good correlation with experimental data. It was shown that, in addition to confining core concrete, the transverse reinforcement in plastic hinge regions should also be capable of restraining longitudinal reinforcement against buckling. The vertical spacing between layers of transverse reinforcement to avoid buckling of bars in the first mode (between two layers) depends on the size and effective modulus of elasticity of bars in the strain-hardening region, and the peak compression strain.

- The coupon tests provide strength and elongation capacity of material used in manufacturing grids, whereas bursting test provides the elongation capacity of a grid as whole, under a representative load condition. Bursting tests should be conducted to assess the integrity of joints in grid reinforcement.

- Pullout tests should be used to verify the weld connection of steel head-plates to the studs.

- Bursting tests showed that the steel grids used in this experimental project exhibited an overall elongation of above approximately 7%. The failure was characterized by either a rupture near the weld joint of weld failure following significant yielding. While the

bursting test is representative of grid behavior in columns, it may be more critical on the weld. Therefore, it may be viewed as a conservative approach to verifying weld strength.

9.2 Recommendations

- Welded grids offer an economical alternative to conventional ties with reduced construction time, especially for earthquake resistant construction where the tie details may be prohibitively complex. The experience with cage assembly in a laboratory environment has been most favorable in terms of dimensional tolerances and speed of construction. This aspect may be a significant asset in the field. Therefore construction advantages, combined with superior performance observed in column tests make welded reinforcement grids a viable alternative to conventional ties. However, the conclusions drawn in this investigation may be limited to the materials considered in this research project. The extension of the results to other columns, especially with welded reinforcement grids having significantly different material properties, should be done with caution. Deformability of grid reinforcement and the strength of welded joints remain to be two important parameters to be specified before such a material is authorized for use in reinforced concrete columns. The observations made in this research program indicate that welded grids must have welded joints stronger that the steel itself, and a minimum elongation of 4%, when determined by a standard coupon test where the coupon contains a welded joint in the center.

- The anchor heads of DHS studs were originally designed to prevent crushing of concrete and not to restrain longitudinal bars against buckling. Large size heads is recommended to be used to confine concrete columns and more tests are needed.

- An improvement of the FRP grid joints is needed by using either stronger epoxy resin or round continuous fibers. Further tests are required to establish design recommendations for columns confined with FRP grids.

- Experimental studies are needed to establish bond slip of longitudinal reinforcing steel bars in high strength concrete.

- More precise experimental research is needed on the cyclic behavior of reinforcing steel bars including inelastic buckling.

REFERENCES

1. Abdel-Fattah, H., and Ahmed, S.H., "Behavior of Hoop Confined High-Strength Concrete Under Axial and Shear Loads," *ACI Structural Journal*, V.86, No. 6, Nov. - Dec. 1989, pp. 652 – 659.

2. ACI Committee 224, "Cracking of Concrete Members in Direct Tension," *ACI Journal*, Jan.-Feb. 1986, pp. 3 –1 3.

3. ACI Committee 318, "Building Code Requirements for Reinforced Concrete and Commentary (ACI 318-95)," *American Concrete Institute*, Detroit, 1995, pp. 369.

4. ACI Committee 363, "State-of-the-Art Report on High-Strength Concrete," *ACI Journal*, Proceedings V. 81, No. 4, July - Aug. 1984, pp. 364 - 411.

5. ACI Committee 440, "State-of-the-Art Report on Fiber Reinforced Plastic Reinforcement for Concrete Structures," *American Concrete Institute*, Detroit, 1996, pp. 68.

6. Ahmad, S.H., and Shah, S.P., " Behavior of Hoop Confined Concrete Under High Strain Rates," *ACI Journal*, Sept. - Oct. 1985, 634 – 647.

7. Ahmed, S.H. and Shah, S.P., "Stress-Strain Curves of Concrete Confined by Spiral Reinforcement," *Journal of the American Concrete Institute*, Vol. 79, No. 6, Dec. 1982, pp. 484 – 490.

8. Al-Hussaini, A., Regan, P.E., Xue, H.Y., Ramdame, K.E., "The Behavior of HSC Columns Under Axial Load," *Proceedings of the Symposium on High-Strength Concrete*, June 1993, Norway, pp. 83 – 90.

9. Azizinamini, A., Kuska, S.S., Brungardt, P., and Hatfield, E., "Seismic Behavior of Square High-strength Concrete Columns," *ACI structural Journal*, May-June 1994, pp. 333-345.

10. Baingo, D., "Performance of Circular High-Strength Concrete Columns Under Lateral Load Reversals," M.A.Sc. Thesis, *Department of Civil Engineering, University of Ottawa*, Ottawa, Ontario, Canada, May 1996, pp. 211.

11. Baingo, D. and Saatcioglu, M., "Tests of Circular High-Strength Concrete Columns Under Reversed Cyclic Loading," Research Report 97-12, *Ottawa-Carleton Earthquake Engineering Research Center, Department of Civil Engineering, the University of Ottawa, Ottawa, Canada, 1997.*

12. Baker, A., and Amarakone, A.M.N., "Inelastic Hyperstatic Frames Analysis," Flexural Mechanics of Reinforced Concrete, SP-12, *American Concrete Institute/ America Society of Civil Engineers*, Detroit, 1965, pp. 85 – 142.

13. Balmer, G.G., "Shearing Strength of Concrete Under High Triaxial Stress-Computation of Mohr's Envelope as a Curve, " *Structural Research Lab., Report No. SP-23, U.S. Bureau of Reclamation, Denver,* Co., 1949.

14. Banthia, N., Al. Asaly, M., and Ma, S., "Behavior Of Concrete Slabs Reinforced With Fiber-Reinforced Plastic Grid," *ASCE Journal of Materials in Civil Engineering*, Vol. 7, No. 4, November, 1995, pp. 252 – 257.

15. Basset, R., and Uzumeri, S.M., "Effect of Confinement on the Behavior of High-Strength Lightweight Concrete Columns," *Canadian Journal of Civil Engineering*, V. 13, No. 6, Dec. 1986, pp. 741 - 751.

16. Baumann, H.U., "Performance of Prefabricated High-Strength Welded Wire Grids in Ductile Concrete Shear Wall Boundary Elements," *The Structural Design of Tall Buildings*, Vol. 2, John Wiley & Sons Lt., 1993, pp. 33 – 52.

17. Bedard, C., and Aitcin, P.C., " A la Recherche d'un Beton de 150 MPa," *Canadian Journal of Civil Engineering*, October 1983, pp. 600 – 613.

18. Bertero, V.V., and Felippa, C., Discussion of "Ductility of Concrete," by Roy, H.E., and Sozewn, M.A., *Proceedings of the International Symposium on the Flexural Mechanics of Reinforced Concrete, ASCE-ACI,* Miami, Nov. 1964, pp. 227 – 234.

19. Bjerkeli, L., Tomaszewica, A., and Jensen, J.J., "Deformation Properties and Ductility of High Strength Concrete," *High Strength Concrete, Second International Symposium*, ACI SP-121-12, Detroit, 1990, pp. 215-238.

20. Bleich, F., "Buckling Strength of Metal Structures," *McGraw-Hill Book Company, Inc.*, New York, 1952, pp. 508.

21. Bortolotti, L., "Influence of Concrete Tensile Ductility on Compressive Strength of Confined Columns," *Journal of Material in Civil Engineering*, ASCE, 6(4), 1994, pp. 542 - 563.

22. Bresler, B. and Gilbert, P.H., "Tie Requirements for Reinforced Concrete Columns", *Journal of the American Concrete Institute*, Vol. 58, No. 5, Nov. 1961, pp. 555 - 569.

23. Burdette, E.G. and Hilsdorf, H.K., " Behaviour of Laterally Reinforced Concrete Columns", *Journal of the Structural Division*, ASCE, Vol. 97, No. ST2, Feb, 1971, pp. 687 – 602.

24. Carino, N.J., and Lew, H.S., "Re-examination of the Relation Between Splitting Tensile and Compressive Strength of Normal Weight Concrete," *ACI Journal*, May-June 1982, pp. 214 - 219.

25. Carreira, D.J., and Chu, K.H., "Stress-Strain Relationship for Plain Concrete in Compression," *ACI Journal*, Nov. - Dec. 1985, pp. 797 - 804.

26. Carreira, D.J., and Chu, K.H., "Stress-Strain Relationship for Plain Concrete in Tension ," *ACI Journal*, Jan. - Feb. 1986, pp. 21 - 28.

27. Carreira, D.J., and Chu, K.H., "The Moment-Curvature Relationship of Reinforced Concrete Members," *ACI Journal*, Mar. - Apr. 1986, pp. 191-198.

28. Chajes, A., "Principles of Structural Stability Theory," *Prentice-Hall, Inc.*, Englewood Cliffs, New Jersey, 1974, pp. 336.

29. Chan, W.W.L., "The Ultimate Strength and Deformation of Plastic Hinges in Reinforced Concrete Frameworks," *Magazine of Concrete Research*, Vol. 7, No. 21, Nov. 1955, pp. 121 – 132.

30. Chang, G.A., and Mander, J.B., "Seismic Based Fatigue Damage Analysis of Bridge Columns: Part I - Evaluation of Seismic Capacity", *Technical Report NCEER-94-0006*, March 14, 1994.

31. Cheok, G.S., and Stone, W.C., "Performance of 1/3-Scale Model Precast Concrete Beam Column Connections subjected to cyclic Inelastic Loads," *Report No. 4, Research Report NISTIR 5436, Building and Fire Research Laboratory, National Institute of Standards and Technology*, Gaithersburg, Maryland, June 1994.

32. Collins, M.P., Mitchel D., and MacGregor, J.G., "Structural Design Considerations for High-Strength Concrete", Network of Cenres of Excellence on High-Performance Concrete, October 4-7, 1992, Toronto, pp. 18.

33. Comite Euro-International du Beton (CEB), "CEB model code 90," *Bull. D'information, No. 203*, Paris, France, 1990.

34. Corley, W. G., "Rotational Capacity of Reinforced Concrete Beams," *Proceedings, ASCE*, V. 92, ST5, Oct. 1966, pp. 121 - 146.

35. CSA, Design of Concrete Structures for Buildings (CAN3-A23.2-94), *Canadian Standards Association*, Ontario, 1994, pp. 199.

36. Cusson, D., and Paultre, P., "Experimental Study of High-Strength Concrete Columns Confined by Rectangular Ties," *Proceedings of the Symposium on High-Strength Concrete*, June 1993, Norway, pp. 136 – 145.

37. Cusson, D., and Paultre, P., "High-Strength Concrete Columns Confined by Rectangular Ties," *Journal of Structural Engineering, ASCE*, Vol. 120, No. 3, March 1994, pp. 783 – 804.

38. Dilger, W.H., and Ghali, A., " Double Head Studs as Ties in Concrete," *Concrete International*, June 1997, pp. 59 - 66.

39. Dilger, W.H., and Ghali, A., "Shear Reinforcement for Concrete Slabs," *Proceedings, ASCE*, V.107, ST 12, Dec. 1981, pp. 2403 - 2420.

40. Diniz, S.M., and Frangopol, D.M., "Strength and Ductility Simulation of High-Strength Concrete Columns," *Journal of Structural Engineering*, ASCE, October, 1997, pp. 1365 - 1374.

41. Djukic, D.S., and Atanackovic, T.M., (1993). "Effect of Shear on Simple Buckling Problem," *Journal of Engineering Mechanics , ASCE*, 119(5), pp. 1108 - 1115.

42. Dodd, L.L., and Restrepo-Posada, (1995), "Model for Predicting Cyclic Behavior of Reinforcing Steel," *Journal of Structural Engineering, ASCE*, 121 (3), pp. 433 - 445.

43. Fafitis, A., and Shah, S.P., "Predictions of Ultimate Behavior of Columns Subjected to Large Deformations," *ACI Journal*, July-Aug. 1985, pp. 423 - 433.

44. Foraboschi, P. (1995), "Modeling of Collapse Mechanisms of Thin Reinforced Concrete Shells," Journal of Structural Engineering, ASCE, 121(1), pp. 15 - 27.

45. Fujisaka T., Kobayashi, K.M., "Application of New Fiber Reinforced Composite Material (NFM) to Shear wall of Concrete Structures," *Proceeding of Ninth World Conference on Earthquake Engineering*, Aug. 2-9, 1988, Tokyo-Kyoto, Japan, Vol. 4.

46. Furlong, R.W., Fenves, G.L., and Kasl, E.P., "Welded Structural Wire Reinforcement for Columns," *ACI Structural Journal*, Sept. - Oct. 1991, pp. 585 – 591.

47. Gopalaratnam, V.S., and Shah, S.P.," Softening Response of Plain Concrete in Direct Tension," *ACI Journal*, May- June 1985, pp. 310 – 323.

48. Grira M. and Saatcioglu M., "Concrete Confined with Welded Reinforcement Grids," *Research Report OCEERC 96-05, Ottawa Carleton Earthquake Engineering Research Center, Department of Civil Engineering, University of Ottawa, Ottawa*, Ontario, pp. 89.

49. Hognestad, E., "A Study of Combined Bending and Axial Load in Reinforced Concrete Members," *Bulletin 399, University of Illinois Engineering Experiment Station*, Urbana, Ill., Nov. 1951, pp. 128.

50. Hoshikuma, J., Kawashima, K., Nagaya, K., and Taylor, A.W., "Stress-Strain Model for Confined Reinforced Concrete in Bridge Piers," *Journal of Structural Engineering, ASCE*, May 1997, pp. 624 - 633.

51. Hudson, F.M., "Reinforced Concrete Columns: Effects of Lateral Tie Spacing on Ultimate Strength," *Paper No. 10, Symposium on Reinforced Concrete Columns, ACI, SP-13*, 1966, pp. 235 – 244.

52. Imran, I., and Pantazopoulou S.J., "Experimental Study of Plain Concrete under Triaxial Stress," ACI Materilas Journal, V.93, No. 6, Nov. – Dec. 1996, pp. 589 – 601.

53. Johnston, B.G., "Column Buckling Theory: Historical Highlights," *Journal of Structural Engineering, Structural Division, ACSE*, Vol. 109, No. 9, September 1983, pp. 2086 - 2096.

54. Karabinis A.I. and Kiousis P.D. (1996), "Strength and Ductility of Rectangular Concrete Columns: A Plasticity Approach," *Journal of Structural Engineering., ASCE*, 122 (3), pp. 267 -274.

55. Karsan, I.D. and Jirsa, J.O., "Behaviour of Concrete Under Varying Strain Gradients," *Journal of the Structural Division, ASCE*, Vol. 96, No. ST8, Aug. 1970, pp. 1675 – 1697.

56. Kent D.C. and Park R. (1971), "Flexural Members with Confined Concrete," *Journal of Structural Division, ASCE*, 97 (ST7), pp. 1969-1990.

57. Kuramoto, H., and Kabeyasawa, T., and Shen, F.H., "Influence of Axial Deformation on Ductility of High-Strength Reinforced Concrete Columns Under Varying Triaxial Forces," *ACI Structural Journal*, Sept. - Oct., 1995, pp. 610-618.

58. Legeron. F., and Paultre, P., "Seismic Behaviour of Columns Made of High-Strength Concrete," *Proceedings of Seventh Canadian Conference on Earthquake Engineering, Montreal*, June 5 – 7, 1995, pp. 469 – 476.

59. Li, B., "Strength and Ductility of reinforced Concrete Members and Frames Constructed Using High-Strength Concrete," *Research Report No. 94-5, University of Canterbury*, Christchurch, New Zealand, May 1994, pp. 389.

60. Lim, F.K., and Rangan, V., "Studies on Concrete Slabs With Stud Shear Reinforcement in the Vicinity of Edge and Corner columns," *ACI Structural Journal*, Sept. - Oct., 1995, pp. 515-525.

61. Lipien, W., "Behavior of Square High Strength Concrete Columns Under Load Reversals," *M.A.Sc. thesis, Department of Civil Engineering, University of Ottawa*, Ottawa, Ontario, Canada, month 1995, pp. 183.

62. Lipien, D. and Saatcioglu, M., "Tests of Square High-Strength Concrete Columns Under Reversed Cyclic Loading," Research Report 97-11, *Ottawa-Carleton Earthquake*

Engineering Research Center, Department of Civil Engineering, the University of Ottawa, Ottawa, Canada, 1997.

63.

64. Lloyd, N.A., and Rangan, B.V., "High Strength Concrete Columns Under Eccentric Compression," *Research Report No. 1/95, School of Civil Engineering, Curtin University of Technology*, Australia, 1995, pp. 199.

65. MacGregor, James, "Reinforced Concrete: Mechanics and Design," Prentice Hall, 1988, pp.799.

66. Madas, P. and Elnashai, A.S., "A New Passive Confinement Model For the Analysis of Concrete Structures Subjected to Cyclic and Transient Dynamic Loading," *Earthquake Engineering. and Structural Dynamics*, 1992, vol. 21, pp. 409 - 431.

67. Mander, J.B., Panthaki, F.D., Kasalanati, A., "Low-Cycle Fatigue Behavior of Reinforcing Steel," *Journal of Material in Civil Engineering., ASCE*, 1994, 6(4), pp. 453 - 468.

68. Mander, J.B., Priestley, M.J.N., and Park, R., "Observed Stress-Strain Behavior of Confined Concrete," *Journal of Structural Engineering., ASCE*, 1988, 114 (8), pp. 1827 - 1849.

69. Mander, J.B., Priestley, M.J.N., and Park, R., "Theoretical Stress-Strain Model for Confined Concrete, " *Journal of Structural Engineering., ASCE*, 1988, 114(8), pp. 1804 - 1826.

70. Martinez, S., Nilson, A.H. and Slate, F.O., "Spirally Reinforced High-Strength Concrete Columns," *Research Report No. 82 – 10, Department of Structural Engineering, Cornell University*, Ithaca, Aug. 1982, 255 pp.

71. Martinez, S., Nilson, A.H. and Slate, F.O., "Spirally Reinforced High-Strength Concrete Columns," *ACI Journal*, Sept. – Oct. 1984, pp. 431 – 442.

72. Martinez, S., Nilson, A.H., and Slate, F.O., "Spirally Reinforced High-Strength Concrete Columns," *ACI Journal*, Sept. - Oct. 1984, pp. 431-442.

73. Mau S.T. (1990), "Effect of Tie Spacing on Inelastic Buckling of Reinforcing Bars," ACI Structural Journal,..... 1990, pp. 671 - 677.

74. Mau, S.T., and El-Mabsout, M., "Inelastic Buckling of Reinforcing Bars," *Journal of Engineering. Mechanics, ASCE*, 1989, 115(1), pp. 1 - 17.

75. Miranda, E., Thompson, C.L., and Bertero, V.V., "Cyclic Behavior of Shear Wall Boundary Elements Incorporating Prefabricated Welded Wire Hoops," *Research Report, Earthquake Engineering Research Center, College of Engineering, university of California*, Berkeley, Jan. 1990, pp. 66.

76. Mitchel, D., Adams, J., DeVall, R., Lo, R., and Weichert, D., "Lessons from the 1985 Mexican Earthquake," *Canadian Journal of Civil Engineering*, Vol. 13, No. 5, Oct. 1986, pp. 535 – 557.

77. Moehle, J.P,. and Cavanagh, T, "Confinement Effectiveness of Cross-ties in RC," *Journal of Structural Engineering., ASCE*, 1985, 111 (10), pp. 2105 - 2119.

78. Montgomery, J.C., 1981. "Influence of P-Delta Effects on Seismic Design," *Canadian Journal of Civil Engineering.*, 8,1981, pp. 31-43.

79. Monti, G., and Nuti, C., "Nonlinear Cyclic Behavior of Reinforcing Bars Including Buckling", *Journal of Structural Engineering, ASCE*, 1992, 118(12), pp. 3268 - 3279.

80. Muguruma, H., Nishiyama, M., Watanabe, F., and Tanaka, H., "Ductile Behavior of High Strength Concrete Columns Confined by High Strength Transverse Reinforcement," *ACI International conference on Evaluation and Rehabilitation of Concrete Structures and Innovations in Design*, SP-128-54, Vol. 2, Hong Kong, Dec. 1991, pp. 877 - 891.

81. Muguruma, H., Watanabe, F., and Komuro, T., "Ductility Improvement of High Strength Concrete Columns with Lateral Confinement," *High Strength Concrete, Second International Symposium*, ACI SP-121-4, Detroit, 1990, pp. 47 – 60.

82. Muguruma, H., Watanabe, F., Iwashimizu, T., and Mitsueda, R., "Ductility Improvement of High-Strength Concrete by Lateral Confinement," *Transactions of the Japan Concrete Institute*, Vol. 5, 1983, pp. 403 - 410.

83. Nagasaki T, Fukuyama H., and Tanigaki M., "Shear Performance of Concrete Beams Reinforced with FRP Stirrups," 1993, *ACI, SP-138-47*, pp. 789-811.

84. Nagashima, T. Sugano, S., Kimura, H., Ichikawa, A., "Monotonic Axial Compression Test on Ultra-High-Strength Concrete Tied columns," *Proceedings of 10th World Conference on Earthquake engineering*, Madrid, 1992, pp. 2983 - 2988.

85. Nanni, A., Norris, M.S., and Bradford, N.M. "Lateral Confinement of Concrete Using FRP Reinforcement," *ACI, SP-138-13*, 1993, pp. 193 - 209.

86. Neville, A.M., "Properties of Concrete," Fourth and Final Edition, Longman Group Limited, England, 1995, pp. 844.

87. Neville, Adam M., "Aggregate Bond and Modulus of Elasticity of Concrete," ACI Material Journal, Vol. 94, No. 1, Jan. – Feb. 1997, pp. 71 – 74.

88. Ooya, H., Kato, D., " Experimental Study on Buckling Behavior of Intermediate Longitudinal Bars in R/C Members," *Transactions of the Japan Concrete Institute*, 1994, Vol. 16, 365-372.

89. Otter, D., and Naaman, O., "Model for Response of Concrete to Random Compressive Loads," *Journal of Structural Engineering*, ASCE, November, 1989, pp. 2794 – 2809.

90. Ozawa, K., Sekijima, K., and Okamura, H., "Flexural Fatigue Behavior of Concrete Beams With FRP Reinforcement," *Transactions of the Japan Concrete Institute*, 1987, Vol. 9, pp. 289 - 296.

91. Ozcebe, G., and Saatcioglu, M., "Confinement of Concrete Columns for Seismic Loading," *ACI Structural Journal*, Vol. 84, No.4, 1987, pp. 308 – 315.

92. Ozden, S., "Behaviour of High-Strength Concrete Under Strain Gradient," *M.A. Sc. Thesis, Department of Civil Engineering, University of Toronto*, Toronto, Aug. 1992, pp. 165.

93. Pantazopoulou, S.J., "Detailing for Reinforcement Stability in RC Members," *Journal of Structural Engineering., ASCE*, 1998, 124(6), pp. 623 - 632.

94. Pantazopoulou, S.J., "Role of Expansion on Mechanical Behavior of Concrete," *Journal of Structural Engineering., ASCE*, 1995, 121(12), pp. 1795 - 1805.

95. Papia, M., and Russo, G., "Compressive Concrete Strain at Buckling of Longitudinal Reinforcement," *Journal of Structural Engineering., ASCE*, 1989, 115(2), pp. 382 - 383.

96. Papia, M., Russo, G., and Zingone, G., "Instability of Longitudinal Bars in R/C Columns," *Journal of Structural Engineering., ASCE*, 1988, 114(2), pp. 445 - 461.

97. Park, R., and Paulay, T., "Reinforced Concrete Structures," John Wiley and Sons, 1975, pp. 769.

98. Paulay, T. and Priestly M.J.N., "Seismic Design of Reinforced Concrete and Masonry Buildings", *John Wiley & Sons Inc.*, 1992, pp. 744.

99. Paulay, T., "A Critique of the Special Provisions for Seismic Design of the Building Code Requirements for Reinforced Concrete (ACI 318-83)," *ACI Journal*, Mar. - Apr. 1986, pp. 274 - 283.

100. Paulay, T., "Development in the Seismic Design of Reinforced Concrete Frames in New Zealand," *Canadian Journal of Civil Engineering*, Aug. 1981, pp. 91 - 113.

101. Paulay, T., "Earthquake-Resisting Shear Walls - New Zealand Design Trends," *ACI Journal*, May-June 1980, pp. 144 - 180.

102. Paulay, T., "Lapped Splices in Earthquake-Resisting Columns," *ACI Journal*, Nov. - Dec., 1982, pp. 458-469.

103. Paultre, P., and Cusson, D., "Stress-Strain Model for Confined High-Strength Concrete," *Journal of Structural Engineering, ASCE*, 1995, 121 (3), pp. 468 - 477.

104. Pfister, J.F., "Influence of Ties on the Behaviour of Reinforced Concrete Columns," *ACI Journal, Proceedings*, Vol. 61, No. 5, May 1964, pp. 521 – 536.

105. Polat, M.B., "Behavior of Normal and High Strength Concrete Under Axial Compression," *M.A.Sc. thesis, Department of Civil Engineering, University of Toronto*, Ontario Canada, 1992, pp. 175.

106. Popovics, S., "Analytical Approach to Complete Stress-Strain Curves," *Cement and Concrete Research*, Vol. 3, No. 5, Sept. 1973, pp. 583 - 599.

107. Priestley, J.N., and Benzoni, G., "Seismic Performance of Circular Columns with Low Longitudinal Reinforcement Ratios," *ACI Structural Journal.*, July – Aug. 1996, pp. 474 - 485.

108. Priestly, M.J.N., Sieble, S., and Calvi, G.M., "Seismic Design and Retrofit of Bridges," *Jhon Wiley & Sons Inc.*, 1996, pp.686.

109. Rahman, A.H., Taylor, D.A., "Deflections of FRP-Reinforced Slabs-A finite Element Study," *Proceedings of the first International Conference on Advanced Composite Materials in Bridges and Structures*, Sherbrooke, 1992, pp. 607 - 616.

110. Rahman, A.H., Taylor, D.A., and Kingley, C.Y., 1993. "Evaluation of FRP as Reinforcement for Concrete Bridges," *ACI, SP-138*-47, pp. 71-86.

111. Rangan, B.V., Sauders, P., and Seng, E.J., "Design of High Strength Concrete Columns", *Evaluation and Rehabilitation of Concrete Structures and Innovations in Design, ACI SP 128-52*, 1991, pp. 851-862.

112. Rangan, B.V., Sauders, P., and Seng, E.J., "Design of High Strength Concrete Columns," *Evaluation and Rehabilitation of Concrete Structures and Innovations in Design*, ACI SP 128-52, 1991, pp. 851-862.

113. Raphael, J.M., "Tensile Strength of Concrete," *ACI Journal, Proceedings*, Vol. 81, No. 2, March - April 1984, pp. 158 - 165.

114. Razvi, S., "Behavior of Confined Concrete Columns Confined with Welded Wire Fabric," *M.A.Sc. thesis, Department of Civil Engineering, University of Ottawa*, Ottawa, Ontario, Canada, 1988, pp. 152.

115. Razvi, S., "Behavior of Reinforced Concrete Columns Confined With Welded Wire Fabric and/or Rectilinear Ties," *Research Report No. 8902, Department of Civil Engineering, University of Ottawa, Ottawa*, Ontario, Canada, Dec. 1989, pp. 65.

116. Razvi, S., "Confinement of Normal and High-Strength Concrete Columns," *Ph.D. thesis, Department of Civil Engineering, University of Ottawa*, Ottawa, Ontario, Canada, May 1995, pp. 415.

117. Razvi, S., and Saatcioglu, M., "Discussion of Deformation Properties and Ductility of High-Strength Concrete," *ACI Material Journal*, Vol. 88, No. 6, 1991, pp. 674 - 675.

118. Razvi, S.R., and Saatcioglu, M., "Design of R/C Columns for Confinement Based on Lateral Drift," *Research Report OCEERC 96-02, Ottawa Carleton Earthquake*

Engineering Research Center, Department of Civil Engineering, University of Ottawa, Ottawa, Ontario, Canada, Feb. 1996, pp. 92.

119. Razvi, S.R., and Saatcioglu, M., "Strength and Deformability of Confined High-Strength Concrete Columns," *ACI Structural Journal*, Nov. - Dec. 1994, pp.???

120. Razvi, S.R., and Saatcioglu, M., 1996. "Tests of High-Strength Concrete Columns Under Concentric Loading," *Research Report OCEERC 96-03, Ottawa Carleton Earthquake Engineering Research Center, Department of Civil Engineering, University of Ottawa*, Ottawa, Ontario, March 1996, pp. 147.

121. Richart, F.E., Brandtzaeg, A., and Brown, R.L., "A Study of the Failure of Concrete Under Combined Compressive Stresses," *Bulletin No. 185, University of Illinois Engineering*, Experimental Station, Urbana, Ill., 1928.

122. Richart, F.E., Brandtzaeg, A., and Brown, R.L., "The Failure of Plain and Spirally Reinforced Concrete in Compression," *Bulletin No. 190, University of Illinois Engineering, Experimental Station*, Urbana, Ill., 1929.

123. Roy, H.E.H. and Sozen, M.A., "Ductility of Concrete," *Proceedings of the International Symposium on the Flexural Mechanics of Reinforced Concrete, ASCE-ACI*, Miami, Nov. 1964, pp. 213 – 224.

124. Rubinsky, I.A., and Rubinsky, A., "An Investigation into the use of Fiber-Glass for Prestressed Concrete," *Magazine of Concrete research*, 1954, V.6

125. Saatcioglu, M., "Deformability of Reinforced Concrete Columns," *Earthquake Resistant Concrete Structures - Inelastic Response and Design, American Concrete Institute*, 1991, SP 127 -10, pp. 421- 452.

126. Saatcioglu, M., Alsiwat, J., and Ozcebe, G., "Hysteretic Behavior of Anchorage Slip in R/C Members," *Journal of Structural Engineering., ASCE*, 1992, 118(9), pp. 2439 - 2458.

127. Saatcioglu, M., and Alsiwat, J., "Reinforcement Anchorage Slip Under Monotonic Loading," *Journal of Structural Engineering., ASCE*, 1992, 118(9), pp. 2421 - 2438.

128. Saatcioglu, M., and Grira, M., "Concrete Confined with Welded Reinforcement Grids", *ACI Structural Journal*, under press.

129. Saatcioglu, M., and Ozcebe, G., "Response of Reinforced Concrete Columns to Simulated Seismic Loading," *ACI Structural Journal*, Jan.- Feb. 1989, pp. 3 - 12.

130. Saatcioglu, M., and Razvi, S., "Strength and Ductility of Confined Concrete," Journal of Structural Engineering, ASCE, 1992, 118(6), pp. 1590 - 1607.

131. Saatcioglu, M., Salamat, A.H., and Razvi, S.R., "Confined Columns Under Eccentric Loading," *Journal of Structural Engineering., ASCE*, 1995, 121 (11), pp. 1547 - 1556.

132. Sakai, K., and Kakuta, Y., "Moment-Curvature Relationships of Reinforced Concrete Members Subjected to Combined Bending and Axial Force," *ACI Journal*, May - June 1980, pp. 189 - 194.

133. Sakai, Y., Hibi, J., Otani, S., and Aoyama, H., "Experimental Study of Flexural Behavior of Reinforced Concrete Columns Using High Strength Concrete," *Transaction of the Japan Concrete Inst.*, Vol. 12, 1990, pp 323 – 330.

134. Samra, R.M., and Deeb, N.A.A., and Madi, U.R., "Transverse Steel Content in Spiral Concrete Columns Subjected to Eccentric Loading," *ACI Structural Journal*, July – Aug. 1996, pp. 412 - 419.

135. Sargin, M., "Stress-Strain Relationships for Concrete and the Analysis of Structural Concrete Sections," *Study No. 4, Solid Mechanics Division, University of Waterloo*, 1971, pp. 167.

136. Schmeckpeper, E., "Performance of Concrete Beams and Slabs Reinforced with FRP Grids," *Ph.D. thesis, University of New Hampshire*, USA, 1992.

137. Scott, B.D., Park, R., and Priestley, J.N. "Stress-Strain Behavior of Concrete Confined by Overlapping Hoops at Low and High Strain Rates," *ACI Journal*, Jan. - Feb. 1982, pp. 13 - 27.

138. Scribner, C.F., "Reinforcement Buckling in Reinforced Concrete Flexural Members," *ACI Journal*, Nov. - Dec. 1986, pp. 966 - 973.

139. Seible, F., and Karbhari, V., "Advance Composites Build on Success," *Civil Engineering*, Aug. 1996, pp. 44 - 47.

140. Seible, F., Priestley, J.N., Kingsley, G.R., and Kurkchubashe, A.G, "Seismic Response of Full-Scale Five-Story Reinforced-Masonry Building," *Journal of Structural* Engineering, ASCE 1994, 120(3), pp. 925 - 946.

141. Sekijima, K., Ikeda, K., Nakura, K., and Sekine, K., "Application of FRP Grid Reinforcement for Concrete Supports in Tunnel," *Transactions of the Japan Concrete Institute*, Vol. 10, 1988, pp. 29 - 34.

142. Setty, B.R.H., and Rangan, B.V., "Strength of High Strength Concrete Columns Under Eccentric Compression", *Research Report No. 2/95 Aug. 1995, School of Civil Engineering, Curtin University of Technology, Perth*, Western Australia, pp. 102.

143. Shah, S.P. and Rangan, B.V., "Effects of Reinforcements on Ductility of Concrete", *Journal of the Structural Division, ASCE*, Vol. 96, No. ST6, June 1970, pp. 1167 – 1184.

144. Shah, S.P., and Ahmad, S.H., " Stress-Strain Curves of Concrete Confined by Spiral Reinforcement", *ACI Journal*, Nov. - Dec. 1982, pp. 484 - 490.

145. Sheikh, S.A. "A Comparative Study of Confinement Models," *ACI Journal*, Jul. - Aug. 1982, pp. 296 - 306.

146. Sheikh, S.A., and Khoury, S.S., "Confined Concrete Columns with Stub," *ACI Structural Journal*, Vol. 90, No. 4, 1993, pp. 414 – 431.

147. Sheikh, S.A., and Uzumeri, S.M., " Strength and ductility of tied concrete columns," *ASCE Structural Division*, Vol. 106, No. ST5, May 1980, pp. 1079 - 1102.

148. Sheikh, S.A., and Uzumeri, S.M., "Analytical Model for Concrete Confinement in Tied Columns," *Journal of Structural Division*, ASCE 1982, 108 (ST12), pp. 2703 – 2722.

149. Sheikh, S.A., and Yeh, C.C., "Flexural Behavior of Confined Concrete Columns," *ACI Journal*, May-June 1986, pp. 389 - 404.

150. Sheikh, S.A., Shah, D.V., and Khoury, S.S., "Confinement of High-Strength Concrete Columns," *ACI Structural Journal*, Jan. - Feb. 1994, pp. 100 - 111.

151. Sheikh, S.A., Yeh, C.C., and Menzies, D., "Confined Concrete Columns," *Pacific Conference on Earthquake Engineering, Wairakei, New Zealand,* Aug. 27, 1986, Vol. 1, pp. 177-188.

152. Soliman, M.T.M., Yu, C.W., "The Flexural Stress-Strain Relationship of Concrete Confined by Rectangular Transverse Reinforcement," Magazine of Concrete Research, Vol. 19, No. 61, Dec. 1967, pp. 223 - 238.

153. Soroushian, P. and Sim, J., "Axial Behavior of Reinforced Concrete Columns Under Dynamic Loads," ACI Journal, Nov. -Dec. 1986, pp. 1018 - 1025.

154. Stockl, S., Discussion of "Ductility of Concrete," by Roy, H.E., and Sozen, M.A., Proceedings of the International Symposium on the Flexural Mechanics of Reinforced Concrete, ASCE-ACI, Miami, Nov. 1964, pp. 225 – 227.

155. Sturman, G.M., Shah, S.P. and Winter, G., "Effects of Flexural Strain Gradients on Microcracking and Stress-Strain Behavior of Concrete", journal of the American Concrete Institute, Vol. 62, No. 7, July 1965, pp. 805 – 822.

156. Suda, K., Murayama, Y., Ichinomiya, T., and Shinbo, H., "Buckling Behavior of Longitudinal Reinforcement Bars in Concrete Column Subjected to Reverse Lateral Loading," 11th World Conference on Earthquake Engineering, 1996, Paper No. 1753.

157. Sugano, S., Nagashima, T., Kimura, H., Tamura, A., and Ichikawa, A., "Experimental Studies on Seismic Behavior of Reinforced Concrete Members of High Strength Concrete," High Strength Concrete, second International Symposium, ACI SP-121-5, Detroit, 1990, pp. 61 – 87.

158. Szulcynski, T., and Sozen, M.A., "Load-Deformation Characteristics of reinforced Concrete Prisms with Rectilinear Transverse Reinforcement," Structural Research Series No. 224, Civil Engineering Studies, University of Illinois, Urbana, Set. 1961, 54 pp.

159. Timoshenko, S.P., and Gere, J.M., "Theory of Elastic Stability," 2nd Ed., McGraw-Hill Book Company, Inc., New York, 1961, pp. 541.

160. Tsai, W.T., "Unixail Compressional Stress-Strain Relation of Concrete," Journal of Structural Engineering, Vol. 114, No. 9, Sept. 1988, pp. 2133-2136.

161. Vallenas, J., Bertero, V.V., and Popov, E.P., (1977), Concrete Confined by Rectangular Hoops Subjected to Axial Loads, University of California, Berkeley, Report No. UBC/EERC-77/13, August 1977.

162. Wang, P.T., Shah, S.P., and Naaman, A.E., "Stress-Strain Curves of Normal and Lightweight Concrete in Compression", ACI journal, November 1975, pp. 603 - 611.

163. Watanabe, F., Muguruma, H., Tanaka, H., and Katsuda, S., "Improving the Flexural Ductility of Prestressed Concrete Beam by Using the High Yield Strength Lateral Hoop Reinforcement," Symposia on Partial Prestressing and Practical Construction in Prestressed and Reinforced Concrete, proceedings: Part 2, Sept. 1980, Bucuresti-Romania, pp. 398 – 406.

164. Wee, T.H., Chin, M.S., and Mansour, M.A., "Stress-Strain Relationship of High-Strength Concrete in Compression," Journal of Material in Civil Engineering, ASCE, 1996, 8 (2), pp. 70 - 76.

165. Woodward, K.A., and Jirsa, J.J., "Influence of Reinforcement on RC Short Column Lateral Resistance," Journal of Structural Engineering, ASCE, 1994, 110 (1), pp. 90 - 104.

166. Yalcin, C., "Seismic Evaluation and Retrofit of Existing Reinforced Concrete Bridge Columns," Ph.D. thesis, Civil Engineering Department, University of Ottawa, Ontario, Canada, 1997, pp. 306.

167. Yong, Y.K., Nour, M.G., and Nawy, E.G., "Behavior of Laterally Confined High-Strength Concrete Under Axial Loads," Journal of Structural Engineering, ASCE, 1988, 114 (2), pp. 332 - 351.

168. Zahn, F.A., Park, R., and Priestly, M.J.N.,"Flexural Strength and Ductility of Circular Hollow Reinforced Concrete Columns without Confinemet on Inside Face," ACI Structural Journal, Vol. 87, No.2, April 1990, pp. 156 - 166.